VYSOKÉ UČENÍ TECHNICKÉ V BRNĚ

Fakulta elektrotechniky a komunikačních technologií

Habilitační práce

Brno, 2020

Ing. et Ing. Vilém Neděla, Ph.D.

VYSOKÉ UČENÍ TECHNICKÉ V BRNĚ
BRNO UNIVERSITY OF TECHNOLOGY

FAKULTA ELEKTROTECHNIKY A KOMUNIKAČNÍCH TECHNOLOGIÍ
FACULTY OF ELECTRICAL ENGINEERING AND COMMUNICATION

ÚSTAV ELEKTROTECHNOLOGIE
DEPARTMENT OF ELECTRICAL AND ELECTRONIC TECHNOLOGY

ADVANCED ENVIRONMENTAL SCANNING ELECTRON MICROSCOPY FOR STUDY OF SUSCEPTIBLE SAMPLES IN THEIR NATIVE STATE AND UNDER DYNAMICALLY CHANGING CONDITIONS.

HABILITAČNÍ PRÁCE
HABILITATION THESIS

AUTOR PRÁCE
AUTHOR

Ing. et. Ing. Vilém Neděla, Ph.D.

BRNO, 2020

Abstrakt

Habilitační práce dokumentuje vědecké výsledky autora dosažené v oblasti Environmetální rastrovací elektronové mikroskopie za posledních dvacet let. Úvodní část práce obsahuje komentovaný přehled těchto výsledků v kontextu mezinárodního výzkumu a definuje přínos autora pro rozvoj vědního oboru. Současně popisuje klíčové výhody a nevýhody výše uvedené metody a dále se zaměřuje na výzvy pro současný a budoucí rozvoj tzv. pokročilé environmentální rastrovací elektronové mikroskopie. Ta umožní zobrazovat povrchy velmi citlivých, často vlhkých biologických nebo polymerních vzorků v nativním stavu bez poškození. Vzorky budou studovány ve statických nebo dynamicky se měnících podmínkách, nebo při působení různých fyzikálních či chemických vlivů. Pro zobrazování povrchů s velkým rozlišením a hloubkou ostrosti budou použity velmi nízké proudy a energie elektronového svazku minimalizující radiační poškození vzorků. Systematický vývoj pokročilé environmentální rastrovací elektronové mikroskopie od prototypu elektronového mikroskopu AQUASEM II až po současný, modifikovaný mikroskop QUANTA 650 FEG včetně výsledků použití této metody v různých vědních oborech popisuje druhá část práce, tvořená souborem vybraných vědeckých článků.

Klíčová slova

Environmnetální rastrovací elektronová mikroskopie, detekční systémy, matematicko-fyzikální simulace, dynamické in-situ experimenty, citlivé vzorky.

Abstract

The habilitation thesis presents the scientific results of the author in the field of Environmental Scanning Electron Microscopy in the last twenty years. The first part provides a commented overview of the international research results and defines the author's contribution to the development within the scientific field. It also describes the key advantages and disadvantages of the above-mentioned method and focuses on the challenges of current and future development of so-called Advanced Environmental Scanning Electron Microscopy. This should allow surfaces of very sensitive, often wet biological or polymeric samples to be imaged in their native state without damage. Samples will be studied under static or dynamic conditions or under various physical and chemical influences. Very low currents and electron beam energy minimizing radiation damage to the samples will be used for imaging of high resolution and depth of field observation of surfaces. The second part describes the systematic development of advanced environmental scanning electron microscopy from the prototype of the AQUASEM II electron microscope to the current modified QUANTA 650 FEG microscope, including the results of application of this method in various scientific fields.

Keywords

Environmental scanning electron microscopy, detection systems, mathematical and physical simulations, dynamical in-situ experiments, susceptible samples.

Prohlášení

Prohlašuji, že jsem svou habilitační práci na téma „Advanced environmental scanning electron microscopy for study of susceptible samples in their native state and under dynamically changing conditions“ vypracoval samostatně a s použitím literatury, kterou jsem uvedl v seznamu literatury.

V Brně, dne 23.04.2020 ……

Ing. et. Ing. Vilém Neděla, Ph.D.

Poděkování

Chtěl bych především poděkovat mým kolegům, členům vědecké skupiny Environmentální elektronová mikroskopie ÚPT AVČR, v.v.i v Brně za spolupráci a pomoc v oblasti výzkumu a vývoje Environmentální rastrovací elektronové mikroskopie a také spoluautorům mých vědeckých článků, které prezentují možnosti a využití této metody napříč vědními obory.

Vilém Neděla

Acknowledgment

I would particularly like to thank my colleagues, members of the scientific group Environmental Electron Microscopy of ISI ASCR in Brno for cooperation and assistance in the field of research and development of the Environmental Scanning Electron Microscopy and also co-authors of my scientific articles presenting the possibilities and applications of this method across scientific fields.

Vilém Neděla

Obsah

1 Úvod

Environmentální rastrovací elektronová mikroskopie je jedním z novějších vývojových stádií rastrovací elektronové mikroskopie, a proto jedna z elektronově mikroskopických metod. Z instrumentálního hlediska představuje environmentální rastrovací elektronový mikroskop (EREM) nadstavbu/rozšíření klasického rastrovacího elektronového mikroskopu (REM) a to zejména o systém diferenciálně čerpaných komor, speciální detektory, systémy pro regulaci tlaku plynu v komoře vzorku, systémy pro chlazení vzorku a hydratační systémy. EREM ve svých volitelných pracovních režimech/modech umožňuje práci v podmínkách relativně vysokého tlaku různých plynů v komoře vzorku (obvykle od 10 Pa do 2700 Pa), ovšem také v podmínkách tlaku blížícímu se vakuu tak, jako klasický REM. EREM proto nabízí veškeré výhody klasického REM a současně další výhody i nevýhody spojené s přítomností vyššího tlaku plynů v komoře vzorku. Výhodou EREM pracujícího v podmínkách vyššího tlaku plynů je možnost pozorovat přirozeně vlhké vzorky bez jejich poškození dehydratací v podmínkách termodynamické rovnováhy, elektricky izolační vzorky nebo polovodiče bez nutnosti zvodivění jejich povrchu, ale také v podmínkách vyšších energií a proudů svazku analyzovat prvkové složení nenabíjejících se elektricky izolačních vzorků pomocí energiově disperzního X-Ray analyzátoru. Další výhodou je možnost detekovat, v optimálních podmínkách tlaku vodních par a intenzity elektrického pole detektoru až 1000x zesílený signál převážně sekundárních elektronů. Hlavní výhodou EREM je však možnost přímého pozorování vzorků v dynamicky se měnících podmínkách a studium jejich změn při působení různých fyzikálních či chemických vlivů v komoře vzorku EREM. Hlavní nevýhodou EREM je nižší rozlišení než v REM, komplikovanější a těžko automatizovatelné ovládání mikroskopu a při pozorování vlhkých vzorků v nativním stavu nebo realizaci dynamických in-situ experimentů možná vyšší kontaminace mikroskopu. EREM má také v důsledku přítomnosti tlak omezující clony omezené zorné pole, což může komplikovat orientaci na vzorku. Reálný proces pozorování vzorků v podmínkách vysokého tlaku a relativní vlhkosti plynů v komoře vzorku EREM je velmi odlišný od REM. Zásadně jiná je metodika pro studium vlhkých vzorků, které jsou-li v nativním stavu, jsou extrémně citlivé na radiační poškození i podmínky, v nichž jsou pozorovány. Specifická je i práce s detektory pracujícími na principu nárazové ionizace plynů. Oproti ovládání klasického REM je navíc nutné regulovat tlak plynu, teplotu vzorku a výsledně i jeho relativní vlhkost, a to často v dynamicky se měnících podmínkách. Vzhledem k výše uvedeným specifikům, a to i přes relativně velký počet instalovaných EREM ve světě, existuje jen velmi málo vědeckých laboratoří, které

dokáží potenciál EREM plně využít. V současné době je většina těchto laboratoří čistě aplikačních a vývojem EREM se pro jeho náročnost, nákladnost a absenci know-how téměř nikdo nezabývá. V tomto ohledu a také vzhledem k více než třicetileté tradici výzkumu a vývoje zaměřeného na EREM a detekční systémy je laboratoř Environmentální elektronové mikroskopie ÚPT AVČR v Brně světovým unikátem.

2 Introduction

The environmental scanning electron microscopy is one of the newer developmental stages of scanning electron microscopy and therefore one of the electron microscopic methods. From an instrumental point of view, the Environmental Scanning Electron Microscope (ESEM) is an extended version of the conventional scanning electron microscope (SEM) additionally equipped with a system of differential pumping chambers, special detectors, gas chamber pressure control systems, sample cooling and hydration systems. In its selectable operating modes, ESEM allows operation under relatively high pressure conditions of various gases in the specimen chamber (usually from 10 Pa to 2700 Pa of water vapours), but also under near-vacuum conditions like conventional SEM. ESEM therefore offers all the advantages of conventional SEM and at the same time other advantages and disadvantages associated with the presence of higher gas pressure in the specimen chamber. The advantage of ESEM operating under higher gas pressure conditions is the possibility to observe naturally wet samples under the conditions of thermodynamic equilibrium without damaging them by dehydration, electrically insulating samples or semiconductors without the need to conduct their surface and also the possibility to analyse samples under conditions of higher energies and beam currents using an energy-dispersive X-Ray analyser. Another advantage is the possibility to detect (under optimal conditions of water vapor pressure and electric field intensity of the ionisation detector) up to 1000x amplified signal of mostly secondary electrons. However, the main advantage of ESEM is the possibility of direct observation of samples under dynamically changing conditions and study of their changes under various physical or chemical influences in the specimen chamber of ESEM. The main disadvantage of ESEM is lower resolution than SEM, difficult-to-automate microscope control and possibly higher contamination of the microscope when observing wet samples in native state or performing dynamic in-situ experiments. ESEM also has a limited field of view due to the presence of a pressure limiting aperture, which may complicate the orientation on the sample. The actual process of observation of samples under conditions of high pressure and relative humidity of gases in the ESEM specimen chamber differs greatly from that of SEM. The methodology of studying wet samples that are extremely sensitive to radiation damage and the conditions under which they are observed is fundamentally different. The work with detectors working on the principle of impact ionization of gases is also specific. In addition to operating SEM, it is also necessary to regulate gas pressure, sample temperature and, consequently, its relative humidity, often under dynamically changing

conditions. Given the specificities mentioned above and despite the relatively large number of ESEMs installed worldwide, there are very few scientific laboratories that can fully exploit the potential of ESEM. At present, most of these laboratories are purely application-oriented and almost no one is involved in the development of ESEM due to its demandingness, cost and lack of know-how. With regard to more than thirty years of tradition in research and development focussed on ESEM and detection systems, the Laboratory of Environmental Electron Microscopy of the ISI ASCR in Brno is a unique one in the world.

3 Author's scientific contribution in field of environmental scanning electron microscopy

The ability to observe three-dimensional-like structures of heterogeneous organic and inorganic materials from a few hundred picometres to millimeters and the possibility of their characterization makes a scanning electron microscope (SEM) a well-established and widely used instrument within branches of science (Goldstein et al. 2017). Primary electrons are emitted from the electron source, accelerated to energy from hundreds of eV to tens of keV and focused by electrostatic or magnetic lenses to a final spot size from tenths to tens of nm in diameter. Beam electrons which are scanned over the sample surface undergo many inelastic and elastic collisions and generate several types of signals. Sample surface topography/morphology, material/Z, voltage, magnetic or crystallographic contrasts, as well as other types of information, are gained by detection of signal electrons. Detection of ultraviolet, visible or infrared light is used for cathodoluminescence characterisation of samples, while chemical/elemental analysis is obtained by detection of characteristic X-rays, (Reimer 1998). Utke et al. (2012) showed that SEMs equipped with a focused ion beam and gas injectors allow precise 3D machining or electron beam induced deposition of new structures. Advanced sample chemical analysis can be made by a combination of the SEM with Raman spectroscopy (Wille et al. 2014) or cyclic voltammetry (Jensen et al. 2013).

While the conventional SEM allows the study of samples in vacuum-close conditions (better then 10-3 Pa) only, an environmental scanning electron microscope (ESEM) (working principle was first introduced by Lane (1970) and Robinson (1975) and later described in detail by Danilatos 1988) also enables the sample observation in various gaseous environments with the pressure ranges from tens to thousands of Pa. The sizeable gas pressure difference (six or more orders) between the ESEM specimen chamber (from tens to thousands of Pa) and the area of the electron source (from 10-3 to 10-9 Pa, depending on the type of electron source) can be maintained through a sophisticated system of differentially pumped chambers separated by gas pressure limiting apertures (Danilatos et al 1979). This system is most often integrated into the bottom part of the microscope column, as in the case of our microscope QUANTA 650 FEG or situated just below the objective of the ESEM as in the case of our microscope AQUASEM II (Neděla 2007). The pressure limiting apertures are referred to as PLA1 to PLAX in sequence from the sample, and their diameter is chosen as a compromise between the ability

to limit gas flow from sample to column of the microscope as much as possible and ESEM field of view. The largest, final aperture PLA 1 most often has a diameter of 500 μm and according to the pivot point position of a particular microscope and working distance of the sample allows to achieve a minimum magnification from 500 times to 800 times, while a minimum magnification in the case of SEM is less than 100 times.

The advantages of ESEM (Danilatos 1988) are in the possibility of a direct observation of electrically non-conductive samples without charging artefacts (Danilatos 1991), fully hydrated wet samples (Cameron et al. 1994, Royall et al. 2002), plants (Danilatos 1981; Stabentheiner et al. 2010; Popielarska-Konieczna et al. 2010; Vlašínová et al. 2017) or microgel particles (Garcia-Salinas et al. 2010) and realization of „in situ“ dynamical experiments (Danilatos 1982; Huggett et al. 1994). The principal disadvantage of ESEM is the scattering of the primary electron (PE) beam in the gaseous environment (Wight et al 2000). Danilatos (1983) claimed that the image resolution at a high pressure can be comparable with that of the resolution in conventional SEM. However, the “skirting effect” causes a decrease in the probe current in the focused spot so that the signal to noise ratio (SNR) in detected signal is lowered.

This problem can be mitigated by decreasing the distance in the gaseous environment which PEs pass through, increasing the PE energy and the probe current, using a lower scanning speed and choosing a suitable gas type and its pressure (Gauvin 2005, Le Berre et al. 2007). In such cases there is a necessity to improve the detection efficiency of the useful signal and minimise the “skirting effect”. On the basis of the mentioned solutions the gas scattering phenomena are studied (Mansour et al. 2013, Neděla et al. 2020) and computed results are utilized for optimizations of the ESEM resulting in increasing the detection efficiency and minimizing the “skirting effect” (Neděla et al. 2018).

So far, the most efficient secondary electron (SE) detector for ESEM is based on the principle of gas ionisation (Danilatos 2013). It uses an amplification through an ionization cascade between a grounded specimen holder and a positively biased signal electrode placed under the pole piece of the objective lens (Danilatos 1992, 1994, 2000; Thiel et al. 2003, Neděla 2010a; Neděla et al. 2010b). The amplification of the SEs depends mainly on the intensity of the electrostatic field between the detection electrode and the grounded sample holder as well as on the pressure and the type of gas (Meredith et al. 1996; Thiel et al 2003; Fletcher et al. 1997; Neděla et al. 2011a,b).

Our team has examined several methods and detectors for the detection of the signal electrons in SEM and ESEM. Autrata et al. (1992, 1997) designed a very sensitive backscattered electrons (BSE) detector using the original YAG (yttrium aluminium garnet) and YAP (yttrium aluminium perovskite) scintillators for the study of the material/Z contrast. This scintillator photomultiplier detector is commonly used in SEMs and also in the Hitachi VP-SEM. The YAG scintillator with a small opening in its centre was used as the PLA1 in our prototype of ESEM AQUASEM II (Neděla 2007, 2010) for studying wet biological samples (Neděla et al. 2013). The YAG BSE detector has been adapted for topographical SE contrast detection by gas ionization, and finally designed as the so called combined detector (Romanovský et al. 1999, 2000). For topographical contrast observation, the combined detector was equipped with a thin electrode deposited on the bottom of the YAG. If the electrode is positively biased (Autrata et al. 2003), this detector works similarly to the Environmental Secondary Detector (ESD) (Danilatos 1988).

Suitable methods for suppressing the BSE background in the detected signal by the ionisation detector have been also investigated by our team (Neděla et al 2006). Similarly, to Danilatos´ concept ESD, multiple circular electrodes are used for detection in the ionisation detector (Neděla 2010a; Neděla et al. 2010b; Neděla et al. 2011a, b).

Ground-breaking innovation in the field of research and development of detection systems for ESEM represents a new Combined System for high-efficiency detection of Secondary and Backscattered Electrons (CSSBE) (Neděla et al. 2018). The CSSBE consists of three combined detectors allowing very high efficiency detection of secondary and backscattered electrons (surface topography and material contrasts) at the same time under very low-dose conditions in ESEM. One of these detectors is the Ionisation Secondary Electron Detector with the electrostatic Separator (ISEDS) (Neděla et al. 2006). This detector allows recording a strongly amplified signal of SEs with a minimal influence of the BSEs and, as the world's first detector, allows an energy separated detection of signal electrons for the gas pressure from 50 Pa to 300 Pa (Neděla et al. 2010b). The outstanding efficiency of the ISEDS allows imaging of susceptible samples with low emissivity of signal electrons (biological samples, latex particles) under low beam energy 5 keV, up-to-date lowest beam current of 0.2 pA, dwell time of 1.5 ms and pressure of hundreds of Pa (Neděla et al. 2018). Another detector we developed is scintillation SE detector for SEM and ESEM (Jirák et al. 2010). The main advantage of this detector is very high detection efficiency in the both SEM and ESEM modes

(gas pressure from 0.001 Pa up to 1,000 Pa) without the need to exchange the detectors (Jirák et al. 2010).

In order to understand the signal generation in a gaseous environment, the program EOD (Lencová et al. 2007), used for the design of charged particle optics devices and detectors, has been extended with a Monte Carlo (MC) module to include the collision phenomena of electrons with the gases in the specimen chamber of the ESEM (Neděla et al. 2011a).

Neděla et al. published computed dependencies of signal amplification of detected electrons with selected energies and total signal amplification by including a realistic simulation of the secondary emission from sample on the water vapor pressure in ESEM (Neděla et al. 2011b, 2015c. Results of the simulations computed using the EOD software equipped with a Monte Carlo plug-in were compared with experimental measurements and the dependencies of published analytical models. Our latest work in the field of electron optical computations focused on the design of aberration corrected objective lenses for the new generation of the ESEM (Oral et al. 2015).

Electron-gas interaction in ESEM results not only in the ionization of gas molecules and the emission of new accelerated and cascade-amplified signal electrons (Fletcher et al. 1999, Jirák et al. 2010) by the detectors' electrostatic field (Neděla et al. 2011a,b), but also in the production of positive and negative ions (Toth et al. 2002). Positive ions return to the sample surface where its negative charge is neutralized and allows the observation of electrically non-conductive samples free of a conductive layer. Ion bombardment also reduces surface contamination of samples (Rice and Knowles 2005). Decontamination processes in ESEM, as well as the possibilities to observe electrically non-conductive samples without conducive coating, allow studying specific, for SEM invisible, contrasts as was referred by Williams and Donald (2004).

If the samples can be simultaneously cooled (usually down to 10°C) and observed under the environment of water vapour (values of temperature and water vapour pressures are set according to the values of the thermodynamic equilibrium, e.g. 2°C and 705 Pa), then the samples can be observed in their fully wet state, without the need for any chemical fixation, i.e. in their native state in ESEM. The ability to precisely control the thermodynamic conditions in the vicinity of the sample opens possibilities for studying samples in dynamically changing conditions, alternatively also under the influence of various physical and chemical processes (Neděla et al 2020). Tihlaříková et al. (2013) introduced new methods for the gentle in-situ study

of live and surviving mites observed under low beam currents in ESEM. The possibility to study the morphology of the extracellular matrix covering early somatic embryos of conifers (hundred nm thin layer of biopolymer) in their native state by ESEM was shown by Neděla et al. (2015a). We also introduced new methods for additive in-situ hydration of wet samples in ESEM. This method is based on the usage of small needle connected to hydration system situated outside the ESEM specimen chamber. Alternatively, we can use a wet agar sample holder, which extends observation time of wet biological samples by additional hydration of the sample caused by water evaporating from the agar (Neděla 2007). A great contribution to the morphological characterization of surfaces of fresh plant sample was the introduction of the Low Temperature method for ESEM (LTM) (Neděla et al 2015a). This method allows the increase of resistance of plant sample to radiation damage as well as its shape fixation and stabilization without necessity to use chemicals for long-term observation in ESEM (Neděla et al 2012). The results of LTM were validated by other methods such as cryo-SEM and light microscopy (Neděla et al 2016). The LTM for ESEM was also used for the study of morphological abnormalities caused by copper and arsenic stress on the development of Norway spruce somatic embryos (Đorđević et al. 2019). Using LTM in combination with a new high-efficiency Ionisation Secondary Electron Detector with an electrostatic Separator (ISEDS) for ESEM (Neděla et al 2018), we recorded the world´s first images of unaffected fresh water rotifers in their native state, and two new species of rotifers were subsequently discovered (Michaloudi et at 2018). An extended version of the LTM (ELTM) allows in-situ preparation of close-to-native state plant samples and repetitive topographical and material analysis at a higher resolution in the vacuum conditions of SEM or in the low gas pressure conditions of ESEM (Tihlaříková et al. 2019). The ELTM was also utilized for in-situ preparation of plant samples analysed using an EDX analyzer in an ESEM with no coating or chemical fixation. We were able to quantify traces of silicon, which are not measurable in a conventional manner. We also clarified the relationship between colossal synthesis and transport into the cell wall of the trichomes and the ability to store silicon there. The original use of micromanipulators and EDX analysis in ESEM has a crucial contribution to the application of X-Ray EDS micro-analysis for plant biology (Kulich et al. 2018).

In the field of dynamical in-situ experiments, we published several articles with outstanding results. We showed morphological changes of rat tongue at changing thermodynamic conditions in the specimen chamber of ESEM equipped with a new prototype of hydration system (Neděla 2010a). We were the first ones to observe the dynamic in-situ process of sublimation of uncoated frost flowers using our

environmental SEM AQUASEM II. Based on this observation we experimentally disproved a suspected major role of frost flowers in ozone depletion events as a source of sea-salt aerosol (Yang et al. 2017). Ice contamination processes at grain boundaries in environmentally compatible conditions of a high gas pressure and a relatively high temperature in ESEM in a combination with fluorescence microscopy were studied (Krausko et al. 2014, Vetráková et al. 2019). We also reported partial vitrification of the freeze concentrated solution and the pH change during freezing of NaCl solutions. The ESEM study provided us a unique insight into the morphology of the frozen samples revealing lamellar arrangement of ice and salt (Imrichová et al. 2019). Morphological and size/shape changes of various types of bentonites and micro-pores inside the bentonite observed under various relative humidity in ESEM were published in collaboration with our partners (Sun et al. 2019a, b). The study of various preparation procedures of lime putties and their surface microstructures monitored by our ESEM was published by Navrátilová et al. (2017). The new way of lime putty preparation was introduced. The preparation consists of mechanical crash of the lime particles immediately after hydration.

One of the most important problems of the study of beam susceptible samples like polymers by electron beam is radiation damage (Grubb 1974), predominately resulting from inelastic collisions between beam electrons and the sample (Egerton et al. 2004). This causes temporary or permanent chemical and physical changes resulting in the formation of volatile products, mass loss and formation of unsaturated structures, chain scissions and cross-linking described by Kitching & Donald (1998). Sawyer and Grubb (1987) stated that the primary event leading to damage is the ionization of atoms present in the sample with the subsequent formation of molecular ions and radicals. The radiation damage is also increased by the presence of liquid water on the electron beam irradiated sample surface in ESEM (Kitching and Donald 1998, Arnoult et al. 2012). Biological samples can also be studied in a frozen state and imaged in liquid nitrogen in Cryo-SEM. Under irradiation, ice acts as a source of small, highly mobile free radicals, which provide more mechanisms for radiation damage described by Talmon (1987). Water in ESEM behaves in similar way; however, the mobility of reactive species is substantially increased due to the liquid medium, as was described by Royall et al. (2001). Owing to ionization or excitation of the water molecules during inelastic scattering events, their decay into free radicals or ions may occur (Talmon 1987). Hill and Smith (1994) reported that each inelastic scattering event produces typically six reactive species in the space of a few nm. The radial concentration profile for dominant species produced after electron beam-water interaction using

typical beam energies for ESEM was published by Royall et al. (2001). These authors also found out that the dominant reactive species is the hydroxyl radical (•OH). Annihilation of this species is suppressed due to the lower concentration of reactants. By comparing two beam energies, 5 keV and 25 keV, Royall et al. (2001) found a drastic increase in the quantities of reactive species produced by beam energy. Resent results of our group focused on low-dose morphological characterization of extremely beam and environmentally susceptible polyelectrolyte complex particles containing live E. coli cells under lowered radiation damage were published by Neděla et al (2020). We showed that application of lower beam energy enhances electron energy loss and beam scattering in the ESEM, hence the final interaction volume in the sample is smaller. Consequently, the number of free radicals decreases, but their concentration increases, and so the probability of recombination increases. The decrease of beam energy also causes an increase of the emission coefficient of secondary electrons from the sample; however, in the case of a 500 nm water layer, all of the secondary electrons are absorbed by the layer.

Another inevitable consequence of electron beam-sample interactions is local heating of the inspected area. Due to the relatively low heat conductivity of biological samples and polymers, the real temperature of the electron beam affected area, as well as the ESEM observation conditions (beam current, gas type and pressure, working distance, etc), is higher and different for each sample (material composition, homogeneity, etc.). The local increase in the surface temperature, especially when thin polymer layers or hollow beats are observed, can cause irreversible sample dehydration due to the violation of the thermodynamic equilibrium between gas pressure and sample temperature. (Neděla 2010a). It has not yet been possible to measure the actual temperature and gas pressure close to the sample surface (or directly in the beam-scanned area on the sample) in a satisfactory manner in the ESEM (Neděla et al. 2015a). However, there have been some attempts to specify these conditions. One such attempt was the integration of micro sensors for temperature and pressure measurement into the sample holder, described by Leary and Brydson (2010).

Moreover, the samples in ESEM are covered with aqueous layer, which may contain other substances. According to Raoult's Law, conditions for the thermodynamic equilibrium of clean water did not correspond with the liquid on the sample (Tihlaříková et al. 2013). Furthermore, the presence of the liquid layer can also influence the sample temperature. Calculation of the total amount of heat delivered by the beam to the sample per exposed area is also complicated, because

the electron beam is in high pressure conditions of ESEM scattered out from the initially focused spot to the diffused skirt. Also, the chemical composition of the liquid which the beam goes through is difficult to define and its composition can be changed during the experiment.

To enhance the quality of the observation the gas flow and the environment in the specimen chamber of ESEM during pumping needs to be precisely described. Typically, a controlled sequence of vacuum pumping and water vapour flooding is repeated until most of the dry air is replaced by water vapour (Cameron et al 1994). Danilatos (2011) introduced modifications to the differentially pumped chamber of the ESEM. They compared two commercial microscopes in terms of pumping efficiency of the pumped volume using a program based on the Direct Simulation Monte Carlo (DSMC) method (Bird 1994) and the scattering of the primary beam within it (Danilatos 2012). The results of Danilatos' simulations were validated by Maxa et al. (2016) using a different counting method and ANSYS software. Furthermore, our group published the results of the simulation of gas flow in a differentially pumped chamber in the environmental SEM AQUASEM II (Maxa and Neděla 2011) and of a scintillation secondary electron detector for the ESEM (Jirák et al 2010, Maxa et al. 2012, Vyroubal et al. 2013).

Given the above-mentioned findings the current level of commercially available environmental scanning electron microscopes prohibits the study of very susceptible samples like polyelectrolyte complex capsules/beads (PEC) in their native, fully wet, hence unfrozen, state free of damage. The Scientific Group of Environmental Electron Microscopy of the ASCR in Brno currently represents the world's leading workplace in the field of environmental scanning electron microscopy. In an effort to push the boundaries of application capabilities of ESEM, a breakthrough results have recently been published by our group (Neděla et at 2020). We introduced the most complex analysis and optimization of thermodynamic conditions in the specimen chamber of ESEM to allow in-situ observation of extremely delicate wet PEC particles in their native state. Based on all experimental and simulation results we also introduce a Delicate Sample Observation Strategy for the ESEM. We show how this strategy can be applied to the characterization of polyelectrolyte complex spherical particles containing immobilized recombinant cells E. coli overexpressing cyclohexanone monooxygenase, used as a model biocatalyst (Bertóková et al. 2015). We present the first native-state electron microscopy images of the viscous core of a halved polyelectrolyte complex capsule containing living cells. The exceptionality of our methods (Neděla et al. 2015b, Tihlaříková et al. 2013) and the ESEM AQUASEM

II were also demonstrated by the possibility to image and measure dimensions of unaffected PEC beds prepared by a novel two-step reaction of oppositely-charged polymers including highly defined cellulose sulphate (Krajčovič et al. 2017). Polyvinyl alcohol lens-shaped particles were also imaged for the first time using our microscope under reduced temperature and at the air pressure 540 Pa (Schenkmayerova et al. 2014).

Some modern electron microscopes allow not only the high-resolution observation or usage of the focused ion beam to etch or machine surfaces of samples under vacuum conditions, but also enabling easy switching to the environmental mode and take full advantage of the ESEM described above. These advantages today lie mainly in the possibility of in-situ characterization of samples in conditions of dynamically changing environment, under various physical or chemical influences, all in combination with the possibility to directly measure electrical and non-electrical quantities. Local injection of liquids and gases on the sample, integrated into micromanipulators, is also possible. Transmission scanning electron microscopy of nanoparticles in liquids with sub nanometre resolution, highly sensitive elemental micro analysis of native and uncoated samples, and in combination with other microscopic methods also correlative microscopy represent a group of specialized equipment.

New technologies are being developed for the world´s unique low-energy ESEM system to observe samples using 1 keV electron beam energy, which will be presented by the ISI ASCR Environmental Electron Microscopy group in the next few years. This will enable to study sensitive samples in an even more gentle way and bring several advantages when studying semiconductors and other electrically non-conductive samples. These technologies will be implemented into our modified ESEM QUANTA 650 FEG equipped with Schottky electron source allowing high resolution imaging of samples.

REFERENCES:

Arnoult, C., Di Martino, J. & Ruch, D. Prediction and limitation of polymer degradation in Environmental SEM. *Ultramicroscopy* **122**, 32-36 (2012).

Autrata, R., Hermann, R. & Müller, M. An efficient single crystal BSE detector in SEM. *Scanning* **14**, 127-135 (1992).

Autrata, R., Hutar, O., & Schauer, P. Low Voltage single crystal backscatter electron detectors. *Journal of computer-assisted microscopy* **9.2** 105-107 (1997).

Autrata, R., Jirák, J. & Schneider, L. Usage of Segmental Ionization Detector in Environmental Conditions. *Microscopy and Microanalysis* **9**, 142-143 (2003).

Bertóková, A. *et al.* Biooxidation of 2-phenylethanol to phenylacetic acid by whole-cell Gluconobacter oxydans biocatalyst immobilized in polyelectrolyte complex capsules. *Biocatalysis and Biotransformation* **33**, 111-120 (2015).

Bird, G. A. *Molecular gas dynamics and the direct simulation of gas flows*. (Oxford University Press, 1994).

Cameron, R. E. & Donald, A. M. Minimizing sample evaporation in the environmental scanning electron microscope. *Journal of Microscopy* **173**, 227-237 (1994).

Danilatos, G. D. & Robinson, V. N. E. Principles of scanning electron microscopy at high specimen chamber pressures. *Scanning* **2**, 72-82 (1979).

Danilatos, G. D. The examination of fresh or living plant material in an environmental scanning electron microscope. *Journal of Microscopy* **121**, 235-238 (1981).

Danilatos, G. D. & Postle, R. The environmental scanning electron microscope andits applications. *Scanning Electron Microscopy* 1-16 (1982).

Danilatos, G. D. A Gaseous Detector Device for an Environmental SEM. *Micron and Microscopica Acta* **14,** 307-318 (1983).

Danilatos, G. D. Foundations of Environmental Scanning Electron Microscopy. *Advances in Electronics and Electron Physics Volume 71* 109-250 (1988).

Danilatos, G. D. Review and outline of environmental SEM at present. *Journal of Microscopy* **162**, 391-402 (1991).

Danilatos, G. D.: Secondary-electron imaging by Scintillating Gaseous Detection device. *Proc. 50th Annual Meeting EMSA* 1302-1303 (1992)

Danilatos, G. D. Environmental scanning electron microscopy and microanalysis. *Mikrochimica Acta* **114-115**, 143-155 (1994).

Danilatos, G. D. Radiofrequency Gaseous Detection Device. *Microscopy and Microanalysis* **6**, 12-20 (2000).

Danilatos, G. D. Figure of merit for environmental SEM and its implications. *Journal of Microscopy* **244**, 159-169 (2011).

Danilatos, G. D. Velocity and ejector-jet assisted differential pumping: Novel design stages for environmental SEM. *Micron* **43**, 600-611 (2012).

Danilatos, G. D. Electron scattering cross-section measurements in ESEM. *Micron* **45**, 1-16 (2013).

Đorđević, B., Neděla, V., Tihlaříková, E., Trojan, V. & Havel, L. Effects of copper and arsenic stress on the development of Norway spruce somatic embryos and their visualization with the environmental scanning electron microscope. *New Biotechnology* **48**, 35-43 (2019).

Egerton, R. F., Li, P. & Malac, M. Radiation damage in the TEM and SEM. *Micron* **35**, 399-409 (2004).

Fletcher, A. L., Thiel, B. L. & Donald, A. M. Amplification measurements of alternative imaging gases in environmental SEM. *Journal of Physics D: Applied Physics* **30**, 2249-2257 (1997).

Fletcher, Thiel & Donald. Signal components in the environmental scanning electron microscope. *Journal of Microscopy* **196**, 26-34 (1999).

Garcia-Salinas, M. J. & Donald, A. M. Use of Environmental Scanning Electron Microscopy to image poly(N-isopropylacrylamide) microgel particles. *Journal of Colloid and Interface Science* **342**, 629-635 (2010).

Gauvin, R. X-ray microanalysis of real materials using Monte Carlo simulations. *Surface and Interface Analysis* **37**, 875-886 (2005).

Goldstein, J. I. *et al. Scanning Electron Microscopy and X-ray Microanalysis*. (Springer US, 2017).

Grubb, D. T. Radiation damage and electron microscopy of organic polymers. *Journal of Materials Science* **9**, 1715-1736 (1974).

Hill, M. A. & Smith, F. A. Calculation of initial and primary yields in the radiolysis of water. *Radiation Physics and Chemistry* **43**, 265-280 (1994).

Huggett, J. M. & Uwins, P. J. R. Observations of water-clay reactions in water-sensitive sandstone and mudrocks using an environmental scanning electron microscope. *Journal of Petroleum Science and Engineering* **10**, 211-222 (1994).

Imrichová, K. *et al.* Vitrification and increase of basicity in between ice I h crystals in rapidly frozen dilute NaCl aqueous solutions. *The Journal of Chemical Physics* **151**, (2019).

Jensen, E., Køber, C., Jensen, P. S. & Mølhave, K. In-situ SEM microchip setup for electrochemical experiments with water based solutions. *Ultramicroscopy* **129**, 63-69 (2013).
Jirák, J., Neděla, V., Černoch, P., Čudek, P. & Runštuk, J. Scintillation SE detector for variable pressure scanning electron microscopes. *Journal of Microscopy* **239**, 233-238 (2010).

Kanaya, K. & Okayama, S. Penetration and energy-loss theory of electrons in solid targets. *Journal of Physics D: Applied Physics* **5**, 43-58 (1972).

Kitching, S. & Donald A.M. Beam damage of polypropylene in the environmental scanning electron microscope: an FTIR study. *Journal of Microscopy* **190**, 357-365 (1998).

Krajčovič, T. *et al.* Polyelectrolyte Complex Beads by Novel Two-Step Process for Improved Performance of Viable Whole-Cell Baeyer-Villiger Monoxygenase by Immobilization. *Catalysts* **7**, (2017).

Krausko, J., Runštuk, J., Neděla, V., Klán, P. & Heger, D. Observation of a Brine Layer on an Ice Surface with an Environmental Scanning Electron Microscope at Higher Pressures and Temperatures. *Langmuir* **30**, 5441-5447 (2014).

Kulich, I. *et al.* Exocyst Subunit EXO70H4 Has a Specific Role in Callose Synthase Secretion and Silica Accumulation. *Plant Physiology* **176**, 2040-2051 (2018).

Lane, W.C. The environmental wet stage. *Proceedings of the Third Scanning Electron Microscopy Symposium, IIT Reserch Institute, Chicago, IL* 60616 (1970).

Leary, R. & Brydson, R. Characterisation of ESEM conditions for specimen hydration control. *Journal of Physics: Conference Series* **241**, (2010).

Le Berre, J. F., Demopoulos, G. P. & Gauvin, R. Skirting: A Limitation for the Performance of X-ray Microanalysis in the Variable Pressure or Environmental Scanning Electron Microscope. *Scanning* **29**, 114-122 (2007).

Lencová, B. & Zlámal, J. The development of EOD program for the design of electron optical devices. *Microscopy and Microanalysis* **13**, 2 (2007).

Mansour, O., Kadoun, A., Khouchaf, L. & Mathieu, C. Monte Carlo simulation of the electron beam scattering under water vapor environment at low energy. *Vacuum* **87**, 11-15 (2013).

Maxa, J. & Neděla, V. The impact of critical flow on the primary electron beam passage through differentially pumped chamber. *Adv. Mil. Technol.* **6** (2011).

Maxa, J., Neděla, V., Jirák, J., Vyroubal, P. & Hladká, P. Analysis of gas flow in a secondary electron scintillation detector for ESEM with a new system of pressure limiting apertures. *Adv. Mil. Technol.* **7** (2012).

Maxa, J., Bílek, M., Hlavatá, P., Vyroubal, P. & Lepltová, K. Comparisons Using Methods of Continuum Mechanics and Monte Carlo at Differentially Pumped Chamber. *Advances in Military Technology* **11**, (2016).

Meredith, P., Donald, A. M. & Thiel, B. Electron-gas interactions in the environmental scanning electron microscopes gaseous detector. *Scanning* **18**, 467-473 (1996).

Michaloudi, E. *et al.* Reverse taxonomy applied to the Brachionus calyciflorus cryptic species complex: Morphometric analysis confirms species delimitations revealed by molecular phylogenetic analysis and allows the (re)description of four species. *PLOS ONE* **13**, 1-25 (2018).

Navrátilová, E., Tihlaříková, E., Neděla, V., Rovnaníková, P & Pavlík, J. Effect of the preparation of lime putties on their properties. *Scientific Reports* **7**, 1-9, 17260 (2017).

Neděla, V., Linhart, J. & Autrata, R. Detection of the True Secondary Electrons with a Newly Designed lonization Detector for ESEM. *In Proceedings of the 16th International Microscopy Congress – IMC16. Sapporo: Japanese Society of Microscopy* 982 (2006)

Neděla, V. Methods for additive hydration allowing observation of fully hydrated state of wet samples in environmental SEM. *Microscopy Research and Technique* **70**, 95-100 (2007).

Neděla, V. Controlled dehydration of a biological sample using an alternative form of environmental SEM. *Journal of Microscopy* **237**, 7-11 (2010a).

Neděla, V. & Jirák, J. Newly Designed Ionisation Secondary Electron Detector with Electrostatic Separators for VP-ESEM. *In Proceedings of the 17th IFSM International Microscopy Congress. Rio de Janeiro : Sociedade Brasileira de Microscopia e Microanilise,* 1-2 (2010b)

Neděla, V., Konvalina, L., Lencová, B. & Zlámal, J. Simulation of Energy Selective signal Amplification in Gas Environment of Variable Pressure SEM. *Microscopy and Microanalysis* **17**, 920-921 (2011a).

Neděla, V., Konvalina, I., Lencová, B. & Zlámal, J. Comparison of calculated, simulated and measured signal amplification in a variable pressure SEM. *Nuclear Instruments and Methods in Physics Research Section A: Accelerators, Spectrometers, Detectors and Associated Equipment* **645**, 79-83 (2011b).

Neděla, V., Hřib, J. & Vooková, B. Imaging of early conifer embryogenic tissues with the environmental scanning electron microscope. *Biologia Plantarum* **56**, 595-598 (2012).

Neděla, V., Hrib, J., Havel, L. & Runštuk, J. Early state of spruce somatic embryos in native state observed using the ESEM and Cryo-SEM. *Microscopy and Microanalysis* **19**, 20-21 (2013).

Neděla, V., Tihlaříková, E. & Hřib, J. The low-temperature method for study of coniferous tissues in the environmental scanning electron microscope. *Microscopy Research and Technique* **78**, 13-21 (2015a).

Neděla, V., Bučko, M., Tihlaříkova, E., Krajčovič, T. & Gemeiner, P. The Size and Morphological Study of Spherical Polyelectrolyte Complex Beads Using Environmental Scanning Electron Microscopy. *Microscopy and Microanalysis* **21**, 1697-1698 (2015b).

Neděla, V., Konvalina, I., Oral, M. & Hudec, J. The Simulation of Energy Distribution of Electrons Detected by Segmental Ionization Detector in High Pressure Conditions of ESEM. *Microscopy and Microanalysis* **21**, 264-269 (2015c).

Neděla, V., Hřib, J., Havel, L., Hudec, J. & Runštuk, J. Imaging of Norway spruce early somatic embryos with the ESEM, Cryo-SEM and laser scanning microscope. *Micron* **84**, 67-71 (2016).

Neděla, V., Tihlaříková, E., Runštuk, J. & Hudec, J. High-efficiency detector of secondary and backscattered electrons for low-dose imaging in the ESEM. *Ultramicroscopy* **184**, 1-11 (2018).

Neděla, V. *et al.* Simulation-based optimisation of thermodynamic conditions in the ESEM for dynamical in-situ study of spherical polyelectrolyte complex particles in their native state. *Ultramicroscopy* **211**, (2020).

Oral, M., Neděla, V. & Danilatos, G. D. Dynamic Correction of Higher-Order Deflection Aberrations in the Environmental SEM. *Microscopy and Microanalysis* **21**, 194-199 (2015).

Popielarska-Konieczna, M., Bohdanowicz, J. & Starnawska, E. Extracellular matrix of plant callus tissue visualized by ESEM and SEM. *Protoplasma* **247**, 121-125 (2010).

Rice, T. & Knowles, R. Ultra High Resolution SEM on Insulators and Contaminating Samples. *Microscopy Today* **13**, 40-43 (2005).

Reimer, L. *Scanning electron microscopy: physics of image formation and microanalysis*. (Springer, c1998).

Robinson, V. N. E. The elimination of charging artefacts in the scanning electron microscope. *Journal of Physics E: Scientific Instruments* **8**, 638-640 (1975).

Romanovský, V. & Autrata, R. Scintillation and Ionisation Detectors for Environmental SEM. *European Microscopy and Analysis* 59,19 (1999).

Romanovský, V. & Autrata, R. Combined scintillation and ionisation detectors for environmental scan-ning electron microscopes. *Fine mechanics and optics* **45** (10), 273-274 (2000).

Royall, C. P., Thiel, B. L. & Donald, A. M. Radiation damage of water in environmental scanning electron microscopy. *Journal of Microscopy* **204**, 185-195 (2001).

Royall, C. P. & Donald, A. M. Optimisation of the environmental scanning electron microscope for observation of drying of matt water-based lacquers. *Scanning* **24**, 305-313 (2002).

Sawyer, L.C. & Grubb, D. T. *Polymer microscopy*. (London, Great Britain: Chapman and Hall, 1987).

Schenkmayerová, A. *et al.* Physical and Bioengineering Properties of Polyvinyl Alcohol Lens-Shaped Particles Versus Spherical Polyelectrolyte Complex Microcapsules as Immobilisation Matrices for a Whole-Cell Baeyer–Villiger Monooxygenase. *Applied Biochemistry and Biotechnology* **174**, 1834-1849 (2014).

Stabentheiner, E., Zankel, A. & Pölt, P. Environmental scanning electron microscopy (ESEM)—a versatile tool in studying plants. *Protoplasma* **246**, 89-99 (2010).

Sun, H., Mašín, D., Najser, J., Neděla, V. & Navrátilová, E. Bentonite microstructure and saturation evolution in wetting–drying cycles evaluated using ESEM, MIP and WRC measurements. *Géotechnique* **69**, 713-726 (2019a).

Sun, H., Mašín, D., Najser, J., Neděla, V. & Navrátilová, E. Fractal characteristics of pore structure of compacted bentonite studied by ESEM and MIP methods. *Acta Geotechnica* 1-17 (2019b).

Talmon, Y. Electron Beam Radiation Damage to Organic and Biological Cryospecimens. in *Cryotechniques in Biological Electron Microscopy* 64-84 (Springer Berlin Heidelberg, 1987).

Thiel, B. L., Bache, I. C., Fletcher, A. L., Meredith, P. & Donald, A. M. An improved model for gaseous amplification in the environmental SEM. *Journal of Microscopy* **187**, 143-157 (2003).

Tihlaříková, E., Neděla, V. & Shiojiri, M. In Situ Study of Live Specimens in an Environmental Scanning Electron Microscope. *Microscopy and Microanalysis* **19**, 914-918 (2013).

Tihlaříková, E., Neděla, V. & Đorđević, B. In-situ preparation of plant samples in ESEM for energy dispersive x-ray microanalysis and repetitive observation in SEM and ESEM. *Scientific Reports* **9**, (2019).

Toth, M., Daniels, D. R., Thiel, B. L. & Donald, A. M. Quantification of electron-ion recombination in an electron-beam-irradiated gas capacitor. *Journal of Physics D: Applied Physics* **35**, 1796-1804 (2002).

Utke, I., Moshkalev, S. & Russell, P. *Nanofabrication using focused ion and electron beams: principles and applications*. (Oxford University Press, 2012).

Vetráková, Ľ., Neděla, V., Runštuk, J. & Heger, D. The morphology of ice and liquid brine in an environmental scanning electron microscope: a study of the freezing methods. *The Cryosphere* **13**, 2385-2405 (2019).

Vlašínová, H., Neděla, V., Đorđević, B. & Havel, L. Bottlenecks in bog pine multiplication by somatic embryogenesis and their visualization with the environmental scanning electron microscope. *Protoplasma* **254**, 1487-1497 (2017).

Vyroubal, P., Maxa, J., Neděla, V., Jirák, J. & Hladká, K. Apertures with Laval nozzle and circular orifice in secondary electron detector for environmental scanning electron microscope. *Advances in military technology* **8**(1), 59-69 (2013).

Wight, S. A. & Zeissler, C. J. Direct measurement of electron beam scattering in the environmental scanning electron microscope using phosphor imaging plates. *Scanning* **22**, 167-172 (2000).

Wille, G., Bourrat, X., Maubec, N. & Lahfid, A. Raman-in-SEM, a multimodal and multiscale analytical tool: Performance for materials and expertise. *Micron* **67**, 50-64 (2014).

Williams, S. J. & Donald, A. M. Investigation of quantitative secondary electron imaging of semiconducting polymer materials using environmental scanning electron microscopy. *Journal of Microscopy* **216**, 241-248 (2004).

Yang, X. *et al.* Evaporating brine from frost flowers with electron microscopy and implications for atmospheric chemistry and sea-salt aerosol formation. *Atmospheric Chemistry and Physics* **17**, 6291-6303 (2017).

4 Controlled dehydration of a biological sample using an alternative form of environmental SEM

V. NEDĚLA
Institute of Scientific Instruments of ASCR, Královopolská 147, 61264, Czech Republic

Key words. Biological sample, dehydration, environmental SEM AQUASEM II, hydration system.

Summary

In this study a non-conductive biological sample is observed free of charging artefacts when placed on a cooled Peltier stage in the specimen chamber of an alternative form of the environmental scanning electron microscope, equipped with a specially designed hydration system. This system was used to create dynamically changing surrounding conditions leading to controlled dehydration of the sample enabling us to visualize the topographical structure of a rat tongue in the transition region between the liquid and the gas state of water in the microscope specimen chamber.

Introduction

The environmental scanning electron microscopy enables us to observe and examine specimens that are difficult or impossible to image in a conventional high vacuum scanning electron microscope (SEM). The basic difference between the environmental scanning electron microscope (ESEM) and SEM is that the specimen chamber of ESEM can contain a certain amount of gas, mostly water vapour, whereas the pressure of gas close to an electron source of the microscope remains sufficiently low (Danilatos,1988). Collisions with gas molecules influence both the primary electrons between the small holes in the pressure-limiting apertures and the sample and the signal electrons emitted from the sample. Due to the high pressure of gases in the specimen chamber of ESEM the conditions for secondary electron detection are completely different from those in a conventional SEM. The construction of detectors must be based on different physical principles, as described by Jacka et al. (2003), Jirák et al. (2008) and Morgan and Phillips (2006). The most efficient detectors of secondary electrons in the high-pressure conditions in the specimen chamber of ESEM use the principle of gas ionization that proceeds as a cascade between a grounded specimen holder and a detector signal electrode supplied with a positive voltage, placed under the pole piece of the objective lens (Danilatos, 1990; Meredithetal.,1996) or inside the objective lens (Thiel, 2006).

In the ESEM the specimens can be observed in a wide range of pressures from vacuum (comparable with the SEM) to high pressure of various gases (over 1000 Pa) in the specimen chamber. In high-pressure conditions very wet nonconductive samples can be observed without a conductive coating covering their surface, and their natural fully hydrated surface structure is preserved (Stokes, 2003). Additionally, more interesting and very useful in situ dynamical experiments as a study of sample solidification, dissolution, chemical reactions, etc. can be conducted as well, as reviewed by Donald (2003).

The pressure of water vapour in the specimen chambre of the ESEM together with the specimen temperature play a crucial role in obtaining and maintaining the state of thermodynamic equilibrium between the environment of the specimen chamber and the sample itself, as demonstrated by Cameron and Donald (1994). In thermodynamic equilibrium of 100% relative humidity we must follow the dependence of saturated water vapour pressure on the specimen temperature. A small change of a sample temperature at the stable pressure of the water vapour can be used for the study of transition between the hydration and dehydration phenomena, but also to a more limited extent for the study of reactions (Donald, 1998). The above mentioned dynamical in situ experiments represent one of the most important advantages of the ESEM microscopes. Unique results, obtained during these experiments, can serve as the basis for interesting cooperation between scientists across scientific disciplines.

Material and methods

The rat tongue has a good structure to maintain natural hydration inside the sample and the change of structure of siliform papillae on its surface can sensitively indicate a decrease of relative humidity; for this reason, the rat tongue is a suitable sample for an experimental study of controlled dehydration of a biological sample. The sample was not treated with any preparation technique and its surface was not covered with a conductive layer. The rat tongue was placed on a cooled specimen holder (Peltier stage) and the temperature of the specimen holder was adjusted and kept at 2◦C. For this temperature the saturated water vapour pressure is 708 Pa.

Our experimental microscope AQUASEM-II, Neděla & Maxa (2006), was designed in the Institute of Scientific Instruments (ISI) of the Academy of Sciences of the Czech Republic as a non-commercial apparatus for research on detection systems and ESEM techniques, see Fig. 1. The electron optical column with a tungsten hairpin filament and Electronics was produced by Tescan Ltd (Brno, Czech Republic). The special specimen chamber, the differentially pumped chamber, the Peltier cooled specimen holder and the hydration system for precise

control of water vapour flow into the chamber, were designed at ISI Brno (Neděla, 2006). A new hydration system, shownˇ in Fig. 2, has been specially developed to maintain the wet environment in the specimen chamber of the microscope, enabling work in the high-pressure conditions of some gases and water vapour in the specimen chamber up to 2000Pa. The pressure measurement is performed by a system of capacity gauges made by the Pfeiffer company. The microscope can also work in the high and low vacuum modes.

Fig. 1 Non-commercial experimental ESEM AQUASEM II

The single crystal YAG:Ce3+ (yttrium aluminium garnet activated with trivalent cerium) has a hole in the centre, so that it simultaneously acts as a pressure-limiting aperture, which restricts the gas flow between the specimen chamber and the differentially pumped chamber (Neděla, 2007). It is used for detection ofˇ backscattered electrons in the low and high vacuum modes, but it is also well suited for the high-pressure conditions in the specimen chamber. In the low vacuum and environmental mode the secondary electron signal was detected by an electrode with the inner diameter of 4 mm deposited on the input surface of the single crystal detector, Danilatos (1993a, b). With a positive bias of 370 V with respect to the sample it acts in a similar manner as the environmental secondary detector (see Fig. 3).

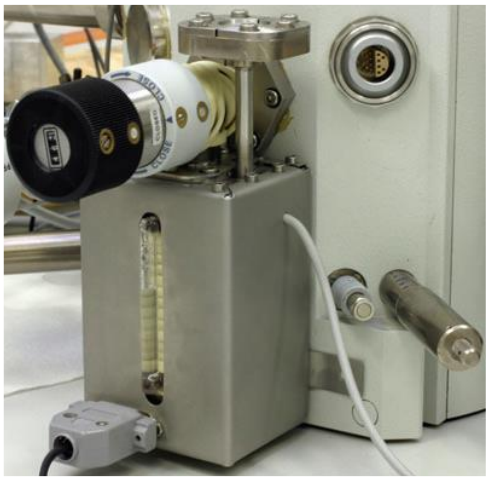

Fig. 2 Hydration system of ESEM AQUASEM II.

The sufficiently high and stable humidity in the specimen chamber during the first pumping stage must be preserved. At the beginning of the pumping the pressure is equal to the atmospheric pressure in all parts of the microscope. A small aluminium cup with distilled water is inserted into the specimen chamber (Danilatos, 1988), and the temperature of the sample is reduced to 2◦C.

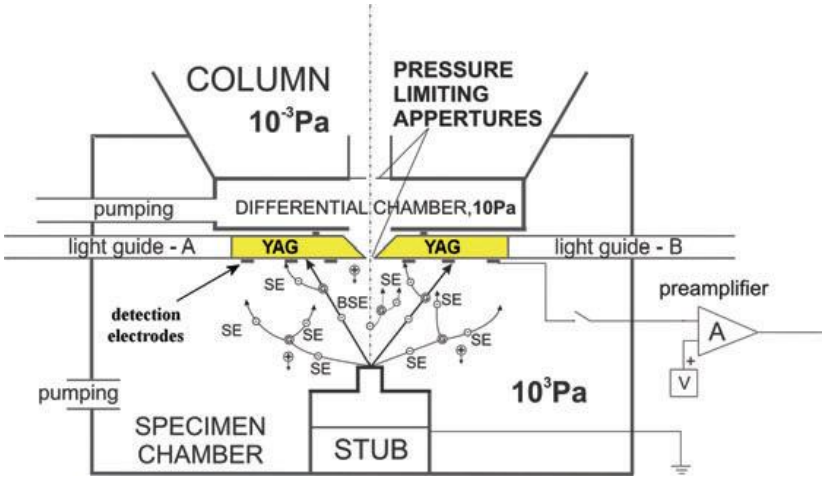

Fig. 3 Configuration of the combined YAG-BSE detector and ionization detector of secondary electrons in ESEM AQUASEM II.

The microscope is pumped using rotary and turbo-molecular pumps and the specimen chamber is pumped only through the small hole (diameter 500 μm) situated in the centre of the YAG:Ce3+ single crystal. The small diameter of this pressure-limiting aperture critically restricts the gas pumping speed and prolongs the time needed to achieve a pressure decrease in the specimen chamber. Then the pressure in the chamber stabilizes at about 2000 Pa; this value is given by the thermodynamic balance corresponding to the pressure of saturated water vapour in the cup. When the water from the cup evaporates, the pressure in the specimen

chamber is decreasing and water vapour is supplied from a hydration system to establish the required pressure in the chamber (Cameron & Donald, 1994).

All experiments were carried out under constant operating conditions of the microscope AQUASEMII (beam accelerating voltage 20kV, probe current 200pA, sampledistance2.5mm between the bottom surface of the YAG single crystal and the surface of the sample, positive bias of the detection electrode system 370 V) and in the water vapour environment with high relative humidity.

Results and discussion

This experiment was focused on study of the transition from the hydration to dehydration state and on study of the topographical changes depending on dehydration using our experimental microscope equipped with a specially designed hydration system. Another objective of the paper is to present the first results obtained with the help of this non-commercial microscope, its hydration system and the cooled specimen holder, test them and demonstrate their performance.

The first image (Fig. 4A) of the sample was recorded after the pressure in the specimen chamber had dropped from 2000 to 730 Pa at the stage temperature of 2◦C and after 10 min of pumping the specimen chamber. The long pumping time (10 min) is the main disadvantage of this experiment. It can be compensated by the use of an additional rotary pump to support gas pumping through the small hole in the YAG:Ce3+ single crystal and increase the speed of gas pumping from the specimen chamber.

The specimen is fully hydrated and its surface is covered with water, so that no topographical details are visible on the surface. Figure 4(B) shows a sample at 715 Pa and 2◦C, which are the conditions slightly above the dependence of the saturated water vapour pressure on the sample temperature (liquid phase region). After that the pressure was decreased to 708 Pa. A slow local temperature increase in the observed area due to the influence of the primary electron beam and low temperature conductivity of the biological sample violates the thermodynamic balance and causes a very slow evaporation of water from the sample surface dependent on the observation time. It can be seen in Fig. 4(A)–(E), recorded at 5-min intervals. With the thinning of the water layer the fine topographical structure is becoming visible.

Water evaporation from the sample is not even and depends on the temperature, pressure, topography and local material properties in the given place.

A very thin layer of water on the surface of siliform papillae and the preservation of their natural undistorted shape demonstrate optimum conditions for the observation of the sample in Fig. 4(E). A further increase of the local sample temperature leads to evaporation of water from inside the sample. It is accompanied by slow sample shifts, which imply the dehydration of its volume and its stronger damage. These shifts are indicated by changing position of the object marked with white circles in Fig. 4(E)–(I) that were recorded at 10min intervals.

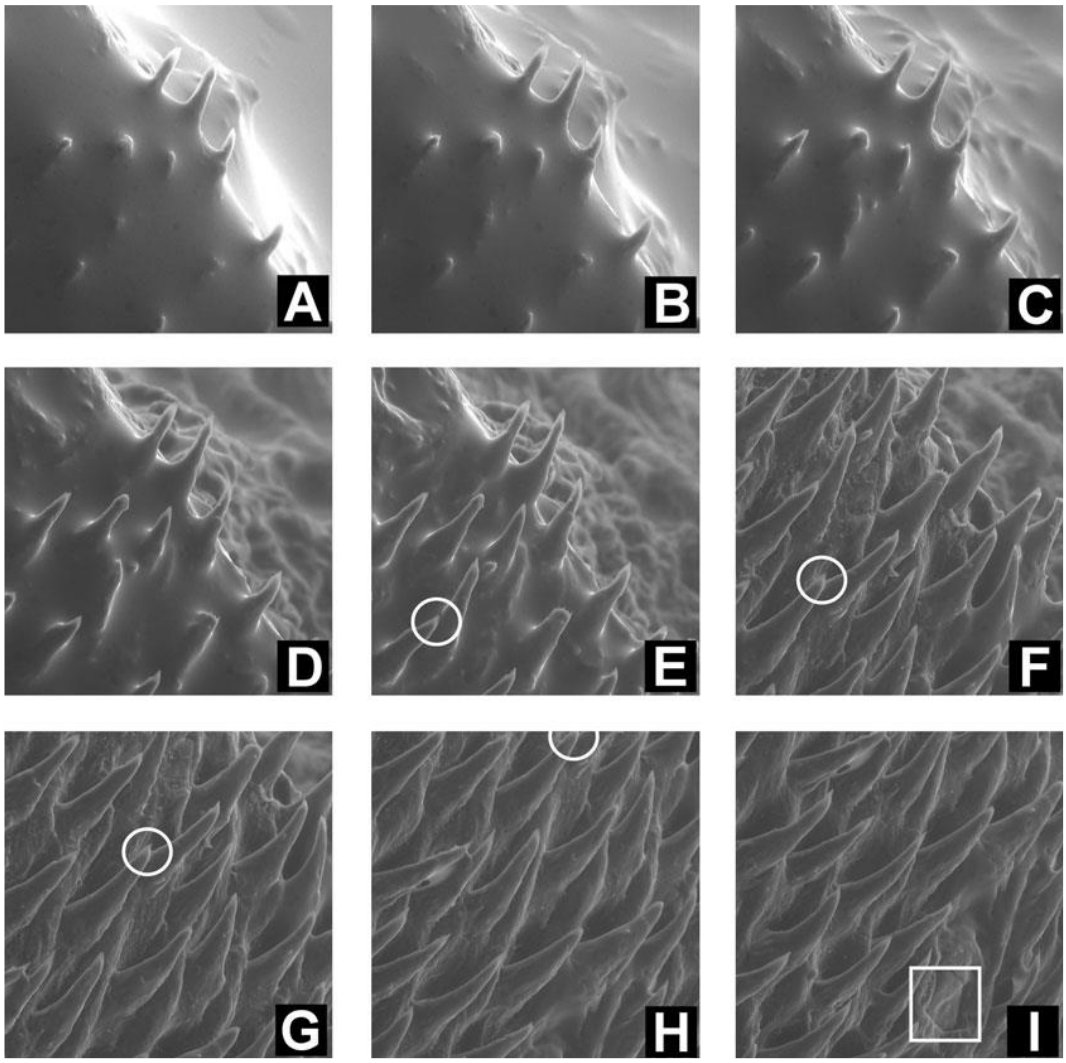

Fig. 4. Siliform papillae on the rat tongue kept at 2◦C observed at different water vapour pressure values. (A) 730 Pa, (B) 715 Pa (C)–(I) 708 Pa. (A)–(E) were recorded at 5-min intervals, (F)–(I) were recorded at 10-min intervals. (Field of view 250 μm, beam voltage 20 kV, probe current 100 pA, sample distance 2.5 mm, bias of the electrode system 370 V.)

Figure 4(I) shows that due to dehydration the sample has shifted so much that the object marked with the white circle is no longer visible; the shape of a taste cell marked with a white square in this final figure and the large inclination of papillae demonstrate that the damage of the sample is already significant. Undamaged, fully

hydrated natural state of a taste cell is characterized by a hemispherical shape without cracks.

Conclusion

The above described experiment focused on transition from the hydration to dehydration state of a biological sample by using the alternative form of ESEM underlined the significance of the thermodynamic stability to in the vicinity of the sample, considering the thermal effects of the beam, temperature conductivity of the specimen, temperature stability of the cooled specimen holder, etc. This experiment also showed the physical conditions for evaporation of a thin water layer from the sample surface and the topographical changes in the sample due to dehydration.

Acknowledgements

This work was supported by Grant CEZ: AV0Z20650511. I express my gratitude to Ing. L. Ilkovics from the Institute of Histology and Embryology of the Faculty of Medicine, Masaryk University in Brno for his help during experiments and for preparation of the specimens. I also thank Prof. B. Lencová for numerous discussions and advice connected with the preparation of the paper.

References

Cameron, R.E. & Donald, A.M. (1994) Minimizing sample evaporation in the environmental scanning electron. J. Microsc. 173, 227–237.

Danilatos, G.D. (1988) Foundations of environmental scanning electron microscopy. Adv. Electron Phys. 71, 109–250.

Danilatos, G.D. (1990) Theory of gaseous detector device in the environmental scanning electron microscope. Adv. Electron Phys. 78, 1–103.

Danilatos, G.D. (1993a) Environmental scanning electron microscope some critical issues. Scanning Microsc. Int. 7, 57–80.

Danilatos, G.D. (1993b) Universal ESEM. Proc. 51st Annual Meeting MSA (ed. by G.W. Bailey & L.C. Rieder), pp. 786–787. San Francisco Press, San Francisco.

Donald, A.M. (1998) Environmental Scanning electron microscopy for the study of “wet” systems. Curr. Opin. Coll. Interface Sci. 3, 143–147.

Donald, A.M. (2003) The use of environmental scanning electron microscopy for imaging wet and insulating materials, Nature Mater. 2, 511–516. ISSN 1476–1122.

Jacka, M., Zadražil, M. & Lopour, F. (2003) A differentially pumped secondary electron detector for low-vacuum scanning electron microscopy. Scanning 25, 243–246.

Jirák, J., Černoch, P., Neděla, V.& Špinka, J. (2008) Scintillation se detector for variable pressure scanning electron microscope. In Proceedings of 14th European Microscopy Congress, Aachen, Germany (ed. by M. Luysberg, K. Tillmann and T. Weirich), pp. 559–560. European Microscopy Society.

Meredith, P., Donald, A.M. & Thiel, B. (1996) Electron-gas interactions in the environmental scanning electron microscopes gaseous detector. Scanning. 18, 467–473.

Morgan, S.W. & Phillips, M.R. (2006) Gaseous scintillation detection and amplification in variable scanning electron microscope. J. App. Phys. 100, 074910–07491

Neděla, V. (2006) Hydratační systém pro environmentální rastrovací elektronové mikroskopy. Fine Mech. Opt. 11–12, 329–331.

Neděla, V. (2007) Methods for additive hydratation allowing observation of fully hydrated state of wet samples in environmental SEM. Microsc. Res. Tech. 70, 95–100.

Neděla, V.& Maxa, J. (2006) Environmental scanning electron microscope AQUASEM II – the design and applications. Proc 10th International Seminar Skalský Důr 2006 (ed. by I. Müllerová), pp. 55–56. ISI AS CR, Brno.

Stokes, D.J. (2003) Investigating Biological Ultrastructure Using Environmental Scanning Electron Microscopy (ESEM). In Science, Technology and Education of Microscopy an Overview (ed. by A. Méndez-Vilas), pp. 564–570. Formatex, Badajos.

Thiel, B.L., et al. (2006) Two-stage gas amplifier for ultrahigh resolution low vacuum scanning electron microscopy. Rev. of Sci. Ins. 77,033705.1–033705.7.

5 Methods for Additive Hydration Allowing Observation of Fully Hydrated State of Wet Samples in Environmental SEM

VILÉM NEDĚLA

Institute of Scientific Instruments, Academy of Sciences of the Czech Republic, Brno, Czech Republic

KEY WORDS agar; natural structure; biological specimens; environmental SEM

ABSTRACT Methods for additive hydration are presented that enable long time observation of very wet biological specimens in an environmental scanning electron microscope. The changes of structure due to dehydration for specimens placed on a Peltier-cooled holder, put on a special agar base or embed-ded in it or blown over by water vapor are compared. The degree of dehydration damage of the observed specimen structures is evaluated and compared with the structure of a non-destructively dried specimen, prepared by the critical point drying method. Microsc. Res. Tech. 70:95–100, 2007.

INTRODUCTION

The basic difference between the environmental scanning electron microscope (environmental SEM) and the scanning electron microscope (SEM) is that the specimen chamber of environmental SEM contains a certain amount of gas in which collisions occur between the primary beam electrons, signal electrons emitted from the specimen surface, and gas molecules (Danilatos, 1988, 1990). The negative charge on the surface of the nonconductive specimen is compensated by positive ions created by the collisions, as described by Robinson (1975a) and Moncrieff et al. (1978). Another advantage of environ-mental SEM arises from the presence of water vapor, namely the possibility of observing wet specimens, particularly under higher pressures in the specimen chamber around 757 Pa (5.7 Torr) at specimen temperature 38C.

The modern environmental SEM allows specimens to be observed in two high-pressure modes, the \low vacuum," or \variable-pressure or natural mode," in which the pressure ranges from 13.3 to 330 Pa (0.1–2.5 Torr) and the environmental mode, in which the pressure is over 330 Pa, as well as in the high vacuum mode. The environmental mode enables very wet nonconductive specimens to be observed without covering the surface with a conductive coating, and their natural, fully hydrated surface structure is preserved. The first attempts to maintain specimen

humidity in the environment of a relatively high pressure of saturated water vapor (611 Pa at 08C) were made by Lane (1970) and by Robinson (1975b). The pressure of water vapor in the specimen chamber of the environmental SEM plays a crucial role, together with specimen temperature, for obtaining and maintaining the state of thermodynamic equilibrium between the environment of the specimen chamber and the specimen itself, as demonstrated by Cameron and Donald (1994). To reach the state of thermodynamic equilibrium, of 100% relative humidity, we must respect the dependence of saturated water vapor pressure on the specimen temperature (Fig. 1). The region below the curve of 100% relative humidity corresponds to physical conditions for specimen dehydration. Stokes (2003) has demonstrated that environmental SEM enables biological specimens

to be studied without sophisticated or time-consuming preparation techniques, such as chemical fixation, freezing, and metallic coating, and the natural state of wet specimen surfaces can be recorded. One of the remaining problems is the accurate determination of the surface temperature of the biological specimen, particularly when the latter is comparatively thick, which makes it difficult to obtain and maintain the thermodynamic equilibrium between the specimen sur-face and the specimen chamber environment. The step-by-step drying of the specimen results in irreversible changes of its surface microstructure. Preservation of the maximum specimen hydration during the initial pump-down of the specimen chamber as well as throughout the time of observation is a necessary pre-requisite. Observation of sensitive biological structures at temperatures higher than the optimum 38C (Stokes, 2003) can also be a problem, if it is not suitable or possible to cool the specimen additionally, immediately after placing it into the microscope, in order to minimize evaporation of water from the specimen. The use of a Peltier-cooled stage and purge-flood cycle, introduced by Cameron and Donald (1994), has been proposed, but their performance may not be sufficient in some cases.

Here, we present suitable additive hydration methods to optimize the conditions for long-time study of sensitive wet biological specimens in environmental SEM.

MATERIALS AND METHODS

Biological specimens were observed in the experimental environmental scanning electron microscope AQUASEM-II designed in the Institute of Scientific Instruments (ISI) of the Academy of Sciences of the Czech Republic as a non-commercial apparatus for research on SEM and environmental SEM detection systems and environmental SEM techniques (Neděla and Maxa, 2006). The micro-scope uses the electron optical column with tungsten hairpin filament and electronics delivered by Tescan.

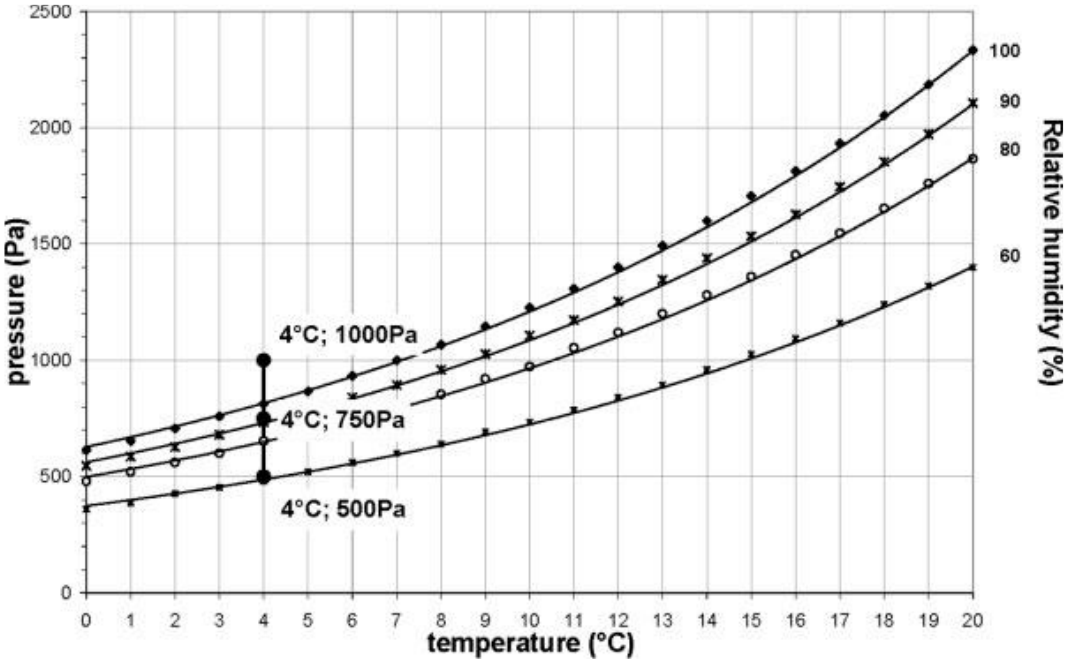

Fig. 1 Dependence of water vapor pressure with a relative humidity of 60, 80, 90, and 100% on temperature. The points correspond to temperature and pressures for individual experiments. The zone above the curve for 100% relative humidity corresponds to physical conditions for specimen hydratation.

The special specimen chamber, the differentially pumped chamber, the Peltier-cooled specimen holder, and hydration system, allowing precise control of water vapor flow into the chamber, (Neděla, Hydration system for environ-mental scanning electron microscopes. J Microsc, submit-ted for publication), were designed at ISI Brno. Pressure control is provided by the system of capacity gauges made by the Pfeiffer company. The microscope works also in high and low vacuum modes. The single crystal YAG:Ce3+ (yttrium aluminum garnet activated with trivalent cerium), used for the detection of back scattering electrons (BSE), has a hole in the middle, so that it simultaneously acts as a pressure-limiting aperture restricting the gas flow between the specimen chamber and the differentially pumped chamber (Romanovský and Autrata, 2000). The secondary electron (SE) signal was detected by the environmental secondary detector (ESD); this detector uses a circular, axial-symmetric undivided electrode system, diameter 4 mm, deposited on the input surface of the single crystal YAG:Ce3+.

All experiments were carried out under constant operating conditions of environmental SEM (beam accelerating voltage: 20 kV, probe current: 200 pA, working distance: 2.5 mm, positive bias of the electrode system of ESD: 350–370 V) and in the water vapor environment with high relative humidity. Small intestine villi with fine surface epithelium that respond sensitively to dehydration were selected as the test specimen. Each specimen was prepared in the form of a cylinder, diameter 7 mm and height 4 mm. The specimens were not subjected to any

preparation technique. The hydration system and the cooled specimen holder (Peltier stage) are used for all the experiments. The temperature of the thin tissue is decreased to 48C and the appropriate amount of distilled water (around 0.6 mL for our specimen chamber) is inserted into the specimen chamber before beginning of the pumping process, to ensure that its natural moisture is preserved during the initial pump down of the chamber. The specimen chamber is pumped down through the pressure-limiting aperture, which separates the differentially pumped chamber and the specimen chamber. This pumping is accompanied by a decrease of the pressure down to the value of the pressure of saturated water vapor, 2,062 Pa (15.5 Torr), corresponding to the temperature of dis-tilled water in the specimen chamber (188C). Another decrease of pressure in the specimen chamber occurs after evaporation of the distilled water. From then on, water vapor must be supplied from the external hydration system, regulated by a micrometrical valve. It is therefore usual to perform a sequential pump down such that air is purged from the chamber and successively replaced with water vapor (purge-flood cycle), according to Cameron and Donald (1994). A typical regime involves cycling eight times between a set pressure, 1,000 Pa (7.5 Torr) and flood pressure, 2,000 Pa (15 Torr). As a test, we used the surface structure of the small intestine specimen prepared with the standard method of Critical Point Drying (CPD) on the device CPD 030 Balzers. The specimen was observed at the pressure of 40 Pa (0.3 Torr) of air, using the YAG-BSE detector, which was more suitable than ESD with respect to the detected signal level at the pressure of 40 Pa. The specimen surface was not coated (Fig. 2).

During the first experiment the small intestine specimen was placed on the cooled specimen holder and the specimen temperature was reduced to 4°C. The specimen chamber was pumped down in conformity with the purge-flood cycle described by Cameron and Donald (1994).

During the second experiment the specimen was placed on the surface of a special agar base. The agar powder (1.3%—Sigma Aldrich Chemie GmbH, Ger-many) was mixed in the aluminum cylindrical cup (diameter 18 mm and height 5 mm) with water and heated to a temperature over 508°C. At this tempera-ture the agar was in the liquid state. After the cup was cooled outside the environmental SEM specimen chamber, the agar solidified and the cup was fixed on the cooled specimen holder (Fig. 3). The specimen was then put on the agar surface and the temperature was reduced to 48C; the pumping process, again in conformity with the purge-flood cycle method, was started.

Fig. 2. Surface structure of small intestine villi. The sample was dried non-destructively by the CPD method, uncoated, and observed at 40 Pa of air with a YAG-BSE detector, field of view 200 μm.

During the third experiment the specimen was put into the aluminium cup, after which agar was poured around it. A part of the specimen explored by the primary beam was thus not covered by agar (Fig. 4). For better position fixing, the cup was provided with a fixing pin to hold the specimen in constant position. The cup was then fixed into the cooled specimen holder and after its temperature was reduced, the agar became solid. The pumping process, always in conformity with the purge-flood cycle method, was then started.

The fourth experiment resembled the first experiment except that now, water vapor was blown over the specimen. The water vapor was brought close to the specimen surface by a thin heated capillary. The capillary tube was connected to the hydration system placed outside the environmental SEM specimen chamber and a second separately heated hydration system was thus created.

All experiments were started at a pressure of 1,500 Pa (11.25 Torr) in the environmental SEM specimen chamber. The water vapor pressure was reduced in steps of 50 Pa (0.38 Torr) down to the value of 200 Pa (1.5 Torr) when the specimen completely dried. After each pressure reduction, micrographs of the specimen surface structure were taken. The experiments were carried out in the same time steps and individual micrographs were recorded chronologically from the beginning of each experiment to ensure that the conditions of all the experiments were identical.

RESULTS AND DISCUSSION

The aim of our experiments was to check the efficiency of the additive hydration methods and to provide experimental data for extended long-time observation of sensitive biological and other special specimens in environmental SEM in conditions that would preserve their naturally hydrated surface structures.

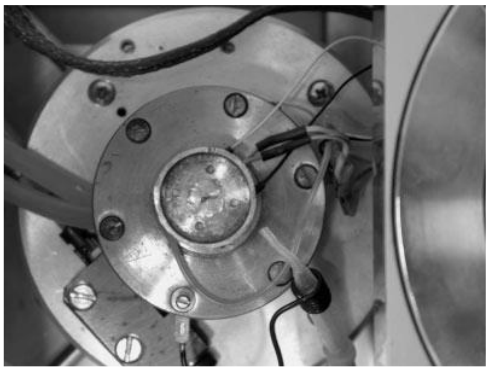

Fig. 3. The solidified agar base in a special cup placed on the Peltier cooled specimen holder of the environmental SEM AQUASEM II.

Fig. 4. Specimen of the small intestine embedded in agar; the cup is placed on the Peltier-cooled holder.

The observation of the biological specimen prepared by the CPD method in Figure 2 shows the dried but undamaged biological specimen microstructure. It enables us to determine criteria for the evaluation of the degree of damage of small intestine villi microstructure by dehydration, the emergence of hydration craters on the specimen surface and the suitability of individual methods of additive hydration.

In the first experiment, where the small intestine specimen observed in the water vapor environment of high relative humidity is placed on the Peltier-cooled holder, partial microstructure damage (dehydration craters) is seen after some 40 min at the pressure of 750 Pa (5.63 Torr) and temperature 4°C (Fig. 5B). With respect to pressure and specimen temperature value, in Figures 5B and 5C, the specimen dehydration according to the curve on Figure 1 conforms to expectations. On the contrary, in the case of Figure 5A, the thermodynamic condition is set in the

hydration zone of Figure 1; the water vapor condenses on the specimen surface and the specimen is covered by a thin layer of water, which hides the specimen surface and the relevant topographic structure information remains invisible.

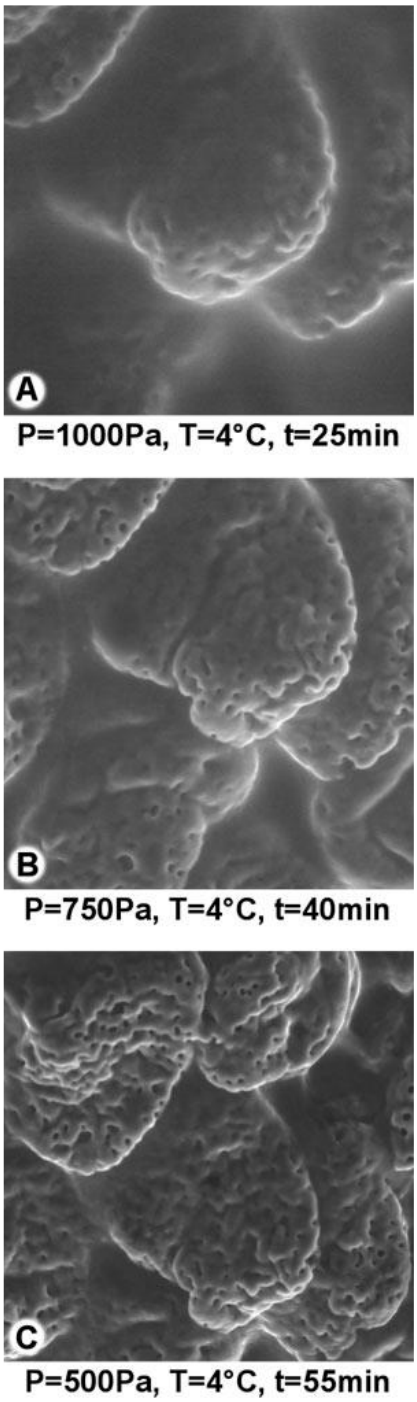

Fig. 5. Specimen of the small intestine placed on the Peltier-cooled specimen holder, at selected times and at changing water vapor pressure ESD, field of view 200 μm.

The results of the second experiment, in which the specimen is placed on the agar base, show surprisingly that the same specimen has not been damaged by dehydration at the same pressure of 750 Pa (5.63 Torr), temperature 4°C and

observation time of 40 min (Fig. 6B). This can be explained by the influence of additive hydration resulting from water evaporating from the agar, demonstrated by Sanger et al. (2003). The evaporation keeps the specimen and its close vicinity sufficiently wet, up to the critical pressure and temperature values, namely from the first pressure reduction in the environmental SEM specimen chamber. The presence of the agar close to the specimen creates differences in equilibrium vapor pressures, which is the key parameter for hydration or dehydration of specimen as discussed by Cameron and Donald (1994). It implies that agar preferentially evaporates to provide vapor for the particular specimen used. If the conditions of specimen temperature and water vapor pressure are set as in Figure 6C, the agar containing a large quantity of water is nevertheless unable to compensate the lack of humidity and the specimen will be dehydrated and damaged.

In Figure 6A whose thermodynamic condition is in the hydration zone, the relevant topographic structure is also invisible by the covered water on the specimen surface.

By surrounding the specimen by the agar so that most of the specimen is covered by agar and only the specimen surface being examined protrudes slightly from the agar surface, the additive hydration of the whole volume is maximized. This arrangement also enables us to minimize the temperature difference between the observed specimen surface and the agar, measured on the Peltier-cooled holder. Knowledge of the real temperature of the specimen allows us to set and maintain the optimum thermodynamic conditions so that long-time observation without dehydration is possible (Figs. 7A–7C). The only disadvantage of this method is the relatively high instability of the specimen position caused by the change of volume and shape of the agar as it dries. This disadvantage can be minimized by using the position-fixing pin to hold the specimen in the same position. The positive influence of the additive wetting arises from the agar hydration in this experiment. Figure 7B and particularly Figure 7C (500 Pa, 48C, 55 min) show neither specimen dehydration nor damage of its microstructure.

During the last experiment, the specimen was again placed on the Peltier-cooled holder and water vapor from a thin heated capillary tube brought close to the specimen surface was blown over it. The positive influence of additive hydration can be seen in Figures 8B and 8C and it is comparable with the results of the preceding experiment. Moreover, the position of the specimen does not have to be fixed. The surface microstructure of small intestine villi remains undamaged even after the thin water coating has evaporated from the specimen surface (see Figure 8C), which enables us to obtain higher-quality topographic information about the specimen. The complexity of the last method, in particular the design of the heated thin capillary tube, is its only disadvantage.

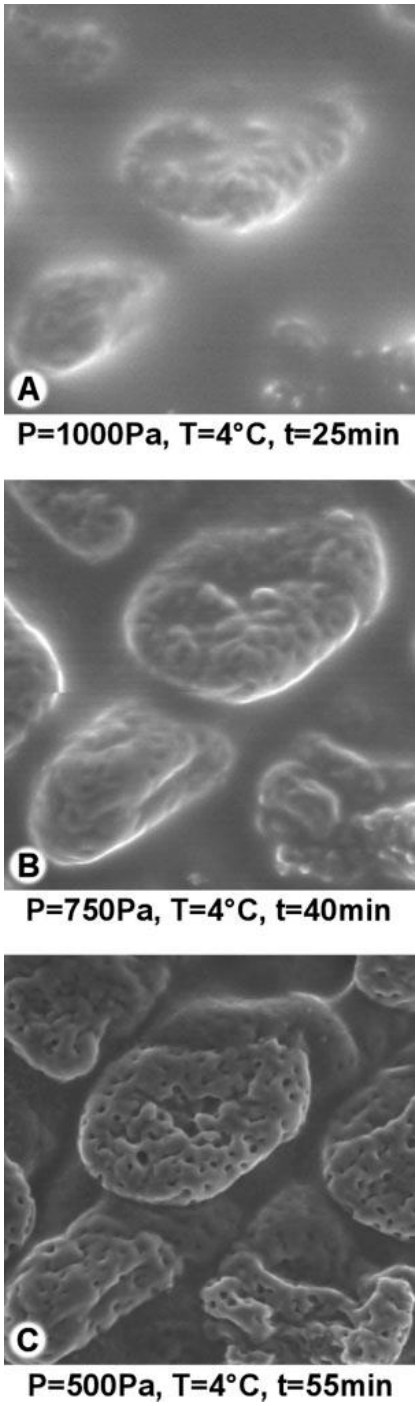

Fig. 6. Specimen of the small intestine placed on the cooled agar plate, at selected times and at changing water vapor pressure, ESD, field of view 200 μm.

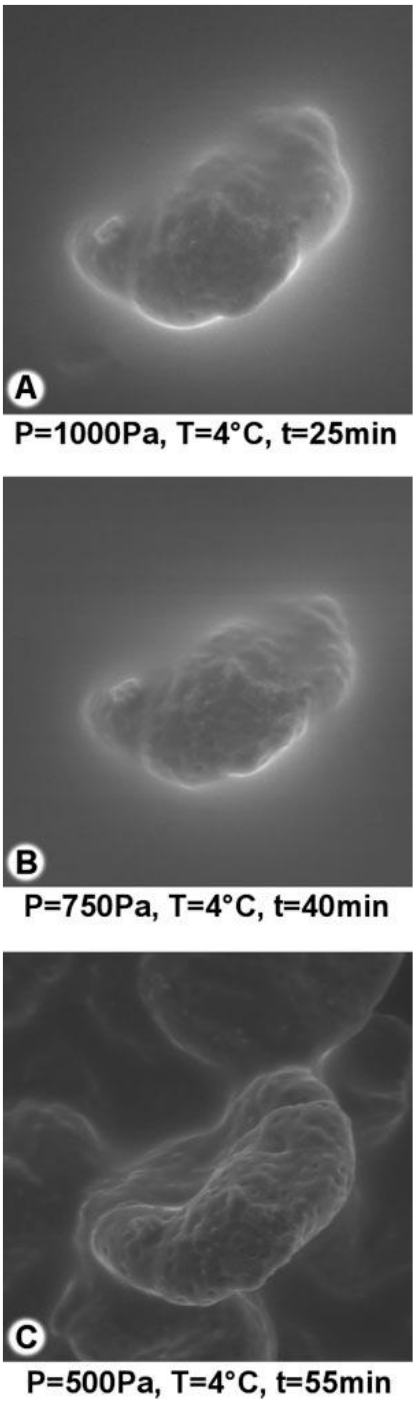

Fig. 7. Specimen of the small intestine surrounded by the cooled agar plate, at selected times and at changing water vapor pressure, ESD, field of view 200 μm.

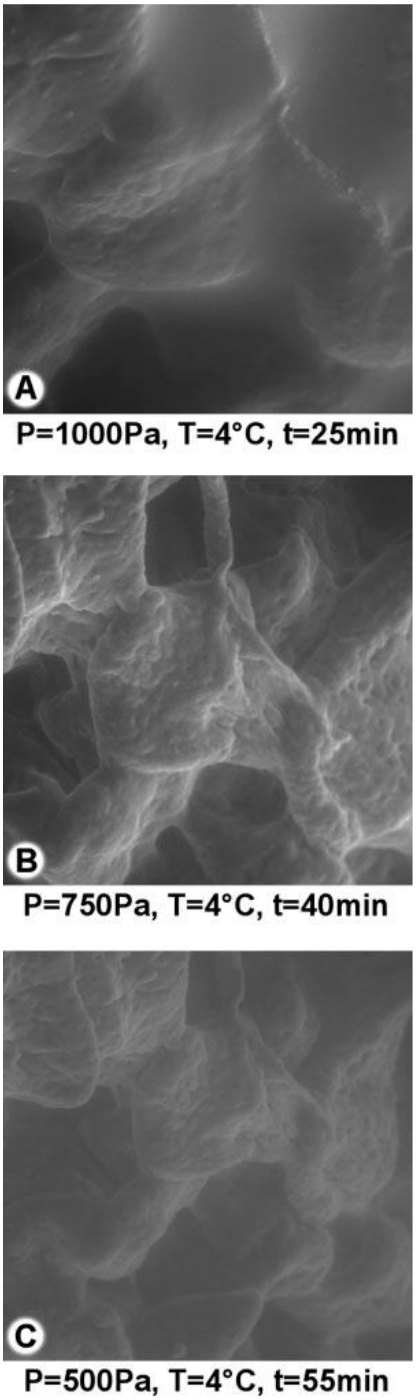

Fig. 8. Specimen of the small intestine placed on the Peltier-cooled specimen holder and water vapor blown from the thin capillary tube on the specimen, at selected times and at changing water vapor pressure, ESD, field of view 200 μm.

The suitability of the additive hydration methods for observing sensitive biological specimens in environmental SEM emerges clearly from these experiments. In particular, the method in which the specimen is surrounded by agar can be recommended, because it is very cheap and efficient. The method provides maximum additive hydration of a large specimen area, and thanks to the good

thermal conductivity of agar that minimizes the gradient between the temperature measured on the Peltier-cooled specimen holder and that of the surface, resulting from the poor thermal conductivity of thick biological specimens. Good results were also obtained by blowing water vapor from the thin capillary tube over the specimen, but this is more complex from the application point of view.

These additive hydration methods enable us to optimize the thermodynamic conditions of the specimen and yield satisfactory results. They can be recommended particularly for use in older or noncommercial electron microscopes of the environmental SEM type, where the control system of water vapor transfer into the specimen chamber has not been optimized.

ACKNOWLEDGMENTS

The author thanks Ing. L. Ilkovics from the Institute of Histology and Embryology of the Faculty of Medicine of the Masaryk University in Brno for his help during experiments and for preparation of the specimens. He also thanks Prof. B. Lencová for numerous consultations and much advice connected with the preparation of the paper. His special thanks are to the late Prof. R. Autrata, who supervised his PhD research and who contributed a great deal to this investigation and to whom he would like to dedicate this paper.

REFERENCES

Cameron RE, Donald AM. 1994. Minimizing sample evaporation in the environmental scanning electron microscope. JMicrosc 173:227–237.

Danilatos GD. 1988. Foundations of environmental scanning electron microscopy. Adv Electron Electron Phys 71:109–250.

Danilatos GD. 1990. Theory of the gaseous detector device in the environmental scanning electron microscopy. Adv Electron Electron Phys 78:1–102.

Lane WC. 1970. The environmental control stage. Scan Electron Microsc 1970:43–48.

Moncrieff DA, Robinson VNE, Harris LB. 1978. Charge neutralisation of insulating surfaces in the SEM by gas ionisation. J Phys D 11:2315–2325.

Neděla V, Maxa J. 2006. Environmental scanning electron microscope AQUASEM II—The design and applications. In: Proceedings of the 10th International Seminar Skalsky´ Dvu˚ r, ISI AS CR Brno, 2006 pp. 55–56.

Robinson VNE. 1975a. The elimination of charging artefacts in the SEM. J Phys E 8:638–640.

Robinson VNE. 1975b. Awet stage modification to a scanning electron microscope. J Microsc 103:71–77.

Romanovský V, Autrata R. 2000. Combined scintillation and ionisation detectors for environmental scanning electron microscopes. In: Proceedings of the 12th EUREM, Czechoslovak Society of Electron Microscopy, 2000, Vol. 3, pp. 241–242.

Sanger P, Ritter M, Hohenberg H. 2003. Water reservoirs (matrices) prevent rapid dehydration of native samples in the environmental scanning electron microscope (ESEM). Microsc Microanal 9 (Suppl. 3):494–495.

Stokes DJ. 2003. Investigating biological ultrastructure using environmental scanning electron microscopy (ESEM). In: Méndez-Vilas A, editor. Science, technology and education of microscopy: An overview. Badajoz, Spain: Formatex. pp. 564–570.

6 The Impact of Critical Flow on the Primary Electron Beam Passage through Differentially Pumped Chamber

J. Maxa[1] and V. Neděla[2]

[1] *Department of Electrotechnology, Faculty of Electrical Engineering and Communication, Brno University of Technology, Brno, Czech Republic*

[2] *Institute of Scientific Instruments of the ASCR, Academy of Sciences of the Czech Republic, Brno, Czech Republic*

Abstract

Environmental scanning electron microscope creates new possibilities in the field of examination of various types of specimens and their phases. The article analyses and compares the results of air pumping measurement for selected shapes of the differentially pumped chamber to create vacuum, using the Cosmos FloWorks system.

Keywords

EREM, CAE, SolidWorks, Cosmos, FEI, Differentially Pumped Chamber

Introduction

High pressure in gases (up to 3000 Pa) in the specimen chamber of the variable pressure scanning electron microscope (VP-SEM) sets specific requirements for construction of the microscope and its pumping system. The design of individual construction parts of VP-SEM, mainly the differentially pumped chambers must meet specific requirements for efficient pumping of their interior and minimization of pressure. The specific technological requirements are sufficiently compensated by a wide scope of applications in both the vacuum mode and the high pressure mode [1].

The rather big difference in pressure originating between the specimen chamber ($3 \square 10^3$ Pa) and around the source of electrons ($10^{-3} \square 10^{-9}$ Pa, according to source type) in VP-SEM, can be maintained only due to the system of differentially pumped chambers, pressure limiting screens (PLA1 and PLA2 in Fig. 2) and an efficient gas pumping system. In the screens there are holes of the order of tens to hundreds of micrometres in diameter that can effectively restrict the gas flow between the individual parts of the micro-scope, and at the same time allow the passage of electrons from the source to the specimen [2]. The system of chambers and screens is usually integrated in the column of EREM. For pumping, usually a system of rotary, diffusion or turbomolecular vacuum pumps (the interior of the specimen chamber and adjacent differentially pumped chambers), or possibly ion vacuum pumps (the source of electrons) are used.

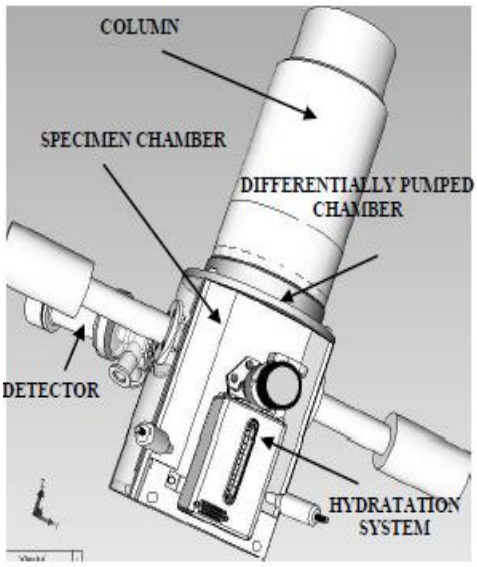

Fig. 1 AQUASEM II [2]

Due to the high pressure of gases in the EREM specimen chamber, there is an increased occurrence of interactions of electrons with molecules and atoms of gases (mainly water vapours). Subsequently the original primary electron beam diffuses. The diffusion of primary electrons increases with increasing pressure, average atomic number of gas, working distance and decreasing accelerating voltage in the beam. The diffusion results in an increased diameter of the trajectory of the primary electron beam. Consequently the signal/noise ratio in the detected signal is less favourable, and the final effect may be a deteriorated resolution of the microscope [3].

AQUASEM

The construction of now fully operating experimental VP-SEM AQUAEM II as a successor of the previous version of this microscope was completed, in cooperation with TESCAN Ltd, in 2007 at the Institute of Instrument Techno-logy, Academy of Sciences in Brno [1]. The key application of the microscope is testing new detection systems opera ting in conditions of high pressure in gas or vacuum, study of special water containing or non-conducting specimens difficult to monitor and dynamic „in-situ“ experiments.

Because of the above-mentioned reasons, an optimal variant of the shape of the differentially pumped chamber was sought as the chamber is the principal construction element for adaptation of the microscope for work in high pressure conditions. Pumping the chamber efficiently is the crucial requirement affecting the qualitative parameters of the microscope, such as the maximal magnitude of gas

pressure in the specimen chamber, amount of noise in the detected signal closely associated with microscope resolution, etc.

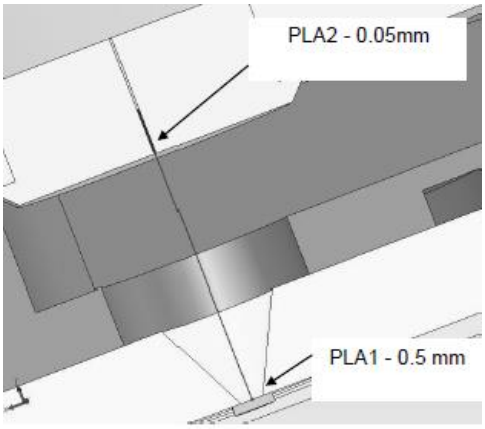

Fig. 2 Electron path leading through the high pressure environment in the differentially pumped chamber of AQUAESM II.

A vital parameter for the final design of the differentially pumped chamber is the minimum gas pressure in the microscope optical axis. In Fig. 2, this trajectory is drawn in red. The area is the same in all variants (see Fig. 3). There are differences in the shape and in the manner of pumping. On the basis of our previous experience, three preliminary shapes were proposed.

Variant 1 (closed) – Gas from the passage area of the primary electron beam through the differentially pumped chamber is pumped in one direction and through the area between the microscope lens and the differentially pumped chamber (Fig. 3A). In this variant, the delimited area for gas passage is constructed in such a way that gas can follow the shortest possible path to the rotary vacuum pump.

Variant 2 (open) – Gas is pumped from the passage area of the primary electron beam through the differentially pumped chamber in one direction, similarly to the first variant C. It passes, however, through the entire area between the microscope lens and the differentially pumped chamber (see Fig. 3B).

Variant 3 (conical) – Gas is pumped from the space for passage of the primary electron beam through the differentially pumped chamber in all directions over the maximal possible free area and it goes away in the same way (Fig. 3C). The gas off take in this variant is identical with variant 2.

the variants were modelled using the SolidWorks system and the Cosmos FloWorks module for analysis of gas flow in seeking an optimal shape.

For calculations executed using the Cosmos FloWorks the following marginal requirements were defined. On the PLA 2 screen with a hole 0.05 mm in diameter, located between the microscope column and the differentially pumped chamber, the static pressure of 0.01 Pa is required. Analogically, in the case of the PLA 1 screen with a hole 0.5 mm in diameter separating the differentially pumped chamber and the specimen chamber (Fig. 2, Fig. 3E), the gradually set pressure values were 200, 400, 600, 800, 1000 Pa. These values are most frequently required for the VP-SEM specimen chamber.

For the pumping hole in the differentially pumped chamber the mass flow of the pumped gas was set at 0.00347 kg/s. in dependence on the selected rotary vacuum pump. In symmetrical objects, Cosmos FloWorks can be used to set computation for only a half of the symmetrical objects, and thus the computing time can be substantially reduced. In real conditions, therefore, the mass flow value is doubled.

Pressure in Primary Electron Beam Area in Monitored Variants

In order to select an optimal variant, it is necessary to evaluate the pressure and mainly the density trends directly in the trajectory of the primary electron beam. That is why line C was drawn in the trajectory (Fig. 2) where the system will evaluate pressure and density values and transform them into a table to be used for plotting on graphs.

Results in Fig. 4 show that the conical variant is not suitable for our purpose. Important information obtained from Fig. 4 is the fact that the pressure in the specimen chamber has no particular effect on the magnitude of average pressure in the trajectory of the primary beam.

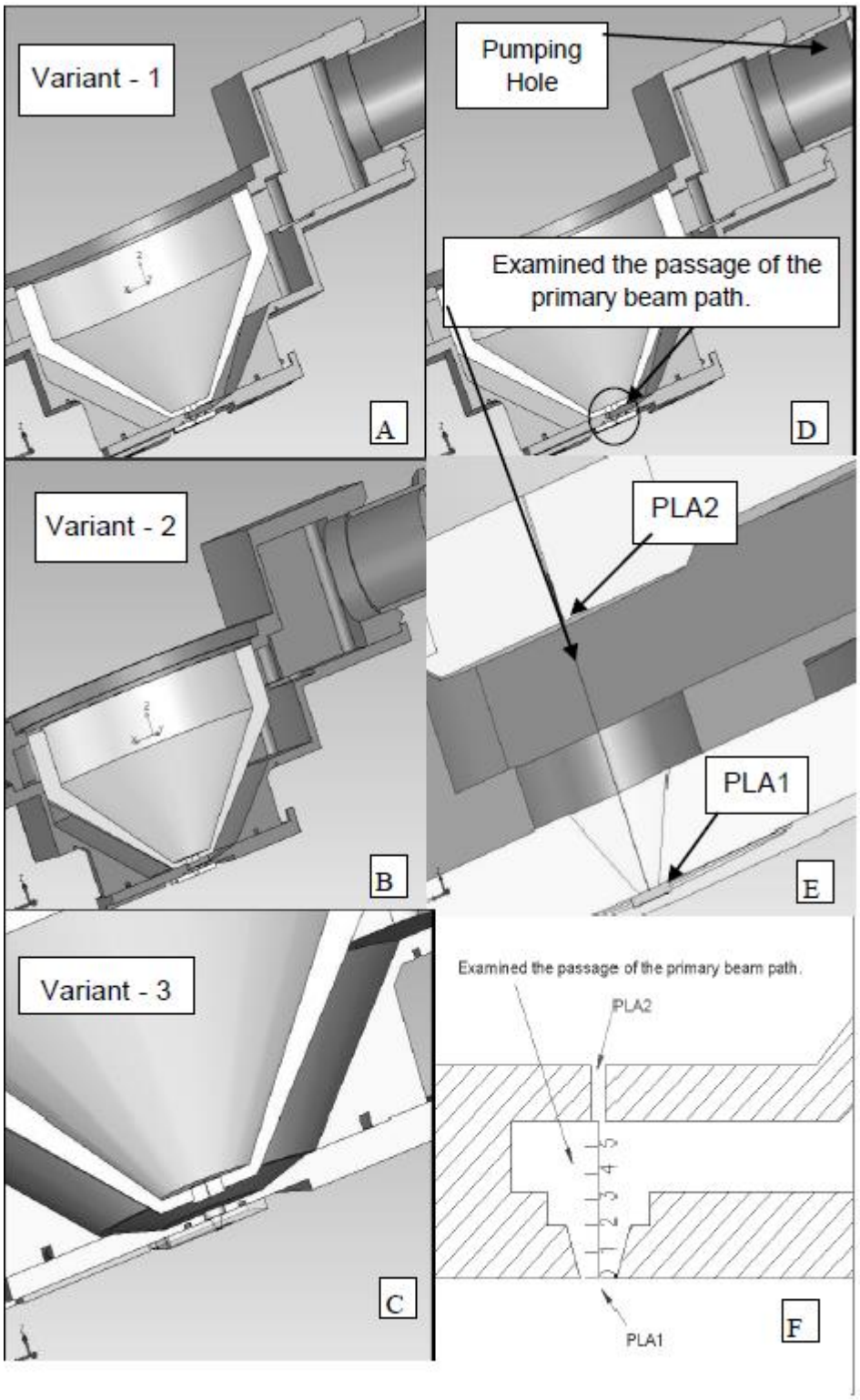

Fig. 3 Variants of differentially pumped chambers

This phenomenon is based on the principle of so-called critical flow originating at the edge of a small dimension hole separating areas of high pressure fall. In our

case, it is the fall between the specimen chamber and the differentially pumped chamber on screen PLA 1.

As can be seen from the results, in both open and closed variant of the differentially pumped chamber at the edge of PLA 1 screen, all values of the set pressures reach the above mentioned critical values of flow. Behind PLA 1 screen, the flow beam first widens in the mode of supersonic gas flow up to a certain distance in dependence on the variant and pressure in the specimen chamber. Then the supersonic flow beam narrows to the point where the beam passes into under sonic gas flow. This fact is of great importance as in the area of supersonic flow the pressure of the environment decreases. The drop of pressure between the specimen chamber and the differentially pumped chamber is directly proportional to the dimensions of the expansion cone of supersonic flow behind PLA 1, therefore the low pressure area is longer. This observation for the studied case is shown in Fig. 5. Fig. 5 shows the expansion cone for the closed variant for the pressure of 200 Pa in the specimen chamber in the left part of the figure, and for the pressure of 1000 Pa on the right. The cone thus eliminates a direct relationship of pressure in the specimen chamber and average pressure in the trajectory of the primary beam in the differentially pumped chamber.

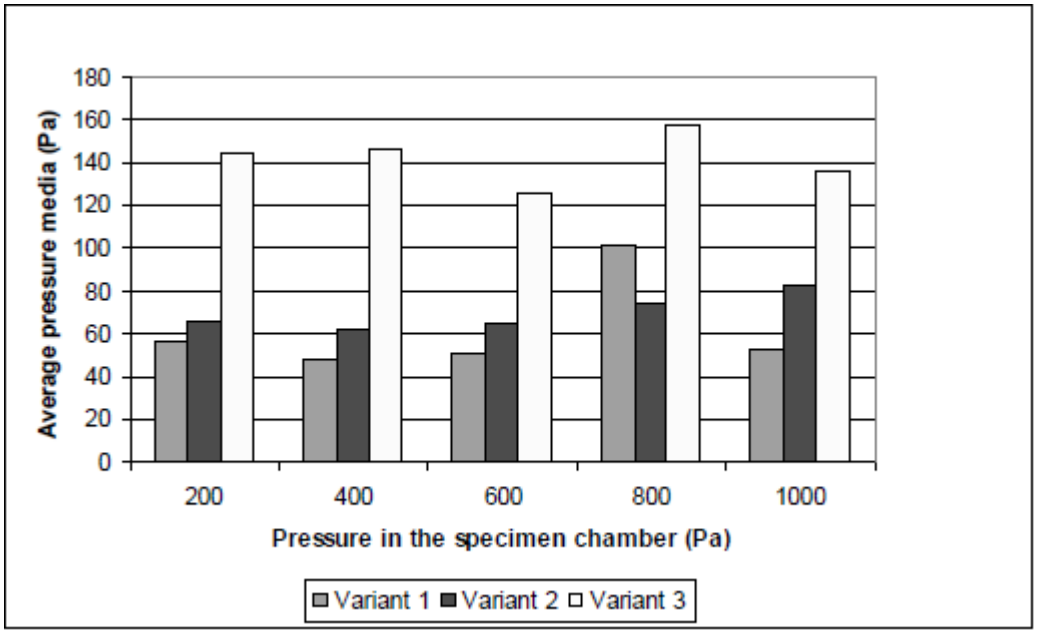

Fig. 4 Average pressure in the trajectory of the primary electron beam

This observation is described in detail in the graph in Fig. 6, where another observation is apparent. In case of large reductions of pressure, there is not only a

longer expansion cone but also a certain pulsation – drop and subsequent increase – of flow rate. It is a monitored characteristic of supercritical flow that can be used for more efficient passage of the primary beam through the differentially pumped chamber at a higher pressure in the specimen chamber as it extends the low pressure area.

The flow behind PLA1 screen can be described using Fig. 7. The edges of the output cross section A-A1 cause the turbulence in the output flow. Behind the cross section, the gas flow is affected by pressure in the vicinity of P_{amb}, which is lower than the critical pressure P_{cr}. At this gate P_{cr} changes into P_{amb} and two expansions A-A1-B and A1-A-B1 formed by elementary expansion waves appear. They intersect at point D.

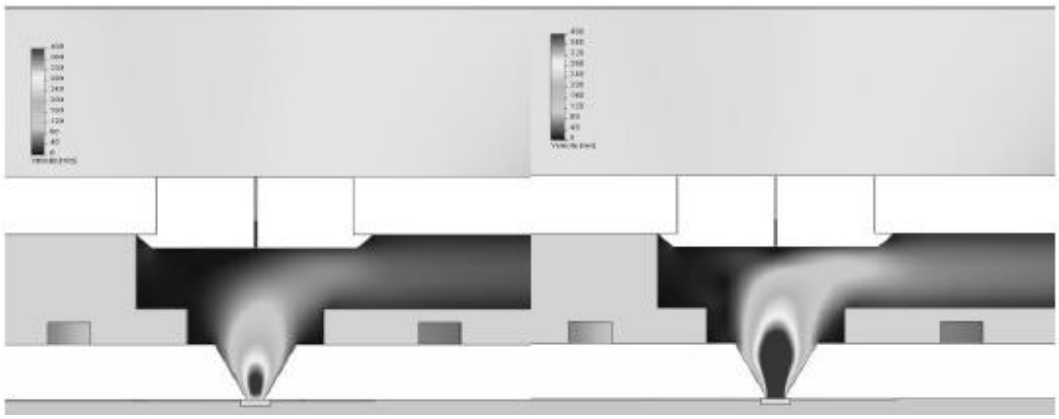

Fig. 5 Expansion of supersonic flow for 200 Pa and 1000 Pa

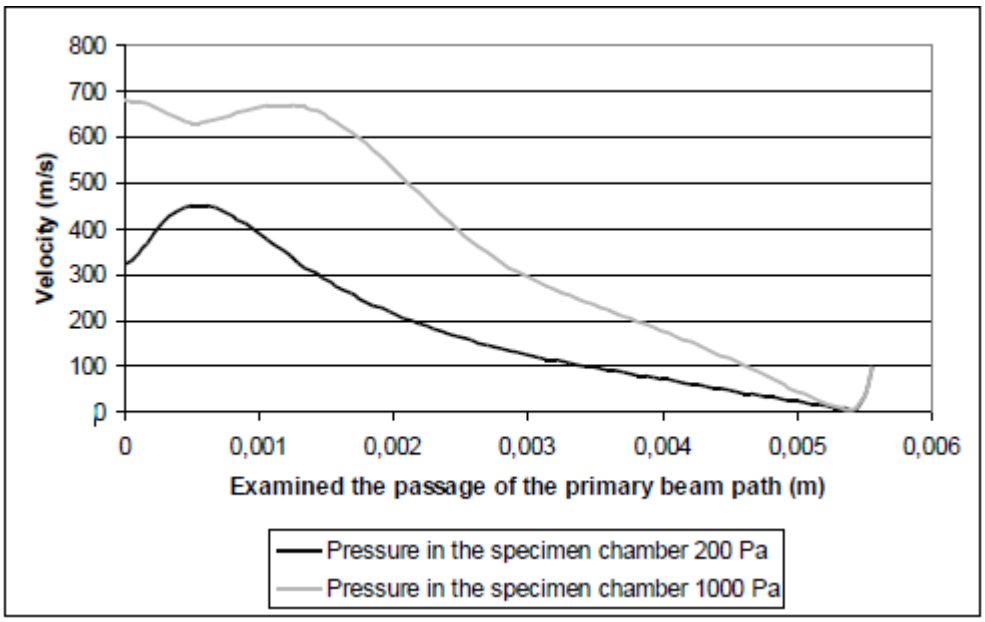

Fig. 6 Flow rate in the trajectory of the primary beam.

The result of this process is the wedge of thinning A-A1-D. Inside it, the pressure is substantially reduced. Then the pressure is lower than P_{amb}. In the second wedge DB- B1, the pressure increases and in section B-B1 it reaches the value of P_{cr}. Thus the wedge of thinning passes into the wedge of thickening. In this section the reiteration of the cycle starts, then P_{cr} changes into P_{amb} again. In the mentioned graph the pulsation is apparent in the variant for the

pressure of 1000 Pa in the specimen chamber. The graphic representation is in Fig. 8. The results show that in the closed variant pulsation starts at 600 Pa in the specimen chamber, in the open variant at 500 Pa. In the conical variant, due to lower rates, pulsation does not occur.

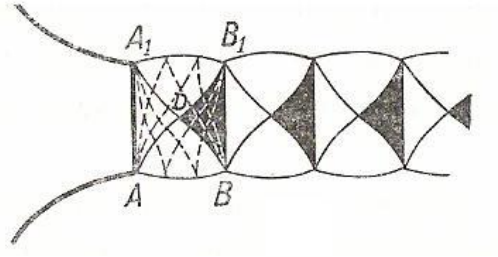

Fig. 7 Expansion waves behind the edge of the jet [4].

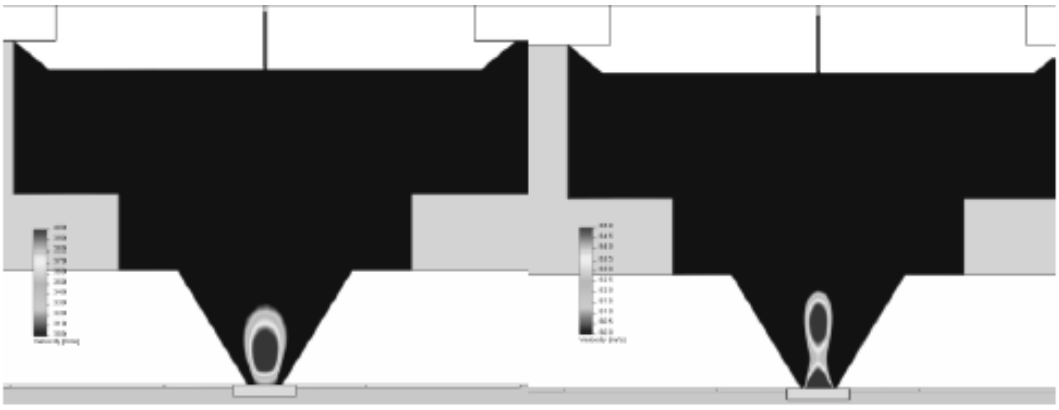

Fig.8 Double expansion wave in the 1000 Pa variant.

The given characteristics of the critical flow are used in the design of the differentially pumped chamber as they substantially affect the density of the medium in the trajectory of the primary beam, as it follows from elementary equations. One directional flow of an ideal gas in a tube of a variable flow diameter can be described by equation:

$$p = r\rho T$$

and three laws:

law of conservation of mass:

$$Q_m = \rho v A = const. \text{ [kg/s]}$$

law of conservation of motion:

$$e = \frac{v^2}{2} + \frac{\kappa}{\kappa - 1}\frac{p_0}{\rho_0}\left(\frac{p}{p_0}\right)^{\frac{\kappa-1}{\kappa}} \text{ [J/kg]}$$

and law of conservation of energy:

$$e = \frac{v^2}{2} + c_p T = const. \text{ [J/kg]}$$

with P – static pressure, r – universal gas constant, ρ – density, T – temperature, A – area, v – *velocity*, Q_m – mass flow, e – internal energy, κ – Poisson constant, c_p – specific heat.

The average values of medium density in the trajectory of the primary beam, as well as the average values of the pressure, show that the conical shape of the chamber is absolutely unsuitable, mainly because of the low flow rates, which means that the physical laws associated with critical flow in the medium behind a small hole, in our case PLA1screen, are not taken into account.

The results for the remaining two variants are very similar, though on the whole, the closed variant is the more acceptable one.

Tab. 1 Results for the density of secondary electrons on the track in the detector

PRESSURE IN THE SPECIMEN CHAMBER (Pa)	ARITHMETIC MEAN OF MEDIUM DENSITIES (g/m^3)		
	VARIANT 1	VARIANT 2	VARIANT 3
200	0.75	0.81	1.73
400	0.63	0.92	1.68
600	0.84	0.88	1.60
800	0.79	1.05	2.20
1000	1.10	1.20	1.52

Conclusion

On the basis of the above analyses, we could evaluate also those spots in sections of the differentially pumped chamber where gauges for experimental measurements cannot be placed, however information on flow conditions is indispensable for construction.

Results of analyses offer new possibilities for modifications of construction of the differentially pumped chamber.

References

[1] NEDĚLA, V. and AUTRATA, R. Environmental Scanning Electron Microscopy (in Czech). *Československý časopis pro fyziku*, 2005, vol. 55, no. 3, p. 251-251. ISSN 0009-0700.

[2] NEDĚLA, V., MAXA, J. and AUTRATA, R. Environmental Scanning Electron Microscope Aquasem II – the Design and Applications. In *Proceedings of 10th Seminar Recent Trends in Charged Particle Optics and Surface Physics Instruments*. Brno : Institute of Scientific Instruments of AS CR, 2006, p. 55-56, ISBN 80-239-6285-X

[3] NEDĚLA, V. and MAXA, J. Hydration System for Environmental Scanning Electron Microscopes (in Czech). *Jemná mechanika a optika*, 2006, vol. 2006, no. 11-12, p. 329-332. ISSN 0447-6441.

[4] DEJČ, ME. *Technical Dynamics of Gases* (in Czech). Praha : SNTL, 1967.

7 Apertures with Laval Nozzle and Circular Orifice in Secondary Electron Detector for Environmental Scanning Electron Microscope

P. Vyroubal[1], J. Maxa[1], V. Neděla[2], J. Jirák[1,2] and K. Hladká[1]

[1] *Department of Electrotechnology, Faculty of Electrical Engineering and Communication, Brno University of Technology, Brno, Czech Republic*

[2] *Institute of Scientific Instruments of the ASCR, Academy of Sciences of the Czech Republic, Brno, Czech Republic*

Abstract

Environmental scanning electron microscopes offer wide possibilities for the exploration of various types of specimens, especially non-conductive and wet specimens containing different material phases. The evaluation of pressure on the secondary electrons trajectory is one of the important parameters in design of scintillation detector of secondary electrons. The final process is influenced by the size and the shape of the apertures used to separate areas with different pressure gradient. This article is focused on the comparison of the aperture with circular orifice and aperture with Laval nozzle.

Keywords

Aperture, Laval nozzle, circular orifice, pressure, detector, Mach number, flow, trajectory of secondary electrons.

Introduction

Scintillation and ionization detectors are used to detect secondary electrons. The ionization detector works on the principle of impact ionization. The scintillation detector contains a scintillator (e.g. YAG, CRY 18, etc.) which releases electrons when they hit a flash of light whose intensity is proportional to the energy of incident electrons [1].

The scintillator in the scintillation detector of secondary electrons is placed in a separately pumped chamber separated from the specimen chamber by apertures C1 and C2 (Fig. 1). Electric potential of hundreds of volts is applied on the apertures.

Apertures form electrostatic lens. Secondary electrons are directed by the electrodes to the lens in the mouth of the detector and then the electrons pass through it. Apertures also prevent gas flow from the sample chamber into the scintillator chamber. In the specimen chamber there is a gas pressure from 0.01 to 1,000 Pa.

At the maximum pressure of 5 Pa in the scintillator chamber, a voltage up to 8 kV can be attached to the scintillator without causing a gas discharge. This voltage accelerates the electrons through the apertures with an energy which is sufficient to generate scintillation. Photons created by scintillation are kept in the light guide into photomultiplier, where they are amplified and converted into an electrical signal [2].

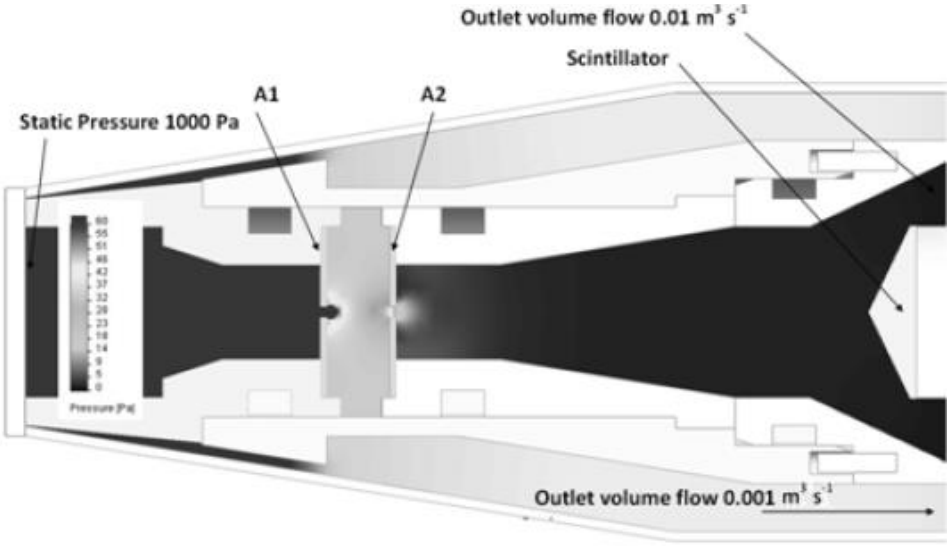

Fig. 1 Functional scheme of the scintillation detector of secondary electrons

The orifices of small dimensions are found in the construction of the electron microscope, where it is necessary to separate areas with a large pressure gradient without the possibility of perfect isolation (Fig. 2). The pressure in the fluid flow depends on the speed of flow. The higher the speed is, the lower gas pressure can be achieved by reducing the size of the orifice in apertures or changing their shape [3-5].

In terms of detectors, the following aspects are important:

1. The pressure in the area of a scintillation crystal must be higher than 5 Pa to avoid electric discharge in the gas because of the high voltage on the scintillator (up to 8 kV).

2. Average pressure on the trajectory of secondary electrons must be low to avoid scattering of electrons.

Mathematical Interpretation

For the modelling of individual apertures, the SolidWorks detector and SolidWorks Flow Simulation were used and thus the flow can be calculated using the finite

volumes method. Flow Simulation solves a system of three partial differential equations, completed with a fourth equation of state. It is a type of three-dimensional flow of compressible viscous fluid. Basic equations describing the flow of viscous compressible fluid written in conservative form are three conservation laws, law of conservation of mass, momentum and energy completed with the fourth equation of state of the considered fluid [6].

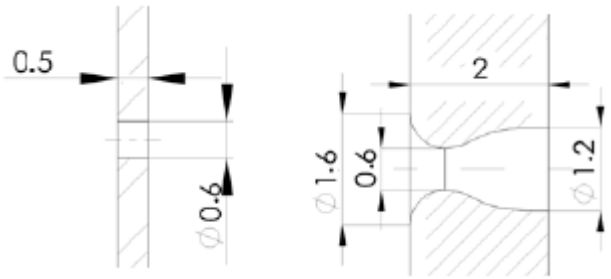

Fig. 2 Illustration of the detector and investigated apertures in Flow Simulation

Continuity equation (1) expresses the law of conservation of mass and it takes the form

$$\frac{\partial \rho_d}{\partial t} + \frac{\partial}{\partial x_i}(\rho_d u_i) = 0$$

where r_d is the symbol of density, u_i is the velocity.

Navier-Stokes equations (2) express Newton's theorem applied to the change of momentum in the form

$$\frac{\partial(\rho_d u_i)}{\partial t} + \frac{\partial}{\partial x_j}(\rho_d u_i u_j) + \frac{\partial p}{\partial x_i} = \frac{\partial}{\partial x_j}(\tau_{ij} + \tau_{ij}^R) + S_i$$

where p is the symbol of pressure, τ_{ij} is the viscous stress tensor.

Energy equation (3) expresses the law of conservation of energy for compressible fluid and it takes the form

$$\frac{\partial \rho_d E}{\partial t} + \frac{\partial \rho_d u_i}{\partial x_i}(-\bar{l} + P) = \frac{\partial}{\partial x_i}\left[u_j(\tau_{ij} + \tau_{ij}^R) + 9i\right] + \tau_{ij}^R \frac{\partial u_i}{\partial x_j} + \rho_d \varepsilon + S_i u_i + Q_H$$

The equation of state (4) for the considered ideal gas is as follows:

$$\rho_d = \frac{pM}{RT}$$

In the above mentioned equations *ui* is the fluid velocity, *p* is the fluid pressure, r_d the fluid density, *M* the molar mass of the fluid, *T* the temperature of the fluid, *E* the internal energy, S_i the external mass forces (gravity, centrifugal), *Q*H the supply and heat dissipation per volume unit, *qi* the flow heat, τ_{ij} the viscous stress tensor and indexes *ij* indicate summation variables in three directions according to the coordinates (Einstein summation) [7].

The Mathematical – physical model

The forces acting on a moving electric charge in an electromagnetic field can be expressed by the specific Lorentz force according to relation [8]

$$\boldsymbol{f}_e = \rho(\boldsymbol{E} + \boldsymbol{v} \times \boldsymbol{B})$$

where $\boldsymbol{B}$ is the magnetic flux density vector in the space of a moving electrically charged particle with the volume charge density r, $\boldsymbol{v}$ is the mean velocity of the particle, and $\boldsymbol{E}$ is the electric intensity vector [9]. Then, the specific force acting on the moving of electrically charged particles with charge q_e and number N_e and – in the monitored area – with volume *V* is

$$\boldsymbol{f}_e = \frac{d(N_e q_e)}{dV}(\boldsymbol{E} + \boldsymbol{v} \times \boldsymbol{B})$$

On the moving particle in the system *A'*, the relativity effect from the place of the observer system *A* must still be applied. The model (6) includes this effect. In the example provided by reference [10], current density in the *A* system is $\boldsymbol{J} = \rho\,\boldsymbol{v}$, for mutually moving Cartesian coordinate system *A*-*A´* in the component form [11]

$$\boldsymbol{J} = J'_x\boldsymbol{u}_x + J'_y\boldsymbol{u}_y + J'_z\boldsymbol{u}_z + jc\rho'\boldsymbol{u}_t$$

where $\boldsymbol{J}$ is the current density 4-vector, $J'_{x,y,z}$ are its components in the Cartesian coordinates *A´*, *j* is a symbol which indicates an imaginary part of the complex variable (in a harmonious state of phase-shifted by p/2), *c* is the velocity of light and r´ is the volume density of electric charge in the system *A´*.

The continuity equation can be formulated as follows

$$div\,\boldsymbol{J} = -\frac{\partial \rho}{\partial t}$$

After applying the Lorentz transformation to simplify the moving systems in the direction of *x*, current density (7) can be written in the form

$$\boldsymbol{J} = \frac{J'_x + j\frac{v_x}{c}J'_t}{\sqrt{1-\left(\frac{v}{c}\right)^2}}\boldsymbol{u}_x + J'_y\boldsymbol{u}_y + J'_z\boldsymbol{u}_z + j\frac{c\rho' - \frac{v_x}{c}J'_x}{\sqrt{1-\left(\frac{v}{c}\right)^2}}\boldsymbol{u}_t$$

where v is the instantaneous particle velocity module (system A) and v_x is its component in the direction of the x axis. To eliminate possible errors in the nondynamic system of Maxwell reduced equations, it is suitable to include the term which respects Faraday's law of induction [11]

$$rot\boldsymbol{E} = -\frac{\partial \boldsymbol{B}}{\partial t} + rot(\boldsymbol{v} \times \boldsymbol{B})$$

and for the magnetic field relation (10)

$$rot\boldsymbol{H} = \boldsymbol{J} + \frac{\partial \boldsymbol{D}}{\partial t} + rot(\boldsymbol{v} \times \boldsymbol{D})$$

The complete Maxwell equations are covariant in all systems, therefore it is not important to specify the system within which the observer moves, because the described relations always hold true. After the derivation of the four-vector and respecting the Lorentz transformation [12], for the moving electric charge with density r from the viewpoint of two individual systems relatively moving at the velocity $\boldsymbol{v}$ of A and A', the source current density is written in the form

$$\boldsymbol{J} = \rho\frac{\partial \boldsymbol{s}}{\partial t}jc\rho\boldsymbol{u}_t$$

where $\boldsymbol{s}$ is the position vector of a material point in the coordinate system A. Then equation (5) or (6) for the specific force acting on an elementary particle with an electric charge q_e and current density $\boldsymbol{J} = N_e q_s \boldsymbol{v}$ is

$$\boldsymbol{f}_e = \boldsymbol{J}v^{-1}(\boldsymbol{E} + \boldsymbol{v} \times \boldsymbol{B})$$

with respect to relative movement systems A-A' the specific power is (14)

$$\boldsymbol{f}_e = \left(\rho\frac{\partial \boldsymbol{s}}{\partial t} + jc\rho\boldsymbol{u}_t\right)v^{-1}(\boldsymbol{E} + \boldsymbol{v} \times \boldsymbol{B})$$

The total specific force acting on the moving electrically charged particles with respect to the velocity of moving electrically charged particles $\boldsymbol{v}$ in the magnetic field is:

$$\boldsymbol{f}_e = \left[\frac{d(N_e q_e)}{dV}\frac{\partial \boldsymbol{s}}{\partial t} + jc\frac{d(N_e q_e)}{dV}\boldsymbol{u}_t - \frac{\partial(\varepsilon \boldsymbol{E})}{\partial t} + rot(\boldsymbol{v}\times\boldsymbol{D})\right] v^{-1}\left[\boldsymbol{E} + \frac{1}{N_e q_e}\left(\frac{m d\boldsymbol{v}}{dt} + l\boldsymbol{v} + k\int \boldsymbol{v}\, dt\right)\right] + \left[\frac{d(N_e q_e)}{dV}\frac{\partial \boldsymbol{s}}{\partial t} + jc\frac{d(N_e q_e)}{dV}\boldsymbol{u}_t - \frac{\partial(\varepsilon \boldsymbol{E})}{\partial t} + rot(\boldsymbol{v}\times\boldsymbol{D})\right]\times\boldsymbol{B}$$

where *m* is the particle mass which is given by the relation

$$m = \frac{m_0}{\sqrt{1-\frac{v^2}{c^2}}}$$

Further q_e is the electric charge of the moving particle, *l* is the damping coefficient, and *k* is the coefficient of stiffness of the ambient environment. Material relations for the macroscopic part of the model are represented by the expressions

$$\boldsymbol{B} = \mu_0\mu_r\boldsymbol{H}$$

and

$$\boldsymbol{D} = \varepsilon_0\varepsilon_r\boldsymbol{E}$$

where the indexes of quantities of permeabilities and permittivities *r* denote the quantity of the relative value and the 0 value of quantity for vacuum. By applying the Galerkin method to find the functional minimum and respecting the boundary conditions, the numerical model is obtained as a system of non-linear equations. It will be possible to solve the system of equations using standard methods.

The description of the coupled model with macroscopic properties is perceived inarea W_F with the pressure parameters which express a body balance (5) [11]

$$div\bar{\bar{T}} + \boldsymbol{f} = \frac{\partial(\rho_d \boldsymbol{v})}{\partial t} \text{ in the are } W_{F,}$$

where r_d is the fluid density and $\boldsymbol{v}$ is the vector of instantaneous velocity. Stress tensor of the relationship (19) can be written as follows (generalized Hooke's law)

$$\bar{\bar{T}} = \overline{\overline{D_F}}\cdot\bar{\bar{e}}$$

Specific deformation tensor is expressed in the form

$$\bar{\bar{e}} = \begin{bmatrix} \frac{\partial s_x}{\partial x} & \frac{\partial s_x}{\partial y} - \frac{\partial s_y}{\partial x} & \frac{\partial s_x}{\partial z} - \frac{\partial s_z}{\partial x} \\ \frac{\partial s_x}{\partial y} - \frac{\partial s_y}{\partial x} & \frac{\partial s_y}{\partial y} & \frac{\partial s_y}{\partial z} - \frac{\partial s_z}{\partial y} \\ \frac{\partial s_x}{\partial z} - \frac{\partial s_z}{\partial x} & \frac{\partial s_y}{\partial z} - \frac{\partial s_z}{\partial y} & \frac{\partial s_z}{\partial z} \end{bmatrix}$$

Putting the stress tensor (20) and power density (15) into equation (19) and itemizing this equation we obtain

$$(\lambda_1 + \lambda_2) grad\ div\boldsymbol{s} + \lambda_2 \nabla^2 \boldsymbol{s} + \boldsymbol{f}_s = \frac{\partial(\rho_d \boldsymbol{v})}{\partial t}$$

where λ_1, λ_2 are

$$\lambda_1 = \frac{E_u \sigma}{(1+\sigma)(1-2\sigma)}$$

and

$$\lambda_2 = \frac{E_u}{2(1+\sigma)}$$

For Poisson ratio s appliess ¹ -1Ùs ¹ 0.5 .

This work does not deal with particle trajectories; however, it is focused on the evaluation of the pressure gradient in a small nozzle area. Then it is possible to linearize this model piecewise.

Finite Element/ Volume Method

The finite volume method is a discretization method which is well suited for the numerical simulation of various types of conservation laws. It has been extensively used in several engineering fields, such as fluid mechanics, heat and mass transfer or petroleum engineering. Some of the important features of the finite volume method are similar to those of the finite element method. The method may be used on arbitrary geometries, using structured or unstructured meshes, and it leads to robust schemes.

The finite volume method is a numerical method for solving partial differential equations that calculates the values of the conserved variables averaged across the volume. One advantage of the finite volume method over finite difference methods is that it does not require a structured mesh (although a structured mesh can also be used). Furthermore, the finite volume method is preferable to other methods as a result of the fact that boundary conditions can be applied noninvasively. This is true because the values of the conserved variables are located within the volume element, and not at nodes or surfaces. Finite volume methods are especially powerful on coarse nonuniform grids and in calculations where the mesh moves to track interfaces or shocks [13-15]. The method is used in many computational fluid dynamics packages [16].

A supersonic flow created by apertures with circular orifices is accompanied by a local reduction in pressure (Fig. 3). This is an advantage in relation to the scattering of secondary electrons. There is a slight local decrease in pressure. Some energy is lost to the free expansion of gas around the nozzle mouth due to its geometry (Figs 4 and 5).

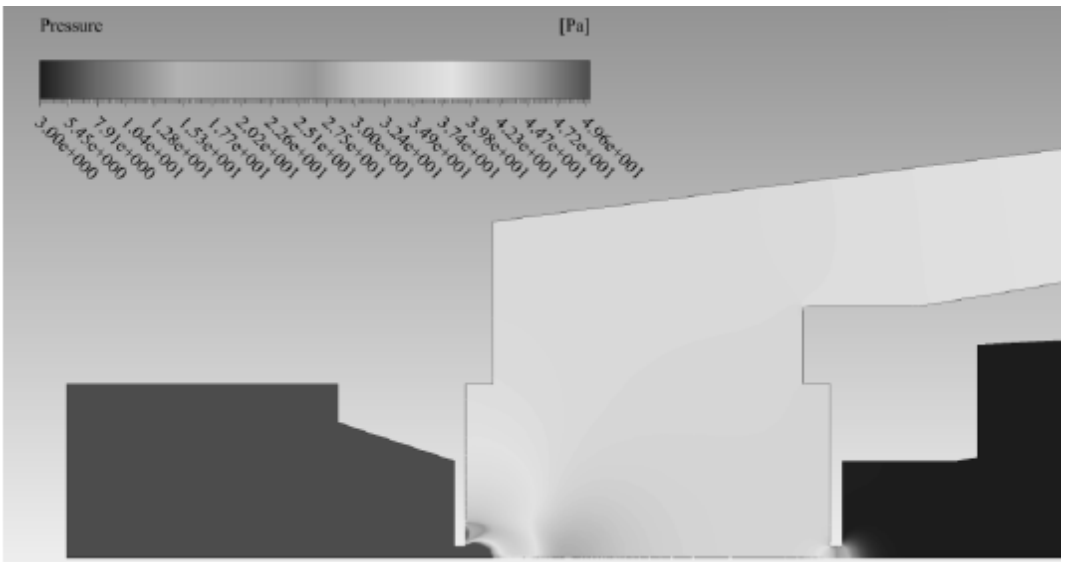

Fig. 3 The pressure as it passes through the first aperture (circular orifice)

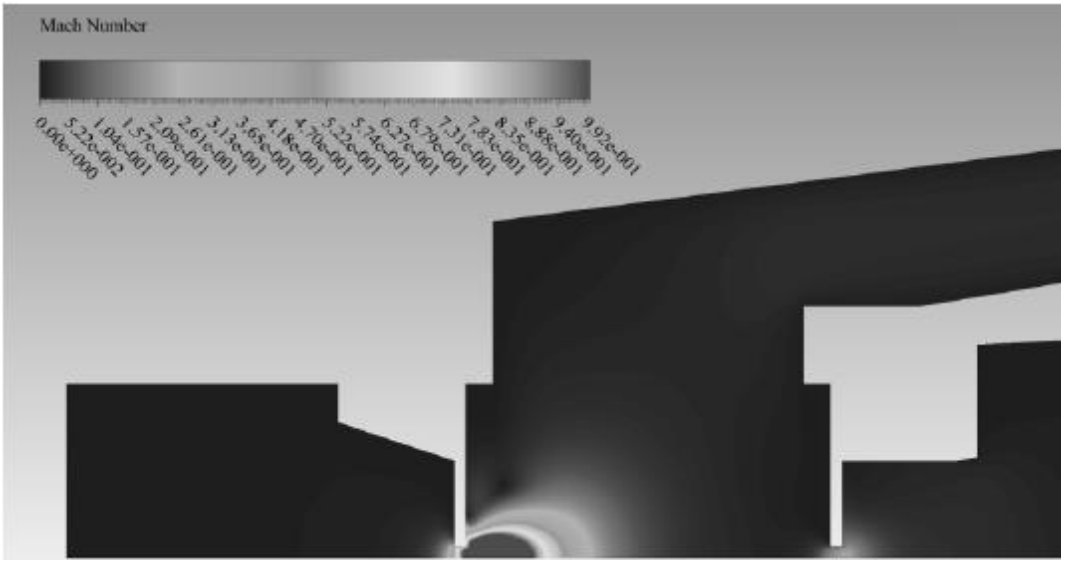

Fig. 4 The Mach number as it passes through the first aperture (circular orifice)

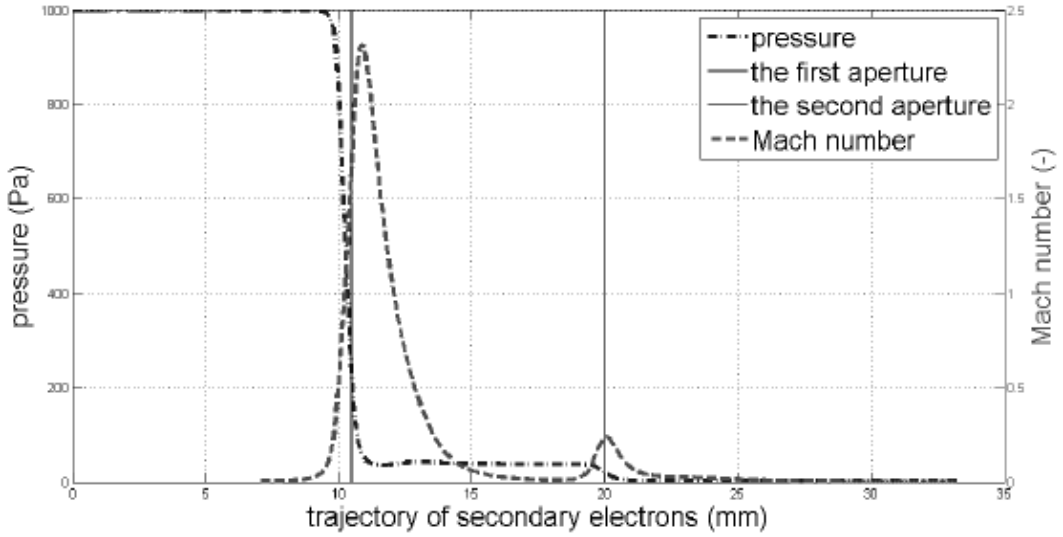

Fig. 5 Pressure profile and Mach number in apertures with circular orifice

The energy lost in uncontrolled expansion allows the use of the Laval nozzle, which consists of a convergent part (tapers to a critical section) and divergent part, which directs the gas expansion to the critical cross section (Fig. 6). In the convergent part the gas reaches the critical speed and in the divergent part the gas is further accelerated (Fig. 7).

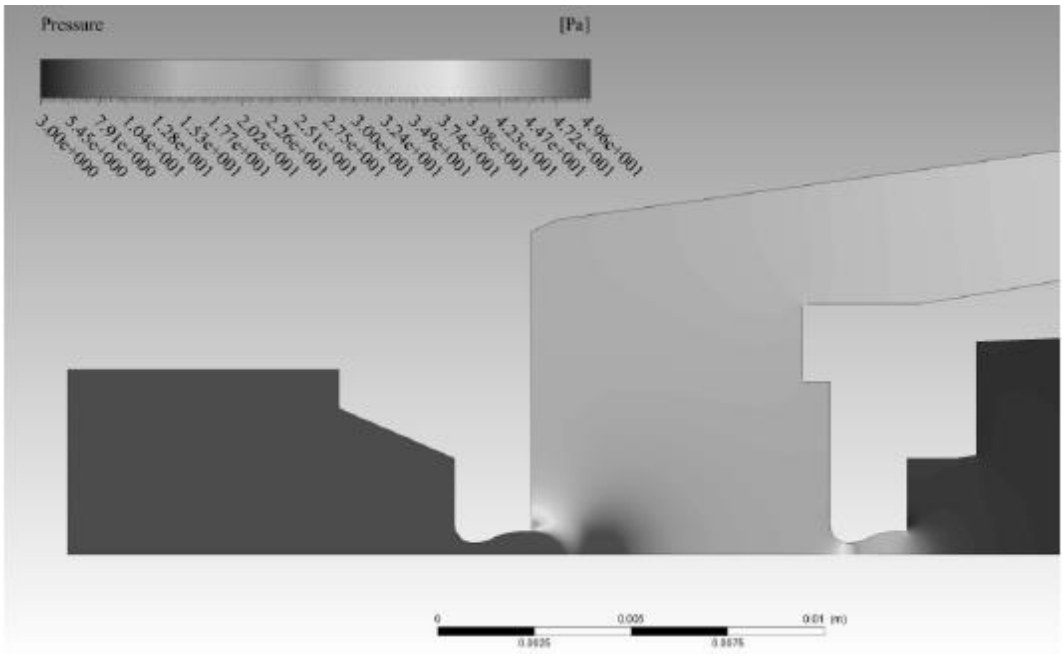

Fig. 6 The pressure as it passes through the first aperture (Laval nozzle)

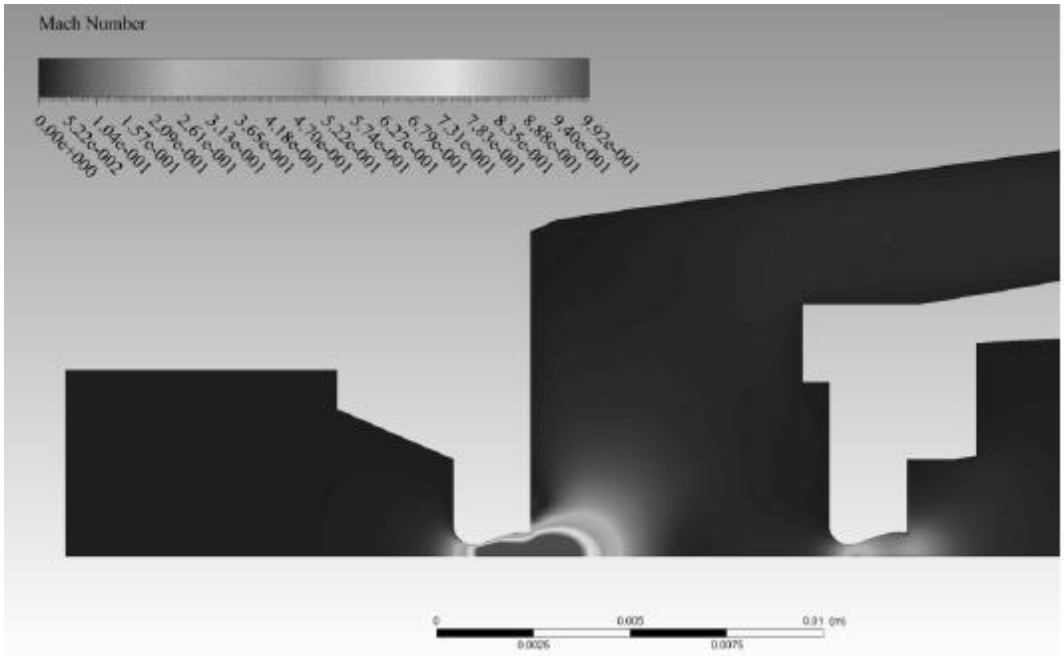

Fig. 7 The Mach number as it passes through the first aperture (Laval nozzle)

The characteristic feature of the Laval nozzle is called a double expansion wave, which can be used to streamline the passage of the secondary electrons through the detector at a higher pressure in the specimen chamber (Fig. 8). Double expansion wave extends the area of low pressure. This affects the media pressure conditions entering into the second aperture and thus the pressure at the scintillator.

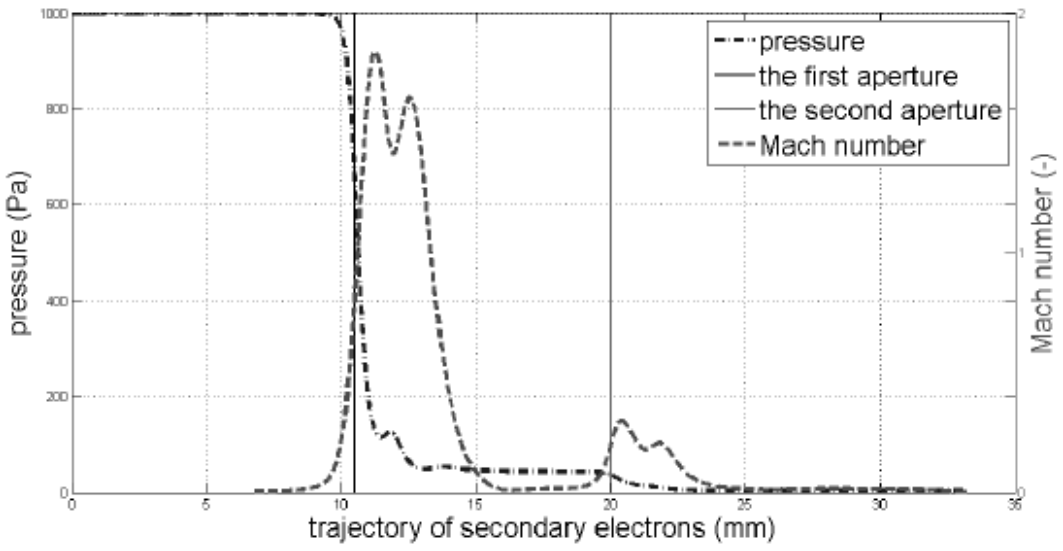

Fig. 8 Pressure profile and Mach number in apertures with Laval nozzle.

Discussion

The supersonic flow through the aperture can cause shock waves. This is a significant compression of gas at short distances, which may create a barrier to the passage of electrons. The shock wave is a step change value (pressure, density), and it creates a discontinuity which in the calculations by the finite volume method cannot be described without a correct approximation type. The second order upwind method was used to investigate shock waves. Figures 3, 4, 6, and 7 show us the pressure compression behind the aperture. It assumes that shock waves can occur in these places.

Conclusion

When setting up pressures in the range of 200 to 1000 Pa at the inlet of the scintillator, the results show that at the Laval nozzle pressure drops faster than at an aperture with a circular orifice. Due to the requirement to maintain the pressure on a lower trajectory of secondary electrons in the scintillator chamber, the aperture with the Laval nozzle appears to be better.

Aperture C1 determines the pressure ratios across the detector. Gas that enters into it is moving into a critical state and moves at supersonic speed. Gas entering into aperture C2 is already moving at subsonic speeds, far below the Mach number. In some cases, swirls are formed directly in apertures or even before the entry into the first aperture, which again affects the pressure in the detector.

References

[1] JIRÁK, J., NEDĚLA, V., ČERNOCH, P., ČUDEK, P. and RUNŠTUK, J. Scintillation SE detector for variable pressure scanning electron microscopes. *Journal of Microscopy,* 2010, vol. 239, no. 3, p. 233-238. DOI: 10.1111/j.1365- 2818.2010.03377.x.

[2] DANILATOS, G. Design and construction of an atmospheric or environmental SEM (part 3). *Scanning,* 1985, vol. 7, no. 1, p. 26-42. DOI: 10.1002/sca.4950070102.

[3] DANILATOS, G. Velocity and ejector-jet assisted differential pumping: Novel design stages for environmental SEM. *Micron*, 2012, vol. 43, no. 5, p. 600-611. DOI:10.1016/j.micron.2011.10.023.

[4] MAXA, J., NEDĚLA, V., JIRÁK, J., VYROUBAL, P. and HLADKÁ, K. Analysis of Gas Flow in a Secondary Electron Scintillation Detector for ESEM with a new system of Pressure limiting Apertures. *Advances in Military Technology*, 2012, vol. 7, no. 2, p. 39-44. ISSN 1802-2308.

[5] MAXA, J., NEDĚLA, V. and JIRÁK, J. Analysis of Gas Flow in the new system of Apertures in the Secondary Electron Scintillation Detector for ESEM. *Microscopy and Microanalysis*, 2012, vol. 18, supplement 2, p.1264-65. ISSN 1431-9276.

[6] VERSTEEG, K. and MALALASEKERA, W. *An Introduction to Computational Fluid Dynamics: The Finite Volume Method*. Reading, Addison- Wesley, 1995. 257 p.

[7] VYROUBAL, P. and MAXA, J. Analysis of the Impact of Supersonic Flow in Detector of Secondary Electrons ESEM. In *Proceedings 2nd Computer Science On-Line Conference*. Ithaca: Cornell University 2012, p. 149-155.

[8] FIALA, P. Pulse-powered virtual cathode oscillator. *Transactions on Dielectrics and Electrical Insulation*, 2011, vol. 18, no. 4, p. 1046-1053. ISSN 1070-9878.

[9] BAČA, P. Possibilities of electric power storage from renewable sources. *Acta Montanistica Slovaca,* 2010, vol. 15, special issue no, 2, p. 100-104. ISSN1335- 1788.

[10] FIALA, P., FRIEDL, M. and SZABÓ, Z. EMHD Models Respecting Relativistic Processes of Trivial Geometries. *Progress in Electromagnetics*, 2011, vol. 2011, p. 96-99. ISSN 1559- 9450.

[11] STRATTON, JA. *Electromagnetic Theory*. New York: Mc Graw-Hill, 1941. 630 p.

[12] KIKUCHI, H. *Electrohydrodynamics in dusty and dirty plasmas, gravitoelectrohydrodynamics and EHD*. Kluwer Academic Publishers, 2001, 228 p.

[13] MAXA, J. and NEDĚLA, V. Impact of the critical Flow on Conditions of the Primary Electron Beam passage through the Differentially Pumped Chamber. *Advances in Military Technology*, 2011, vol. 6, no. 1, p. 39-47. ISSN 1802- 2308.

[14] HYMAN, M. and KNAPP, R. High Order Finite Volume Approximations of Differential Operators on Nonuniform Grids. *Physica D: Nonlinear Phenomena*, 1992, vol. 60, no. 1-4, p. 112-138. ISSN 0167-2789.

[15] RÜBENKÖNIG, O. *The Finite Volume Method (FVM)*. [cited 2012-12-12]. Available from: <www.imtek.unifreiburg. de/simulation/mathematica/imsReferencePointers/FVM_introDocu.htm>

[16] MAXA, J., VYROUBAL, P., VANĚK, J. and SOLČANSKÝ, M. The finite volume method in photovoltaic – The cooling system of concentrator solar panels. *ECS Transactions*, 2013. ISSN 1938-6737 (in print).

Acknowledgement

This work was supported by the EU project No. CZ.1.05/2.1.00/01.0014, project FEKT-S-11-7 and Czech Science Foundation: grant No. GAP 102/10/1410.

8 Scintillation SE detector for variable pressure scanning electron microscopes

J. JIRÁK,*†, V. NEDĚLA∗, P. ČERNOCH†, P. ČUDEK† & J . RUNŠTUK∗

∗ *Institute of Scientific Instruments of ASCR, Královopolská, Czech Republic*
† *Department of Electrical and Electronic Technology FEEC BUT, Údolní, Czech Republic*

Keywords Scintillation detector, secondary electrons detection, variable pressure scanning electron microscope.

Summary

We present results obtained with a new scintillation detector of secondary electrons for the variable pressure scanning electron microscope. A detector design is based on the positioning of a single crystal scintillator within a scintillator chamber separated from the specimen chamber by two apertures. This solution enables us to decrease the pressure to several Pa in the scintillator chamber while the pressure in the specimen chamber reaches values of about 1000 Pa (7.5 Torr). Due to decreased pressure, we can apply a potential of the order of several kV to the scintillator, which is necessary for the detection of secondary electrons. Simultaneously, the two apertures at appropriate potentials of the order of several hundreds of volts create an electrostatic lens that allows electrons to pass from the specimen chamber to the scintillator chamber. Results indicate a promising utilization of this detector for a wide range of specimen observations.

Introduction

The variable pressure scanning electron microscopes (VPSEMs) can be used for observation of wet specimens, insulators without conductive layer coating as well as for dynamic in situ experiments (Robinson, 1978; Danilatos, 1988; Stokes, 2003; Postek & Vladár, 2004; Mathews, 2002; Rice & Knowles, 2005; Toth et al., 2005a,b; Neděla, 2007, 2008).

In high-pressure conditions of the VPSEM, a signal of backscattered electrons (BSEs) can be detected by the same means as in the high-vacuum conditions, but detection of secondary electrons (SEs) becomes complicated if a potential of several kV in the specimen chamber is required for their additional acceleration. For the detection of SEs in the VPSEM, several new detectors have been developed since the first experiments with the gaseous environment surrounding specimens were published (Robinson, 1978). These detectors can be divided into two groups: (i) the

detectors that take advantage of a cascade amplification of signal electrons in the gaseous environment in an electrostatic field at the electric field strength typically from tens to hundreds of V/mm (Danilatos, 1990; Fletcher *et al*., 1999; Morgan & Phillips, 2006a; Thiel *et al.*, 2006) and (ii) the scintillation detectors.

The detectors of the group (i) can be designed for the detection of charged particles generated predominantly by SEs or by BSEs or generated by a mixture of these electrons (Danilatos, 1990; Morgan&Phillips, 2006a). It is also possible to detect photons, originated in excitation processes in cascade collisions of signal electrons with gaseous environment (Danilatos, 1988, 1990; Morgan & Phillips, 2006b). Both the charged particles and the photon detection systems contain electrodes that are placed near the specimen and are usually positively biased in respect to the specimen so the electrostatic field causing the cascade amplification of electrons is created (Knowles, 1995; Heinz, 2004a; Morgan & Phillips, 2006a,b; Thiel *et al.*, 2006). In specific conditions, the cascade amplification of electrons can be enhanced by a magnetic field (Thiel *et al*., 2006).

In the scintillation SE detectors, the SEs have to be accelerated to the energy of the order of several keV by an electrostatic field in order to efficiently produce scintillations in a scintillation material. For positioning of these detectors in the specimen chamber of the VPSEM, complications with electric discharges that originate in the gaseous environment in the electrostatic field of a high electric field strength must be solved. A way to prevent electric discharges can be found in an arrangement, in which the scintillator is emplaced, and the mentioned electrostatic field is created in a scintillator chamber of the pressure of several Pa at the most.

This chamber must be separated from the specimen chamber by one or more ‘barriers’ that restrict a gas flow but allow the signal electrons to pass through. Such barriers can be made from a thin aluminium foil reinforced by a Mylar grid (Heinz, 2002, 2004b), from a metal grid or a metal-coated polyimide grid (Jacka *et al*., 2003), from a combination of an aperture and a microporous plate (Slówko, 2001, 2007) or from two apertures (Jirák & Skřivánek, 2003). The pressures in the individual chambers separated from the specimen chamber by these barriers are lowered towards the scintillator by appropriate vacuum pumping.

In this article, we present a scintillation detector designed for the detection of the SE signal and positioned in the specimen chamber of the VPSEM. The transmission of the electrons and the restriction of the gas flow towards the scintillator are achieved by two apertures that are hundreds of micrometres in diameter and at potentials of hundreds of volts.

Scintillation SE detector for VPSEM

The idea presented here of using the SE scintillation detector at high-pressure conditions of the VPSEM is based on the design in which the scintillator chamber is separated from the specimen chamber by two apertures A1 and A2, as shown in Fig. 1. The chamber between the apertures and the scintillator chamber is vacuum pumped by a rotary and turbomolecular pump in order to achieve a minimal pressure in the vicinity of the scintillator, with respect to the pressure in the specimen chamber. The two apertures, A1 and A2 (Fig. 1), set at appropriate potentials, create an electrostatic lens for transmission of the signal electrons from the specimen chamber towards the scintillator of the detector.

Collection efficiency of the detector as well as focusing of detected electrons to the optical axis of the detector are optimized using an electric field created by voltages on electrodes E1 and E2, which are, like apertures A1 and A2, electrically insulated from the grounded metal body of the detector.

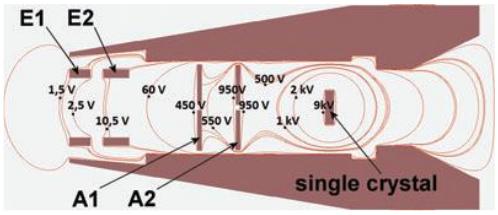

Fig. 1. Detector cross-section with equipotential lines. E1, E2 – focusing electrodes with voltages of 1.5 V and 10 V, respectively. A1, A2 apertures with voltages of 500V and 1000V, respectively. Scintillation single crystal with a voltage of 10 kV. Equipotential lines were simulated by program Simion 3D ver. 7.

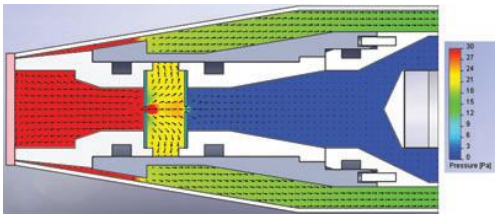

Fig. 2. Pressure distribution and pressure flow lines obtained by simulation of gas flow in scintillation SE detector. Input simulation parameters: pressure of 600 Pa (4.5 Torr) in specimen chamber, set of apertures A1 and A2, diameters 0.6 mm and 0.6 mm, set of vacuum pumping speeds 1.1 l/s for chamber between apertures and 10 l/s for scintillator chamber.

Distribution of equipotential lines in the detector computed for commonly used working conditions by the program SIMION 3D 7.0 (Bechtel BWXT Idaho, LLC, Idaho Falls, ID, U.S.A.) is shown in Fig. 1.

To optimize gas flow and pumping of the detector, computer simulations of the gas flow by the program Cosmos FloWorks (SolidWorks Corp., Concord, MA, U.S.A.) were utilized. The pressure distribution, pressure flow lines and pressure values at

chosen positions for input parameters corresponding to experimental set-up are shown in Fig. 2.

Results and discussion

The new SE scintillation detector for the VP SEM was installed to our experimental AQUASEM-II microscope (Neděla, 2008), which was designed in the Institute of Scientific Instruments (ISI) of the Academy of Sciences of the Czech Republic as a non-commercial apparatus for research on detection systems and ESEM techniques. This microscope is equipped with a tungsten hairpin filament and can be used for work at high pressure conditions of water vapour and some gases in the specimen chamber up to 2000 Pa.

Measurements of pressure in individual parts of the detector in dependence on pressure of water vapour in the specimen chamber were realized at first. A turbomolecular pump with the pumping speed 10 l/s supported by a membrane pump and a rotary pump with the pumping speed 1.1 l/s were chosen for the evacuation of the scintillator chamber and of the chamber between the apertures, respectively.

As seen from Fig. 3, the measured values of the pressure in the scintillation chamber were in a good accordance with the simulated ones, and a positive voltage of several kV could be attached to the scintillator without the risk of discharges in the gas. For the pressures in the chamber between the apertures, the measured values match the simulations only roughly.

Subsequently, we conducted a study of the dependence of the detected signal on the change of the potentials of the detector electrode system for the pressure range from 100 to 1000 Pa (0.75 to 7.5 Torr) in the specimen chamber. The detected signals were considered as signal levels recorded from chosen materials of a specimen by means of the greyscale mean values analysed in the specimen images (Jirák *et al*., 2005; Morgan & Phillips, 2006a). No post-processing image enhancements were applied for the analysis of greyscale mean values. The utilized specimen contained gold, copper and carbon sections. A hole in the carbon section was used for a primary electron beam current measurement. Position of the detector in the specimen chamber at the carried out measurements is shown in Fig. 4.

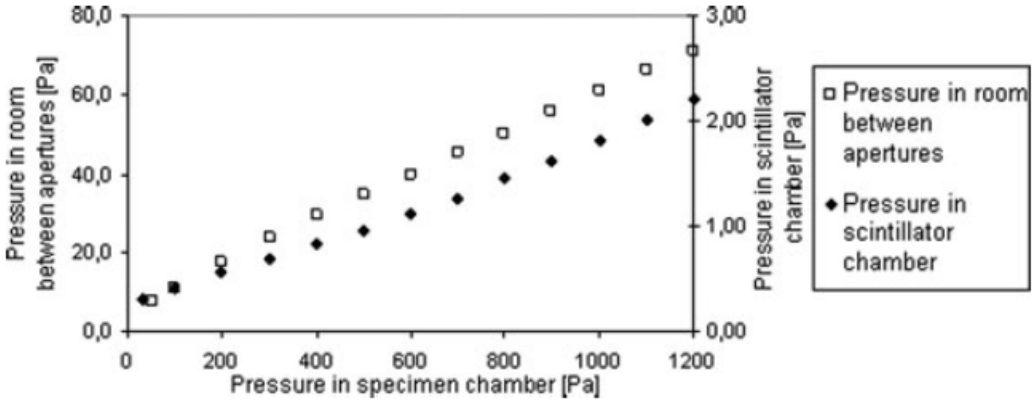

Fig. 3. Dependences of water vapour pressure in chamber between apertures and in scintillator chamber on pressure in specimen chamber for experimented set of apertures A1 and A2, diameters 0.6 and 0.6 mm.

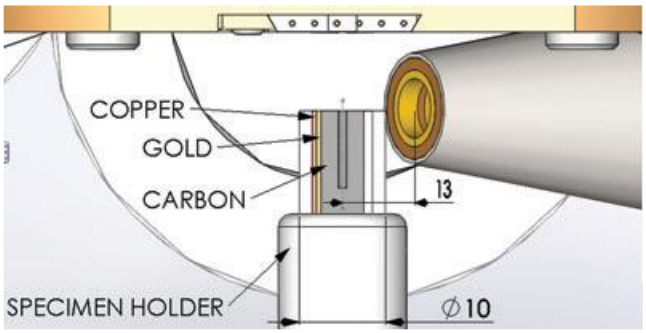

Fig. 4. Positions of detector and specimen in specimen chamber of microscope. Specimen consists of carbon cylinder with gold and copper wires.

For initial experimental measurements, the voltage on electrode E1 was 1.5V. Apparent from Fig.5a–eis the influence of voltage on the other electrodes of the detector and on the scintillator as well as the influence of the distance between the pressure limiting aperture (PLA) and the specimen on the signal level. The potentials of the detector electrode system used to obtain results in Fig. 5 are shown in Table 1.

It is apparent from the shape of the dependences in Fig. 5a that cascade amplification occurs mainly in the space of the detector before electrode A1 and is beneficial for the gain of the signal. It is also visible from the dependences in Fig. 5c that the increase of the voltage on the electrode E2 above the optimal value (15 V) brings the decrease of the signal level which is caused by the decrease of the strength of electric field between electrodes E2 and A1 resulting in lower amplification of the signal in the process of impact ionization in gaseous environment. Effect of the increase of the voltage on electrode A2 on the signal level growth is evident from Fig. 5b but the further growth of this voltage is accompanied by signal detection instability. Figure 5e shows dependences of signal

level for two different distances between the PLA and the specimen. However, the growth of this distance contributes to higher scattering of primary beam electrons and is accompanied by the growth of noise in the detected signal. Expected signal increment is connected with the increase of the voltage on the scintillator as seen in Fig. 5d.

As seen from Fig. 5a–e the detector with values of voltages introduced in Table 1 is capable to operate efficiently in the specimen chamber pressure range from 200 to 1000 Pa (1.5 to 7.5 Torr).

Subsequently, the way was searched how to increase the signal level also at pressures under 200 Pa in the specimen chamber. It is possible by increasing the voltage on electrode E1 to a value in the range from 100 to 300 V and by creating an electric field between the specimen and the detector that attracts SEs to the detector more efficiently. The change of the voltage on E1 brings the necessity of certain changes of voltages on the other electrodes compared to the values mentioned in Table 1.

The possibility of signal detection by this detector from the water vapour pressure value of50Pain the specimen chamber is evident from Figs 6 and 7. Figure 6 shows a 3-nm-thick carbon layer sputtered through the grid mask on silicone substrate. Figure 7 demonstrates the possibility of observing the voltage contrast on the pn emitter base junction of a power transistor. It is widely known that this carbon layer and the voltage contrast can be observed only when SEs are detected (Reimer, 1998).

The possibility to record image of specimens by this detector in the pressure range from 50 to 900 Pa is apparent from Fig. 8, where tin spheres on carbon are shown. Resolution of recorded images is limited by the parameters of experimental microscope equipped with hairpin tungsten cathode.

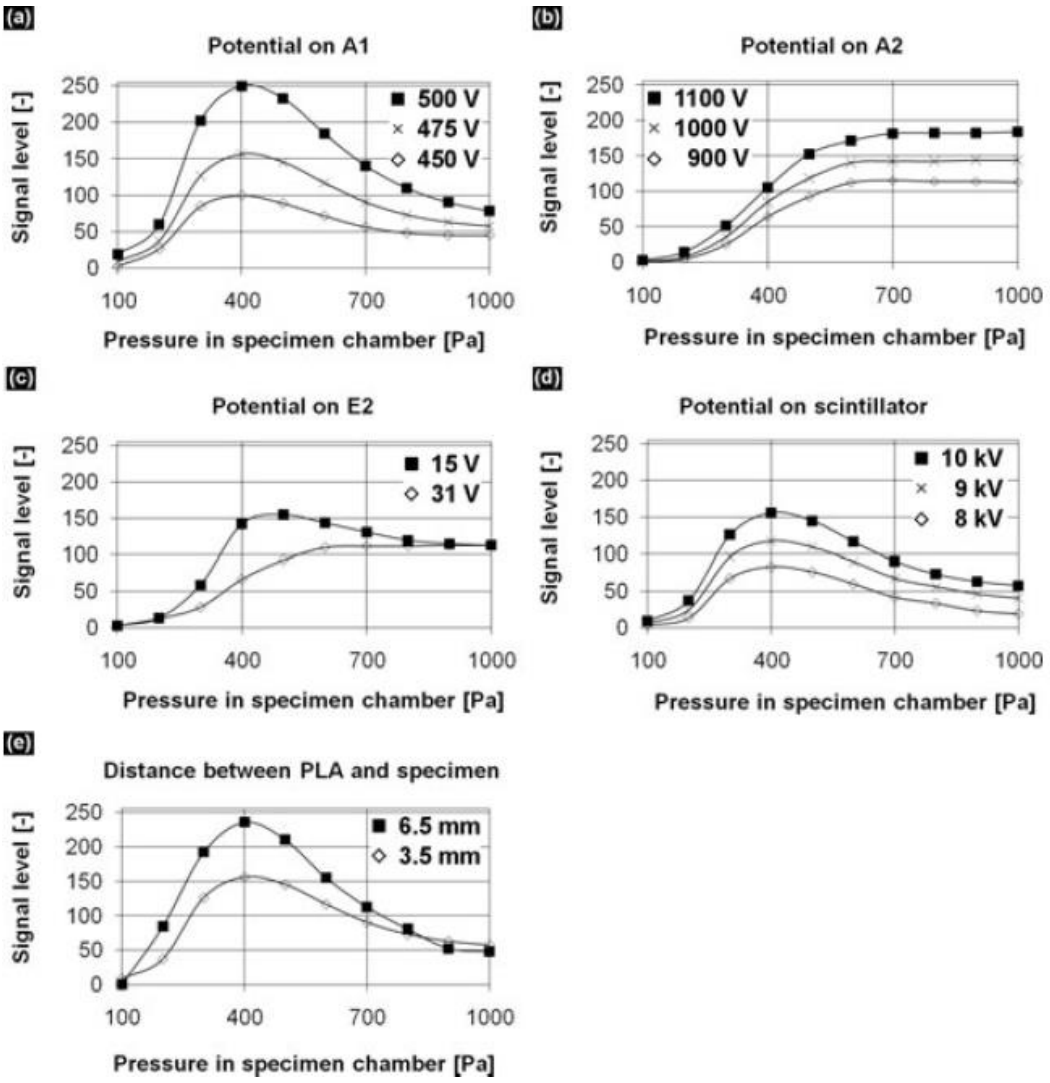

Fig. 5. (a), (b), (c), (d), (e) Dependences of signal level in units of greyscale mean values detected from gold on pressure of water vapour in specimen chamber; potentials on electrodes – see Table 1; beam current 100 pA, accelerating voltage 20 kV.

Conclusion

In this article, we briefly summarized the current development in signal detection in VPSEMs. We introduced a new scintillation SE detector, which differs from other concepts by having two pressure limiting apertures acting as an electrostatic lens for transmission of signal electrons to the scintillator. The detector is capable to operate at water vapour pressures in the specimen chamber from 10 Pa up to 1000 Pa.

With several sets of the electrode voltages it is possible to optimize the maximal level of the detected signal for the used pressure conditions.

Table 1. Parameters of measured dependences displayed in Fig. 5a–e.

	(a)	(b)	(c)	(d)	(e)
Potential on A1 [V]	**450, 475, 500**	475	475	475	475
Potential on A2 [V]	1000	**900, 1000, 1100**	1000	1000	1000
Potential on E1 [V]	1.5	1.5	1.5	1.5	1.5
Potential on E2 [V]	10	31	**15, 31**	10	10
Potential on scintillator [kV]	10	10	10	**8, 9, 10**	10
Distance between PLA and specimen [mm]	3.5	3.5	3.5	3.5	**3.5, 6.5**
Electrode arrangement	#1	#1	#1	#1	#1

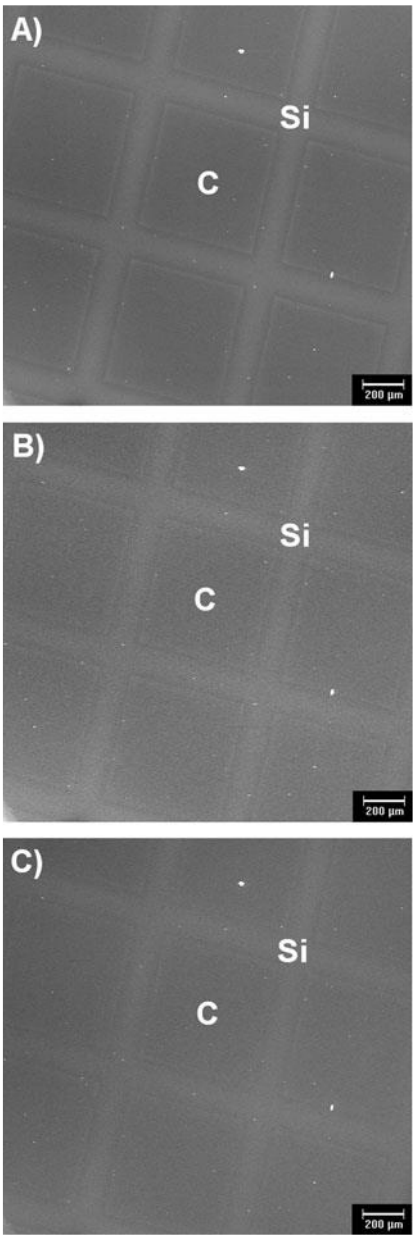

Fig. 6. Observationof3-nm-thick carbon layer on silicon substrate. Water vapour pressure (a) 100 Pa, (b) 200 Pa and (c) 300 Pa. Beam current 100 pA, beam accelerating voltage 20 kV.

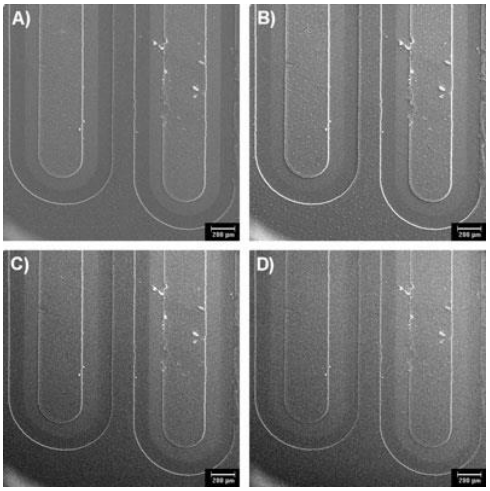

Fig. 7. Observation of voltage contrast on emitter base junction of power transistor. Voltage 9 V. Water vapour pressure (a) 50 Pa, (b) 150 Pa, (c) 300 Pa and (d) 400 Pa. Beam current 120 pA, beam accelerating voltage 20 kV.

It justifies the relatively complicated design of this detector, which is, however, necessary for its function. The electric field of the detector electrode system is also beneficial for signal electron cascade amplification within the detector. Low collection aperture of detector lowers the probability of detection of BSEs, but the detection and multiplication of low-energy SEs are enabled; see Figs 6 and 7. SEs are selectively attracted by an extended electrical field with optional intensity. The effect of relatively low collection efficiency with respect to the low collection aperture of the detector is compensated by a combination of both the positive influence of signal amplification due to the electric field inside the detector and the use of the highly efficient scintillation single crystal.

In our experiments, we successfully operated the scintillation SE detector for the VPSEM with the single crystal YAG:Ce^{3+} scintillator, but generally this detector can be modified in order to replace scintillation material by another one, such as single crystal YAP:Ce^{3+}, P47. Detection efficiency can be substantially increased by using new types of scintillation single crystals in combination with an optimum shape and material of the light guide. The detector equipped with this high-efficient YAG:Ce^{3+} scintillator followed by the light guide and by the photomultiplier provides fast and easy to- use solution to record the specimen images. The assembled detector is shown in Fig. 9.

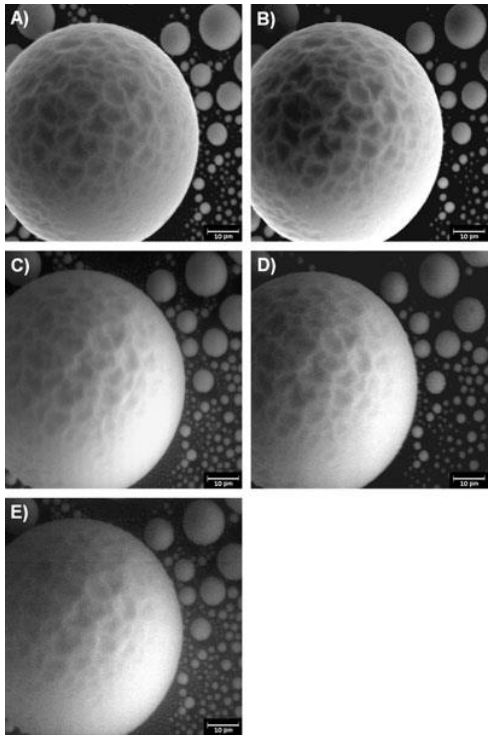

Fig. 8. Tin spheres on carbon. Water vapour pressure (a) 50 Pa, (b) 200 Pa, (c) 400 Pa, (d) 600 Pa and (e) 900 Pa. Beam current 80 pA, beam accelerating voltage 20 kV.

Fig. 9. Scintillation SE detector for VPSEM (total length of detector is 360 mm).

Acknowledgements

The authors thank J. Spinka and J. Kozák for their help during experiments. This work was supported by Grant Agency of the Czech Republic, grant No. P 102/10/1410 and by the project MSM 0021630516.

References

Danilatos, G.D. (1988) Foundations of environmental scanning electron microscopy. *Adv. Electron Phys.* **71**, 109–250.

Danilatos, G.D. (1990) Theory of gaseous detector device in the environmental scanning electron microscope. *Adv. Electron Phys.* **78**, 103.

Fletcher, A.L., Thiel, B.L.&Donald, A.M. (1999) Signal components in the environmental scanning electron microscope. *J. Microsc.* **196**, 26–34.

Heinz, A.H. (2002) Particle detectors. *Patent No. US2002088939*.

Heinz, A. H. (2004a) Particle detectors. *Patent No. US2004026621*.

Heinz, A.H. (2004b) Particle detectors. *Patent No. US2004227080*.

Jacka, M., Zadrazil, M. & Lopour, F. (2003) A differentially pumped secondary electron detector for low-vacuum scanning electron microscopy. *Scanning* **25**, 243–246.

Jirák, J. & Skřivánek, J. (2003) Use of scintillation detector in ESEM. *In Proceedings of 6thMultinational Congress on Microscopy, Pula.* 491–492.

Jirák, J., Černoch, P. & Autrata, R. (2005) Segmental Ionization Detector in Environmental SEM. *In Proceedings of 7th Multinational Congress on Microscopy* 367–368.

Knowles, W.R. (1995) Environmental scanning electron microscope. *Patent No. 5412211*.

Mathews, R.G. & Donald, A.M. (2002) Conditions for imaging emulsions in the environmental scanning electron microscope. *Scanning* **24**, 75– 85.

Morgan, S.W. & Phillips, M.R. (2006a) Transient analysis of gaseous electron-ion recombination in the environmental scanning electron microscope. *J. Microsc.* **221**, 183–202.

Morgan, S.W.&Phillips, M.R. (2006b) Gaseous scintillation detection and amplification in variable pressure scanning electron microscope. *J. App. Phys.* **100**, 16.

Neděla, V. (2007) Methods for additive hydratation allowing observation of fully hydrated state of wet samples in environmental SEM. *Microsc. Res. Tech.* **70**, 96–100.

Neděla, V. (2008) Dynamical “in situ” observation of biological samples using variable pressure scanning electron microscope. *J. Phys.: Conf. Ser.* **62**, 1–4.

Postek, M.T. & Vladár, A.E. (2004) New application of variable-pressure environmental microscopy to semiconductor inspection and metrology. *Scanning* **26**, 11–17.

Reimer, L. (1998) *Scanning Electron Microscopy: Physics of Image Formation and Microanalysis* (2nd edn). Springer Verlag, Berlin Heidelberg.

Rice, T., Knowles, W.R. (2005) Ultra high resolution SEM on insulators and contaminating samples. *Microsc. Today* **13**, 40–42.

Robinson, V. N. E. (1978) The SEM examination of wet specimens. *Scanning* **1**, 149–156.

Slówko,W.(2001) Secondary electron detector with a micro-porous plate for environmental SEM. *Vacuum* **63**, 457–461.

Slówko, W. (2007) New system for secondary electron detection in variable-pressure scanning electron microscopy. *J. Microsc.* **224**, 97– 99.

Stokes, D.J. (2003) Recent advances in electron imaging, image interpretation and applications: environmental scanning electron microscopy. *Phil. Trans. R. Soc. Lond. A.* **361**, 2771–787.

Thiel, B.L., *et al*. (2006) Two-stage gas amplifier for ultrahigh resolution low vacuum scanning electron microscopy. *Rev. Sci. Ins.* **77**, 033705- 1–033705-7.

Toth,M., Thiel, B.L.&Knowles, W.R. (2005a) Imaging of non-conductors by ultra-high resolution immersion lens SEM. *Microsc. Microanal.* **11**(2), 2.

Toth, M., *et al*. (2005b) Artifact-free imaging of photolithographic masks by evnironmental scanning electron microscopy. *Microsc. Microanal.* **11**(2), 2.

9 Comparison of calculated, simulated and measured signal amplification in a variable pressure SEM

V. NEDĚLA [a], I. KONVALINA [a], B. LENCOVÁ [a], J. ZLÁMAL [b]

a *Institute of Scientific Instruments ASCR ,v.v.i, Královopolská 147, 61264Brno, Czech Republic*

b *Institute of Physical Engineering, Faculty of Mechanical Engineering, Brno University of Technology, Technická 2, 61696 Brno, Czech Republic*

Keywords

Electron–gas interactions, Monte Carlo simulations, Signal amplification, Analytical models

Abstract

This paper presents computed dependencies of signal amplification of detected electrons on the water vapor pressure in a variable pressure SEM using the EOD software equipped with a Monte Carlo plug-in. We analyze the amplification at selected energies of signal electrons going through a high-pressure water vapor and total signal amplification by including a realistic simulation of the secondary emission from sample. The results are compared with experimental measurements and the dependencies of published analytical models.

Introduction

Relatively high pressure (up to 3000 Pa) of gases (mostly water vapor) in the specimen chamber of variable pressure scanning electron microscopes (VP-SEM), environmental scanning electron microscopes (ESEM), etc., enables examination of non-conductive, partially or fully wet samples as well as the study of dynamically changing physical or chemical conditions [1]. Besides these advantages scattering of primary electrons (PE) in a gaseous environment [2] causes worsening of the signal to noise ratio and it negatively influences the image resolution. This problem can be solved by decreasing the length in which the PE passes through the gas environment, increasing the PE accelerating voltage and probe current, using lower scanning speed and by choosing a suitable gas type and pressure [3,4]. Nevertheless, decrease in the probe current in the focused spot due to the primary electron–gas interactions lowers the number of the unscattered beam electrons and decreases the useful signal from the specimen. In such cases there are higher demands on the efficiency of the detection system.

So far the most efficient detectors for the detection of the secondary electrons (SE) in environmental conditions use the principle of gas ionization that proceeds as a cascade between a grounded specimen holder and the signal electrode supplied with a positive voltage [5]. Signal electrons are accelerated by the electrostatic field and ionize gas molecules and generate positive ions; the secondary electrons strongly contribute to the amplifica-tion of signal detected by the detector. The amplification of the detected signal depends on the intensity of the electrostatic field between the detection electrode and the grounded sample, on the gas path length of the signal electrons through the gas as well as on the pressure and type of the ionization gas [6].

High-pressure gases in the specimen chamber of electron microscopes create completely different and more complicated conditions for the detection of SEs than in a conventional SEM. Signal amplification arises due to ionization of gas molecules not only by various types of secondary and backscattered electrons, but also by the primary and the diffused electrons. Moreover, experimental results cannot provide quantitative information about separate types of signal electrons from the detected signal and any improvement of detection systems with the aim to discriminate unwanted signal components cannot be simply made. It requires computer simulations using properly defined and correct mathematical algorithms.

Simulation method

In order to understand the signal generation in the gaseous environment, the program EOD [7], used for the design of imaging, scanning and detection systems in electron microscopes, has been extended with a MC module to include the collision phenomena of electrons with the gases in the specimen chamber of the micro-scope. For this we use the data of cross-sections from the NIST database for ionization. Dissociation, vibration, rotation and momentum-transfer cross-sections for water molecules are included in the simulation algorithm.

The simulation uses integration of the equation of motion of electrons with variable and sufficiently small step, much smaller than the steps necessary to trace electrons in a non-gaseous environment. The step size is determined by the probability in which the interaction of electron with a gas molecule may occur, typically around 10%, and the interaction cross-section for given electron energy. According to the particle energy the MC routine selects if and which type of collision happens. After elastic collisions the electron energy is not changed, only its direction. If an ionization collision happens, a new electron is generated with a random angle and a small energy gain relevant for the ionization type. The energy of the first electron is decreased by the ionization energy and the energy transferred to the second electron; its direction is changed, depending on ionization level involved and

electron energy. A correct simulation of these effects is vital for obtaining correct results for the signal amplification. A detailed description of the effects involved is given by Thiel et al. [8]. In our computations we do not include any effects related to generated ions (space charge, generation of secondary electrons as an impact on the sample, recombination of ions and electrons) and the secondaries arising from the impacts of BSEs on the micro-scope parts.

The computation starts with a set of electrons with given initial position, energy and angle. New ‘‘environmental’’ electrons are then added to the set. For each selected energy 2000 particles are started and then the amplification is determined from the total number of detected electrons. The results were calculated for SE energies of 3, 10, 20 and 50 eV and BSE energies of 100, 250, 500, 750, 1000, 3000, 10 000 and 18 000 eV; see Fig. 3.

Analytical models

A recent analytical model used to calculate the total amplified ion current detected with the environmental secondary electron detector was published by Meredith et al. [6]. An improved version of this model taking into account the nonlinearity of the Town-send’s first ionization coefficient as well as newly calculated specific gas type coefficients was published by Thiel et al. [8]; see Eq. (1). Small modification of Thiel’s model, reducing its total signal amplification by inclusion of the SE and BSE emission coefficients, was published by Morgan [9]; see Eq. (2).

The total amplified ion current I_{ion} or the total current of electrons emitted from the sample and amplified in partially ionized gases I_{ese} and detected with the detection electrode of the detector is stated by Thiel et al. [8] as

$$I_{ion} = I_{PE}\left(e^{\alpha_{ion}^{sw} d_{eff}} - 1\right)\left\{\frac{S_{PE}p}{\alpha_{ion}^{sw}} + \frac{\eta S_{BSE}p}{\alpha_{ion}^{sw}}\left(\frac{\bar{d}_{BSE}}{d}\right) + \delta\right\}k \qquad (1)$$

The total amplification of the ionization detector A_{ESD} is defined by Morgan [9] as a ratio of the I_{ion} to the total amount of emitted electrons from the sample.

$$A_{ESD} = \frac{I_{ion}}{I_{PE}(\eta+\delta)} \qquad (2)$$

Here I_{PE} is the primary beam current, p is the specimen chamber pressure in Pa, d and Z are the SE and BSE emission coefficients, d is the sample to detection electrode gap in mm, d_{BSE} is the average BSE path length in mm, S_{PE} and S_{BSE} are the field-independent ionization efficiencies of the primary electrons and BSEs in ion pairs/(mm Pa). For the calculation of S_{PE} an energy equal to 75% energy of primary electrons was used. The factor α_{ion}^{sw} is called Townsend’s first ionization coefficient and gives an average value of ion pairs per unit of length, created by the

SEs and their products in electron–gas interactions accelerated by the field of the detection electrode. The quantity k relates to the effect of positive ion impact at the sample. It is a gas-specific amplification factor related to the inelastic scattering cross-section. The pressure- and field-dependent effective gap distance d_{eff} represents a specific fraction of d when the value of α_{ion}^{sw} is approximately constant.

All the above mentioned analytical models use a simplified description of processes accompanying the impact ionization of gas molecules by signal electrons and its signal amplification in high-pressure conditions and they demonstrate the influence of micro-scope parameters on the shape of signal detected by an ionization detector. These models are based on simplified assumptions for the gas plate capacitor and use a physical theory for partially ionized gases published by von Engel [10]. The grounded sample, ideally straight and smooth, acts as a bottom electrode of the gas capacitor regardless of the existence of recombination sample processes, gas pressure distribution between the sample and the pressure-limiting aperture, nonlinear processes of signal amplification, etc.

Experiment

An experimental measurement investigating the dependence of the detected signal from a thin gold plate on the water vapor pressure as well as on other parameters was carried out using a special sample. Two holes were bored into a carbon cylinder with the diameter of 4 mm and the length of 8 mm. First, an eccentrically situated hole with the diameter of 0.5 mm and depth of 6 mm was used as a Faraday cage for measuring the absorbed primary electron current. The primary current was kept constant and measured precisely at the pressure of 0.01 Pa for each experiment using the pico-amperemeter KEITHLEY 485. The second hole situated approximately at the center of the carbon cylinder was used for the measurement of a reference signal. The thin gold plate was placed closely to the second hole so that its surface was at the same level as the surface of the carbon. The thin gold plate was fixed to the carbon using a liquid conductive carbon paste. Both surfaces were roughly polished. The following experimental conditions were set: an accelerating voltage of the primary electron beam of 20 kV, a probe current of 25 pA, a gas path length of 6 mm and the potential applied to the detection electrode of the ionization detector was 300 V.

All experiments were carried out using our non-commercial experimental microscope AQUASEM-II [11]; see Fig. 1. It was designed at the Institute of Scientific Instruments (ISI) of the ASCR as an experimental instrument for research of detection systems and ESEM techniques. The microscope can work in high and

Fig. 1. Non-commercial experimental scanning electron microscope AQUASEM-II.

low vacuum modes. The single crystal YAG:Ce^{3+} (yttrium aluminium garnet activated with trivalent cerium) has a hole in the center, so that it simultaneously acts as a pressure-limiting aperture, which restricts the gas flow between the specimen chamber and the differentially pumped chamber [12]. It is used for the detection of backscattered electrons in both low and high vacuum modes, and it is well suited for the high-pressure conditions in the specimen chamber. In the low vacuum and environmental mode the secondary electron signal was detected by an electrode with the inner diameter of 4 mm deposited on the input surface of the single crystal detector [13,14]; see Fig. 2. With a positive bias of 300 V with respect to the sample, it acts similarly to the environmental secondary electron detector.

Results

Dependencies of signal amplification in gas environment on the water vapor pressure and on the energy of electrons going through the gas, shown in Fig. 3, were calculated using the EOD software equipped with a Monte Carlo plug-in. It is seen that the highest amplification of the signal is for electrons with energy of 250 eV. The lowest amplification was obtained for signal with the highest energy of 20 keV. Generally, by increasing the energy of electrons, up to the energy of 250 eV, their signal amplification increase. We suppose that the amplification maxima is approximately between 200 and 250 eV. For higher energy the amplification decreases. Computed results considerably depend on the geometry and parameters of the detection system as well as on the geometry of the specimen chamber of the microscope. Fig. 3 also shows that the maxima of amplified signal are shifted to a higher pressure with the increase in electron energy.

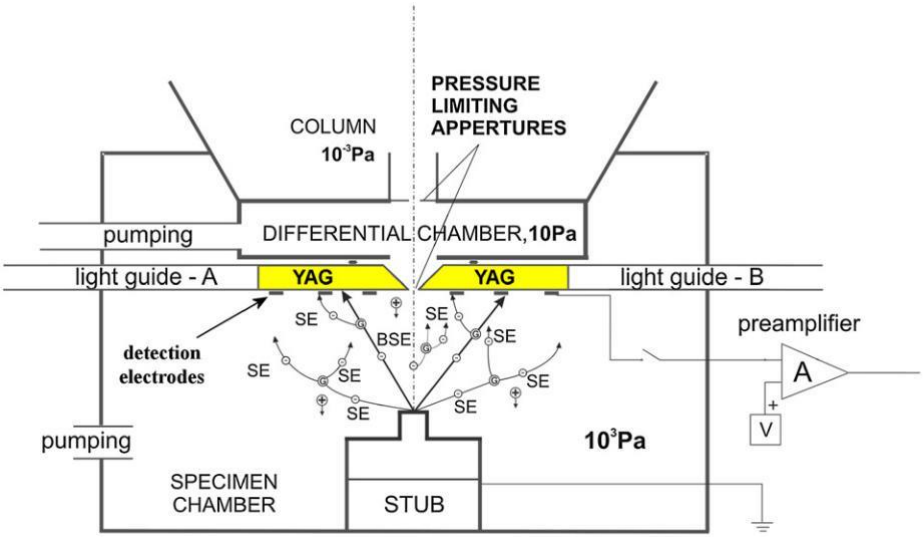

Fig. 2. Configuration of the combined YAG-BSE detector and ionization detector of SE in scanning electron microscope AQUASEM-II.

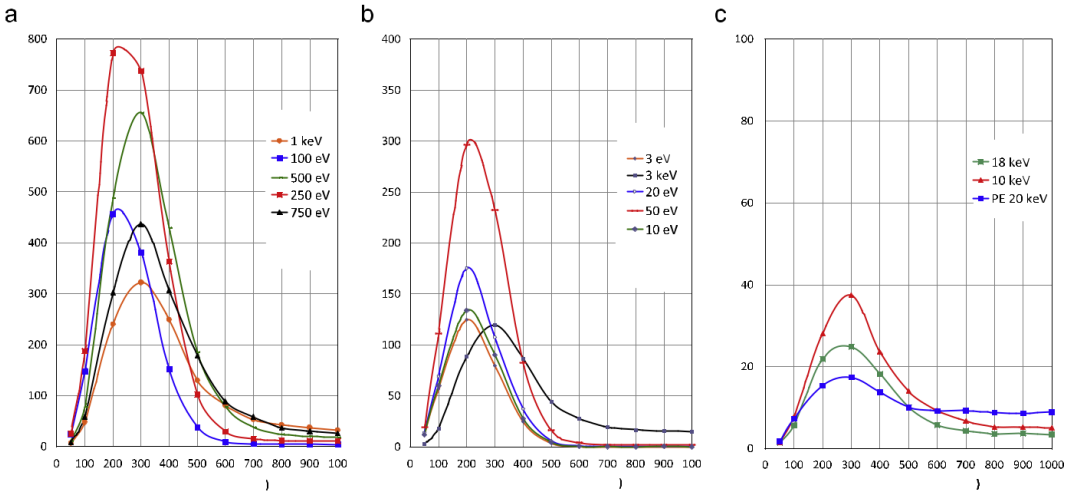

Fig. 3. (a–c) Dependencies of signal amplification in gaseous environment on the water vapor pressure and on the energy of electrons. Two thousand electrons were simulated for each value of pressure. Sample to detection electrode distance is 6 mm and potential on the detection electrode is 300 V.

Our results show that the gas environment acts as a selective amplifier with highest amplification for relatively low-energy electrons, but not for secondary electrons. The results in Fig. 3 describe electron–gas interactions, without the influence of real energy distribution of the signal electrons emitted from the sample. For this reason, emission spectra of signal electrons from a gold sample were also simulated using the Monte Carlo method. As a result, the secondary electron emission coefficient δ and the backscatter electron emission coefficient η were calculated for selected energies of electrons to obtain a realistic number of emitted electrons propagating through the gas. Fig. 4 shows the dependence of normalized number of detected

electrons on the water vapor pressure for selected energy of electrons emitted from the sample. These results were calculated with respect to the simulated energy distribution of signal electrons from gold at the accelerating voltage of 20 keV. It can be seen that the largest detected signal was indeed found for secondary electrons with the energy of 3 eV, and the lowest signal curves come from 3 keV electrons. These calculated results confirm that the ionization detector is predominantly a detector of secondary electrons.

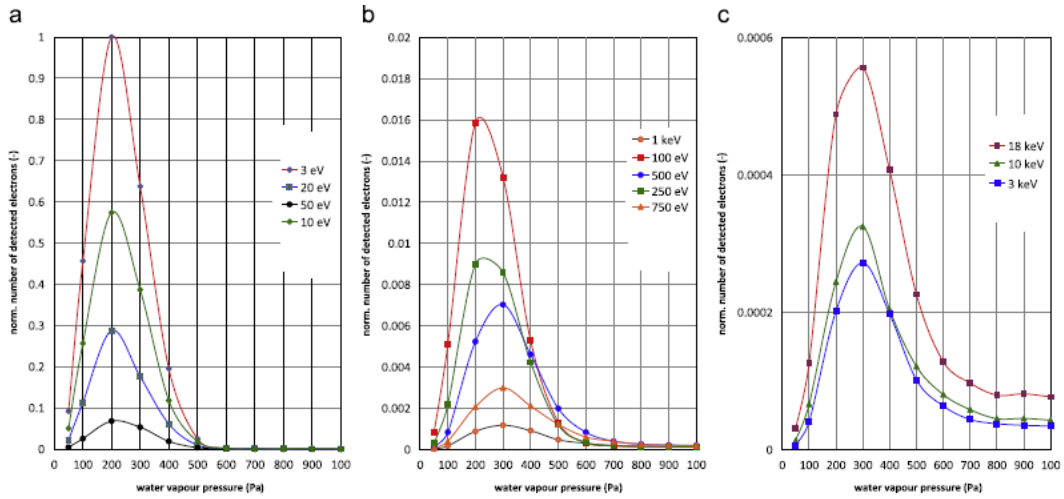

Fig. 4. (a–c) Dependence of the normalized number of detected electrons on the water vapor pressure and the energy of electrons emitted from the gold. It is calculated with respect to simulated energy distribution of signal electrons from gold, energy of primary electrons 20 keV, sample to detection electrode distance 6 mm, potential on the detection electrode 300 V.

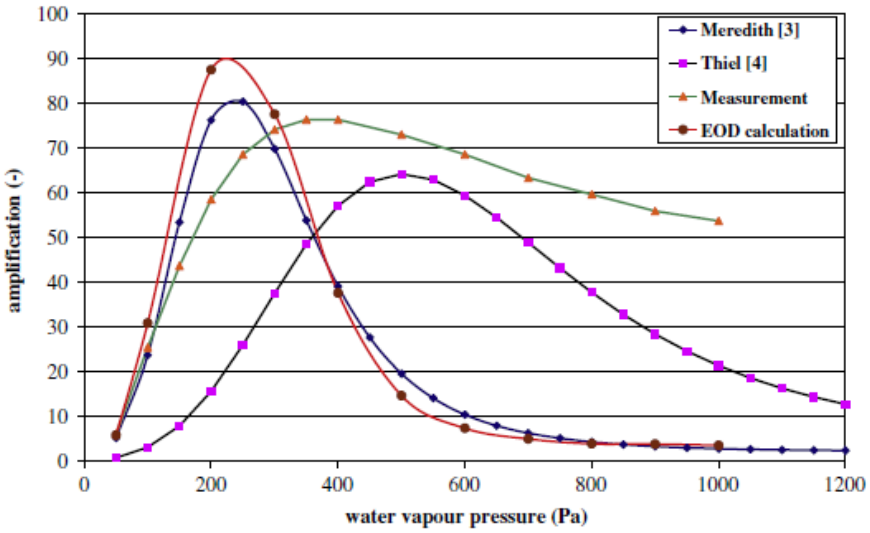

Fig. 5. Dependence of signal amplification obtained from the numerical models published by Meredith et al. [6] and Thiel et al. [8], calculated by the program EOD and measurement on the water vapor pressure (acceleratingvoltage20kV, probe current 25pA, gas path length 6mm, ionization detector 300V, water vapor environment).

Finally, Fig. 5 shows the comparison of results calculated according to the models of Meredith et al. [6] and Thiel et al. [8], the results simulated with EOD, and measured dependencies of signal amplification.

The results obtained by EOD were processed so that each value of the signal amplification at a certain pressure was computed by integrating the spectral amplification function over the entire energy interval. The spectral amplification is given by the energy distribution of the secondary emission multiplied by the dependence of the amplification on energy.

This figure shows a good agreement between the curve simulated with EOD software and that with the model of Meredith.

Conclusion

This paper shows the current possibilities of a plug-in of the EOD program that enables to simulate electron–gas interactions as well as amplification of signal electrons going through the gas to the ionization detector. Almost all presented results are new and still not published by other authors. Due to the simplification of the complicated physical processes in the algorithm, some deficiencies in the results are expected. The final amplification of the signal detected with ionization detector, as shown in Fig. 5, was calculated from the results of twelve selected energies, each one simulated for 2000 electrons emitted from the sample. Restricted number of energies, covering the energy interval from 0 to 20 keV was used for the time-consuming Monte Carlo computations, but the presented results are already in a good agreement with experimental results as well as with the results calculated using the analytical models.

Acknowledgements

This work was supported by the Grant Agency of the Czech Republic, Grant no. P102/10/1410 and by the Ministry of Industry and Trade of the Czech Republic: Grants FR/TI1/118 and FR/TI1/305. I would like to thank Dr. Filip Mika for help with Monte Carlo in the solid sample and Dr. Martin Oral for help in data interpretation.

References

[1] A.M. Donald, Nature Materials 2 (2003) 511.

[2] A.Wight Scott, Scanning 23 (2001) 320.

[3] G.D. Danilatos, Foundations of Environmental Scanning Electron Microscopy, Academic Press, Sydney, 1988, p. 249.

[4] R. Gauvin, Surf. Interface Anal. 37 (2005) 875.

[5] G.D. Danilatos, Micron and Microscopica Acta 14 (1983) 307.

[6] P. Meredith, A.M. Donald, B.L. Thiel, Scanning 18 (1996) 467.

[7] B. Lencová, J. Zlámal, Physics Procedia 1 (2008) 315.

[8] B. Thiel, et al., Journal of Microscopy 187 (1997) 143.

[9] S.W. Morgan, Gaseous secondary electron detection and cascade amplification in the environmental scanning electron microscope, PhD Thesis, Faculty of Science, University of Technology, Sydney, Australia, 2005.

[10] A. von Engel, Ionized Gasses, second edition, Oxford University Press, 1965 p. 325.

[11] V. Neděla, J. Maxa, Proceedings of the 10th International Seminar Skalský Dvůr 2006, ISI AS CR Brno, 2006, pp. 55–56.

[12] V. Neděla, Microscopy Research and Technique 70 (2007) 95.

[13] G.D. Danilatos, Scanning Microscopy International 7 (1993) 57.

[14] G.D. Danilatos, in: G.W. Bailey, L.C. Rieder (Eds.), Proceedings of the 51st Annual Meeting MSA, San Francisco Press, San Francisco, 1993, pp. 786–787.

10 The Simulation of Energy Distribution of Electrons Detected by Segmental Ionization Detector in High Pressure Conditions of ESEM

V. Neděla, I. Konvalina, M. Oral and J. Hudec

Institute of Scientific Instruments ASCR, v.v.i, Brno, Czech Republic

Abstract

This paper presents computed dependencies of the detected electron energy distribution on the water vapour pressure in an environmental scanning electron microscope obtained using the EOD software with a Monte Carlo plug-in for the electron-gas interactions. The software GEANT was used for the Monte Carlo simulations of the beam-sample interactions and the signal electron emission from the sample into the gaseous environment. The simulations were carried out for selected energies of the signal electrons collected by two electrodes with two different diameters with the voltages of +350 V and 0, respectively, and then 0 and +350 V, respectively, and for the distance of 2 mm between the sample and the detection electrodes of the ionization detector. The simulated results are verified by experimental measurements. Consequences of the simulated and experimental dependencies on the acquisition of the topographical or material contrasts using our ionization detector equipped with segmented detection electrode are described and discussed.

Introduction

Environmental scanning electron microscope (ESEM) is indispensable for many experimental uses, including dry and electrically non-conductive samples. Apart from the compensation of the negative charge by positive ions from electron-gas interactions, ESEM allows studying fully hydrated, mostly biological samples at high pressures (units to thousands Pa) [1], semiliquid or liquid samples as well as sample changes and reactions during dynamical in-situ experiments [2]. Danilatos claimed [3] that the image resolution in a high pressure in the ESEM can be comparable to that in the conventional scanning electron microscope (SEM). The resolution in ESEM is limited due to beam scattering, and also the signal-to-noise ratio in the detected signal is lower, but it can be mitigated by various adjustments: a decrease in the path length of the primary electrons (PE) through the high pressure region, an increase in the PE accelerating voltage and the probe current, a lower scanning speed or a suitable choice of the gas and its pressure.

Nevertheless, the high pressure conditions support amplification and detection of low energy signal electrons [4]. The detection principle is based on gas ionization which proceeds in a cascade between a grounded specimen holder and positively biased electrodes, commonly placed under the pole piece of the objective lens [5-7]. So far almost all detectors for ESEM use an electrostatic field to accelerate electrons and, consequently, a higher ionization of gas molecules, generation of signal electrons and positive ions, and increased signal amplification. Amplification of the detected signal is strongly influenced by the strength of the electric field between the grounded sample and the detection electrode as well as by the pressure and the type of gas in the specimen chamber of the ESEM. It was found that the optimal conditions are created by the presence of water vapour in the specimen chamber of ESEM [8].

The first commercial detector for ESEM based on this amplification phenomenon was called the environmental secondary detector (ESD) [9]. Unfortunately, the original version of the detector records a signal which is a mixture of SEs and backscattered electrons (BSEs); therefore the image is composed of SE topographical and BSE material contrasts [10]. For this reason the ESD was modified into the gaseous secondary electron detector (GSED) by using a suppressor electrode which allows detecting a cleaner SE signal [10]. Danilatos proposed a multi-electrode configuration of the detector to separate various detected signals [9]. The physical principle of a multi-electrode configuration was implemented into a technical design by Knowles and was used commercially in an ESEM by the FEI Company. Meredith et al. simulated contribution of PEs, BSEs and SEs to the total amplification from the ionisation [11]. Thiel et al. calculated the signal-to-background ratio for amplification of SEs in the GSED and the ESD [12]. Fletcher published curves showing a lower contribution of BSEs to the gas cascade amplified electron signal collected using the GSED as a function of the gas type and pressure in comparison with the ESD [10].

Some methods for the detection of separated SE and BSE signal have been examined also by our team. Autrata et al. designed a very sensitive BSE detector using the original YAG (yttrium aluminium garnet) scintillator for recording the material contrast [13]. The so-called combined ionization detector capable of detecting BSEs in SEM and ESEM by scintillation and SEs in ESEM by electron-gas ionization was realised [14,15]. If the specimen surface is to be observed in a topographical contrast, the ionisation function of the combined detector can be used. For this reason, a thin electrode is deposited on the bottom base of the YAG scintillator. If the electrode is at a positive voltage, the signal electrons initiate an ionisation cascade with gas molecules which amplifies the signal. Even if this detector was primarily designed as the SE detector for topographical observation a

portion of BSE background is still detected. The small hole in the YAG scintillator can simultaneously serve as a second pressure limiting aperture (PLA 2) of the ESEM, an arrangement utilized in our AQUASEM II microscope [15]. The length of the high pressure region between the PLAs is decreased, and the diffusion of the electron beam in the differentially pumped chamber is minimised for this configuration.

The main objective of this work is to simulate signal electron trajectories for selected energies from several eV to tens of keV in gaseous environment for a specially designed ionisation detector equipped with two circular electrodes in order to better understand the connection between the configuration of the detection electrode or their segmented parts and the type of the detected information. The EOD program extended with our Monte Carlo module for electron-gas interactions and signal amplification is used to simulate trajectories of the signal electrons from a realistic sample model [4]. That is followed by an analysis of the energy distribution of the detected electrons by the detection electrodes.

In this paper, simulations of the detection efficiency for various conditions, detector configurations and types of detected electrons are presented. Simulated results are compared and verified by experiments, based on the assumption that the topographical contrast created by SEs can be observed using the detection electrode closest to the optical axis of the ESEM column. The material contrast, created by BSEs, is partially suppressed. On the other hand, a predominantly material contrast is detected by the detection electrode with a higher distance from the ESEM optical axis.

Material and Methods

The emission of the signal electrons from the gold surface was simulated using the GEANT Monte Carlo software [16] for 1 000 000 particles, the energy of the primary beam was 20 keV. The trajectories of the signal electrons emitted from the sample to water vapour environment between the sample and the segmented ionization detector and the signal amplification of the detected electrons were calculated using the EOD [17] (Electron Optical Design) software equipped with a Monte Carlo plug-in [4]. 10 000 signal electrons with the energies of 1.7, 2.7, 4.7, 7.6, 10, 20, 50, 100, 300, 500, 900, 1000, 2000, 3000, 5000, 7500, 10000, 15000 and 20000 eV were traced through a 2 mm thick water vapor region (the sample to detection electrode distance) with the pressure of 50, 100, 200, 300, …, 1000 Pa.

The electrons detected by the individual segments of the detector provide information about their final energy. The distribution of the electrostatic fields between the detector and the specimen, the spatial distribution of the signal electron

emission from the sample as well as the gas type and the pressure all have a significant influence on the detected type of the signal electrons.

All experiments were made using our non-commercial experimental microscope, the AQUASEM-II [18]. The custom-built segmented ionization detector of secondary electrons with two ring detection electrodes was used for the detection of the signal electrons. The first electrode B with the inner diameter of 1.5 mm and the outer diameter of 4.5 mm was situated close to the optical axis of the ESEM, whereas the second electrode A with the inner diameter of 16 mm and the outer diameter of 20 mm was situated as far as possible from the microscope optical axis (Figures 1A, 1C). The detection system was made from 2 mm thick FR-4 copper clad laminate board. The electrodes A and B were made by etching and connected to a signal preamplifier. The detection system also has a small hole (600 μm in diameter, with its surface electrically conductive and grounded) situated in the centre of the detection system. The detection system simultaneously acts as the PLA 2 of the ESEM AQUASEM II [15].

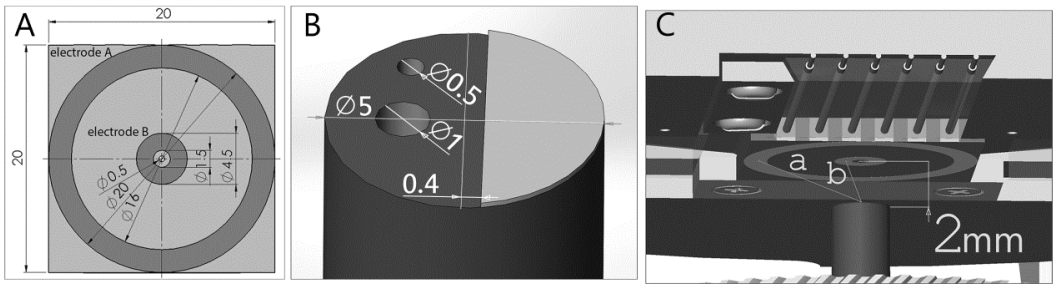

Figure 1. A: Detection electrodes of ionization detector for ESEM, B: Experimental sample consisting with two holes and gold plate, C: Experimental setup in ESEM AQUASEM II.

Two configurations of the detection system were used for the experiment. First, the positive potential of 350 V was applied on electrode A while electrode B was grounded. Second, the positive potential of 350 V was applied on electrode B and electrode A was grounded. An application of a positive bias of 350 V on the electrodes of the presented detection system acts similarly as the ESD. The detector is relatively simple both to construct and to model in simulations, therefore it was selected for a comparison of numerical results with experimental data and to help understanding the detection principles based on electron-gas interactions in ESEM.

The testing sample was made from a carbon rod (5 mm diameter, 8 mm width) with two holes and a small gold plate (Figure1B). An eccentrically situated hole (0.5 mm diameter, 6 mm deep) was used as the Faraday cup. The probe current was measured at the pressure of 0.01 Pa using the picoampermeter Keithley 485 before each experiment. Another hole (1 mm diameter, 6 mm deep) was used for the measurement of the background signal induced by beam diffusion in gas.

Dependences of detected signal from gold on the gas pressure were measured (Figure 3B, dashed line) and also this signal with subtracted background (recorded by electrode A or B from the Faraday cup) was calculated and plotted (Figure 3B, full line).

The following experimental conditions were set: the beam accelerating voltage of 20 kV, the beam current of 25 pA, 2 mm sample to detection electrode distance. For the experimental comparison a sample containing three metals with different atomic numbers and, therefore, different SE and BSE emission coefficients, was used. The three elements were mixed in alloys using different ratios, and these alloys are then in different areas on the sample – areas I, II and III, see Figure 4A. An energy dispersion X-ray analysis revealed that area I contains 57 % of Al, 1 % of Cr and 42 % of Pd, area II contains 70 % of Al, 1 % of Cr and 29 % of Pd, and area III contains 74 % of Al, 17 % of Cr and 9 % of Pd. The signal at the electrodes A and B from the three areas were determined from a line scan (Fig. 4A, B). The beam accelerating voltage was 20 kV, the probe current had a value of 120 pA, the sample to PLA distance was 2 mm and the water vapor pressure was 500 Pa.

Results

The simulation consisted of two steps. First, the spectrum of the signal electrons was computed by the Monte-Carlo method in the Geant. Second, a dependence of the amplification coefficient on the energy and the pressure was obtained in the EOD (Figure 2). For each pressure, this dependence was used as a weight function in the integration of the signal electron emission spectrum, providing a value of the signal amplification coefficient for signal electrons of any emission energy (Figure 3A). The influence of the primary beam scattering was not considered in the simulations, as that would make them significantly even more time consuming.

The simulated results of the signal electrons at selected energies in a gas show that electrodes A and B collect signal electrons in the whole emission spectrum, recording a mixed contrast. Electrode B detects a higher number of low-energy electrons (Figures 2B, 2D), whereas electrode A with a higher diameter predominantly detects backscattered electrons, especially for the pressure of 300 Pa and higher (Figures 2A, 2C). All the results indicate that the proportion of the high-energy electrons increases with an increasing pressure. Multiplying the signal amplification in the gas by the simulated emission coefficients at a given energy gives the detection efficiency as a function of the initial energy of the signal electrons (Figures 2C, 2D). These dependencies help understanding contrast formation in the images in Figure 4, that were obtained using electrodes A and B and by evaluating differences between them.

The results were verified with an experiment. Using electrodes A and B the image of the sample was acquired for the three areas with different alloy ratios (Figure 4). The measured difference in the detected signal at the water vapour pressure of 500 Pa from electrode A from area II (point L1) and area I (point L3) is almost by 50 % higher that the corresponding difference from electrode B under the same conditions (Figures 4A, 4B). The signal from electrode A contains a higher BSE contribution; BSE yield is higher for higher atomic numbers. To verify these conclusions, the sample was examined under the same conditions in vacuum in the Jeol JSM 6700F SEM, using a BSE-YAG detector which detects just BSEs (Figure 4C), and using an in-lens SE detector which obtains just the topographical contrast (Figure 4D). The signal from area II was calibrated for the same level during the experiments (Figures 4A-D).

The shift in the signal intensity maxima from electrode A towards higher pressure values compared to electrode B (Figures 3A and 3B) is caused mainly by a higher average length of the signal electron trajectories. The distances from the sample centre to the electrodes A and B are 9.22 mm and 2.50 mm, respectively. The initially low-energy signal electrons are more influenced by the electrostatic field and collisions are more probable. Their trajectories then can be significantly longer.

Figures 3A and 3B, dashed line, show a good agreement between the curve simulated with EOD software and experimental data. Computed and experimental results considerably depend on the geometry and the parameters of the detection system as well as on the geometry of the specimen chamber of the microscope.

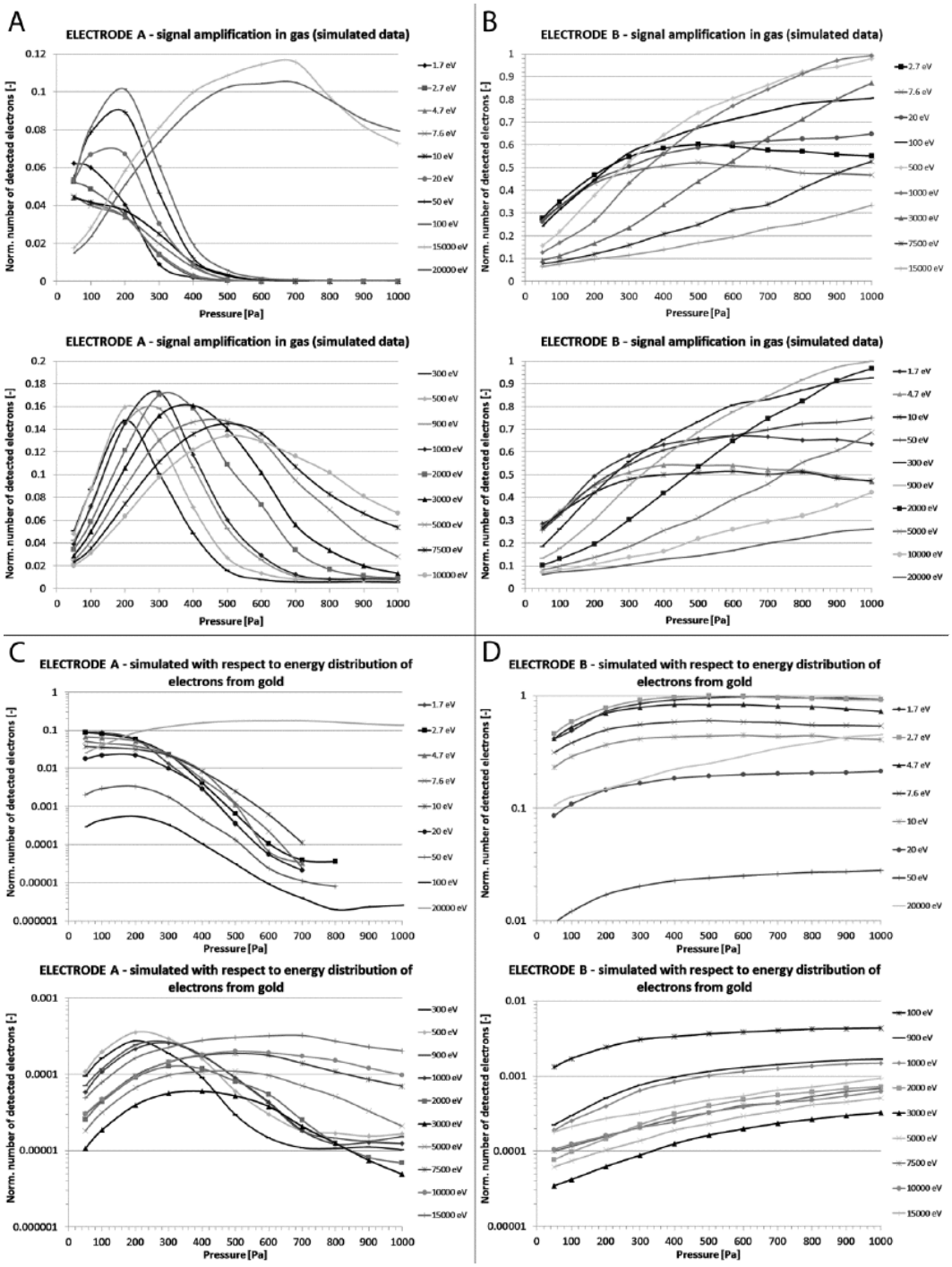

Figure 2. The dependence of the normalized number of electrons detected by electrodes A and B, Figure1, on the water vapor pressure and the energy of the signal electrons using a gold sample.

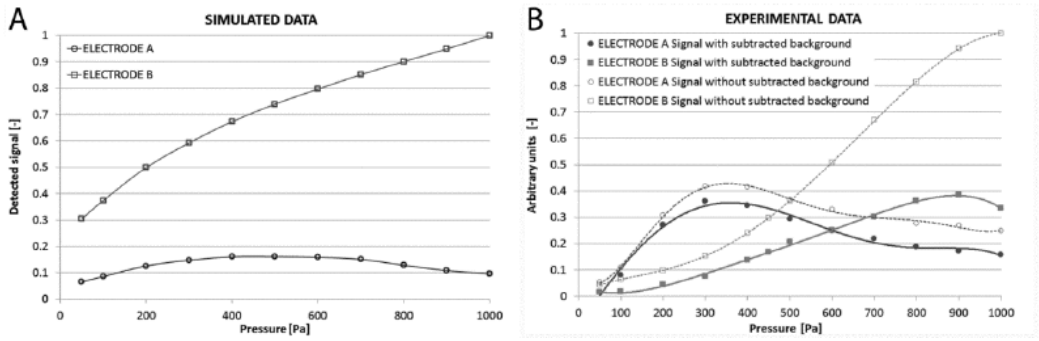

Figure 3. The dependence of the detected signal calculated by the EOD program (A) and obtained by the experiment (B) on the water vapour pressure; acc. voltage 20 kV; probe current 15 pA, sample to PLA distance 2 mm, ionization detector at 350 V for detection electrodes A and B, see Figure 1

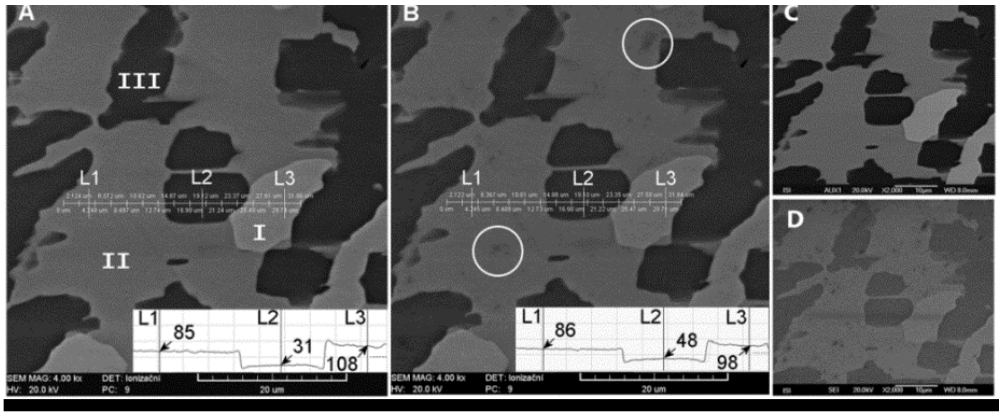

Figure 4. Three types of materials with different Z (I,II,III); A: using electrode A, B: using electrode B in ESEM, ionization detector, acc. voltage 20 keV, vapor pressure 500 Pa. C: using BSE-YAG detector, D: using in-lens SE detector in Jeol JSM 6700F; acc. voltage 20 keV, vacuum.[19]

References

[1] V Neděla, Microscopy Research Technique **70** (2007), p. 95.

[2] AM Donald, Nat. Mater. **2** (2003), p.511.

[3] GD Danilatos, J. Microsc. **160** (1990), p.9.

[4] V Neděla *et al*, Nucl. Instrum. Meth. A **645** (2011), p. 79.

[5] GD Danilatos, Microsc. Microanal. **6** (2000), p. 12.

[6] M Toth *et al*, Ultramicroscopy **94** (2003), p. 71.

[7] J Jirák *et al*, J. Microsc. **239** (2010), p. 233.

[8] AL Fletcher *et al*, J.Phys. D: Appl.Phys. **30** (1997), p. 2249.

[9] US Patent No. 4,897,545.

[10] AL Fletcher *et al*, J. Microsc. **196** (1999), p.26.

[11] P Meredith *et al*, Scanning **18** (1996), p.467.

[12] BL Thiel *et al*, J. Microsc. **187** (1997), p.143.

[13] R Autrata *et al*, Scanning **14** (1992), p.127.

[14] V Romanovský *et al*, European Microscopy and Analysis **59** (1999), p. 19.

[15] V Neděla *et al*, Microsc. Microanal. **17** (S2) (2011), p. 920.

[16] S Agostinelli *et al*, Nucl. Instr. Meth. A **506** (2003), p. 250.

[17] B Lencová *et al*, Phys. Procedia **1** (2008), p.315.

[18] V Neděla, J. Microsc. **237** (2010), p. 7.

[19] This work was supported by the Grant Agency of the Czech Republic, grant No. GA14-22777S.

11 High-efficiency detector of secondary and backscattered electrons for low-dose imaging in the ESEM

Vilém Neděla, Eva Tihlaříková, Jiří Runštuk, Jiří Hudec

Environmental electron microscopy group, Institute of Scientific Instruments of the CAS, v.v.i., Královopolská147, 612 64 Brno, Czechia

Keywords

Detectors, Scintillators, Low-dose imaging, Energy filtration, MC simulations

Abstract

A new Combined System for high-efficiency detection of Secondary and Backscattered Electrons (CSSBE) in the ESEM consists of three detectors: an ionisation SE detector, an improved scintillation BSE detector, and a new Ionisation Secondary Electron Detector with an electrostatic Separator (ISEDS). The ISEDS optimizes conditions for electron-gas ionisation phenomena in the ESEM to achieve a strongly amplified signal from the secondary electrons with a minimal contribution from backscattered and beam electrons. For this purpose, it is originally equipped with an electrostatic separator, which focuses signal electrons towards a detection electrode and controls the concentration of positive ions above the sample. The work- ing principle of the ISEDS is explained by simulations of signal electron trajectories in gas using the EOD program with our Monte Carlo module. The ability to detect the signal electrons in a selected range of energies is described with Geant4 Monte Carlo simulations of electron-solid interactions and proven by experimental results. High-efficiency detection of the ISEDS is demonstrated by imaging a low atomic number sample under a reduced beam energy of 5 keV, very low beam currents of up to 0.2 pA, and gas pressure of hundreds of Pa.

Introduction

The ability to perform research on most natural and synthetic materials in their native or minimally treated state, in different phases of matter, or during phase transitions emphasises the in- dispensability of an Environmental Scanning Electron Microscope (ESEM) in science and industry. The ESEM [1] allows direct observation of natural, electrically non-conductive and semi-conductive samples free of charging artefacts [2,3] , fully hydrated or wet samples [4,5] , plants [6,7] ,

small live animals [8] , or microgel particles [9] in conditions of thermodynamic equilibrium [10] , as well as in-situ investigation of chemical reactions and samples under dynamically changing conditions (mostly in water vapour pressures of ones to thousands of Pa, sample temperature commonly from −20 °C to 1500 °C, and relative humidity up to 100%) [11,12].

Inevitable beam diffusion in gas causes unscattered beam electron fraction to decrease as well as probe current in a focused spot. It can be mitigated by lowering the distance in the gaseous environment which beam electrons (BE) pass through, increasing the BE energy, probe current and dwell time, or choosing a suit- able gas type and its pressure [13,14] . Nevertheless, a useful signal from a beam spot region is supplemented with an unwanted background signal generated by inelastic beam-gas interactions and elastically scattered BE, generally governed by the Poisson distribution probability in the skirt region [15] . It can cause worsening of signal-to-noise ratio (SNR), image resolution, as well as the X-ray microanalysis spatial resolution in the ESEM. Investigation of samples with a low atomic number (low Z samples) or wet samples in their native state susceptible to radiation damage increases demand on new high-efficiency and energy-sensitive detection systems. Given the above, research and development of new detection systems for the characterisation of samples in a wide range of working conditions is one of the most important topics for future progress in the ESEM.

So far, the most efficient detectors of secondary electrons (SE) in the ESEM use a principle of gas ionisation that proceeds as a cascade or avalanche between a grounded sample holder and a detection electrode supplied with a positive voltage, placed under a pole piece of an objective lens [16–18] . The signal electrons are accelerated by an electrostatic field. They then ionize gas molecules, generate ions and new electrons and thus amplify the detected signal [19] . The amplification depends namely on three factors: the intensity of the electrostatic field between the detection electrode and the grounded sample, the path length of the signal electrons through the gas, and the pressure and type of ionisation gas [20,21] . This principle was used in the Environmental Secondary Detector (ESD) [22] . Unfortunately, the ESD is unable to detect SE and backscattered electrons (BSE) separately [23] . For this reason, the ESD was developed into the Gaseous Secondary Electron Detector (GSED) [24] . The GSED provides a cleaner SE signal, but it still detects some BSE signal [23] . A multi-electrode configuration of the gaseous detector device was proposed by Danilatos to separate various signals emitted from the sample surface [25] . The physical principle of the multi-electrode configuration was implemented in the technical design by Armstrong et al. [24] , and it is used commercially in the ESEMs of FEI Inc. Nevertheless, the BSE are not yet separated completely from the SE image. The contribution of BE, SE, and BSE to the total amplification of the

signal by the ionisation of the gas was simulated by Meredith et al. [26] . Toth et al. [27] introduced a system for the detection of SE at gas pressures exceeding 1 kPa. This system uses a stainless steel needle-shaped anode with a radius of curvature of approx. 50 μm, which allows an optimal gradient of the electrostatic field for electron impact ionisation of gas molecules and detection of the amplified signal to be made free of dielectric breakdown. A similar detection system based on a biased nano-wire situated in close proximity to the sample and used as a detection electrode was introduced by LEO (Zeiss Company) [28] . An SE detector working on the same principle as the two detectors mentioned above, but with the detection electrode situated on the sample stage at a fixed distance from the sample, was designed by Fitzek et al. [29] The best of the commercially available detection systems of SE in the ESEM is the Helix (FEI Inc). This system uses the magnetic field of an ultra-high resolution magnetic immersion objective lens and the electrostatic field of an annular detection electrode placed at the bottom part of the objective [30]. The Helix detector allows a high resolution image (1.8 nm at the energy of BE 3 keV) at a short working distance (up to 3 mm) and low gas pressure (up to 200 Pa) to be recorded. A recent study in the field of generation and detection of a signals in high pressure conditions implies the significant role of positive ions [31]. For this reason, the Helix detector is equipped with an “ion trap electrode”, which allows a number of ions in the vicinity of the sample and detection electrode to be controlled. The utilization of the magnetic field to the signal selection and amplification of the SE signal are very promising for the future detection of the signal electrons in the ESEM.

The Two-Stage SE Detector and Intermediate SE Detector were introduced by Slówko [32] . These detectors contain a scintillation detector of the Everhart–Thornley type combined with a micro- sphere plate [33] . The same author also published a Combined Directional Detector [34] for the three-dimensional imaging of electrically non-conductive and semi-liquid samples in the ESEM, newly equipped with a coaxial ion micro-source [35] . This detector comprises two quadruple (4Q) semiconductor BSE detectors for the detection of high take offangle BSE1 and an ionisation type of detector for the detection of BSE2 and SE.

The Low Vacuum Secondary Tescan Detector (LVSTD) was developed by Jacka et al. [36] . This detector is based on the modified design of the Everhart-Thornley detector with a vacuum separated and differentially pumped detection chamber located behind a Microlens Differential Barrier and pumped by a small turbo-molecular pump. A similar working principle is used in the scintillation SE detector developed by Jirák et al. [37] from the Institute of Scientific Instruments of the Czech Academy of Sciences (ISI of the CAS). In this detector, the biased scintillator (8–12 keV) is located in the differentially pumped chamber, separated from the

specimen chamber by a system of two pressure limiting apertures (PLA). These apertures, with applied voltage, create an electrostatic lens which focuses the signal electrons through to the scintillator.

The study of specimens under the high pressure conditions in the ESEM need not be necessarily associated with "direct" signal electron detection. As was pointed out by Danilatos [38], photons can also be detected. Luminescence in gas ("gaseous scintillation"), a consequence of inelastic excitation collisions of the signal electrons with the gas molecules and their subsequent deexcitation (a process lasting approx. 10^{-8} s), is accompanied by the emission of light quanta in the range from ultraviolet to infrared radiation, as shown by Takahashi et al. [39] and Fraga et al. [40] . This principle is applied in the Variable Pressure Secondary Electron Detector (VPSE detector), patented by the Zeiss company [41], and the Gaseous Scintillation Detector (GSD), presented and described by Morgan et al. [42], which collect and transfer the detected photons via a light-guide to a photomultiplier. A comparison of the GSED and GSD in the operating conditions of the ESEM was published by Morgan et al. [42].

Autrata et al. introduced a very sensitive BSE detector using the original YAG: Ce^{3+} (yttrium aluminium garnet, $Y_3Al_5O_{12}$ doped with Ce^{3+}) [43] and YAP: Ce^{3+} (yttrium aluminium perovskite, $YAlO_3$ doped with Ce^{3+}) [44] scintillators for the study of the material contrast of samples. This allows the observation of wet bio- logical samples at lower energies of BE [45, 46].

Due to a demand for the simultaneous detection of SE and BSE, the YAG BSE detector was developed into the combined detector. BSE are detected by the scintillator and SE by the ionisation detector [47]. A hole in the scintillator of the combined detector creates the PLA for differential pumping of the ESEM [48]. The ionisation SE detector of the combined detector is created by a thin electrode from indium tin oxide (ITO), deposited on the bottom side of the scintillator. Many types of materials and shapes of detection electrodes were tested for the separation of BSE and SE signals [49] , for the recording of spatial distribution of signal electrons [50] , and for the study of biological samples [51,52] in our non-commercial ESEM AQUASEM II. Another version of the combined detector al- lows the signals from lateral sides of the scintillator to be detected separately using a halved scintillation single crystal. A comparison of YAG: Ce^{3+}, YAP: Ce^{3+} and plastic scintillator NE102A [53], as well as a design of an optimum shape of light-guides [54], were published by Danilatos. These detectors are mostly situated be- low the ESEM objective lens. Some special "in lens" versions were also designed and situated inside the differentially pumped chamber for detection of SE going through the PLA2 up to the ESEM objective [55,56].

This paper introduces a new Combined System for high- efficiency detection of Secondary and Backscattered Electrons (CSSBE) in the ESEM. The description of the detection system is focused on a new Ionisation Secondary Electron Detector with an electrostatic Separator (ISEDS); however, the other parts of the CSSBE (the combined ionisation detector and the improved scintillation BSE detector) will be briefly mentioned.

Materials and methods

The CSSBE detector

The CSSBE for simultaneous high-efficiency detection of SE and BSE in the ESEM contains three mutually integrated detectors (see Fig. 1). The first part of the CSSBE detector consists of a halved scintillator with a small hole in the centre (typical diameter 500 μm). It is possible to use standard scintillators of YAG: Ce^{3+}, YAP: Ce^{3+}, or CRY018 (unpublished chemical formula) with appropriate light-guides (fused-silica and decolourised methyl methacrylate monomer with no ultraviolet absorbing additives). The scintillator can be used to separate the signal coming from its right and left side in the same way as the conventional scintillation BSE detector introduced by Autrata et al. [43,44] and the PLA2 of the ESEM AQUASEM II [47] . A simplified version of this part of the CSSBE may consist of an undivided scintillator and one light-guide.

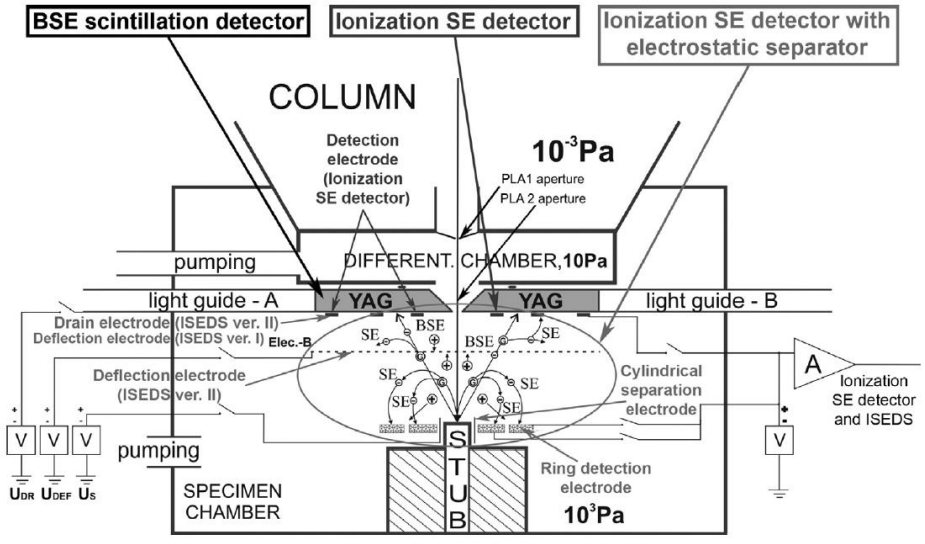

Fig. 1. Schematic of the position of the individual parts of the CSSBE in the ESEM specimen chamber.

The second part of the CSSBE is created with segmented ITO electrodes deposited on the input surface of the scintillator. These shape and size optimized electrodes

can be used for the detection of the signal electrons by a conventional ionisation SE detector, working on a similar principle as ESD, but also as electrodes of the ISEDS.

The third part of the CSSBE is the ISEDS that consists of three electrodes: a ring detection electrode placed close to the sample holder, a cylindrical separation electrode, and a deflection electrode deposited on the bottom side of the scintillator. The positively biased single ring detection electrode (U_D, hundreds volt), whose active side faces BE and surrounds the sample substantially in or under the sample plane, may also have a concentric ring de- sign or be divided into sectors. In the case of the sectors, the secondary electron signal distribution may be studied on the basis of the spatial angle. Before the signal electrons reach the detection electrode, their trajectories are curved by the electrostatic field of the deflection electrode. The sample is further surrounded by the separation electrode for reinforcement of the effects of the deflection electrode and better focusing of signal electrons to the detection electrode. The vertical position of the separation electrode is adjustable in relation to the sample and is supplied with a low positive or negative voltage (U_S). Regarding the position of the separation electrode, which is slightly above or in the plain of the sample, this electrode could be made from carbon or metal with a thin carbon layer similarly to the deflection electrode. The signal of electrons detected by the detection electrode is amplified un- der an increased amount of electron-gas collisions occurring along their extended trajectories in the gaseous environment from the sample to the detection electrode.

The ISEDS ver. I allows sample observation with high resolution at very short sample-to-PLA2 distances (1-4 mm). Its modification for working under longer distances is called ISEDS ver. II. It differs in the moving of the deflection electrode closely to the sample and using the drain electrode (see Fig. 1). The deflection electrode can be designed as a shape and size optimised and conductively isolated grid, supplied with negative voltage typically from one to ten volts (U_{DEF}). For lowering electron emission from the interaction of BSE or diffused BE with deflection electrode, its surface can be covered with a resistant thin carbon layer. The detection of the electrons emitted from the interaction of BSE or BE with the scintillator or metal parts of the objective is prevented by the fact that they are attracted back with a positively biased drain electrode (U_{DR}, one to ten volts).

The ISEDS is being further improved; a magnetic circuit generating a directed magnetic field opened towards the sample chamber has been added. A subsequent spiral motion of the signal electrons in the magnetic field causes further extension of the electron trajectories and hence increases the signal amplification in the gas. These results will be published in a forthcoming paper.

Samples for measurements

The CSSBE working principle and ability for high-efficiency detection were demonstrated by the measurement of the signal intensity in its dependency on various detector configurations, set- tings, and gas pressure. A testing sample was created from a car- bon cylinder with two holes (with diameters of 0.5 mm and 1 mm, respectively, and 6 mm in length); small gold and nickel plates were placed closely to the larger hole and on the same surface level. The surfaces of both the plates were roughly polished.

The first eccentrically situated hole was used as a Faraday cage for measuring the absorbed BE current. The beam current was kept constant and precisely measured at the pressure of 0.01 Pa for each experiment using the KEITHLEY 485 pA m. Owing to necessity to measure the beam current exactly, it was measured by beam blanking first, and then this value was subtracted from the value of the absorbed BE current.

The second concentrically situated hole was used for measuring the background signal (noise) induced by beam diffusion in gas. The background signal was measured with the same detector parameters and under the same conditions as they were during the experiment. The background signal was subtracted from the raw signal detected from the sample to obtain the pure signal intensity from Au and Ni, respectively.

The ISEDS's capability for energy separation was demonstrated by the observation of a six-nanometre-thin carbon layer sputtered through a grid on a silicon wafer. The thin carbon layer was made by the Leybold Heraeus-Z550 magnetron sputtering system with a precision below 1 nm and checked by the Atomic Force Microscope Pacific Nanotechnology Nano-R.

The high detection efficiency of the ISEDS was demonstrated by the imaging of non-coated polystyrene microspheres (Agar scientific, diameters 2, 5, and 10 μm, respectively) placed on carbon or silicon substrates.

All experiments were performed on the experimental, non- commercial ESEM AQUASEM II [5] equipped with a hairpin cathode and developed by the Environmental electron microscopy group at the ISI of the CAS.

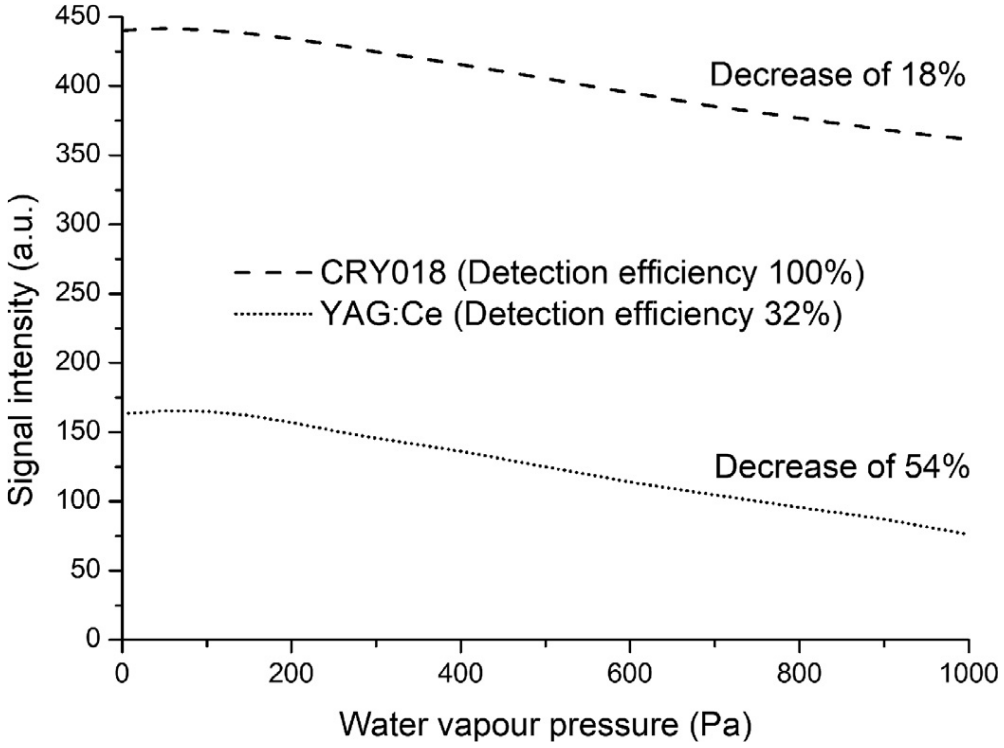

Fig. 2. Signal intensity as a function of the water vapour pressure for different scintillators. The gold sample, beam energy 20 keV, beam current 25 pA, PLA2 to sample distance 1 mm, scintillators CRY018 and YAG: Ce^{3+}.

Results and discussion

The BSE scintillation detector

The practical impact of different scintillators with identical position and geometry and special improvements for maximum efficiency of BSE detection in the high gas pressure conditions of the ESEM were tested.

The detection efficiency can be derived from measuring the level of the detected signal from the gold part of the first testing sample (see Fig. 2).

A substantial increase in the detection efficiency between the two scintillators is evident. This significant difference was obtained due to several improvements to the BSE detectors (the know-how of ISI of the CAS); for example, the ITO coated surface on the bot- tom side of the scintillators for the ESEM was minimised (over 80% of the BSE bottom surface is free of any conductive coating for CRY018). These improvements were invented and experimentally proven by our group many years ago, although unpublished to date. The subsequent decrease in the signal intensity during the in- crease in water vapour pressures from 10^{-3} Pa to 10^{3} Pa (see Fig. 2) is caused by the gradual decrease in BSE energy due to inelastic collisions with gas molecules before reaching the scintillator. The number of collisions

significantly increases with the length of the traversed gap between the sample and the scintillator (in our case, from the PLA2 to the sample surface) and also with gas pressure, as can be seen in Fig. 2. The difference between the decrease rate of signal intensity from CRY018 and YAG: Ce^{3+} (18% for CRY018 and 54% for YAG: Ce^{3+}) when increasing the gas pressure is caused by the increased sensitivity of CRY018 to low energy BSE. The in- creased sensitivity was confirmed by the experiment in which the BSE YAG: Ce^{3+} detector was incapable of recording the image of the experimental sample at beam energies below of 2 kV (beam current 25 pA), while the same detector equipped with CRY018 in- stead of YAG: Ce^{3+} could be used down to beam energies of 1 keV. Signal of electrons with the energy of around 1 keV amplified in the gas significantly contributes to the signal intensity detected by the CRY018. These results will be discussed in more detail in a forthcoming paper.

The ISEDS - Working principle

The first draft of the ISEDS was developed on the basis of simulations of the signal electron trajectories in a vacuum using the SIMION 3D program. Despite the inaccurate and partially misleading results of the simulations in a vacuum, this method is useful for rough design optimization and quick estimation of results for various developmental versions. Moreover, simplified results can also be helpful for a basic explanation of the ISEDS working principle (see Fig. 3). Another development of the CSSBE with the ISEDS was based on a combination of experimental results and simulations in the EOD program [57], extended with an MC module [49] to include the collision phenomena of electrons with gasses, as will be shown later.

SE emitted from the sample at the spatial angle of 0 to 180 are deflected by the electrostatic field of the deflection electrode supplied with a negative voltage and the separation electrode with a negative or positive voltage towards the space above the detection electrode placed in the same plane or below the sample (see Fig. 3 A). The high-energy BSE are not affected by the electrostatic field of the deflection electrode and pass through the grid and hit the scintillator, with the drain electrode supplied with a positive voltage.

The ISEDS ver. II equipped with the drain electrode represents an optimised version allowing minimisation of the detection of SE type III, which are generated after the BSE interactions with the metal parts of the microscope or the scintillator as well as the “environmental” electrons resulting from the interactions of the BSE and BE with the gas atoms or molecules in the detected signal. The low-energy BSE, whose energy is reduced after passing through the high-pressure environment and then

also by the influence of the electrostatic field of the deflection electrode (grid), can generate an increased number of low energy "environmental" electrons in the space above the deflection electrode. All of the above- mentioned types of electrons are caught by the drain electrode and are thus prevented from being attracted by the electrostatic field of the detection electrode (see Fig. 3B). The efficiency of the drain electrode is further multiplied by the electrostatic field of the de- flection electrode supplied with negative voltage.

The electrostatic field of the deflection electrode allows the regulation of a number of generated positive ions whose presence, not only lowers the number of the detectable SE, but also allows compensation of the negative charge on the surface of electrically non- conductive samples. If a negative voltage is supplied to the separation electrode, the recombination processes between the electrons and the positive ions may be controlled. If the low positive voltage is supplied to the separation electrode, the influence of the deflection electrode is reinforced and the bending of the low energy SE's trajectories in the direction of the space above the detection electrode of the ISEDS is supported. This effect is also supported by the electrostatic field of the positively biased detection electrode. In this case, the electrostatic field of the separation electrode and detection electrode jointly increase the energy of the SE above its minimal energy necessary for gas ionisation.

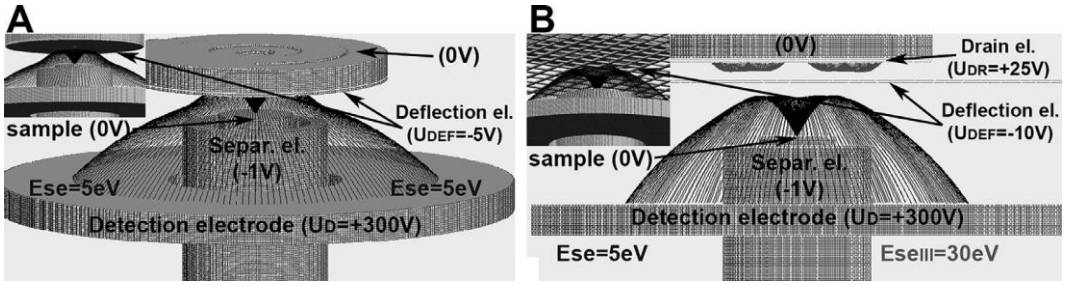

Fig. 3. A) The ISEDS ver. I –without the drain electrode, B) The ISEDS ver. II –with the drain electrode. A rough, preliminary simulation: trajectories of detected SE with the energy 5 eV simulated using the software SIMION 3D in the vacuum.

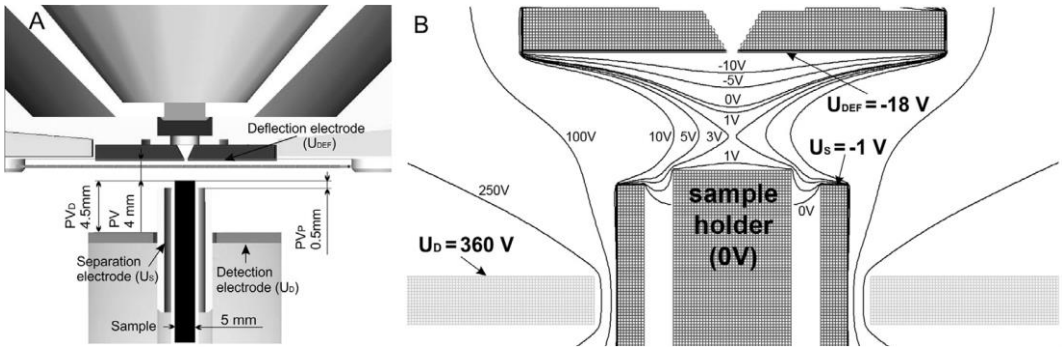

Fig. 4. The model of the ISEDS ver. I A) description of experimental distances B) electrostatic field distribution calculated by SIMION 3D.

The detection electrode distance (PVd) is variable, however, and should always be longer than the sample-to-PLA2 distance (PV), commonly termed the environmental distance. In this case, low energy signal electrons, which are continually accelerated by the electrostatic fields of the detector, are moving in the direction of the detection electrode along significantly longer trajectories than the BE from the PLA2 to the sample. This enables the detection of the strongly amplified signal with high SNR at a low PV and, therefore, at low beam energies as well.

The geometric configuration of the electrodes (Fig. 4A) and their potentials define the distribution of the electrostatic field (Fig. 4B), which has a crucial influence on the type of the detected signal. Changes in the electrode potentials adapt the detector for a specific use, such as for a requested type of the detected information, or for the pressure facilitating the strongest signal at thermodynamic equilibrium, etc.

ISEDS—Experimental measurement

The impact of the different potentials and distances of the ISEDS's electrodes on the signal intensity will be described in this part of the paper. Both types of the ISEDS have been experimentally tested. Despite the fact that the design of the ISEDS ver. II brings benefits for the detection of a very high portion of SE, the presence of an additional electrode makes the ISEDS ver. II difficult for practical use. For this reason, only the ISEDS ver. I will be described in more detail. The strongest signal was measured for PV = 4 mm and $U_{DEF} = -18$ V (Fig. 5) due to the electrostatic field that efficiently deflects most low-energy SE towards the detection electrode and maximizes the detector's collection efficiency. The electrons reach the peak ionisation probability of gas molecules [1] after travelling about half of their trajectories (see Fig. 4 B, the 100 V equipotential). Low energy SE are accelerated and follow longer paths towards the detection electrode. The path prolongation of the SE is evidenced, not only by the maximized detected signal

intensity, but also by the characteristic shift in the signal peak towards lower gas pressure (Fig. 5). The high-energy electrons are not affected and thus are not directly detected. The ability to focus the signal electrons onto the detection electrode depends on their emission direction from the sample as well as their initial energy and the strength of the electrostatic field. At PV ≤ 2 mm and U_{DEF} = −18 V, the majority of the slow SE with energies from 3 eV to 5 eV are repelled by the deflection electrode and return back onto the sample. The majority of the SE emitted from the sample at a higher energy and a small angle from the sample surface normal escape through the PLA2 or hit the deflection electrode. In this case, the detector's col- lection efficiency is minimal. For an increase, it is advantageous to decrease U DEF to −3 V (Fig. 5).

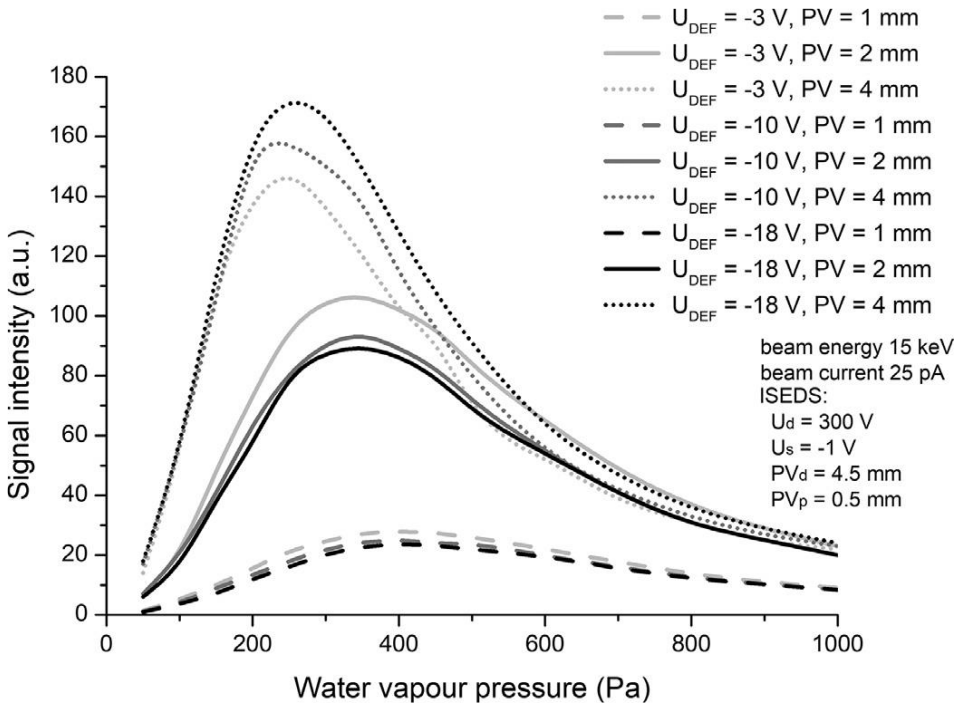

Fig. 5. Signal intensity as a function of water vapour pressure for different U DEF and PV, gold sample.

As has been mentioned above, a significant advantage of the ISEDS is its ability to alter (increase) PV_d while PV is preserved or decreased (Fig. 4 A). This enables maximization of the signal amplification of the detected electrons in the gas and, simultaneously, minimization of BE scattering on their way to the sample.

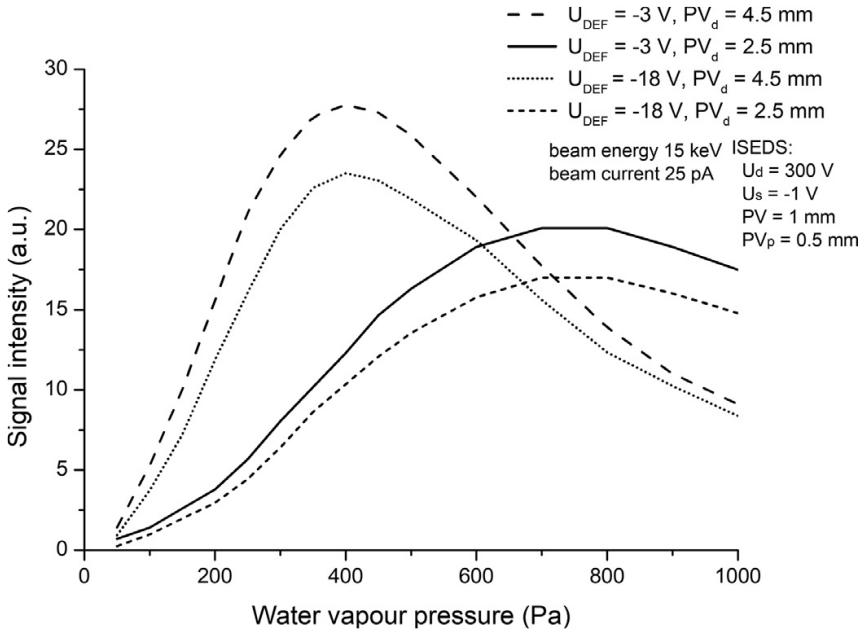

Fig. 6. Signal intensity as a function of water vapour pressure for different and U_{DEF}, PV d , gold sample.

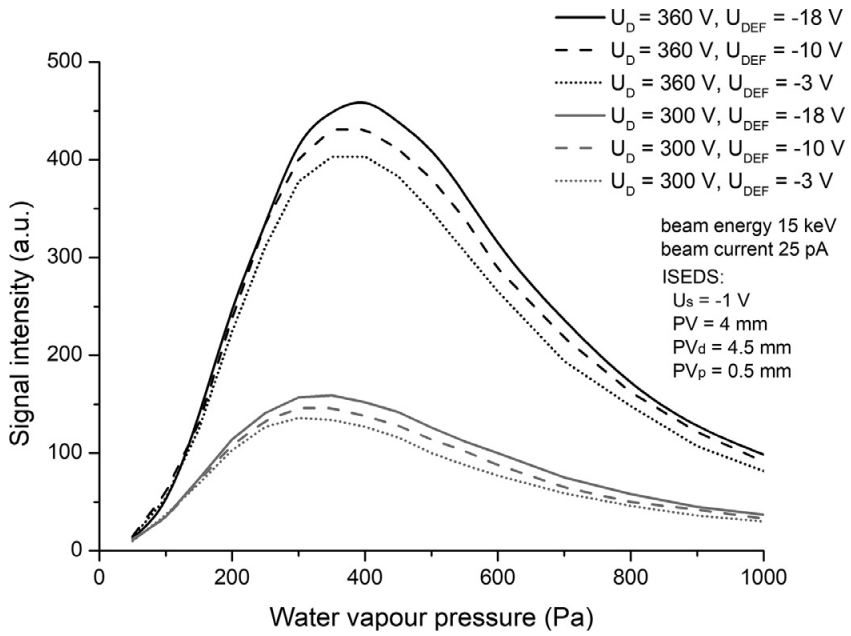

Fig. 7. Signal intensity as a function of water vapour pressure for different U D and U_{DEF}, gold sample.

The dependence of the signal strength detected by the ISEDS on the PV $_d$ and the water vapour pressure at different U $_{DEF}$ is in Fig. 6. An increase in PV $_d$ from 2.5 mm to 4.5 mm leads to an increase in the signal strength by about 32% (maximum vs. maximum). The signal intensity maximum is also shifted to a lower water vapour pressure, from 750 Pa to 400 Pa, which indicates a prolongation of the signal electron paths. An even higher increase in the signal amplification can be achieved

by increasing the PV (Fig. 5). In this case, electrons emitted at smaller angles from the sample surface normal, travelling in even longer paths in the gas, will also be detected.

An increase in detection electrode potential (theoretically up to the value of dielectric breakdown) is another way of improving the detection efficiency of the ISEDS (Fig. 7). This effect is well known, and it can be observed in all detector types based on the principle of impact ionisation in gas in the ESEM. In the ISEDS, mainly SE with the energy of 3 eV to 5 eV are retracted from the sample by the high-strength electrostatic field above the detection electrode (Fig. 4 B). The increase in the detected signal (by about 280% when comparing the maximum vs. maximum) after changing U_D from 300 V to 360 V at U DEF = 18 V is caused, firstly, by a better penetration of the electrostatic field into the region around the sample (Fig. 4 B) and, secondly, by an increase in the electrostatic field strength above the detection electrode, where the majority of the ionisation collisions occur.

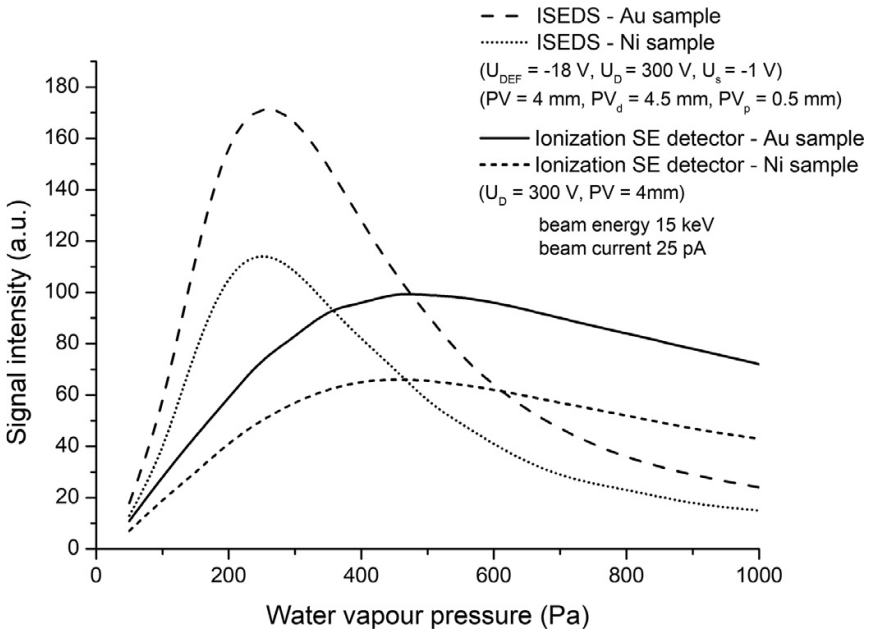

Fig. 8. Signal intensity measured with different detectors as a function of water vapour pressure.

The ISEDS—comparison with ionisation SE detector

In order to assess the detection efficiency of the new ISEDS, the detected signal intensity at different water vapour pressures was measured and compared with results from the ionisation SE detector (see Fig. 8). Measurements were made under the same beam conditions and optimal PV for both detectors. The detected signals of both detectors are correctly comparable because they utilize the same physical principles: the signals are amplified by the same preamplifier and are connected to the same signal input of the ESEM, unlike the BSE YAG:Ce^{3+} detector.

Measured dependencies of the signal detected by both detectors on water vapour pressure show a greatly amplified signal detected with the ISEDS. The detected signal from nickel as well as gold is higher by about 73% (maximum vs. maximum) (see Fig. 8). The shapes of the detected signals as well as the positions of the maxima are different. Therefore, it was advantageous to combine the detectors within the CSSBE and use them for specific applications. It is highly recommended to use the ISEDS for the high resolution study of small samples at pressures of up to 500 Pa. Fig. 9 A and B confirm the above-mentioned difference between the level of the detected SE signal by the ISEDS and the Ionisation SE detector. For comparison, BSE imaging (the CSSBE BSE YAG: Ce^{3+} detector) of polystyrene spheres with very low BSE coefficients are in Fig. 9 C.

The ISEDS—low dose imaging in the ESEM

The very high detection efficiency of the ISEDS is presented by Fig. 10 A and B. These are polystyrene spheres on a silicon wafer imaged at a water vapour pressure of 300 Pa, a beam energy of 5 keV, and a beam current of 1 pA in the ESEM AQUASEM II. The ability to detect a high portion of SE signal is presented by clear topographical contrast allowing small particles on the surface of the spheres, which is highlighted by white arrows in Fig. 10 A, or thin carbon film on the surface on the lower left sphere, which is highlighted by the dashed white arrow in Fig. 10 B, to be seen. The image of the polystyrene spheres recorded under an extremely low beam current of 0.2 pA, a beam energy of 5 keV, PV 4 mm, and a water vapour pressure of 300 Pa in the ESEM AQUASEM II is presented in Fig. 10 C. In ultra low-dose conditions (probe cur- rent 0.2 pA, dwell time 1.5 ms), the electron dose is 0.106 Cm −2. At higher probe current and appropriate dwell time (1 pA, 1 ms) the electron dose rises to the still relatively small value of 0.368 Cm −2 in comparison with commonly used parameters in the ESEM (for example: 100 pA, 0.23 ms, 8.332 Cm −2). Longer dwell times (1 and 1.5 ms, Fig. 10 B, C) were used to increase SNR and due to impossibility to apply special modes like scan integration, noise reduction etc. The ability to work well also at higher water vapour pressures is confirmed by Fig. 10 D, E, and F and was taken by the ISEDS equipped with a larger detection electrode.

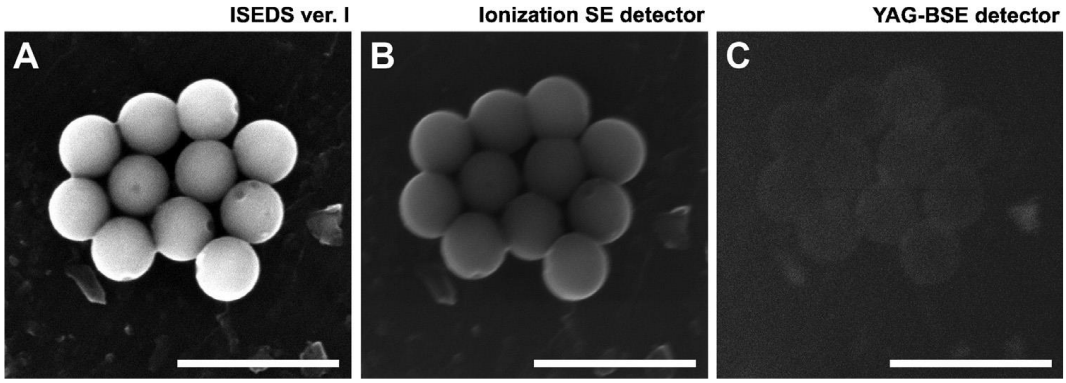

Fig. 9. Polystyrene spheres observed using A) ISEDS ver.I: U_{DEF} = −10 V; U_D = 300 V; U_S = −1 V, PV = 4 mm, PV_d = 4.5 mm, PV_p = 0.5 mm. B) Ionization SE detector: U_D = 300 V, PV = 4 mm. (C) BSE YAG:Ce^{3+} detector. Beam energy 20 keV, beam current 40 pA, water vapour pressure 300 Pa, dwell time 0.63 ms, databar 5 μm.

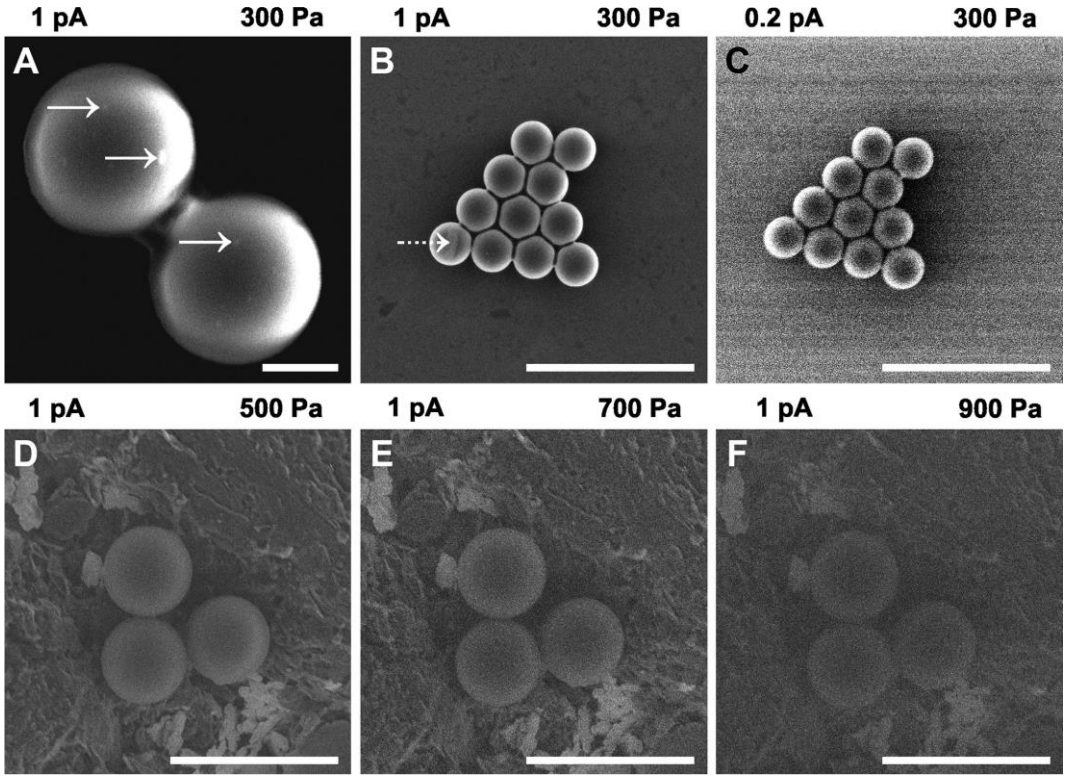

Fig. 10. Polystyrene spheres observed using ISEDS ver.I: U_S = −1 V, PV = 4 mm, PV_d = 4.5 mm, PV_p = 0.5 mm, beam energy 5 keV; A,B,C) U_{DEF} = −18 V, U_D = 360 V; A) dwell time 0.63 ms, B) dwell time 1 ms, C) dwell time 1.5 ms; D,E,F) U_{DEF} = 0 V, dwell time 0.38 ms; D) U_D = 313 V, E) U_D = 364 V, F) U D = 390 V. Databar A) 2 μm; B,C,D,E,F) 20 μm.

The ISEDS energy-selective detection in the ESEM

The possibility to precisely adjust the intensity and shape of the electrostatic fields along the path of signal electrons allows low energy electrons to be deflected with varying efficiency, depending on their energy and emission angle, as well as the intensity of the electrostatic fields of the ISEDS. Consequently, the resulting energy of the signal electrons with the energy in the selected range is affected and the shape and length of their trajectories are modified or, more specifically, elongated or shortened. Thanks to this effect, the detected electrons may be filtered on the basis of their energy (see Fig. 11 A). For the simulation of the signal electron trajectories in our ISEDS, the EOD program, extended with a plug-in module including electron-gas collision phenomena [49], was used. According to the simulations, the electrons with energy lower (higher) than required move along more (less) curved trajectories and fall on the less (more) distant ring of the detection electrode, i.e. the ring with smaller or bigger diameters, or return back to the sample, missing the detection electrode (see Fig. 11 B, C). If the detection electrode is also divided into segments, signal electrons could be detected, not only according to their energy, but also according to their emission angle.

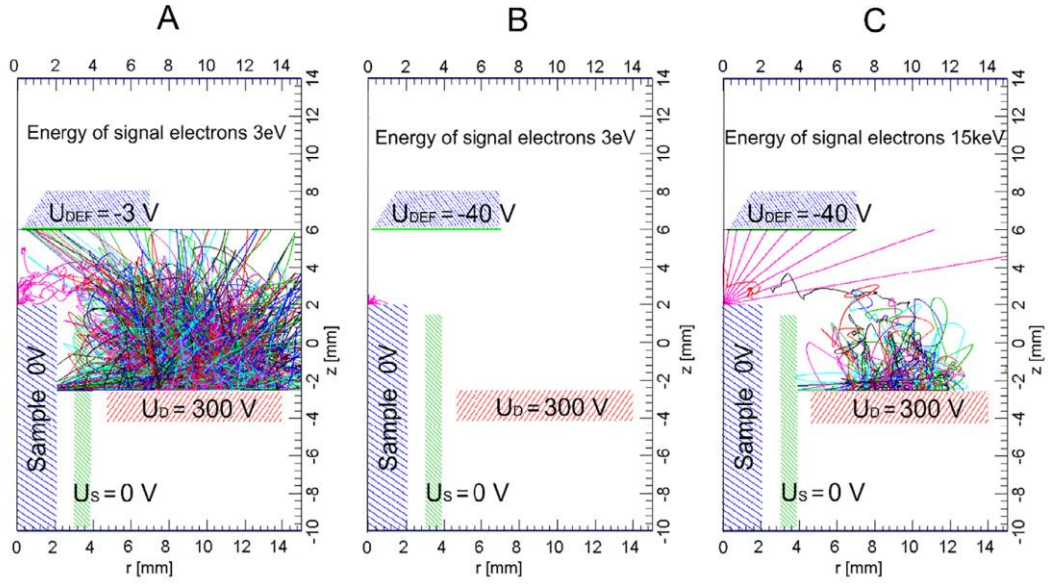

Fig. 11. Simulations of signal electron trajectories in the ISEDS ver. I using the EOD software extended with the Monte Carlo plug-in module. Trajectories of 20 electrons were traced in water vapour pressure 100 Pa. PV = 4 mm, PV_d = 4.5 mm, PV_p = 0.5 mm.

For confirmation of MC simulations, an experimental observation was made. A thin carbon layer (6 nm) on a silicon wafer was observed at different voltages on the deflection electrode (see Fig. 12).

If the thin carbon structure is visible, a great proportion of the SE is detected. On the other hand, a great proportion of detected BSE or environmental electrons produced by them, which are emit- ted from the deeper bulk of the sample, cause the disappearance of the carbon structure in the recorded picture. This assumption is supported by the results of the Monte Carlo simulations of inter- action volume (imaged up to 100 nm) showing the dependence of signal electron energy on the escaped depth when the U_{DEF} is ap- plied, see Fig. 13 A (U_{DEF} = -3 V) and Fig. 13 B (U_{DEF} = −40 V). These simulations are in accordance with experimental conditions and results in Fig. 12 A–F.

The increasing intensity of the electrostatic field between the deflection electrode and the sample causes filtering of low energy electrons (mainly SE) in the detected signal, and the silicon mesh in the carbon stays invisible. Even if the silicon surface is located 6 nm lower than the surrounding carbon layer (Fig. 12 A–E, the cross-shaped pattern), it appears brighter due to the stronger signal electron emission and can create the impression of structure elevated above the surface (see Fig. 12 A-D).

The lower quality of Fig. 12 A–F is caused by the low emission of signal electrons from the C/Si sample observed under relatively low beam current at a gas pressure of 300 Pa by the ESEM AQUASEM II, which is equipped with a hairpin cathode. For comparison, the same sample was imaged by the in-column SE detector (see Fig. 12 G) and the BSE-YAG:Ce^{3+} detector (see Fig. 12 H) in high vacuum conditions of high resolution SEM JEOL JSM 670F, equipped with an immersion objective and cold field emission gun. Our experimental results confirm that the deflection electrode acts as an adjustable high-pass filter for the selected range of energies of signal electrons. According to the strength of the electrostatic fields, the ISEDS allows signal electrons with energies from one to a hundred eV to be filtered out (see Fig. 13).

Given the above-mentioned results, that is, the level of ability to filter the detected signal in gas pressure conditions, the ISEDS allows visualising information from various ranges of depth in low Z samples such as silicon or carbon. Using diverse beam energies, the information range of accessible depth can be adjusted and more specified. The filtering efficiency is increased by the patented configuration of ISEDS electrodes [56], allowing a reduction in the ionisation of gas molecules in the space above the sample, and strongly increasing in the space above the detection electrode (see Fig. 11 A). Nevertheless, the ability to detect selectively filtered signal electrons decreases with increasing gas pressure in the specimen chamber of the ESEM. For this reason, the practical usability of the filtering of signal electrons, as well as the ability to detect a very high portion of SE signals, is limited by a gas pressure of about 500 Pa at PV < 5 mm. Even though these versions of ISEDS are

optimised for the detection of SE, complete suppression of BSE in the detected signal is not possible as yet.

The shape of the sample and particularly its charging has an appreciable influence on the ISEDS's functionality. The electrostatic field in the proximity of the sample surface has a major influence on the trajectories of the signal electrons. The charging of the sample also changes the electrostatic field around it and may prevent the filtering of the detected electrons. In the case of electrically non-conductive samples, it is always necessary to adjust the detector for optimal conditions. If the charging of the sample is stronger, the electron filtering, which uses the ISEDS, becomes impossible.

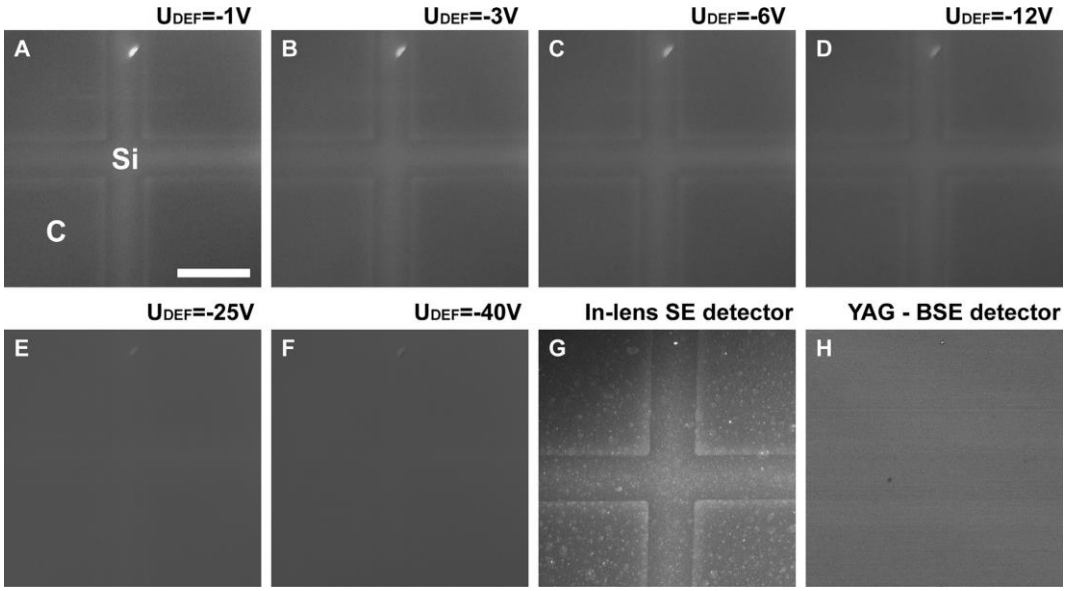

Fig. 12. Six nanometres thin carbon layer sputtered through the grid on the silicon wafer. Recorded using ISEDS ver.I in AQUASEM II, water vapour pressure 300 Pa, U_D = + 360 V, U_S = −1 V, PV = 4 mm, PV_d = 4.5 mm, beam current = 50 pA, U_{DEF} = A) −1 V, B) -3 V, C) −6 V, D) −12 V, E) −25 V, F) −40 V. G) recorded with in-lens SE detector and H) BSE-YAG detector of SEM JEOL JSM 6700F. Beam energy 15 keV. Databar 100 μm.

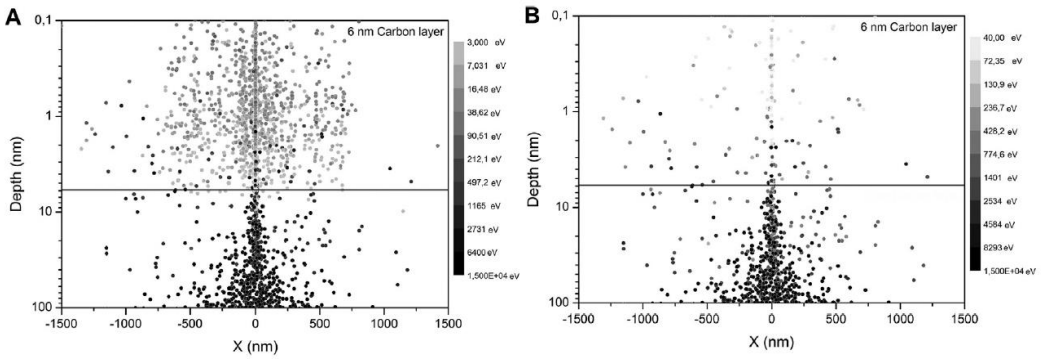

Fig. 13. The Monte Carlo simulation of interaction volume inside 6 nm thin carbon layer on the silicon wafer and escape depth of signal electrons with energies from A) 3 eV to 15 keV and B) from 40 eV to 15 keV. Beam energy 15 keV, 50 0 0 0 electrons were traced by Geant4 software.

Conclusion

Research and development of novel detection systems is among the crucial disciplines which widen the capabilities of contemporary electron microscopy. This paper presents a new CSSBE in several modifications that have been developed, simulated, and experimentally tested for over ten years at the Department of Electron Microscopy at the ISI of the CAS. Thanks to the use of special scintillation material and other improvements for high-efficiency detection of BSE in the ESEM, an average increase in the detected signal of 312% was achieved at water vapour pressures from 100 Pa to 10 0 0 Pa, a beam energy of 15 keV, and a beam current of 25 pA. For collecting a signal with a high proportion of SE in gas pressures of up to 500 Pa in the ESEM, a new ISEDS was introduced. The use of a patented electrode configuration [56] and optimized impact ionisation on prolonged SE trajectories increases the ability of the ISEDS to produce a signal stronger by 73% from nickel as well as gold (maximum vs. maximum) compared to the ionisation SE detector. In the case of electrically conductive samples or semiconductors, the ISEDS is able to filter low-energy electrons and provide contrast that can vary continuously between more topographic and material, or, in other words, the signal from various ranges of the depth of low Z samples at water vapour pressures of up to 500 Pa. In view of the above, this is the world's first detection system allowing the filtering of detected low-energy signal electrons according to their energy in the gas pressure conditions of the ESEM. The very high detection efficiency of the ISEDS was experimentally confirmed by the imaging of low atomic number samples (polystyrene spheres) at a beam energy of 5 keV, a beam current of 1 pA, and also at, so far, the lowest beam cur- rent of 0.2 pA at a water vapour pressure of 300 Pa in the ESEM AQUASEM II. In ultra low-dose conditions (probe current 0.2 pA, dwell 1.5 ms), the electron dose is 78 times lower than commonly used conditions (e.g. 100 pA, dwell 0.23 ms). The new CSSBE com- bines the enhanced BSE detector and two SE detectors that supplement each

other due to their different underlying concepts and intended purposes. This encompasses the concept of the highly efficient and universal detector for the ESEM for wide-ranging applications in science and industry.

Acknowledgements

The work was supported by the Ministry of Education, Youth and Sports of the Czech Republic [LO1212]. The research infrastructure was funded by Ministry of Education, Youth and Sports of the Czech Republic and European Commission [CZ.1.05/2.1.0 0/01.0 017] and by the Czech Academy of Sciences [RVO:68081731].

References

[1] G.D. Danilatos, Foundation of environmental scanning electron microscopy, in: Advances in Electronics and Electron Physics, Academic Press, Boston, 1988, pp. 109–250. http://dx.doi.org/10.1016/S0065-2539(08)60902- 6.

[2] A.M. Donald, The use of environmental scanning electron microscopy for imaging wet and insulating materials, Nat. Mater. 2 (2003) 511–516. http://dx.doi. org/10.1038/nmat898.

[3] G.D. Danilatos, Review and outline of environmental SEM at present, J. Microsc. 162 (1991) 391–402. http://dx.doi.org/10.1111/j.1365-2818.1991.tb03149.x.

[4] D.J. Stokes, Investigating biological ultrastructure using environmental scanning electron microscopy (ESEM), in: A. Méndez-Vilas (Ed.), Science, Technology and Education of Microscopy an Overview, Formatex Research Center, Spain, 2003, pp. 564–570.

[5] V. Neděla, Controlled dehydration of a biological sample using an alternative form of environmental SEM, J. Microsc. 237 (2010) 7–11. http://dx.doi.org/10. 1111/j.13652818.2009.03216.x.

[6] E. Stabentheiner, A. Zankel, P. Pölt, Environmental scanning electron microscopy (ESEM) –a versatile tool in studying plants, Protoplasma 246 (2010) 89–99. 10.10 07/s0 0709- 010- 0155- 3.

[7] V. Neděla, E. Tihlaříková, J. Hřib, The low-temperature methode for study of coniferous tissues in the environmental scanning electron microscope,

Microsc. Res. Tech. 78 (2015) 13–21. http://dx.doi.org/10.1002/jemt.22439.

[8] E. Tihlaříková, V. Neděla, M. Shiojiri, In situ study of live specimens in an environmental scanning electron microscope, Microsc. Microanal. 19 (4) (2013) 914–918. http://dx.doi.org/10.1017/S14319276130 0 0603.

[9] M.J. Garcia-Salinas, A.M. Donald, Use of environmental scanning electron mi- croscopy to image poly (N-isopropylacrylamide) microgel particles, J. Colloid Interface Sci. 342 (2010) 629–635. http://dx.doi.org/10.1016/j.jcis.2009.10.064.

[10] R.E. Cameron, A.M. Donald, Minimizing sample evaporation in the environ- mental scanning electron microscope, J. Microsc. 173 (1994) 227–237. http: //dx.doi.org/10.1111/j.1365-2818.1994.tb03445.x.

[11] G.D. Danilatos, R. Postle, The environmental scanning electron microscope and its applications, Scan Electron Microsc. 1 (1982) 1–16.

[12] J.M. Huggett, P.J.R. Uwins, Observation of water-clay reactions in water sen- sitive sandstone and mudrocks using an ESEM, J. Petrol Sci. Eng. 23 (1994) 255–266. http://dx.doi.org/10.1016/0920-4105(94)90082-5.

[13] R. Gauvin, X-Ray microanalysis of real materials using Monte Carlo simula- tions, Surf. Interface Anal. 37 (2005) 875–886. http://dx.doi.org/10.1002/sia. 2105.

[14] J.F.Le Berre, G.P. Demopoulos, R. Gauvin, Skirting: a limitation for the performance of X-ray microanalysis in the variable pressure or environmental scanning electron microscopy, Scanning 29 (2007) 114–122. http://dx.doi.org/10. 10 02/sca.20 052.

[15] A. Zoukel, L. Khouchav, J.Di. Martino„D. Ruch, Skirting effects in the variable pressure scanning electron microscope: limitations and improvements, Micron 44 (2013) 107–114. http://dx.doi.org/10.1016/j.micron.2012.05.004.

[16] G.D. Danilatos, Secondary-electron imaging by Scintillating Gaseous Detection device, in: G.W. Bailey, J. Bentley, J.A. Small. (Eds.), Proc. 50th Annual Meeting EMSA, San Francisco Press, San Francisco, 1992, pp. 1302–1303.

[17] G.D. Danilatos, Environmental scanning electron microscopy and microanalysis, Mikrochim. Acta 114 (1994) 143–155. http://dx.doi.org/0.1007/BF01244538.

[18] G.D. Danilatos, Radiofrequency gaseous detection device, Microsc Microanal. 6 (20 0 0) 12–20. http://dx.doi.org/10.1017.S143192760 0 0 0 0 015.

[19] G.D. Danilatos , Theory of the gaseous detector device in the ESEM, in: Advances in Electronics and Electron Physics, Vol. 78, Academic Press, Boston, 1990, pp. 1–102 . [20] B.L. Thiel, I.C. Bache, A.L. Fletcher, P. Meredith, A.M. Donald, An improved model for gaseous amplification in the environmental SEM, J. Microsc 187 (1997) 143–157. http://dx.doi.org/10.1046/j.1365-2818.1997.2360794.x.

[20] B.L. Thiel, I.C. Bache, A.L. Fletcher, P. Meredith, A.M. Donald, An improved model for gaseous amplification in the environmental SEM, J. Microsc 187 (1997) 143–157. http://dx.doi.org/10.1046/j.1365-2818.1997.2360794.x.

[21] A.L. Fletcher, B.L. Thiel, A.M. Donald, Amplification measurement of alternative imaging gasses in environmental SEM, J. Phys. D. 30 (1997) 2249–2257. http: //dx.doi.org/10.1088/0022-3727/30/15/018.

[22] G.D. Danilatos, Electron detector for use in a gaseous environment, U.S. Patent 4 (January 1990) 897,545.

[23] A.L. Fletcher, B.L. Thiel, A.M. Donald, Signal components in the environmental scanning electron microscope, J. Microsc 196 (1999) 26–34. http://dx.doi.org/ 10.1046/j.1365-2818.1999.00590.x.

[24] A.E. Armstrong , R.W. Knowles , W.G. Schultz , Detector assembly for a scanning electron microscope, Euro. Patent EP (June 1999) 0924743 .

[25] G.D. Danilatos, Mechanisms of detection and imaging in the ESEM, J. Microsc 160 (1990) 9–19.

[26] P. Meredith, A.M. Donald, B.L. Thiel, Electron-Gas Interaction in the Environmental Scanning Electron Microscopes Gaseous Detector, Scanning 18 (1996) 467–473. http://dx.doi.org/10.1002/sca.1996.4950180701.

[27] M. Toth, M. Unčovský, R. Knowles, Secondary electron imaging at gas pressure in excess of 1 kPa, Appl. Phys. Lett. 91 (2007) 053122. http://dx.doi.org/10.1063/ 1.2768031.

[28] LEO Electron Microscopy Limited, GB Patent application, Heinz, A.H., GB 2 391 696, 2003–5-29.

[29] H. Fitzek, H. Schroettner, J. Wagner, F. Hofer, J. Rattenberger, High-quality imaging in environmental scanning electron microscope–optimizing the pressure limiting system and the secondary electron detection of a commercially available ESEM, J. Microsc. 262 (2016) 85–91. http://dx.doi.org/10.1111/ jmi.12347.

[30] B.L. Thiel, M. Toth, R.P.M. Schroemges, J.J. Scholtz, G. Veen, W.R. Knowles, Two- stage gas amplifier for ultrahigh resolution low vacuum scanning electron microscopy, Rev. Sci. Instrum. 77 (2006) 033705. http://dx.doi.org/10.1063/1. 2183082.

[31] M. Toth, B.L. Thiel, A.M. Donald, On the Role of Electron-ion Recombination in Low Vacuum Scanning Microscopy, J. Microsc. 205 (2002) 86–95. http://dx.doi. org/10.1046/j.0 022-2720.20 01.0 0968.x.

[32] W. Slówko, M. Krysztof, Electron detection in the intermediate chamber of the variable pressure SEM, J. Microsc. 237 (2010) 292–298. http://dx.doi.org/ 10.1111/j.1365-2818.2009.03245.x.

[33] W. Slówko, H. Prasoł, Micro-sphere plate as an electron detector at low vacuum, Vacuum 67 (2002) 191–198. http://dx.doi.org/10.1016/S0042-207X(02) 00113-6.

[34] W. Slówko, M. Krysztof, Detector system for three-dimensional imaging in the variable pressure/environmental SEM, Acta Physica Polonica A 123 (2013) 877–879. http://dx.doi.org/10.12693/APhysPolA.123.877.

[35] W. Slówko, A. Wiatrowski, Coaxial ion micro-source for VP/ESEM –E-beam impact mode, Vacuum 132 (2016) 53–61. http://dx.doi.org/10.1016/j.vacuum.2016. 07.027.

[36] M. Jacka, M. Zadražil, F. Lopour, Differentially Pumped Secondary Electron Detector for Low-Vacuum Scanning Electron Microscopy, Scanning 25 (2003) 243–246. http://dx.doi.org/10.1002/sca.4950250505.

[37] J. Jirák, P. Černoch, V. Neděla, Scintillation SE detector for variable pressure scanning electron microscopes, J. Microsc. 239 (3) (2010) 233–238. http://dx. doi.org/10.1111/j.1365-2818.2010.03377.x.

[38] G.D. Danilatos, Cathodoluminescence of gaseous scintillation in the environmental SEM, Scanning 8 (1986) 279–284. http://dx.doi.org/10.1002/sca. 4950080605.

[39] T. Takahashi, S. Himi, M. Suzoki, J. Ruan, S. Kubota, Emission spectra from ArXe, ArKr, ArN_2, $ArCH_4$, $ArCO_2$ and XeN_2 gas scintillation proportional counters, Nucl. Instrum. Meth. in Phys. Res. 205 (1983) 591. http://dx.doi.org/10.1016/ 0167- 5087(83)90028- 5.

[40] M.M.F.R. Fraga, F.A.F. Fraga, A.J.P.L. Ppolicarpo, Modelling of an IR scintillation counter, Nucl. Instr. and. Meth. in Phys. Res. A442 (20 0 0) 423–427. http://dx. doi.org/10.1016/S0168-9002(99)01267-X.

[41] P. Sudraud, A. Corbin, R. Sailer, D.J. Bate, Scanning electron microscope, US 6,365,898, 2002, April 2002.

[42] S.W. Morgan, M.R. Phillips, Transient analysis of gaseous electron-ion recombination in the environmental scanning electron microscope, J. Microsc. 221 (3) (2006) 183–202. http://dx.doi.org/10.1111/j.1365-2818.2006.01554.x.

[43] R. Autrata, P. Schauer, Jos Kvapil, Ji. Kvapil, A single crystal of YAG- new fast scintillator in SEM, J. Phys. E 11 (1978) 707. http://dx.doi.org/10.1088/ 0022-3735/11/7/028/meta.

[44] R. Autrata, P. Schauer, J. Kvapil, J. Kvapil, A Single crystal of $YAlO_3$:Ce^{3+} as a fast scintillator in SEM, Scanning 5 (1983) 91–96. http://dx.doi.org/10.1002/sca. 4950050204.

[45] T. Ushiki , H. Hashizume , S. Itoh , K. Kuboki , S. Saito , K. Tanaka , Low-voltage backscattered electron imaging of non-coated biological samples in a low–vacuum environment using a variable-pressure scanning electron microscope with a YAG-detector, J. Electron. Micrsc. 47 (4) (1998) 351–354.

[46] H. Hashizume, S. Itoh, K. Tanaka, T. Ushiki, Direct observation of t-butyl alcohol frozen and sublimated samples using low-vacuum scanning electron microscopy, Arch Histol. Cytol. 61 (2) (1998) 93–98. http://dx.doi.org/10.1679/ aohc.61.93.

[47] R. Autrata, J. Jirák, V. Romanovský, J. Špinka, Signal Detection in Environmental SEM with Ionisation Detector, J. Comput. Assist. Microsc. 9 (2) (1997) 115–116.

[48] R. Autrata, J. Jirák, L. Schneider, Usage of segmental ionization detector in environmental conditions, Microsc. Microanal. 9 (3) (2003) 142–143.

[49] V. Neděla, I. Konvalina, B. Lencová, J. Zlamal, Comparison of calculated, simulated and measured signal amplification in a variable pressure SEM, Nucl. Instrum. Method Phys. A 645 (1) (2011) 79–83. http://dx.doi.org/10.1016/j.nima. 2010.12.200.

[50] V. Neděla, I. Konvalina, M. Oral, J. Hudec, Monte Carlo simulations of signal electrons collection efficiency and development of new detectors for ESEM, Microsc. Microanal. 21 (3) (2015) 1109–1110. http://dx.doi.org/10.1017/ S1431927615006339.

[51] V. Neděla, Dynamical "in situ" observation of biological samples using variable pressure scanning electron microscope, J. Phys. 62 (2008) http://dx.doi.org/1-4. 10.1088/1742-6596/126/1/012046.

[52] Š. Mašová, E. Tihlaříková, V. Neděla, In situ dynamic esem observation of basic groups of parasites, J. Adv. Img. El Phys. 190 (2015) 92–94.

[53] GD Danilatos , Backscattered electron detection in environmental SEM, J. Microsc. 245 (2012) 171–185.

[54] G.D. Danilatos, Design and construction of an atmospheric or environmental SEM (part 3), Scanning 7 (1985) 26–42.

[55] R. Autrata, J. Jirák, J. Špinka, Backscattered electron detector for environmental scanning electron microscopes, Beitr. Elektronenmikroskop. Direktabb. Oberfl. 26 (1993).

[56] V. Neděla, J. Jirák, Ionisation detector for environmental scanning electron microscope, European Patent EP 2195822 and Czech Patent 299864 B6, July 2010.

[57] B. Lencová, J. Zlámal, A new program for the design of electron microscopes, Phys. Procedia 1 (2008) 315–324. http://dx.doi.org/10.1016/j.phpro.2008.07.111.

12 In Situ Study of Live Specimens in an Environmental Scanning Electron Microscope

Eva Tihlaříková[1], Vilém Neděla[1], and Makoto Shiojiri[2]

1 *Institute of Scientific Instruments of the ASCR, v.v.i., Královopolská 147, Brno 612 64, Czech Republic*

2 *Kyoto Institute of Technology, Matsugasaki, Sakyo-ku, Kyoto 606-8585, Japan*

Keywords

live biological sample, high-pressure environment, hydration system, *in situ* observation, Monte Carlo simulation, methodology

Abstract

In this paper we introduce new methodology for the observation of living biological samples in an environmental scanning electron microscope (ESEM). The methodology is based on an unconventional initiation procedure for ESEM chamber pumping, free from purge–flood cycles, and on the ability to control thermodynamic processes close to the sample. The gradual and gentle change of the working environment from air to water vapor enables the study of not only living samples in dynamic *in situ* experiments and their manifestation of life (sample walking) but also its experimentally stimulated physiological reactions. Moreover, Monte Carlo simulations of primary electron beam energy losses in a water layer on the sample surface were studied; consequently, the influence of the water thickness on radiation, temperature, or chemical damage of the sample was considered.

Introduction

Biological samples are commonly chemically fixed, dried (Bozzola & Russell, 1999; Hayat, 2000), sputter coated (Robards & Wilson, 1993), or rapidly frozen (Roos & Morgan, 1990) and observed by electron irradiation within a vacuum in conventional transmission or scanning electron microscopes. To overcome the problem of charging and to potentially observe samples close to their natural state, scientists have used a gas environment in electron microscopes such as the environmental scanning electron microscope (ESEM) (Danilatos & Robinson, 1979; Danilatos, 1988), to observe samples under various environmental atmospheric conditions (Ruska, 1942; Hashimoto et al., 1968; Lane, 1970; Robinson, 1975; Danilatos, 1981*b*; Danilatos & Postle, 1982; Fukushima et al., 1985; Donald, 2003; Stokes, 2003; Neděla, 2007; de Jonge & Ross, 2011).

The presence of a high-pressure environment and the possibility to adjust pressure, gas type, sample temperature, etc. opens a wide field of *in situ* or dynamic *in situ* experiments such as growth or reaction processes of nanoparticles in a solution and observation of fully wet and then slowly dried biological materials with minimal treatment. When observing sensitive biological samples with a high moisture content, care must be exercised to minimize the extent to which they are allowed to dry, both during pumping at initialization and during the observation process itself. Quick and effective replacement of air by water vapor in the ESEM specimen chamber is ensured by the generally used method of purge–flood cycles, introduced by Cameron & Donald (1994). For this method, the sample has to undergo several cycles of pressure change as the specimen chamber is periodically pumped and flooded with water vapor. Dehydration of the sample is kept to a minimum due to reduction in its temperature. This methodology is suitable for observation of lifeless and highly wet samples, but for observation of living organisms, it can be a source of complications. Even though optimum conditions for observation of wet and live samples in the ESEM have been published (Danilatos, 1981*a*; Stokes, 2006; McGregor & Donald, 2010), the long-term study of movement in a living animal in an ESEM has not yet been reported. Noncommercial or adapted commercial microscopes can be used for *in situ* experiments where nonstandard adjustments of some parameters of the microscope are necessary.

An example of this device is our experimental ESEM AQUASEM II (Neděla, 2010), constructed from a conventional high-vacuum Tescan VEGA SEM equipped with a hairpin cathode. The uniqueness of our instrument is based on the original differentially pumped chamber, which enables us to evacuate the specimen chamber very slowly and hence gently for the sample. Our microscope is also equipped with a specific detection system, consisting of four detectors. The first part of the detection system is a scintillation secondary electron (SE) detector for ESEM, the only one in the world working continuously under conditions of both SEM and ESEM (gas pressure from 0.001 to 1,000 Pa) (Everhart & Thornley, 1960; Jirák et al., 2010) without the need to change the detector. The second part consists of three integrated detectors: a scintillation backscattered SE (BSE) detector and two ionization SE detectors. The BSE YAG:Ce^{3+} (yttrium aluminum garnet activated with trivalent cerium) scintillation single-crystal detector (Autrata et al., 1978) has a small hole in the center of the scintillator used as the second pressure-limiting aperture (PLA 2) of our microscope. The newly patented ionization SE detector with an electrostatic separator (Neděla & Jirák, 2012) uses a biased indium tin oxide electrode sputtered on the YAG:Ce^{3+} single crystal of the BSE detector. This electrode can also work as a detection electrode of the second ionization SE detector (Neděla et al., 2011), which was used for our observations.

In addition, the AQUASEM-II is equipped with a sophisticated device to measure water vapor pressure in the specimen chamber, a Peltier stage for the cooling of wet biological samples, and an originally designed efficient hydration system with temperature and vapor flow control.

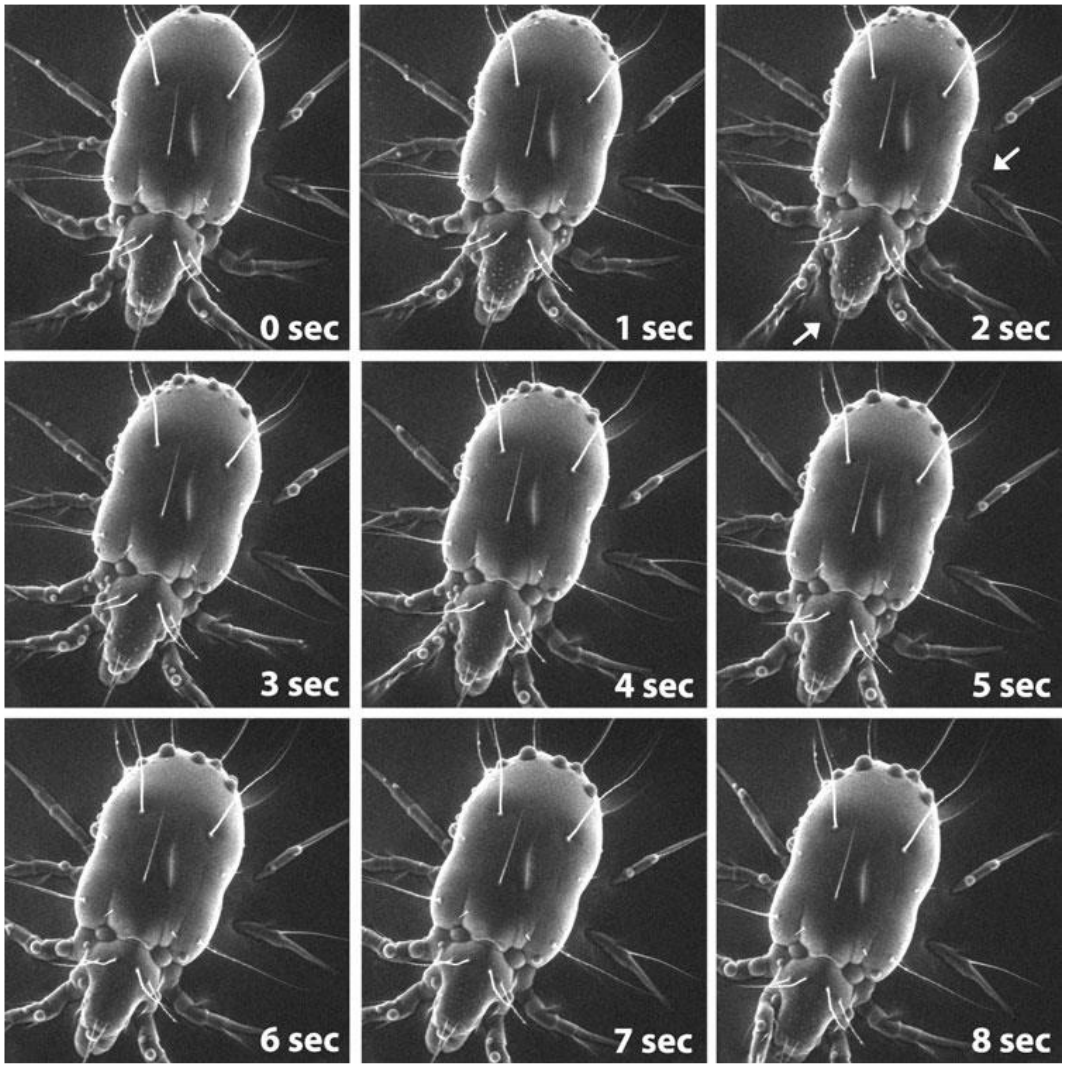

Figure 1. Observation of a live mite in an environmental scanning electron microscope (SEM). Frames recorded at marked times and selected from the moving image documenting movement of the mite. All frames show the liquid water underlay in which the mite is immersed, marked by white arrows in a frame of 2 s. Activity of the mite is obvious in the change in its leg

position, which was observed in the AQUASEM II ESEM. Images showing movement were recorded at a vapor pressure of 950 Pa, sample temperature of 78C, beam voltage of 20 kV, probe current of 80 pA, and sample distance of 3 mm from second pressure limiting aperture. Horizontal field of view is 440 mm for each frame.

Materials and methods

Observations were carried out on a sample of mites in the early part of their life cycle. This type of sample is unstable and susceptible to rapid pressure changes; thus, it is hard to observe in a natural state in the gas environment of an ESEM. Samples of mites were redeployed together with water from a reservoir near Brno, Czech Republic. In view of the fact that our aim was to observe fully natural samples, no treatments were used. The mite was laid on a drop of liquid placed on tiny piece of silicon on the cooled specimen holder of the microscope. The initial holder temperature was about 2°C and the mite was partially submerged in water in a state of suspended animation. Then, the sample was stabilized for 2 min.

The specimen chamber was evacuated only through the small hole in the PLA 2 very slowly and gently with respect to the sample. When the sample-specific pressure in the specimen chamber was achieved, controlled injection of water vapor from our hydration system was started. The sample was installed in the microscope for about 15 min, 5 min of which were spent on taking pictures. During the course of observation, there was water vapor pressure of 950 Pa, a 20 keV accelerating voltage of primary electrons (Pes), and a distance from the PLA 2 of 3 mm. In accordance with the conditions of thermodynamic equilibrium on the sample surface, the live mite was observed at a humidity of ;95%, where the thin water layer above the sample was evaporated and the native structure was exposed.

The ability of the water layer to protect the sample against the destructive influence of the PE beam was studied by Monte Carlo simulation. Simulations for the parameters were carried out by shooting a PE beam with an energy of 20 keV through water layers with a thickness from 500 nm to 12 μm. The Geant4-DNA package, an extension to the free open source Geant4 Monte Carlo toolkit, which allows the coverage of electron interaction in the range 0.025 eV–1 MeV with an accuracy of 3% for total energy deposition (Ivanchenko et al., 2011), was used.

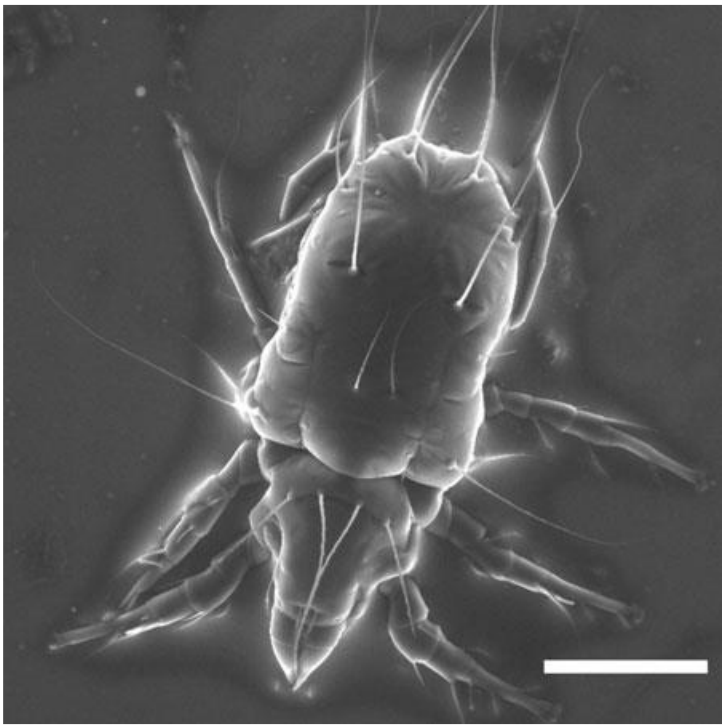

Figure 2. A still environmental scanning electron microscope image of the mite. To obtain a higher signal-to-noise ratio the scanning speed was reduced, and the pressure was slightly decreased. As a consequence, structures on the back of the mite slightly shrank. Experimental conditions: vapor pressure of 850 Pa, sample temperature of 7°C, beam voltage of 20 kV, probe current of 80 pA, and sample distance of 3 mm from second pressure limiting aperture. Scale bar is 100 μm.

Results

Images in Figure 1 are frames from a moving mite (Supplementary Movie 1) that represent a sequence of the mite walking as shown from its leg movement. The mite remained partially immersed in the original liquid. Figure 2 shows a still ESEM image of the mite that was about 320 mm in length. To obtain a higher signal-to-noise ratio, the scanning speed was reduced, the pressure of gas was slightly decreased, and a larger amount of water was evaporated. Reduced humidity in the specimen chamber caused slight shrinkage of the surface structure, as can be seen in the mite's rear side in Figure 2.

Supplementary Material

To view supplementary material for this article, please visit http://dx.doi.org/10.1017/S1431927613000603.

Since the AQUASEM II is equipped with a thermo emission hairpin cathode, the resolution of images taken under the above-mentioned conditions is relatively low. This deficiency is consequently multiplied by energy losses and scattering of PEs in the water layer on the sample surface. The impact of water layer thickness on these mechanisms is shown in Figure 3. The water layer has a strong absorption effect on the PE beam; for the water layer thickness of 4 μm absorption is 50% of the PE energy. The level of lost energy is proportional to the thickness of the water layer and the presence of water has an additional effect on the scattering of PE, which causes enlargement of probe size, in the case of Figure 3B, approximately 10,000 times laterally.

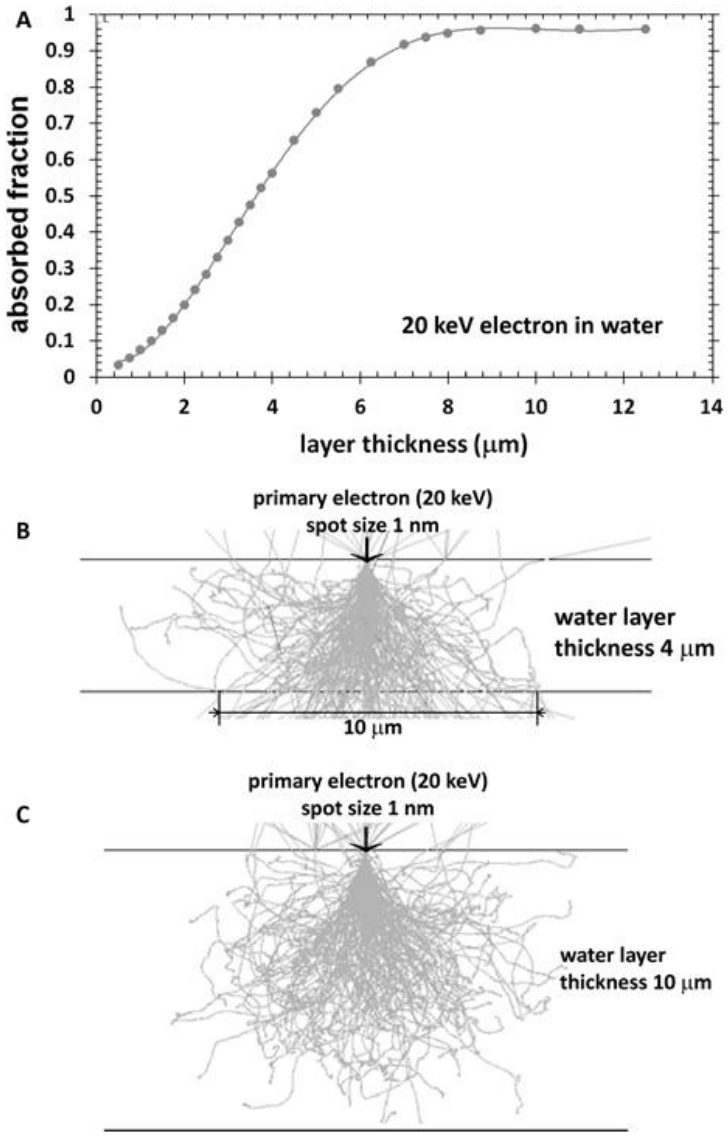

Figure 3. Monte Carlo simulation of primary electron scattering in water. Distribution of absorbed fraction in growing thickness of the water layer (**A)**. Interaction volumes in thin (**B**) and thick layers (**C**). The initial electron energy was 20 keV; to obtain reasonable statistics, results were averaged over 50,000 tracks.

Discussion

In this paper we show that live animal observation, including observation of mite movement in an ESEM, is possible, but with some limitations. A specific procedure, which is difficult to realize in standard commercial microscopes, had to be used. It involves the gradual replacement of air by water vapor, free from pressure, and surges that occur during purge–flood cycles.

Use of our thermally stabilized hydration system with accurate regulation of water vapor flow and our custombuilt detection systems is essential for observation.

A significant part of observation is the initialization process, which needs to be performed so that the sample is covered and protected by surrounding liquid during microscope pumping. Liquid surface tension partially maintains the position of the sample free from damage or artefact formation. Regulated gradual pumping of the specimen chamber through the PLA 2 aperture allows maintenance of a stable environment of high relative humidity in the sample surrounding, which keeps the sample covered by liquid. A water layer with a thickness from tens to thousands of micrometers is intentionally maintained in this phase of observation in order to minimize sample drying and consequently to protect against heat and radiation damage.

As shown by Monte Carlo simulations in the Geant4 (DNA package), the entire energy from 20 keV PE is absorbed in a 10 μm thickness of water layer due to beam– water interactions. As a consequence of preventing high energy electron penetration into the sample, radiation damage is negligible. Heat energy is conducted away through the water layer, simultaneously cooled by the Peltier stage. The secondary effect of PE–water interaction is the creation of highly mobile free radicals that can create a hostile environment. However, as described by Royall et al. (2001), the concentration of radicals tends toward a neutral state in a displacement below 20 μm. In the case of expected water layer thickness (tens to thousands of micrometers) and working conditions (accelerating voltage 20 keV, dwell time 3.5 _10^{-6} s, and probe current 80 pA), the sample is also protected against the impact of these radicals.

The next phase of observation involves slow drying, which leads to exposure of the sample surface structure. Owing to reduced temperature, the sample was in hibernation.

Only gradual evaporation of the cooled water layer from the sample surface will expose the sample to the influence of PEs, resulting in a local increase in sample temperature of ;7°C and subsequent reawakening of the sample from hibernation.

This is visible from its leg movement and overall shifting in direction to an edge of the field of view. The proof of the high relative humidity in the sample's surrounding is the presence of liquid under the sample and also condensation of drops of water on the sample surface during observation (Fig. 1). In the case of Figure 1, a relatively high water vapor pressure (900– 1,000 Pa) was used in the sample chamber of the ESEM and images of the living sample were taken with high scanning speed to record the sample's movement.

The reduced image quality is due to the low signal-tonoise ratio, scattering of PE in the high-pressure vapor environment, and sample movement. Decreasing gas pressure and partial evaporation of water near the sample induce more efficient cooling, leading to a recurrence of hibernation and positional stabilization. However, the possibility of drying of the sample has to be taken into account.

Applications of ESEM on studies of dynamically changing physical or chemical conditions on the manifestation of life of different samples could be of great benefit to biology, medicine, and pharmacy. The future of high-resolution live sample microscopy can be seen in low-energy beam ESEM (Danilatos, 2012) and correlative light and transmission electron microscopy (Peckys et al., 2011).

Acknowledgements

This work was supported by the Grant Agency of the Czech Republic: Grant No. GAP 102/10/1410. We would like to thank all our colleagues from ISI ASCR and from Brno University of Technology, Department of Electrotechnology, for cooperation with the design and rebuilding of our experimental ESEM AQUASEM II and all new detection systems. We would also like to thank Mrs. Silvie Svidenská for her help during preparation of the paper. Our special thanks are due to the late Prof. R. Autrata, who contributed a great deal to the realization of the ESEM AQUASEM II and some special detectors.

References

Autrata, R., Schauer, P., Kvapil, J. & Kvapil, J. (1978). A single crystal of YAG—New fast scintillator in SEM, *J Phys E: Sci Instrum* **11**, 707–708.

Bozzola, J.J. & Russell, L.D. (1999). *Electron Microscopy: Principles and Techniques for Biologists*. Sudbury, MA, USA: Jones & Bartlett Learning.

Cameron, R.E. & Donald, A.M. (1994).Minimizing sample evaporation in the environmental scanning electron microscope. *J Microsc* **173**, 227–237.

Danilatos, G.D. (1981*a*). The examination of fresh or living plant material in an environmental scanning electron microscope. *J Microsc* **121**, 235–238.

Danilatos, G.D. (1981*b*). Design and construction of an atmospheric or environmental SEM (part 1). *Scanning* **4**, 9–20.

Danilatos, G.D. (1988). *Foundations of Environmental Scanning Electron Microscopy*. Sydney, Australia: Academic Press.

Danilatos, G.D. (2012). Velocity and ejector-jet assisted differential pumping: Novel design stages for environmental SEM. *Micron* **43**, 600–611.

Danilatos, G.D. & Postle, R. (1982). The environmental scanning electron microscope and its applications. *Scan Electron Microsc* **1982**, 1–16.

Danilatos, G.D. & Robinson, V.N.E. (1979). Principles of scanning electron microscopy at high specimen pressures. *Scanning* **2**, 72–82.

De Jonge, N. & Ross, F.M. (2011). Electron microscopy of specimens in liquid. *Nat Nanotech* **6**, 695–704.

Donald, A.M. (2003). The use of environmental scanning electron microscopy for imaging wet and insulating materials. *Nat Mater* **2**, 511–5 16.

Everhart, T.E. & Thornley, R.F.M. (1960). Wide-band detector for micro-microampere low-energy electron currents, *J Sci Instrum* **37**, 246–248.

Fukushima, K., Ishikawa, A. & Fukami, A. (1985). Injection of liquid into environmental cell for *in situ* observations. *J Electron Microsc* **34**, 47–51.

Hashimoto, H., Naiki, T., Eto, T. & Fujiwara, K. (1968). High temperature gas reaction specimen chamber for an electron microscope. *Jpn J Appl Phys* **7**, 946–953.

Hayat, M.A. (2000). *Principles and Techniques of Electron Microscopy: Biological Applications*. UK: Cambridge University Press.

Ivanchenko, V., Apostolakis, J., Bagulya, A., Abdelouahed, H.B., Black, R., Bogdanov, A., Burkhard, H., Chauvie, S., Cirrone, P., Cuttone, G., Depaola, G., Di Rosa, F., Elles, S., Francis, Z., Grichine, V., Gumplinger, P., Gueye, P., Incerti, S., Ivanchenko, A., Jacquemier, J., Lechner, A., Longo, F., Kadri, O., Karakatsanis, N., Karamitros, M., Kokoulin, R., Kurashige, H., Maire, M., Mantero, A., Mascialino, B., Moscicki, J., Pandola, L., Perl, J., Petrovic, I., Ristic-Fira, A., Romano, F., Russo, G., Santin, G., Schaelicke, A., Toshito, T., Tran, H., Urban, L.,

Yamashita, T. & Zacharatou, C. (2011). Recent improvement in Geant4 electromagnetic physics models and interfaces. *J Nucl Sci Technol* **2**, 898–903.

Jirák, J., Neděla, V., Černoch, P., Čudek, P. & Runštuk, J. (2010). Scintillation SE detector for variable pressure scanning electron microscopes. *J Microsc* **239**, 233–238.

Lane,W.C. (1970). The environmental control stage. *Scan Electron Microsc* **1970**, 43–48.

McGregor, J.E. & Donald, A.M. (2010). ESEM imaging of dynamic biological processes: The closure of stomatal pores. *J Microsc* **239**, 135–141.

Neděla, V. (2007). Methods for additive hydration allowing observation of fully hydrated state of wet samples in environmental SEM. *Microsc Res Tech* **70**, 95–100.

Neděla, V. (2010). Controlled dehydration of a biological sample using an alternative form of environmental SEM.*J Microsc* **237**, 7–11.

Neděla, V. & Jirák, J. (2012). Ionisation detector for environmental scanning electron microscope. Patent EP 2195822, Czech Patent No. 299864.

Neděla, V., Konvalina, I., Lencová, B. & Zlámal, J. (2011). Comparison of calculated, simulated and measured signal amplification in a variable pressure SEM. *Nucl Instrum Methods Phys Res A* **645**, 79–83.

Peckys, D.B., Mazur, P., Gould, K.L. & Jonge, N. (2011). Fully hydrated yeast cells imaged with electron microscopy. *Biophys J* **100**, 2522–2539.

Robards, A.W. & Wilson, A.J. (1993). *Procedures in Electron Microscopy*. Chichester, UK: Wiley.

Robinson, V.N.E. (1975). A wet stage modification to a scanning electron microscope. *J Microsc* **103**, 71–77.

Roos, N. & Morgan, A.J. (1990). *Cryopreparation of Thin Biological Specimens for Electron Microscopy*. Oxford, UK: Oxford Science Publications.

Royall, C.P., Thiel, B.L. & Donald, A.M. (2001). Radiation damage of water in environmental scanning electron microscopy. *J Microsc* **204**, 185–195.

Ruska, E. (1942). Beitrag zur übermikroskopischen Abbildung bei höheren Drucken. *Kolloid* **100**, 212–219.

Stokes, D.J. (2003). Investigating biological ultrastructure using environmental scanning electron microscopy (ESEM). In *Science, Technology and Education of Microscopy an Overview*, Méndez-Vilas, A. (Ed.), pp. 564–570. Spain: Formatex Research Center.

Stokes, D.J. (2006). Progress in the study of biological specimens using ESEM. *Infocus* **2**, 64–72.

13 The Low-Temperature Method for Study of Coniferous Tissues in the Environmental Scanning Electron Microscope

VILÉM NEDĚLA[1], EVA TIHLAŘÍKOVÁ[1], AND JIŘÍ HŘIB[2]

1 ASCR, Institute of Scientific Instruments, Kralovopolska 147, 612 00 Brno, Czech Republic

2 Department of Plant Biology, Faculty of Agronomy, Mendel University of Agriculture and Forestry, Zemedelska 1, 613 00 Brno, Czech Republic

Keywords

methodology; conifer; embryogenic tissue; extracellular matrix; Oxalis acetosella

Abstract

The use of non-standard low-temperature conditions in environmental scanning electron microscopy might be promising for the observation of coniferous tissues in their native state. This study is aimed to analyse and evaluate the method based on the principle of low temperature sample stabilization. We demonstrate that the upper mucous layer is sublimed and a microstructure of the sample surface can be observed with higher resolution at lower gas pressure conditions, thanks to a low-temperature method. An influence of the low-temperature method on sample stability was also studied. The results indicate that high-moisture conditions are not suitable for this method and often cause the collapse of samples. The potential improvement of stability to beam damage has been demonstrated by long-time observation at different operation parameters. We finally show high applicability of the low-temperature method on different types of conifers and Oxalis acetosella. Microsc. Res. Tech. 78:13–21, 2015.

Introduction

Somatic or asexual embryogenesis is a recently developed biotechnology technique whereby genetically identical trees are produced through the production of embryolike structures from somatic cells without gamete fusion, and works as the primary enabling technology for all conifer biotechnology products (Klimaszewska et al., 2007). The rapid improvement in this method allows the use of somatic embryos in plant micropropagation as synthetic seeds. A well-established and commonly used method for the study of coniferous embryogenic samples is light optical microscopy. However, the study of embryo micromorphology, or the advanced characterization of developmental changes of the embryo surface

structure in the process of embryogenesis, requires a profound structural analysis by electron beam inspection. Nevertheless, complex preparation processes is required to make the sample stable in vacuum conditions, and also electrically conductive. Each step of sample preparation, from chemical fixation, dehydration and drying up to metal coating, can cause various artefact formation and/ or destruction of the finer features (Timp and Matsudaira, 2008), particularly in a case of early somatic embryos of conifers covered with an extracellular matrix (ECM) (Pathan et al., 2008).

Problems caused by sample preparation or unwanted dehydration, can be overcome by using an environmental scanning electron microscope (ESEM). High pressure of gas, mostly water vapor in a specimen chamber of the ESEM, allows the direct study of fully hydrated or electrically non-conductive samples in their native state, without the necessity of their surface covering by a conductive layer (Donald, 2003; Stokes, 2003). The presence of a high-pressure environment is allowed by addition of differentially pumped chamber/chambers with pressure limiting apertures, thus separation of the specimen chamber from the high-vacuum conditions in the microscope column and the electron source is reached. The working conditions in the ESEM (gas pressure, gas type, accelerating voltage, length of electron trajectories in the gas, etc.) as well as using of special types of detectors (Danilatos, 1983, 1986; Fletcher et al., 1997; Jirák et al., 2010) have a significant impact on electron beam diffusion, the signal to noise ratio and signal amplification (Danilatos, 1988). Moreover, many samples require proper working conditions and methodology of observation which respect their specificities (Tihlaříková et al., 2013).

Water vapor pressure in the specimen chamber, in combination with the specimen temperature, plays the principal role in reaching and maintaining the state of thermodynamic equilibrium of saturated water vapor in the immediate vicinity of the specimen (Cameron and Donald, 1994; Mathews and Donald, 2002). The dependency between these parameters in Figure 1 maps the course of thermodynamic equilibrium between the solid, liquid, and gas phase of water. Unfortunately, this dependency is not fully applicable for aqueous phases with dissolved solutes contained in the majority of biological samples. According to the Raoult's Law, the vapor pressure of a solution is proportional to the mole fraction of the pure solute. Consequences of this statement are that: different parts of the sample are thermodynamically stable at different condition, especially in a case of biological samples and the phase diagram should be supplemented by equilibrium vapor pressures for the solution which is specific for the actually observed sample (Tabor, 1991). To reach the appropriate environmental conditions, the specimen should be held in an atmosphere corresponding to its equilibrium state, in order to

be stabilized against moisture loss or gain over time, see Stokes (2008). Thus, it is necessary to respect the dependence of saturated water vapor pressure on specimen temperature (Fig. 1), which places increased demands on the fine control of gas flow from the hydration system, advanced regulation of specimen chamber pumping, and thermal stability of a Peltier cooled specimen holder.

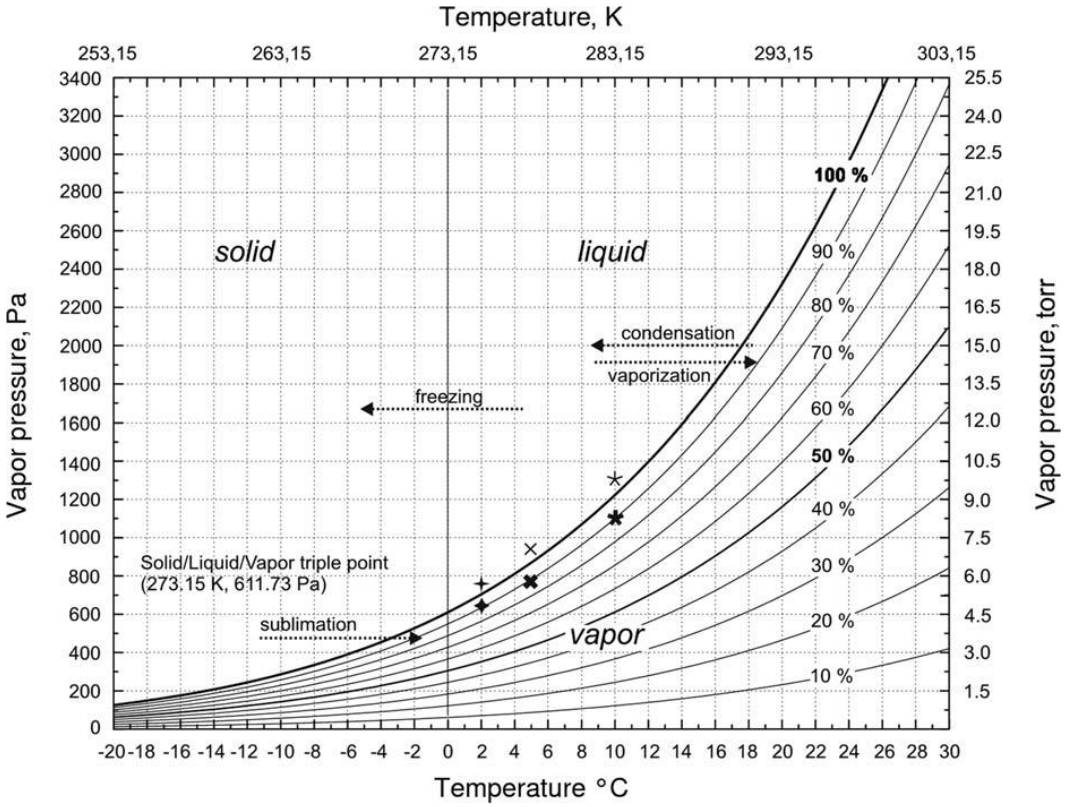

Fig. 1. The saturated water vapor pressure curve with marked relative humidity and water phase changes. Symbols on relative humidity curves correspond with an ESEM part of the first experiment, see first line in Table 1. Light symbols indicate high-relative humidity conditions at the start of observation and bold symbols denote decreasing of water vapor pressure in order to expose sample structure. Conditions for the low-temperature method are not included due to different gas (air) in the specimen chamber.

The great potential of the ESEM for the investigation of plants was demonstrated in the recent works of Popielarska-Konieczna et al. (2008, 2010) focused on the study of the susceptible ECM; Stabentheiner et al. (2010) and McGregor and Donald (2010) published results of observation of various plant tissue surfaces, wax and dynamic behavior of plants. The samples were examined in commonly used high-pressure conditions of the ESEM, with a tendency to cool the samples to a temperature slightly higher than 0°C, with a quite low rate of moisture loss. This combination allows the thermodynamic stability of moist and fresh specimens to be controlled. Nevertheless in the case of specific samples or special experiments, different temperatures and gasses can be more useful (Neděla et al. 2012). This article briefly reports about new methodology and points out the possibility to

observe the conifer samples in their native state in conditions of 220°C and 400 Pa of air. The aim of this work is to provide a detailed description and methodological analysis of the low-temperature method, and also a discussion about its results and its correctness as well as demonstration of applicability of the method for observation of plant samples in their native states.

Materials and methods

Plant Material and culture conditions

The embryogenic culture of Norway spruce (Picea abies (L.) Karst.) from the collection of Institute of Plant Biology, Mendel University (Brno) was originally derived from a mature zygotic embryo of tree No. 12345 of spruce mountain climate type, from the experimental area in the Beskydy Mountains, Moravia, Czech Republic. The culture's embryonic tissues were maintained on medium designated LP/2 in 100 mm diameter Petri dishes (Havel and Durzan, 1996), with 9 μmol 2,4-dichlorophenoxyacetic acid (2,4-D) and 4.4 μmol benzylaminopurine (BAP). The embryogenic tissues from the upper parts of their aggregates (2.5– 5.0 mg) were sub-cultured in 10–14 day periods. The cultures were maintained in the dark at 23 ± 1°C.

The embryogenic tissue of silver fir (Abies alba Mill) was initiated from immature zygotic embryos of cones from open-pollinated trees. Immature seeds were surface-sterilized for 10 min in 10% (v/v) H_2O_2, and then, rinsed several times with sterile distilled water. The immature cones of Abies alba were collected on July 26th, 2006 in the Dobroč primeval forest. The embryogenic tissue was initiated and proliferated on the medium published by Vooková and Kormut'ák (2009).

Immature cones of Scots pine (Pinus sylvestris L.) were collected on June 28th, 2010, from trees in Ostravsky Biely Potok, Slovakia. Megagametophytes which included embryos were cultured on DCR medium (Gupta and Durzan, 1985) containing 0.5 mg/dm3 BAP, 2 mg/dm^3 2,4-D, 200 mg/dm^3 myo-inositol, 500 mg/dm^3 casein hydrolysate, 50 mg/dm^3 L-glutamine, 20 g/dm^3 sucrose, solidified with 3 g/dm^3 Phytagel. The pH was adjusted to 5.8 before autoclaving. The cultures were grown in darkness at 25±1°C, and transferred to a fresh medium at 2–3 week intervals. The embryogenic tissue was initiated and proliferated on the same medium.

TABLE 1. Parameters of individual experiments in ESEM

	Temperature (°C)	Pressure	RH (%)	Gas type	Sample	Images
Wet ESEM|	2	760 Pa → 630 Pa	108 → 90	Water vapor	*Picea abies*	2A
	5	930 Pa → 760 Pa	107 → 90			2B
	10	1300 Pa → 1100 Pa	106 → 90			2C
Low-temperature ESEM	−20	400 Pa	–	Air	*Picea abies*	2 D 3A–3C
					Abies alba	2E
					Pinus sylvestris	2F and 2G
Light microscopy	23	101 kPa	30	Air	*Picea abies*	2G and 2H
Beam resistance testing	3	715 Pa	94	Water vapor	*Picea abies*	5A–5F
	−20	400 Pa	–	Air		5G–5I
Study of ice crystal formation	−20	400 Pa	–	Air	*Pinus sylvestris*	6A and 6B
					Abies alba	6C and 6D
					Picea abies	6E and 6F
Different plant sample	3	715 Pa	94	Water vapor	*Oxalis*	7A
	−20	400 Pa	–	Air	*acetosella L.*	7B and 7C

Light microscopy

The embryogenic tissue of Picea abies in its native state was observed with the Olympus BX51 microscope equipped with the Olympus DP70 camera.

Environmental Scanning Electron Microscopy

Experiments were realized using the noncommercial ESEM AQUASEM II. The microscope was adjusted to the research of detection systems and ESEM instrumentation (Neděla, 2010). The microscope equipped with a hairpin cathode is capable to operate with high pressure of the water vapor in the specimen chamber. Backscattered electrons (BSE) are detected with the scintillation YAG:Ce^{3+} (yttrium aluminium garnet activated with trivalent cerium) single crystal, simultaneously used as a pressure-limiting aperture of the microscope (Neděla, 2007). The signal of secondary electrons (SE) is detected by an ionization detector, using an electrode with the inner diameter of 4 mm deposited on an input surface of the scintillation YAG single crystal (Neděla et al., 2011). The hydration system, mounted on the specimen chamber allows the sample vicinity to be supplied with a sufficient amount of water vapor with controlled and regulated initial temperature. The hydration system is also equipped with a special warming unit providing heating of the micrometric valve with a water reservoir, and ensuring fine control of the flow of water vapor, and prevention of valve freezing.

All experiments were carried out under constant operating conditions: beam accelerating voltage 20 kV, probe current 110 pA and 60 pA (measured in high vacuum with a Faraday cup), distance between the sample surface and the bottom surface of the YAG single crystal (the second pressure limiting aperture) 2.7 mm, and the positively biased electrode of the ionization detector (330 V). In the case of beam damage evaluation, focus and astigmatism adjustments were made to a near uninteresting area. The blind displacement to the observed position was performed with a blanked beam.

Embryogenic tissues of conifers in their native state were observed in the cooled or frozen state using the water cooled Peltier stage with a silicone surface. Before observation, samples with dimensions of 2– 4 mm^2 and thickness of 2 mm were gently rinsed by distilled water to minimize and dissolve a mucous layer. Samples were put into a drop of 2 μL of water (micropipette Eppendorf) to obtain better thermal contact between the sample and the Peltier stage, and for better sample hydration. The environment working conditions were adjusted according to the following experiments, summarized in Table 1. The actual value of pressure in the specimen chamber was measured with the capacity gauges (Pfeiffer CMR 261 and 262).

ESEM and the Low-temperature Method

Procedures

A custom pumpdown procedure described by Tihlaříková et al. 2013, which is more suitable for observation of wet samples with ESEM AQUASEM II than the pumpdown procedure by Cameron and Donald (1994), was used to minimize sample evaporation and degradation caused by fast pressure changes. The working parameters were selected with regard to the most widely used range of sample temperatures with relative humidity (RH) of 100%: ***** = 10°C, 1,300 Pa; × = 5°C, 930 Pa; + = 2°C, 760 Pa. Consequently, RH was decreased to 90%: * =10°C, 1,100 Pa; × = 5°C, 810 Pa, † = 2°C, 630 Pa (see Fig. 1).

We devised a low-temperature method for observation of conifers and samples at temperature around – 20°C using air instead of water vapor. The initial procedure was different from that described above. Cooling of the Peltier stage was started after sample placement, and when the temperature reached 0°C, the pumping process was begun. The first state lies in fast pumping of the specimen chamber (up to 1,000 Pa) to allow relatively rapid decreasing of gas pressure as well as the sample temperature and to reach the conditions needed for sample freeze stabilization. At the second state, the specimen chamber is gradually filled up with air to maintain the work environment of 400 Pa. This value of working pressure is a good compromise between suitable conditions for detection of signal electrons by the ionization detector (high signal to noise ratio), and conditions for safe observation of this type of sample in a frozen state.

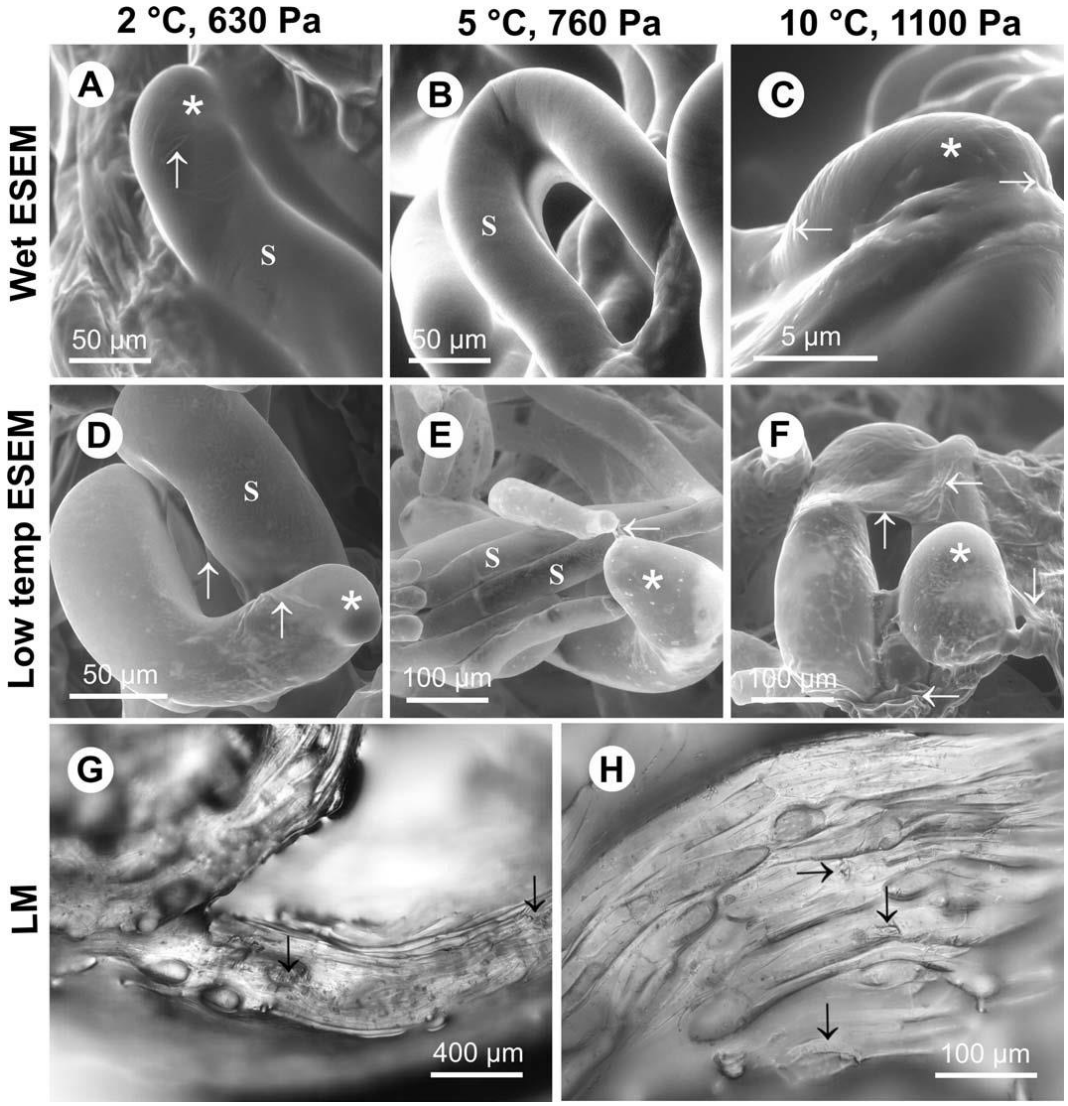

Fig. 2. The series of pictures illustrate the differences between methods. Images **A–C** were taken under the standard ESEM observation and show the fully hydrated surface of embryonic tissue of Picea abies. Structure specifics (the ECM indicated by white arrows) are covered by the water-mucous layer. Parameters of the observation are situated above the pictures and correspond with points in Figure 1. Images **D–F** display the exposed surface taken under the low temperature method, where the study of the ECM on the surface of the embryogenic cells is possible (white arrows). (D–F: - 20°C, air pressure 400 Pa). ESEM working conditions: accelerating voltage 20 kV, probe current 60 pA, the ionization detector. A–D: Picea abies; E: Abies alba; F: Pinus sylvestris, S-suspensor cell, white star-somatic head. Images **G, H** from the light microscope supplement ESEM observations. Results show that the structures resembling artefacts in ESEM are nature structural features of somatic embryos (Picea abies) indicated by black arrows.

Result and discussions

ESEM, the Low-temperature Method and Light Microscopy Observation

The comparison between the traditional ESEM and the low-temperature method is visible in Figure 2 (conditions were summarized in Table 1). The upper triplet shows the embryogenic tissue of Picea abies observed under several suitable

conditions for observation of wet biological samples in ESEM. Due to the requirement for very high-relative humidity, the samples were observed under the conditions of thermodynamic equilibrium. RH was 100% at the beginning of the observation, then it was gradually decreased to approximately 90% in a controlled way to expose the microstructure: pressure from 760 Pa to 630 Pa for 2°C, (Fig. 1, Fig. 2A), from 930 Pa to 760 Pa for 5°C (Fig. 1 , Fig. 2B), and from 1,300 Pa to 1,100 Pa were used for the holder temperature 10 C, (Fig. 1 , Fig. 2C). RH in the microscope was calculated regardless of the real temperature of the inspected part of the sample. Study of coniferous samples at different temperatures showed that the increasing sample temperature makes observation under thermodynamic equilibrium more difficult. The signal to noise ratio in the detected signal decreases with increasing gas pressure, which is necessary for observation at higher sample temperatures. The surface of the characteristic vacuolated suspensor cells (white S, Figs. 2A and 2B) is noticeably fully hydrated. The ECM in Figure 2C (a white arrow) can be assessed on the edges of the early somatic embryo (a white star). However, structure details and distribution of the ECM are not well visible. The results are partially depreciated by the highly hydrated ECM covering early somatic embryos, and mainly by the presence of a water-mucous layer of specific extracellular proteins which are secreted by the somatic embryos (Mo et. al, 1996). The secretion is permanent but uneven, and decreasing RH is inapplicable because of the collapse of the exposed structure. This state is usual for the observation of wet samples in the ESEM and is the reason that the observation of highly hydrated samples with higher resolution is impractical.

Figures 2D–2F contain results obtained by the low temperature method (temperature around – 20°C, air pressure 400 Pa). Direct comparison cannot be realized on the same sample because of the different starting procedures needed for each method, and high susceptibility of the sample. The method was tested on three different members of the Pinaceae family with the aim to show methods versatility. Results show that the detailed morphological characterization of embryogenic cells is possible, the presence of the water-mucous layer is minimized and the surface presents no damage. Moreover, connections between the suspensor cells (white S) and the somatic heads (white star) created by the ECM are visible in Figures 2D and 2E (white arrow). The high-density layer of the ECM covering a great part of the embryonic tissue is well visible in Figure 2F. This figure can bring new information about the distribution and function of the ECM during cell development. Figures 2A (upper part, white star) and 2D (bottom part, white star) illustrate the same situation of the creation of new embryonic heads. The head should be fully covered by the protected layer of the ECM.

The presence of the ECM on embryogenic cells was confirmed and depicted in SEM by Šamaj et al. (2008), however surface was affected by SEM treatments. In the standard ESEM, the thin and highly hydrated layer of the ECM is not well recognizable while the usage of the low-temperature method makes the border of the ECM and differences between the structures of the suspensor cells as well as newly formed head well visible (Figs. 2D–2F). Specifics of exposed surfaces can evince signs of artefacts, but according to the complementary light microscope observation and discussion with professor Havel (a specialist on somatic embryogenesis from Mendel University in Brno, Faculty of Agronomy, Department of Plant Biology), the structures resembling artefacts in ESEM are nature structural features of somatic embryos, see Figures 2G and 2H; black arrow.

Thanks to differences in signal contrast, the low temperature method allows to reveal areas with various inner structures. The presence of different materials or functional blocks inside the embryonic tissue can be reflected by these differences. Nevertheless, the formation of artefacts due to the use of low temperature must be considered.

If the low-temperature method is used incorrectly and the embryonic tissues are cold earlier, then the water-mucous layer remains on the sample surface in a frozen state. The process of surface exposure during low-temperature observation is documented in Figures 3A–3C. The high-density water-mucous layer was gradually sublimated from the surface of the suspensor cells. The whole process takes 4 minutes and was probably accelerated by exposing the sample to the focused electron beam. The shrinkage-like structures highlighted by white circles are natural and were formed due to the cell division, before observation. The accurate sublimation is the most important part of the low-temperature method and essential to observation of surface morphology. It is usually done during initial pumping, then no water layers are exposed to primary electrons, and beam damage of the sample due to the influence of free radicals is decreased. Due to good thermal contact of the bottom part of sample with Peltier cooling stage, the drying is slow. Nevertheless, sublimation through the cell wall is highly probable.

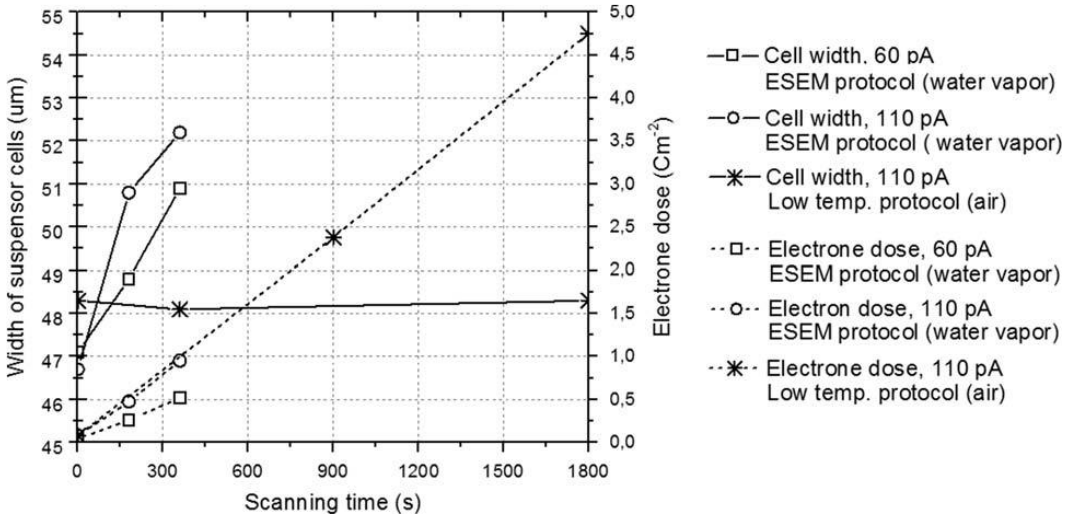

Fig. 4. Calculated electron dose in comparison with measured width changes of imaged suspensor cells. The sample observed using the low-temperature method shows high stability for the longest period.

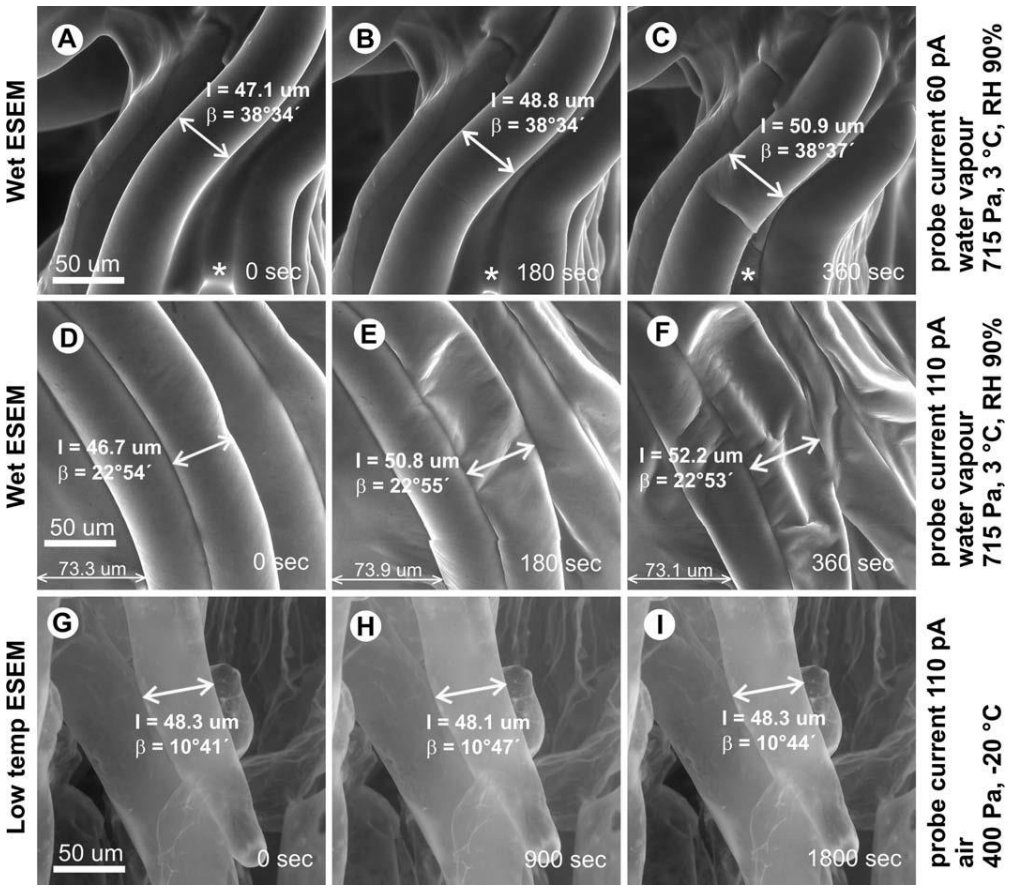

Fig. 5. Evaluation of wet ESEM and low-temperature methods to their ability to sample stabilization. The suspensor cells of Picea abies, used as referent samples were continuously scanned by electron beam with different current probes (marked on the left side of triplets). The width of suspensor cells served as an indicator of the sample destruction and was measured in marked times (Tescan measuring software). Microscope parameters were identical for every sample: accelerating voltage 20 kV as well as dwell time.

Test of Sample Resistance to Beam Damage

The noticeable growth of the probe current, the small size of the scanning area, and slow scanning speed have a damaging impact on the inspecting area of most of the biological wet samples, resulting in the creation of artificial-like structures. The electron beam impact was quantified by the electron dose (D, in cm^{-2}) represented by the number of electrons reaching the sample's surface for an irradiation time (Eq. (1)) and is directly proportional to the current density (j, Am^{-2}), and the irradiation time (t, s). The term of electron dose was used for the determination of sample resistance to electron irradiation. Then the I_0 (A) is the incident current measured by a Faraday cup in vacuum conditions, S (m^2) is the total scanned surface, and t_{total} (s) is the total irradiation time.

$$D = jt_{total} = \left(\frac{I_0}{s}\right) t_{total} \quad (1)$$

Calculated results of electron dose in comparison with results of measurement of suspensor cell width are presented in Figure 4. Due to high stability of the sample observed using the low-temperature method see Figure 5, two time scales were used.

The evaluation and demonstration of an ability of the low-temperature method to sample stabilization was realized via exposing of the sample to the repeated beam irradiation. Structural changes of samples were observed and measured during continuous scanning, until the sample was destroyed. In the case of sample observation with the standard ESEM procedure (Figs. 5A–5F), pictures of embryogenic tissue of Picea abies were taken after 180 seconds. The temperature of the Peltier stage was 3°C, the vapor pressure 715 Pa, and beam current 60 pA (Figs. 5A–5C) and 110 pA (Figs. 5D–5F). In the case of observation using the low temperature method, the images were taken chronologically after 900 seconds (Figs. 5G–5I) at the beam current 110 pA.

Changes in the structure, position, and shape of the suspensor cells appearing as a drift are the results of the cumulative impact of radiation damage and increased temperature in the irradiated area. Due to amount of the vapor pressure and hence the quantity of generated positive ions coming back to the sample, the drift of the sample caused by the negative surface charging is negligible. The charging drift-like behaviour in Figures 5A–5C is caused by gradual sample drying (marked with a white star). A small drift was also confirmed by measurement of the suspensor cell position marked in lower left side of Figures 5D–5F.

The common manifestation of the gradual sample destruction process under beam irradiation can be observed in Figure 5. For a better evaluation of the sample degradation, widths of the suspensor cells were measured and compared. The variation of suspensor cell width and the suspensor cell wall subsidence clearly shows the rate of sample destruction separately. As was expected, the rate of sample destruction is proportional to the accumulated electron dose (Fig. 4). The observation using the low-temperature method demonstrates a high resistance of the sample to beam irradiation. This is apparent from Figures 5G–5I where the suspensor cell width remains approximately constant through the whole duration of the experiment.

The problem of beam damaging lies in many destructive factors (Royall et al., 2001). Regardless of radiation and ionization damages related to the electron beam dose, local heating of the inspected area also causes sample destruction in the ESEM. Due to relatively low heat conductivity of conifer samples, the real temperature of the part of the sample affected by the electron beam can be higher. Regarding the experimental results with condensation and evaporation of water droplets on the same sample, the real temperature on the surface affected by the electron beam is approximately two degrees Celsius higher, than the temperature of the cooled Peltier stage if the probe current was 110 pA. In view of this fact, RH of the inspected sample surface is lower than that adjusted from Figure 1. Moreover, the sample is covered with aqueous phases with dissolved solutes containing a mixture of water and biological secrete. According to Raoult's Law, conditions for thermodynamics equilibrium of pure water do not correspond with liquid from the sample. The real temperature of the beam inspected sample area is different for each sample with low-temperature conductivity, for example biological samples. The direct measurement of real temperature of sample surface is not possible with any equipment available at the time of this study. Local temperature depends on many parameters. The most important variables are: the quality of thermal contact between the sample and the Peltier stage, the sample's heat-transferring ability, the gas type and pressure in the specimen chamber (thermal conductivity of gas and the presence of water, especially ice, improve the heat transfer, and the sample is cooled better), parameters of the Peltier stage and parameters of the primary electron beam (due to especially inelastic scattering of primary electrons, the sample temperature is increased). Finally, the real temperature of the inspected area is also strongly influenced by the total sample volume, and location of the observed place. Uneven samples and protrusions (for example insect feeler, heads of length suspensor cells, etc.) are predisposed to local heating, causing irreversible sample damage by dehydration, as in the case of the experiment.

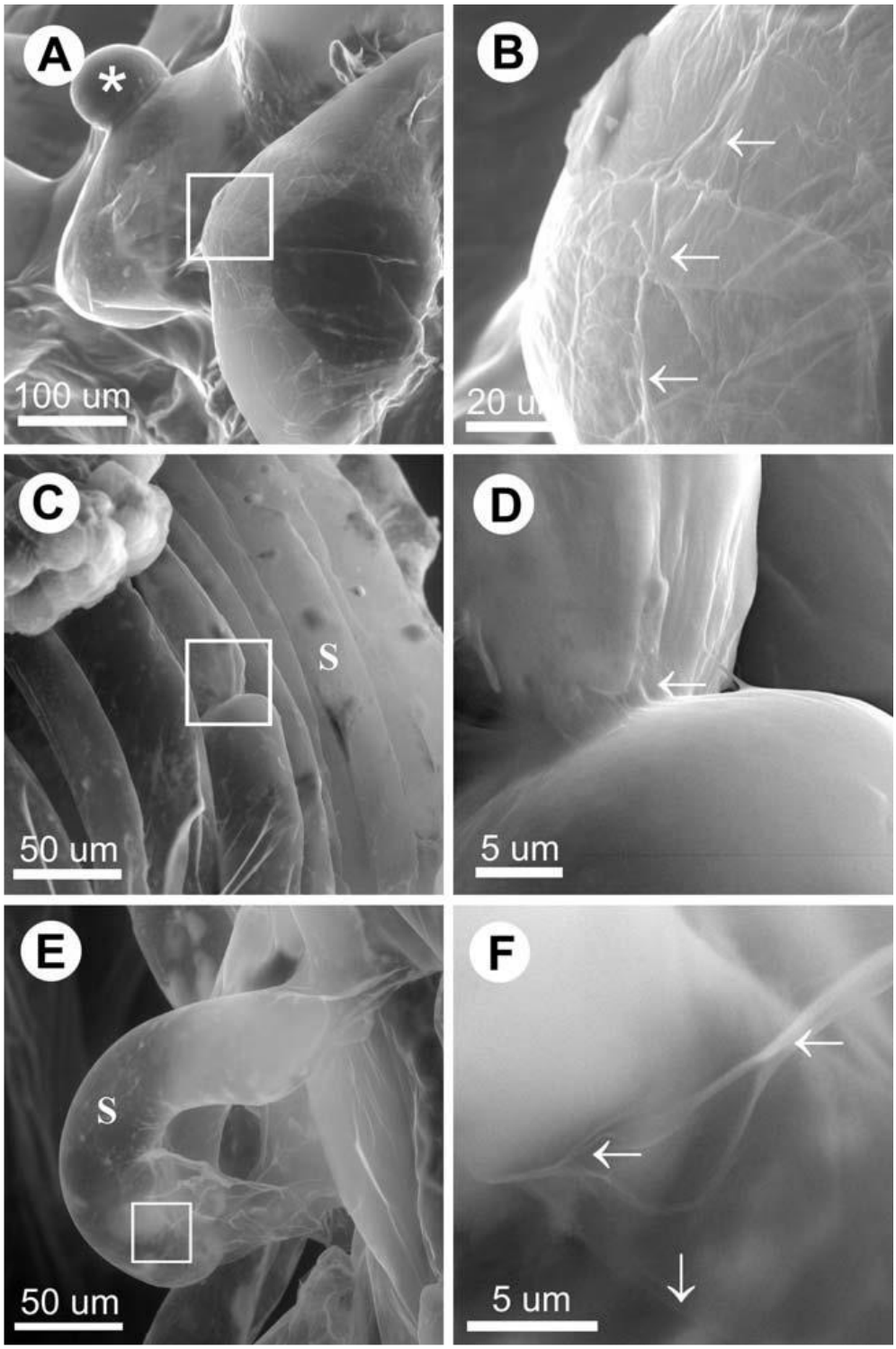

Fig. 6. Study of ice crystal formation on figures obtained with higher resolution. The layers of the ECM on the top of the embryonal head of Pinus sylvestris (**A,B**), the suspensor cell division of Abies alba (**C,D**) and the detail of the cell of the Picea abies partially covered with the ECM (**E,F**). Results demonstrate the capability of the low-temperature method to provide higher resolution imaging than a common wet sample observation. No ice crystal formation is evident from the smooth surface of the samples. Observation parameters: accelerating voltage 20 kV, probe current 60 pA, 400 Pa of air, temperature -20°C, ionization detector. S-suspensor cell, white arrow extracellular matrix, white star-somatic head.

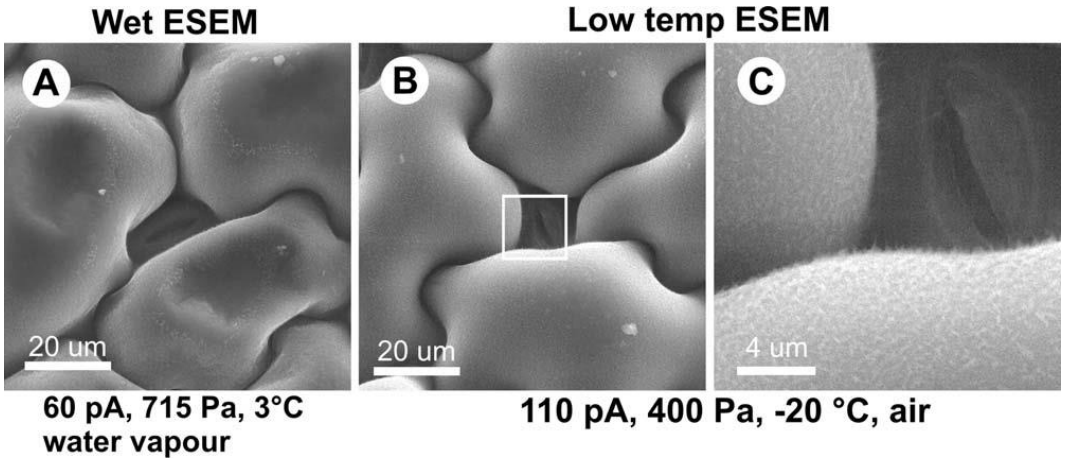

Fig. 7. Demonstration of applicability of the low-temperature method on plant sample observation. The lower epidermis of Oxalis acetosella L. imaged by ESEM method (**A**) and by the low temperature method (**B,C**). In Figure 7A, the probe current (60 pA) induces a dose which was still too high for this sample. One scan (30 s) leads to the collapse of the structure, clearly visible in the picture. At the probe current of 110 pA (Figures 7B and 7C) the sample showed a resistance to the beam when using the low-temperature method. Figure 7C shows the difficultly observable detail of epicuticular waxes on the leaf surface. The accelerating voltage of 20 kV and the ionization detector were used.

Evaluation of Damage Rate due to Ice Crystal Formation (Study of Ice Crystal Formation)

The structural and dimensional changes due to the freezing process, especially intracellular or extracellular ice formations, can be expected. However, Figures 5G–5I show the minimal dimensional differences between individual suspensor cells (considering the fact that the samples are identical in type and age). Moreover, samples of susceptible embryogenic tissue observed with the low-temperature method show high steadiness, and also the possibility for detailed observation of microstructures with a markedly higher resolution. It is also possible to conclude that no significant growth of ice crystals occurs. It is demonstrated in Figure 6 with its image of smooth structure, free of ice crystals or indication of crystal formation. Figure 6A shows the head of embryonic cells of Pinus Sylvestris (white stars) partially covered by the ECM and the cell covered with many layers of ECM (detail marked with a white box). Figure 6B shows the detail of mutually overlapping ECMs as well as a single layer of the ECM (white arrows).

Figures 6C and 6D depict early somatic embryonic tissue of Abies alba at the moment of cell division. The undamaged ECM on embryogenic tissue of Picea abies is apparent in Figures 6E and 6F. The observation of the ECM is comparable to the results presented by Šamaj et al. (2008). However, samples are unaffected by the SEM treatments. Unfortunately, resolution is limited by the capabilities of the AQUASEM II microscope, equipped with a hairpin cathode.

Many types of plant samples, especially conifers, are resistant to cold stress around – 20°C due to their specific cell features, such as fluidity of biomembranes, synthesis and accumulation of low-molecular weight (Hansen et al., 1997; Nanjo et al., 1999), and highmolecular weight of cryoprotectants (Strimbeck and Schaberg, 2009). For example, sugar (oligosaccharides, raffinose, and stachyose) accumulation has cryoprotective effects on proteins and membranes (Arakawa and Timasheff, 1982; Caffrey et al., 1988).

The temperature used in the experiments (- 18/–20°C) is generally unusual from the ESEM point of view, nevertheless results in Figure 7 demonstrate its suitability not only for plant somatic embryogenesis and conifer sample observation. The comparison between wet ESEM observation—see Figure 7A (3°C, 715 Pa of water vapor, RH 94%, probe current 60 pA)— and the low-temperature method—see Figures 7B and 7C (- 20°C, 400 Pa of air, probe current 110 pA)—was carried out on the sample of Oxalis acetosella L. with the aim to show the sample's stabilization as well as higher resistance to beam damaging as a result of the low-temperature method. The detail of epidermical waxes which are difficult to observe in ESEM (Stabentheiner et al., 2010) is clearly visible in Figure 7C.

Conclusion

The functionality and wide range of applicability of the low-temperature method was demonstrated by the study of different types of embryogenic tissues of conifers (Pinaceae). Results demonstrate that the ESEM is useful method in the study of plant samples in their native state, and the presented low-temperature method has a potential to extend ESEM observation based on the specific hardiness of plant samples at low-temperatures around – 20°C. Nevertheless, low temperature may impose stress due to cell and tissue dehydration during the freezing of cellular water, and intracellular or extracellular ice formation in the intercellular space, so the conditions of ESEM observation have to be carefully examined and selected. Freezing artefacts can be created by an incorrect method procedure and are identifiable by changing of image contrast when changing the electron dose.

The usage of the low-temperature method for observation of other plant samples was demonstrated on the sample of Oxalis acetosella L. The results indicate that applicability of the low-temperature method could be feasible for various other plant samples with the aim to improve the sample's stability as well as resistance to beam damage.

Acknowledgements

This work was supported by the Grant Agency of the Czech Republic: grant No. GA14–22777S. We would like to express many thanks to Professor Havel from Mendel University in Brno, Faculty of Agronomy, Department of Plant Biology for description of light microscopic microphotography and consultation of potential artefacts in ESEM pictures. For cooperation with the cultivation of plant material, we would like to express many thanks to Dr. Vlašínová from Mendel University in Brno, Faculty of Agronomy, Department of Plant Biology and Dr. Vooková from The Institute of Plant Genetics and Biotechnology of the Slovak Academy of Sciences. We would also like to express our gratitude to Dr. Mašová from ASCR, Institute of Scientific Instruments, for her help with light microscopy.

References

Arakawa T, Timasheff SN. 1982. Stabilization of protein structure by sugar. Biochemistry 21:6536–6544.

Caffrey M, Fonseca V, Leopold A. 1988. Lipid-sugar interactions. Relevance to anhydrous biology. Plant Physiol 86:754–758.

Cameron RE, Donald AM. 1994. Minimizing sample evaporation in the environmental scanning electron microscope. J Microsc 173:227–237.

Danilatos GD. 1983. A gaseous detector device for an environmental SEM. Micron and Microsc Acta 14:307–319.

Danilatos GD. 1986. Cathodoluminescence and gaseous scintillation in the environmental SEM. Scanning 8:279–284.

Danilatos GD. 1988. Foundations of environmental scanning electron microscopy. Adv Electronics and El Phys 71:109–250. Academic press.

Donald AM. 2003. The use of environmental scanning electron microscopy for imaging wet and insulating materials. Nature Mater 2:511–516.

Fletcher AL, Thiel BL, Donald AM. 1997. Amplification measurements of alternative imaging gases in environmental SEM. J Phys D Appl Phys 30:2249–2257.

Gupta PK, Durzan DJ. 1985. Shoot multiplication from mature trees of Douglas-fir (Pseudotsuga menziesii) and sugar pine (Pinus lambertiana). Plant Cell Rep 4(4):177–179.

Hansen J, Tuerk R, Vogg G, Heim R, Beck E. 1997. Conifer carbohydrate physiology: Updating classical views. In: Rennenberg H, Eschrich W, Ziegler H, editors. Trees: Contributions to modern tree physiology. Leiden: Backhuys Publ, pp. 97–108.

Havel L, Durzan DJ. 1996. Apoptosis during diploid parthenogenesis and early somatic embryogenesis of Norway spruce. Int J Plant Sci 157(1):8–16.

Jirák J, Neděla V, Černoch P, Čudek P, Runštuk J. 2010. Scintillation SE detector for variable pressure scanning electron microscopes. J Microsc 239:233–238.

Klimaszewska K, Trontin JF, Becwar MR, Devillard C, Park YS, Lelu-Walter AM. 2007. Recent progress in somatic embryogenesis of four Pinus spp. Tree For Sci Biotech 1:11–25.

Mathews RG, Donald AM. 2002. Conditions for imaging emulsion in the environmental scanning electron microscope. Scanning 24:75–85.

McGregor JE, Donald AM. 2010. ESEM imaging of dynamic biological processes: The closure of stomatal pores. J Microsc 239(2):135–141.

Mo LH, Egertsdotter U, Von Arnold S. 1996. Secretion of specific extracellular proteins by somatic embryos of Picea abies is dependent on embryo morphology. Ann Bot 77:143–152.

Nanjo T, Kobayashi M, Yoshida Y, Kakubari Y, Yamaguchi- Schinozaki K, Shinozaki K. 1999. Antisense suppression of proline degradation improves tolerance to freezing and salinity in Arabidopsis thaliana. FEBS Lett 461:205–210.

Neděla V. 2007. Methods for additive hydration allowing observation of fully hydrated state of wet samples in environmental SEM. Microscope Res Tech 70:95–100.

Neděla V. 2010. Controlled dehydration of a biological sample using an alternative form of environmental SEM. J Microsc 237 (1):7–11.

Neděla V, Hřib J, Vooková B. 2012. Imaging of early conifer embryogenic tissues with the environmental scanning electron microscope. Biol Plantarum 56(3):595–598.

Neděla V, Konvalina I, Lencová B, Zlámal J. 2011. Comparison of calculated, simulated and measured signal amplification in a variable pressure SEM. Nucl Instrum Meth A 645(1):79–83.

Pathan AK, Bond J, Gaskin RE. 2008. Sample preparation for scanning electron microscopy of plant surfaces-horses for courses. Micron 39:1049–1061.

Popielarska-Konieczna M, Bohdanowicz J, Starnawska E. 2010. Extracellular matrix of plant callus tissue visualized by ESEM and SEM. Protoplasma 247:121–125.

Popielarska-Konieczna M, Kozieradzka-Kiszkurno M, Świerczyńska J, Góralski G, Ślesak H, Bohdanowicz J. 2008. Are extracellular matrix surface network components involved in signaling and protective function? Plant Signal Behav 3(9):707–709.

Royall CP, Thiel BL, Donald AM. 2001. Radiation damage of water in environmental scanning electron microscopy. J Microsc 204(3): 185–195.

Šamaj J, Salaj T, Matúšová R, Salaj J, Takáč T, Šamajová O, Volkmann D. 2008 Arabinogalactan-protein epitope Gal4 is differentially regulated and localized in cell lines of hybrid fir (Abies alba x Abies cephalonica) with different embryogenic and regeneration potential. Plant Cell Rep 27:221–229.

Stabentheiner E, Zankel A, Polt P. 2010. Environmental scanning electron microscopy (ESEM) – a versatile tool in studying plants. Protoplasma 246:89–99.

Stokes DJ. 2003. Recent advances in electron imaging, image interpretation and applications: Environmental scanning electron microscopy. Phil Trans R Soc Lond A 361(1813):2771–2787.

Stokes DJ. 2008. Principles and practice of variable pressure: Environmental scanning electron microscopy (VP-ESEM). John Wiley & Sons and Cambridge University Press. p 234.

Strimbeck GR, Schaberg PG. 2009. Going to extremes: Low temperature tolerance and acclimation in temperate and boreal conifers. In: Gusta L, Wisniewski M, Tanino K, editors. Plant cold hardiness: From the laboratory to the field. Oxfordshire, UK: CAB International, pp. 226–239.

Tabor D. 1991. Gases, liquid and solids, and other states of matter. John Wiley & Sons and Cambridge University Press. p 444.

Tihlaříková E, Neděla V, Shiojiri M. 2013. In situ study of live specimens in an environmental scanning electron microscope. Microsc Microanal 19(4):914–918.

Timp W, Matsudaira P. 2008. Electron microscopy of hydrated samples. Methods Cell Biol 89:391–407.

Vooková B, Kormut'ák A. 2009. Improved plantlet regeneration from open-pollinated families of Abies alba trees of Dobroč primeval forest and adjoing managed stand via somatic embryogenesis. (Bratislava) Biologia 64:1136–1140.

14 Imaging of Norway spruce early somatic embryos with the ESEM, Cryo-SEM and laser scanning microscope

Vilém Neděla[a], Jiří Hřiba, Ladislav Havel[b], Jiří Hudec[a], Jiří Runštuk[a]

a *Environmental Electron Microscopy Group, Institute of Scientific Instruments of the CAS, Brno, Czech Republic*

b *Department of Plant Biology, Faculty of Agronomy, Mendel University in Brno, Brno, Czech Republic*

Keywords

ESEM, Cryo-SEM, Bright field/dark field microscopy, Extracellular matrix, Picea abies, Somatic embryogenesis

Abstract

This article describes the surface structure of Norway spruce early somatic embryos (ESEs) as a typical culture with asynchronous development. The microstructure of extracellular matrix covering ESEs were observed using the environmental scanning electron microscope as a primary tool and using the scanning electron microscope with cryo attachment and laser electron microscope as a complementary tool allowing our results to be proven independently. The fresh samples were observed in conditions of the air environment of the environmental scanning electron microscope (ESEM) with the pressure from 550 Pa to 690 Pa and the low temperature of the sample from −18°C to −22°C. The samples were studied using two different types of detector to allow studying either the thin surface structure or material composition. The scanning electron microscope with cryo attachment was used for imaging frozen extracellular matrix microstructure with higher resolution. The combination of both electron microscopy methods was suitable for observation of "native" plant samples, allowing correct evaluation of our results, free of error and artifacts.

Introduction

The suitability of an environmental scanning electron micro-scope (ESEM) to the examination of plant samples was demonstrated by Danilatos (1981) and Stabentheiner et al. (2010).

The ESEM (Danilatos, 1988) can open up a wide range of new applications in electron microscopy which rely on being able to image samples in, or close to, their fully hydrated and native state (Stokes, 2003; Neděla, 2010). However, for reaching

and maintaining the thermodynamic equilibrium, it is important to respect basic dependences of the gas pressure on the sample temperature as well as the influence of other operating parameters in the ESEM. Important is also the type of detected information, strongly influenced by the detector geometry or its position in the specimen chamber of an ESEM (Neděla et al., 2015a). The possibility to study specific and susceptible samples in the ESEM is based on advanced methodologies (Neděla et al., 2012, 2015b; Kirk et al., 2009; Tihlaříková et al.,2013), mostly developed as an extension of conventional proto-cols. Using the ESEM to study dry or hydrated somatic and zygotic embryos was reported by Reid et al. (1999). For the observation of zygotic and somatic embryos of Algerian fir, the first version of the ESEM AQUASEM was used by (Hřib, 2005). A detailed study of native extracellular matrix (ECM) structures of early somatic embryos (ESEs) using ESEM AQUASEM II equipped with a custom-built ionization detector of secondary electrons combined with the YAG:Ce^{3+}detector of backscattered electrons was presented by Neděla et al. (2012).

The scanning electron microscope with cryo-attachment (cryo-SEM) involves the examination of biological material below ambient temperature (typically between −100°C and −175°C),allowing the life-like appearance of the sample to be preserved and recorded in a fully hydrated and chemically unmodified state. The cryo-method has a great advantage. The material is rapidly frozen, so volatile and sensitive biological structures are well preserved. Additionally, images of fracture surfaces inside the sample can be obtained (Roos and Morgan, 1990). The field emission SEM with cryo-attachment enables the highest resolution attainable with this type of microscope to be reached and is comparable with the routine 100 kV scanning transmission electron microscope (STEM).High quality of freezing of biological samples produces minimal dimensional changes, such as shrinkage and distortion caused by drying (Pšenička et al., 2010).

ESEs of the Norway spruce were first described by Chalupa (1985). The embryogenic culture was white and mucilaginous. Later on it was observed that the culture comprised bipolar structures composed of structures resembling early zygotic embryo — embryonal group, embryonal tubes and embryonal suspensor (Durzan et al., 1994; Havel and Durzan, 1996). One of structural features of ESEs is the presence of an extracellular matrix network on the surface of embryogenic cells (Šamaj et al., 2008). Presence of a continuous fibrillar layer on the outer cell surface cultured in vitro has been reported in several plant species e.g. maize (Šamaj et al., 1995), peach palm (Steinmacher et al., 2012), black pine (Jasik et al., 1995), Trifolium nigrescens (Pilarska et al., 2013). Bobák et al. (2004) reported that extracellular matrix network has been specifically related to induction and early stages of somatic embryogenesis.

The role of extracellular matrix network during embryogenesis is still uncertain, but cell adhesion, a protective function and coordinating developmental stages have been proposed (Verdeil et al., 2001).

The aim of this paper was to publish a confirmation study of the morphology of cultured ESEs using our newly published Low- Temperature Method (LTM) for ESEM (Neděla et al., 2015b) and owing to many requests of plant-biologists to compare our results with light microscopy and cryo-SEM which is currently still a preferred method for studying biological samples. This is the first report of ESEM, cryo-SEM and reflected light microscopy with contrast method bright-field/dark-field of extracellular matrix surface network (ECMSN) in ESEs of the Norway spruce.

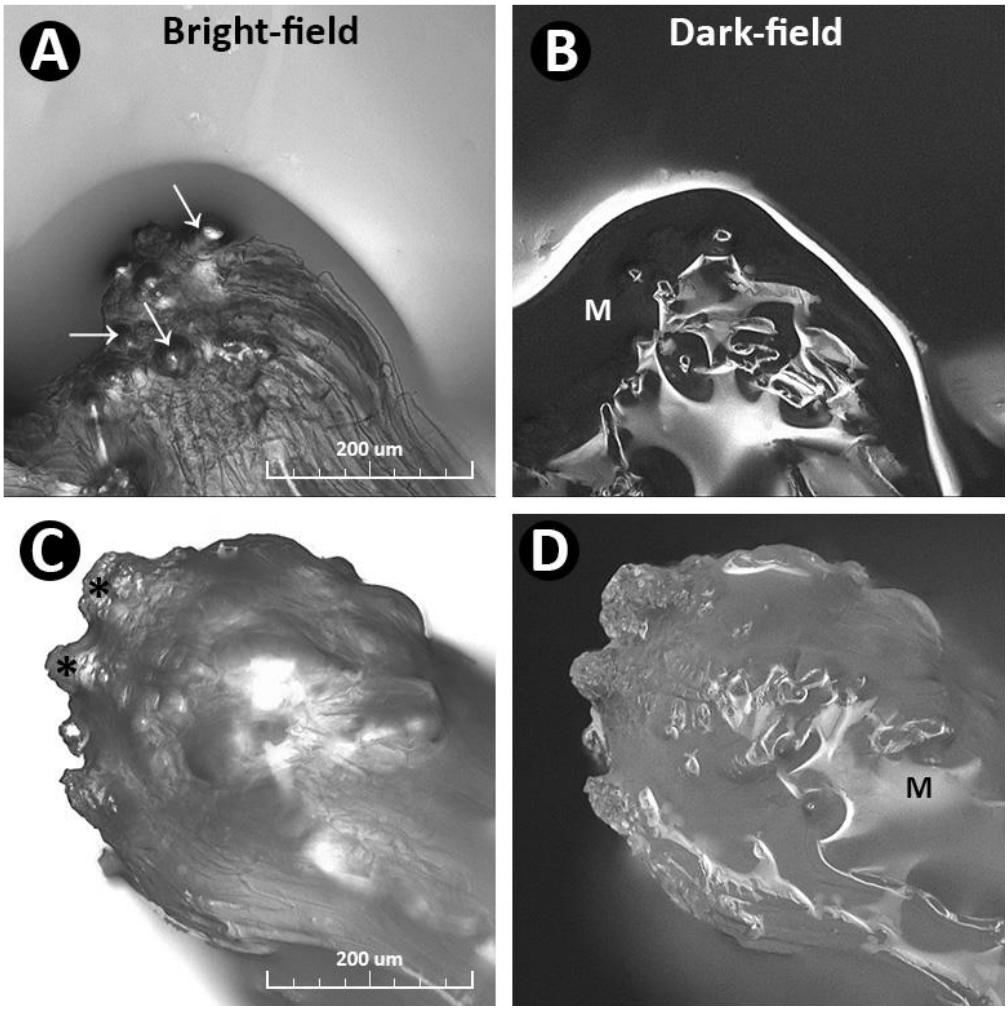

Fig. 1. Aggregates of ESEs, clone 2/32 of the Norway spruce (Picea abies/L./Karst.) after one week from last passage reflected light microscopy (A,C—contrast method bright-field, B,D—contrast method dark-field, the presence of the mucilaginous matrix is indicated by M, heads of ESEs is indicated by * and somatic embryo development from meristematic layer is indicated by arrows).

Materials and method

Plant material

Early somatic embryos, clone 2/2 and clone 2/32 from the col-lection of the Department of Plant Biology of Mendel University in Brno, were originally derived from a mature zygotic embryo of tree of the Norway spruce (Picea abies/L./Karst.) mountain cli-mate type of experimental area in the Beskyd Mountains, Moravia, Czech Republic. The ESE cultures were maintained on medium designated LP/2 in 100 mm diameter Petri dishes (Havel and Durzan, 1996) with 9 _M 2.4 D and 4.4 _M BAP. The ESEs from the upper parts of their aggregates (2.5–5.0 mg) were subcultured in 10–14 day periods. The cultures were maintained in the dark at 23 ± 1 °C.

ESEM

Samples of collected ESEs, clone 2/2 were placed on a cooled specimen holder (Peltier stage) and their temperature was gradually decreased. After application of special procedure for study of plant biological samples using the LTM for ESEM, described in detail by (Neděla et al., 2015b) based on combination of influence of controlled slow gas pressure evacuation of the ESEM specimen chamber and low temperature effect, the temperature of samples was stabilized and maintained between −18 °C and −22 °C. This experimentally discovered and for many plant samples environmentally acceptable temperature causes well stabilization of plant cells on the sample surface as well as their better resistance for radiation damage (Neděla et al., 2015b). The ESE samples were examined under low vacuum conditions (air pressure 550 Pa) by the non-commercial ESEM AQUASEM-II, equipped with the custom-built ionization detector of secondary electrons (Danilatos, 1990) and the halved YAG:Ce^{3+} scintillation single crystal used as the principal part of the detector of backscattered electrons (BSE-YAG). This detection system is very thin (2 mm) and allows sample observation with a very short distance from the sample to final pressure limiting aperture, typically 1 mm to 5 mm. Due to shortening the path length of the primary electrons (PE) in the gas, PE-gas scattering decreases and the SNR in the detected signal increases.

All experiments in the ESEM were carried out under constant operating conditions (beam accelerating voltage 20 kV, probe cur-rent 70 pA, sample distance 2.5 mm between the bottom surface of the YAG single crystal and the surface of the sample, positive bias of the detection electrode system 270 V) and in the gas environment with relative humidity equal to 40%.

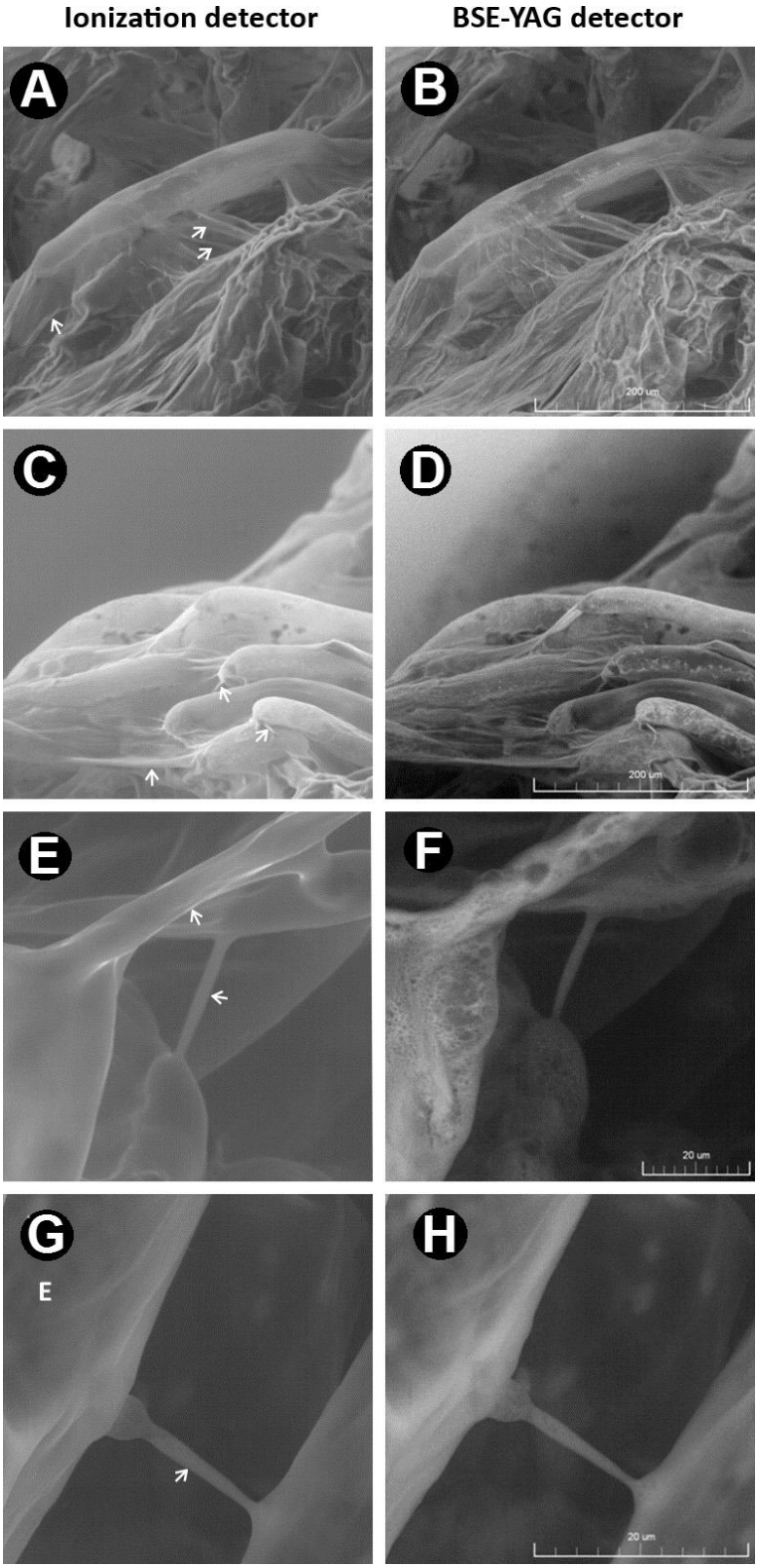

Fig. 2. Comparison of early somatic embryogenic culture of the Norway spruce using the ESEM AQUASEM II with two detectors with the focus on the ECM (A, C, E and G—the ionization detector; B, D, F and H—the BSE-YAG detector; accelerating voltage 20 kV, air pressure in the specimen chamber 550–690 Pa; the presence of the ECM is indicated by arrows; E—embryonic tube cells).

Cryo-SEM

For comparison, our samples were observed by using the field emission scanning electron microscope with cryo-attachment. The sample was placed on the aluminium target and the excess liquid drained. Then the sample was frozen by plunging into liquid nitrogen and immediately transferred under vacuum into the chamber of the cryo-attachment CryoALTO 2500 (Gatan). At a temperature of −95 ◦C vacuum sublimation was performed for 2 min to decontaminate the surface of the sample. The frozen sample was observed free of sputtering by the conductive layer in the FESEM JEOL 7401F operated at acceleration voltage 1 kV for the detector of secondary electrons situated in the specimen chamber of the microscope and 4 kV for the BSE-YAG detector. The working distance was around 18.3 mm for low magnification mode and 8.5 mm for classic SEM mode and the stage temperature −130 °C.

Laser scanning microscopy

Samples approximately 2 × 2 × 2 mm of spruce embryogenic tissue were placed on slide of the LEXT OLS-3100 laser scanning microscope. This microscope is a 408 nm laser-based confocal microscope for nondestructive imaging and measurements of sub-micron surface structures. As well as for above mentioned electron microscopy methods no samples preparation is required to achieve mutually comparable images.

We used reflected light microscopy with contrast method bright-field/dark-field using white LED illumination for the imaging of the samples for this paper.

Results ad discussion

Usage of contrast method bright-field and dark-field may clearly show different morphological structures of Norway spruce ESEs (Fig. 1). This figure was recorded by the laser scanning micro-scope LEXT OLS-310 in order to visualize structures of the same plant biological material with contrasting techniques. Appearance of embryonal heads is present on Fig. 1A and C while on Fig. 1B and D the presence of the mucilaginous matrix is visible. On Fig. 3A and B bundles of vacuolated suspensor cells are presented whereas on Fig. 3C–F embryonal tubular cells with extracellular matrix. More-over, compact clump of densely cytoplasmic cells which comprises embryonal head is recorded. Micrographs by FESEM Jeol JSM 7401F with cryo-attachment enabled visualization of extracellular matrix microstructure but as well cover of ESE (Fig. 4A–D). On Fig. 4E developed ESE is shown while on Fig. 4F detailed structure of embryonal head and embryonal tubular cells was recorded. Morphology of the inner surface of suspensor cells is presented on Fig. 4G and H.

To obtain a detailed image of ECMSN in-situ, we applied the techniques and conditions described above and used two different types of detectors to record images. The results are arranged in two rows side by side for an easy comparison. First, the BSE-YAG detector allows the detection of high-energy BSEs emitted from deep bulk of the sample (mostly up to tens of micrometers) and thus yielding information on the material contrast. Second, ionization detector records signals composed of predominantly low energy secondary electrons mostly emitted from the depth from units to tens of nanometers and giving topographic contrast. The individual micrographs from morphology groups of ESEs of the Norway spruce show images of suspensor cells and their surface with extracellular matrix obtained by the ionization detector (Fig. 2A and C) and also the same structures by the BSE-YAG detector (Fig. 2B and D) with a higher resolution. Moreover, the BSE-YAG detector is able to distinguish two elements differing by 0.09 mean atomic number (Autrata et al., 2001) and therefore can be used for rough qualitative material analysis of the samples. Structures (of particles) on cells with a higher level of brightness are particularly apparent in Fig. 3A and C. These figures show small and larger structures occur-ring in the cells of the embryonic group. For comparison, the same structures recorded by the ionization detector of secondary electrons are shown in Fig. 3B and D. The transition of suspensor cells is visible in Fig. 3E and F. The early somatic embryo is shown in Fig. 3G and H. The extracellular matrix was studied firstly on the surface of the embryonal group as a membranous layer or reticulated network, see Fig. 2A and C and secondly, as stretched compact fibers between cells, see Fig. 2E and G (using the ionization detector of secondary electrons) and Fig. 2F and H (using the BSE-YAG detector). The smooth and compact surface layer was observed using the ionization detector of low energy secondary electrons, see Fig. 2E, while the detector of backscattered electrons, giving the information about the material contrast from the bulk of sample, shows structure looking like surface-porosity, see Fig. 2F. But in fact the figure shows under surface matrix distribution of fibers containing high atomic number elements.

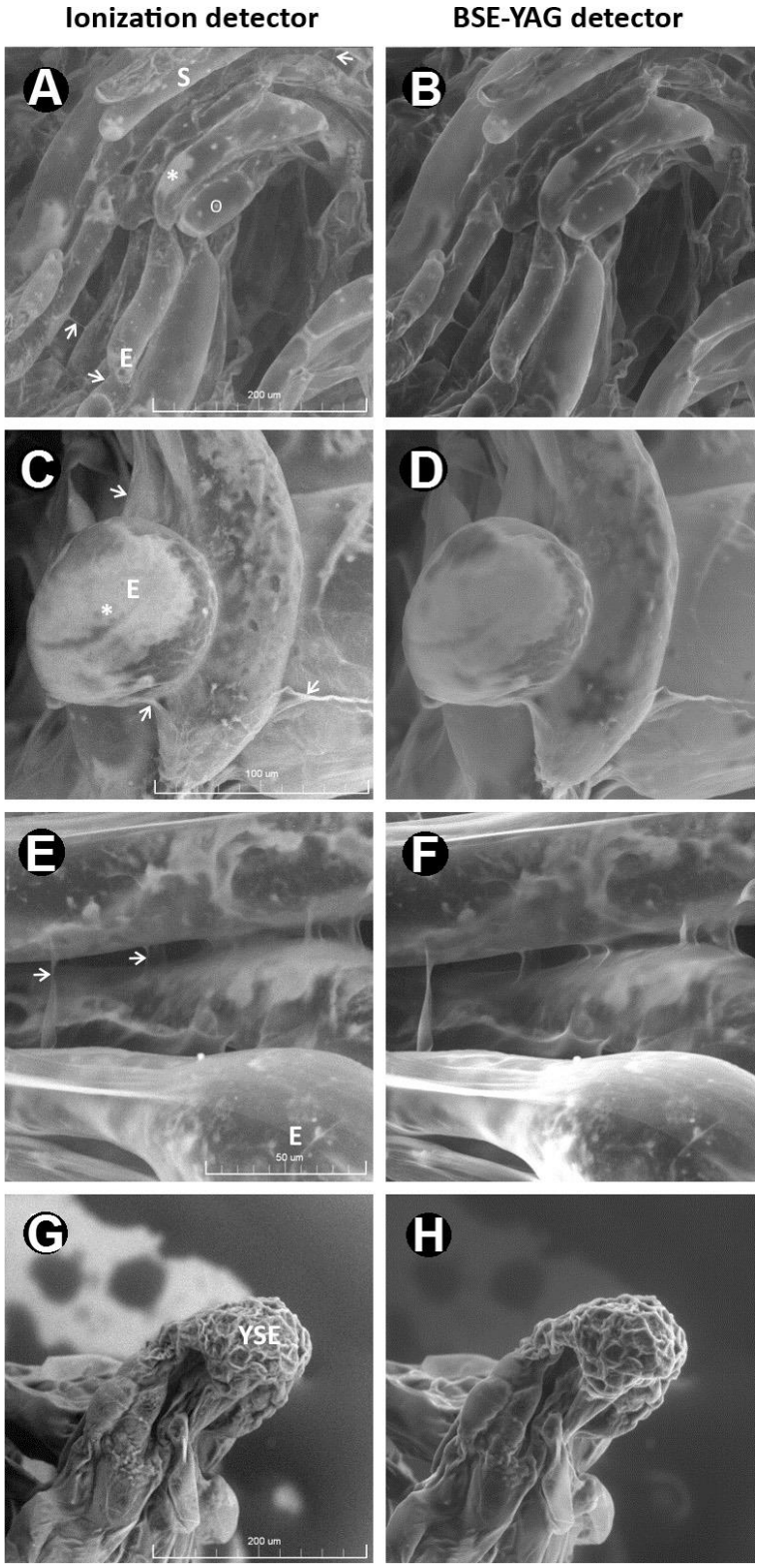

Fig. 3. Comparison of ESEs of the Norway spruce using the ESEM AQUASEM II with two detectors with the focus on the aspect of development of the somatic embryo (A, C, E and G—the BSE-YAG detector; B, D, F and H—the ionization detector; accelerating voltage 20 kV, air pressure in the specimen chamber 550–690 Pa; the presence of the extracellular matrix is indicated by arrows; E—embryonic tube cells, S—suspensor cell, YSE—new young somatic embryo is formed).

The presence of a smooth and compact surface of extracellular matrix was also proven by our results obtained using the Cryo- SEM, see Fig. 4A and B. The early somatic embryo fully covered by the ECM is apparent from Fig. 4C and D, where Fig. 4D shows its elongated state. Fig. 4E shows the forming head of the early somatic embryo. Its more developed phase is apparent from Fig. 4F. The fracture of frozen somatic embryo tissue shows the inner structure of suspensor cells, recorded by the BSE-YAG detector in the SEM with cryo-attachment (Fig. 4G and H).

The cell wall of higher plants is a dynamic cellular compartment. This active structure, referred to as the ECM (Roberts, 1994), is an integral part of the ECM-plasma membrane-cytoskeleton continuum and plays fundamental roles in intercellular interactions of the multicellular organism.

Recently there has been considerable interest in the ECM surface network, its chemical composition and the structural arrangement on the cell surface may play significant roles in morphogenesis. Additionally, the inner composition of suspensor cells was uniquely shown in its fracture part using the Cryo-SEM.

The ECM of Actinidia deliciosa was observed using the ESEM and Cryo-SEM on the surface of cell clusters as a membranous layer or reticulated network, shrunken or wrinkled, depending on the procedure. Smoother surface layers without visible fibrils and showing porosity were published by (Popielarska-Konieczna et al., 2010). Thus, by combining the two detectors in the ESEM, and by additional proving of our results using the Cryo-SEM, the existence of porosity on the ECM surface was negotiated; on the other hand the smoother surface of the ECM without visible fibrils was probed. It is beneficial to present our methodology of the research on another species of the Pinaceae family (Neděla et al., 2012).

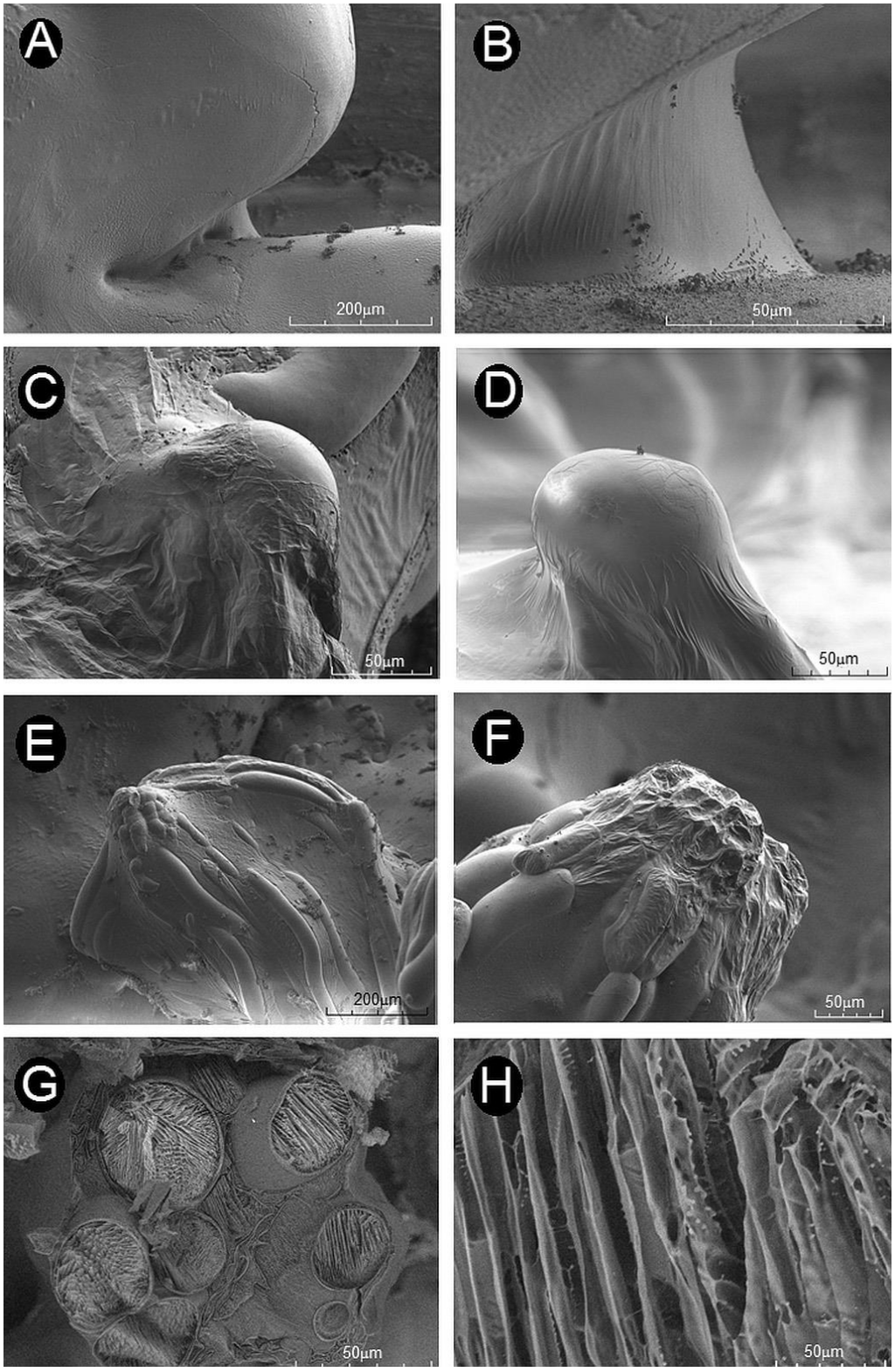

Fig. 4. Spruce embryogenic culture (Picea abies) micrographs by FESEM Jeol JSM 7401F with cryo-attachment. Figures A–F—the detector of secondary electrons in low magnification mode, working distance 18.3 mm and figures G and H—the BSE-YAG detector, working distance 8.3 mm (A and B—early somatic embryo with microstructure of the ECM; C and D—early somatic embryo covered by the ECM; E and F—early somatic embryo; G and H fracture morphology of the inner surface of suspensor cells).

Acknowledgements

We would like to express many thanks to Dr. Jana Nebesářová from the Institute of Parasitology of the Biology Centre ASCR, v.v.i. for her help during experiments with Cryo-SEM and preparation of the specimens. We would also like to thank to Ing. Biljana Đordević for consultations in the field of plant biology. This work was supported by the Grant Agency of the Czech Republic, grant No. GA14-22777S.

References

Autrata, R., Schauer, P., Jirák, J., 2001. Detection of backscattered electrons for biological specimens study. In: 5th Multinational Congress on Electron Microscopy, Lecce, Italy, pp. 519–520.

Bobák, M., Šamaj, J., Pretová, A., Blehová, A., Hlinková, E., Oveˇcka, M., Kutarnová, Z., Hlavačka, A., 2004. The histological analysis of indirect somatic embryogenesis on Drosera spathulata Labill. Acta Physiol. Plant. 26, 353–361.

Chalupa, V., 1985. Somatic embryogenesis and plantlet regeneration from cultured immature and mature embryos of Picea abies/L./Karst. Comm. Inst. For. Čechosloveniae 14, 65–90.

Danilatos, G.D., 1981. The examination of fresh or living plant material in an environmental scanning electron microscope. J. Microsc. 12, 235–238.

Danilatos, G.D., 1988. Foundation of environmental scanning electron microscopy. Advances in Electronics and Electron Physics, 71. Academic Press, Boston, pp. 109–250.

Danilatos, G.D., 1990. Theory of the gaseous detector device in the environmental scanning electron microscopy. Advances in Electronics and Electron Physics, 78. Academic Press, Boston, pp. 1—102.

Durzan, D.J., Jokinen, K., Guerra, M., Santerre, A., Chalupa, V., Havel, L., 1994. Latent diploid parthenogenesis and parthenote cleavage in egg-equivalents in Norway spruce. Int. J. Plant Sci. 155 (6), 677–688.

Havel, L., Durzan, D.J., 1996. Apoptosis during diploid parthenogenesis and early somatic embryogenesis of Norway spruce. Int. J. Plant Sci. 157, 8–16.

Hřib, J., 2005. Study of somatic and zygotic embryos of Algerian fir (Abies numidica De Lann. Carriére) by AQUASEM. In: Libiaková, G., Gajdošová, A. (Eds.), Book of Abstracts COST 843 Final Conference, COST 843 and COST 851

Joint Meeting. Organized by Institute of Plant Genetics and Biotechnology SAS, June 28–July 3, Stará Lesná, Slovakia, pp. 269–271.

Jasik, J., Salajova, T., Salaj, J., 1995. Developmental anatomy and ultrastructure of early somatic embryos in European black pine (Pinus nigra Arn.). Protoplasma 185, 205–211.

Kirk, S.E., Skepper, J.N., Donald, A.M., 2009. Application of environmental scanning electron microscopy to determine biological surface structure. J. Microscopy 233, 205–224.

Neděla, V., 2010. Controlled dehydration of a biological sample using an alternative form of environmental SEM. J. Microsc. 237, 7–11.

Neděla, V., Hřib, J., Vooková, B., 2012. Imaging of early conifer embryogenic tissues with the environmental scanning electron microscope. Biol. Plant. 56, 595–598.

Neděla, V., Konvalina, I., Oral, M., Hudec, J., 2015a. The simulation of energy distribution of electrons detected by segmental ionization detector in high pressure conditions of ESEM. Microsc. & Microanal. 21 (Suppl. 4), 264–269.

Neděla, V., Tihlaříková, E., Hřib, J., 2015b. The Low-Temperature method for study of coniferous tissues in the environmental scanning electron microscope. Microsc. Res. Tech. 78, 13–21.

Pilarska, M., Knox Paul, J., Konieczny, R., 2013. Arabinogalactan-protein and pectin epitopes in relation to an extracellular matrix surface network and somatic embryogenesis and callogenesis in Trifolium nigrescens Viv. Plant Cell Tissue Organ Culture 115, 35–44.

Popielarska-Konieczna, M., Bohdanowicz, J., Starnawska, E., 2010. Extracellular matrix of plant callus tissue visualized by ESEM and SEM. Protoplasma 247, 121–125.

Pšenička, M., Tesařová, M., Těšitel, J., Nebesářová, J., 2010. Size determination of Acipenser ruthenus spermatozoa in different types of electron microscopy. Micron 41, 455–460.

Reid, D.A., Lott, J.N.A., Attree, S.M., Fowke, L.C., 1999. Imbibition of white spruce seeds and somatic embryos: a study of morphological changes in an environmental scanning electron microscope and potassium leakage. In Vitro Cell. Dev. Biol. Plant 35, 303–308.

Roberts, K., 1994. The plant extracellular matrix: in an expansive mood. Curr. Opin. Cell Biol. 6, 688–694.

Roos, N., Morgan, A.J., 1990. Cryopreparation of thin biological specimens for electron microscopy: methods and applications. In: Royal Microscopical Society Microscopy Handbooks 21. Oxford University Press, Oxford, pp. 109.

Šamaj, J., Salaj, T., Matúšová, R., Salaj, J., Takáč, T., Šamajová, O., Volkmann, D., 2008. Arabinogalactan-protein epitope Gal 4 is differentially regulated and localized in cell lines of hybrid fir (Abies alba × Abies cephalonica) with different embryogenic and regeneration potential. Plant Cell Rep. 27, 121–229.

Šamaj, J., Bobák, M., Blehová, A., Krińtin, J., Auxtova-Šamajova, O., 1995. Developmental SEM observations of an extracellular matrix in embryogenic calli of Drosera rotundifolia and Zea mays. Protoplasma 186, 45–49.

Stabentheiner, E., Zankel, A., Polt, P., 2010. Environmental scanning electron microscopy (ESEM)—a versatile tool in studying plants. Protoplasma 246, 89–99.

Steinmacher, D.A., Saare-Surminski, K., Lieberei, R., 2012. Arabinogalactan proteins and the extracellular matrix surface network during peach palm somatic embryogenesis. Physiol. Plant 146, 336–349.

Stokes, D.J., 2003. Investigating biological ultrastructure using environmental scanning electron microscopy (ESEM). In: Mendez-Vilas, A. (Ed.), Science, Technology and Education of Microscopy: An Overview, vol. 1. FORMATEX Publ., Badajoz, Spain, pp. 564–570.

Tihlaříková, E., Neděla, V., Shiojiri, M., 2013. In situ study of live specimens in an environmental scanning electron microscope. Microsc. and Microanal. 19, 914–918.

Verdeil, J.L., Hocher, V., Huet, C., Grosdemange, F., Escoute, J., Ferriere, N., Nicole, M., 2001. Ultrastructural changes in coconut calli associated with the acquisition of embryogenic competence. Ann. Bot. 88, 9–18.

15 Bottlenecks in bog pine multiplication by somatic embryogenesis and their visualization with the environmental scanning electron microscope

Helena Vlašínová[1], Vilém Neděla[2], Biljana Đorđević[1], Ladislav Havel[1]

1 Faculty of AgriSciences, Mendel University in Brno, Zemědělská 1, Brno 613 00, Czech Republic

2 Institute of Scientific Instruments, Academy of Sciences of the Czech Republic, Královopolská 147, Brno 61264, Czech Republic

Keywords

Somatic embryogenesis, Pinus uncinata subsp. uliginosa, Abnormalities, Environmental scanning electron microscope

Abstract

Somatic embryogenesis (SE) is an important biotechnological technique used for the propagation of many pine species in vitro. However, in bog pine, one of the most endangered tree species in the Czech Republic, limitations were observed, which negatively influenced the development and further germination of somatic embryos. Although initiation frequency was very low—0.95 %, all obtained cell lines were subjected to maturation. The best responding cell line (BC1) was used and subjected to six different variants of the maturation media. The media on which the highest number of early-precotyledonary/cotyledonary somatic embryos was formed was supplemented with 121 μM abscisic acid (ABA) and with 6 % maltose. In the end of maturation experiments, different abnormalities in formation of somatic embryos were observed. For visualization and identification of abnormalities in meristem development during proliferation and maturation processes, the environmental scanning electron microscope was used. In comparison to the classical light microscope, the non-commercial environmental scanning electron microscope AQUASEM II has been found as a very useful tool for the quick recognition of apical meristem disruption and abnormal development. To our knowledge, this is the first report discussing somatic embryogenesis in bog pine. Based on this observation, the cultivation procedure could be enhanced and the method for SE of bog pine optimized.

Introduction

Pinus uncinata subsp. uliginosa (G.E. Neumann) Businský is a subendemic taxon in the Czech Republic (CR) (Businský 2009). Over the last decades, spontaneous interspecific hybridization with the ecologically more flexible Scots pine (Pinus sylvestris L.) has seriously affected rare populations of bog pine in the CR (Businský and Kirschner 2010). Moreover, the long-term disruption of the groundwater level and transformation of biotopes after the removal of peat supports Norway spruce and white birch and suppress bog pine. The surviving fragment of bog pine forest consists of old forest vegetation, which is constantly under the invasion of insect pests (Lukášová et al. 2012; Vejsadová and Lukášová 2010). Due to rapid decline, bog pine is considered greatly endangered and it is included in the red list of vascular plants of the Czech Republic (Grulich 2012). Considering that classical propagation of bog pine by cuttings is problematic, newer methods need to be studied in order to preserve populations in the CR. Plant tissue culture systems represent an excellent possibility for the study and conservation of threatened and endangered species (Perullo et al. 2015; Hill et al. 2015). Both in vitro methods, organogenesis and somatic embryogenesis proved to be efficient methods for the regeneration of conifers but somatic embryogenesis (SE) is more preferable. Moreover, in our previous research, we studied the induction of organogenesis from mature seeds of bog pine (Vejsadová et al. 2008) while Vejsadová and Šedivá (2002) induced organogenesis from isolated winter buds of adult individuals. However, shoot propagation was not very successful and problems with rhizogenesis appeared. SE as a biotechnological technique has important implications in tree improvement and breeding programs. It is a powerful tool for clonal propagation of economically important species and is being scaled up for commercial application in conifers (Klimaszewska et al. 2009). Furthermore, SE has been described in many pine species including Scots pine (Häggman et al. 2009; Aronen et al. 2009), maritime pine (Klimaszewska et al. 2009), sugar pine (Gupta and Durzan 1985), Monterey pine (Minocha et al. 1999), white pine (Finer et al. 1989), and European black pine (Salajová and Salaj 1992).

Propagation via SE has many advantages over other ways of vegetative propagation, but the main ones are that embryogenic tissue can be cryopreserved while field testing is still in progress, production of unlimited numbers of somatic embryo, artificial seeds, and genetically modified plants with improved traits (Trontin et al. 2007; Lelu-Walter et al. 2013; Smertenko and Bozhkov 2014). Despite the many advantages of SE, several major bottlenecks still exist to scale up propagation of pine species. Klimaszewska et al. (2009) reported that for several pine species, initiation frequency is very low, the ability for production of mature somatic embryos is lost after the tissue was cultured for over a certain period of

time, and a major limitation is in the low quality of cotyledonary somatic embryos. It was found that morphological abnormalities are responsible for the poor yield of somatic embryos in several species such as Quercus robur (Zegzouti et al. 2001), Acacia mangium (Xie and Hong 2001), Carica papaya (Fernando et al. 2001), Pisum sativum (Griga 2002), Vitis sp. (Bharathy and Agrawal 2008), and Citrus reticulata (Benelli et al. 2010). Morphological alterations, which occur during somatic embryo development, increase the risk of morphological abnormalities, resulting in cotyledons fusion, lack of shoot apical meristem (SAM), cup-shaped cotyledons, and loss of bipolarity (Benelli et al. 2010).

For studying those obstacles, new microscopical techniques can be used. The combination of optical and environmental scanning electron microscopy (ESEM) allows the study of fully fresh samples by the routinely used optical microscopy with higher resolution and depth of field for better understanding of the uneven surface sample microstructure. For the study of the development and abnormalities in somatic embryogenesis of a palm Areca catechu, scanning electron microscopy was used (Wang et al. 2010). Samples were subjected to fixation and dehydration using a critical point dryer while coated with gold in an ion coater.

The aim of this study was to develop the most suitable protocol for SE in bog pine. The other goal was related to observation of the fresh and artifact-free shoot apical meristem distribution connected with abnormal cotyledon development using the original low-temperature method for ESEM and by optical microscopy. Based on these results, the cultivation procedure could be enhanced and the method for SE optimized.

Material and methods

Initiation and maintenance of embryogenic tissue

Embryogenic tissue was initiated from immature zygotic embryos excised from cones of an open-pollinated Pinus uncinata subsp. uliginosa mother tree. The cones were collected in two terms (20 June and 30 June) from the northern and southern side of the tree. The origin of the mother tree was the Dendrological Garden of the Silva Tarouca Institute for Landscape and Ornamental Gardening, Pruhonice, Czech Republic. Embryogenic cell lines of bog pine were established in 2011. For initiation of embryogenic tissue of bog pine, a full-strength DCR medium with certain modifications was used (Gupta and Durzan 1985). Basal DCR medium was composed of 200 mg l^{-1} of inositol, 500 mg l^{-1} casein hydrolysate, 500 mg l^{-1} glutamine, and 0.3 % of gelling agent Gelrite (Duchefa); pH was adjusted from 5.5 to 5.8 before autoclaving. Three variants of DCR media were tested: the first (further denoted as media B) was supplemented with 5 μM2.4-

dichlorophenoxyacetic acid (2.4-D) and 2.5 μM benzyladenine (BA); the second (further denoted as media BAC) was composed of 5 μM 2.4-D, 2.5 μM BA, and with 100 mg l^{-1} activated charcoal (AC); and the third (further denoted as B/2) was with half concentration of growth regulators, 2.5 μM 2.4-D, and 1.25 μM BA. Once sufficient tissue had been initiated, it was transferred onto B maintenance medium.

Maturation

Experiments were performed following the standard procedure as described by Ramarosandratana et al. (2001). At the beginning of the maturation experiment, 3–5 g of fresh embryogenic tissue was transferred to sterile Falcon flasks with 20 ml of liquid proliferation media without plant growth regulators. The suspension was gently mixed by vortex and allowed to settle. After removal of supernatant, 1 ml of suspension containing approximately 250 mg of embryogenic tissue (fresh weight) was plated onto sterile Whatman filter paper on maturation media. Basal maturation medium DCR was supplemented with sucrose or maltose as a carbon source, with/without 3.5 % (w/v) polyethylene glycol (PEG) 4000 (Duchefa, Harleem, the Netherlands) (Table 2). pH was adapted to 5.8 before autoclaving (121 °C, 100 kPa, 20 min). The media were solidified with 0.55 % (w/v) gellan gum (Sigma Aldrich). Into cooled media, 3.4 mM glutamine and 60 or 121 μMabscisic acid (ABA) was filter sterilized and added. Sub-culturing was performed every 3 weeks during maturation for up to 15 weeks. The cultures were kept in the dark at a temperature 23 ± 1 °C.

Morphological observation

Samples of embryos, mainly abnormally developed ones, were moved to Petri dishes with basal medium, and the first informative photos were taken with an Olympus E-450 camera connected with a stereomicroscope Olympus SZH10 using Olympus software Quick Photo micro 2.3. For comparison, some photographs were taken also by digital scanning 3D microscope—HIROX KH-7700. For detailed observation, the non-commercial environmental scanning electron microscope AQUASEM II was used. It was designed as a non-commercial apparatus in the Institute of Scientific Instruments of the Academy of Sciences of the Czech Republic for research into detection systems and advanced ESEM techniques. Besides others, the microscope is equipped with non-commercial systems for the detection of backscattered and secondary electrons used for sample characterization in this work (Neděla et al. 2011).

For the early stage of embryo development, treatment with liquid medium and short exposition in a drop of distilled water had been used for removing the layer of mucilage before ESEM observation. Samples were transferred with a strip of

medium by scalpel and placed on the cooled specimen holder (Peltier stage) of the ESEM. The temperature of the specimen holder was gradually decreased and maintained between −18 and −22 °C according to our newly introduced low-temperature method for ESEM (Neděla et al. 2015). Due to the relatively low-temperature conductivity of the samples, the real temperature of the electron beam-impacted sample surface can be slightly higher. At the beginning of the pumping, the pressure was equal to the atmospheric pressure in all parts of the microscope. Approximately 1 min after the decrease of the sample holder temperature, the pumping process started (Neděla et al. 2012). The samples were examined under low-vacuum conditions in the specimen chamber (air pressure 589 Pa) of the non-commercial ESEM AQUASEM II. All experiments were carried out under constant operating conditions (beam accelerating voltage 20 kV, probe current 100 pA, sample distance 2.5 mm between the bottom surface of the YAG single crystal. and the surface of the sample and ionization detector bias 320 V).

Experimental design

Initiation

For evaluation of initiation frequency in bog pine somatic embryogenesis, different parameters were analyzed: (1) the effect of the sampling date, which represents the effect of the developmental stage of the embryos; (2) the effect of the tree side from which immature cones were collected, which also correspond with the stage of embryo; and (3) nutritional media with supplements in different concentrations. From more than 1000 megagametophytes excised, only 12 embryogenic cell lines were induced.

Maturation

The maturation abilities of nine embryogenic cell lines were analyzed. The best responding cell line (BC1) was used and subjected to different variants of maturation media. The effects of ABA concentrations (60 and 121 μM), sucrose (1 and 6 %), maltose (0 and 6 %), and PEG concentrations (0 and 3.5 %), on the response of embryogenic cell masses, were examined. Maturing ECMs were monitored and characteristics evaluated were as follows: the presence or absence of developing somatic embryos in ECMs, i.e., the response of ECMs to maturation media; the presence of early-precotyledonary and cotyledonary embryos; and the total number of somatic embryos formed. In the end of maturation experiment, it was observed that many somatic embryos were formed in the abnormal way. Abnormally formed embryos were divided into different morphological categories and were studied by ESEM.

Results

Embryogenic cultures were initiated on immature zygotic embryos of bog pine. After 3 weeks on induction medium, the first signs of somatic embryo initiation were observed (Fig. 1a). The majority of embryogenic tissues were initiated between the 3rd and 6th week of culture. In general, from 1000 megagametophytes excised in the first and 160 in the second term, only twelve cell lines were established; initiation frequency was very low—0.95 %. From twelve cell lines induced, five were on media with full concentration of BA (media denoted as B), five on media BAC, and two on media B/2 (Table 1). Considering the term of cone collection—in the first term (June 20), zygotic embryos were mostly in the cleavage stage (seven cell lines were induced but one cell line lost proliferation ability during the 5th transfer and cell line BC1 started spontaneous maturation in proliferation phase), while in second term (June 30), most of zygotic embryos were in the late precotyledonary stage, which resulted that five cell lines were initiated (one cell line lost proliferation ability during the 3rd transfer) (Table 1). According to explants used, eight cell lines were induced directly from immature embryos (BE), one from immature megagametophytes (BM1), while three cell lines were developed on parts of zygotic embryos cultured on induction medium—on the cotyledon (BC1), hypocotyl (BH1), and radicle (BR1) (Table 1; Fig. 1b–e). Two weeks after induction of the embryogenic tissue, the cell lines were transferred to the proliferation medium for long-term culture (Fig. 1f, g).

After transfer of the embryogenic tissue to the maturation medium, all cell lines were tested for their maturation abilities (data not shown). The best responding cell line (BC1) was used and subjected to six different variants of maturation media, e.g., with 60 or 121 μM ABA, and with or without different concentrations of sucrose, maltose, and PEG (Table 2). The media on which the highest number of earlyprecotyledonary/ cotyledonary SE was formed was supplemented with 121 μM ABA and with 6 % maltose. Conversely, the lowest number of somatic embryos formed was recorded on media enriched with 60 μM ABA and with 6 % sucrose. Even if the embryos matured, the development of the cotyledons showed great variability and many embryos developed in an abnormal way (Fig. 2c). According to a morphological point of view, abnormally developed embryos were sorted into the following groups, i.e., cup-shaped cotyledons (Fig. 3a, b), fused cotyledons (Fig. 3c, d), and single cotyledon (Fig. 3e). Furthermore, the obtained fully developed abnormal embryos were subjected to microscopical observation where meristem less SE (Fig. 3f) and SE with disrupted meristem (Fig. 3g, h) were detected. In each group, the shoot apical zone was studied on the basis of the transverse section and under ESEM.

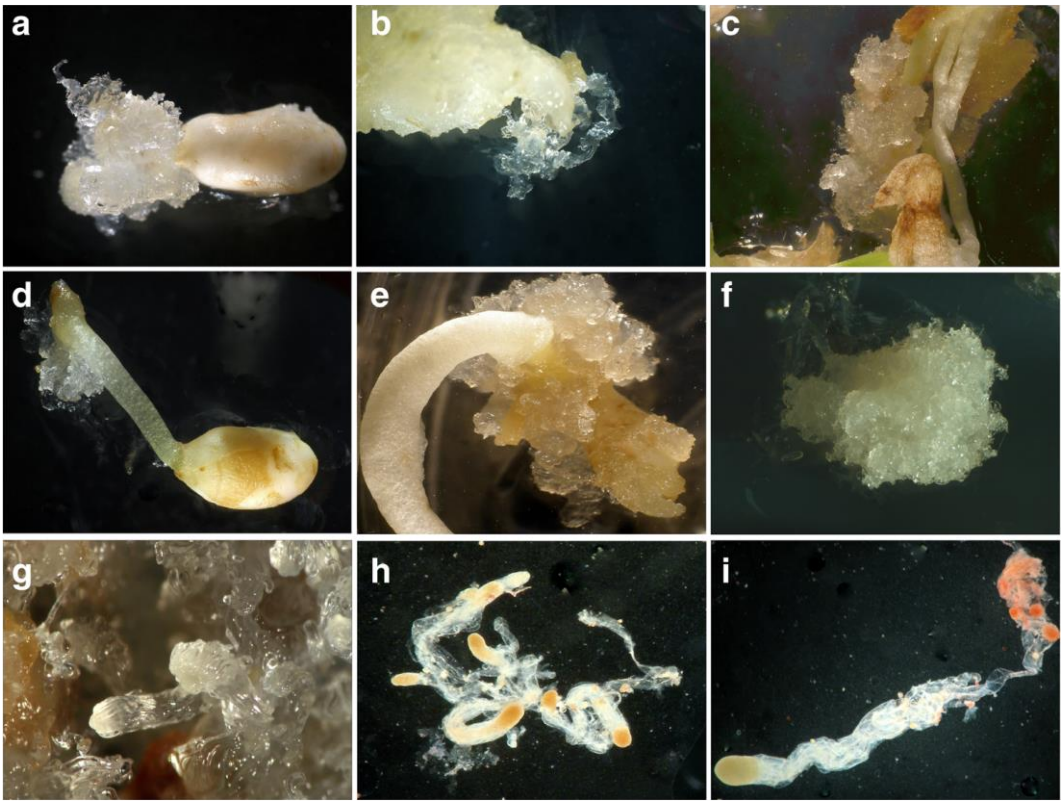

Fig. 1 Initiation and proliferation of early somatic embryos excised from immature cones of bog pine on DCR medium. a Embryogenic tissue initiation on zygotic embryo of bog pine; b initiation of embryogenic tissue on megagametophyte; c initiation of embryogenic tissue on cotyledon; d initiation of embryogenic tissue on hypocotyl; e initiation of embryogenic tissue in the region of radicle; f maintaining of embryogenic tissue on proliferation media; g proliferating embryogenic tissue; h cleavage polyembryony; i early somatic embryo stained with acetocarmine

Discussion

In the present study, the SE developmental pathways of bog pine were used in order to develop the most suitable protocol.

Table 1 Frequency of embryogenic cultures initiated on immature embryos excised from cones of open-pollinated Pinus uncinata subsp. uliginosa mother tree. Embryogenic culture induction was monitored and parameters evaluated were as follows: sampling date (June 20th and June 30th), side of the tree South (S) and North (N), and effect of induction media (BAC, B/2, and B). Data are presented as a total number of immature embryos able to produce embryogenic cell masses

Sampling date	Tree side	Medium			Total number of embryogenic cell lines
		BAC	B/2	B	
June 20th	S	1 (BE_1)	0	3 (BE_3; BE_4; BE_6*)	3 + 1*
June 20th	N	0	1 (BE_7)	2 (BE_2; BE_8)	3
June 30th	S	2 (BM_1*; BH_1)	0	0	1 + 1*
June 30th	N	2 (BC_1°; BR_1)	1 (BE_5)	0	2 + 1°
Total per side	S	3	0	3	6
Total per side	N	2	2	2	6
Total per sampling date (June 20th)		1	1	5	7
Total per sampling date (June 30th)		4	1	0	5
Total lines		5	2	5	9 (2* + 1°)

Cell lines induced on parts of zygotic embryos: on embryo (BEn), cotyledon (BCn), radicle (BRn), hypocotyl (BHn), and megagametophyte (BMn) where n is number of induced cell lines. Cell lines which lost proliferation ability (*) and where spontaneous maturation in proliferation phase (°) were observed

Table 2 Effect of ABA, PEG, and sugar on maturation of bog pine somatic embryos (cell line BC1)

Medium	ABA (μM)	Sucrose (%)	Maltose (%)	PEG (%)	Total number of SE early-precotyledonary/cotyledonary
M1	121	6	0	0	5/2
M2	121	1	0	3.5	6/2
M3	60	6	0	0	3/0
M4	60	1	0	3.5	5/0
M5	121	0	6	0	32/48
M6	60	0	6	0	10/18

We have evaluated somatic embryo initiation frequencies using different variants of DCR media, two terms of cone collection, and different explants source. Our results suggest that the highest initiation frequency for bog pine was achieved on DCR media (Gupta and Durzan 1985) supplemented with 5 μM 2.4-D and 2.5 μM BA and with/without activated charcoal (media denoted as B and BAC). From previous reports of SE in Pinus spp., it was found that the most responsive media is DCR (Gupta and Durzan 1985) with/without small modifications (Miguel et al. 2004; Aronen et al. 2009; De Diego et al. 2010; Montalbán et al. 2013). Similar concentrations of plant growth regulators (PGR) were tested in Pinus nigra where the best initiation response was also achieved (Salaj et al. 2014). Conversely, Klimaszewska et al. (2001), in experiments with Pinus strobus, have found that with decreasing the concentration of PGR, initiation frequencies were increased from 20

to 53 %. A lower concentration of PGR did not show any beneficial effect in the case of bog pine initiation, since we tested half concentrations of PGR (media denoted as B/2), and as a result, we obtained only two cell lines. As mentioned previously, initiation frequency in bog pine was very low, only 0.95 %. Low initiation frequency was reported in several studied species in the genus Pinus, e.g., in P. sibirica, 0.2–0.5 % (Tret'yakova and Voroshilova 2014); in P. pinea, from 0.5 to 7.2 % (Carneros et al. 2009); in Pinus armandii across nine open-pollinated families, initiation frequency ranged from 0 to 20 % with an average of 1.5 % (Maruyama et al. 2007); in Pinus nigra (maximum 10.3 and 10.4 %) (Salaj et al. 2014); in Pinus sylvestris, the initiation frequencies varied from 0 to 26.7 % (Aronen et al. 2009); for Pinus radiata with 55 % initiation frequency on average (Hargreaves et al. 2009); and 20–53 % for Pinus strobus (Klimaszewska et al. 2001). Low initiation frequencies are often obtained because many desired seed sources are recalcitrant and tissue survival is often poor (Pullman et al. 2009). In our experiments, the megagametophytes with immature zygotic embryos were excised from open-pollinated seeds, so the exact genetic background is unknown. MacKay et al. (2006) reported that initiation is the step in the SE process, which is the most highly influenced by genetic background. In their experiments with open and control pollinated loblolly pine, they suggested that seeds produced in the second growth season after pollination should be used as explants in order to obtain the optimum somatic embryo response. Initiation frequencies could be significantly affected by the date of cone collection and stage-specific response of zygotic embryo explants. In preliminary experiments with mature seeds of bog pine, no embryogenic cultures were initiated (data not shown). Moreover, as can be seen from our results, in the first term initiation frequency was a little higher than that in the second. In most pine species, initiation of embryogenic cultures is limited to the first period of zygotic embryo development during the cleavage stage or prior to the development of the cotyledons. Our results are in agreement with results reported on several Pinus species (Klimaszewska et al. 2001; Lelu-Walter et al. 2008; Hargreaves et al. 2009; Carneros et al. 2009; Montalbán et al. 2012; Salaj et al. 2014).

Fig. 2 Different developmental stages of bog pine somatic embryos observed during the maturation process; a, b early-precotyledonary and cotyledonary somatic embryos; c different abnormalities

In order to obtain cotyledonary somatic embryos, all induced cell lines were tested for their maturation abilities (data not shown). The yield of matured somatic embryo was strongly dependent on the embryogenic cell line, a phenomenon common to all conifer species. During development of mature somatic embryos into plantlets, megagametophyte as a major organ for storage of both proteins and lipids is absent, and the only way to substitute it is a nutritional medium (Montalbán et al. 2011). The best responding cell line (BC1) was subjected to effect of different ABA concentrations, PEG, and as a carbohydrate source maltose or sucrose. From our results, it can be seen that the best media for maturation of bog pine somatic embryos was supplemented with 121 μMABA and 6 % maltose. Maltose in a concentration of 6 % was a significantly better carbohydrate source for bog pine in comparison with sucrose. It might be because maltose has a slower break down and thus provides longer-lasting high osmolarity required for maturation (Salaj et al. 2014). Maltose was reported as the dominant metabolite in late embryogeny of P. abies embryogenic line producing normal somatic embryos; about half of this level was recorded in a line producing aberrant embryos, but in the line producing no embryos, only a low level of isomaltose and nomaltose was detected (Businge et al. 2012). Regarding the concentration of ABA, the amount used for maturation differs among different species in Pinus spp. Lelu-Walter et al. (2008) in experiments with P. strobus tested two concentrations (80 and 120 μM) with the addition of sucrose. In some cases, a lower ABA concentration (80 μM) and higher sucrose had better response. Montalbán et al. (2013) recently published that with P. halepensis, a higher yield of matured somatic embryos was recorded when 6 % of sucrose and 75 μM ABA was used while in P. nigra, the best results were achieved with 6 % maltose and 95 μM ABA (Salaj et al. 2014). Conversely, in Pinus radiata, the slightly lower concentration 60 μM of ABA and 6 % of sucrose was used (Montalbán et al. 2011).

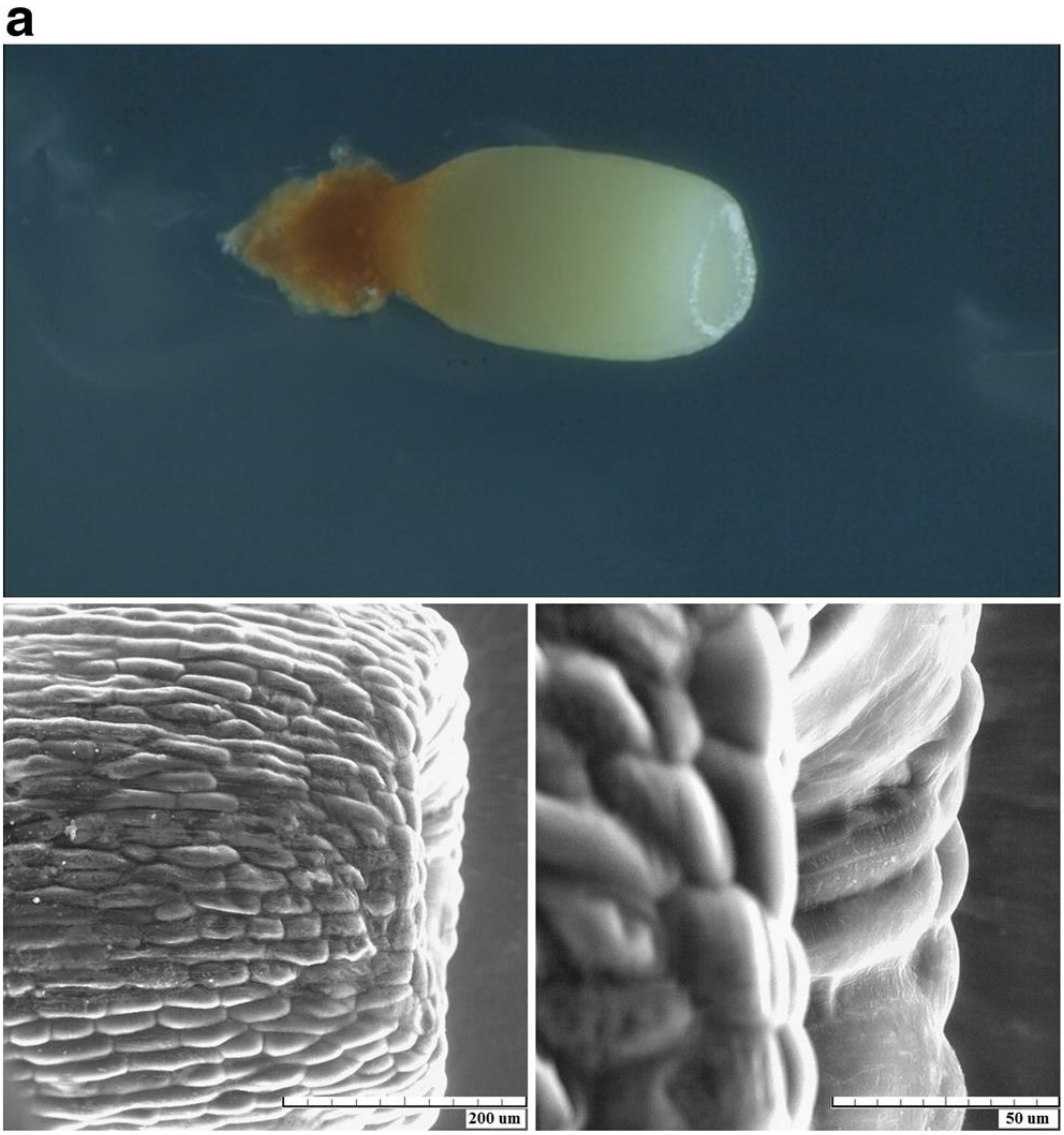

Fig. 3 Abnormal development observed during maturation of bog pine—the shoot apical zone was studied on base of transverse section and under environmental scanning electron microscope AQUASEM II (using ionization/BSE detector; gas pressure 450 Pa; beam energy 20 keV). Abnormal developed embryos were sorted to five groups, i.e., cup-shaped cotyledons (a, b), fused cotyledons (c, d), single cotyledon (e), meristemless SE (f), and SE with disrupted meristem (g, h)

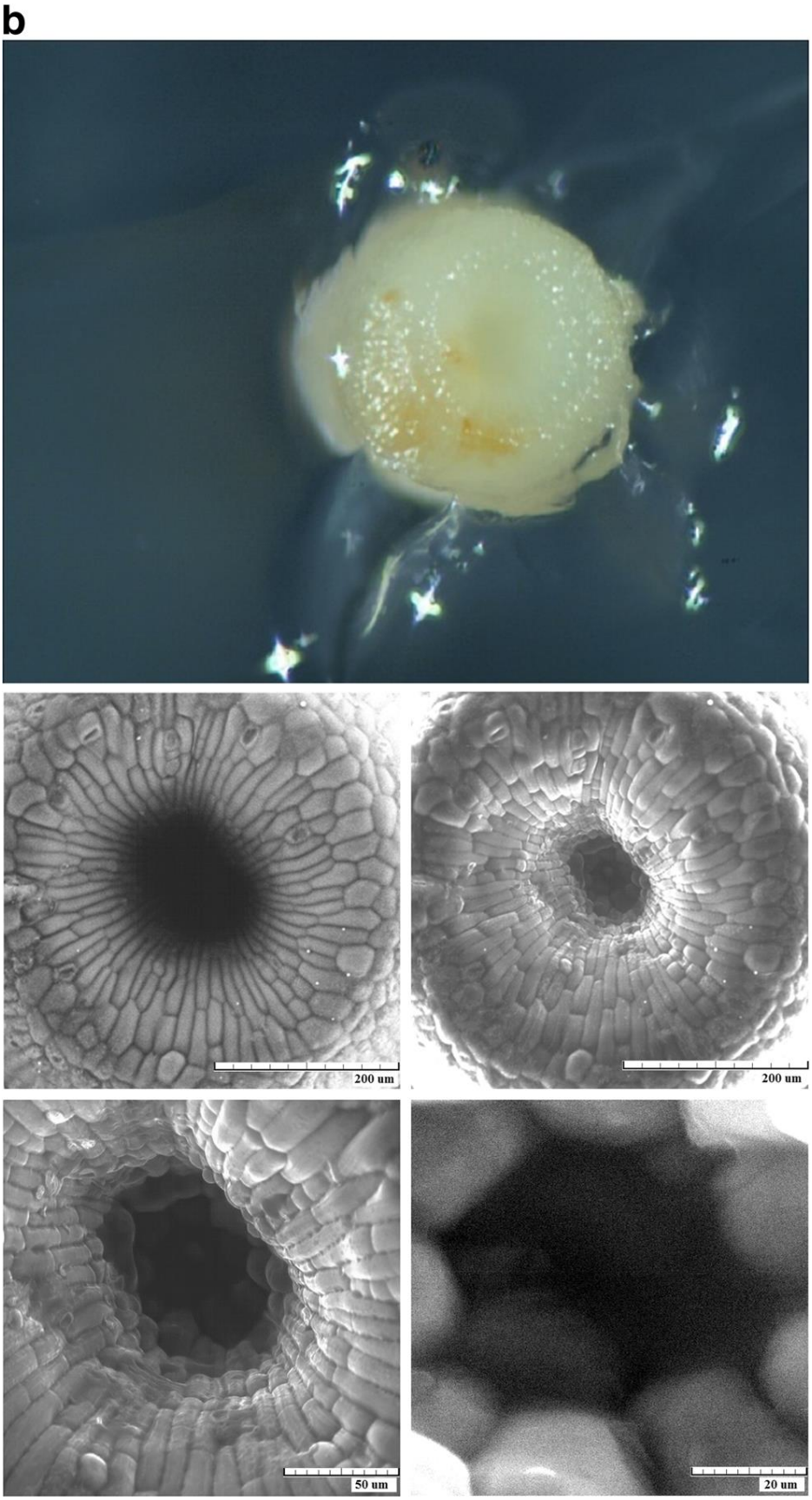

Fig. 3 (continued)

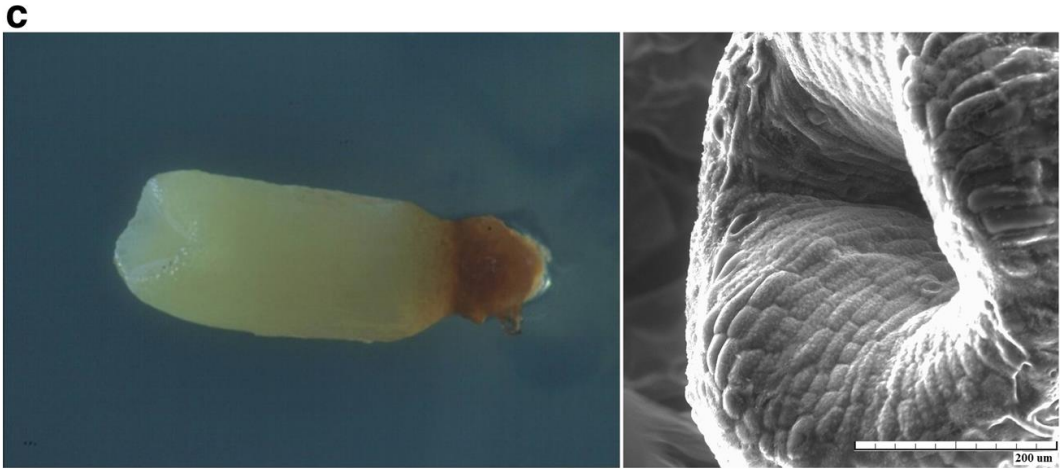

Fig. 3 (continued)

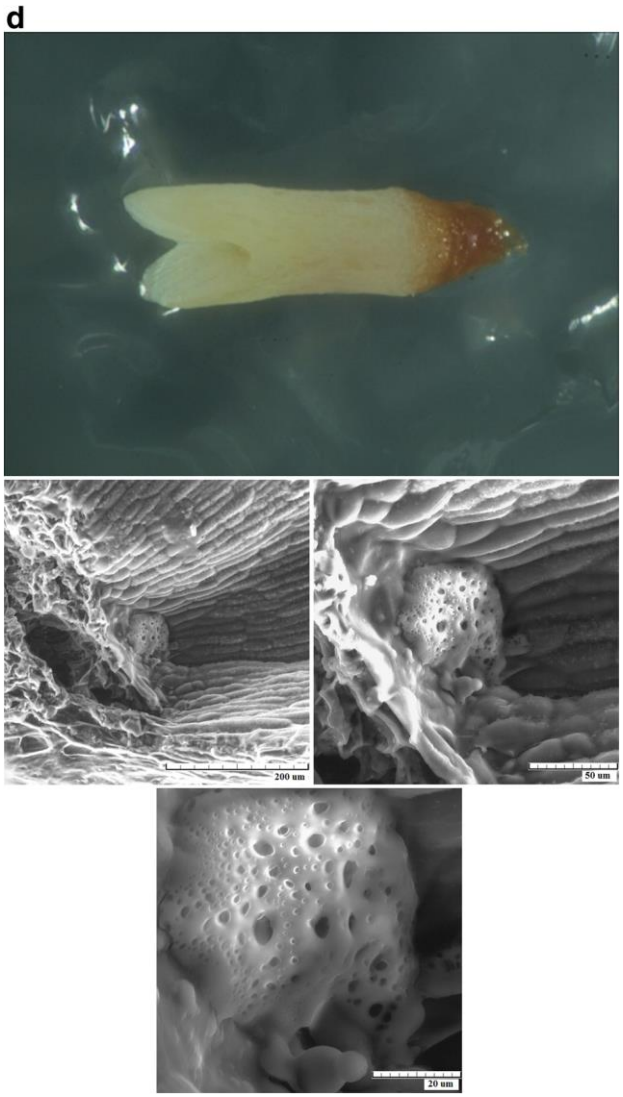

Fig. 3 (continued)

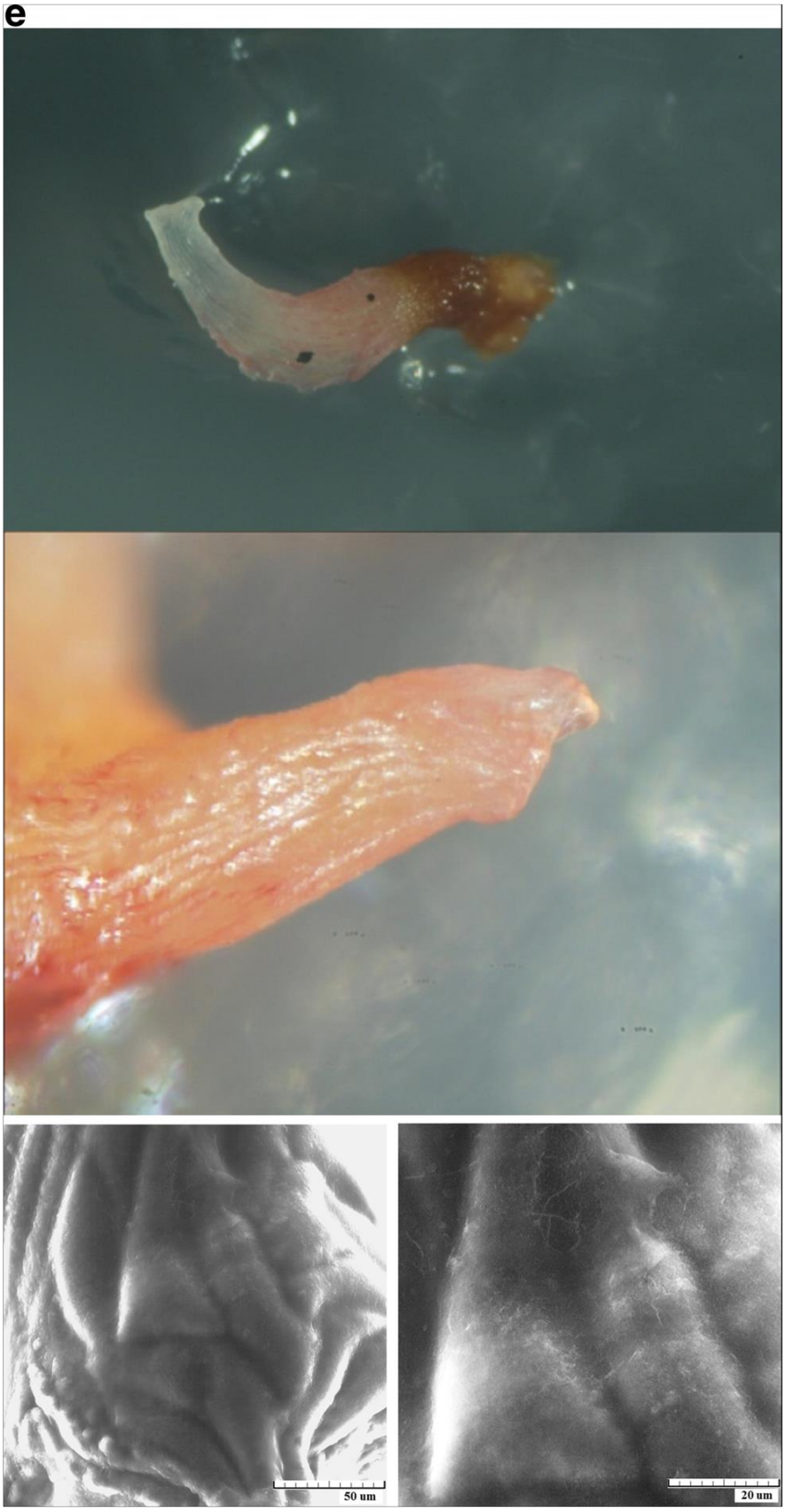

Fig. 3 (continued)

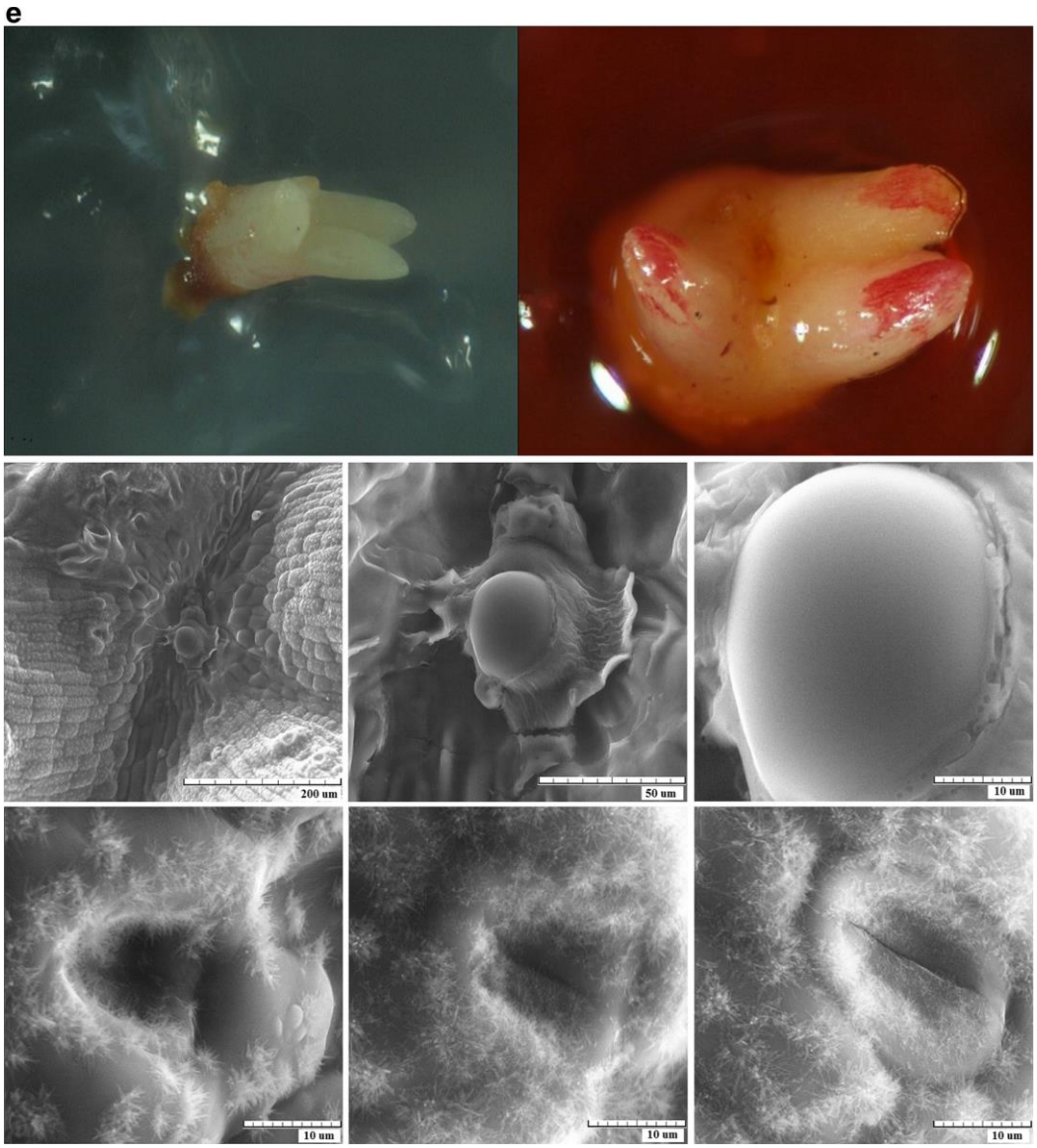

Fig. 3 (continued)

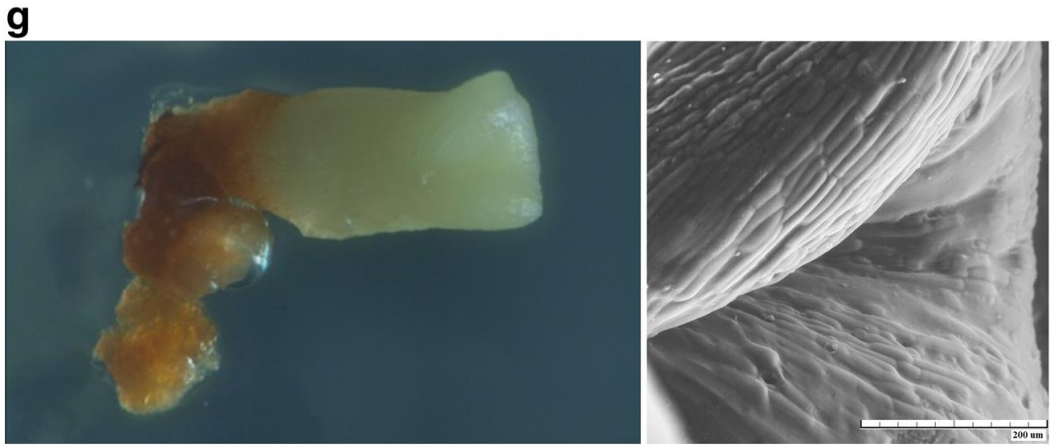

Fig. 3 (continued)

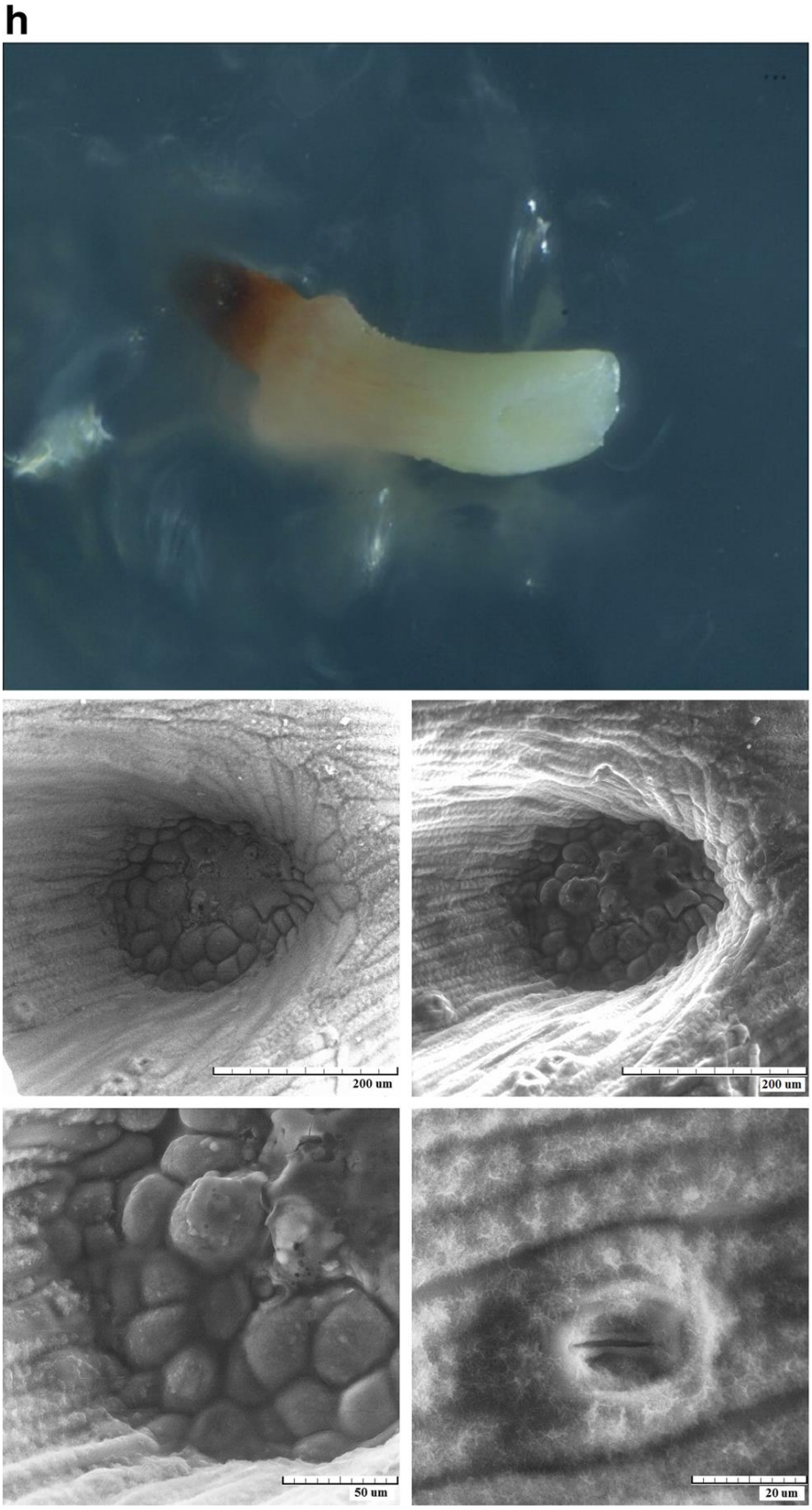

Fig. 3 (continued)

However, the major bottleneck in Pinus SE is maturation of the embryogenic tissue. In several pine species, it was found that the somatic embryos obtained feature abnormal morphology and even when they resemble their zygotic counterparts, they appear in very low numbers and lost their maturation abilities after 6 months in culture (Choudhury et al. 2008; Carneros et al. 2009; Klimaszewska et al. 2009). In our work, we obtained somatic embryos but nearly all of them had abnormal development. Similar abnormalities were observed after inhibition of auxin transport by 1-N-naphthylphthalamic acid (NPA) in Larix (Li et al. 2013) and in Picea abies (Larsson et al. 2008). Larsson et al. (2008) proved that during early embryo development, NPA treatment led to increased indole-3-acetic acid (IAA) content, abnormal cell divisions, and decreased programmed cell death (PCD), resulting in aberrant development of embryonal tube cells and suspensors. Mature embryos that had been treated with NPA showed both apical and basal abnormalities. Typically, the embryos had abnormal cotyledon formation, fused cotyledons, and aborted SAM. Moreover, irregular cell divisions in the area of the root meristemwere also observed. In Pinus sylvestris, Abrahamsson et al. (2012) studied in detail the morphology of embryogenic cell lines and their maturation. The presence of supernumerary suspensor cells in early somatic embryos of P. sylvestris has been found as a marker of disturbed polar auxin transport that results in aberrant embryo development. It correspond with our observation with bog pine embryogenic lines, where after 2 years in culture, almost all early embryos showed abnormal suspensor cell development. The reason for that changes could be found in long-term 2,4-D application and could be connected with changes in gene expression, as was observed by Businge et al. (2012) in Norway spruce.

However, usage of optical microscopy and ESEM for studying detailed morphology of abnormal mature somatic embryos was shown to be very beneficial. Moreover, considering our latest findings, where different plant samples were studied, it was also shown that combination of these methods is the best option to perform studies on wet and fresh plant materials. ESEM allows observation of samples with high resolution and depth of field, despite the fact that primary electrons are scattered in relatively high gas pressure conditions in comparison with scanning electron microscope (SEM). Accessible resolution of modern ESEMs equipped with Schottky cathode is from once to tens nm considering sample type, gas pressure, and distance of the sample from the ESEM objective. This resolution is more than sufficient for investigation of wide range of samples including plants as was shown by Stabentheiner et al. (2010) in study of different plant surfaces orNeděla et al. (2016) in study of coniferous embryogenic tissues. However, the possibility to obtain high quality images is also highly depending on experimental experiences with the ESEM (usually complicated to reach and maintain correct thermodynamic conditions in the close vicinity of the sample), good knowledge of applied physics

(optimization of working conditions as well as detection efficiency, mostly based on Monte Carlo simulations as was published by Tihlaříková et al. (2013)) and necessity to develop new methods for hardly observable, mostly low emissive biological (Neděla et al. 2015) or very susceptible polymeric samples (Bertóková et al. 2015). As it can be seen in Fig. 3, resolution of images is also lowered if ESEM is equipped with thermoemission hair pin cathode (the beam current density in focused spot is significantly lower). Further difficulties may arise when imaging deeper cavities in biological samples since signal electrons are absorbed by the sample and are hardly detectable. Such special places in the samples as bottom of deeper cavities (see Fig. 3b, h) can be displayed only by using special detectors, i.e., ionization detector of secondary electrons for ESEM AQUASEM II as was used in this paper. Regardless the abovementioned difficulties, the ESEM as a method is very beneficial for exploration of the true, natural micro-morphology of untreated, mostly electrically nonconductive wet samples. Moreover, metal-conductive layers applied on biological samples for SEM enhance the level of detected signal, harden the soft samples, and drain out the electric charge but increase the risk of artifact appearance (Belz and Auchterlonie 1995). Consequently, the natural surface microstructure of uncoated samples in the ESEM does not have to appear as sharp as in the SEM. However, it is still questionable to what extent surface microstructure sharpness corresponds to real structure of the sample, when done by SEM and/or existing artifacts are formed by conductive coating. According to our experiences, very rugged surfaces of plant biological samples are necessary to provide with a relatively thick layer (20 nm or thicker) of conductive coating. In these cases, the probability of artifact appearance is very high, especially if gold or platinum coating is used.

To our knowledge, this is the first report discussing somatic embryogenesis in bog pine. An improved protocol could be used as a helpful tool for preservation of weak populations of rare bog pine. However, controlled pollination of selected mother trees is demanded for the development of verified cultures, and the optimization of this method based on morphological observation is needed.

Acknowledgements

The research was supported by the Ministry of the Environment of the Czech Republic (project no. SP-2d4-83-07) and by theGrantAgency of the Czech Republic (project no.GA14-22777S). The authors are grateful to the company HIROX for making photos with their instruments for comparative visualization of embryo development.

Compliance with ethical standards

Conflict of interest

The authors declare that they have no conflict of interest.

References

Abrahamsson M, Valladares S, Larsson E, Clapham D, von Arnold S (2012) Patterning during somatic embryogenesis in Scots pine in relation to polar auxin transport and programmed cell death. Plant Cell Tissue Org Cult 109(3):391–400

Aronen T, Pehkonen T, Ryynänen L (2009) Enhancement of somatic embryogenesis from immature zygotic embryos of Pinus sylvestris. Scand J For Res 24:372–383

Belz GT, Auchterlonie GJ (1995) An investigation of the use of chromium, platinum and gold coating for scanning electron microscopy of casts of lymphoid tissues. Micron 26(2):141–144

Benelli C, Germana MA, Ganino T, Beghe D, Fabbri A (2010) Morphological and anatomical observations of abnormal somatic embryos from anther cultures of Citrus reticulata. Biol Plant 54(2):224–230

Bertóková A, Vikartovská A, Bučko M, Gemeiner P, Tkáč J, Chorvát D, Štefuca V, Neděla V (2015) Biooxidation of 2-phenylethanol to phenylacetic acid by whole-cell Gluconobacter oxydans biocatalyst immobilized in polyelectrolyte complex capsules. Biocatal Biotransform 33(2):111–120

Bharathy PV, Agrawal DC (2008) High frequency occurrence of single cotyledonary embryo morphotype and repetitive somatic embryogenesis in ‘Thompson Seedless’ crossed with seven grapevine male parents. Vitis 47(3):169–174

Businge E, Brackmann K, Moritz T, Egertsdotter U (2012) Metabolite profiling reveals clear metabolic changes during somatic embryo development of Norway spruce (Picea abies). Tree Physiol 32(2): 232–244

Businský R (2009) A new concept in bog pine. Zprávy Čes Bot Společ Praha 44:35–43

Businský R, Kirschner J (2010) Pinus mugo and P. uncinata as parents of hybrids. A taxonomic and nomenclatural survey. Phyton (Horn, Austria) 50:27–57

Carneros E, Celestino C, Klimaszewska K, Parky S, Toribio M, Bonga JM (2009) Plant regeneration in stone pine (Pinus pinea L.) by somatic embryogenesis. Plant Cell Tiss Organ Cult 98:165–178

Choudhury H, Kumaria S, Tandon P (2008) Induction and maturation of somatic embryos from intact megagametophyte explants in Khasi pine (Pinus kesiya Royle ex. Gord.). Curr Sci 95:1433–1438

De Diego N,Montalbán IA, Moncaleán P (2010) In vitro regeneration of adult Pinus sylvestris L. trees. S Afr J Bot 76:158–162

Fernando J, MeloM, Soares M, Appezzato-da-Glória B (2001) Anatomy of somatic embryogenesis in Carica papaya L. Braz Arch Biol Technol 44(3):247–255

Finer J, Kriebel H, BecwarM(1989) Initiation of embryogenic callus and suspension cultures of eastern white pine (Pinus strobus). Plant Cell Rep 8:203–206

Griga M (2002) Morphology and anatomy of Pisum sativum somatic embryos. Biol Plant 45(2):173–182

Grulich V (2012) Red list of vascular plants of the Czech Republic: 3rd edition. Preslia 84:631–645

Gupta PK, Durzan DJ (1985) Shoot multiplication from mature trees of Douglas-fir (Pseudotsuga menziesii) and sugar pine (Pinus lambertiana). Plant Cell Rep 4:177–179

Häggman H, Pirttilä AM, Niemi K, Sarjala T, Julkunen-Tiitto R (2009) Medicinal properties, in vitro protocols and secondary metabolite analyses of Scots pine. Methods Mol Biol 547:35–52

Hargreaves CL, Reeves CB, Find JI, Gough K, Josekutty P, Skudder DB, Van der Maas SA, Sigley MR, Menzies MI, Low CB, Mullin TJ (2009) Improving initiation, genotype capture, and family representation in somatic embryogenesis of Pinus radiata by a combination of zygotic embryo maturity, media, and explant preparation. Can J For Res 39:1566–1574

Hill P, Gutierrez B, Carmack L, Kopp OR (2015) Micropropagation of Astragalus holmgreniorum (Holmgren milkvetch), an endemic and endangered species. Plant Cell Tissue Org Cult 121(2):381–387

Klimaszewska K, Park Y-S, Overton C, Maceacheron J, Bonga J (2001) Optimised somatic embryogenesis in Pinus strobus. In Vitro Cell Dev Biol Plant 37:392–399

Klimaszewska K, Noceda C, Pelletier G, Label P, Rodriguez R, LeluWalter MA (2009) Biological characterization of young and aged embryogenic cultures of Pinus pinaster (Ait.). In Vitro Cell Dev Biol Plant 45:20–33

Larsson E, Sitbon F, Ljung K, von Arnold S (2008) Inhibited polar auxin transport results in aberrant embryo development in Norway spruce. New Phytol 177(2):356–366

Lelu-Walter MA, Bernier-Cardou M, Klimaszewska K (2008) Clonal production from self-and cross pollinated seed families of Pinus sylvestris (L.) through somatic embryogenesis. Plant Cell Tissue Org Cult 92:31–45

Lelu-Walter MA, Thompson D, Harvengt L, Sanchez L, Toribio M, Pâques LE (2013) Somatic embryogenesis in forestry with a focus on Europe: state-of-the-art, benefits, challenges and future direction. Tree Genet Genomes 9:883–899

LiWF, Zhang SG, Han SY,Wu T, Zhang JH,Qi LW(2013) Regulation of LaMYB33 by miR159 during maintenance of embryogenic potential and somatic embryo maturation in Larix kaempferi (Lamb.) Carr. Plant Cell Tissue Org Cult 113(1):131–136

Lukášová M, Businský R, Vejsadová H (2012) Bog pine (Pinus uncinate susbp. uliginosa) protection using morphometric, genetic and micropropagation methods. Acta Pruhoniciana 100:147–153

MacKay JJ, Becwar MR, Park YS, Corderro JP, Pullman GS (2006) Genetic control of somatic embryogenesis initiation in loblolly pine and implications for breeding. Tree Genet Genomes 2:1–9

Maruyama E, Hosoi Y, Ishii K (2007) Somatic embryogenesis and plant regeneration in yakutanegoyou, Pinus armandii Franch. Var. Amamiana (Koidz.) Hatusima, an endemic and endangered species in Japan. In Vitro Cell Dev Biol Plant 43:28–34

Miguel C,Gonçalves S, Tereso S, Marum L, Maroco J,OliveiraM(2004) Somatic embryogenesis from 20 open-pollinated families of Portuguese plus trees of maritime pine. Plant Cell Tiss Org Cult 76:121–130

Minocha R, Smith DR, Reeves C, Steele KD, Minocha SC (1999) Polyamine levels during the development of zygotic and somatic embryos of Pinus radiata. Physiol Plant 105:155–164

Montalbán IA, De Diego N, Aguirre Igartua E, Setién A, Moncaleán P (2011) A combined pathway of somatic embryogenesis and organogenesis to regenerate radiata pine plants. Plant Biotechnol Rep 5(2):177–186

Montalbán IA, De Diego N, Moncaleán P (2012) Enhancing initiation and proliferation in radiata pine (Pinus radiata D. Don) somatic embryogenesis through seed family screening, zygotic embryo staging and media adjustments. Acta Physiol Plant 34:451–460

Montalbán IA, Setién-Olarra A, Hargreaves CL, Moncaleán P (2013) Somatic embryogenesis in Pinus halepensis Mill.: an important ecological species from the Mediterranean forest. Trees 27(5):1339–1351

Neděla V, Konvalina I, Lencová B, Zlámal J (2011) Comparison of calculated, simulated and measured signal amplification in variable pressure SEM. Nucl Instrum Methods Phys Res Sect A 645(1): 79–83

Neděla V, Hřib J, Vooková B (2012) Imaging of early conifer embryogenic tissues with the environmental scanning electron microscope. Biol Plant 56:595–598

Neděla V, Tihlaříková E, Hřib J (2015) The low-temperature method for study of coniferous tissues in the environmental scanning electron microscope. Microsc Res Tech 78(1):13–21

Neděla V, Hřib J, Havel L, Hudec J, Runštuk J (2016) Imaging of Norway spruce early somatic embryos with the ESEM, Cryo-SEM and laser scanning microscope. Micron 84:67–71

Perullo N, Determann RO, Cruse-Sanders JM, Pullman GS (2015) Seed cryopreservation and micropropagation of the critically endangered species swamp pink (Helonias bullata L.). In Vitro Cell Dev Biol Plant 51(3):284–293

Pullman GS, Chase KM, Skryabina A, Bucalo K (2009) Conifer embryogenic tissue initiation. Improvements by supplementation of medium with D-xylose and D-chiro-inositol. Tree Physiol 29:147–156

Ramarosandratana A, Harvengt L, Bouvet A, Calvayrac R, Paques M (2001) Effects of carbohydrate source, polyethylene glycol and gellan gum concentration of embryonal-suspensor mass (ESM) proliferation and maturation of maritime pine somatic embryo. In Vitro Cell Dev Biol Plant 37(1):29–34

Salaj T, Fráterová L, Cárach M, Salaj J (2014) The effect of culture medium formulation on Pinus nigra somatic embryogenesis. Dendrobiology 71:119–128

Salajová T, Salaj J (1992) Somatic embryogenesis in European black pine (Pinus nigra Arn.). Biol Plant 34(3):213–218

Smertenko A, Bozhkov PV (2014) Somatic embryogenesis: life and death processes during apical-basal patterning. J Exp Bot 65: 1343–1460

Stabentheiner E, Zankel A, Pölt P (2010) Environmental scanning electron microscopy (ESEM)—a versatile tool in studying plants. Protoplasma 246:89–99

Tihlaříková E, Neděla V, ShiojiriM(2013) In situ study of live specimens in an environmental scanning electron microscope. Microsc Microanal 19(4):914–918

Tret'yakova IN, Voroshilova EV (2014) Embryo initiation from Pinus sibirica megagametophytes in in vitro culture. Russ J Dev Biol 45(2):93–100

Trontin JF,Walter C, Klimaszewska K, Park YS, Lelu-WalterMA(2007) Recent progress in genetic transformation of four Pinus spp. Transgenic Plant J 1:314–329

Vejsadová H, Lukášová M (2010) Shoot organogenesis induction from genetically verified individuals of endangered bog pine (Pinus uncinata subsp. uliginosa). J For Sci 56(8):341–347

Vejsadová H, Šedivá J (2002) Micropropagation of endangered bog pine species (Pinus rotundata Link). Acta Pruhoniciana 73:37–47 (in Czech)

Vejsadová H, Vlašinová H, Havel L (2008) Preservation of a rare bog pine genotype using micropropagation techniques. Acta Universitatis Agriculturae et Silviculturae Mendelianae Brunensis LVI(4):197–206

Wang HC, Chen JT, Chang WC (2010) Morphogenetic routes of longterm embryogenic callus culture of Areca catechu. Biol Plant 54(1): 1–5

Xie DY, Hong Y (2001) Regeneration of Acacia mangium though somatic embryogenesis. Plant Cell Rep 20:34–40

Zegzouti R, ArnouldM-F, Favre J-M(2001) Histological investigation of the multiplication step in secondary somatic embryogenesis of Quercus robur L. Ann For Sci 58:681–690

16 The Response of Picea abies Somatic Embryos to UV - B Radiation Depends on the Phase of Maturation

Kateřina Eliášová[1], Zuzana Vondráková[1], Lenka Gemperlová[1], Vilém Neděla[2], Jiří Runštuk[2], Lucie Fischerová[1], Jiří Malbeck[1], Alena Trávníčková[1], Milena Cvikrová[1] and Martin Vágner[1]

1 Institute of Experimental Botany of the Czech Academy of Sciences, Prague, Czechia,

2 Institute of Scientific Instruments of the Czech Academy of Sciences, Brno, Czechia

Keywords

ferulic acid, Picea abies (L.) Karst., polyamines, somatic embryogenesis, viability

Abstract

Ultraviolet-B (UV-B) radiation is a key environmental signal which initiates diverse responses that affect the metabolism, development, and viability of plants. In keeping with our previous studies, we concentrated primarily on how UV-B radiation affects Norway spruce [Picea abies (L.) Karst.] somatic embryo maturation and how phenolics and polyamines (PAs) are linked to the defense response invoked by UV-B irradiation. We treated clusters of Norway spruce embryogenic culture (EC) with UV-B during the five stages of embryo maturation (early, cylindrical, precotyledonary, cotyledonary, and mature embryos). For the first time, we take an advantage of the unique environmental scanning electron microscope AQUASEM II to characterize somatic embryos in their native state. The severity of the irradiation effect on embryonal cell viability was shown to be dependent on the intensity of radiation as well as the stage of embryo development and might be related to the formation of protoderm. The response of early embryos was characterized by an increase in malondialdehyde (MDA), a marked decrease in PA contents and a decline in phenolics. The reduced ability to activate the defense system seems to be responsible not only for the severe cell damage and decrease in viability but also for the inhibition of embryo development. The significant reduction in spermidine (Spd), which has been reported to be crucial for the somatic embryo development of several coniferous species, may be causally linked to the limited development of embryos. The pronounced decrease in cell wall-bound ferulic acid might correspond to failure of somatic embryos to reach more advanced stages of development. Embryos at later stages of development showed stress defense responses that were more efficient against UV-B exposure.

Introduction

Ultraviolet-B (UV-B) radiation affects plants both directly and indirectly, and can, for example, damage DNA, proteins, and membranes, alter transpiration and photosynthesis, and lead to changes in growth, development, and morphology (Jansen et al., 1998). Oxidative stress is a common response to unfavorable environmental conditions such as UV radiation (Hideg et al., 2013). The scavenging of active oxygen and other radical species, either through enzymatic or non-enzymatic systems, can alleviate UV stress (Jansen et al., 1996).

Polyamines (PAs), which constitute a group of low molecular weight aliphatic amines, are key to regulating growth and developmental processes in plants, as well as the response to biotic and abiotic stresses (Kusano et al., 2008; Gill and Tuteja, 2010; Takahashi and Kakehi, 2010; Hussain et al., 2011). Studies using loss-of-function mutants and transgenic plants to modulate PA metabolic pathways have confirmed that PAs play a protective role during plant responses to abiotic stress (Shi and Chan, 2014). Possibly the radical-scavenging activity of PAs moderates UV-B radiation stress, as has been demonstrated for other free-radical scavengers (Jansen et al., 1996). Moreover, species-specific and age-dependent differences in the quantitative and qualitative composition of PAs could affect the susceptibility of a plant to abiotic stresses (Reifenrath and Müller, 2007).

One of the most frequently observed responses to increased UV-B exposure is the activation of the phenylpropanoid biosynthetic pathway (Takshak and Agrawal, 2015). Many phenylpropanoids have both antioxidant and UV-B screening properties (Jansen et al., 2008; Agati and Tattini, 2010), and mutants deficient in the accumulation of these compounds (e.g., Arabidopsis transparenta testa) are considerably more susceptible to UV-B radiation than the corresponding wild-type lines (Booij- James et al., 2000). Phenolic compounds are generally viewed as harmful for in vitro cultures (both in micropropagation and somatic embryogenesis) since their exudation and oxidation negatively affects explants, causing browning and necrosis, especially when mature explants of woody plants are used (Martin and Madassery, 2005). However, Reis et al. (2008) provided evidence that phenolic compounds are involved in certain in vitro morphogenic processes, including the induction of somatic embryogenesis in Feijoa sellowiana. Somatic embryos were formed in the proximity of phenolic-rich cells which, in more advanced stages of development, formed a zone isolating the embryo from the maternal tissue. Furthermore, according to Cvikrová et al. (2008, 2010), phenolic compounds participate in resistance mechanisms that are important for P. abies ECs.

We have previously reported that the accumulation of Pas in fully developed P. abies somatic embryos may be causally linked to better tolerance of UV-B irradiation (Cvikrová et al., 2016). The research presented in this paper focused on the variable sensitivity of an EC to UV-B radiation during the course of maturation. More specifically, the research aimed to determine whether irradiation affects the development of spruce somatic embryos and to evaluate the ability of an EC to activate the stress defense response upon UV-B exposure. We exposed EC clusters to UV-B during the embryo maturation. The effects of UV-B irradiation were described on the morphological and biochemical levels. We used the unique environmental scanning electron microscope AQUASEM II, which enables the observation of beam sensitive samples as wet biopolymers (Schenkmayerová et al., 2014), plant extracellular matrix (Neděla et al., 2012), or plant waxes (Neděla et al., 2015b) in their native states, to characterize the developmental stages. This permitted us to study how the pattern of surface cell layers, which is crucial to plant defenses against radiation, develops. The morphological evaluation methods included light, fluorescence, and electron microscopy, while the biochemical analyses focused on monitoring changes in the contents of PAs and phenolic acids.

Materials and methods

Plant material

An EC of Norway spruce (Picea abies L. Karst.), genotype AFO 541, was obtained from AFOCEL (Nangis, France). The cultivation of the EC followed a protocol described by Cvikrová et al. (2016). During proliferation, the EC was cultivated in plastic Petri dishes (10 cm in diameter) on GD medium (Gupta and Durzan, 1986) solidified with 0.75% agar and supplemented with sucrose (30 g/L) and the phytohormones 2,4-D (5 mM), kinetin (2 mM), and BAP (2 mM) (all Duchefa, Haarlem, Netherlands). To initiate the maturation phase, cytokinins and auxin in the medium were replaced with abscisic acid (20 mM) and 3.75% polyethylene glycol 4000 (all Sigma-Aldrich, St. Louis, MO, United States). The cultures were kept in darkness at 23 ± 1°C during both proliferation and maturation and were subcultured onto fresh medium once per week.

UV-B Irradiation and Collection of Plant Material for Analysis

Closed plastic Petri dishes with cultures were exposed to UV-B irradiation at the third day after regular 1-week subcultivation in the first, second, third, fourth, and fifth weeks of maturation. These time points corresponded to stages I, II, III, IV, and V of embryo development. UV-B treatment was performed in a box (BIO-LINK, BLX-312, Vilber Lourmat, France) equipped with 312 nm UV lamps. Each treatment represented one short-term exposure (15 and/or 75 s of UV-B radiation).

Precise measurement of the amount of UV energy that samples were exposed to was ensured by a UV sensor cell within the radiation chamber. The exposures, 15 and 75 s, are equivalent to intensities of 0.1 and 0.6 W m^{-2}, respectively, acting for 1 h. The transmittance of the plastic Petri dishes was measured on a defined wavelength (312 ± 2 nm) and statistically evaluated [T = (63 ± 0.6)%]. The average transmittance was then used to recalculate the UV-B dose that the ECs had been exposed to.

In order to avoid the effect of UV-B irradiation on media composition, the ECs were transferred onto fresh medium and returned to the original light regime immediately after UV-B treatment. The same cultivation regime was applied to the control variant.

Material from two independent experiments was analysed at anatomical and biochemical level. At least four biological replicates of control (non-treated) and irradiated ECs were collected for malondialdehyde (MDA), PA, and phenolic acid analyses on the seventh day after treatment. The control and irradiated ECs were further analyzed for phenolic acids at the end of maturation (i.e., after 6 weeks). Material from each variant was dried on cotton wool, divided into samples and frozen in liquid nitrogen. The samples were stored at -80°C until the biochemical analysis.

Microscopic Analysis

Specification of Developmental Stages

The developmental steps of spruce somatic embryos were documented on the morphological and anatomical levels using a Jenaval transmission light microscope (Zeiss, Jena, Germany) after staining with 0.4% Trypan Blue (Sigma-Aldrich) as described elsewhere (Vondráková et al., 2014).

The Yield of Embryos

Small clusters (0.1 g FW) of EC were placed on medium in Petri dishes at the start of maturation and whole intact clusters were weekly subcultured. The number of mature embryos was estimated after 6 weeks of maturation from 10 clusters corresponding to 1 g of EC inoculated. Images of 10 clusters per variant that contained mature embryos were recorded and the total number of embryos (including those that were malformed or only partially developed) in each image was counted, along with the number of fully developed mature embryos.

An SMZ 1500 stereomicroscope (Nikon, Tokyo, Japan) was used to observe EC morphology and determine embryo yield. All of the images were recorded using a

Nikon DS-5M digital camera and processed using the Nis-Elements AR 3.2 (Laboratory Imaging, Prague, Czechia) computer image analysis system.

Environmental Scanning Electron Microscopy (ESEM)

A non-commercial environmental scanning electron microscope AQUASEM II (Institute of Scientific Instruments of the CAS, Brno, Czechia) equipped with self-developed ionization detectors of secondary electrons (Neděla et al., 2015a) was used for the micro-morphological description of the embryo surface and to study how embryos – in their native state without any chemical fixation, dehydration, or coating – change during maturation. Norway spruce somatic embryos were placed onto the water-cooled Peltier stage with a silicone surface. Before observation with the ESEM, samples with dimensions of 3–6 mm^2 and a thickness of 2 mm were rinsed with distilled water for 20 min to minimize and dissolve the mucous layer. Before specimen chamber evacuation, samples were put into a drop of 2 ml of distilled water to both obtain better thermal contact between the sample and the Peltier stage and to achieve better sample hydration. The working conditions for observations were: water vapor pressure from 500 to 580 Pa; sample temperature - 1°C; beam energy 20 keV; beam current 60 pA; and environmental distance 3– 4 mm.

Viability Assay

Viability assay was performed at the first, second, third, fourth, and fifth weeks of maturation on the seventh day after irradiation with 0.1 and 0.6 W m^{-2} h^{-1} UV-B and in the corresponding un-treated samples. Cell viability was determined using double staining with fluorescein diacetate (FDA) and propidium iodide (PI) (both Sigma-Aldrich) according to a modified version of the protocol presented by Vondráková et al. (2010). A small piece of EC was suspended in cultivation medium and stained with 2.25 mM PI (stock solution 1 mg mL^{-1} H_2O) and freshly diluted 4.8 mM FDA (stock solution 2 mg mL^{-1} acetone). Within 5 min, the samples were observed using an LSM 5 Duo confocal laser-scanning microscope (Zeiss) equipped with an Argon/2 laser (FDA excitation at 488 nm, emission filter-set BP 505–550) and a DPSS laser (PI excitation at 561 nm, emission filter-set LP 650). The viable cells were observed based on the enzymatic hydrolysis of FDA to form fluorescein, which exhibits bright green fluorescence. PI intercalates with nucleic acids of non-viable or dead cells to form complexes that emit bright red fluorescence. All images are shown at maximum intensity projections of confocal optical sections of the whole embryos.

Biochemical Analyses

Polyamine Analysis

The extraction and HPLC/MS analysis of benzoylated PAs was performed as described by Eliášová et al. (2017).

Phenolic Acid Analysis

Phenolic acids were extracted as described by Cvikrová et al. (1991). Briefly, free, ester-bound (those released after alkaline hydrolysis) and glycoside-bound (those released after acid hydrolysis) phenolic acids were obtained from a methanol extract of tissue ground in liquid nitrogen. The cell wall-bound phenolic acids were obtained through alkaline hydrolysis of the residual material following methanol extraction. The detection and quantification of phenolic acids was carried out using an HPLC/MS system as described by Eliášová et al. (2017).

Malondialdehyde Assay

The MDA content of the samples was determined using an NWLSS-Malondialdehyde Assay kit (cat. no. NWK-MDA01, Northwest Life Science Specialties LLC, Vancouver, BC, Canada) as described in detail by Cvikrová et al. (2013).

Statistical Analysis

The mean ± SE of two independent experiments with a minimum of four biological replicates per experiment are shown in the figures. Standard descriptive statistics were used when analyzing the data. To assess the significance of between-treatment differences, we used a two-step procedure: a preliminary F-test of standard deviations (classical F-test hypothesis H_0: $\sigma_1^2=\sigma_2^2$, H_1: $\sigma_1^2 \neq \sigma_2^2$; $R < F\ \alpha/2$) and t-test of averages (hypothesis H_0:$\mu_1^2=\mu_2^2$, H_1: $\mu_1^2 \neq \mu_2^2$; $|R| < t\ \alpha$). Asterisks above bars indicate significant differences ($P < 0.05$) between the contents observed in irradiated somatic embryos and the contents observed in the corresponding controls.

Results

Description of Somatic Embryo Development

The characterization of every stage of embryo development is crucial for determining the extent of stress response as it provides indications of anatomical dissimilarity among the irradiated ECs. The EC contained embryos in different developmental stages over the course of maturation. A detailed assessment of embryo development during each week of maturation enabled us to characterize the

EC based on particular developmental stages of predominant embryos as EC I–VI. Six distinct developmental stages, denoted EC I–EC VI, were identified during Norway spruce somatic embryo maturation based on EC morphology, including the constitution of surface layers (Figures 1, 2).

At the start of maturation, the clusters of EC are white and filamentous with macroscopically invisible embryos (Figure 1 – EC Ia). The embryonal heads of early embryos are enlarged and individual embryos begin to release from the polyembryogenic complexes (Figure 1 – EC Ib). The embryonal heads are compact, created from small meristematic cells (Figure 2 – EC Ia) that are linked to elongated suspensor cells (Figure 2 – EC Ib).

During the next step of development, globular and cylindrical embryos predominate in EC: the clusters are similar to that observed during the first stage (Figure 1 – EC IIa), but the polyembryogenic complexes have disintegrated and embryos become visible by naked eye. The embryonal heads continue to elongate (Figure 1 – EC IIb); the bigger embryonal heads of cylindrical embryos have a smooth surface formed by polyhedral cells of the early protoderm (Figure 2 – EC IIa). Suspensors' complexes are composed of long suspensor cells (Figure 2 – EC IIb).

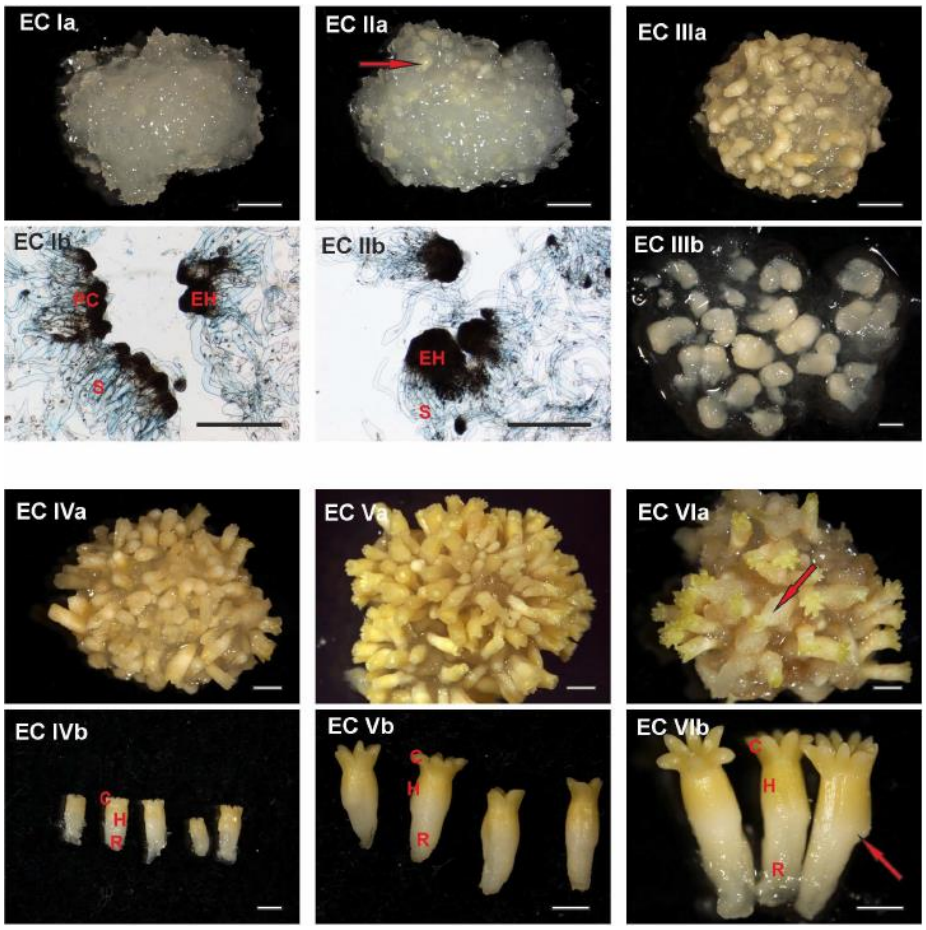

FIGURE 1 | Documentation of Picea abies somatic embryos at distinct phases of somatic embryo maturation. (EC Ia) Cluster of embryogenic suspensor mass during the first week of maturation; (EC Ib) detailed morphology of early embryos, with individual embryonal heads (EH) connected to elongated suspensor cells (S); large polyembryogenic centers, i.e., meristematic zone from which embryonal heads can be separated (PC). (EC IIa) Cluster of embryogenic suspensor mass during the second week of maturation (the arrow highlights a somatic embryo that is visible on the surface of the cluster); (EC IIb) detailed morphology of elongated early embryos, with enlarged embryonal heads (EH) still connected to the suspensor (S). (EC IIIa) Cluster of embryogenic suspensor mass with visible somatic embryos during the third week of maturation; (EC IIIb) detailed morphology of precotyledonary embryos. (EC IVa) Cluster of maturing somatic embryos during the fourth week of maturation; (EC IVb) detailed morphology of cotyledonary embryos demonstrating a circle of cotyledons (C), hypocotyl (H) and radicle (R). (EC Va) Cluster of mature somatic embryos during the fifth week of maturation; (EC Vb) detailed morphology of mature embryos showing a circle of longer cotyledons (C), hypocotyl (H), and radicle (R). (EC VIa) Cluster of post-mature somatic embryos during the sixth and seventh weeks of maturation (the arrow highlights a malformed embryo on the surface of the cluster in which the process of callogenesis has begun); (EC VIb) detailed morphology of post-mature embryos, with an open crown of long cotyledons (C), elongated hypocotyl (H), and radicle (R); the arrow identifies a malformation in the hypocotyl. Ia, IIa, IIIa, IVa, Va, and VIa. Scale bar = 5 mm; Ib, IIb Scale bar = 500 mm; IIIb, IVb, Vb, VIb. Scale bar = 1 mm.

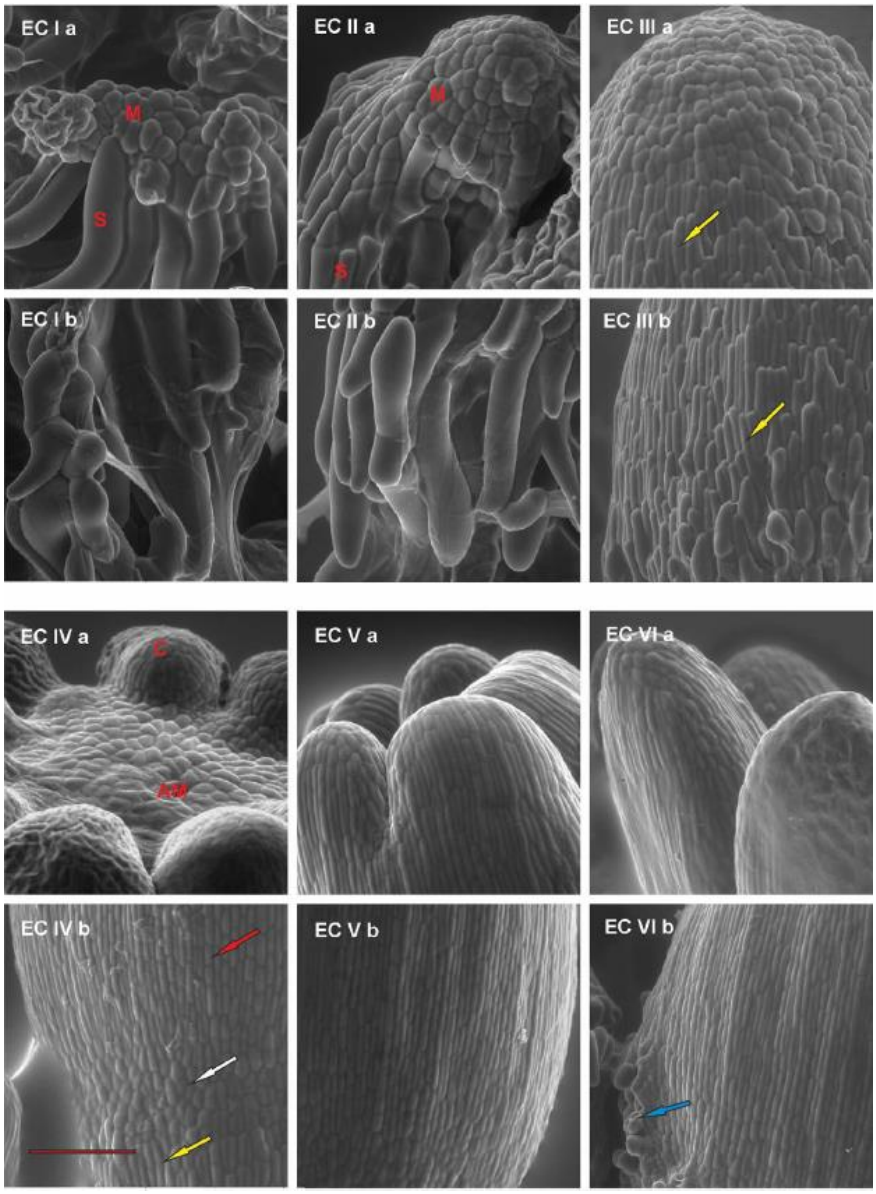

FIGURE 2 | Documentation of the development of the outermost cell layers in Picea abies somatic embryos at distinct phases of somatic embryo maturation. (EC Ia) Well-arranged meristematic embryonal heads (M) of polyembryogenic center are connected to suspensor cells (S); (EC Ib) a suspensor is composed of long suspensor cells. (EC IIa) A compact embryonal head (M) covered by polyhedral cells of early protoderm that are typical for globular embryos; (EC IIb) elongated suspensor cells, which are distally located from the meristematic embryonal head. (EC IIIa) An apical part of the precotyledonary embryo that is covered by polyhedral cells of the protoderm; note the elongated cells of the root cap reaching almost the top of the embryo in the left lower part of the image (yellow arrow); (EC IIIb) lower part of the embryo covered by elongated and overlapping cells of the root cap (yellow arrow). (EC IVa) Apical meristem of cotyledonary embryo (AM) surrounded by cotyledons (C); (EC IVb) junction zone between the hypocotyl and the root cap of cotyledonary embryo; polyhedral cells of protoderm (white arrow) are characteristic of this zone, they are surrounded proximally by elongated cells of hypocotyl (red arrow) and distally by elongated cells of the root cap (yellow arrow). (EC Va) Cotyledons of a mature embryo covered by elongated, well-arranged protodermal cells. The polyhedral cells are present on the very tip of cotyledons; (EC Vb) well-arranged pattern of elongated protodermal cells on the hypocotyl. (EC VIa) Elongated cotyledons of a post-mature embryo; (EC VIb) hypocotyl presenting with a sign of callus formation (blue arrow). Scale bar = 200 mm.

The third step of development is characterized by rapidly developing precotyledonary embryos that are localized to the surface of EC clusters (Figure 1 – EC IIIa and EC IIIb). The embryonal heads have elongated considerably and the suspensors have disintegrated. This developmental step includes the establishment of new embryonic inner structures as described in our previous studies (Svobodová, 1999; Cvikrová et al., 2016). Apical meristem develops and root meristem, with the root cap, forms at the basal pole of the embryo. The protoderm of the embryo proper is now established and demonstrates a tile pattern (Figure 2 – EC IIIa). The elongated root cap cells cover twothirds of embryo proper in layers that overlap and resemble the pattern of roof tiles (Figure 2 – EC IIIb).

Cotyledonary embryo development proceeds with the emergence of a ring of cotyledon primordia that grow and differentiate around the apical meristem (Figure 1 – EC IVa and EC IVb; Figure 2 – EC IVa). Tightly connected protodermal cells cover the entire embryo and form its smooth surface. These cells at the tips of cotyledons (Figure 2 – EC IVa) and at the junction zone between the hypocotyl and root cap (Figure 2 – EC IVb) have a polyhedral shape whereas the protodermal cells of the hypocotyl have an elongated shape as they extend parallel to the embryonic axis (Figure 2 – EC IVb).

At the end of maturation, the development of mature somatic embryos morphology is completed (Figure 1 – EC Va and EC Vb). All of the structural parts of the embryo (well-developed cotyledons surrounding apical meristem, hypocotyl, and root meristem covered by the root cap) are now established and no further organ primordia will appear. The elongation of the embryos, as well as cotyledons, continues. Both the cotyledons and hypocotyl of the mature embryos have fully developed protoderm (Figure 2 – EC Va and EC Vb).

Mature embryos are not able to continue their development when cultivation on the maturation media is prolonged, the disintegration process of embryos and callogenesis on embryo surfaces can start (Figure 2 – VIa and VIb).

Ultraviolet-B radiation was applied to ECs in stages I, II, III, IV, and V.

Viability

In the control embryos, a majority of meristematic cells that forms the embryo proper was viable throughout maturation, although some individual dead cells were observed at all stages of embryo development. On the contrary, the amount of dead suspensor cells increased throughout maturation due to the natural process of programmed cell death (PCD), which is required for normal embryo development (Figures 3A,D,G,J). UV-B irradiation had the largest effect on the viability of

somatic embryos in EC I. Exposure to 0.1 W m^{-2} h^{-1} UV-B led to both death of some or all meristematic cells (depending on the size of embryo) and to the release of compact structure of embryonal heads; the suspensor cells were severely injured (Figure 3B). A higher dose of UV-B radiation caused lethal damage to all cells of the embryonal head; suspensor cells were either dead or exhibited signs of disintegration (Figure 3C). Developmentally more advanced cylindrical and precotyledonary embryos (EC II and III) were less affected by UV-B treatment than EC I embryos. Irradiation with 0.1 W m^{-2} h^{-1} UV-B caused the death of only certain individual cells in the embryo surface layers (Figures 3E,H). However, after the application of 0.6Wm^{-2} h^{-1} UV-B, the embryonal heads of EC II embryos were severely injured. Surprisingly, a part of the suspensor cells that were distally located from the embryonal head remained viable even though a majority of the suspensor cells might have already undergone PCD at this stage (Figure 3F). The surface cells of precotyledonary embryos (EC III) that had been directly exposed to radiation exhibited damage, but this was only noticeable at the higher UV-B dose (Figure 3I). Cotyledonary embryos (EC V) were much less affected by UV-B radiation, although individual dead cells could be observed in both hypocotyls and cotyledons (Figure 3K). Exposure to 0.6 W m^{-2} h^{-1} UV-B was more harmful for cells located on the tips of cotyledons and probably caused the ruptures on the hypocotyl surface that were filled with dead cells (Figure 3L).

Malondialdehyde Content

Changes in MDA content, determined 7 days after irradiation in EC I–V, are presented in Figure 4. Irradiation of EC I and II with 0.1 W m^{-2} h^{-1} UV-B prompted MDA content to increase by 30 and 35%, respectively, while the MDA contents of the same ECs rose by 60 and 50%, respectively, following 0.6 W m^{-2} h^{-1} UV-B exposure. The MDA contents of EC III and IV increased by 20 and 30% following exposure to 0.1 and 0.6 W m^{-2} h^{-1} UV-B, respectively. All of these changes are reported relative to MDA content in control ECs.

Polyamine Contents

Throughout maturation, the spermidine (Spd) content of EC continuously increased; however, statistically significant increase was observed in EC IV and EC V only (results for the controls are indicated with the label “0” in the figures) (Figure 5). Significant differences in Spd content between controls and irradiated EC (both with 0.1 and 0.6 W m^{-2} h^{-1} UV-B) were noted 7 days after irradiation. The Spd content of EC I and II declined approximately 40% following irradiation with 0.1 W m^{-2} h^{-1} UV-B. A higher dose of UV-B, 0.6 W m□2 h□1, decreased Spd contents in EC I and II by 50 and 40%, respectively. UV-B radiation also had a substantial effect on EC III, with Spd contents in cultures decreasing by about 35

and 50% after exposure to 0.1 and 0.6 W m^{-2} h^{-1} UV-B, respectively. In EC IV, a significant decrease in Spd content was only observed after the culture was exposed to the higher dose of UV-B. All of the reported changes are relative to Spd content in control ECs. In EC II and III, spermine (Spm) levels were substantially higher after the higher dose of UV-B was applied. Only slight differences in the levels of putrescine (Put) were observed in both control and irradiated ECs throughout maturation. The control EC was characterized by a stable Spd/Put ratio, with values ranging from 1.8 to 2.4 (Supplementary Figure S1). The decline in Spd contents observed in irradiated EC I–III markedly decreased the Spd/Put ratio. The Spd/Put ratios of control EC and EC IV that had been irradiated with 0.6 W m^{-2} h^{-1} UV-B differed significantly. EC V demonstrated non-significant changes in the Spd/Put ratio that were irrespective of the applied UV-B dose.

Phenolic Acid Contents

The phenolic acids present in ECs I – V were determined on the seventh day after irradiation (Figure 6) and at the end of maturation (i.e., after 6 weeks of maturation, when the yield of embryos was estimated, Figure 7). Analyses revealed that seven phenolic acids were present in the EC extracts: two cinnamic acid derivatives, p-coumaric acid and ferulic acid, and five benzoic acid derivatives, p-hydroxybenzoic, protocatechuic, vanillic, gallic, and anisic acids. The benzoic acid derivatives extracted by methanol were mainly in free, ester-bound (those released after alkaline hydrolysis) and glycoside-bound (those released after acid hydrolysis, mainly glycosides of p-hydroxybenzoic, protocatechuic, and vanillic acids) forms. The most abundant phenolic acid liberated from the cell walls with alkali was ferulic acid, followed by p-coumaric acid. Exposure with 0.6 W m^{-2} h^{-1} UV-B clearly decreased free and soluble esterand glycoside-bound phenolic acids in EC I and II (Figure 6). A significant increase in cell-wall bound phenolic acids was observed in EC I–III 7 days after irradiation (both 0.1 and 0.6 W m^{-2} h^{-1} UV-B treatments) and was mostly a result of elevated ferulic acid levels (Figure 8). No marked differences in phenolic acid contents were observed in EC V following UV-B treatment, with the exception of an increase in the amount of phenolic glycosides, which increased by about 30% relative to the control after exposure to 0.1 and 0.6 W m^{-2} h^{-1} UV-B. The irradiation effect on the levels of phenolics determined at the end of maturation was strikingly different. Significant decreases in phenolic acids, which were dependent on the UV-B dose, were observed in irradiated EC I–III (Figure 7). A noticeable decrease in cell wall-bound phenolics, potentially arising from the pronounced decrease in cell wall-bound ferulic acid, was also observed after EC IV was treated with 0.6 W m^{-2} h^{-1} UVB. These changes correspond to the failure of somatic embryos to reach advanced stages of development (Figures 7 and 9). In EC IV and V, treatment with both 0.1 and 0.6 W m^{-2} h^{-1} UV-B caused the

accumulation of phenolic glycosides, as levels of these compounds increased approximately 30–45% relative to the controls (Figure 7). An increase in the glycosides of p-hydroxybenzoic acid and vanillic acid coincided with a decline in glycoside-bound protocatechuic acid (Figure 10).

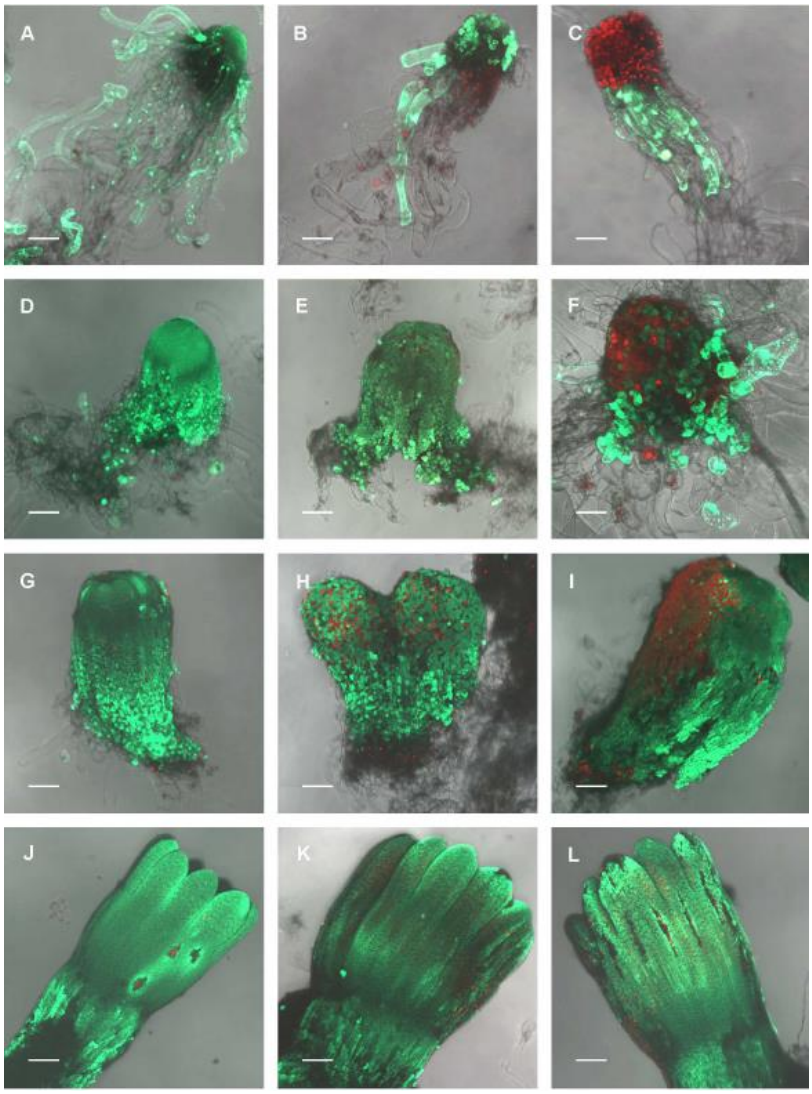

FIGURE 3 The effect of UV-B radiation on the viability of Picea abies somatic embryo cells at distinct phases of somatic embryo maturation. (A–C) Control, non-treated embryo, and irradiated embryos at EC I phase of maturation. (D–F) Control, non-treated embryo, and irradiated embryos at EC II phase of maturation. (G–I) Control, non-treated embryo, and irradiated embryos at EC III phase of maturation. (J–L) Control, non-treated embryo, and irradiated embryos at EC IV phase of maturation. First column – control embryos. Second column – embryos on the seventh day after irradiation with 0.1 W m^{-2} h^{-1} UV-B. Third column – embryos on the seventh day after irradiation with 0.6 W m^{-2} h^{-1} UV-B. Green fluorescence indicates living cells (vital staining with fluorescein diacetate), whereas red fluorescence indicates dead cells (staining with propidium iodide). All images are shown at maximum intensity projection of confocal optical sections of the whole embryos; the focal step size between optical sections was 7–16 mm. (A,D,E,G–L) Scale bar = 200 mm; (B,C,F) scale bar = 100 mm.

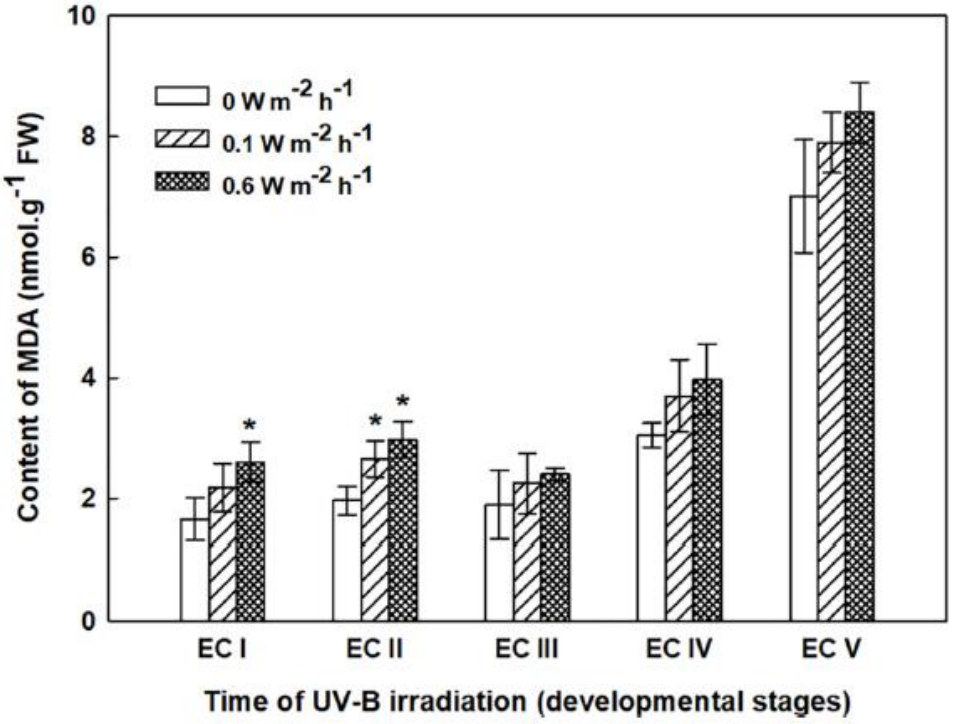

FIGURE 4 | Malondialdehyde (MDA) content in control and irradiated ECs at stages I–V of maturation, determined on the seventh day after UV-B irradiation. Data indicate mean _ SE ($n \geq 4$). Asterisks above the bars indicate significant differences ($P < 0.05$) between the MDA contents observed in irradiated ECs and the corresponding controls. 0 W m^{-2} h^{-1}, control – untreated EC at stages I–V.

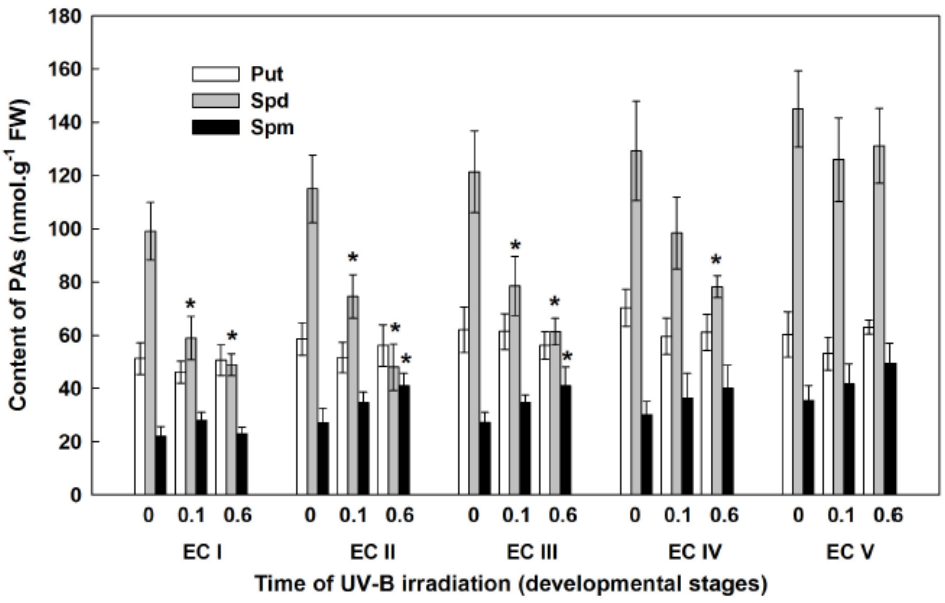

FIGURE 5 | Levels of free polyamines (PAs) in control and irradiated ECs at stages I–V of maturation, analyzed on the seventh day after UV-B irradiation. Data indicate mean _ SE ($n \geq 4$). Asterisks above the bars indicate significant differences (P ? 0.05) between the values observed in irradiated ECs and the corresponding controls. 0 W m^{-2} h^{-1}, control – untreated EC at stages I–V; 0.1–0.1 W m^{-2} h^{-1} UV-B; 0.6–0.6 W m^{-2} h^{-1} UV-B; Put, putrescine; Spd, spermidine; Spm, spermine.

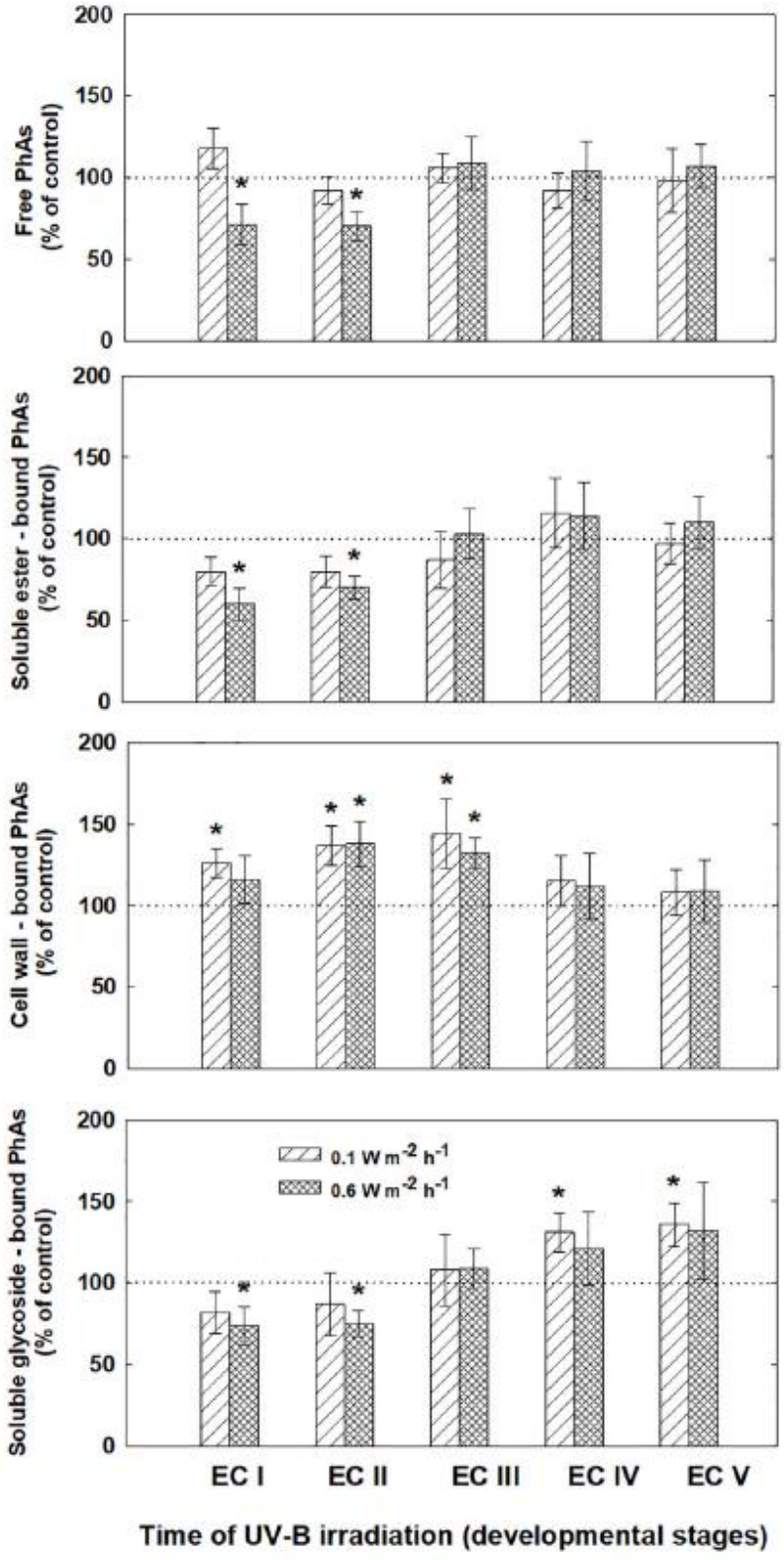

FIGURE 6 | Levels of phenolic acids (PhAs) in ECs irradiated at stages I–V of maturation determined on the seventh day after UV-B application. Changes are expressed relative to the values of untreated EC at stages I–V, which represent 100%. Data are shown as mean _ SE ($n \geq 4$). Asterisks above bars indicate significant differences ($P < 0.05$) between the contents observed in irradiated ECs and the untreated corresponding controls.

Yield of Somatic Embryos

The yield of embryos was estimated after 6 weeks of maturation, i.e., 1–5 weeks after EC irradiation. UV-B treatment affected the total yield of embryos as well as the number of fully developed mature embryos (Figure 11). The most pronounced effect and/or absolute inhibition of somatic embryo development was observed after irradiation of EC I. A marked decrease in the total amount of embryos was also observed in irradiated EC II, as the total amount of embryos reached 41% (lower dose) and 12% (higher dose) of what was observed in the control. Irradiation of EC III and EC IV decreased embryo yield to approximately 50% (lower dose) and 45% (higher dose of UV-B). UV-B treatment only exerted a weak effect on EC V as the total amount of embryos was 80% compared to the control.

Comparing the total number of embryos with the amount of fully developed embryos enabled us to determine how UV-B exposure, as well as its intensity, affects embryo development. In non-treated controls, 50% of all embryos were fully developed. The lower dose of irradiation (0.1 W m^{-2} h^{-1}) decreased the number of fully developed embryos to 20–30% in EC II–IV. Treatment with 0.6 W m^{-2} h^{-}1 UV-B had an even more pronounced effect; it stopped the further development of irradiated embryos so that only a limited number of fully developed mature embryos could be found [representing only a few (0–7%) percent of all embryos]. Irradiation did not affect EC V severely, as 40% of all the embryos were fully developed embryos, and there was only a small difference between the two UV-B doses (Figure 11).

Discussion

Our recent results indicate that UV-B light-induced polyphenolic deposition in epidermal cells and specialized idioblastic cells growing within the subepidermal and procambial regions of mature Norway spruce somatic embryos is likely to be part of the protective response to UV-B exposure (Eliášová et al., 2017). The research presented in this paper concentrated on how irradiation affects the development of Norway spruce somatic embryos in terms of the yield of mature embryos and changes in the contents of phenolics and PAs as a defense response to UV-B exposure.

The sequence of morphogenetic events during the development of embryos allowed us to correlate embryo morphology with the stress defense response to UV-B exposure. Generally, a lower dose of UV-B applied to EC I and EC II caused only part of meristematic and suspensor cells to die, whereas a higher dose of UV-B caused either lethal injury to entire embryonal heads or severe damage to individual meristematic cells. However, this result depended on the size of treated embryos.

Very small embryos were injured by lower dose of radiation similar to those ones treated by higher dose of UV-B radiation. The reason for the damage of meristematic cells that are mitotically active could consist in their higher sensitivity to UV-B radiation. The fate of suspensor cells is elimination during embryo proper development (Filonova et al., 2002). UV-B radiation might accelerate the process of PCD in these cells. The lesser extent of the damage of some suspensor cells might be related to their less sensitivity and stage of PCD through they underwent. The extent of embryo proper damage could be linked to the differentiation of the outermost cell layers (Eliášová et al., 2017). Protoderm formation begins very early in conifer somatic embryogenesis (Svobodová, 1999; Stasolla et al., 2002) and its establishment is important for further embryo development and maturation (Zhu et al., 2016). Differentiation of Norway spruce protodermal cells proceeded during embryogenesis. Precotyledonary embryos (EC III) were injured on the surface, which was likely the part of the embryo that was directly exposed to UV-B radiation. Cotyledonary embryos (EC IV) and mature embryos (EC V) were affected minimally as the protoderm was already more developed. We can assume that there is some correlation between the process of protoderm formation and the increasing ability of protodermal cells to protect somatic embryos from the harmful effects of UV-B radiation. The outermost cell layer gradually acquire features of mature epidermis; however, this process is only complete after germination (Javelle et al., 2011).

The increase in MDA content, indicating the extent of lipid peroxidation, noted for cultures containing early somatic embryos (EC I, II, and partly III) coincided with changes in the composition of the phenolic substances pool (Figure 4). A decrease in free and ester-bound phenolic acids determined in these cultures (Figure 6) coupled with a significant rise in cell wall-bound phenolics, such as esters of ferulic acid (Figure 8), supports the hypothesis that phenolics incorporated into the cell walls protect cells against UV-B radiation (Schweiger et al., 1996; Semerdjieva et al., 2003). The localization of high levels of phenolic compounds in the epidermal cells of plants subjected to UV-B radiation has been associated with a strategy of protection against UV-B radiation by many authors (Laakso et al., 2000; Martínez-Abaigar et al., 2015). Direct evidence that phenolic accumulation has a role in conferring UV tolerance has been obtained from Arabidopsis thaliana (L.) Heynh. mutants containing inactive forms of specific phenolic biosynthetic enzymes (Sheahan, 1996). In conifers, the synthesis of phenolics is crucial to various inducible defense systems. We have recently proposed that the deposition of polyphenolics in intact epidermal cells located in the vicinity of damaged cells may mean that injured cells can transmit a signal to evoke defense response in other tissues (Eliášová et al., 2017). However, the observed increase in glycoside-bound p-hydroxybenzoic acid and vanillic acid levels could be considered to be a general

antioxidative defense mechanism rather than a specific consequence of UV-B light perception (Figure 10). The observed increases correspond well with results of experiments in which callus cultures of Pinus sylvestris were treated with mycelial extracts of Fusarium nivale reported by Shein et al. (2003) who, in an earlier contribution (Shein et al., 2001), concluded that the accumulation of p-hydroxybenzoic acid plays an important role in the protection of conifer cells.

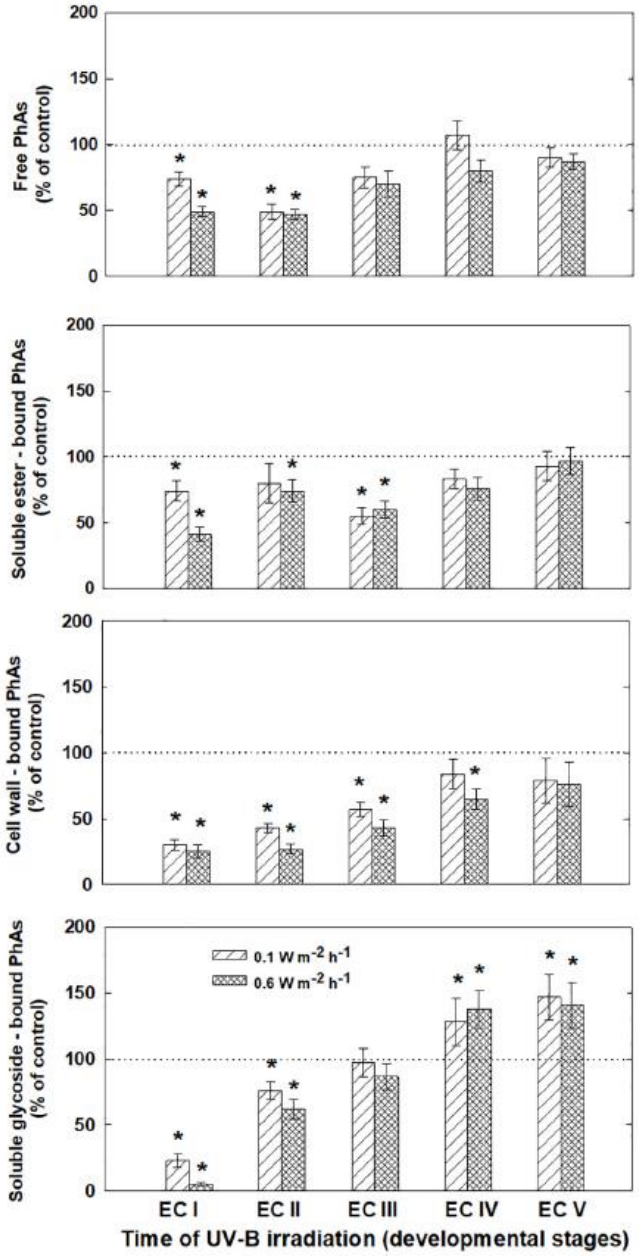

Figure 7 Levels of phenolic acids (PhAs) in ECs irradiated at stages I–V of maturation, determined at the end of maturation. Changes are expressed relative to the values of untreated control EC at the end of maturation, which represent 100%. Data are shown as mean ± SE ($n \geq 4$). Asterisks above bars indicate significant differences ($P < 0.05$) between the contents observed in irradiated ECs and the untreated control.

Significant changes in phenolic substance contents caused by the UV-B treatment of EC I–V, determined at the end of maturation, might be involved in the inhibition of somatic embryo development. Phenolic acids are important to successful embryo development as they are involved in alterations of the cell wall composition during differentiation and morphogenesis (Fry, 1987). Lozovaya et al. (1996) reported that differences between the cell walls of regenerable and non-regenerable callus tissues of Zea mays, Fagopyrum esculentum, and F. tataricum may be associated with differences in levels and localization of cell wall phenolics. They assumed that alterations in cell wall phenolics during morphogenesis can be used as biochemical markers to demonstrate cell differentiation capacity. A significant decrease in cell wall-bound phenolics arising from the pronounced decrease in cell wall-bound ferulic acid, which was observed after UV-B exposure in EC II–IV, might correspond to failure of somatic embryos to reach more advanced stages of development (Figure 9). We previously found that the cell walls of embryogenic alfalfa calli grown over long periods of time on medium containing glyphosate (an inhibitor of shikimate pathway enzyme 5-enolpyruvylshikimate- 3-phosphate synthase) show increased amounts of hydroxybenzoic acids, which replaced p-coumaric and ferulic acids, and the concomitant gradual loss of calli embryogenic potential (Binarová et al., 1994).

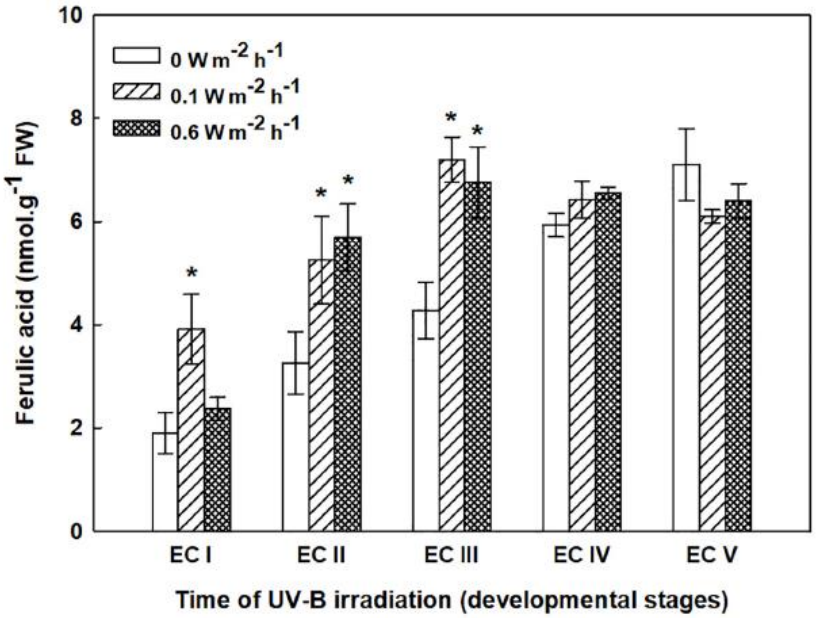

Figure 8 Ferulic acid content in the cell wall-bound fractions from control and irradiated ECs at stages I–V of maturation, determined on the seventh day after irradiation. Data indicate mean ± SE ($n \geq 4$). Asterisks above bars indicate significant differences ($P < 0.05$) between the contents observed in irradiated ECs and the corresponding controls. 0 W m^{-2} h^{-1}, control – untreated EC at stages I–V.

Polyamines have multiple essential functions in plant. They not only facilitate cell division and growth but can also induce cell death by producing H2O2 as a response to abiotic stressinduced Spd oxidation, which results in the induction of either tolerance responses or the overexpression of certain genes involved in PCD cascades (Moschou et al., 2008, 2012). Pas should no longer be considered only as protective molecules, but rather as multifaceted compounds, which have a key role in the regulation of stress tolerance and are involved in direct interactions with other metabolic routes and hormonal crosstalk (Pál et al., 2015). The accumulation of PAs provoked by UV-treatment has previously been discussed in relation to their role in the prevention of oxidative damage (Lütz et al., 2005; Sfichi-Duke et al., 2008, Schweikert et al., 2011). Several studies have shown that exogenous Spd and Spm applications improve the stress tolerance of plants (Yiu et al., 2009; Hu et al., 2012). As a signaling molecule, H2O2 subsequently induces expression of antioxidant enzyme genes and their increased activities result in the reduction of oxidative damage. However, the role of PA-derived H2O2 is still controversial due to its dual functions, and the distinction between the two functions needs to be studied further. Various environmental stresses can cause the accumulation of PAs in plant tissues; however, high stress can lead to a decrease in PA synthesis and may indicate the sensitivity to UV-B radiation (Smith et al., 2001). The significant decrease in the Spd contents of irradiated EC I and II, which contained somatic embryos in early developmental stages, correlated to an increase in MDA levels (Figures 4, 5). On the contrary, a higher dose of UV-B substantially increased the levels of Spm in EC II and III (Figure 5). An increase in MDA and a marked decrease in Spd contents pointed to the fact that early embryos were not well protected against UV-B damage. Alterations in individual PA levels occur in response to a wide variety of stress situations. It has been shown that Put is effective at increasing the activities of antioxidant enzymes (Papadakis and Roubelakis-Angelakis, 2005) while Spd and especially Spm, biologically more dynamic than the other PAs, seem to be involved in preventing injury to membranes under stress conditions (Bouchereau et al., 1999; Kuthanová et al., 2004; Silveira et al., 2004). The relatively high content of Spm (compared with the levels of Put and Spd) as a consequence of cryoprotectant treatment of P. abies embryogenic suspensor mass (ESM) also corroborates suggestions that Spm participates in cellular membrane stabilization (Vondráková et al., 2010).

The involvement of PAs in various plant growth and developmental processes, including a crucial role in somatic embryo development, has been reported for several coniferous species (Minocha et al., 2004; Silveira et al., 2004). The variable responses of EC containing early somatic embryos (I and II) and EC containing prevailing cotyledonary embryos (IV and V) to UV-B radiation markedly influenced the yield of somatic embryos (Figure 11). The limited development of

embryos caused by UV-B radiation was a result of the decreased viability of irradiated EC I and II and the extent of cell damage in EC III– V, consequences which both coincided with a marked decrease in Spd contents. Spd has been shown to exert a specific morphogenic role in many plant systems. Significant increases in Spd levels were associated with the formation of somatic embryos in P. abies (Santanen and Simola, 1992) and P. radiata (Minocha et al., 1999) The relationship between embryogenic capacity and the total content of free PAs confirmed that Spd is a crucial part of P. abies somatic embryo development and is in agreement with our previous findings (Gemperlová et al., 2009; Vondráková et al., 2015).

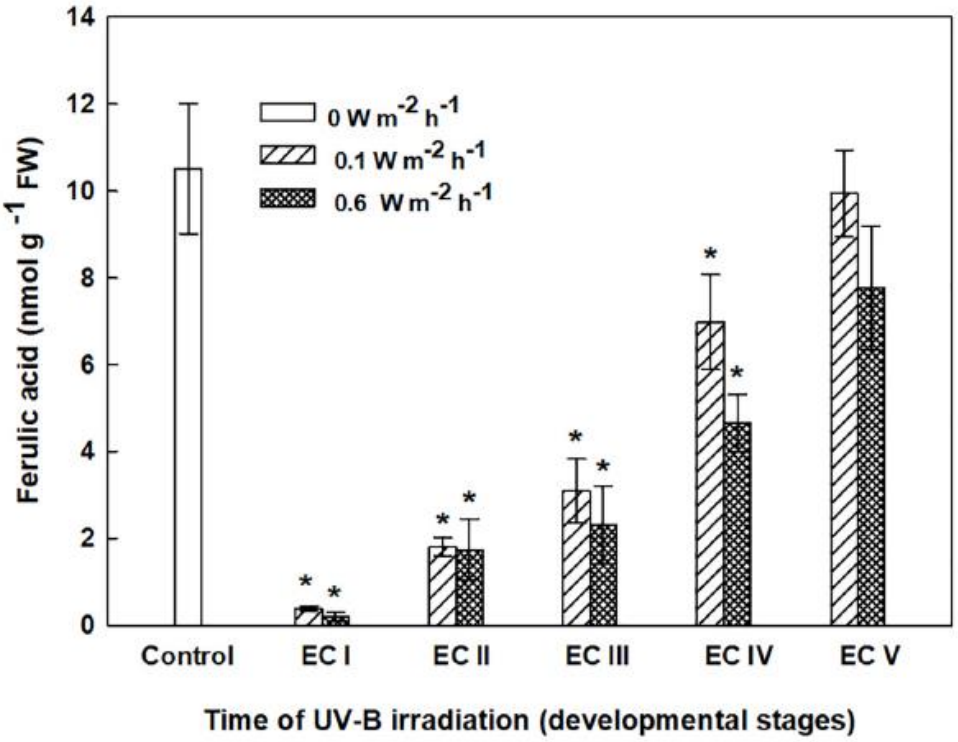

Figure 9 Ferulic acid content in cell wall-bound fractions from control EC and irradiated ECs at stages I–V of maturation, determined at the end of maturation. Data indicate mean ± SE ($n \geq 4$). Asterisks above bars indicate significant differences ($P < 0.05$) between the contents observed in irradiated ECs and the untreated control. 0 W m^{-2} h^{-1}, control – untreated EC at the end of maturation.

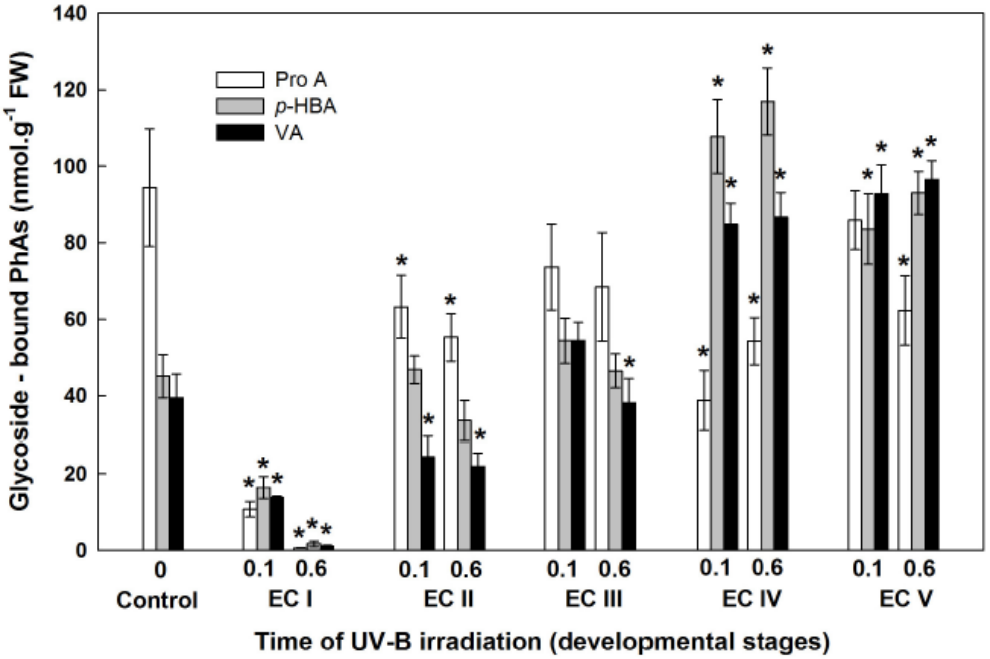

Figure 10 Glycoside-bound methanol-soluble protocatechuic (ProA), p-hydroxybenzoic (p-HBA), and vanillic (VA) acid contents of control EC and irradiated ECs at stages I–V of maturation, determined at the end of maturation. Data indicate mean ± SE ($n \geq 4$). Asterisks above bars indicate significant differences ($P < 0.05$) between the contents observed in irradiated ECs and the untreated control. 0 W m^{-2} h^{-1}, control – untreated EC at the end of maturation; 0.1–0.1 W m^{-2} h^{-1} UV-B; 0.6–0.6 W m^{-2} h^{-1} UV-B.

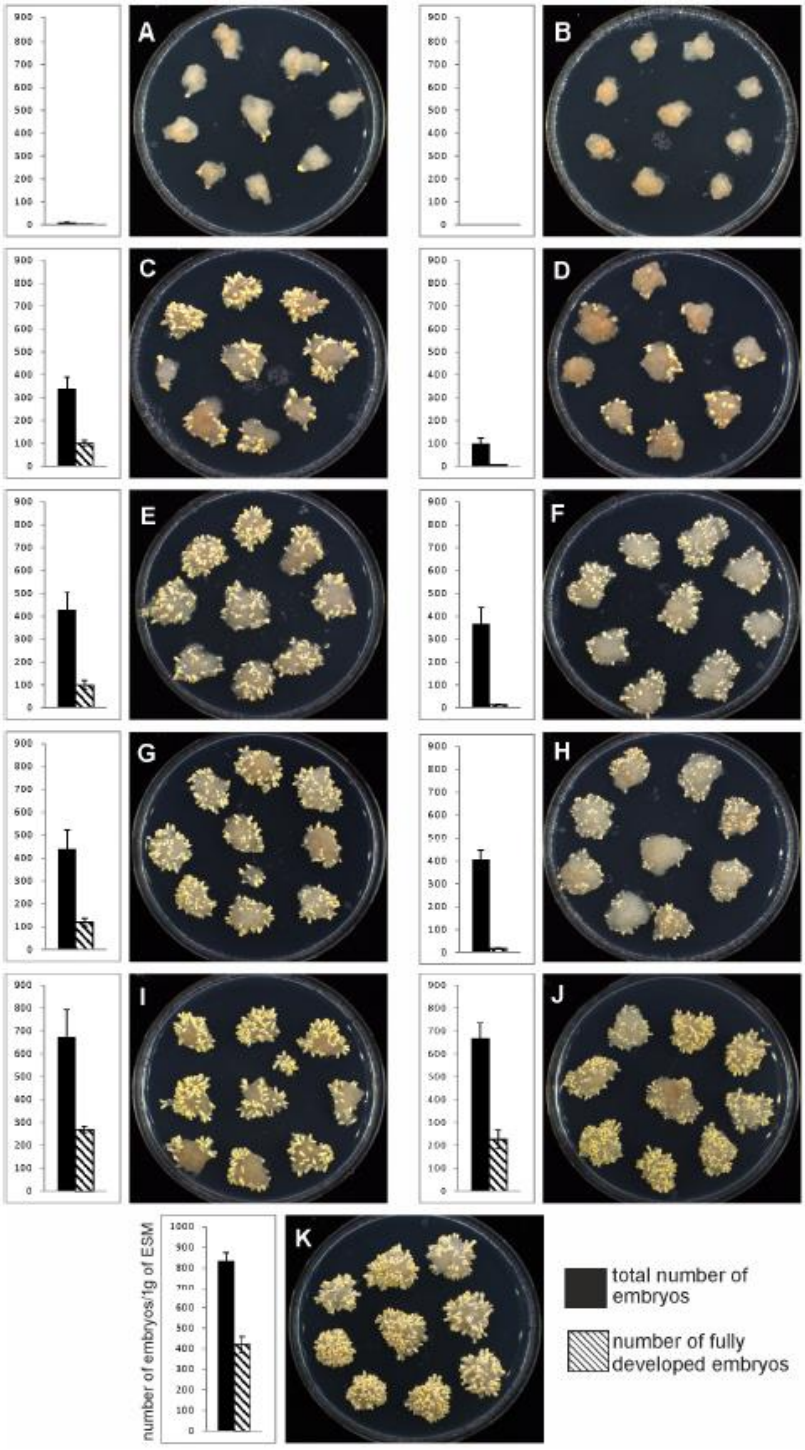

Figure 11 The yield of mature somatic embryos obtained from EC irradiated in distinct phases of maturation. The number of embryos at the end of maturation was expressed on a per-gram basis relative to the fresh mass of embryogenic culture at the start of the experiment. The presented graphs demonstrate the proportion of embryos that are morphologically fully developed (hatched columns) to all embryos (black columns). (A,B) UV-B treatment at EC I phase of maturation. (C,D) UV-B treatment at EC II phase of maturation. (E,F) UV-B treatment at EC III phase of maturation. (G,H) UV-B treatment at EC IV phase of maturation. (I,J) UV-B treatment at EC V phase of maturation. (K) Untreated control. First column – 0.1 W m^{-2} h^{-1} UV-B treatment. Second column – 0.6 W m^{-2} h^{-1} UV-B treatment. The Petri dishes were 90 mm in diameter.

Conclusion

In summary, the exposure of Norway spruce EC to UV-B radiation at different stages of maturation had the strongest effect on cell viability of embryos at early stages of development and resulted in the inhibition of somatic embryo development and/or the substantial decrease in the number of embryos. The extent of cell damage was dependent on the UV-B dose applied, as well as the embryo developmental stage, and might be related to differentiation of the outermost cell layers and formation of protoderm. Developmentally more advanced embryos were superior to early embryos in terms of a more efficient stress defense response to UV-B exposure. The response of early embryos was characterized by an increase in MDA, a marked decrease in PA contents and a decline in phenolics. The reduced ability to activate the defense system seems to be responsible not only for the severe cell damage and decrease in viability but also for the inhibition of embryo development. The significant reduction in Spd, which has been shown to be crucial in the somatic embryo development of several coniferous species, seems to be causally linked to the limited development of embryos. Furthermore, decreased levels of cell wall-bound phenolics arising from the pronounced decrease in cell wall-bound ferulic acid might correspond to failure of somatic embryos to reach more advanced stages of development.

Author Contributions

ZV, KE, and MC designed the experiments. MV and MC have written the first draft of the manuscript. ZV has participated in collection of plant material for biochemical analysis and has cowritten the manuscript. KE has performed and interpreted the data of histological analysis. LG and LF performed the extraction of polyamines and phenolic substances. JM and AT have done HPLC/MS analysis of phenolic acids and polyamines. VN and JR performed the micro-morphological study with ESEM. KE, ZV, and MC wrote the manuscript with contributions from all the authors. MV reviewed the manuscript.

Funding

This work was supported by the Ministry of Education, Youth and Sports of the Czechia (grant nos. LTC 17030 and LTC 17036).

Acknoledgments

The authors would like to thank Sees-Editing Ltd. for linguistic editing. They also thank technicians Jana Kališová and Jaroslava Špačková for their excellent work.

Supplementary Material

The Supplementary Material for this article can be found online at: https://www.frontiersin.org/articles/10.3389/fpls.2018.01736/ full#supplementary-material

References

Agati, G., and Tattini, M. (2010). Multiple functional roles of flavonoids in photoprotection. New Phytol. 186, 786–793. doi: 10.1111/j.1469-8137.2010. 03269.x

Binarová, P., Cvikrová, M., Havlický, T., Eder, J., and Plevková, J. (1994). Changes of shikimate pathway in glyphosate tolerant alfalfa cell lines with reduced embryogenic ability. Biol. Plant. 36, 65–73. doi: 10.1007/BF0292 1271

Booij-James, I. S., Dube, S. K., Jansen, M. A. K., Edelman, M., and Mattoo, A. K. (2000). Ultraviolet-B radiation impacts light-mediated turnover of the photosystem II reaction center heterodimer in Arabidopsis mutants altered in phenolic metabolism. Plant Physiol. 124, 1275–1283. doi: 10.1104/pp.124.3. 1275

Bouchereau, A., Aziz, A., Larher, F., and Martin-Tanguy, J. (1999). Polyamines and environmental challenges: recent development. Plant Sci. 140, 103–125. doi: 10.1016/S0168-9452(98)00218-0

Cvikrová, M., Gemperlová, L., Eder, J., and Zažímalová, E. (2008). Excretion of polyamines in alfalfa and tobacco suspension-cultured cells and its possible role in maintenance of intracellular polyamine contents. Plant Cell Rep. 27, 1147–1156. doi: 10.1007/s00299-008-0538-5

Cvikrová, M., Gemperlová, L., Martincová, O., and Vaˇcková, R. (2013). Effect of drought and combined drought and heat stress on polyamine metabolism in proline-over-producing tobacco plants. Plant Physiol. Biochem. 73, 7–15. doi: 10.1016/j.plaphy.2013.08.005

Cvikrová, M., Malá, J., Hrubcová, M., Martincová, O., Cvrčková, H., and Lipavská, H. (2010). Defence responses induced in embryogenic cultures of Norway spruce by two fractions of Gremmeniella abietina mycelia. For. Pathol. 40, 467–484. doi: 10.1111/j.1439-0329.2009. 00622.x

Cvikrová, M., Meravý, L., Macháčková, I., and Eder, J. (1991). Phenylalanine ammonia-lyase, phenolic acids and ethylene in alfalfa (Medicago sativa L.) cell cultures in relation to their embryogenic ability. Plant Cell Rep. 10, 251–255. doi: 10.1007/BF00232569

Cvikrová, M., Vondrákova, Z., Eliášová, K., Pešek, B., Trávníčková, A., and Vágner, M. (2016). The impact of UV-B irradiation applied at different phases of somatic embryo development in Norway spruce on polyamine metabolism. Trees 30, 113–124. doi: 10.1007/s00468-015-1280-6

Eliášová, K., Vondráková, Z., Malbeck, J., Trávníčková, A., Pešek, B., Vágner, M., et al. (2017). Histological and biochemical response of Norway spruce somatic embryos to UV-B irradiation. Trees 31, 1279–1293. doi: 10.1007/s00468-017-1547-1

Filonova, L. H., von Arnold, S., Daniel, G., and Bozhkov, P. V. (2002). Programmed cell death eliminates all but one embryo in a polyembryonic plant seed. Cell Death Differ. 9, 1057–1062. doi: 10.1038/sj.cdd.4401068

Fry, S. C. (1987). Intracellular feruloylation of pectic polysaccharides. Planta 171, 205–211. doi: 10.1007/bf00391095

Gemperlová, L., Fischerová, L., Cvikrová, M., Malá, J., Vondráková, Z.,Martincová, O., et al. (2009). Polyamine profiles and biosynthesis in somatic embryo development and comparison of germinating somatic and zygotic embryos of Norway spruce. Tree Physiol. 29, 1287–1298. doi: 10.1093/treephys/tpp063

Gill, S. S., and Tuteja, N. (2010). Polyamines and abiotic stress tolerance in plants. Plant Signal. Behav. 5, 26–33. doi: 10.4161/psb.5.1.10291

Gupta, P. K., and Durzan, D. J. (1986). Somatic polyembryogenesis from callus of mature sugar pine embryos. Biotechnology 4, 643–645.

Hideg, É., Jansen, M. A. K., and Strid, Å. (2013). UV-B exposure, ROS, and stress: inseparable companions or loosely linked associates? Trends Plant. Sci. 18, 107–115. doi: 10.1016/j.tplants.2012.09.003

Hu, X. H., Zhang, Y., Shi, Y., Zhang, Z., Zou, Z. R., Zhang, H., et al. (2012). Effect of exogenous spermidine on polyamine content and metabolism in tomato exposed to salinity–alkalinity mixed stress. Plant Physiol. Biochem. 57, 200–209. doi: 10.1016/j.plaphy.2012.05.015

Hussain, S. S., Ali, M., Ahmad, M., and Siddique, K. H. M. (2011). Polyamines: natural and engineered abiotic and biotic stress tolerance in plants. Biotechnol. Adv. 29, 300–311. doi: 10.1016/j.biotechadv.2011.01.003

Jansen, M. A. K., Babu, T. S., Heller, D., Gaba, V., Mattoo, A. K., and Edelman, M. (1996). Ultraviolet-B effects on Spirodela oligorrhiza: induction of different protection mechanisms. Plant Sci. 115, 217–223.

Jansen, M. A. K., Gaba, V., and Greenberg, B. M. (1998). Higher plants and UVB radiation: balancing damage, repair and acclimation. Trends Plant Sci. 3, 131–135.

Jansen, M. A. K., Hectors, K., O'Brien, N. M., Guisez, Y., and Potters, G. (2008). Plant stress and human health: do human consumers benefit from UV-B acclimated crops? Plant Sci. 175, 449–458. doi: 10.1016/j.plantsci.2008.04.010

Javelle, M., Vernoud, V., Rogowsky, P. M., and Ingram, G. C. (2011). Epidermis: the formation and functions of a fundamental plant tissue. New Phytol. 189, 17–39. doi: 10.1111/j.1469-8137.2010.03514.x

Kusano, T., Berberich, T., Tateda, C., and Takahashi, Y. (2008). Polyamines: essential factors for growth and survival. Planta 228, 367–381. doi: 10.1007/ s00425-008-0772-7

Kuthanová, A., Gemperlová, L., Zelenková, S., Eder, J., Machá˘cková, I., Opatrný, Z., et al. (2004). Cytological changes and alterations in polyamine contents induced by cadmium in tobacco BY-2 cells. Plant Physiol. Biochem. 42, 149–156. doi: 10.1016/j.plaphy.2003.11.003

Laakso, K., Sullivan, J. H., and Huttunen, S. (2000). The effects of UV-B radiation on epidermal anatomy in loblolly pine (Pinus taeda L.) and Scots pine (Pinus sylvestris L.). Plant Cell Environ. 23, 461–472. doi: 10.1046/j.1365-3040.2000. 00566.x

Lozovaya, V., Gorshkova, T., Yablokova, E., Zabotina, O., Ageeva, M., Rumyantseva, N., et al. (1996). Callus cell wall phenolics and plant regeneration ability. J. Plant Physiol. 148, 711–717. doi: 10.1016/S0176-1617(96)80373-7

Lütz, C., Navakoudis, E., Seidlitz, H. K., and Kotzabasis, K. (2005). Simulated solar irradiation with enhanced UV-B adjust plastid- and thylakoid-associated polyamine changes for UV-B protection. Biochim. Biophys. Acta Bioenerg 1710, 24–33. doi: 10.1016/j.bbabio.2005.09.001

Martin, K. P., and Madassery, J. (2005). Direct and indirect somatic embryogenesis on cotyledon explants of Quassia amara L., an antileukaemic drug plant. In Vitro Cell. Dev. Biol. Plant 41, 54–57. doi: 10.1079/IVP2004588

Martínez-Abaigar, J., Monforte, L., Del-Castillo-Alonso, M. Á., Fabón, G., Tomás-Las-Heras, R., and Núñez-Olivera, E. (2015). Ultraviolet-absorbing compounds from the cell walls of an aquatic liverwort are more efficiently extracted by alkaline than by enzymatic digestion. J. Bryol. 37, 1–14. doi: 10.1179/ 1743282014Y.0000000112

Minocha, R., Minocha, S. C., and Long, S. (2004). Polyamines and their biosynthetic enzymes during somatic embryo development in red spruce (Picea rubens sarg.). In Vitro Cell. Dev. Biol. Plant 40, 572–580. doi: 10.1079/ IVP2004569

Minocha, R., Smith, D. R., Reeves, C., Steele, K. D., and Minocha, S. C. (1999). Polyamine levels during the development of zygotic and somatic embryos of Pinus radiata. Physiol. Plant. 105, 155–164. doi: 10.1034/j.1399-3054.1999. 105123.x

Moschou, P. N., Paschalidis, K. A., Delis, I. D., Andriopoulou, A. H., Lagiotis, G. D., Yakoumakis, D. I., et al. (2008). Spermidine exodus and oxidation in the apoplast induced by abiotic stress is responsible for H2O2 signatures that direct tolerance responses in tobacco. Plant Cell 20, 1708–1724. doi: 10.1105/tpc.108. 059733

Moschou, P. N., Wu, J., Cona, A., Tavladoraki, P., Angelini, R., and Roubelakis-Angelakis, K. A. (2012). The polyamines and their catabolic products are significant players in the turnover of nitrogenous molecules in plants. J. Exp. Bot. 63, 5003–5015. doi: 10.1093/jxb/ers202

Neděla, V., Hřib, J., and Vooková, B. (2012). Imaging of early conifer embryogenic tissues with the environmental scanning electron microscope. Biol. Plant. 56, 595–598. doi: 10.1007/s10535-012-0062-x

Neděla, V., Konvalina, I., Oral, M., and Hudec, J. (2015a). The simulation of energy distribution of electrons detected by segmental ionization detector in high pressure conditions of ESEM. Microsc. Microanal. 21, 264–269. doi: 10. 1017/S1431927615013483

Neděla, V., Tihlaříková, E., and Hřib, J. (2015b). The low-temperature method for study of coniferous tissues in the environmental scanning electron microscope. Microsc. Res. Tech. 78, 13–21. doi: 10.1002/jemt.22439

Pál, M., Szalai, G., and Janda, T. (2015). Speculation: polyamines are important in abiotic stress signaling. Plant Sci. 237, 16–23. doi: 10.1016/j.plantsci.2015. 05.003

Papadakis, A. K., and Roubelakis-Angelakis, K. A. (2005). Polyamines inhibit NADPH oxidase-mediated superoxide generation and putrescine prevents programmed cell death induced by polyamine oxidase-generated hydrogen peroxide. Planta 220, 826–837. doi: 10.1007/s00425-004-1400-9

Reifenrath, K., and Müller, C. (2007). Species-specific and leaf-age dependent effects of ultraviolet radiation on two Brassicaceae. Phytochemistry 68, 875–885. doi: 10.1016/j.phytochem.2006.12.008

Reis, E., Batista, M. T., and Canhoto, J. M. (2008). Effect and analysis of phenolic compounds during somatic embryogenesis induction in Feijoa sellowiana berg. Protoplasma 232, 193–202. doi: 10.1007/s00709-008-0290-2

Santanen, A., and Simola, L. K. (1992). Changes in polyamine metabolism during somatic embryogenesis in Picea abies. J. Plant Physiol. 140, 475–480. doi: 10. 1016/S0176-1617(11)80828-X

Schenkmayerová, A., Buˇcko, M., Gemeiner, P., Trel'ová, D., Lacík, I., Chorvát, D., et al. (2014). Physical and bioengineering properties of polyvinyl alcohol lensshaped particles versus spherical polyelectrolyte complex microcapsules as immobilisation matrices for a whole-cell Baeyer–Villiger monooxygenase. Appl. Biochem. Biotechnol. 174, 1834–1849. doi: 10.1007/s12010-014-1174-x

Schweiger, J., Lang, M., and Lichtenthaler, H. K. (1996). Differences in fluorescence excitation spectra of leaves between stressed and non-stressed plants. J. Plant Physiol. 148, 536–547. doi: 10.1016/S0176-1617(96)80073-3

Schweikert, K., Sutherland, J. E. S., Hurd, C. L., and Burritt, D. J. (2011). UVB radiation induces changes in polyamine metabolism in the red seaweed Porphyra cinnamomea. Plant Growth Regul. 65, 389–399. doi: 10.1007/s10725- 011-9614-x

Semerdjieva, S. I., Sheffield, E., Phoenix, G. K., Gwynn-Jones, D., Callaghan, T. V., and Johnson, G. N. (2003). Contrasting strategies for UV-B screening in subarctic dwarf shrubs. Plant Cell Environ. 26, 957–964. doi: 10.1046/j.1365-3040. 2003.01029.x

Sfichi-Duke, L., Ioannidis, N. E., and Kotzabasis, K. (2008). Fast and reversible response of thylakoid-associated polyamines during and after UV-B stress: a comparative study of the wild type and a mutant lacking chlorophyll b of unicellular green alga Scenedesmus obliquus. Planta 228, 341–353. doi: 10.1007/ s00425-008-0741-1

Sheahan, J. J. (1996). Sinapate esters provide greater UV-B attenuation than flavonoids in Arabidopsis thaliana (Brassicaceae). Am. J. Bot. 83, 679–686. doi: 10.2307/2445845

Shein, I. V., Andreeva, O. N., Polyakova, G. G., and Zrazhevskaya, G. K. (2003). Effect of pine callus elicitation by the Fusarium strains of various pathogenicity on the content of phenolic compounds. Russ. J. Plant Physiol. 50, 634–639. doi: 10.1023/A:1025688023862

Shein, I. V., Polyakova, G. G., Zrazhevskaya, G. K., Pashenova, N. V., and Vetrova, V. P. (2001). Accumulation of phenolic compounds in conifer callus cultures in response to wood blue-stain fungi. Russ. J. Plant Physiol. 48, 216–221. doi: 10.1023/A:1009056201926

Shi, H., and Chan, Z. (2014). Improvement of plant abiotic stress tolerance through modulation of the polyamine pathway. J. Integr. Plant Biol. 56, 114–121. doi: 10.1111/jipb.12128

Silveira, V., Floh, E. I. S., Handro, W., and Guerra, M. P. (2004). Effect of plant growth regulators on the cellular growth and levels of intracellular protein, starch and polyamines in embryogenic suspension cultures of Pinus taeda. Plant Cell Tissue Organ Cult. 76, 53–60. doi: 10.1023/A:102584751 5435

Smith, J., Burrit, D., and Bannister, P. (2001). Ultraviolet-B radiation leads to a reduction in free polyamines in Phaseolus vulgaris L. Plant Growth Regul. 35, 289–294. doi: 10.1023/A:1014459232710

Stasolla, C., Kong, L., Yeung, E. C., and Thorpe, T. A. (2002). Maturation of somatic embryos in conifers: morphogenesis, physiology, biochemistry, and molecular biology. In Vitro Cell. Dev. Biol. Plant 38, 93–105. doi: 10.1079/IVP200 1262

Svobodová, H., Albrechtová, J., Kumstýřová, L., Lipavská, H., Vágner, M., and Vondráková, Z. (1999). Somatic embryogenesis in Norway spruce: anatomical study of embryo development and influence of polyethylene glycol on maturation process. Plant Physiol. Biochem. 37, 209–221. doi: 10.1016/S0981-9428(99)80036-9

Takahashi, T., and Kakehi, J. I. (2010). Polyamines: ubiquitous polycations with unique roles in growth and stress responses. Ann. Bot. 105, 1–6. doi: 10.1093/aob/mcp259

Takshak, S., and Agrawal, S. B. (2015). Defence strategies adopted by the medicinal plant Coleus forskohlii against supplemental ultraviolet-B radiation: augmentation of secondary metabolites and antioxidants. Plant Physiol. Biochem. 97, 124–138. doi: 10.1016/j.plaphy.2015.09.018

Vondráková, Z., Cvikrová, M., Eliášová, K., Martincová, O., and Vágner, M. (2010). Cryotolerance in Norway spruce and its association with growth rates, anatomical features and polyamines of embryogenic cultures. Tree Physiol. 30, 1335–1348. doi: 10.1093/treephys/tpq074

Vondráková, Z., Eliášová, K., and Vágner, M. (2014). The anti-actin drugs latrunculin and cytochalasin affect the maturation of spruce somatic embryos in different ways. Plant Sci. 221, 90–99. doi: 10.1016/j.plantsci.2014. 02.006

Vondráková, Z., Eliášová, K., Vágner, M., Martincová, O., and Cvikrová, M. (2015). Exogenous putrescine affects endogenous polyamine levels and the development of Picea abies somatic embryos. Plant Growth Regul. 75, 405–414. doi: 10.1007/s10725-014-0001-2

Yiu, J.-C., Liu, C. W., Fang, D. Y. T., and Lai, Y. S. (2009). Waterlogging tolerance of Welsh onion (Allium fistulosum L.) enhanced by exogenous spermidine and spermine. Plant Physiol. Biochem. 47, 710–716. doi: 10.1016/j.plaphy.2009. 03.007

Zhu, T., Moschou, P. N., Alvarez, J. M., Sohlberg, J. J., and von Arnold, S. (2016). WUSCHEL-RELATED HOMEOBOX 2 is important for protoderm and suspensor development in the gymnosperm Norway spruce. BMC Plant Biol. 16:19. doi: 10.1186/s12870-016-0706-7

Conflict of Interest Statement: The authors declare that the research was conducted in the absence of any commercial or financial relationships that could be construed as a potential conflict of interest.

17 Reverse taxonomy applied to the Brachionus calyciflorus cryptic species complex: Morphometric analysis confirms species delimitations revealed by molecular phylogenetic analysis and allows the (re) description of four species

Evangelia Michaloudi[1], Spiros Papakostas[2], Georgia Stamou[1], Vilém Neděla [3], Eva Tihlaříková[3], Wei Zhang[4], Steven A. J. Declerck[4]

1 *Department of Zoology, School of Biology, Aristotle University of Thessaloniki, Thessaloniki, Greece,*
2 *Division of Genetics and Physiology, Department of Biology, University of Turku, Turku, Finland*
3 *Institute of Scientific Instruments, Academy Of Sciences of the Czech Republic, Brno, Czech Republic*
4 *Netherlands Institute of Ecology, Department of Aquatic Ecology, Wageningen, The Netherlands*

Abstract

The discovery and exploration of cryptic species have been profoundly expedited thanks to developments in molecular biology and phylogenetics. In this study, we apply a reverse taxonomy approach to the *Brachionus calyciflorus* species complex, a commonly studied freshwater monogonont rotifer. By combining phylogenetic, morphometric and morphological analyses, we confirm the existence of four cryptic species that have been recently suggested by a molecular study. Based on these results and according to an exhaustive review of the taxonomic literature, we name each of these four species and provide their taxonomic description alongside a diagnostic key.

Introduction

Species recognition has been revolutionized by the advent of DNA sequence analysis and barcoding [1, 2]. DNA sequences have helped reveal the existence of cryptic species in a wide variety of taxa [3, 4, 5], and in so doing, have drawn attention to the limitations of traditional species recognition based solely on morphological characteristics. To render species delimitations and descriptions more robust, molecular methods are nowadays increasingly combined with morphology, ecology, cross-fertilization data as well as with other sources of information (e.g., behavioural data, biogeography) in the framework of a taxonomical approach coined as integrative taxonomy [6, 7]. However, even when

identified by modern methods, cryptic species often remain taxonomically cryptic [8] because current research practice typically ignores the need of providing a formal description of their diagnostic morphological traits and to suggest a valid taxonomic name. The taxonomic identity of a name is nevertheless fundamental for nomenclatural stability [9, 10, 11]. Unambiguous recognition of cryptic species is further essential for many research purposes, ranging from species diversity inventories and the interpretation of community phylogenetic and biogeographical patterns to the assessment of species' ecological tolerance or evolutionary potential [12], and the set-up of experiments [13]. To this end, reverse taxonomy consists of an approach that largely uses molecular evidence to guide the morphological description of cryptic species [14]. As such, it provides a powerful tool to discover, describe and assign taxonomically valid names to previously unknown species and thus resolve many of the problems associated to taxonomic crypsis [8, 15].

Rotifera is a phylum of microscopic organisms commonly found in inland waters throughout the world [16] and often harbour high levels of cryptic species diversity [17, 18, 19, 20]. Molecular phylogenetics has proven to be a very effective strategy in recognizing evolutionary significant units of diversity of putative species status in rotifers [18, 21]. An illustrative example of the successful deciphering of a rotifer cryptic species complex is the case of the euryhaline *Brachionus plicatilis* Müller, 1786 [17, 19]. By inspecting molecular phylogenies, at least nine divergent lineages were initially recognized in this taxon [17], which then, by using samples from additional geographic regions, were increased to present-day 15 putative species [19]. Boundaries between most of these species were also confirmed by the results of cross-fertilization experiments [22]). By applying modern phylogenetic species delimitation methods (e.g., reviewed in Fontaneto et al., [23]), the species status of these cryptic species was further supported in a recent study [19]. Such molecular evidence combined with morphometric analysis has also been fundamental to the taxonomic description of some of these species [24, 25, 26].

Of all freshwater monogonont rotifers, *Brachionus calyciflorus* Pallas, 1766 is probably the most widely studied in ecology (e.g. [27, 28]), evolutionary biology (e.g. [29, 30, 12]), ecotoxicology (e.g. [31, 32, 33]), and aquaculture (e.g. [34, 35]). Indicative of its importance, *B. calyciflorus* was the first monogonont rotifer of which the genome was published [36]. Nevertheless, its taxonomy remains particularly confused. Since *B. calyciflorus* served as type species for the *Brachionus* genus [37], numerous morphological variants on subspecies and infrasubspecific level have been described (e.g., [38, 39]). This situation has led [40] to express the need for a thorough revision of the taxon and the validation of these numerous variants recorded worldwide in ecological studies (Table A in S1 Text). A lot of the confusion undoubtedly arises from its high phenotypic variability

[37]. Recently, the taxon was suggested to consist of a cryptic species complex [41, 42]. By applying an integrative taxonomy approach, Papakostas et al. [20] coupled the analysis of a large dataset of DNA sequences with morphometric data. The molecular analyses revealed frequent cases of discordant patterns between the mitochondrial cytochrome *c* oxidase subunit I (COI) and nuclear internal transcribed spacer 1 (ITS1) markers, a phenomenon often described as mitonuclear discordance. Combined with microsatellite analysis, the possibility of hybrid introgression between four cryptic species of the *B. calyciflorus* complex, coded as 'A', 'B', 'C', and 'D', was suggested [20]. In light of this evidence, an intriguing observation was that the nuclear marker ITS1 was found to be a more reliable predictor of the species than the mitochondrial marker COI as it explained a much higher proportion of the morphometric variation (71% vs. 36%), with the variation explained by COI being also entirely redundant to that explained by ITS1 [20].

Papakostas et al. [20] mainly studied the morphometry of two of the four species, those coded as 'B' and 'C'. In this study, we aim at comprehensively studying the morphometry and morphology of all four *B. calyciflorus* cryptic species recognized by Papakostas et al. [20]. For this purpose, we collected and cultured additional rotifer clones representing multiple populations for each of the four suggested species. We then measured several morphometric traits under standardized conditions and tested for the existence of morphometric differentiation among each of the four species pairs. We additionally proceeded to an elaborate morphological investigation, which entailed an exhaustive review of the taxonomic literature, comparing the morphology of the groups with previously published descriptions of forms and variants within the taxon. This effort has resulted in the description of two new species, *B. elevatus* sp. nov. and *B. fernandoi* sp. nov., and the redescription of two earlier described taxa, *B. calyciflorus* Pallas, 1766 and *B. dorcas* Gosse, 1851. Furthermore, we provide a key to guide the identification of the species using diagnostic morphological traits. We also provide in the supplementary materials an organized collection of ITS1 sequences available in GenBank that may be used to facilitate identification of each of these species using this particular molecular marker. Altogether, this study resolves the taxonomic identity of a much-studied freshwater monogonont rotifer species complex, it suggests distinct valid names that should be used to refer to each of these species, and provides morphological and genetic resources to facilitate the recognition and thus study of each of these species.

Material and methods

Resting egg collection and clone line establishment

Surficial sediment samples were collected from lakes and ponds in The Netherlands (Table 1). All samples analysed for this study were taken from public waterways in The Netherlands and therefore do not require permission. The field studies did not involve endangered or protected species. *Brachionus* sp. resting eggs were separated using the sugar flotation method [43]. Resting eggs hatched under continuous light in Petri dishes with distilled water. The dishes were checked at 12-hour intervals, and hatchlings were removed when present. Clonal lines were initially established by individually transferring hatched *Brachionus calyciflorus* females from the dishes into wells of a 24-well plate filled with chemostat grown *Chlamydomonas reinhardtii* (1000 μmol C L^{-1}). After clonal lines had established, cultures were upscaled by transferring the populations into 20 mL coulter cups (Beckman Coulter1) with 8 mL of food. These populations served as stock cultures, were maintained at room temperature (22–24˚C) under continuous light and supplied with fresh medium and food every two days. After a few months of growth in the lab, these stock cultures served as the source of individuals for morphometric analysis.

Molecular species identification

To identify the species of the additional clonal cultures used in this study, we employed an extensive database of species-delimited ITS1 unique sequences, called haplotypes, available in Papakostas et al. [20] (Appendix 2: S2 and S3 Tables; available at: http://datadryad.org/ resource/doi:10.5061/dryad.8rc4r). For the sake of continuity, we will henceforth use the term, haplotype, to describe unique sequences of ITS1. DNA was extracted from single rotifers, and the ITS1 region was PCR-amplified as described in Papakostas et al. [20]. Amplicons were then Sanger-sequenced to both primer directions by Macrogen Europe (Amsterdam, The Netherlands), and sequencing chromatograms were aligned and manually inspected with Sequencher 4 (Gene Codes). Double peaks and length variance that may indicate heterozygotes was noted and co-occuring sequences were distinguished as described in Papakostas et al. [20]. ITS1 sequences were then appended to the ITS1 haplotypes of Papakostas et al. [20] (available within the file "1_Alignments.zip" through the Dryad repository: http://datadryad. org/resource/doi:10.5061/dryad.8rc4r), and the whole dataset was re-aligned using the mlocarna function of the LocARNA v. 1.9.1 tool [44] with default settings. The alignment was reduced to contain only the complete ITS1 region and identical sequences, referred to as haplotypes, were recognized with DNAsp v. 5 [45]. Newly sequenced clonal cultures with same ITS1 haplotypes as in Papakostas et al. [20]

were assigned to the species that has been already deduced. For newly discovered haplotypes, a simple delimitation analysis was run using the generalized mixed-Yule coalescent model (GMYC; [46] as described in Papakostas et al. [20]. The species of these new ITS1 haplotypes was that of already analyzed ITS1 haplotypes by Papakostas et al. [20] grouped in the same species category suggested by the GMYC analysis.

Table 1. Overview of the materials used for each of the species described in this study. nuITS1 delimitation: Putative species as suggested by [20]; coordinates are WGS84.

nuITS1 delimitation	Species	Population ID	Clone ID	n	Data origin	Latitude	Longitude	Sampling time
'A'	*B. dorcas*	NL7	J	10	Papakostas et al. [20]	N 51.854065°	E 5.893175°	Jun. 2011
		NL68	C01	13	present study	N 52.083253°	E 4.323353°	Apr. 2016
		NL68	C09	17	present study	N 52.083253°	E 4.323353°	Apr. 2016
		NL68	C10	18	present study	N 52.083253°	E 4.323353°	Apr. 2016
		NL128	C25	17	present study	N 52.640324°	E 4.730287°	Mar. 2014
		NL128	C30	10	present study	N 52.640324°	E 4.730287°	Mar. 2014
		NL129	C21	13	present study	N 52.652613°	E 4.776304°	Mar. 2014
		NL129	C43	13	present study	N 52.652613°	E 4.776304°	Mar. 2014
		NL134	C01	16	present study	N 52.734063°	E 4.883798°	Mar. 2014
		NL134	C02	11	present study	N 52.734063°	E 4.883798°	Mar. 2014
		NL134	C04	13	present study	N 52.734063°	E 4.883798°	Mar. 2014
'B'	*B. elevatus* sp. nov.	NL7	B	19	Papakostas et al. [20]	N 51.854065°	E 5.893175°	Jun. 2011
		NL7	C24	14	present study	N 51.854065°	E 5.893175°	Apr. 2016
		NL7	E	17	Papakostas et al. [20]	N 51.854065°	E 5.893175°	Jun. 2011
		NL7	G	20	Papakostas et al. [20]	N 51.854065°	E 5.893175°	Jun. 2011
		NL67	E	18	Papakostas et al. [20]	N 52.080972°	E 4.313722°	Aug. 2012
		NL69	B	20	Papakostas et al. [20]	N 52.090694°	E 4.338444°	Aug. 2012
		NL69	C25	17	present study	N 52.090694°	E 4.338444°	Apr. 2016
		NL69	D	19	Papakostas et al. [20]	N 52.090694°	E 4.338444°	Aug. 2012
		NL69	G	19	Papakostas et al. [20]	N 52.090694°	E 4.338444°	Aug. 2012
		NL69	H	19	Papakostas et al. [20]	N 52.090694°	E 4.338444°	Aug. 2012
		NL69	K	20	Papakostas et al. [20]	N 52.090694°	E 4.338444°	Aug. 2012
		NL69	L	18	Papakostas et al. [20]	N 52.090694°	E 4.338444°	Aug. 2012
		NL69	M	18	Papakostas et al. [20]	N 52.090694°	E 4.338444°	Aug. 2012
		NL69	R	16	Papakostas et al. [20]	N 52.090694°	E 4.338444°	Aug. 2012
'C'	*B. calyciflorus* s.s.	NL7	C01	20	present study	N 51.854065°	E 5.893175°	Apr. 2016
		NL7	K	12	Papakostas et al. [20]	N 51.854065°	E 5.893175°	Jun. 2011
		NL7	R	2	Papakostas et al. [20]	N 51.854065°	E 5.893175°	Jun. 2011
		NL22	A	17	Papakostas et al. [20]	N 51.985263°	E 5.665691°	Jul. 2012
		NL22	D	20	Papakostas et al. [20]	N 51.985263°	E 5.665691°	Jul. 2012
		NL22	F	19	Papakostas et al. [20]	N 51.985263°	E 5.665691°	Jul. 2012
		NL22	K	14	Papakostas et al. [20]	N 51.985263°	E 5.665691°	Jul. 2012
		NL67	B	14	Papakostas et al. [20]	N 52.080972°	E 4.313722°	Aug. 2012
		NL69	C	12	Papakostas et al. [20]	N 52.090694°	E 4.338444°	Aug. 2012
		NL69	E	14	Papakostas et al. [20]	N 52.090694°	E 4.338444°	Aug. 2012
		NL69	F	4	Papakostas et al. [20]	N 52.090694°	E 4.338444°	Aug. 2012
		NL128	C01	17	present study	N 52.640324°	E 4.730287°	Mar. 2014
		NL168	C01	18	present study	N 51.491438°	E 4.306801°	Mar. 2014
'D'	*B. fernandoi* sp. nov.	NL128	C05	18	present study	N 52.640324°	E 4.730287°	Mar. 2014
		NL128	C06	17	present study	N 52.640324°	E 4.730287°	Mar. 2014
		NL129	C01	7	present study	N 52.652613°	E 4.776304°	Mar. 2014
		NL129	C02	19	present study	N 52.652613°	E 4.776304°	Mar. 2014
		NL129	C42	16	present study	N 52.652613°	E 4.776304°	Mar. 2014
		NL129	C44	16	present study	N 52.652613°	E 4.776304°	Mar. 2014
		NL181	C02	15	present study	N 51.839032°	E 4.144425°	Feb. 2014
		NL181	C03	9	present study	N 51.839032°	E 4.144425°	Feb. 2014
		NL181	C07	8	present study	N 51.839032°	E 4.144425°	Feb. 2014
		NL181	C10	11	present study	N 51.839032°	E 4.144425°	Feb. 2014

Morphometry

Morphometric analysis was performed on formalin-fixed females (4% formalin). The 724 individuals used for the analysis were isolated from 48 clonal cultures (23 of them established by Papakostas et al. [20]). Twenty, whenever possible (range 2–20 Table 1), randomly picked individuals from each clonal culture were examined under a LeitzLaborlux S optical microscope. Microphotographs for each individual were taken with an adjusted camera Canon Power shot A650 IS, and morphometric measurements were obtained using ImageJ [47]. A total of 19 lorica dimensions (Fig 1) were measured based on Fu et al. [48], Ciroz-Perez et al. [24], Proios et al. [49], and Michaloudi et al. [26] with additional measurements made on the anterodorsal and anteroventral side. Two measurements of the anterodorsal side, namely 'd' and 'f', were not included in the further analysis due to high distortion of the placement of the anterior spines during preservation. All the rotifer microphotographs analyzed for Papakostas et al. [20] are available within the file "9_Rotifer_microphotographs.zip" through the Dryad repository: http://dx.doi.org/10.5061/dryad.8rc4r. All the additional rotifer microphotographs analysed for the present study are publicly available via the online Dryad repository (accession link: http://datadryad.org/review?doi=doi:10.5061/dryad.4ng70).

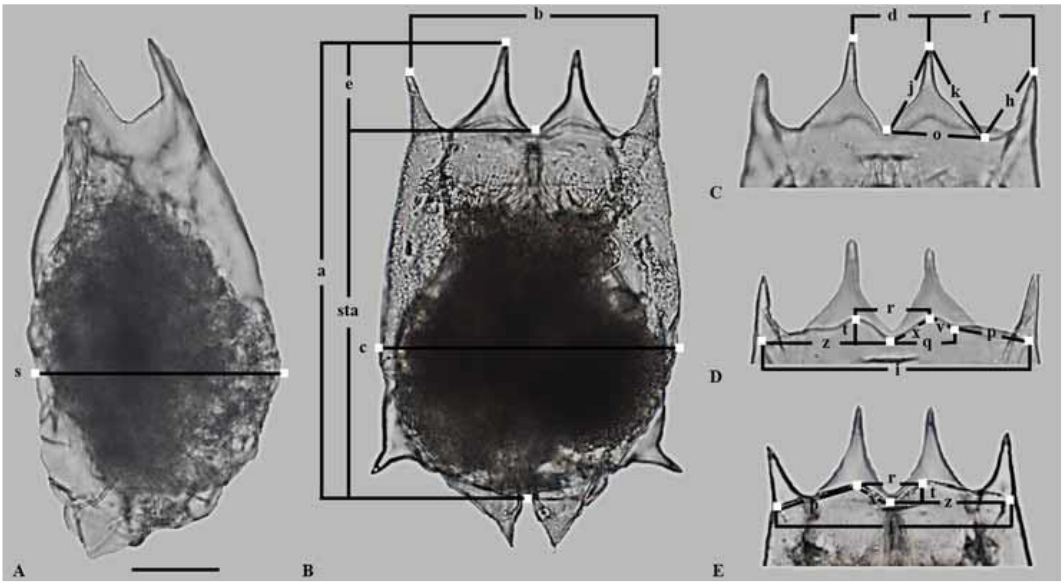

Fig 1. Microphotographs of a Brachionus calyciflorus individual. A and B show the major lorica dimensions measured, C the dimensions measured of the anterodorsal margin, D and E the dimensions measured of the anteroventral margin.

Taxonomy

In order to investigate the taxonomic status of *B. calyciflorus* variants since its description (1766) a literature review was conducted until 2016 using Google scholar search engine and the following synonyms as keywords i.e. "*Arthracanthus biremis*", "*Arthracanthus quadriremis*", "*Anuraea palea"*, "*Anuraea divaricata"*, "*Brachionus calyciflorus borgerti*", "*Brachionus calyciflorus amphiceros*", "*Brachionus calyciflorus anuraeiformis*", "*Brachionus calyciflorus calyciflorus*" "*Brachionus calyciflorus dorcas*", "*Brachionus calyciflorus giganteus*", "*Brachionus calyciflorus spinosus*", "*Brachionus decipiens*", "*Brachionus margoi*", "*Brachionus pala*", "*Brachionus pala mucronatus*", "*Brachionus palea*" and "*Brachionus pentacanthus*". Only studies indicating the existence of at least one of the above species in a zooplankton community was included. In the cases where the same dataset was included in more than one articles, all the articles were included. 'Grey' literature (i.e. conference proceedings, theses) was avoided when there was a peer-reviewed published source. For each case, when possible, we provide the specific name of the species, the country, and the area, lake or river in which it was recorded together with the reference source (Table A in S1 Text).

All taxonomic information provided (i.e. spelling, authors names, synomys) in the text have been verified with the List of Available Names [9, 50] and the Rotifer World Catalog [51].

Nomenclatural acts

The electronic edition of this article conforms to the requirements of the amended International Code of Zoological Nomenclature (ICZN), and hence the new names contained herein are available under that Code from the electronic edition of this article. This published work and the nomenclatural acts it contains have been registered in ZooBank, the online registration system for the ICZN. The ZooBank LSIDs (Life Science Identifiers) can be resolved and the associated information viewed through any standard web browser by appending the LSID to the prefix "http://zoobank.org/". The LSID for this publication is: urn:lsid:zoobank.org:pub: 73FED4F9-11F0-43C0-9AD0-8D4C14CAE1D3. The electronic edition of this work was published in a journal with an ISSN, and has been archived and is available from the following digital repositories: PubMed Central, LOCKSS.

Scanning Electron Microscopy (SEM)

Full-body. Environmental scanning electron microscopy (ESEM) was applied to each clone using custom modified Quanta 650 FEG microscope equipped with and a non-commercial high-efficiency detector for low dose imaging [52]. Rotifers of each clone were pipped into 5 μL drop of distilled water to clean their surface prior the observation. Live animals were individually transferred on a cooling Peltier stage in the microscope and observed using the Low Temperature Method for ESEM (LTM) [53] that was originally developed for the study of plant samples [54] and optimised for the samples of the present study. Additional purging process of water vapour was applied during LTM to ensure higher relative humidity in a specimen chamber of the ESEM to prevent a sample collapse before its low temperature stabilisation. Samples were observed under following conditions: temperature of the cooling stage was -20˚C, air pressure in the ESEM specimen chamber was 200 Pa, beam energy of 10 keV and beam current bellow 20 pA.

Trophi. Trophi SEM stub mounts were prepared for clones of each of the four species based on the methodology described by De Smet [55]. Five 50 μL beads of distilled water were pipetted onto a glass slide. A total of six individual rotifers were pipetted into the first 50 μL drop of distilled water, and 10 μL of domestic bleach (3% sodium hypochlorite solution) was added. Animals were observed under a dissecting microscope. Once all trophi had been expelled from the lorica, they were pipetted between the remaining four 50 μL beads of distilled water. Each individual trophi was finally picked up in 1 μL of distilled water and pipetted onto a round coverslip of 12 mm diameter. The pipette tip was changed after each transfer. Once all of the trophi had been transferred, they were left on the bench to dry. Once desiccated, the round coverslip was stuck to a SEM stub that had been prepared with an adhesive tape; the sample was then sputter coated with gold using Agar Sputter Coater. Photographs were taken by JSM-6300 Scanning Electron Microscope.

Statistical analysis

We applied principal components analysis (PCA) to explore for systematic morphometric differences among the hypothetical species. Redundancy analysis (RDA) was then used to formally test for statistical differences among species. Furthermore, to identify which combinations of morphometric traits discriminate best between species we applied stepwise discriminant function analysis (DFA). Applying DFA on all four species revealed a particularly strong differentiation between species ‘A’ and the other three species, potentially overwhelming differences among the species ‘B’, ‘C’, and ‘D’; thus in order to discriminate the rest of the species as well DFA was applied on two different datasets: (a) including

data of all four species and (b) including only the data of species ‘B’, ‘C’ and ‘D’. To account for the unequal representation of species in the dataset, the weight of species was adjusted according to prior probabilities. To assess the robustness of the DFA model, we applied the leave-one-out cross-validation approach. Finally, for each of the individual morphometric variables, we tested for the significance of differences among the four species using ANOVA combined with Turkey post hoc test.

Data were standardized prior to PCA, RDA and DFA statistical analysis and log(x+1) transformed prior to ANOVA. RDA and ANOVA were performed on clonal averages to avoid inflated type I error whereas PCA and DFA were based on data of individual rotifers. PCA and RDA were performed using the function *rda* of the package “vegan” [56] in R. DFA and ANOVA were performed using IBM SPSS Statistics 22 [57].

Results

Molecular species identification

All clonal cultures used in this study were categorized to one of the four *B. calyciflorus* species previously recognized in Papakostas et al. [20], and no evidence for a new species was found (Table 1; supplementary material of [20]). All but one of the newly generated ITS1 sequences were identical to one of the ITS1 haplotypes previously reported by Papakostas et al. [20] (supplementary material of [20]), which suggests that a large portion of the ITS1 polymorphism has been already covered for the studied geographic region. Only four genotypes were heterozygotes for ITS1 (supplementary material of [20]). Newly generated ITS1 sequences were submitted to GenBank (accession numbers: MF776636-MF776664), while ITS1 alignment, sequencing information and other information relevant to the species delimitation are freely available via the online Dryad repository (accession link: http://datadryad.org/review?doi= doi:10.5061/dryad.4ng70).

Morphometry

Principal Components analysis positioned the clones into separate clusters that corresponded well with the species delimitation as suggested by Papakostas et al. [20] (Fig 2). The first two axes represented 72.41% (PC1 57.67%, PC2 14.74%) of the total observed variation. According to RDA, the factor ‘species’ explained 53% of the total morphometric variation (F: 16.861; $P < 0.001$). Additional tests showed significant differences among each pair of species with R2- values ranging between 19 and 55% (S1 Table).

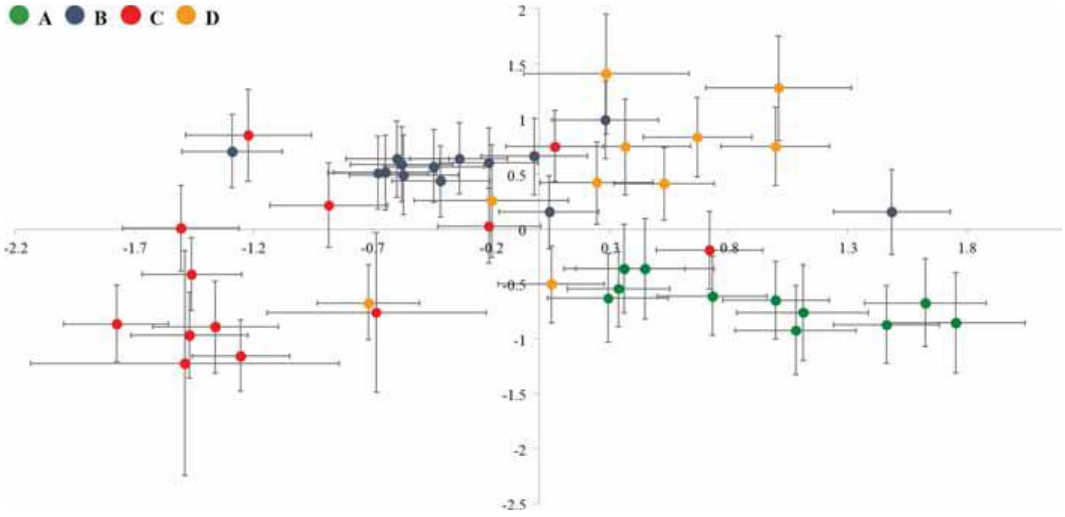

Fig 2. Analysis of the association between molecular species delimitation and morphometry. Representation of sample score averages of each of the studied clones along the first two axes (axis x: PC1, axis y: PC2) of the principal components analysis (PC1 explained 57.67% and PC2 explained 14.74% of the recorded variation) performed on standardized morphometric data. Error bars represent variation between individuals of the same clone (twice the standard error of the mean).

The range of the dimensions measured for the four species is shown in S2 Table. In agreement with the RDA analysis, most of the variables showed statistically significant differences among the four groups, despite a large overlap in values (Table 2, S2 Table). Tables 3 and 4 show the results of the discriminant analysis. When applied to all four species Classification Function I accounted for 58.5% of the total variance (Table 3) and clearly distinguished the species previously reported as 'A' from the rest of the species (Fig 3A). The variables weighing the most in this function were traits from the anteroventral margin, namely 'q', 'v', 'r' and 'i', traits representing overall body size (i.e. standard length 'sta' and width 'c'), and the length of the anterodorsal spines 'h' and 'k' (Table 3). Species 'B', 'C' and 'D' were separated from each other when DFA was applied to these three species only (Fig 3B). In this case Classification Function I accounted for 57.2% of the total variance (Table 4) and distinguished species 'B' from species 'C' and 'D'. The variable weighting the most in this function were traits from the anteroventral margin, namely 'q' and 'v' and body width 'c'. Classification Function II accounted for 42.8% (Table 4) of the variance and mainly differentiated between species 'C' and 'D' (Fig 3B). The variable weighting the most in this function was the distance of the lateralanterodorsal spines 'b' and the width of the medial sinus of the anteroventral margin 'r'. Cross-validation of the individuals' classification based on the classification functions (S3 and S4 Tables) of the discriminant analysis correctly identified 96% of 'A' species, 95.7% of 'B' species, 90.7% of 'C' species and 88.2% of 'D' species individuals, suggesting that the identification of species based on morphometric variables might be possible with reasonable success.

Table 2. Results of ANOVA and Turkey post-hoc test for differences in lorica traits between the four species of the B. calyciflorus cryptic species complex.

	Bonferroni post-hoc test				ANOVA		
Measurement	'A'	'B'	'C'	'D'	df	F	*p*
s	a	b	c	a	3	138.13	<0.0001
c	a	b	c	d	3	143.38	<0.0001
e	a	b	c	b	3	223.68	<0.0001
b	a	b	bd	d	3	72.27	<0.0001
o	a	b	b	d	3	54.18	<0.0001
h	a	b	b	d	3	76.44	<0.0001
k	a	b	c	d	3	187.06	<0.0001
j	a	b	c	b	3	217.83	<0.0001
t	a	b	c	a	3	135.89	<0.0001
i	a	b	c	d	3	142.75	<0.0001
p	a	b	c	bc	3	109.86	<0.0001
v	bd	b	c	d	3	28.49	<0.0001
x	a	b	c	d	3	146.10	<0.0001
z	a	b	c	d	3	152.93	<0.0001
q	a	a	c	a	3	72.76	<0.0001
r	a	b	c	d	3	128.70	<0.0001
sta	a	b	c	a	3	83.39	<0.0001

The redundancy and discriminant function analyses provide robust formal statistical support for the existence of four different morphometric groups that correspond strongly to the evolutionary units as proposed by Papakostas et al. [20]. Our detailed morphological investigation confirms these conclusions and results in the redescription of two formerly described species, *B. calyciflorus* Pallas, 1766 and *B. dorcas* Gosse, 1851, and the description of two new species, *B. elevatus* sp. nov. and *B. fernandoi* sp. nov. These species correspond to the evolutionary units that were revealed by Papakostas et al. [20] based on nuITSI sequence data: species 'A': *B. dorcas*; species 'B': *B. elevatus* sp. nov.; species 'C': *B. calyciflorus* sensu stricto (s.s.); species 'D': *B. fernandoi* sp. nov.

Redescription of Brachionus calyciflorus s.s. Pallas, 1766

Taxonomy. Class: Eurotatoria De Ridder, 1957

Subclass: Monogononta Plate, 1889

Superorder: Pseudotrocha Kutikova, 1970

Order: Ploima Hudson & Gosse, 1886

Family: Brachionidae Ehrenberg, 1838

Brachionus calyciflorus Pallas, 1766

Brachionus calyciflorus Pallas 1766 [58], p. 96,

Brachionus palea, Ehrenberg 1830 [59], p. 68,

Anuraea palea, Ehrenberg 1830 [59], p.68

Brachionus amphiceros, Ehrenberg 1838 [60], p. 511, pl 63, Fig 2

Brachionus calyciflorus var. *amphiceros*, Ehrenberg 1838 [60]

Brachionus pala, Ehrenberg 1838 [60], p. 511, pl 63, Fig 1, pl 50, Fig 2

Anuraea divaricata, Weisse 1845 [61], p. 142, pl 2, Fig 13–14

Arthracanthus biremis, Schmarda 1854 [62], p. 22, pl 6, Fig 5

Arthracanthus quadriremis, Schmarda 1854 [62], p.12, pl 5, Fig 1

Brachionus margoi, Daday 1883 [63], p. 290

Brachionus decipiens, Plate 1886 [64], p 73

Brachionus pentacanthus, France 1894 [65], p. 172, pl 5, Figs 3 and 4

Brachionus pala anuraeiformis, Brehm 1909 [66], p. 308, Fig 1

Brachionus calyciflorus f. *anuraeiformis*, Brehm 1909 [66], p. 210, text-Fig

Brachionus pala mucronatus, Spandl 1922 [67], p. 275, text-Fig.

Etymology. The name ‘calyciflorus’ originates from the latin words ‘calyx’ (originally coming from the greek ‘κάλυξ’) and ‘flos’ meaning flower. Probably it was used due to the resemblage of *B. calyciflorus* to the shape of a flower-calyx.

Material examined. A total of 183 individuals were examined coming from 13 clones established from resting eggs collected in 6 water bodies from The Netherlands (Table 1). Permanent glycerin glass slide mounts, each containing a single specimen, were prepared according to Jersabek et al. [68], and deposited in the Frank J. Myers collection at the Academy of Natural Sciences in Philadelphia (ANSP) with catalogue numbers ANSP [2100–2104]. Based on the literature review (S1 Text) and the information available in the List Available Names (LAN) [9, 50] we conclude that no type material of *B. calyciflorus* is available. Following the guidelines of ICZN, since we are dealing with a species complex, we decided to designate a specific slide as neotype.

Table 3. Stepwise discriminant analysis based on the morphometric data of species ‘A’, ‘B’, ‘C’ and ‘D’ of the B. calyciflorus species complex.

	Function 1		Function 2		Function 3	
Measurement	Coefficient	Correlation	Coefficient	Correlation	Coefficient	Correlation
s	-.488	.102	-.202	.050	.622	.646
c	.912	.290	.485	.133	-.650	.497
e	.364	.401	.186	.054	.238	.506
b	.165	.235	-.492	-.219	-.577	.292
o	-.269	.200	-.104	-.112	-.410	.278
h	-.884	.152	-.498	-.097	.093	.424
k	.564	.344	-.216	-.061	.387	.557
j	.454	.402	.345	.051	-.099	.493
t	-.113	.024	.429	.443	-.476	-.012
i	.819	.302	-.276	.007	-.448	.570
p	.526	.240	.897	-.181	.579	.212
v	-1.346	.026	-.785	.102	.713	.158
x	-.264	-.041	.457	.437	.091	.498
z	-.199	.299	-.745	.017	.500	.607
q	1.871	.082	1.858	.252	-.298	.197
r	-.813	-.097	.419	.324	.566	.592
sta	-.810	.133	-.286	-.005	.470	.568
Eigenvalue	4.291		1.794		1.248	
% variance	58.5		24.5		17.0	

Table 4. Stepwise discriminant analysis based on the morphometric data of species ‘B’, ‘C’ and ‘D’ of the B. calyciflorus species complex.

	Function 1		Function 2	
Measurement	Coefficient	Correlation	Coefficient	Correlation
s	.650	.118	.695	.544
c	-1.127	-.097	-.657	.398
e*		-.054		.328
b	.035	.167	-.829	.060
o	.102	.086	-.281	.114
h	.918	.140	.136	.249
k*		.080		.299
j	-.792	-.087	.198	.333
t	-.499	-.389	-.129	.213
i*		.047		.407
p*		.121		-.019
v	2.093	-.044	-.104	.162
x	-.072	-.187	.261	.643
z*		.026		.400
q	-2.293	-.174	.063	.248
r	.229	-.036	.803	.684
sta	.794	.122	.411	.429
Eigenvalue	2.247		1.683	
% variance	57.2		42.8	

Neotype: A parthenogenetic female in a permanent glycerin glass with catalogue number [2100]

Description. The original description of *B. calyciflorus* [58] lacks details. More recent authors [38, 30] describing a typical form of *B. calyciflorus* indicated a great variation in the morphology of the antero-dorsal spines. Of all the material examined in the present study and Papakostas et al. [20], species ‘C’ also exhibited the greatest variation in the morphology of the antero-dorsal spines (Fig 4) and was also characterized by the undulated anteroventral margin that is also mentioned by Koste [38] and Kutikova and Fernando [39]. Thus, species ‘C’ was identified as *B. calyciflorus*.

Parthenogenetic female: Lorica saccate soft and ovoid- shaped with a smooth surface (Figs 4–6). Anterior dorsal margin with four spines, two on each side of a U-shaped sinus (Figs 4– 6). All spines are triangular with a wide base and relatively sharp apices. The anterior ventral margin is smooth with a medial sinus (Figs 4–6). Foot aperture sub-terminal on the ventral surface of the lorica between two triangular protrusions. Three antennae are present: one found in the U-shaped sinus between the medial anterodorsal spines when the coronal disc is extended, and two others on either lateral side of the lorica at the posterior part of the animal length.

Trophi: Malleate type (Fig 7) bearing the characteristics of the genus as described by Segers et al. [69]. Fulcrum short and hollow. Rami asymmetrical. Unci with four or five teeth decreasing in size from the ventral one. Subuncus brush-like. Manubria are triangular in shape, rounded at the external sickle-shaped margin, flattened and slightly bend at their distal end.

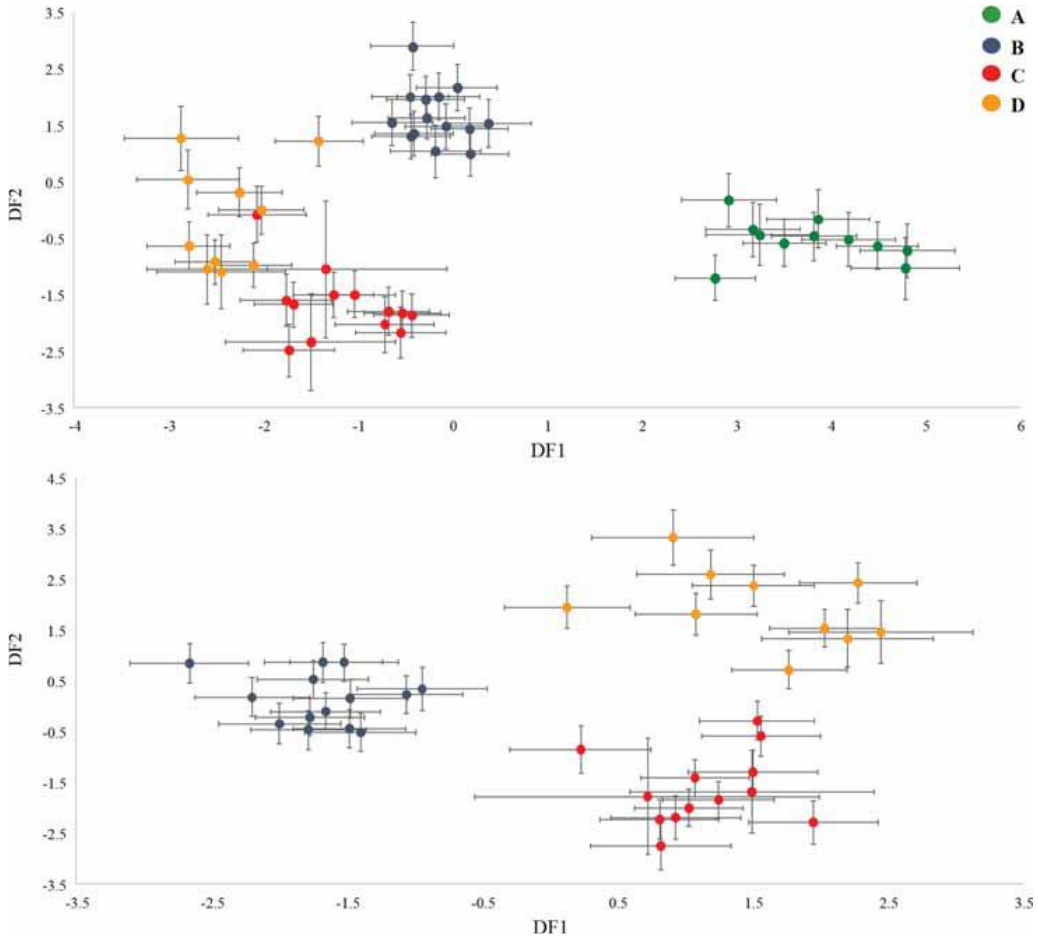

Fig 3. Analysis of the association between molecular species delimitation and morphometry. Scatterplot showing the discrimination of species groups based on the canonical discriminant functions of the discriminant analysis performed on all measured individuals of the studied clones (upper) for species ‘A’, ‘B’, ‘C’, ‘D’ and (lower) for species ‘B’, ‘C’, ‘D’. Error bars represent variation between individuals of the same clone (twice the standard error of the mean).

Comments. Kutikova and Fernando [39] in their analysis of the *Brachionus calyciflorus* Pallas, 1766 variations referred to the typical form as the 'd' form. Their depiction of the anteroventral side is not of great accuracy, although the undulated anteroventral margin with only a median notch is depicted. As for the anterodorsal side, the same extent of variation can be seen as the one described in the present study. This can be identified with species 'C' as suggested by the molecular analysis of this study and of Papakostas et al. [20]. A genotype of *B. calyciflorus* s.s. was used as material for the whole genome sequencing by [36].

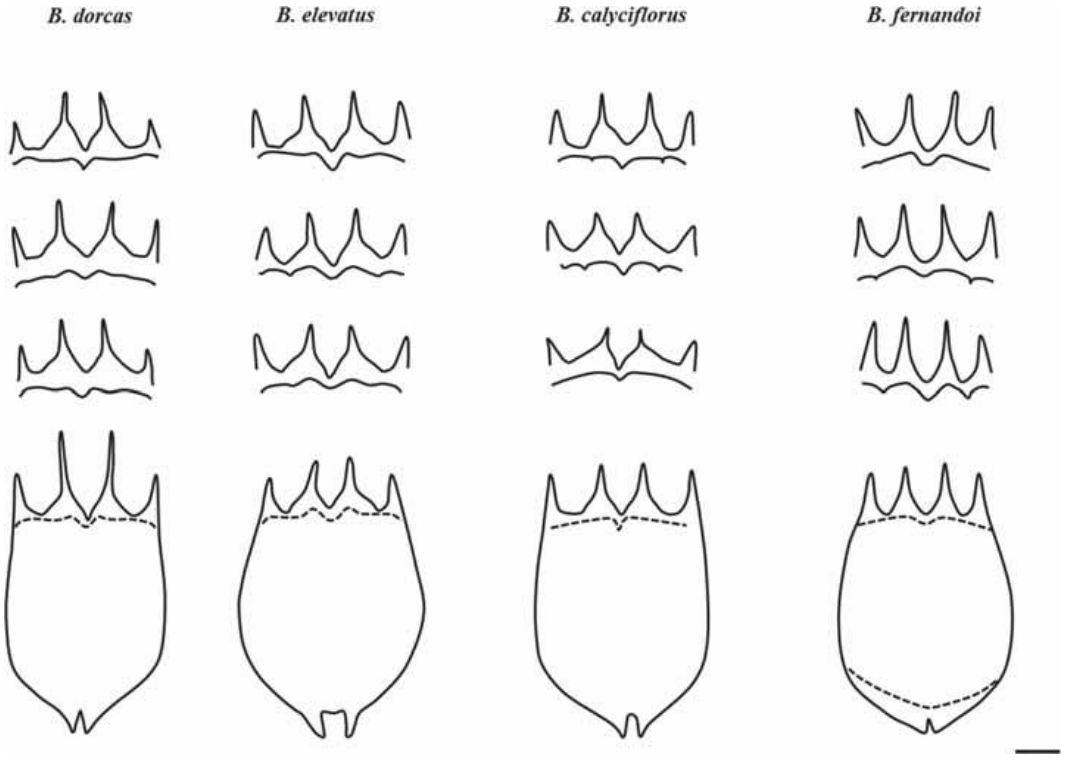

Fig 4. Line drawings of the main variations of the anterodorsal and anteroventral sides encountered for B. dorcas, B. elevatus sp. nov., B. calyciflorus s.s. and B. fernandoi sp. nov.

Distribution-Habitat. *Brachionus calyciflorus* s.s. has a cosmopolitan distribution. Based on the material analysed the present study confirms morphologically and genetically its Palearctic distribution. Relating our species with the typical form of Kutikova & Fernando [39] its Tropical, Oriental and Australian distribution is also confirmed, while it also has a Nearctic distribution (Table A in S1 Text).

It is an euplanctonic species found in freshwater pools, ponds, lakes, and reservoirs, ditches and paddy fields; also in potamoplankton, river estuaries, coastal brackish and marine waters; prefers eu- to hypertrophic waters, circum-neutral to slightly alkaline conditions, tolerates low oxygen [51].

Redescription of Brachionus dorcas Gosse, 1851

Taxonomy. Class: Eurotatoria De Ridder, 1957

Subclass: Monogononta Plate, 1889

Superorder: Pseudotrocha Kutikova, 1970

Order: Ploima Hudson & Gosse, 1886

Family: Brachionidae Ehrenberg, 1838

Brachionus dorcas Gosse, 1851

Brachionus dorcas Gosse 1851 [70], p. 203,

Brachionus calyciflorus dorcas, Gosse 1851 [70], p. 203

Brachionus dorcas spinosus, Wierzejski 1891 [71], p. 52, Fig 4

Etymology. The name 'dorcas' comes from the Greek word 'δορκάς' which is an antelope. Its use refers to the middle anterodorsal spines which resembled the horns of an antelope according to the description made by Gosse [70] '*Lorica ovate or subconical; occipital edge with four long slender spines, the middle pair curving forwards, and bent first from, and then towards, each other, like horns of an antelope; mental edge undulated, with a notch in the centre'*

Material examined. A total of 151 individuals were examined coming from 11 clones established from resting eggs collected in 5 water bodies in The Netherlands (Table 1). Permanent glycerin glass slide mounts (voucher specimens), each containing a single specimen, were prepared according to Jersabek et al. [68], and deposited in the Frank J. Myers collection at the Academy of Natural Sciences in Philadelphia (ANSP) with catalogue numbers ANSP [2105–2110].

Based on the literature review (S1 Text) and the information available in the LAN [9, 50] we conclude that no type material of *B. calyciflorus* is available. Following the guidelines of ICZN, since we are dealing with a species complex, we decided to designate a specific slide as neotype. Neotype: A parthenogenetic female in a permanent glycerin glass with catalogue number [2105]

Description. Of all the examined material Clones 7J and C02NL134 were identified as the *B. dorcas* Gosse, 1851 first described by Gosse [70] due to its biggest median anterodorsal spines; thus the following description is based on those individuals.

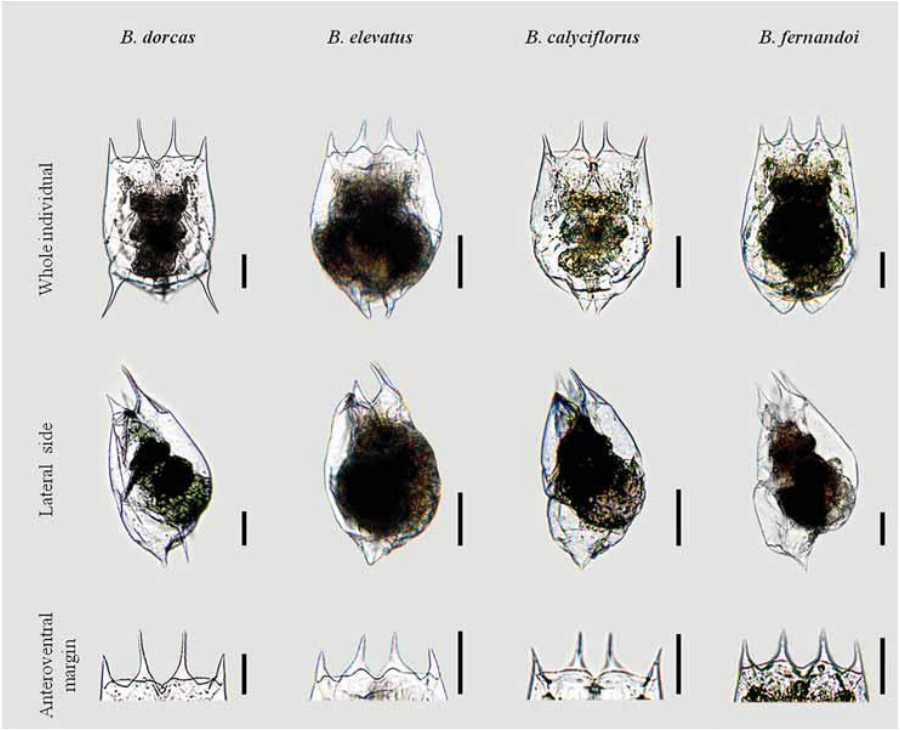

Fig 5. Photomicrographs of B. calyciflorus s.s., B. dorcas, B. elevatus sp. nov., B. fernandoi sp. nov. Whole individual, Lateral side, Anteroventral margin.

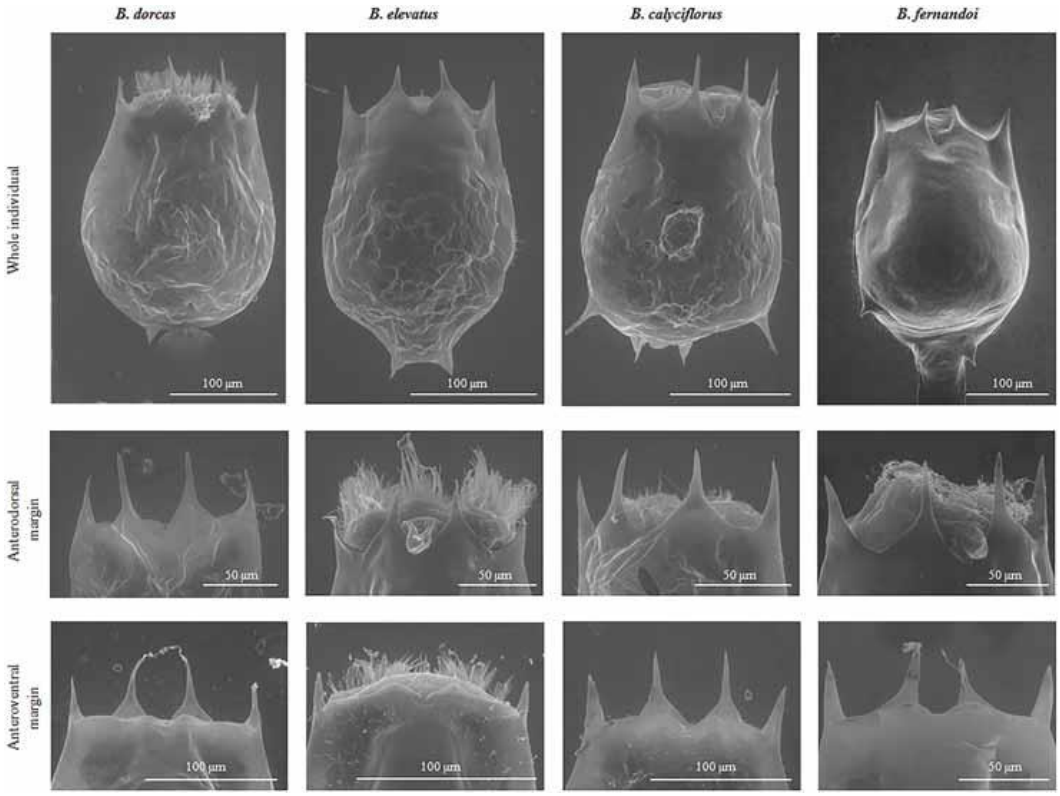

Fig 6. Scanning electron micrographs of B. calyciflorus s.s., B. dorcas, B. elevatus sp. nov., B. fernandoi sp. nov. Whole individual, Anterodorsal margin, Anteroventral margin.

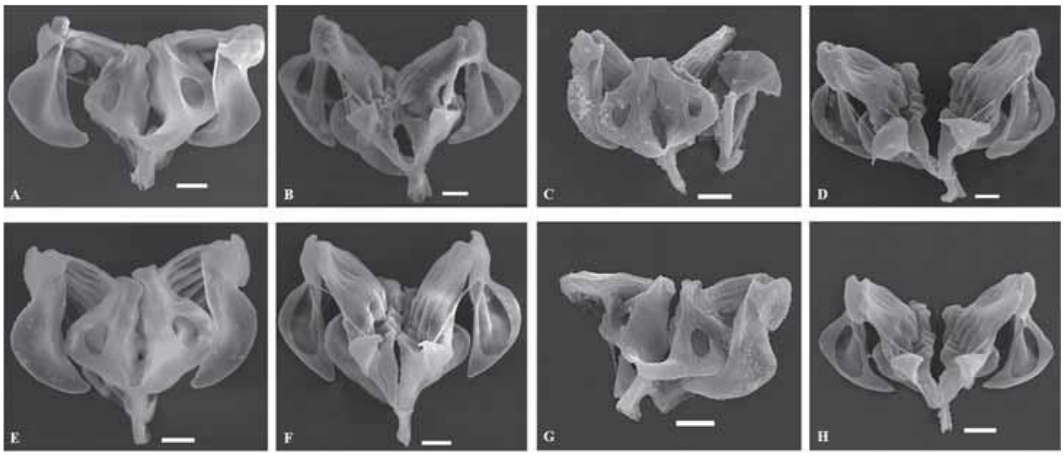

Fig 7. Scanning electron micrographs of the trophi dorsal and ventral view for B. dorcas (A, B), B. elevatus sp. nov. (C, D), B. calyciflorus s.s. (E, F) and B. fernandoi sp. nov. (G, H).

Parthenogenetic female: Lorica saccate soft and ovoid- shaped with smooth surface (Figs 4–6). Anterior dorsal margin with four spines, two on each side of a V-shaped sinus (Figs 4–6). All spines are triangular with a wide base and relatively sharp apices. Median spines are longer compared to the lateral spines. The anterior ventral margin has a wave-like shape on each side of a medial sinus (Figs 4–6). No lateral notches exist. Foot aperture sub-terminal on the ventral surface of the lorica between two triangular protrusions. Three antennae are present: one found in the Vshaped sinus between the medial anterodorsal spines when the coronal disc is extended, and two others on either lateral side of the lorica slightly posterior to the midpoint of the animal length.

Trophi: Malleate type (Fig 7) bearing the characteristics of the genus as described by Segers et al. [69]. Fulcrum short and hollow. Rami asymmetrical. Unci with four or five teeth decreasing in size from the ventral one. Subuncus brush-like. Manubria are triangular, pointed at the external sickle-shaped margin, flattened and bend at their distal end.

Comments. The discriminating factor of the individuals of *Brachionus dorcas* is related to the anterodorsal spines, and specifically the fact that the median spines were much longer compared to the other groups. This character is among the ones used by Koste [38] to describe the *Brachionus calyciflorus* variation *dorcas*. Nevertheless, *Brachionus dorcas* was initially described by Gosse [70] at the species level. Its description can be identified as a match with species ‘A’ of the present study and the study of Papakostas et al. [20]. The results of the present analysis along with the analysis presented by Papakostas et al. [20] justify the establishment of *Brachionus dorcas* as a valid species.

Distribution-Habitat. *Brachionus dorcas* has a Palearctic distribution confirmed genetically and morphologically by the material analysed the present study. It is also known to have a Tropical, Oriental and Australian distribution (Table A in S1 Text).

It is an euplanktonic species found in freshwater pools, ponds, tanks, lakes and reservoirs, ditches and paddy fields; also in potamoplankton, river estuaries, coastal, brackish and marine waters; prefers eu- to hypertrophic waters, circum-neutral to slightly alkaline conditions, tolerates low oxygen; eurytherm but prefers warm waters (Table A in S1 Text).

Description of Brachionus elevatus sp.nov

urn:lsid:zoobank.org:act:624FD96E-9566-4D38-A5CB-86F75649B349

Taxonomy. Class: Eurotatoria De Ridder, 1957

Subclass: Monogononta Plate, 1889

Superorder: Pseudotrocha Kutikova, 1970

Order: Ploima Hudson & Gosse, 1886

Family: Brachionidae Ehrenberg, 1838

Brachionus elevates

Etymology. The name *elevatus* refers to the elevation of the anteroventral margin right before the median notch. It comes form the Latin elevatus, past participle of elevare "lift up, raise".

Type locality. Shallow eutrophic city pond close to city center of The Hague (The Netherlands); N 52.090694˚; E 4.338444˚

Material examined. A total of 254 individuals were examined coming from 14 clones established from resting eggs collected in 3 water bodies from The Netherlands (Table 1).

Of all the clones examined clones 69H and C04NL7 has been chosen to formally describe *Brachionus elevatus* sp. nov. Permanent glycerin glass slide mounts, each containing a single specimen, were prepared according to Jersabek et al. [68], and deposited in the Frank J. Myers collection at the Academy of Natural Sciences in Philadelphia (ANSP).

Holotype: A parthenogenetic female in a permanent glycerin glass slide with catalogue number ANSP [2111].

Paratypes: A total of 9 slides with catalogue number ANSP [2112–2120].

Description. Parthenogenetic female: Lorica saccate soft and ovoid- shaped with a smooth surface (Figs 4–6). Anterior dorsal margin with four spines, two on each side of a Vshaped sinus (Figs 4–6). All spines are triangular with a wide base and relatively sharp apices. The anterior ventral margin has a wave-like shape on each side of a medial sinus (Figs 4–6). The medial sinus is elevated with a well-marked median notch between short oval or nearly triangular protuberances. No lateral notches exist. Foot aperture sub-terminal on the ventral surface of the lorica between two triangular protrusions. Three antennae are present: one found in the V-shaped sinus between the medial anterodorsal spines when the coronal disc is extended, and two others on either lateral side of the lorica slightly posterior to the widest point of the lorica.

Trophi: Malleate type (Fig 7) bearing the characteristics of the genus as described by Segers et al. [69]. Fulcrum short and hollow. Rami asymmetrical. Unci with four or five teeth decreasing in size from the ventral one. Subuncus brush-like. Manubria are more similar in shape with the ones of *B. calyciflorus* with rounded external margin flattened and slightly bend at their distal end.

Comments. In the present study, the anteroventral structure with the marked protuberances of the medial sinus discriminated the individuals of the *Brachionus elevatus* from the individuals of the *B. calyciflorus* s.s. Kutikova & Fernando [39] based on this characteristic describe their ‘b’ form as being intermediate between *Brachionus calyciflorus borgerti* Apstein, 1907 and the typical form in the sense that the ‘b’ form lacks the saw-like basal tooth in the median spines of the anterodorsal margin of *Brachionus calyciflorus borgerti* although they have a broad base. They also hypothesize that this intermediate form might be a hybrid. Based on the analysis of Papakostas et al. [20] and the present study, this hypothesis can be rejected.

Distribution-Habitat. *Brachionus elevatus* sp. nov. has a Palearctic distribution confirmed genetically and morphologically by the material analysed in the present study. Relating the species described in the present study with the ‘b’ form described by Kutikova & Fernando [39] *B. elevatus* sp. nov. can be considered to have an Oriental distribution as well. It is found in freshwater habitats and it is an euplanktonic species.

Description of Brachionus fernandoi sp.nov

urn:lsid:zoobank.org:act:0A4F5205-47ED-47ED-4C72-9686-0E33E0F34DA3

Taxonomy. Class: Eurotatoria De Ridder, 1957

Subclass: Monogononta Plate, 1889

Superorder: Pseudotrocha Kutikova, 1970

Order: Ploima Hudson & Gosse, 1886

Family: Brachionidae Ehrenberg, 1838

Brachionus fernandoi

Etymology. The species is named after dr. C. H. Fernando for his contribution to the description of the *Brachionus calyciflorus* variations in the paper Kutikova & Fernando [39].

Type locality

Eutrophic ditch within residential area, near the town of Hellevoetsluis (The Netherlands); N 51.839032˚; E 4.144425˚

Material examined. A total of 136 individuals were examined coming from 10 clones established from resting eggs collected in 3 water bodies from the Netherlands (Table 1).

Of all the clones examined C02NL181 has been chosen to formally describe *Brachionus fernandoi* sp. nov. Permanent glycerin glass slide mounts, each containing a single specimen, were prepared according to Jersabek et al. [68], and deposited in the Frank J. Myers collection at the Academy of Natural Sciences in Philadelphia (ANSP).

Holotype: A parthenogenetic female in a permanent glycerin glass slide with catalogue number ANSP [2121].

Paratypes: A total of 4 slides with catalogue number ANSP [2122–2125].

Description. Parthenogenetic female: Lorica saccate soft and ovoid- shaped with a smooth surface (Figs 4–6). Anterior dorsal margin with four spines, two on each side of a Ushaped sinus (Figs 4–6). All spines are triangular with a wide base and relatively sharp apices. The anterior ventral margin is smooth with a wide medial

sinus (Figs 4–6). Foot aperture subterminal on the ventral surface of the lorica between two triangular protrusions of varying length. This posterior ventral part is swollen. Three antennae are present: one found in the Ushaped sinus between the medial anterodorsal spines when the coronal disc is extended, and two others on either lateral side of the lorica slightly posterior to the midpoint of the lorica's length.

Trophi: Malleate type (Fig 7) bearing the characteristics of the genus as described by Segers et al. [69]. Fulcrum short and hollow. Rami asymmetrical. Unci with four or five teeth decreasing in size from the ventral one. Subuncus brush-like. Manubria more similar in shape with *B. dorcas*, are triangular, pointed at the external sickle-shaped margin, flattened and bend at their distal end.

Comments. Based on the forms described by Kutikova & Fernando [39] *Brachionus fernandoi* sp. nov. seems to resemble the 'c' form they describe. They mention '*a very swollen posterior part of the dorsal plate*'. In our opinion, the posterior ventral part is swollen giving the impression of the swollen dorsal part. This can be identified as a match with species 'D' of the present study and the study of Papakostas et al. [20].

Distribution-Habitat. *Brachionus fernandoi* sp. nov. has a Palearctic distribution confirmed genetically and morphologically by the material analysed in the present study. Relating the species described in the present study with the 'c' form described by Kutikova & Fernando [39] then *B. fernandoi* sp. nov. can be considered to have an Oriental distribution as well. It is found in freshwater habitats, and it is an euplanktonic species.

Differential diagnosis

The morphology of the anteroventral margin appears to be a powerful trait. This margin is characterized by a wave-like shape in *B. dorcas* and *B. elevatus* sp. nov. whereas in *B. calyciflorus* s.s. and *B. fernandoi* sp. nov. it is mainly completely smooth. This latter character though exhibits a lot of variation (Fig 5).

Brachionus dorcas is discriminated from the other three species based on the size of the anterodorsal spines. *B. dorcas* has much longer median anterodorsal spines compared to the other species. This was the case for all three dimensions measured concerning this characteristic; *B. dorcas*: e (range 43.84–92.62 μm), k (range 52.41–86.21 μm) and j (range 46.32– 98.38 μm), *B. calyciflorus* s.s. e (range 25.17–69.82 μm), k (range 31.14–68.89 μm) and j (range 25.15–74.05 μm), *B. elevatus* sp. nov. e (range 29.54–74.2 μm), k (range 32.77–73.83 μm) and j (range 33.17–75.56

μm). *B. fernandoi* sp. nov. e (range 34.62–72.31 μm), k (range 40.77– 70.96 μm) and j (range 38.07–73.77 μm) (S2 Table).

B. elevatus sp. nov. is characterized by the fact that the medial sinus is elevated with a wellmarked median notch between short oval or nearly triangular protuberances. Further discrimination between *B. dorcas* and *B. elevatus* sp. nov. is based on a combination of traits. In the case of *Brachionus dorcas* the depth of the anterodorsal medial sinus 'e' is usually > 60 μm and the width of the anteroventral medial sinus is smaller than 1/5 of the distance of the lateral anterodorsal spines (i.e., r/b < 0.20). The dimensions measured concerning these characteristics for *B. dorcas* and *B. elevatus* sp. nov. are: *B. dorcas* e (range 43.84–92.62 μm, mean 67.16), r/b (range 0.102–0.253, mean 0.187), *B. elevatus* sp. nov. e (range 29.54–74.2 μm, mean 49.82), r/b (range 0.164–0.424, mean 0.254) (S2 Table).

Brachionus fernandoi sp. nov. compared to *B. elevatus* sp. nov. has no protrusion right before the median sinus of the anteroventral margin which is smooth with no lobes being formed by intermediate notches. The morphological trait that discriminates *B. fernandoi* sp. nov. from *B. calyciflorus* s.s. is the opening of the median sinus of the anterovental margin which has the biggest opening; r range 21.33–45.50 *B. fernandoi* sp. nov., 14.75–40.66 *B. dorcas*, 13.47– 38.25 *B. calyciflorus*, 15.95–49.17 *B. elevatus* sp. nov. Additionally, *B. fernandoi* sp. nov. has a narrower anteroventral opening 'i', while *B. calyciflorus* s.s. has a wider anterodorsal side 'b'.

Key to the identification of the four species of the Brachionus calyciflorus species complex.

1. - Wave-like anteroventral margin. 2

- Anterovental margin either smooth or with notches 3

2. - Median anterodorsal spines longer than lateral anterodorsal spines . .. .

... . ….... . .. .*Brachionus dorcas*

- Anterodorsal spines of more or less equal length; anteroventral margin with an elevation right before the medial sinus .. ..*Brachionus elevatus* sp. nov

3. - Width of the anteroventral medial sinus > 30 μm and more than 1/5 the lorica width (i.e. r/c ratio > 0.2) . . ..*Brachionus fernandoi* sp. nov.

- Width of the anteroventral medial sinus <30 μm and less than 1/5 the lorica width (i.e. r/c ratio < 0.2) . . ..*Brachionus calyciflorus* s.s.

Based on the above key as well as the discriminating characters we performed a blind test on 20 individuals randomly selected from the 724 individuals analysed. Only two cases were misidentified. This 10% of misidentified cases is close to the results of the DFA where in total 91% of the cases where correctly classified.

Discussion

By applying the approach of reverse taxonomy [14], we confirmed the existence of four putative species as predicted by Papakostas et al. [20] based on molecular species delimitation techniques. Indeed, a morphometric analysis of 724 individuals from 48 different clones originating from 10 Dutch water bodies, revealed a clear differentiation among each of the four species pairs. Also, by combining a morphological analysis with an exhaustive literature survey, we were able to link the four species to previously described forms.

Our study highlights specific morphological traits that were found to be particularly useful for the distinction between species of the *B. calyciflorus* species complex. This was especially the case for features of the anteroventral side. Such features have long been suspected a strong diagnostic character for the genus *Brachionus* [37]. Our results thus confirmed the notion by Kutikova and Fernando [39] that aspects of both the anterodorsal and anteroventral side may be useful diagnostic characters for differentiating among *B. calyciflorus* forms. Similarly, these traits were proven valuable for the discrimination between *B. asplanchnoidis* Charin, 1947 and other members of the *B. plicatilis* species complex [26].

Conversely, the presence and size of posterolateral spines proved of little taxonomic value. Historically, these traits have been used to describe certain forms of *Brachionus calyciflorus* (i.e., *B. calyciflorus* f. *anuraeiformis* and *B. calyciflorus* f. *amphiceros* [38, 60, 72]). From our analysis, it was evident that lateral spines cannot be used as a taxonomic character because the frequency of occurrence (ranging within clones between 0 to 100%) as well as the length of these spines varied strongly among clones that belonged to the same species or even among individuals from the same clone. Besides, it is well documented that the lateral spines are the result of exogenous factors, such as predation or food concentration [73, 74, 75, 76]. Thus, the morphological forms that have been previously assigned based on the presence of lateral spines have no taxonomic validity [9].

The validity and applicability of our suggested diagnostic traits still need verification using field samples. Given that the prime objective of this study was to test the hypothesis of four morphospecies as suggested by molecular methods, we excluded as much as possible phenotypic variation associated to environmental variability by culturing the investigated individuals under standardized laboratory

conditions. Whereas this may have strongly increased our ability to differentiate among species it precludes variation resulting from phenotypic plasticity in response to environmental variability under natural conditions. We thus recognize that discrimination of individuals collected from the field may prove less straightforward than suggested by our analyses [26]. For example, in the case of *B. plicatilis* Müller, 1786, morphological identifications based upon individuals raised under laboratory conditions [24] have proven to be inadequate for field studies in some cases [17, 77]. Although our diagnostic traits seemed to provide good resolution to distinguish between the four species of the *B. calycilforus* complex, we anticipate that future research will clarify the extent to which this may be true for field samples.

Another point of consideration when interpreting our conclusions is related to the restricted geographic distribution of our studied samples. In our experimental design, we tried to incorporate interpopulation genetic variation by investigating multiple clones from different populations per species. Such approach prevents that the results of morphometric analyses are contingent on particular genotypes or populations and as such guarantees robustness and generality of reported differences among species. However, all investigated populations originated from a relatively restricted geographic area (i.e., the territory of The Netherlands). Consequently, the morphological and morphometric variation reported in this study may constitute an underrepresentation of what exists for each of the species throughout their biogeographic range. Although this may limit the generality of the diagnostic traits suggested for species identification, this does not disqualify our conclusion that systematic differences between species exist.

Future work should also clarify how hybrid introgression among the species of the *B. calyciflorus* complex impacts morphology. Papakostas et al. [20] provided strong evidence for hybrid formation and introgression among the species of the *B. calyciflorus* complex. However, this has not prevented us from finding clear morphometric differences between the species. Kutikova and Fernando [39] described forms of *B. calyciflorus* that correspond to some of the species described in this work. They also reported the existence of cases with intermediate features and hypothezised them to be the result of hybridization. Investigating how gene flow among species would affect morphometric traits may thus represent an intriguing topic of research to be done.

Supporting information

S1 Text. Records of *Brachionus calyciflorus* synonyms. (DOCX)

S1 Table. Amount of morphometric variation explained by species identity for each pair of the investigated species. (DOCX)

S2 Table. Summary statistics for the selection of morphometric traits measured on individuals of the four species. (DOCX)

S3 Table. Classification functions of the stepwise discriminant analysis performed on species ‘A’, ‘B’, ‘C’, and ‘D’. (DOCX)

S4 Table. Classification functions of the stepwise discriminant analysis performed on species ‘B’, ‘C’, and ‘D’. (DOCX)

Acknowledgments

We cordially thank Dr. Petr Jan Juračka for establishing the first contacts between some of the involved research groups and his initial help with the transportation of samples. We gratefully acknowledge D. Fontaneto whose valuable suggestions were extremely helpful to finally shape the manuscript.

Author Contributions

Conceptualization: Evangelia Michaloudi, Spiros Papakostas, Steven A. J. Declerck.

Data curation: Evangelia Michaloudi, Spiros Papakostas, Steven A. J. Declerck.

Formal analysis: Evangelia Michaloudi, Spiros Papakostas, Georgia Stamou, Wei Zhang, Steven A. J. Declerck.

Funding acquisition: Spiros Papakostas, Vilém Neděla, Steven A. J. Declerck.

Investigation: Spiros Papakostas, Georgia Stamou, Vilém Neděla, Eva Tihlaříková, Wei Zhang.

Methodology: Evangelia Michaloudi, Vilém Neděla, Eva Tihlaříková, Steven A. J. Declerck.

Project administration: Evangelia Michaloudi, Steven A. J. Declerck.

Resources: Evangelia Michaloudi, Spiros Papakostas, Vilém Neděla, Eva Tihlaříková, Wei Zhang, Steven A. J. Declerck.

Supervision: Evangelia Michaloudi, Steven A. J. Declerck.

Validation: Evangelia Michaloudi, Georgia Stamou.

Visualization: Evangelia Michaloudi, Spiros Papakostas, Georgia Stamou, Vilém Neděla, Eva Tihlaříková, Steven A. J. Declerck.

Writing – original draft: Evangelia Michaloudi, Spiros Papakostas, Georgia Stamou, Vilém Neděla, Eva Tihlaříková, Wei Zhang, Steven A. J. Declerck.

Writing – review & editing: Evangelia Michaloudi, Spiros Papakostas, Georgia Stamou, Vilém Neděla, Eva Tihlaříková, Wei Zhang, Steven A. J. Declerck.

References

1. Hajibabaei M, Singer GAC, Hebert PDN, Hickey DA. DNA barcoding: how it complements taxonomy, molecular phylogenetics and population genetics. Trends Genet. 2007; 23(4):167–72. https://doi.org/10.1016/j.tig.2007.02.001 PMID: 17316886

2. Taylor HR, Harris WE. An emergent science on the brink of irrelevance: a review of the past 8 years of DNA barcoding. Mol Ecol Resour. 2012; 12(3):377–388. https://doi.org/10.1111/j.1755-0998.2012. 03119.x PMID: 22356472

3. Knowlton N. Sibling species in the sea. Annu Rev Ecol Evol Syst. 1993; 24(1):189–216.

4. Bickford D, Lohman DJ, Navjot SS, Ng PKL, Meier R, Winker K, et al. Cryptic species as a window on diversity and conservation. Trends Ecol Evol. 2007; 22: 148–155. https://doi.org/10.1016/j.tree.2006.11.004 PMID: 17129636

5. Scheffers BR, Joppa LN, Pimm SL, Laurance WF. What we know and don't know about Earth's missing biodiversity. Trends Ecol Evol. 2012; 27(9):501–510. https://doi.org/10.1016/j.tree.2012.05.008 PMID: 22784409

6. Padial JM, Miralles A, De la Riva I, Vences M. The integrative future of taxonomy. Front Zool. 2010; 7:16. https://doi.org/10.1186/1742-9994-7-16 PMID: 20500846

7. Schlick-Steiner BC, Steiner FM, Seifert B, Stauffer C, Christian E, Crozier RH. Integrative taxonomy: a multisource approach to exploring

biodiversity. Annu Rev Entomol. 2010; 55:421–438. https://doi.org/ 10.1146/annurev-ento-112408-085432 PMID: 19737081

8. Schlick-Steiner BC, Seifert B, Stauffer C, Christian E, Crozier RH. Without morphology, cryptic species stay in taxonomic crypsis following discovery. Trends Ecol Evol. 2007; 22(8): 391–392. https://doi.org 10.1016/j.tree.2007.05.004 PMID: 17573150

9. Segers H, Smet WHD, Fischer C, Fontaneto D, Michaloudi E, Wallace RL, et al. Towards a list of available names in zoology, partim Phylum Rotifera. Zootaxa. 2012; 3179(1):61–68.

10. Cianferoni F, Bartolozzi L. Warning: potential problems for taxonomy on the horizon? Zootaxa. 2016; 4139(1):128–130. https://doi.org/10.11646/zootaxa.4139.1.8 PMID: 27470790

11. Santos CMD, Amorim DS, Klassa B, Fachin DA, Nihei SS, Carvalho CJB, et al. On typeless species and the perils of fast taxonomy. Syst Entomol. 2016; 41(3):511–515.

12. Declerck SAJ, Malo AR, Diehl S, Waasdorp D, Lemmen KD, Proios K, et al. Rapid adaptation of herbivore consumers to nutrient limitation: eco-evolutionary feedbacks to population demography and resource control. Ecol Lett. 2015; 18(6):553–562. https://doi.org/10.1111/ele.12436 PMID: 25913306

13. Declerck SAJ, Papakostas S. Monogonont rotifers as model systems for the study of micro-evolutionary adaptation and its eco-evolutionary implications. Hydrobiologia. 2017; 796(1):131–144.

14. Markmann M, Tautz D. Reverse taxonomy: an approach towards determining the diversity of meiobenthic organisms based on ribosomal RNA signature sequences. Philosophical Transactions of the Royal Society of London B: Biological Sciences. 2005; 360(1462):1917–1924. https://doi.org/10.1098/ rstb.2005.1723 PMID: 16214749

15. Pante E, Schoelinck C, Puillandre N. From Integrative Taxonomy to Species Description: One Step Beyond. Syst Biol. 2015; 64(1):152–60. https://doi.org/10.1093/sysbio/syu083 PMID: 25358968

16. Wallace RL, Snell TW, Ricci C, Nogrady T. Rotifera. 1, biology, ecology and systematics. (2nd ed.). Ghent/Leiden: Kenobi Productions/ Backhuys Publishers; 2006

17. Gómez A, Serra M, Carvalho GR, Lunt DH. speciation in ancient cryptic species complexes: evidence from the molecular phylogeny of *Brachionus Plicatilis* (Rotifera). Evolution. 2002; 56(7):1431–1444. PMID: 12206243

18. Fontaneto D, Kaya M, Herniou EA, Barraclough TG. Extreme levels of hidden diversity in microscopic animals (Rotifera) revealed by DNA taxonomy. Mol Phylogenet Evol. 2009; 53(1):182–189. https://doi.org/10.1016/j.ympev.2009.04.011 PMID: 19398026

19. Mills S, Alcántara-Rodríguez JA, Ciros-Pérez J, Gómez A, Hagiwara A, Galindo KH, et al. Mills S, Alcántara-Rodríguez JA, Ciros-Pérez J, Gómez A, Hagiwara A, Galindo KH, et al. Fifteen species in one: deciphering the *Brachionus plicatilis* species complex (Rotifera, Monogononta) through DNA taxonomy. Hydrobiologia. 2017; 796(1):39–58.

20. Papakostas S, Michaloudi E, Proios K, Brehm M, Verhage L, Rota J, et al. Integrative taxonomy recognizes evolutionary units despite widespread mitonuclear discordance: evidence from a rotifer cryptic species complex. Syst Biol. 2016; 65(3):508–524. https://doi.org/10.1093/sysbio/syw016 PMID: 26880148

21. Fontaneto D. Molecular phylogenies as a tool to understand diversity in rotifers. Internat Rev Hydrobiol. 2014; 99(1–2):178–187.

22. Suatoni E, Vicario S, Rice S, Snell T, Caccone A. An analysis of species boundaries and biogeographic patterns in a cryptic species complex: The rotifer–Brachionus plicatilis. Mol Phylogenet Evol. 2006; 41 (1):86–98. https://doi.org/10.1016/j.ympev.2006.04.025 PMID: 16815046

23. Fontaneto D, Flot J-F, Tang CQ. Guidelines for DNA taxonomy, with a focus on the meiofauna. Mar Biodiv. 2015; 45(3):433–451.

24. Ciros-Pérez J, Gómez A, Serra M. On the taxonomy of three sympatric sibling species of the Brachionus plicatilis (Rotifera) complex from Spain, with the description of *B. ibericus* n. sp. J Plankton Res. 2001; 23(12):1311–1328.

25. Fontaneto D, Giordani I, Melone G, Serra M. Disentangling the morphological stasis in two rotifer species of the *Brachionus plicatilis* species complex. Hydrobiologia. 2007; 583(1):297–307.

26. Michaloudi E, Mills S, Papakostas S, Stelzer C-P, Triantafyllidis A, Kappas I, et al. Morphological and taxonomic demarcation of *Brachionus*

asplanchnoidis Charin within the *Brachionus plicatilis* cryptic species complex (Rotifera, Monogononta). Hydrobiologia. 2017; 796(1):19–37.

27. Gilbert JJ. Competition between Rotifers and Daphnia. Ecology. 1985; 66(6):1943–1950.

28. Guo R, Snell TW, Yang J. Ecological strategy of rotifer *Brachionus calyciflorus* exposed to predatorand competitor-conditioned media. Hydrobiologia. 2011; 658(1):163–171.

29. Becks L, Agrawal AF. The Evolution of Sex Is Favoured During Adaptation to New Environments. PLoS Biol. 2012; 10(5):e1001317. https://doi.org/10.1371/journal.pbio.1001317 PMID: 22563299

30. Scheuerl T, Stelzer C-P. Patterns and dynamics of rapid local adaptation and sex in varying habitat types in rotifers. Ecol Evol. 2013; 3(12):4253–4264. https://doi.org/10.1002/ece3.781 PMID: 24324875

31. Snell TW, Moffat BD. A 2-d Life cycle test with the rotifer Brachionus calyciflorus. Environ Toxicol Chem. 1992; 11(9):1249–1257.

32. Cruciani V, Iovine C, Thomé J-P, Joaquim-Justo C. Impact of three phthalate esters on the sexual reproduction of the Monogonont rotifer, *Brachionus calyciflorus*. Ecotoxicology. 2016; 25(1):192–200. https://doi.org/10.1007/s10646-015-1579-5 PMID: 26666431

33. Han J, Kim D-H, Kim H-S, Kim H-J, Declerck SAJ, Hagiwara A, et al. Genome-wide identification of 31 cytochrome P450 (CYP) genes in the freshwater rotifer Brachionus calyciflorus and analysis of their benzo[α]pyrene-induced expression patterns. Comp Biochem Physiol Part D Genomics Proteomics. 2018; 25:26–33. https://doi.org/10.1016/j.cbd.2017.10.003 PMID: 29126086

34. Lim LC, Wong CC. Use of the rotifer, *Brachionus calyciflorus* Pallas, in freshwater ornamental fish larviculture. Hydrobiologia. 1997; 358(1–3):269–273.

35. Shiri Harzevili A, De Charleroy D, Auwerx J, Vught I, Van Slycken J, Dhert P, et al. Larval rearing of burbot (*Lota lota* L.) using *Brachionus calyciflorus* rotifer as starter food. J Appl Ichthyol. 2003; 19(2):84–7.

36. Kim H-S, Lee B-Y, Han J, Jeong C-B, Hwang D-S, Lee M-C, et al. The genome of the freshwater monogonont rotifer Brachionus calyciflorus. Mol

Ecol Resour. 2018; 18:646–655. https://doi.org/10.1111/1755-0998.12768 PMID: 29451365

37. Ahlstrom EH. A revision of the rotatorian genera Brachionus and Platyias with descriptions of one new species and two new varieties. Bulletin of the American Museum of Natural History. 1940; 77:143–184.

38. Koste W. Rotatoria, die Rãdertiere Mitteleuropas. Berlin: Gebru¨der Borntraeger; 1978.

39. Kutikova LA, Fernando CH. *Brachionus calyciflorus* Pallas (Rotatoria) in Inland Waters of Tropical Latitudes. Int Revue ges Hydrobiol Hydrogr. 1995; 80(3):429–41.

40. Segers H. Annotated checklist of the rotifers (Phylum Rotifera), with notes on nomenclature, taxonomy and distribution. Zootaxa. 2007; 1564: 1–104.

41. Gilbert JJ, Walsh EJ. *Brachionus calyciflorus* is a species complex: mating behavior and genetic differentiationamong four geographically isolated strains. Hydrobiologia. 2005; 546(1):257–65.

42. Xiang X, Xi Y, Wen X, Zhang G, Wang J, Hu K. Patterns and processes in the genetic differentiation of the *Brachionus calyciflorus* complex, a passively dispersing freshwater zooplankton. Mol Phylogenet Evol. 2011; 59(2):386–98. https://doi.org/10.1016/j.ympev.2011.02.011 PMID: 21335094

43. Gomez A, Carvalho GR. Sex, parthenogenesis and genetic structure of rotifers: microsatellite analysis of contemporary and resting egg bank populations. Mol Ecol. 2000; 9:203–214. PMID: 10672164

44. Will S, Joshi T, Hofacker IL, Stadler PF, Backofen R. LocARNAP: Accurate boundary prediction and improved detection of structural RNAs. RNA. 2012; 18:900–914. https://doi.org/10.1261/rna.029041. 111 PMID: 22450757

45. Librado P, Rozas J. DnaSP v5: a software for comprehensive analysis of DNA polymorphism data. Bioinformatics. 2009; 25:1451–1452. https://doi.org/10.1093/bioinformatics/btp187 PMID: 19346325

46. Pons J, Barraclough TG, Gomez-Zurita J, Cardoso A, Duran DP, Hazell S, et al. Sequencebased species delimitation for the DNA taxonomy of undescribed insects. Syst Biol. 2006; 55:595–609. PMID: 16967577

47. Abramoff MD, Magalhaes PJ, Ram SJ. Image processing with ImageJ. Biophotonics International. 2004; 11:36–42.

48. Fu Y, Hirayama K, Natsukari Y. Morphological differences between two types of the rotifer *Brachionus plicatilis* O.F. Móller J. Exp. Mar. Biol. Ecol. 1991; 151:29–41.

49. Proios K, Michaloudi E, Papakostas S, Kappas I, Vasileiadou K, Abatzopoulos TJ. Updating the description and taxonomic status of *Brachionus sessilis* Varga, 1951 (Rotifera: Brachionidae) based on detailed morphological analysis and molecular data. Zootaxa. 2014; 3873:345–370. https://doi.org/10. 11646/zootaxa.3873.4.2 PMID: 25544227

50. International Commission on Zoological Nomenclature [Cited 2018 June]. Available from http://iczn.org/lan/rotifer.hausdernatur.at/

51. Jersabek CD, Leitner MF. The Rotifer World Catalog. World Wide Web electronic publication; 2013 [Cited 2017 December]. Available from http://www.rotifera.hausdernatur.at/

52. Neděla V, Tihlaříková E, Runštuk J, Hudec J. High-efficiency detector of secondary and backscattered electrons for low-dose imaging in the ESEM, Ultramicroscopy. 2018; 184:1–11.

53. Neděla V, Tihlaříková E, Hřib J. The Low-Temperature Method for Study of Coniferous Tissues in the Environmental Scanning Electron Microscope. Microscopy Research Technique. 2015; 78:13–21. https://doi.org/10.1002/jemt.22439 PMID: 25242151

54. Dorđević B, Neděla V, Tihlaříková E, Trojan V, Havel V. Effects of copper and arsenic stress on the development of Norway spruce somatic embryos and their visualization with the environmental scanning electron microscope. 2018; https://doi.org/10.1016/j.nbt.2018.05.005

55. De Smet WH. Preparation of rotifer trophi for light and scanning electron microscopy. Hydrobiologia. 1998; 387/388:117–121

56. Oksanen J, Blanchet FG, Kindt R, Legendre P, Minchin PR, O'Hara RB, et al. 2015. Vegan: Community Ecology Package. R package version 2.3–2. Vienna, Austria: R Foundation for Statistical Computing. Available from: URL http://CRAN.R-project.org/package=vegan

57. IBM Corp. Released 2012. IBM SPSS Statistics for Windows, Version 21.0. Armonk, NY: IBM Corp.

58. Pallas PS. Elenchus zoophytorum, sistens generum adumbrationes generaliores et specierum cognitarum succintas descriptiones: cum selectis auctorum synonymis. Frankfort: Hagae-comitum; 1766.

59. Ehrenberg CG. Organisation, Systematik und geographisches Verha¨ ltnis der Infusionsthierchen. Zwei Vorträge in der Akademie der Wissenschaften zu Berlin gehalten in den Jahren 1828 [Die geographische Verbreitung der Infusionsthierchen in Nord-Afrika und West-Asien, beobachtet auf Hemprich und Ehrenbergs Reisen] und 1830 [Beiträge zur Kenntnis der Organisation der Infusorien und ihrer geographischen Verbreitung, besonders in Sibirien]. Berlin: Druckerei der koniglichen Akademie der Wissenschaften; 1830.

60. Ehrenberg CG. Die Infusionsthierchen als vollkommene Organismen. Ein Blick in das tiefere organische Leben der Natur. Leipzig: Verlag von Leopold Voss; 1838.

61. Weisse JF. Beschreibung einiger neuer Infusorien, welche in stehendenWässern bei St. Petersburg vorkommen. Bulletin de la Classe Physico-Mathe´matique de l'Académie Impériale des Sciences de St.-Pétersbourg. 1845; 4:138–143.

62. Schmarda LK. Zur NaturgeschichteÄ gyptens. Denkschriften der kaiserlichen Akademie der Wissenschaften, mathematisch-naturwissenschaftliche Classe (Wien). 1854; 7/2:1–28.

63. Daday E. Neue Beiträge zur Kenntnis der Rädertiere. Mathematische und Naturwissenschaftliche Berichte aus Ungarn. 1883; 1:261–264.

64. Plate L. Beiträge zur Naturgeschichte der Rotatorien. Jenaische Zeitschrift fur Naturwissenschaft. 1886; 19:1–120.

65. France RH. Beiträge zur Kenntnis der Rotatorienfauna Budapest's. Természetrajzi Fuzetek kiadja a Magyar nemzeti Múzeum. 1894; 17:166–184.

66. Brehm V.U ber die Mikrofauna chinesischer und sudasiatischer Susswasserbecken. Arch Hydrobiol. 1909; 4:207–224.

67. Spandl H. *Brachionus pala* Ehrbg. var. *mucronatus* nov. var. Zool Anz.1922; 54: 275.

68. Jersabek CD, Bolortsetseg E. Mongolian rotifers (Rotifera, Monogononta)– a checklist with annotations on global distribution and autecology. Proceeding of the Academy of Natural Sciences of Philadephia 2010; 159:119–168.

69. Segers H, Murugan G, Dumont HJ. On the taxonomy of the Brachionidae: description of *Plationus* n. gen. (Rotifera, Monogononta). Hydrobiologia. 1993; 268(1):1–8.

70. Gosse PH. A catalogue of Rotifera found in Britain; with descriptions of five new genera and thirty-two new species. Annals and Magazine of Natural History. 1851; 8:197–203.

71. Wierzejski A. Liste de rotifères observes en Galicie (Autriche-Hongrie). Bulletin de la Société zoologique de France. 1891; 16:49–52.

72. Koste W, Shiel RJ. Rotifera from Australian inland waters. II. Epiphanidae and Brachionidae (Rotifera: Monogononta). Invert Systematics. 1987; 1(7):949–1021.

73. Gilbert JJ, Waage JK. *Asplanchna*, *Asplanchna*-substance, and posterolateral spine length variation of the rotifer *Brachionus calyciflorus* in a natural environment. Ecology. 1967; 48(6):1027–31.

74. Gilbert JJ. Further observations on developmental polymorphism and its evolution in the rotifer *Brachionus calyciflorus*. Freshw Biol. 1980; 10(3):281–94.

75. Stemberger RS. Food limitation. spination, and reproduction in Brachionus calyciflorus. Limnol Oceanogr. 1990; 35(1):33–44.

76. Gilbert JJ. Spine development in two taxa of *Brachionus calyciflorus* from Lake Littra, Australia: constitutive and induced defenses against *Asplanchna*. J Plankton Res. 2017; 39(6):962–71.

77. Papakostas S, Michaloudi E, Triantafyllidis A, Kappas I, Abatzopoulos TJ. Allochronic divergence and clonal succession: two microevolutionary processes sculpturing population structure of Brachionus rotifers. Hydrobiologia. 2013; 700(1):33–45.

18 In-situ preparation of plant samples in ESEM for energy dispersive x-ray microanalysis and repetitive observation in SEM and ESEM

Eva Tihlaříková[1], Vilém Neděla[1] & Biljana Đorđević[2]

1 Institute of Scientific Instruments of the Czech Academy of Sciences, Brno, 612 00, Czech Republic.

2 Department of Plant Biology, Mendel University in Brno, Brno, 613 00, Czech Republic.

Abstract

The Extended Low Temperature Method (ELTM) for the *in-situ* preparation of plant samples in an environmental scanning electron microscope enables carrying out repetitive topographical and material analysis at a higher resolution in the vacuum conditions of a scanning electron microscope or in the low gas pressure conditions of an environmental scanning electron microscope. The method does not require any chemical intervention and is thus suitable for imaging delicate structures rarely observable with common treatment methods. The method enables both sample stabilization as close to their native state as possible, as well as the transfer of the same sample from a low vacuum to an atmospheric condition for sample storage or later study. It is impossible for wet samples in the environmental scanning electron microscope. Our studies illustrate the high applicability of the ELTM for different types of plant tissue, from imaging of plant waxes at higher resolution, the morphological study of highly susceptible early somatic embryos to the elemental microanalysis of root cells. The method established here provides a very fast, universal and inexpensive solution for plant sample treatment usable in a commercial environmental scanning electron microscope equipped with a cooling Peltier stage.

Introduction

The scanning electron microscope (SEM) has become a routine technique for the morphological study of a wide range of samples with a resolution up to nanometres; however most plant samples require at least dehydration prior to observation. Therefore, many techniques and methods for the preparation of biological samples have been developed but none of them are universally applicable and artefact-free[1]. In general, samples can be studied after removing or changing the liquids from the samples using various techniques[2], after application of special chemical treatment[3], in their frozen hydrated state (CryoSEM, Low Temperature SEM)[4], or in their fresh

and fully hydrated state in the environmental scanning electron microscope (ESEM)[5,6].

Especially in plant samples, processing a specimen with common preparation techniques can cause different types of artificial changes in the structure arising from chemical fixation, the removal of water and the extraction of soluble components during chemical fixation and drying via solvents. Moreover, structural features of plants can cause a problem with common preparation protocols. The external surface of most plant tissue is protected by a highly water- and chemical-resistant cuticle and the tough cell wall act as a barrier to reagents, and frequently dissection is needed to allow chemical treatment[7]. Cross-linking of the cell wall during the fixation process is less effective due to low protein content so the mechanical strength of the tissue is removed and samples are easily damaged in handling[1]. The classic preparation method based on using fixatives, dehydration with organic solvents and critical point drying is not suitable for wax observation that is dissolved[1].

Currently, a very popular technique for electron microscopy of biological samples is a Low Temperature SEM (LTSEM) or a CryoSEM, which allows the preservation and recording of biological samples in a fully hydrated and chemically unmodified state. These techniques involve the study of samples at temperatures between −100 °C to −175 °C. The preparation of frozen-hydrated samples involves following the operational phases: cryofixation, freeze-drying of fracturing and, if necessary, also coating[8]. The LTSEM/CryoSEM is demanding in terms of the specific hardware composed of cryo-preparation equipment and an SEM specimen stage cooled with liquid nitrogen. Although most artefacts characteristic for a dry specimen were eliminated, the LTSEM/Cryo SEM has its own specific artefacts arising from the behaviour of the water during cryofixation, freeze drying and specimen transfer[9]. A comparison of the ability of a low temperature method for ESEM (LTM), the CryoSEM and optical microscopy to image the early somatic embryo surface microstructure covered with a very fine extracellular matrix has been published[10].

The direct study of fully hydrated or electrically non-conductive dry biological samples, without the necessity of covering their surface with a conductive layer is also possible in a high-pressure environment in the ESEM[11,12]. Observation of fully hydrated biological samples in the ESEM can be limited with a lower resolution in comparison with the SEM and low feasibility for additional analysis or repetitive imaging due to their collapse during or after observation. Moreover, susceptible biological samples which need to be fully hydrated tend to be easily damaged due to the influence of free radicals, local heating and drying[13].

In order to eliminate problems associated with the observation of wet samples, The LTM for ESEM has been developed[13]. This method has been used in the study of plant samples in many studies[14–16]. Recently, it has also been successfully applied in the study of small animals[17]. The LTM for ESEM is based on the low temperature stabilization of a sample using a mutual combination of optimized speeds of gas pumping and sample cooling up to a temperature of −20 °C and pressure of 200 Pa of water vapour instead of the observation of hydrated samples in ESEM (temperature usually from 0 °C to 5 °C and water vapour pressure from 613 Pa to 866 Pa). The low temperature stabilisation of samples benefits from the assumption that the liquid solution inside the sample is unaffected due to its differential pressure contrary to the liquid water on the sample surface which is gently evaporated/sublimated. Moreover, plants are protected owing to their capability of producing components inhibiting ice formation or its growing such as polysaccharides in the cell wall[18] and antifreeze proteins[19]. Although in some species the growth of ice crystals can occur, the cell walls resist collapse in the cellular volume, creating a divergence from the equilibrium[20] and in combination with the high relative humidity in the ESEM, reduce the extent of dehydration.

An advantage of the LTM for ESEM is the capability of preserving sample surface morphology, increasing sample resistance to beam damage and the possibility of higher resolution observation. The LTM for ESEM works with temperatures that are reachable using standard equipment of the ESEM as a cooling Peltier stage in contrast to other low temperature methods (LTSEM/CryoSEM) which involve the use of additional expensive instruments[21]. Moreover, samples do not require any liquid substitution[22].

Recent studies[23–25] have shown that the ESEM and SEM can complement each other. While the ESEM can provide an image of the biological samples in their native state, the SEM can offer a high-resolution image of the treated samples. However, there is a gap between these techniques due to the impossibility of direct transfer between different environmental conditions and different sample preparation requirements. For this case, the LTM for ESEM has been newly extended into the ELTM for further benefits lying in the advanced preparation of plant samples for additional or later analysis in different SEM or ESEM microscopes. This paper proves the applicability of this method for observation of the identical sample in their hydrated state in ESEM and completely dried in SEM with a well-preserved surface morphology. It was not published up to date.

Results and discussion

Commercial ESEMs allow the observation of samples in different modes: (1) in their native-fully hydrated state (2) dried in low vacuum conditions without the necessity of conductive coating (3) dried and coated in high vacuum SEM conditions or without coating under low beam energies. A combination of sample observation in individual ESEM modes enables extending the range of obtainable information for correct evaluation of a sample microstructure or recognizing possible artefacts.

The application possibilities of the ELTM method presented in this paper to prepare plant samples for observation in various ESEM modes are presented in the following paragraphs.

Fully hydrated samples in ESEM and after application of the LTM for ESEM.

ELTM is mutual with the LTM and is based on specimen cooling up to −20 °C during the initial pumping of the microscope up to 200 Pa in the specimen chamber (Fig. 1 – phase diagram, blue arrow). Cooling and pumping run simultaneously. The rate of temperature and pressure changes are crucial parameters and must be set according to the type of sample. More susceptible samples with a higher content of water and with a thicker water layer on its surface need a decreasing of the cooling rate with a later start of pumping (around 0 °C), unlike robust samples with a low content of water and thick cuticles. However, for both cases, it should be ensured that most of water from the sample surface will be evaporated/sublimed and the maximum amount of water in the sample remains. Despite these dynamic changes, the sample is still in conditions close to 100% relative humidity in the specimen chamber.

The effect of the preparation procedure on sample morphology was evaluated by the imaging of an *Oxalis acetosella* leaf microstructure. The leaves are specific due to the low thickness associated with high sensitivity to drying out.

At first, the sample was observed in its fully hydrated state which enables imaging the surface microstructure as close to its natural state as possible (Fig. 2A–C). However, the high-pressure conditions required in the specimen chamber of the ESEM cause electron beam diffusion in the gas, hence the signal to noise ratio in the detected signal decrease. In our study, this was compensated by using higher beam energy (20 keV). At higher magnification, the sample tends to collapse due to radiation damage and the impact of free radicals, see Fig. 2B, C - indicated by white arrows.

The surface morphology of the sample after the application of the first step of the ELTM evinces minimum changes (Fig. 2D–F). Moreover, the sample structure is freeze-stabilized with increased tolerance to radiation damage and allows a higher resolution to be reached. In addition to the study of a wax structure (Fig. 2F) which is prone to be melted by high energy beam electrons, an observation is possible instead Fig. 2C.

Now, the sample is well stabilized in conditions of low pressure and temperature, but not prepared for exposure to atmospheric pressure and ambient temperature. The second step of the ELTM must follow after observation which avoids sample collapse due to the changing of the thermodynamic conditions during the venting process of the ESEM.

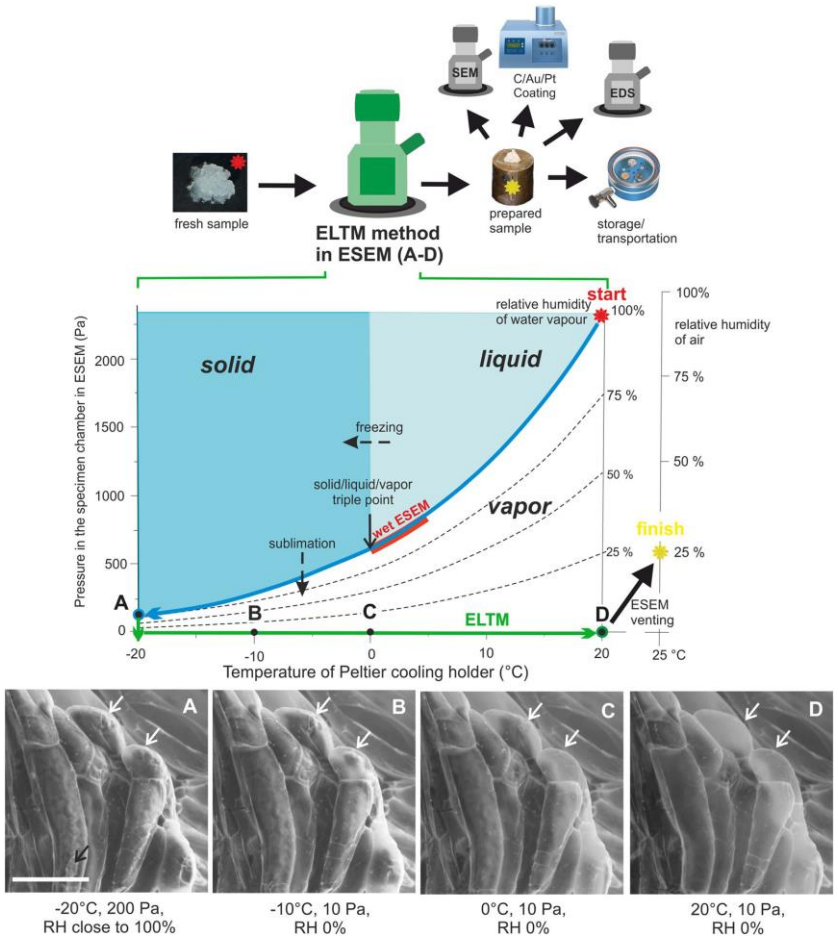

Figure 1. The upper schematic figure shows the introducing of the ELTM in an informative manner. The ELTM is realized during two steps inside the ESEM (green microscope). The steps corresponds with the two lines in the phase diagram (the 1st step of the ELTM - freeze stabilization, blue line; the 2nd step of the ELTM – water sublimation, green line). The state of the sample during the process is visible in images (A–D) placed below the phase diagram. The temperature and pressure conditions of images (A–D) correspond with the letters in the phase diagram. The bar is 50 µm. The white arrows point out places where the changes of the inner structures are well visible during the ELTM, the black arrow points out water residuum on the sample surface during observation in conditions close to 100% relative humidity.

Extended LTM for ESEM

The second step of the ELTM lies in the gentle sublimation of the residual water from the sample inner structure and the transfer of the sample from the low pressure and temperature conditions to atmospheric conditions (Fig. 1 green arrow in the phase diagram). This process starts with a slow decreasing of pressure in the specimen chamber. When the smallest pressure, reachable in ESEM mode (approx. 10 Pa), is achieved the sample temperature can be slowly increased from −20 °C up to 20 °C. An increase in the sample temperature at low gas pressure allows decreasing the relative humidity (RH), thorough removing of the water from the sample and preventing water condensation on the sample surface after opening the specimen chamber of the ESEM. The sample processing with the ELTM is fully realised *in-situ*, inside the specimen chamber of the ESEM, as is visible in the schematic figure in Fig. 1 (above the diagram). The phase diagram of water in Fig. 1 shows temperature/pressure areas where the ELTM is realized from the start of the sample processing to its finish. Changes of the sample were monitored during the ELTM process and are visible on the sample of the suspensor cells of *Abies alba*, see Fig. 1A–D. The letters also correspond to letters in the phase diagrams. Figure 1A depicts the sample in the first step of the ELTM. The hydrated state of suspensor cells (white arrows) as well as the small rest of the ice on the sample surface (black arrow) is well visible there. During the second part of the ELTM (green arrow in the phase diagram) the sublimation is in the ascendant and the inner structure became less visible. If the sample temperature increases sufficiently slowly, minimal changes to the sample morphology are evident, see Fig. 1B–D. Images of similar samples in the wet state in ESEM and light microscopy were presented earlier[13].

Finally, the sample can be moved out from the microscope and stored or used for any further analysis. The prepared samples are usually very fragile and the manipulation can cause artefact or damage formation. The sample can be placed on a thin glass coverslip before mounting on the cooled Peltier sample holder. It enables simple manipulation with the prepared sample and prevents artefact formation.

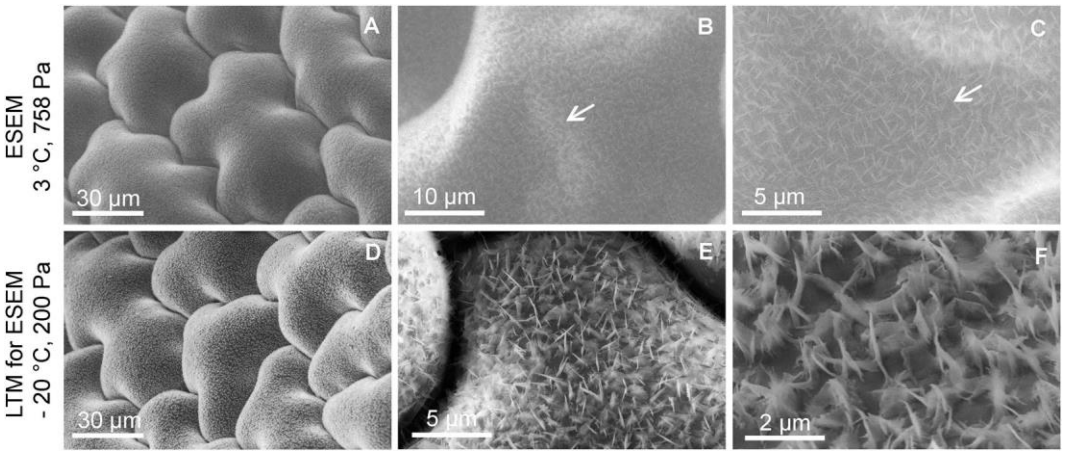

Figure 2. Wax microstructure on the surface of an Oxalis acetosella leaf observed in its fully hydrated state (A–C) and after application of the first step of the ELTM (D–F). The damage (indicated by white arrows) of the fully hydrated sample is evident in higher magnification (B,C) in contrast with the sample prepared using the LTM (E). The method also allows imaging of the high-resolution detail of wax structures (F).

Repetitive observation of biological samples in the ESEM

Samples prepared using the ELTM are dry, with their surface morphology preserved in a state approximate to a fresh state and ready for handling for the purpose of further observation, analysis etc. The possibility to repetitive observation of the identical sample after its observation in the ESEM was demonstrated on early somatic embryos of *Picea abies* in Fig. 3. At first, samples were observed in a freeze stabilized state in conditions of −20 °C and 200 Pa of water vapour. The results show an absence of extracellular ice in all tissues, however achieving a high-resolution image is still limited, see Fig. 3A,D. After finishing the ELTM, samples were removed from the microscope, mounted on double-sided carbon tape, sputter coated with a thin layer of gold and observed in the SEM (10−5 Pa). The following SEM observation provides a more detailed view of the surface microstructure with higher resolution, see Fig. 3B,C,E,F.

The results in Fig. 3 provide tangible evidence that the application of ELTM enables observing the identical sample in both a hydrated and dry state with well-preserved surface micromorphology. The benefit of this method is also the ability to preserve delicate structures such as extracellular matrix (ECM) without any chemical treatments. The ECM is a thin membranous layer on the plant cell surface, see Fig. 3 indicated by arrows. Different preparation techniques (lyophilisation, glycerol substitution, liquid nitrogen substitution, chemical fixation and critical point drying) have been tested in the past but techniques that can avoid artefact formation were not found[26]. Preparation using the ELTM enables observing the ECM without common artefacts such as creating fibrillary structures as well as damage and hole

creation. Structural arrangement of the ECM on the cell surface may play significant roles in morphogenical processes. Morphogenical observation of the samples prepared using the ELTM brings new results and possibilities to its accurate description. Moreover, the high resistance of the sample to repeated pressure changes in a range from atmospheric pressure to the vacuum obtainable during coating and SEM observation was noted after preparation using the ELTM.

Energy dispersive x-ray microanalysis in ESEM

An application of the ELTM as a preparation method of plant samples for elemental microanalysis was demonstrated on a sample of cannabis root grown in a nutritional medium supplemented with Pb2+. In this case, after application of the ELTM, samples were positioned on a carbon stub with regards to the requirements of energy dispersive x-ray microanalysis and analysed in low vacuum conditions to prevent sample charging. Material contrast was observed using the self-designed YAG backscatter electron detector[27] and analysis was realised using an x-ray cone to minimize beam electron scattering in the gas.

A significant impact of Pb2+ treatment was clearly visible via the material contrast of the root cells (Fig. 4D) where a specific element was accumulated between the cell borders in comparison with the control sample (Fig. 4A). A semi-quantitative analysis of several areas of root sections with qualitative x-ray mapping was combined. To describe the impact of Pb2+ treatment on the cannabis root, element localisation and chemical composition of samples were studied. Although no accumulation of Pb2+ was found, a significant variation in the concentration of K and Cl was observed in Pb2+ treated samples (Fig. 4E,F) in comparison with the control (Fig. 4B,C). The analysis confirmed that the elemental distribution of the described component was altered by metal treatment and was due to the affecting of the plant mineral metabolism and induced changes in the nutrient balance.

The sample prepared using the ELTM was observed in conditions of ambient temperature and a low-pressure environment in the specimen chamber of the ESEM. Positive ions generated by electron-gas interactions allow the elimination of charging the electrically non-conductive sample without the necessity of their conductive coating. Thus, the samples prepared using the ELTM in combination with the low-pressure environment are highly suitable for energy dispersive x-ray microanalysis. Generally, the use of the energy dispersive x-ray spectrometer (EDS) in ESEM is possible, but the results are strongly influenced by the scattering of primary electrons with gas. The high-pressure environment can cause the degradation of the effective spatial resolution, absorption of low energy peaks and the spectrum can be extended with X-rays from the gas, so the use of as low a

pressure as possible is recommended. Owing to the ELTM, the EDS analysis could be realised in conditions of 150 Pa of water vapour in which the contribution of a significant artefact is strongly decreased.

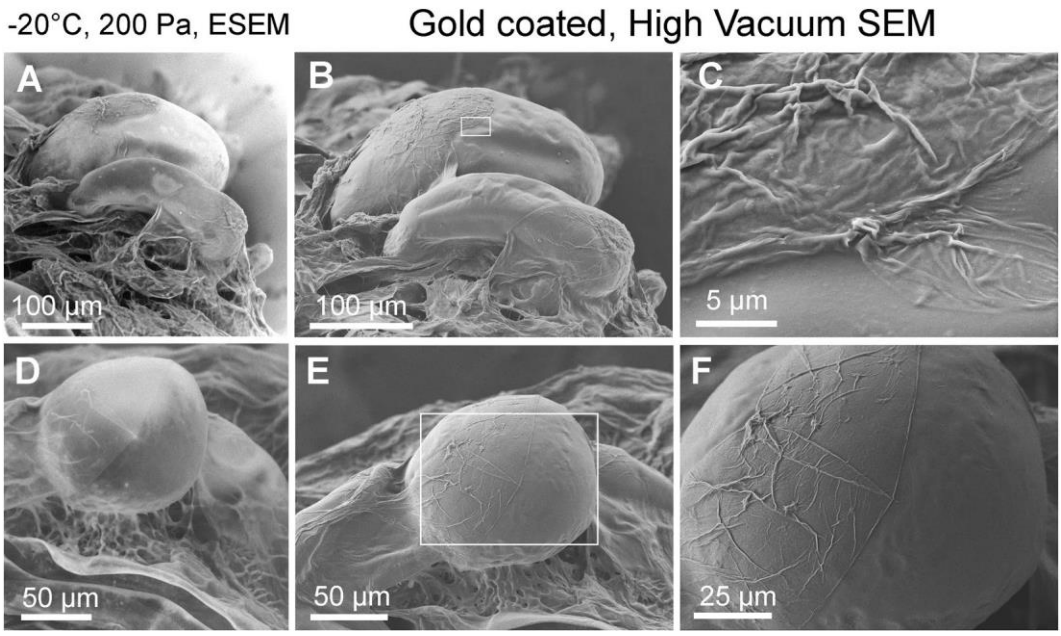

Figure 3. Samples of early somatic embryos of Picea abies observed during different steps of the ELTM. (A,D) Non-commercial ESEM AQUASEM II and conditions of 100% relative humidity. (B–F) SEM JEOL 6700 F with a high vacuum in the specimen chamber. The white arrows indicate the extracellular matrix.

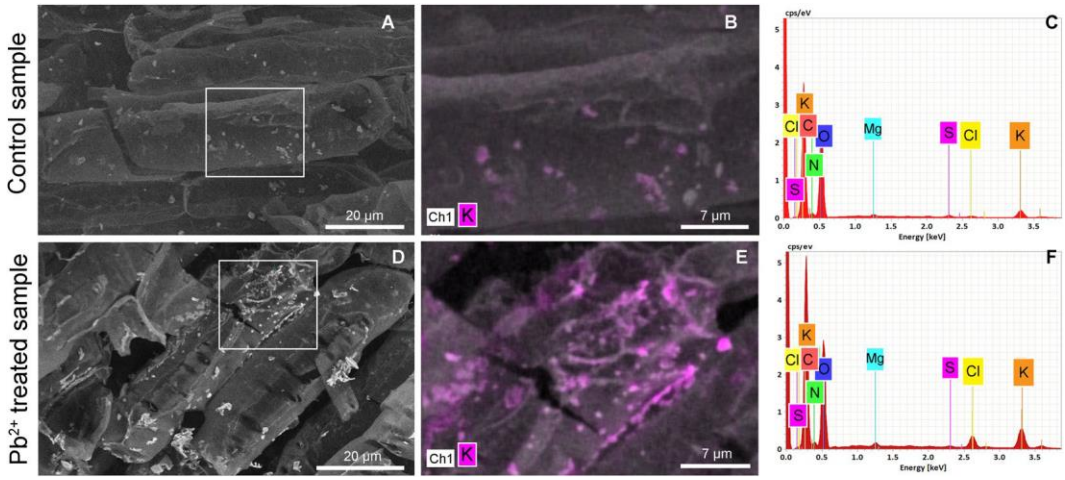

Figure 4. Cells of cannabis roots cultivated in a heavy metal-free medium (A–C) and exposed to Pb2+ (D–F). The material contrast imaged in backscattered electron images (A,D) shows specific element accumulation. Fragments with a map localization of K accumulation (B,E) and corresponding EDS spectra (C,F).

Conclusion

Our paper underlines the wide usability and advantages of the ESEM which can be used not only as a tool for the imaging of conventionally treated or highly susceptible fresh biological samples[28,29] and polymers[30], but also for fast, effective and inexpensive *in-situ* preparation allowing repetitive observation and elemental analysis of plant samples using our new ELTM. The *in-situ* preparation process can be controlled and directly modified according to sample specificity. It allows the amount of sample handling to be reduced to the indispensable minimum, hence contamination, damage or artefact formation is minimalized. Owing to the absence of chemical treatment, the ELTM is highly suitable for EDS microanalysis[31] or observation of specific traits that can be damaged during conventional preparation methods. Sputter-coated free samples analysed under increased gas pressure conditions (up to 300 Pa) in the ESEM may also allow the presence of lower concentrated elements to be revealed, whose signal would be absorbed by the conductive layer. The quality of images is strongly dependent on the working conditions; however, a high variability of ESEM parameters, such as temperature, freezing velocity and humidity, can be found and set. Although this method has many limitations, the surface microstructure is well preserved with minimum artefacts and without expensive and time-consuming chemical treatments. The ELTM method can be applied in any commercial ESEM equipped with a cooled Peltier stage and routinely used for the imaging of plant samples in a higher resolution.

Methods

Plant material and culture conditions

The embryogenic tissue of silver fir (*Abies alba Mill*.) was initiated from immature zygotic embryos of cones from open-pollinated trees. Immature seeds were surface - sterilized for 10 min in 10% (v/v) H2O2 and then rinsed several times with sterile distilled water. The immature cones of *Abies alba* were collected on 26 July 2006 in the Dobroč primeval forest. The cultures were maintained in darkness at 25 ± 1 °C and at 2-3 week intervals transferred to a fresh medium.

The embryogenic culture of Norway spruce (*Picea abies (L.) Karst*.) collected by Plant Biology, Mendel University (Brno) was originally isolated from a mature zygotic embryo of a tree of spruce mountain climate type No. 12345 from an experimental area located in the Beskydy Mountains, Moravia, Czech Republic. The culture of embryonic tissues was maintained on medium designated LP/2 in90 mm diameter Petri dishes with 9 μM 2,4-D and 4.4 μM BAP. The embryogenic

tissues from the upper parts of their aggregates (2.5–5.0 mg) were sub-cultured in 10–14 days periods. The cultures were incubated in the dark at 23 ± 1 °C.

For obtaining hemp plantlets for *in vitro* multiplication, seeds of the Bialobrzeskie variety obtained from Agritec Plant Research Institute Ltd., Šumperk, Czech Republic were used. The seeds were surface sterilized with 6% sodium hypochlorite for 8 minutes and afterwards rinsed three times with sterile distilled water. The sterilized seeds were germinated on half-strength MS medium supplemented with 29.2 mM sucrose and 0.65% agar. The pH value of the media was adjusted to 5.8 before autoclaving at 121 °C, 100 kPa, for 20 min. The seeds were maintained in a cultivation room under 18/6 light dark cycle at 24 ± 2 °C. The shoot tips (approx. 2 cm in length) were taken from 10-14-day-old plantlets and placed on a cultivation medium enriched with full-strength MS salts, 87.6 mM sucrose, 0.8% agar and 2 μM meta-topolin. The pH value of the media was adjusted to 5.7 before autoclaving. The standard cultivation medium was used as a control and experimental variants were supplemented with 750 μl Pb-EDTA. Explants were cultivated for one month on nutritional medium under 18/6 light dark cycle at 24 ± 2 °C when the effect of Pb2+ on the root growth was evaluated. The roots were sectioned at a distance of 1.2–1.5 cm from the apex where the root cells are already developed and this part mostly contributes to the uptake elements[32].

Environmental scanning electron microscopy

Environmental scanning electron microscopy micrographs were obtained with a non-commercial ESEM AQUASEM II and ESEM Quanta 650 FEG equipped with a Bruker QUANTAX EDS XFlash 6 detector. Fresh plant samples were sectioned approximately to 4–8 mm2, placed into a drop of water on the Peltier cooling stage equipped with a special flat cylindrical brass sample holder. In the case of observation of samples in their fully hydrated state, the sample temperature was 3 °C and 760 Pa of water vapour, the accelerating voltage 20 kV, the probe current 80 pA and the environmental distance between the sample surface and the second pressure limiting aperture was 8.5 mm.

In the case of the LTM for ESEM, the accelerating voltage was 10 kV, the probe current was 50 pA and the sample distance between the sample surface and the second pressure limiting aperture was 8.5 mm.

Elemental analysis

The working conditions were: the accelerating voltage 10 kV, the probe current 100 pA, pressure of water vapour 150 Pa, working distance 10 mm. Parameters used for X-ray mapping were: image resolution 200 × 200 pixels, dwell time per pixel 5 ms, magnification 1000x.

Scanning electron microscopy

Observation of dry samples was realized using an SEM JEOL 6700F and conventional vacuum 10−5 Pa. Samples were placed on a carbon tape and coated with gold using a Sputter Coater Q150 (Quorum Technologies).

Acknowledgements

This work was supported by the Czech Science Foundation (19-03909S).

References

1. Pathan, A. K., Bond, J. & Gaskin, R. E. Sample preparation for SEM of plant surfaces. *Mater. Today* 12, 32–43 (2010).

2. Echlin, P. Sample Stabilization for Imaging in the SEM. In Handbook of Sample Preparation for Scanning Electron Microscopy and X-Ray Microanalysis 137–183, https://doi.org/10.1007/978-0-387-85731-2_8 (Springer US, 2009).

3. Golding, C. G., Lamboo, L. L., Beniac, D. R. & Booth, T. F. The scanning electron microscope in microbiology and diagnosis of infectious disease. *Sci. Rep.* 6, 26516, https://doi.org/10.1038/srep26516 (2016).

4. Cocozza, C. *et al*. Distribution and concentration of cadmium in root tissue of Populus alba determined by scanning electron microscopy and energy-dispersive x-ray microanalysis. *iForest-Biogeoscience For.* 1, 96–103 (2008).

5. Tihlaříková, E., Neděla, V. & Shiojiri, M. *In Situ* Study of Live Specimens in an Environmental Scanning Electron Microscope. *Microsc. Microanal.* 19, 914–918 (2013).

6. Neděla, V. Methods for additive hydration allowing observation of fully hydrated state of wet samples in environmental SEM. *Microsc. Res. Tech.* 70, 95–100 (2007).

7. Cox, G., Vesk, P., Dibbayawan, T., Baskin, T. I. & Vesk, M. High-Resolution and Low-Voltage SEM of Plant Cells. In *Biological Low-Voltage Scanning Electron Microscopy* 229–244, https://doi.org/10.1007/978-0-387-72972-5_9 (Springer New York, 2008).

8. Echlin, P. Low temperature scanning electron microscopy: a review. *J. Microsc.* 112, 47–61 (1978).

9. Jeffree, C. E. & Read, N. D. Ambient- and Low-Temperature Scanning Electron Microscopy. *Electron Microsc. Plant Cells* 313–413, https://doi.org/10.1016/B978-0-12-318880-9.50013-2 (1991).

10. Neděla, V., Hřib, J., Havel, L., Hudec, J. & Runštuk, J. Imaging of Norway spruce early somatic embryos with the ESEM, Cryo-SEM and laser scanning microscope. *Micron* 84, 67–71 (2016).

11. Neděla, V. Controlled dehydration of a biological sample using an alternative form of environmental SEM. *J. Microsc.* 237, 7–11 (2010).

12. Stokes, D. J., Rea, S. M., Best, S. M. & Bonfield, W. Electron microscopy of mammalian cells in the absence of fixing, freezing, dehydration, or specimen coating. *Scanning* 25, 181–184 (2003).

13. Neděla, V., Tihlaříková, E. & Hřib, J. The low-temperature method for study of coniferous tissues in the environmental scanning electron microscope. *Microsc. Res. Tech.* 78, 13–21 (2015).

14. Đorđević, B. *et al*. Effects of copper and arsenic stress on the development of Norway spruce somatic embryos and their visualization with the environmental scanning electron microscope. *N. Biotechnol.* 48, 35–43 (2019).

15. Tihlaříková, E., Neděla, V. & Fránková, M. Micro-morphological Characterization of *In-Vivo* Diatoms Using ESEM. *Microsc. Microanal.* 23, 1346–1347 (2017).

16. Vlašínová, H., Neděla, V., Đorđević, B. & Havel, L. Bottlenecks in bog pine multiplication by somatic embryogenesis and their visualization with the environmental scanning electron microscope. *Protoplasma* 254, 1487–1497 (2017).

17. Michaloudi, E. *et al*. Reverse taxonomy applied to the brachionus calyciflorus cryptic species complex: Morphometric analysis confirms species delimitations revealed by molecular phylogenetic analysis and allows the (re) description of four species. *PLoS One* 13, e0203168, https://doi.org/10.1371/journal.pone.0203168 (2018).

18. Olien, C. R. & Smith, M. N. Protective systems that have evolved in plants. In *Advances in Plant Cold Hardiness* (eds Olien, C. R. & Smith, M. N.) 61–88 (CRC Press, 1981).

19. Griffith, M. & Antikienen, M. Extracellular Ice Formation in Freezing-Tolerant Plants. In *Advances in low-temperature biology*. Volume 3 (ed. Steponkus, P. L.) 107–139 (JAI Press, 1996).

20. Zhu, J. J. & Beck, E. Water Relations of *Pachysandra Leaves* during Freezing and Thawing: Evidence for a Negative Pressure Potential Alleviating Freeze-Dehydration Stress. *Plant Physiol.* 97, 1146–1153 (1991).

21. Ensikat, H. J., Ditsche-Kuru, P. & Barthlott, W. Scanning electron microscopy of plant surfaces: simple but sophisticated methods for preparation and examination. In *Microscopy: science, technology, applications and educations* (eds Mendez-Vilas, A. & Diaz, J.) 248–255 (Formatex Research Center, 2010).

22. Ensikat, H. J. & Barthlott, W. Liquid substitution: A versatile procedure for SEM specimen preparation of biological materials without drying or coating. *J. Microsc.* 172, 195–203 (1993).

23. Muscariello, L. *et al*. A critical overview of ESEM applications in the biological field. *J. Cell. Physiol.* 205, 328–334 (2005).

24. Khoshmanesh, K. *et al*. Interfacing Cell-Based Assays in Environmental Scanning Electron Microscopy Using Dielectrophoresis. *Anal. Chem.* 83, 3217–3221 (2011).

25. Tang, S.-Y. *et al*. High Resolution Scanning Electron Microscopy of Cells Using Dielectrophoresis. *PLoS One* 9, e104109, https://doi.org/10.1371/journal.pone.0104109 (2014).

26. Popielarska-Konieczna, M., Bohdanowicz, J. & Starnawska, E. Extracellular matrix of plant callus tissue visualized by ESEM and SEM. *Protoplasma* 247, 121–125 (2010).

27. Neděla, V., Tihlaříková, E., Runštuk, J. & Hudec, J. High-efficiency detector of secondary and backscattered electrons for low-dose imaging in the ESEM. *Ultramicroscopy* 184, 1–11 (2018).

28. Hřib, J., Vooková, B. & Neděla, V. Imaging of native early embryogenic tissue of Scots pine (*Pinus sylvestris L*.) by ESEM. *Open Life Sci.* 10, 285–290 (2015).

29. Neděla, V., Hřib, J. & Vooková, B. Imaging of early conifer embryogenic tissues with the environmental scanning electron microscope. *Biol. Plant.* 56, 595–598 (2012).

30. Schenkmayerová, A. *et al*. Physical and Bioengineering Properties of Polyvinyl Alcohol Lens-Shaped Particles Versus Spherical Polyelectrolyte Complex Microcapsules as Immobilisation Matrices for a Whole-Cell Baeyer–Villiger Monooxygenase. *Appl. Biochem. Biotechnol.* 174, 1834–1849 (2014).

31. Kulich, I. *et al*. Exocyst subunit EXO70H4 has a specific role in callose synthase secretion and silica accumulation. *Plant Physiol.* 176, 2040–2051 (2018).

32. Vaculík, M. *et al*. Root anatomy and element distribution vary between two *Salix caprea* isolates with different Cd accumulation capacities. *Environ. Pollut.* 163, 117–126 (2012).

19 Effects of copper and arsenic stress on the development of Norway spruce somatic embryos and their visualization with the environmental scanning electron microscope

Biljana Đorđević[a], Vilém Neděla[b], Eva Tihlaříková[b], Václav Trojan[a], Ladislav Havel[a]

a *Department of Plant Biology, Mendel University in Brno, Zemědělská 1, Brno 613 00, Czech Republic*

b *Institute of Scientific Instruments of the Czech Academy of Sciences, Královopolská 147, Brno 612 64, Czech Republic*

Keywords

Copper, Arsenic, Somatic embryogenesis, Picea abies (L.) Karst., Environmental scanning electron microscope

Abstract

Somatic embryogenesis is an important biotechnological technique which can be used in studies associated with environmental stress. Four embryogenic cell lines of Norway spruce were grown on media enriched with copper and arsenic in concentration ranges 50–500 μM and 10–50 μM, respectively. The effects were observed during subsequent stages of somatic embryogenesis, the characteristics evaluated being proliferation potential, average number of somatic embryos obtained per g/fresh weight, morphology of developed somatic embryos, metal uptake, and microanalysis of macro- and micronutrients uptake. Copper and arsenic at higher concentrations significantly reduced the growth of early somatic embryos. In almost all treatments, the cell line V-1-3 showed the best performance compared with the other lines tested. Environmental scanning electron microscopy was used to visualize and identify morphological abnormalities in the development of somatic embryos. Abnormalities observed were classified into several categories: meristemless somatic embryos, somatic embryos with disrupted meristem, reduced number of cotyledons, single cotyledon and fused cotyledons. With the application of a low temperature method for the environmental scanning electron microscope, samples were stabilized and whole meristems could be investigated in their native state. As far as we are aware, this is the first report of the effect of copper and arsenic during the process of somatic embryogenesis and the first to evaluate the content of macro and micronutrients uptake in Norway spruce.

Introduction

Trace elements such as copper (Cu) and arsenic (As) are two of the major contaminants that are emitted mainly as a result of various combustion processes and industrial activities [1]. While Cu is an essential micronutrient for growth and development and is a constituent of many plant enzymes, As lacks any biological functions [2,3]. However, both essential and nonessential metals are extremely reactive and toxic in high concentrations [4]. Cu in excess can be very harmful for plant metabolism and can induce oxidative stress, affecting various enzymatic activities and cause different biological defects including biomass reduction [5], decreased photosynthesis and induction of the uptake of other nutrient elements [6], reduction in mitotic index [7], oxidative damage [8], root morphology [9] and growth reduction [10]. As can severely decrease germination, shoot and root elongation [11] and inhibit photosynthetic and respiratory systems and growth [12], which often lead to plant death [13]. The emission trend of the main pollutants has decreased considerably since 1990, primarily due to the implementation of different legislative measures [14]. However, there are still areas where the concentration of heavy metals exceeds permissible limits. Among the coniferous species, Norway spruce (Picea abies (L.) Karst.) is one of the most important in Europe, both from an economic and ecological point of view. Up to now, only a few reports have been published on the effects of heavy metals on conifers [15–19]. Conifers are often used as biomarkers of industrial pollution, including water, air, and soil contamination [20,21].

Somatic embryogenesis (SE) as a biotechnological technique is used for production of a large number of superior plantlets, but enormous potential exists for this method to be used in various environmental studies, including the effects of heavy metal ions. In nature, seed germination is one of the first physiological processes affected by heavy metals and studying embryo development is not an easy task. Since, in conifers, somatic embryos morphologically resemble zygotic embryos, the use of SE can be very valuable for studying cell biology and embryo development in combination with optical and environmental scanning electron microscopy (ESEM), which allows fully fresh somatic embryo samples to be studied by routinely used optical microscopy with higher resolution and depth of the field [22]. Moreover, the ability of embryos to tolerate certain levels of heavy metals in nutritional medium can be very indicative of the tolerance level in contaminated soil.

The aim of this work was to investigate the ability of four different cell lines of Norway spruce to undergo the process of SE under Cu and As stress. The most responsive cell lines could be used in the future for testing in vivo in heavy metal

polluted soils. A further aim was to study embryo development and to observe morphological changes of early somatic embryos during the proliferation phase with ESEM and to detect the effect of Cu and As on macro- and micronutrient uptake. Moreover, apical meristem distribution connected with abnormal cotyledon development in somatic embryos was also observed using the original low-temperature method for ESEM and optical microscopy.

Material and methods

Plant material

Embryogenic cell lines of Norway spruce (V-1-3, V-1-5, I-1-3 and III- 3-3) were established during summer 2011, according to the procedure previously described [23]. The origin of the Norway spruce mother trees was the forest district of Černá Hora, Blansko district, Czech Republic. Embryogenic cultures were cultivated on half strength LP medium [24, modified by 25] and were subcultured every 2 weeks and maintained in a cultivation room in the dark at 23 ± 2 °C. For the set of experiments during the proliferation stage, standard cultivation media (LP) was used as a control and experimental variants were supplemented with an addition of Cu (50, 250 and 500 μM concentrations) and As (10, 25 and 50 μM concentrations), respectively. The stock solution of Cu(II) was prepared by using CuSO4·5H2O and for As (V) $AsHNa_2O_4.7H_2O$. Copper sulfate was mixed with ethylene diamine tetra-acetic acid (EDTA) in a 1:1 molar ratio. The filter-sterilized As(V) and Cu(II)–EDTA complex were added to the autoclaved culture medium, to avoid precipitation. Early somatic embryos were cultivated for 2 weeks on proliferation media enriched with Cu(II) and As(V) and then transferred to the maturation media. The preparation of the maturation media was as previously published [26]. The described maturation media was used as a control, and experimental variants were supplemented with Cu(II) (50, 250 and 500 μM) and As(V) in concentrations (10, 25 and 50 μM), respectively. Subculturing was performed every 2 weeks during the maturation experiment for up to 6 weeks. The mature somatic embryos were subjected to partial desiccation and afterwards were transferred to germination medium [26].

Determination of Cu(II) and As(V) uptake in the early somatic embryos

Determination of Cu(II) and As(V) uptake in the early somatic embryos was as described by [27] with slight modifications. Briefly, the early somatic embryos (about 5 mg) grown for 14 d on nutritional media enriched with Cu(II) or As(V) were freeze dried and digested in a diffused microwave system (MLS 1200 Mega; Milestone S.r.L., Sorisole, Italy). The experiments were carried out using an ICP-MS (Agilent 7700×; Agilent Technologies, Tokyo, Japan) based on a quadrupole

mass analyzer and octopole reaction system (ORS 3). A collision cell in He-mode was used for the elimination of possible polyatomic interferences and was used for isotopes ^{63}Cu and ^{75}As. ^{45}Sc and ^{72}Ge were used as an internal standard. The calibration solutions were prepared by the appropriate dilution of the single element certified reference materials with 1.000 ± 0.002 g/l for each element (Analytika Ltd., Prague, Czech Republic). The certified reference material of strawberry leaves (METRANAL 3, Analytika Ltd., Prague, Czech Republic) was used for control of the decomposition process and for method validation. Measurement accuracy was verified by using certified reference material of water TMDA-64.3 (National Water Research Institute, Ontario, Canada).

Morphological observations and microanalysis of macro and micronutrients uptake

After the maturation experiment, the somatic embryos, mainly abnormally developed ones, were moved to Petri dishes with basal medium, and the first informative photos were taken with an Olympus E-450 camera connected with an Olympus SZH10 stereo microscope using Olympus Quick Photo micro 3.0 software.

For detailed observation in the ESEM, small parts of the early somatic embryos were cut and placed on the cooled specimen holder (Peltier stage). When a temperature of 0 °C was reached, the pumping process of the ESEM specimen chamber started, according to the low-temperature method for ESEM (LTM) described by [28] and used for the study of various plant samples [29,30,31]. All experiments were carried out under constant operating conditions, specimen holder temperature −20 °C and water vapour pressure of 150 Pa in the ESEM QUANTA 650 FEG. Stabilized early somatic embryos using the LTM were observed under a beam accelerating voltage of 15 kV, beam current 53 pA and working distance 10mm using a gaseous secondary electron detector (GSED). Macrographic images of the whole cotyledons were made by composing micrographs using Maps software (Thermo Fisher Scientific).

For the detection of the effect of Cu(II) and As(V) on macro and micronutrient uptake, microanalysis was performed. First, early somatic embryos were stabilized using LTM and observed under the same conditions as matured somatic embryos. In order to maximize detection efficiency and accuracy of semi-quantitative energy dispersive X-Ray microanalysis (EDS) the samples were dried using a modified LTM [28]. This procedure allows minimization of the water content in the samples, use of a higher probe current and longer EDS acquisition time as well as the storage of samples for further analysis. Dried, chemical treatment-free and conductive coating-free samples were analysed using a Bruker Quantax 400 XFlash 6/60 EDS

silicon drift detector under a 10 keV beam energy, beam current 100 pA, working distance 10mm and water vapour pressure 100 Pa. The EDS spectra were obtained from five regions of each sample. The ratio of individual elements in the sample was calculated as the average values obtained from each sample. The regions analyzed were selected with respect to sample morphology (relatively flat surface, suitably situated to the EDS analyzer).

Experimental design and data analysis

The effects of Cu(II) and As(V) at three different concentrations on the proliferation potential of four cell lines were studied and compared to controls. For determination of the proliferation rate, a standard procedure as previously published by [26] was used. All factors, i.e., cell line, concentration and experimental time, together with their interactions, were subjected to analysis of variance (ANOVA, STATISTICA 2013), and differences between treatments were considered significant at $p < 0.05$.

For the maturation experiment three different concentrations in the case of Cu(II) (50, 250 and 500 μM) and three for As(V) (10, 25 and 50 μM) (applied previously during the proliferation stage) were assayed after a maturation period lasting for 6 weeks. At the end of the maturation period, the presence of developing somatic embryos in the early somatic embryos was documented. Somatic embryos were counted per g of fresh weight of the early somatic embryos. All factors, i.e., cell line, concentration together with their interactions, were subjected to analysis of variance (ANOVA, STATISTICA 2013), and differences between treatments were considered significant at $p < 0.05$. For both the proliferation ratio and the number of somatic embryos, pairwise comparisons were judged by the least significant difference test. All statistical analyses were performed using STATISTICA 12.0 software [32].

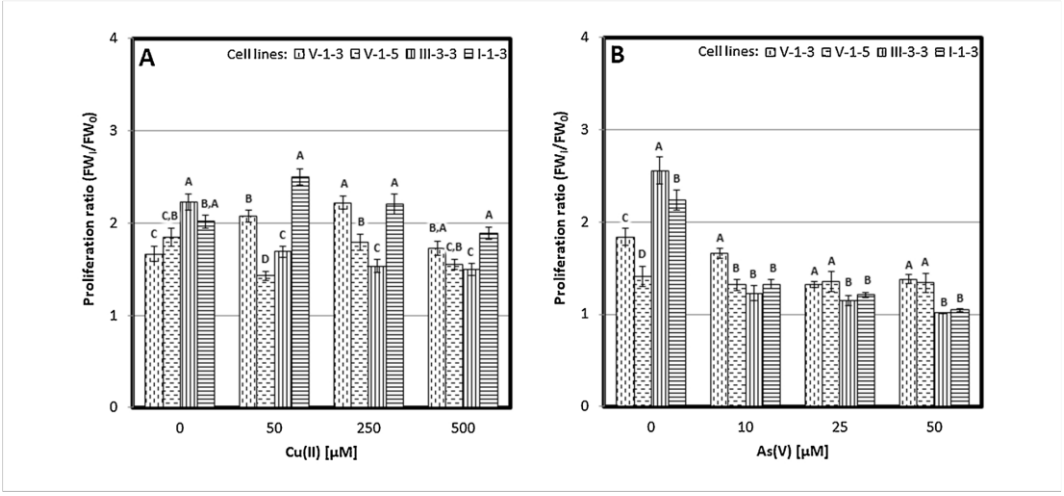

Fig. 1. Proliferation ratios of Norway spruce cell lines V-1-3, V-1-5, III-3-3 and I-1-3 treated with different (A) Cu(II) and (B) As(V) concentrations. Error bars show standard deviation and letters significant differences ($p < 0.05$).

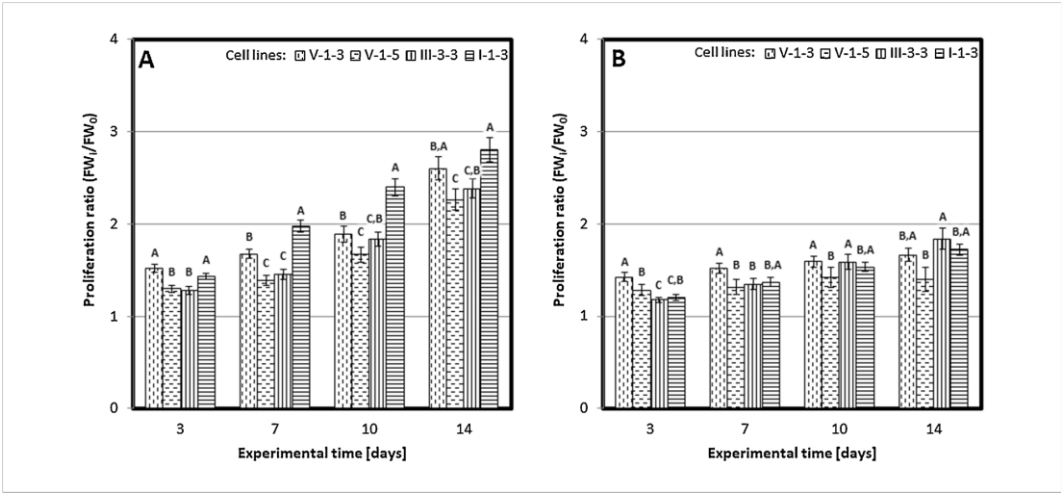

Fig. 2. Proliferation ratios of Norway spruce cell lines V-1-3, V-1-5, III-3-3 and I-1-3 treated with (A) Cu(II) and (B) As(V) for 3, 7, 10 and 14 days. The mean proliferation ratio (FWi/FW0) of experimental variants on the sampling day was divided by the proliferation ratio of the control. Column bars show averages of all concentrations for given cell line on the specific sampling day. Error bars show standard deviation and letters significant differences ($p < 0.05$).

Results and discussion

In this study, Norway spruce embryogenic cell lines V-1-3, V-1-5, III- 3-3 and I-1-3 were treated with different concentrations of Cu(II) and As(V) during the proliferation and maturation processes. To date, relatively few reports have been published in which the effects of heavy metals on conifers were studied under in vitro conditions, e.g., Picea abies [33,26], P. pungens [34], cell suspension cultures of P. rubens [16] and Abies alba [35].

The effect of Cu(II) and As(V) during the proliferation phase and morphological observation of early somatic embryos

In comparison with the control, cell lines treated with Cu(II) showed growth stimulation and/or inhibition depending on the concentration tested (Fig. 1A). Cell lines V-1-3 and I-1-3 treated with 50 and 250 μM concentrations had a higher proliferation ratio compared with the control. Moreover, in V-1-5 a significantly lower proliferation ratio than in the control was observed on treatment with 50 μM and was the lowest of all the cell lines. Interestingly, in the control early somatic embryos, III-3-3 had the highest proliferation ratio compared with other cell lines, while after the treatment with Cu(II) at higher concentrations (250 and 500 μM) it had the lowest. The highest proliferation ratio among all cell lines and Cu(II) concentrations tested was observed for I-1-3 (Fig. 1A). In contrast, treatment with As(V) significantly reduced the proliferation ratio of early somatic embryos in all tested cell lines (Fig. 1B). In the control early somatic embryos, the lowest proliferation ratio was detected in V-1-3 and V-1-5, while after the treatment with As(V) at concentrations 25 and 50 μM, those two cell lines had the highest proliferation ratio among those evaluated. In the presence of 10 μM As(V) a statistically significant difference was observed only in V-1-3 compared to the other cell lines (Fig. 1B).

The proliferation ratio of all cell lines during the Cu(II) treatment showed a time-dependent increase (Fig. 2A). Growth stimulation was observed at the beginning of the experiment, with Cu(II) being highest on the final day 14. During the whole experiment the highest proliferation ratio was observed in I-1-3 and V-1-3. Unlike the Cu(II) treatment, As(V) showed higher toxicity in all tested cell lines (Fig. 2B). At days 3 and 7, a statistically significant difference was observed between V-1-3 and the other cell lines. However, on days 10 and 14, the proliferation ratio in V-1-3, III-3-3 and I-1-3 remained nearly the same and no statistically significant difference was observed. Analysis of variance confirmed that on treatment with both Cu(II) and As(V), the proliferation ratio was significantly ($p < 0.05$) affected by the tested cell lines, experimental time, concentrations and the interactions among these factors (Table 1). The reduction in growth rate under higher concentrations of Cu and As was observed in other plant species [36,37].

Table 1 Analysis of variance of the effects of treatments with Cu(II) and As(V) on the cell lines proliferation ratio in early somatic embryos during the 14-days proliferation period.

Source	DF	*p*-value
Cu(II)		
Cell line	3	< 0.001
Sampling days	3	< 0.001
Concentration	3	< 0.001
Cell line × sampling day × concentration	27	< 0.001
Residual	576	
Total	639	
As(V)		
Cell line	3	< 0.001
Sampling days	3	< 0.001
Concentration	3	< 0.001
Cell line × sampling day × concentration	27	< 0.001
Residual	576	
Total	639	

Table 2 Analysis of variance on the uptake of Cu(II) and As(V) in Picea abies early somatic embryos during the 14-day proliferation period.

Source	DF	*p*-value
Cu(II)		
Cell line	3	< 0.001
Concentration	3	< 0.001
Cell line × concentration	9	< 0.001
Residual	16	
Total	31	
As(V)		
Cell line	3	< 0.001
Concentration	3	< 0.001
Cell line × concentration	9	0.003
Residual	16	
Total	31	

The appearance of early somatic embryos is shown in Fig. 3 and the evaluation was performed at the end of the proliferation experiments. The morphology of early somatic embryos consists of meristematic cells, which give rise to the embryonal head, embryonal tubular cells, and long vacuolized suspensor cells that are often arranged into bundles (Fig. 3, 0 μM concentration). The effect of Cu(II) on the development of early somatic embryos is shown in Fig. 3A. At the highest concentrations of Cu(II), 500 μM, the meristematic cells of the embryonal head and suspensor cells started to disorganize. In contrast, early somatic embryos treated with As(V) concentration of 50 μM, were deformed and completely disintegrated due to the high toxicity (Fig. 3B). It is known that As toxicity can affect numerous

physiological processes including damage to cellular membranes, causing electrolyte leakage [38,13]. Cu in excess can harm cells through the formation of reactive oxygen species (ROS) [39]. However, in order to cope with heavy metals, plants have developed different defensive mechanisms. One of the main strategies is to remove them from the cytoplasm by sequestration in the vacuoles and the cell wall [40]. Plant cell walls are one of the main compartments for heavy metal accumulation, since they can be modified by elevating the amount of pectins, especially low- methylesterified epitopes, which could be regarded as a symptom of the defense strategy and plant adaptation to elevated levels of heavy metals in the substrate [41]. Cell walls were the preferred compartment for Cu accumulation in spruce and Zn accumulation in poplar [42]. Moreover, observations concerning the response of plant cells to heavy metals has provided information about thickened cell walls and/or local cell wall thickening formation which protects plant cells from the toxicity and damaging effects of heavy metals [43]. Heavy metals in the cell walls may result in cell wall stiffening and the inhibition of cell elongation; nevertheless it was found that the presence of Cu and Fe can lead to polysaccharide scission, promoting cell elongation [44]. It is not clear when the presence of heavy metals in plant cell walls can cause their loosening, and when it causes stiffening. It is possible that the reaction of the cell wall could depend on the dose and type of heavy metals [40].

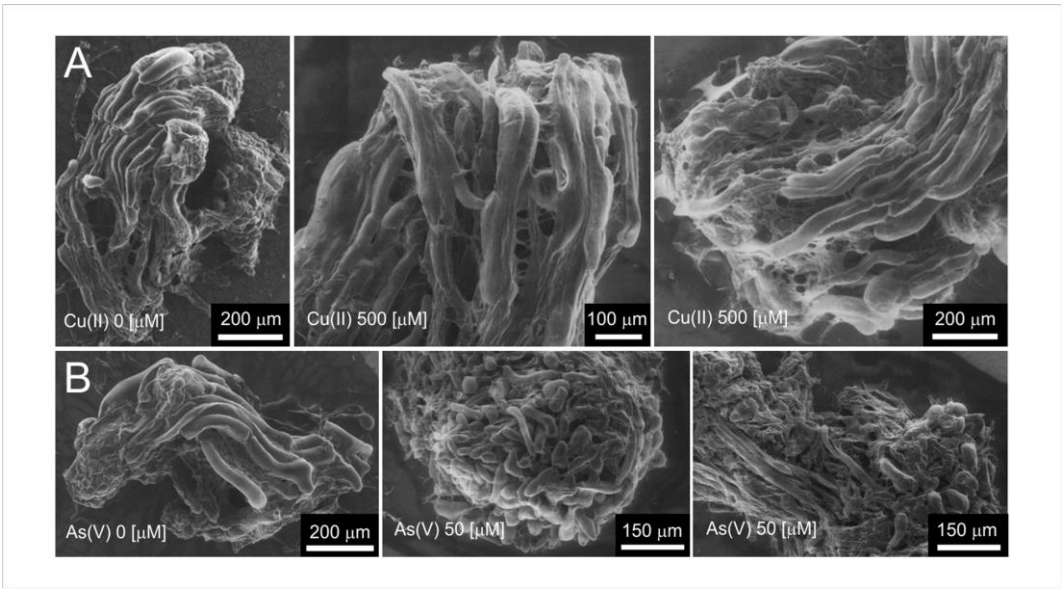

Fig. 3. Morphological observation of control (0 μM) early somatic embryos and after treatment with (A) 500 μM Cu(II) and (B) 50 μM As(V).

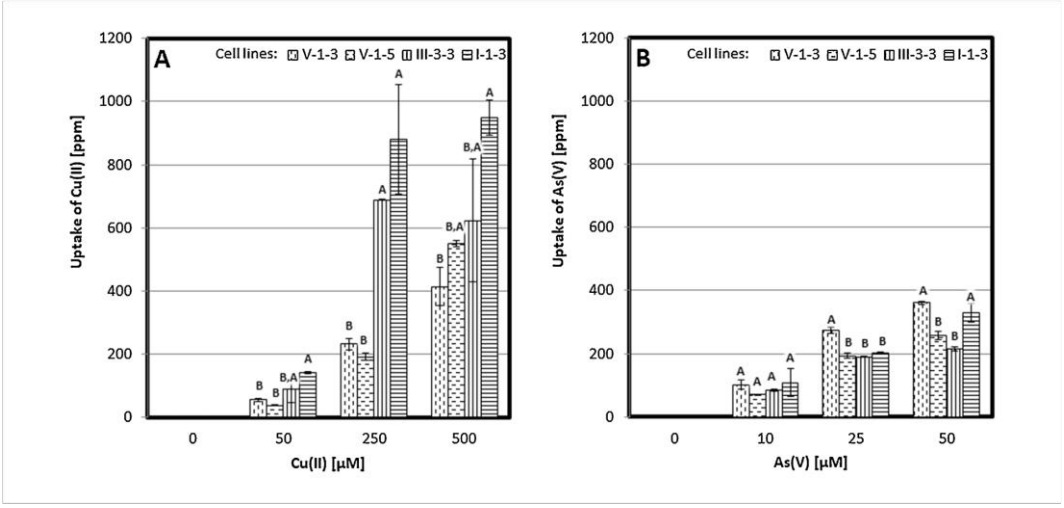

Fig. 4. Uptake of Cu(II) and As(V) in the early somatic embryos of Norway spruce cell lines V-1-3, V-1-5, III-3-3 and I-1-3 treated with different (A) Cu(II) and (B) As (V) concentrations.

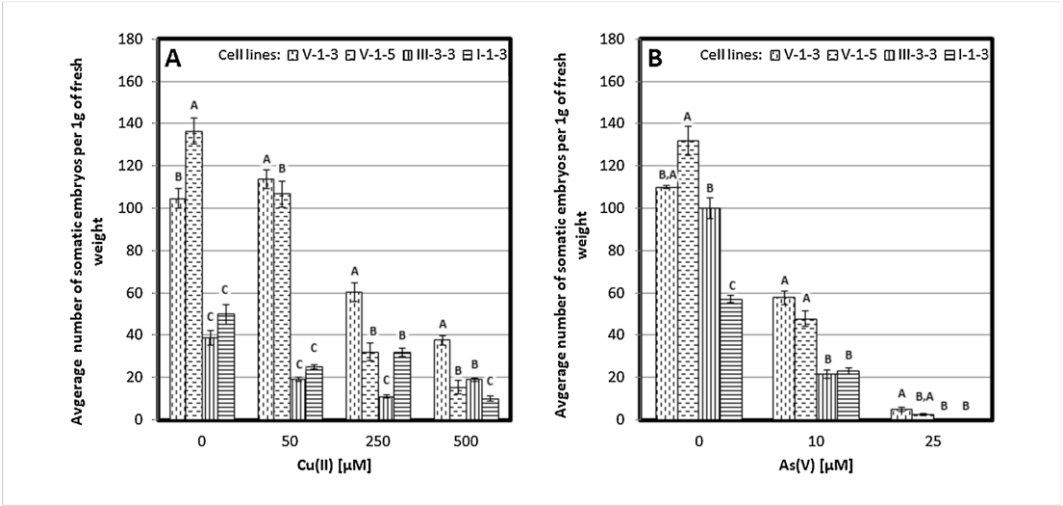

Fig. 5. Average number of Norway spruce somatic embryos formed per g of early somatic embryos fresh weight on maturation media exposed to different (A) Cu(II) and (B) As(V) concentrations. Error bars show standard deviation and letters significant differences ($p < 0.05$).

Uptake of Cu(II) and As(V) in the early somatic embryos

ANOVA on uptake of Cu(II) and As(V) confirmed that the cell line, concentrations and their interactions significantly affected the uptake of the tested metals (Table 2). In early somatic embryos treated with both metals, increasing the concentration in the nutritional media led to increased uptake, being greatest at the highest concentration tested (Fig. 4). In the case of Cu(II), at all concentrations studied the highest uptake was measured in I-1-3 and III-3-3. When concentrations of 250 µM were tested, those two cell lines had a 2-fold higher uptake compared with the other

cell lines tested (Fig. 4A). The lowest uptake of Cu(II) was in V-1-3. In contrast, V-1-3 had the highest uptake of As(V) over the duration of the experiment (Fig. 4B). At a concentration of 10 μM As(V), no statistically significant difference was observed among all the tested cell lines. However, at 25 μM As(V), a significant difference was observed only in V-1-3 compared with the other cell lines. For the highest concentration tested, 50 μM As(V), the highest uptake was observed in V-1-3 and I-1-3.

The effect of Cu uptake was studied on cell suspension cultures of Acer pseudoplatanus, where 78–92% of the Cu added to the media was contained within the callus [45]. Cell suspension cultures of Agave amaniensis were able to grow in media containing 10–240 μM copper ions, and could remove more than 67% copper ions from the media. The cells accumulated up to 106 mg g−1 copper ions in the biomass [46]. The As tolerance and accumulation capacity of Pteris vittata and Arabidopsis thaliana callus cultures were evaluated after 24 h exposure [47]. When a concentration of 0.05mM was applied, the uptake of P. vittata was approximately 500 ppm while in A. thaliana callus cultures it was half. Our results are in agreement with the results of this study.

Table 3 Analysis of variance of the effects of treatments with Cu(II) and As(V) in cell lines on the average number of somatic embryos per g of early somatic embryos fresh weight after the maturation period.

Source	DF	*p*-value
Cu(II)		
Cell line	3	< 0.001
Concentration	3	< 0.001
Cell line × concentration	9	< 0.001
Residual	128	
Total	143	
As(V)		
Cell line	3	0.004
Concentration	2	< 0.001
Cell line × concentration	6	0.118
Residual	96	
Total	107	

The effect of Cu(II) and As(V) during the maturation and germination phase and morphological observation of abnormally developed somatic embryos

The average number of somatic embryos obtained per g of fresh weight varied significantly between the Cu(II) and As(V) concentrations tested (Fig. 5A and B). Comparing the two elements, a considerably higher number of embryos was formed

on treatment with Cu(II) where even at the highest concentration (500 μM) somatic embryos were observed. On the other hand, in treatment with As(V) at the highest concentration tested (50 μM) no embryos were formed in any cell lines. However, in Cu(II) treatments the highest number of embryos was formed in the cell line V-1-3 (Fig. 5A). Similarly to Cu(II) treatment, in treatment with As(V) V-1-3 and V-1-5 performed significantly better compared with the two other cell lines (Fig. 5B). ANOVA showed that in treatment with Cu(II) the formation of embryos was significantly affected ($p < 0.05$) by the cell lines, concentrations and their interactions. For As(V), the number of embryos was affected ($p < 0.05$) by the concentration and cell lines while the interaction of cell lines and concentration did not have significant effect ($p > 0.05$) (Table 3).

Even though the formation of somatic embryos in both treatments was drastically reduced at higher concentrations of both Cu(II) and As (V), upon the completion of the maturation experiments many embryos developed abnormally (Fig. 6). Based on the morphological observation, abnormally developed embryos were divided into the following groups, i.e. meristemless somatic embryos (Fig. 6A, B), somatic embryos with disrupted meristem (Fig. 6C), reduced number of cotyledons (Fig. 6D, E), single cotyledon (Fig. 6F) and fused cotyledons (Fig. 6G, H, I). Our results are in agreement with those of [48,49] who studied the effect of Cu on seed germination, and with [50,51], who studied the effect of As. Moreover, the major effects of heavy metals on seeds are manifested by overall abnormalities and a decrease in germination rate, total soluble protein level, oxidative damage, membrane alteration, altered sugar and protein metabolisms, and nutrient loss all contributing to seed toxicity and productivity loss [52]. After one month on germination medium, development of roots and cotyledons was observed in plantlets treated with Cu(II) in lower concentrations (Fig. 7A). Abnormally developed embryos, mainly obtained in treatment with As (V), were also included for germination experiments but further growth and development was not recorded (Fig. 7B). Moreover, there was no protrusion of the radicle, cotyledons ceased to develop and vitrification was observed. The symptoms of As toxicity include poor seed germination and profound growth inhibition [53]. Maize plants treated with a toxic concentration of As(V) and As(III) produced stunted roots that were thicker and stiffer than controls [54]. On the other hand, root growth in Artemisia annua was stimulated at low As concentrations but inhibited at higher concentrations [55].

Microanalysis of macro and micronutrient uptake

In order to localize the place of accumulation and detect the effect of both Cu(II) and As(V) on the macro- and micronutrient uptake in the early somatic embryos, Cu(II) concentrations of 500 and 1500 μM and As(V) of 50 and 500 μM were tested.

The reason for using such high concentrations was to increase the amount of metals in the samples to be potentially detectable with higher accuracy using EDS. The results of the EDS analysis are given in Tables 4 and 5. For treatment with Cu(II) concentrations at 500 and 1500 μM, the Cl, K, O and N content tended to decrease in comparison with the control, whereas that of C, P and S increased with increasing concentrations of Cu(II) (Table 4). In contrast, in the treatment with As(V) the picture was more complex (Table 5). The content of O and C increased with increasing As(V), while P, Cl and K decreased. N and S decreased in the 50 μM concentration and afterwards increased when a concentration of 500 μM was applied. It is important to note that above mentioned EDS results are semiquantitative and rather indicate possible changes in the concentration of nutrients in the relationship with the various concentrations of tested metals in the samples. EDS was used in other studies related to the localization of heavy metals and their effect on macro and micronutrient uptake [56,57]. A common effect of Cu toxicity in plants is decreased uptake and accumulation of other mineral nutrients [58]. Our results indicated that with increasing the concentration of Cu some elements increased (i.e. C, P and S) while others decreased (Cl, K, O and N) in Norway spruce early somatic embryos. In maize, high concentrations of Cu significantly decreased concentrations of N, P, K, Ca, Zn and Fe in shoots and roots [59,60,61]. On the other hand, Ca and Mg concentrations increased in wheat seedlings in the nutrient solution, which showed a synergistic effect of Cu on Ca and Mg [62]. Furthermore, from our results it can be seen that after application of As in higher concentrations the amount of P decreased. As(V) is an analog of inorganic phosphate (Pi) and is easily transported across the plasmalemma by Pi transporter (PHT) proteins [63]. Furthermore, increasing or decreasing the rate of Pi and As uptake by increasing or decreasing the level of PHT can also increase or decrease the toxicity of As(V) [64]. As(V) and Pi compete for uptake through the same transport systems and under low Pi conditions, As(V) may outcompete Pi for entry into the plant, amplifying Pi deprivation symptoms [65,66]. In rice exposed to lower doses of As, the accumulation of Se, and other nutrients (Fe, P, Zn, S) was enhanced, while a higher dose limited the nutrient uptake of essential nutrients such as Mn, Cu and Zn [67].

Conclusions

As far as we are aware, this is the first report to study the effects of Cu(II) and As(V) on Norway spruce somatic embryogenesis. Furthermore, this provided novel insights into the effect of Cu(II) and As(V) on the appearance and vitality of early somatic embryos during the proliferation stage, and meristem disruption associated with abnormal cotyledon development during the maturation stage. In addition, microanalysis confirmed previous findings that both Cu(II) and As(V) can raise

and/or lower the content of macro- and micronutrient uptake. Besides studying embryo development in treatment with heavy metal ions, somatic embryogenesis could be a novel method for faster, easier, and/or cheaper selection of genotypes of coniferous species which can be tested as potential phytoremediators. The analysis showed that a simple in vitro laboratory test might be an indicative tool to evaluate phytoremediation potential of a considerable number of cell lines in a short period. However, additional experiments in vivo with the selected genotypes should be performed where seedlings growth and root-soil interaction could be studied. Most hyperaccumulators known to date are mainly herbaceous species, although woody species represent attractive models for studying the effect of heavy metals since they have a higher biomass and stronger root system to decontaminate soils. Taking that into consideration, conifers could be an interesting species to test under certain conditions, particularly for polluted sites localized in cold areas and, since there are no known conifers that act as a hyperaccumulator, more detailed studies need to be performed in order to determine if coniferous species might be used for phytoremediation. However, experimentation on tolerance to a metal is the first step towards identification of potential species for phytoremediation.

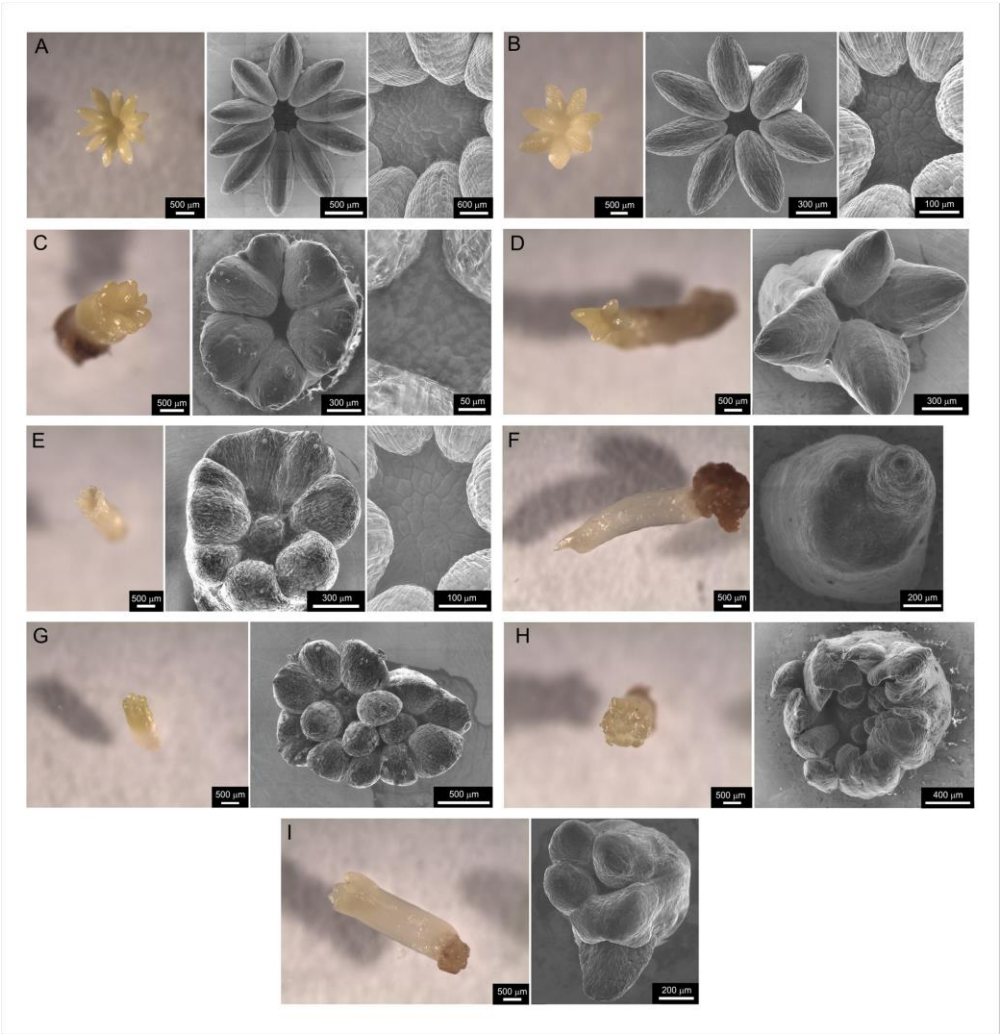

Fig. 6. Morphological observation of abnormally developed embryos−meristemless somatic embryos (A, B), somatic embryos with disrupted meristem (C), reduced number of cotyledons (D, E), single cotyledon (F) and fused cotyledons (G, H, I).

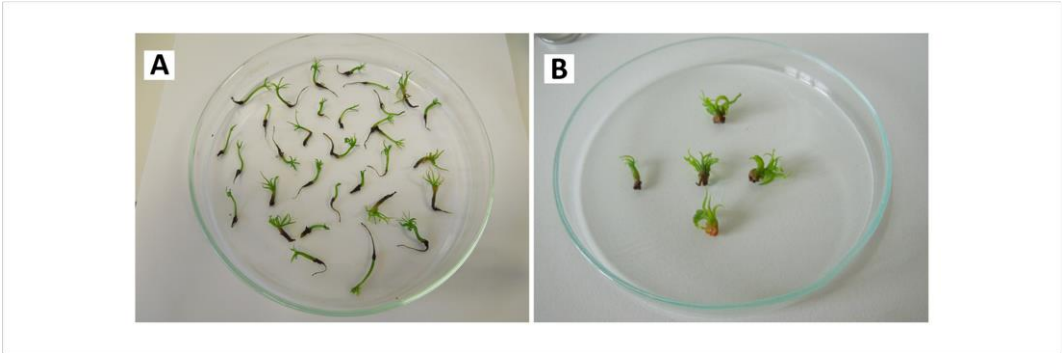

Fig. 7. Plantlets derived (A) from normally developed somatic embryos on treatment with Cu(II) and (B) from abnormally developed somatic embryos obtained on treatment with As(V).

Table 4 Microanalysis of the effect of Cu(II) on macro and micronutrients uptake. The ratio of individual elements in the sample was calculated as the average values obtained from each sample. The mass of the given values are expressed in%.

	C	N	O	P	S	Cl	K
Cu(II) 0 µM	42.0	3.8	45.1	0.5	0.3	1.4	6.4
Cu(II) 500 µM	44.6	3.0	44.8	0.5	0.4	0.5	4.1
Cu(II) 1500 µM	46.2	3.6	43.4	0.9	0.4	0.4	2.3

Table 5 Microanalysis of the effect of As(V) on macro and micronutrients uptake. The ratio of individual elements in the sample was calculated as the average values obtained from each sample. The mass of the given values are expressed in%.

	C	N	O	P	S	Cl	K
As(V) 0 µM	46.0	3.6	44.6	0.7	0.3	0.6	3.9
As(V) 50 µM	44.5	2.5	50.5	0.4	0.2	0.6	2.0
As(V) 500 µM	48.5	3.6	46.9	0.5	0.4	0.3	1.6

Acknowledgements

This work was supported by the Grant Agency of the Czech Republic (project no.GA14-22777S) and by the MEYS CR (LO1212), its infrastructure by the MEYS CR and the EC (CZ.1.05/2.1.00/01.0017) and by the CAS (RVO:68081731). Experiments were performed by using instrumentation which was financed by OP VaVpI CZ.1.05/4.1.00/ 04.0135 “Teaching and research capacities for biotechnology and infrastructure enhancement”.

References

[1] Tchounwou PB, Yedjou CG, Patlolla AK, Sutton DJ. Heavy metals toxicity and the environment. EXS 2012;101:133–64.

[2] Mendoza-Cózatl DG, Jobe TO, Hauser F, Schroeder J. Long-distance transport, vacuolar sequestration, tolerance, and transcriptional responses induced by cadmium and arsenic. Curr Opin Plant Biol 2011;14:554–62.

[3] Chandrasekhar C, Ray JG. Copper accumulation, localization and antioxidant response in Eclipta alba L. in relation to quantitative variation of the metal in soil. Acta Physiol Plant 2017;39:205.

[4] Goswami S, Das S. Screening of cadmium and copper phytoremediation ability of Tagetes erecta, using biochemical parameters and scanning electron microscopy?energy-dispersive X-ray microanalysis. Environ Toxicol Chem 2017;36:2533–42.

[5] Demirevska-Kepova K, Simova-Stoilova L, Stoyanova Z, Holzer R, Feller U. Biochemical changes in barley plants after excessive supply of copper and manganese. Environ Exp Bot 2004;52:253–66.

[6] Alaoui-Sossé B, Genet P, Vinit-Dunand F, Toussaint ML, Epron D, Badot PM. Effect of copper on growth in cucumber plants (Cucumis sativus) and its relationships with carbohydrate accumulation and changes in ion contents. Plant Sci 2004;166(5):1213–8.

[7] Liu D, Jiang W, Meng Q, Zou J, Gu J, Zeng M. Cytogenetical and ultrastructural effects of copper on root meristem cells of Allium sativum L. Biocell 2009;33:25–32.

[8] Bouazizi H, Jouili H, Geitmann A, El Ferjani E. Cupric stress induces oxidative damage marked by accumulation of H_2O_2 and changes to chloroplast ultrastructure in primary leaves of beans (Phaseolus vulgaris L.). Acta Biol Hung 2010;61(2):191–203.

[9] Kopittke PM, Asher CJ, Blamey FPC, Menzies NW. Toxic effects of Cu^{2+} on growth, nutrition, root morphology, and distribution of Cu in roots of Sabi grass. Sci Total Environ 2009;407(16):4616–21.

[10] Cambrollé J, García JL, Figueroa ME, Cantos M. Evaluating wild grapevine tolerance to copper toxicity. Chemosphere 2015;120:171–8.

[11] Shri M, Kumar S, Chakrabarty D, Kumar Trivedi P, Mallick S, Misra P, et al. Effect of arsenic on growth, oxidative stress, and antioxidant system in rice seedlings. Ecotoxicol Environ Saf 2009;72(4):1102–10.

[12] Garg N, Singla P. Arsenic toxicity in crop plants: physiological effects and tolerance mechanisms. Environ Chem Lett 2011;9:303–21.

[13] Finnegan PM, Chen W. Arsenic toxicity: the effects on plant metabolism. Front Physiol 2012;3:182.

[14] EEA, European Environment Agency. Emissions of the main air pollutants in Europe. 2017. Retrieved from URL: https://www.eea.europa.eu/data-and-maps/indicators/main-anthropogenic-air-pollutant-emissions/assessment-5 on 25 September 2017.

[15] Schröder P, Fischer C, Debus R, Wenzel A. Reaction of detoxification mechanisms invsuspension cultured spruce cells (Picea abies L. Karst:) to heavy metals in purevmixture and in soil eluates. Environ Sci Pollut Res 2003;10:225–34.

[16] Thangavel P, Long S, Minocha R. Changes in phytochelatins and their biosynthetic intermediates in red spruce (Picea rubens Sarg:) cell suspension cultures under cadmium and zinc stress. Plant Cell Tissue Organ Cult 2007;88:201–16.

[17] Moudouma CFM, Riou C, Gloaguen V, Saladin G. Hybrid larch (Larix x eurolepis Henry): a good candidate for cadmium phytoremediation. Environ Sci Pollut Res 2013;20:1889–94.

[18] Serbula S, Radojevic A, Kalinovic J, Kalinovic T. Indication of airborne pollution by birch and spruce in the vicinity of copper smelter. Environ Sci Pollut Res 2014;21(19):11510–20.

[19] Golubović Ćurguz V, Raičević V, Veselinović M, Tabaković-Tošić M, Vilotić D. Influence of heavy metals on seed germination and growth of Picea abies L. Karst. Pol J Environ Stud 2012;21:355–61.

[20] Przybysz A, Sæbø A, Hanslin HM, Gawroński SW. Accumulation of particulate matter and trace elements on vegetation as affected by pollution level, rainfall and the passage of time. Sci Total Environ 2014;481:360–9.

[21] Saladin G. Phytoextraction of heavy metals: the potential efficiency of conifers. In: Sherameti I, Varma A, editors. Soil biology Vol 44. Heavy metal contamination of soils – monitoring and remediation. Switzerland: Springer; 2015. p. 333–53.

[22] Vlašínová H, Neděla V, Đorđević B, Havel L. Bottlenecks in bog pine multiplication by somatic embryogenesis and their visualization with the environmental scanning electron microscope. Protoplasma 2016;254(4):1487–97.

[23] Hakman I, von Arnold S. Plantlet regeneration through somatic embryogenesis in Picea abies (Norway Spruce). J Plant Physiol 1985;121:149–58.

[24] Von Arnold S, Ericsson T. In vitro studies of adventitious shoot formation in Pinus contorta. Can J Bot 1981;59:870–4.

[25] Bozhkov P, von Arnold S. Polyethylene glycol promotes maturation but inhibits further development of Picea abies somatic embryos. Physiol Plant 1998;104:211–24.

[26] Đorđević B, Krajňáková J, Hampel D, Gömöry D, Havel L. Effects of cadmium and lead stress on somatic embryogenesis of coniferous species. Part I: evaluation of the genotype dependent response. Acta Physiol Plant 2017;39:140.

[27] Jarosova M, Milde D, Kuba M. Elemental analysis of coffee: a comparison of ICP-MS and AAS methods. Czech J Food Sci 2014;32(4):354–9.

[28] Neděla V, Tihlaříková E, Hřib J. The low-temperature method for study of coniferous tissues in the environmental scanning electron microscope. Microsc Res Tech 2015;78(1):13–21.

[29] Neděla V, Hřib J, Vooková B. Imaging of early conifer embryogenic tissues with the environmental scanning electron microscope. Biol Plant 2012;56(3):595–8.

[30] Hřib J, Vooková B, Neděla V. Imaging of native early embryogenic tissue of Scots pine (Pinus sylvestris L.) by ESEM. Open Life Sci 2015;10(1):285–90.

[31] Neděla V, Hřib J, Havel L, Hudec J, Runštuk J. Imaging of Norway spruce early somatic embryos with the ESEM, Cryo-SEM and laser scanning microscope. Micron 2016;84:67–71.

[32] StatSoft, Inc. STATISTICA (data analysis software system), version 12.0, 2013. Retrieved from URL: http://statistica.io/Assessment on 15 August 2017.

[33] Huska D, Zitka O, Krystofova O, Adam V, Babula P, Zehnalek J, et al. Effects of cadmium(II) ions on early somatic embryos of Norway spruce studied by using electrochemical techniques and nuclear magnetic resonance. Int J Electrochem Sci 2010;5:1535–49.

[34] Supalkova V, Petrek J, Baloun J, Vojtech A, Bartusek K, Trnkova L, et al. Multiinstrumental investigation of the effect of cadmium(II) and lead(II) ions on early somatic spruce embryos. Sensors 2007;7:743–59.

[35] Đorđević B, Prášková M, Hampel D, Havel L. Effects of cadmium and lead stress on somatic embryogenesis of coniferous species. Part II: changes of thiol substances. Acta Physiol Plant 2017;39:141.

[36] Choudhury B, Chowdhury S, Biswas AK. Regulation of growth and metabolism in rice (Oryza sativa L.) by arsenic and its possible reversal by phosphate. J Plant Interact 2011;6(1):15–24.

[37] Gautam S, Anjani K, Srivastava N. In vitro evaluation of excess copper affecting seedlings and their biochemical characteristics in Carthamus tinctorius L. (variety PBNS-12). Physiol Mol Biol Plants 2016;22(1):121–9.

[38] Singh N, Ma LQ, Srivastava M, Rathinasabapathi B. Metabolic adaptations to arsenic induced oxidative stress in Pteris vittata L. and Pteris ensiformis L. Plant Sci 2006;170:274–82.

[39] Lombardi L, Sebastiani L. Copper toxicity in Prunus cerasifera: growth and antioxidant enzymes responses of in vitro grown plants. Plant Sci 2005;168:797–802.

[40] Krzesłowska M. The cell wall in plant cell response to trace metals: polysaccharide remodeling and its role in defense strategy. Acta Physiol Plant 2011;33:35–51.

[41] Muschitz A, Riou C, Mollet JC, Gloaguen V, Faugeron C. Modifications of cell wall pectin in tomato cell suspension in response to cadmium and zinc. Acta Physiol Plant 2015;37:245.

[42] Brunner I, Luster J, Günthardt-Goerg MS, Frey B. Heavy metal accumulation and phytostabilisation potential of tree fine roots in a contaminated soil. Environ Pollut 2008;152:559–68.

[43] Probst A, Liu H, Fanjul M, Liao B, Hollande E. Response of Vicia faba L. to metal toxicity on mine tailing substrate: geochemical and morphological changes in leaf and root. Environ Exp Bot 2009;66:297–308.

[44] Yang JL, Li YY, Zhang YJ, Zhang SS, Wu YR, Wu P, et al. Cell wall polysaccharides are specifically involved in the exclusion of aluminium from the rice root apex. Physiol Plant 2008;146:602–11.

[45] Turner AP, Dickinson NM. Copper tolerance of Acer pseudoplatanus L. (sycamore) in tissue culture. New Phytol 1993;123:523–30.

[46] Kartosentono S, Indrayanto G, Zaini NC. The uptake of copper ions by cell suspension cultures of Agave amaniensis, and its effect on the growth, amino acids and hecogenin content. Plant Cell Tissue Org Cult 2002;68:287–92.

[47] Yang X, Chen H, Xu W, He Z, Ma M. Hyperaccumulation of arsenic by callus, sporophytes and gametophytes of Pteris vittata cultured in vitro. Plant Cell Rep 2007;26:1889–97.

[48] Sfaxi-Bousbih A, Chaoui A, El Ferjani E. Copper affects the cotyledonary carbohydrate status during the germination of bean seed. Biol Trace Elem Res 2010;137(1):110–6.

[49] Pena LB, Azpilicueta CE, Gallego SM. Sunflower cotyledons cope with copper stress by inducing catalase subunits less sensitive to oxidation. J Trace Elem Med Biol 2011;25(3):125–9.

[50] Akhtar S, Shoaib A. Toxic effect of arsenate on germination, early growth and bioaccumulation in wheat (Triticum aestivum L.). Pak J Agric Sci 2014;51:399–404.

[51] Imran MA, Sajid ZA, Chaudhry MN. Arsenic (As) toxicity to germination and vegetative growth of sunflower (Helianthus annuus L.). Pol J Environ Stud 2015;24(5):1993–2002.

[52] Sethy SK, Ghosh S. Effect of heavy metals on germination of seeds. J Nat Sci Biol Med 2013;4(2):272–5.

[53] Smith SE, Christophersen HM, Pope S, Smith FA. Arsenic uptake and toxicity in plants: integrating mycorrhizal influences. Plant Soil 2010;327:1–21.

[54] Rai R, Pandey S, Rai SP. Arsenic-induced changes in morphological, physiological, and biochemical attributes and artemisinin biosynthesis in Artemisia annua, an antimalarial plant. Ecotoxicology 2011;20:1900–13.

[55] Duquesnoy I, Champeau GM, Evray G, Ledoigt G, Piquet-Pissaloux A. Enzymatic adaptations to arsenic-induced oxidative stress in Zea mays and genotoxic effect of arsenic in root tips of Vicia faba and Zea mays. C R Biol 2010;333:814–24.

[56] Kopittke PM, Asher CJ, Blamey FP, Auchterlonie GJ, Guo YN, Menzies NW. Localization and chemical speciation of Pb in roots of signal grass (Brachiaria decumbens) and Rhodes grass (Chloris gayana). Environ Sci Technol 2008;42:4595–9.

[57] Meyers DE, Kopittke PM, Auchterlonie GJ, Webb RI. Characterization of lead precipitate following uptake by roots of Brassica juncea. Environ Toxicol Chem 2009;28:250–5.

[58] Kopittke PM, Menzies NW. Effect of Cu toxicity on growth of cowpea (Vigna unguiculata). Plant Soil 2006;279:287–96.

[59] Ouzounidou G, Ciamporova M, Moustakas M, Karataglis S. Responses of maize (Zea mays L.) plants to copper stress. Growth, mineral content and ultrastructure of roots. Environ Exp Bot 1995;35:167–76.

[60] Ali NA, Bernal MP, Ater M. Tolerance and bioaccumulation of copper in Phragmites australis and Zea mays. Plant Soil 2002;239:103–11.

[61] Azeez MO, Adesanwo OO, Adepetu JA. Effect of Copper (Cu) application on soil available nutrients and uptake. Afr J Agric Res 2015;10(5):359–64.

[62] Azooz MM, Abou-Elhamd MF, Al-Fredan MA. Biphasic effect of copper on growth, proline, lipid peroxidation and antioxidant enzyme activities of wheat (Triticum aestivum'cv. Hasaawi) at early growing stage. Aust J Crop Sci 2012;6:688–94.

[63] Wu Z, Ren H, McGrath SP, Wu P, Zhao FJ. Investigating the contribution of the phosphate transport pathway to arsenic accumulation in rice. Plant Physiol 2011;157(1):498–508.

[64] Catarecha P, Segura MD, Franco-Zorrilla JM, García-Ponce B, Lanza M, Solano R, et al. A mutant of the Arabidopsis phosphate transporter PHT1;1 displays enhanced arsenic accumulation. Plant Cell 2007;19(3):1123–33.

[65] Tu C, Ma LQ. Interactive effects of pH, arsenic and phosphorus on uptake of As and P and growth of the arsenic hyperaccumulator Pteris vittata L. under hydroponic conditions. Environ Exp Bot 2003;50:243–25110.

[66] Esteban E, Carpena RO, Meharg AA. High-affinity phosphate/arsenate transport in white lupin (Lupinus albus) is relatively insensitive to phosphate status. New Phytol 2003;158:165–17310.

[67] Dwivedi S, Tripathi RD, Tripathi P, Kumar A, Dave R, Mishra S, et al. Arsenate exposure affects amino acids, mineral nutrient status and antioxidants in rice (Oryza sativa L.) genotypes. Environ Sci Technol 2010;44:9542–954910. B. Đorđević et al. *New BIOTECHNOLOGY 48 (2019) 35–43*

20 Exocyst Subunit EXO70H4 Has a Specific Role in Callose Synthase Secretion and Silica Accumulation

Ivan Kulich[a], Zdeňka Vojtíková[a], Peter Sabol[a], Jitka Ortmannová[a,b], Vilém Neděla[c], Eva Tihlaříková[c], and Viktor Žárský[a,b]

a *Department of Experimental Plant Biology, Faculty of Sciences, Charles University, Prague, Czech Republic*

b *Institute of Experimental Botany, Academy of Sciences of the Czech Republic, Prague, Czech Republic*

c *Institute of Scientific Instruments of the Academy of Sciences of the Czech Republic, Brno, Czech Republic*

Abstract

Biogenesis of the plant secondary cell wall involves many important aspects, such as phenolic compound deposition and often silica encrustation. Previously, we demonstrated the importance of the exocyst subunit EXO70H4 for biogenesis of the trichome secondary cell wall, namely for deposition of the autofluorescent and callose-rich cell wall layer. Here, we reveal that EXO70H4- driven cell wall biogenesis is constitutively active in the mature trichome, but also can be activated elsewhere upon pathogen attack, giving this study a broader significance with an overlap into phytopathology. To address the specificity of EXO70H4 among the EXO70 family, we complemented the exo70H4-1 mutant by 18 different Arabidopsis (Arabidopsis thaliana) EXO70 paralogs subcloned under the EXO70H4 promoter. Only EXO70H4 had the capacity to rescue the exo70H4-1 trichome phenotype. Callose deposition phenotype of exo70H4-1 mutant is caused by impaired secretion of PMR4, a callose synthase responsible for the synthesis of callose in the trichome. PMR4 colocalizes with EXO70H4 on plasma membrane microdomains that do not develop in the exo70H4-1 mutant. Using energy-dispersive x-ray microanalysis, we show that both EXO70H4- and PMR4-dependent callose deposition in the trichome are essential for cell wall silicification.

Introduction

The exocyst is a protein complex conserved across all eukaryotes, composed of eight subunits with a rod-like shape. Its main function described in yeast is tethering secretory vesicles to the plasma membrane (PM; Munson and Novick, 2006). Two exocyst subunits, SEC3 and EXO70, were described as spatial landmarks for polarized secretion in yeast. It was clearly shown that SEC3 is capable of working as a landmark by itself, whereas EXO70 likely requires additional signalling factors

to work (Luo et al., 2014), such as small GTPases (Wu et al., 2010). The rest of the complex, also referred to as the exocyst core, is associated with secretory vesicles and is regulated via RAB GTPase interactions (Robinson et al., 1999). Most of the time, all exocyst subunits form a relatively stable holocomplex in yeast (Heider et al., 2016; Picco et al., 2017). The interaction of the exocyst core with SEC3 and EXO70 subunits at the PM mediates the tethering of the vesicle to the membrane, followed by the SNARE protein-mediated fusion of the vesicle with the membrane (Heider and Munson, 2012; Yue et al., 2017). Besides conventional roles, the animal EXO70 protein was shown to induce membrane curvature (Zhao et al., 2013).

In comparison with yeast and mammalian genomes, which encode only one or two EXO70s, land plant genomes encode a high number of EXO70 paralogs, which likely emerged during land colonization. The Arabidopsis (Arabidopsis thaliana) genome encodes 23 EXO70 paralogs (Elias et al., 2003; Cvrčková et al., 2012). EXO70A1, the most basal EXO70, has been shown to be involved in the secretion of membrane proteins such as PIN1 or BRI1 (Drdová et al., 2013). It also is crucial for the proper development of the Casparian strip (Kalmbach et al., 2017). EXO70A1 also is recruited to the microtubules decorating xylem secondary cell wall thickenings in a COG/VETHdependent manner, where EXO70A1 recruits the exocyst complex and is responsible for the development of the cell wall thickenings (Oda et al., 2015; Vukašinović et al., 2017). Another example of the exocyst recruitment was shown on EXO70B1, which is recruited to the PM by RIN4 (Sabol et al., 2017). Thus, besides direct lipid interaction, plant EXO70s also seem to be recruited by other proteins. Besides secretion, the EXO70B1 subunit functions in autophagy (Kulich et al., 2013), immune responses (Stegmann et al., 2013; Zhao et al., 2015), and stomatal opening (Hong et al., 2016; Seo et al., 2016). EXO70H1 and EXO70B2 were shown to facilitate the defense papilla buildup (Pecenková et al., 2011). Recently, we showed a role of the EXO70H4 paralog in Arabidopsis trichome cell wall maturation (Kulich et al., 2015).

Arabidopsis leaf trichomes are unicellular outgrowths with very specific polarized shape and two to four (but most frequently three) sharp branches. Their shape is easily and visibly distorted by numerous mutations, which, together with their large size and good accessibility, led to their popularity as a model for studies of plant cell morphogenesis (Hülskamp et al., 1994). They have been especially vital for studies of microtubule- and actin-dependent morphogenetic events (Saedler et al., 2004; Tian et al., 2015), but also serve as a model for deposition of cell wall components (Sinlapadech et al., 2007; Bischoff et al., 2010).

We previously demonstrated that the Arabidopsis trichome cell wall consists of two distinct domains, the basal thin cell wall of the bulb and apical thick cell wall. These domains are separated by a callose-rich structure named the Ortmannian ring (OR). Only the apical cell wall domain consists of an outer and inner layer. We showed that the development of the inner cell wall layer depends on the exocyst subunit EXO70H4 (Kulich et al., 2015). However, we did not provide a detailed description, subcellular localization, and the functional context of EXO70H4. Here, we focused on the EXO70H4-dependent callose deposition, as the lack of callose is one of the most prominent defects of the exo70H4-1 mutant and because callose deposition is of great interest due to its involvement in plant immunity.

Callose is a cell wall polymer, b-1-3-glucan that is involved in many plant developmental processes, such as cell plate formation (Hong et al., 2001), the development of phloem (Bonke et al., 2003), stomata (Guseman et al., 2010), pollen, and pollen tube, as well as regulations of plasmodesmatal permeability (Iglesias and Meins, 2000). It also is deposited in response to abiotic and biotic stress stimuli like wounding, pathogen invasion, or heavy metals exposure (Frye and Innes, 1998; Blümke et al., 2013; Ellinger et al., 2013, 2014).

In contrast to cellulose, a b-1-4-glucan that is crystallized into permanent microfibrils, callose is deposited as an amorphous plug, and often only transiently, because it is specifically and rapidly degraded by the hydrolytic enzymes b-1-3-glucanases (Levy et al., 2007). Callose is synthesized at the PM by large glucan synthase complexes called callose synthases (CalS) or glucan synthase-like (GSL). The Arabidopsis genome contains 12 CalS genes, which fall into two groups (Verma and Hong, 2001). CalS from the first group contain up to 50 exons and are some of the longest genes found in the Arabidopsis genome. The second group consists of CalS11 (GSL1) and CalS12 (GSL5), containing two and three exons, respectively (Hong et al., 2001). Different CalS are expressed in a tissue-specific way in response to diverse physiological conditions (Dong et al., 2008).

It is supposed that callose synthases are transported to the sites of callose synthesis by vesicle trafficking and that the cytoskeleton and endomembrane system are necessary for callose synthase distribution, transport, and positioning (Cai et al., 2011; Drakakaki et al., 2012). Despite pilot observations of callose synthase transport by vesicle-like bodies (Cai et al., 2011; Drakakaki et al., 2012; Nielsen et al., 2012), strong evidence is missing.

In this study, we worked with two callose synthase proteins: CalS9 (GSL10) and CalS12. CalS9 is known to act in male gametophyte development with mutants defective in pollen mitotic division (Töller et al., 2008; Huang et al., 2009), and it

is one of the most transcribed callose synthases in the trichome (Jakoby et al., 2008). CalS12, also known as powdery mildew resistant 4 (PMR4), is a stress-induced callose synthase (Vogel and Somerville, 2000). Knockout mutants lack pathogeninduced callose deposits (Jacobs et al., 2003; Ellinger et al., 2013). One of the possible roles for the callose deposits may be inducing mechanical stiffness in the cell wall by supporting its silicification.

Silica is a nonessential micronutrient absorbed by plants in the form of silicic acid, $Si(OH)_4$, and deposited in different amounts into cell walls of various tissues and structures. Typically, trichome cell walls of many plants are encrusted with silica. Some observations suggest that silica deposition may be related to callose synthesis. The co-occurrence of callose and silica deposition was previously shown in several plant species, including silica hyperaccumulators, for example, in the common horsetail (Equisetum arvense; Law and Exley, 2011), in epidermal trichomes of numerous species (Waterkeyn and Dupont, 1982), Selaginella (Webster, 1992), and Arabidopsis (Brugiére and Exley, 2017). Callose was suggested as an inducing rather than catalysing element of silicification, operating as a supportive matrix for the specific condensation of silicic acid into silica nanoparticles (Brugiére and Exley, 2017). There also is evidence that carbohydrates other than callose can act as organic matrices for silicification (Perry et al., 1987; Leroux et al., 2013; Guerriero et al., 2016), but also that in some cases no carbohydrates are needed (Hodson, 2016).

Despite this considerable evidence for the dependency of silica deposition on callose synthesis, a comprehensive analysis was still missing. In this report, we demonstrate that callose is indispensable for silica deposition in Arabidopsis trichomes.

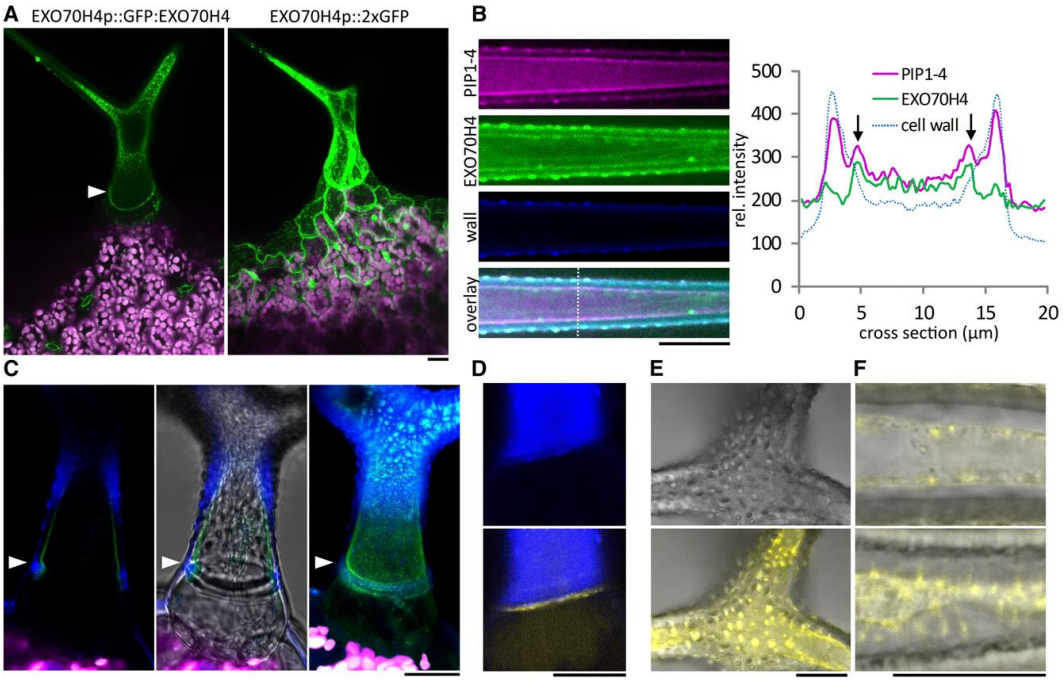

Figure 1. EXO70H4 localization in the trichome. A, EXO70H4 (green) under its native promoter is only visible in the trichome (left), but the EXO70H4 promoter is active also in other epidermal cells (right). Magenta represents chlorophyll; arrowhead points at the OR. B, EXO70H4 colocalizes with PM marker PIP1-4. Graph on the right represents plot of the profile depicted as white dotted line on the left. C, EXO70H4p::mGFP:EXO70H4 (green) localizes to the OR (white arrowheads) and the apical domain above the OR, which produces a highly autofluorescent cell wall (blue). Chlorophyll is in magenta. Left, Single section; middle, single section with transmission; right, z projection. D, A detail of the OR labeled by mCH-EXO70H4 (yellow) and the border of the apical autofluorescent cell wall domain (blue) and the basal domain. Top, Autofluorescence; bottom, autofluorescence and mCH-EXO70H4. E, Detailed view of the mCH-EXO70H4-positive cell wall ingrowths. Top, Transmission; bottom, transmission and mCH-EXO70H4. F, Plasmolysis of a trichome with labeled mCH-EXO70H4, without (top) and with (bottom) developed cell wall ingrowths. The differential attachment of the PM to the cell wall is visible. Bars = 20 µm.

Results

EXO70H4 Is Localized to the OR and a PM Domain above It

To observe the localization of the EXO70H4 protein, we generated native promoter-driven constructs with an N-terminal GFP and with mCHERRY (GFPEXO70H4, mCH-EXO70H4). These constructs were proven to be functional, as they fully complemented the exo70H4-1 mutation described previously (Kulich et al., 2015). In the absence of stress, EXO70H4 constructs were exclusively expressed in the trichome; however, the EXO70H4 promoter also was active in other epidermal cells, showing the capacity of EXO70H4 to be activated elsewhere (Fig. 1A). This also was true for other EXO70 paralogs expressed under the EXO70H4 promoter (see further), suggesting posttranscriptional regulation of EXO70H4. To show whether GFPEXO70H4 localizes to specific PM domains, we

looked for colocalization with the well-established PM marker mCHERRY-PIP1-4 (Geldner et al., 2009; Fig. 1B). Unfortunately, PIP1-4 is almost completely degraded in the mature trichome.

The localization of EXO70H4 very well matches the callose-rich and autofluorescent cell wall shown in Kulich et al. (2015). The XFP-EXO70H4 signal is always present at the OR and above it (apical domain) throughout trichome cell wall development (Fig. 1, A, C, and D). The presence of the EXO70H4 signal was always accompanied by cell wall autofluorescence. The basal PM domain beneath the OR is devoid of GFPEXO70H4 (Fig. 1, A and D). Identical results were obtained using the mCHERRY construct mCHEXO70H4 (Fig. 1, D–F). In young trichomes, the signal above the OR is homogeneous. In older trichomes, the signal becomes more speckled and accumulates at the differential interference contrast-visible cell wall ingrowths, which are a common feature of older trichomes (Fig. 1E). Upon plasmolysis, the mCHEXO70H4 signal is easily separated from the cell wall of the young trichomes but is attached to the cell wall that has developed ingrowths along cytoplasmic strands (Fig. 1F). To confirm that these are actual cell wall ingrowths, we investigated the trichome cell wall from the inside using environmental scanning electron microscopy (ESEM; Supplemental Fig. S1).

On these ingrowths, mCH-EXO70H4 transiently colocalizes with the core exocyst subunits GFP-SEC8 and EXO84-GFP expressed under their respective natural promoters (Fig. 2). The core exocyst subunit signal is, however, visible also in the cytoplasm and in other membrane domains, suggesting their general function in secretion. These data fit with our previous yeast two-hybrid study, where EXO70H4 also physically interacted with the Arabidopsis exocyst subunits SEC5A, SEC6, and EXO84b (Kulich et al., 2015).

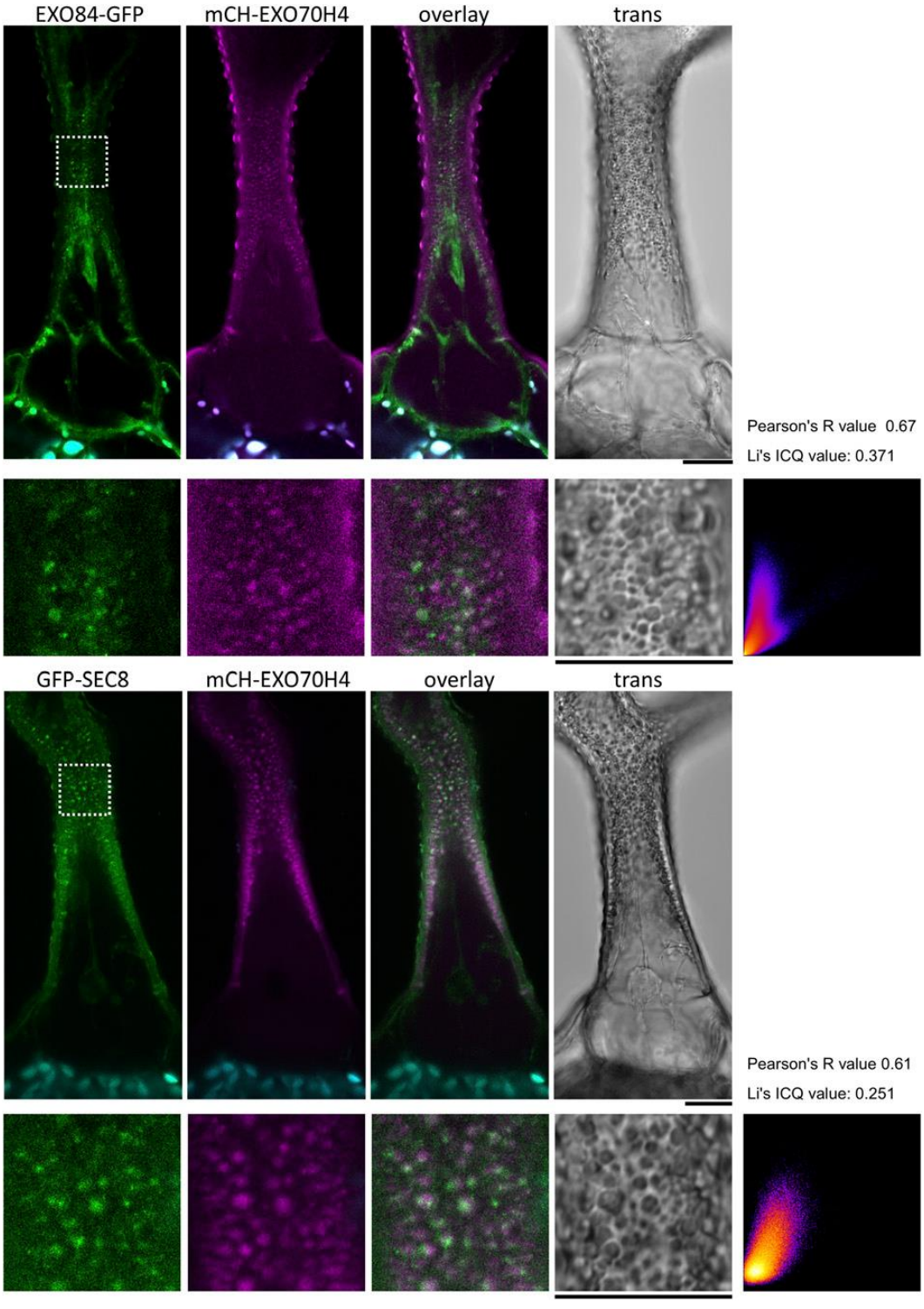

Figure 2. Colocalization of the core exocyst subunits with EXO70H4. SEC8 and EXO84 under their own natural promoters largely localize to the cytoplasm and partially localize to the EXO70H4-positive compartments. The ratio of both signals changes over time. Bars = 20 µm.

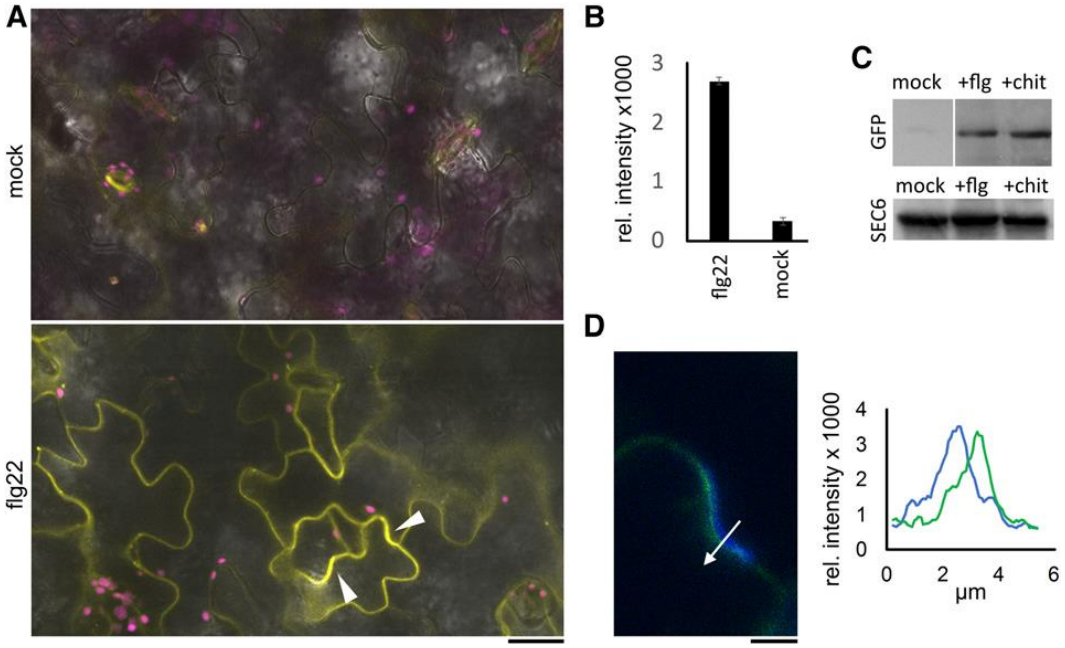

Figure 3. EXO70H4 up-regulation by flg22 in the leaf pavement cells. A, Representative images of leaves 5 h after flg22 treatment (spraying by 1 mM flg22 in 0.05% Silwet and 0.05% Silwet as control). Yellow, mCH-EXO70H4; magenta, chlorophyll; grays, transmission. Arrowheads depict domains with enchiched EXO70H4 signal. Scale bar = 20 mm. B, Quantification of the EXO70H4 signal intensity out of 10 plants and 100 cells. Similar results were obtained in three independent replicates, with both GFP- and mCHERRY-labeled constructs. C, Up-regulation of EXO70H4 in total cell extract from whole rosettes of GFP-EXO70H4 plants, 5 h after flg22 and chitin treatment. The white line is where one empty lane was left on the gel due to overflow. SEC6 was used as a loading control. D, GFP-EXO70H4 (green) forms a microdomain with enriched signal. This is accompanied by development of cell wall autofluorescence (blue). The arrow shows the position of the plot profile in D. Scale bar = 5 µm. Right, Plot profile demonstrating spatial separation of EXO70H4 and cell wall autofluorescence.

Flg22 Induces EXO70H4 Expression in Epidermal Pavement Cells

Because the composition of the trichome inner cell wall layer highly resembles the pathogen-induced cell wall appositions, we investigated whether there is a possible function of EXO70H4 beyond the trichome. As shown in Figure 1A, the EXO70H4 promoter has a capacity to drive EXO70H4 expression in other epidermal cells, but the EXO70H4 protein is absent. Public microarray data suggest an elevation of the EXO70H4 mRNA signal upon flg22 treatment. Therefore, we applied 1 mM flg22 by spraying on the mature Arabidopsis rosettes (24 d old). Four hours after the treatment, the first visible signal appeared in the epidermal pavement cells and peaked approximately 5 h after induction (Fig. 3A). The signal disappeared again 12 h after induction. We got similar results with both GFP and mCHERRYlines and quantified the fluorescence intensity (Fig. 3B). These results are supported by the western blot analysis of the total cell extract using an anti-GFP antibody and document similar up-regulation using chitin as elicitor (Fig. 3C). In many cells, the EXO70H4 signal was not evenly distributed across the cell surface and formed

small domains of higher signal intensity. These domains developed cell wall autofluorescence similar to the autofluorescence of the trichome apical cellwall (Fig. 3D).

EXO70H4 Differs from Other Arabidopsis EXO70 Paralogs in Its Function and Subcellular Localization

To learn more about the specificity of EXO70H4 function, we performed a cross-complementation analysis, in which we subcloned multiple EXO70 paralogs under the EXO70H4 promoter. We subcloned 18 different EXO70 paralogs in the same fashion under EXO70H4 promoter (EXO70H4p::GFP:EXO70XY). We selected at least one gene from each subfamily (A–G) and all members of the subfamily H. Then, we transformed these constructs into the exo70H4-1 mutant background and observed the development of trichome autofluorescence (Fig. 4, A and B) and trichome callose deposition (Supplemental Fig. S2). Both of these parameters provided us with identical results. Apart from EXO70H4, no other paralog could restore either the callose or autofluorescence, suggesting that the function of EXO70H4 is highly specific.

Most EXO70 paralogs showed no PM localization in the trichome (Supplemental Fig. S3). While EXO70A1 was uniformly distributed over the whole PM of the trichome (even beneath the OR; Fig. 4C), EXO70B1 and most of the other EXO70 paralogs showed cytoplasmic and nuclear localization.

Despite using an identical experimental setup, some of the EXO70 proteins (H1, E2, G2, H2, H3, H5, and H6) were not detected in the trichome, and therefore, we cannot exclude that some of these have the capacity to complement EXO70H4 on the protein level (Supplemental Fig. S3). This may be due to microRNA (miRNA) regulation of the EXO70 mRNA. We identified several miRNAs that may interfere with EXO70. The number of predicted interfering RNAs (based on Yi et al. [2015] database) is enhanced in the EXO70H subfamily (Supplemental Table S1).

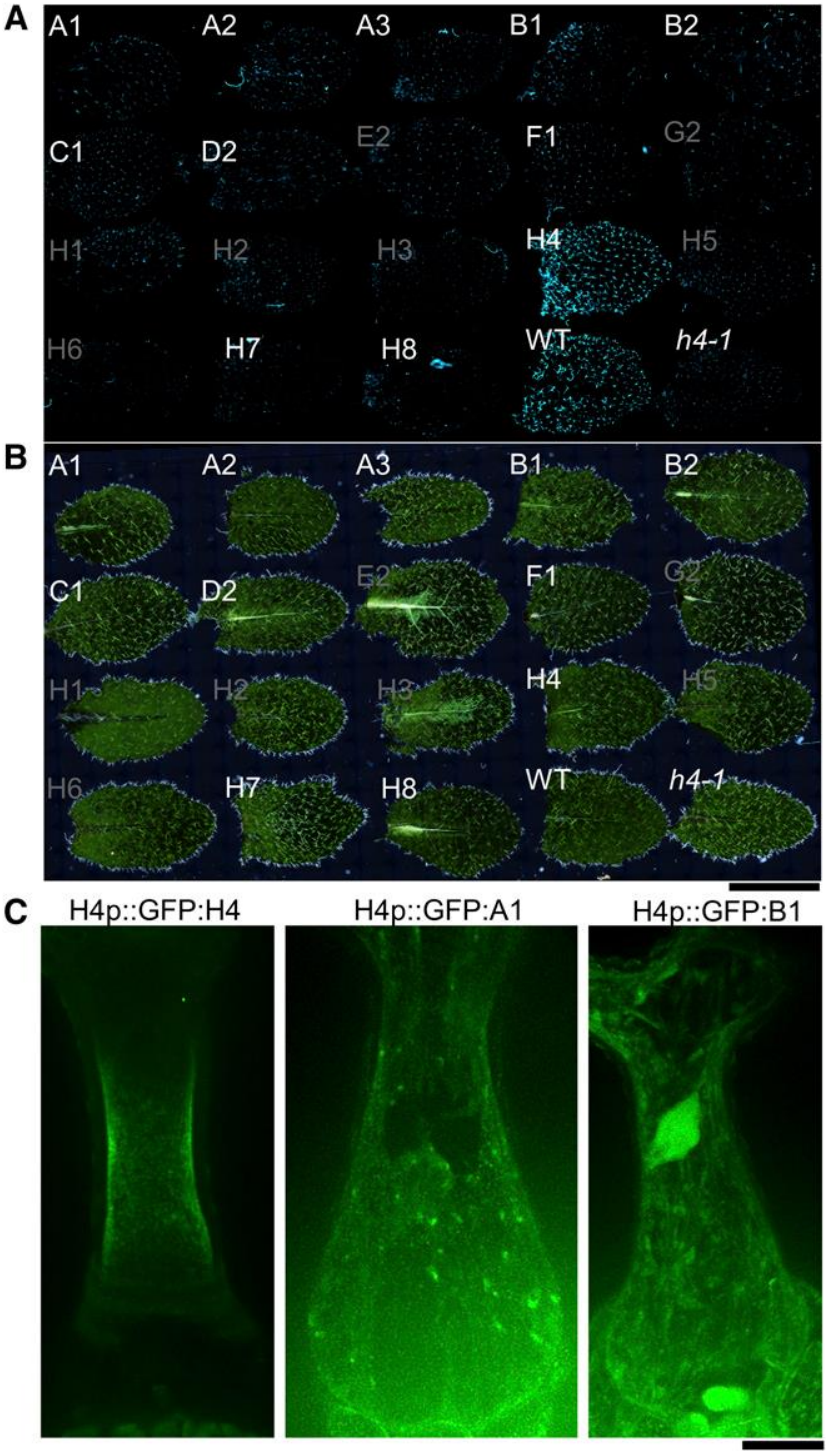

Figure 4. Complementation of the exo70H4-1 mutant by multiple EXO70 paralogs. A, Autofluorescence of trichomes on leaves of individual transgenic lines (A1 stands for exo70H4-1 complemented by EXO70H4p::GFP:EXO70A1, etc.), plus wild-type control (WT) and exo70H4-1 mutant (h4-1). Gray letters label lines where no GFP signal was observed in the trichome. B, Dark-field view of A. Large images (A and B) consist of 475 tiles. Scale bar = 500 mm. C, Localization of selected EXO70 paralogs under the EXO70H4 promoter in exo70H4-1 background (H4p::GFP:H4 stands for EXO70H4p::GFP: EXO70H4, etc.). Localizations of all 18 tested EXO70 paralogs are shown in Supplemental Figure S3.

EXO70H4 Is Essential for PM Localization of Callose Synthases in the Trichome

Since we showed that callose is absent from the exo70H4-1 mutant trichomes (Kulich et al., 2015), we further investigated the callose synthase delivery to the PM. We worked with two callose synthases and generated ubiquitin promoter-driven callose synthase constructs UBQ::GFP:PMR4 (GFP-PMR4) and UBQ::GFP:CALS9 (GFP-CALS9). Here, we focus on PMR4, which is essential for the callose production in the trichome. We obtained similar results using CALS9. These can be found in the supplements (Supplemental Fig. S4).

As reported previously, pmr4 mutants lack pathogen-induced callose deposits (Jacobs et al., 2003; Ellinger et al., 2013). In our hands, pmr4 trichomes also lacked the visible callose, stained with aniline blue (Fig. 5A). This phenotype was complemented by transforming the pmr4 mutant plants with GFP-PMR4 (Fig. 5B), demonstrating the functionality of this construct. In contrast to exo70H4-1, pmr4 trichomes are mechanically stiff and show wild type-like autofluorescence (Fig. 5C).

Next, we introduced UBQ::GFP:PMR4 into the wild type and the exo70H4-1 mutant line. In the wild-type trichome, the signal of both callose synthases was visible in immobile membrane speckles at the PM and also on mobile membrane bodies, possibly representing multiple steps of the secretory pathway (Fig. 6A). To separate mobile PMR4 fraction from the immobile PM dots, we performed time-series imaging and minimal intensity projections (Fig. 6B). In the exo70H4-1 mutant plants, the signal from the PM speckles was lost, suggesting a secretory defect of both of these callose synthases (Fig. 6, B–D).

By colocalization of EXO70H4p::mCHERRY:EXO70H4 with UBQ::GFP:PMR4, we show that the callose synthase speckles also are EXO70H4 positive (Fig. 6A). As described above, the signal of callose synthases was first visible in smaller transient speckles on the PM of young trichomes and developed later into large speckles. Taken together, our data show the dependency of callose synthase secretion on the EXO70H4 protein.

Silica Accumulation Is Dependent on Callose Deposition and Thus on the EXO70H4-Dependent PMR4 Secretion

While doing our ESEM studies of untreated biological samples (Tihla_ríková et al., 2013; Ned_ela et al., 2015), we applied energy-dispersive x-ray spectroscopy for a semiquantitative analysis of elements in the trichome. Surprisingly, apart from heavy metals, we noticed a significant amount of silica in the domain above the OR.

This silica encrustation was absent in exo70H4-1 mutant trichomes. To determine whether this was a direct effect of the exo70H4-1 mutation, we next included a pmr4 mutant (which lacks callose in the trichome), and we increased the amount of silica in the soil by watering with sodium silicate solution (final concentration 2 mM). As shown in Figure 7, both the pmr4 and the exo70H4-1 mutants had dramatically reduced silica levels in the trichomes. Therefore, we conclude that callose deposition is essential for cell wall silicification and that the exo70H4-1 silica phenotype is a secondary phenotype, contingent on the impaired callose synthase delivery and the subsequent absence of callose synthesis.

Discussion

In our previous study, we demonstrated the EXO70H4-dependent development of the callose-rich cell wall in the Arabidopsis trichome. Here, we show that EXO70H4 acts by promoting the secretion of callose synthase. Surprisingly, no other EXO70 subcloned under the EXO70H4 promoter was able to complement the exo70H4-1 phenotype, despite high sequence similarity of some paralogs (Cvrčková et al., 2012). Since EXO70 proteins in general act as spatial landmarks for secretion, it is likely that the specificity of EXO70 paralogs reflects their differential target binding capacities. EXO70H4 decorates a specific PM subdomain in the trichome, while the most ancestral EXO70A1 localizes all over the trichome PM. This is consistent with the previous model of multiple recycling domains within one cell (Zárský et al., 2009). We also observed that some of the EXO70 paralogs with cytoplasmic localization in the trichome localize to the PM in the pavement cells (e.g. EXO70B1), suggesting differential regulatory mechanisms.

The cross-complementation analysis suggests that the EXO70H4-positive trichome PM domains have a highly distinctive character and cannot be recognized by other EXO70 paralogs. Previously, it was proposed that the EXO70 paralogs differ just in their expression pattern (Li et al., 2010). In this study, we demonstrate that there is functional divergence between the paralogs. This also is supported by other studies showing specific EXO70 roles (Kulich et al., 2013; Zhao et al., 2015) and recently by the specific PM domain localizations of NtEXO70A1 and NtEXO70B1 in tobacco (Nicotiana tabacum) pollen tubes (Sekereš et al., 2017).

Since EXO70 proteins are putative landmarks for secretion, the specificity of EXO70 paralogs could mainly be determined by different localization signals. For example, during xylogenesis, EXO70A1 localization to cortical microtubules is maintained by COGVETH proteins (Oda et al., 2015; Vukašinović et al., 2017). Also, as we showed recently, EXO70B1 PM localization can be achieved by

protein-protein interaction with NOI family proteins (Sabol et al., 2017). We speculate that a similar mechanism, but with different proteins, may be responsible for the specific localization of many EXO70 paralogs, causing their functional diversity. Whether the process of EXO70H4 localization is mediated by specific lipid-binding properties or by interacting proteins is the subject of our follow-up study.

The initially homogenous PM signal of GFPEXO70H4 develops later into stable speckles, which then form ingrowths of the cell wall. Similar behavior of the exocyst subunits was observed during xylogenesis, where EXO70A1-tagRFP first localized dispersedly to the PM and later on gradually organized into a bundled pattern (Vukašinović et al., 2017). Such stabilization of the polarity was observed previously in budding yeast (Saccharomyces cerevisiae; Brennwald and Rossi, 2007). The mechanism of this stabilization in plants is not yet known, but in our opinion it may be achieved by a positive feedback loop, whereby the original EXO70 attracts vesicles with more exocyst subunits.

Unfortunately, not all the EXO70 constructs in our cross-complementation study were expressed in the trichome. We explain this by a predicted RNA interference regulation, which is common among stressinduced transcripts (Sunkar and Zhu, 2004), or by ubiquitination, which was previously manifested as a possible step in EXO70 protein regulation (Samuel et al., 2009; Stegmann et al., 2012; Seo et al., 2016). Very likely, EXO70s are subjected to a high degree of regulation at multiple levels.

Here, we show a secretory defect of the exo70H4-1 mutation on one type of cargo: two callose synthases, which both localized and behaved similarly despite their functional classification. Of these, only CALS12 was biologically relevant for callose synthesis in the trichome. More cargo affected by the exo70H4-1 mutation must exist, since the trichomes lacking only callose and silica in the case of the pmr4 mutation are still mechanically relatively stiff and accumulate autofluorescent compounds and metals, unlike exo70H4-1 mutants.

The inner cell wall of the trichome shares many similarities with the pathogen-induced cell wall (being rich in callose, silica, and phenolic compounds; Russo and Bushnell, 1989; Ghanmi et al., 2004), and as we show here, EXO70H4 has the capacity to contribute to such a cell wall biogenesis, since the EXO70H4 protein appears in nontrichome cells upon bacterial elicitor treatment, allowing PMR4 and other cargo secretion and callose synthesis. Deposited callose thereafter acts as a matrix for silica accumulation, which is known to modulate physical properties of the cell wall and acts as an important line of defense against fungal pathogens

(Ghanmi et al., 2004; Fauteux et al., 2006; Vivancos et al., 2015). The exact relationship between callose and the silica accumulation was enigmatic for a long time, although it was clear that these processes are related (Law and Exley, 2011; Exley, 2015). First evidence that callose may be essential for silica deposition was provided recently (Brugiére and Exley, 2017), using chemical staining of silica. In our study, we extend these observations with quantitative and statistically processed data. We also show that callose is not essential for the accumulation of phenolic compounds in the cell wall in contrast to some observations that lignification precedes silicification (Zhang et al., 2013).

While Arabidopsis trichomes contain relatively little silica, trichomes of species such as nettle (Urtica dioica) are well known for their silicified cell wall (Sangster and Hodson, 2007). Cucumber (Cucumis sativus) trichomes also contain silica, and supplementing plants with silica leads to physically stiffer trichomes (Samuels, 1993). In cucumber, basal cells of the trichomes (sometimes referred to as cells surrounding the trichome or the trichome spine) were the site of maximal silica deposition (Samuels et al., 1991a, 1991b; Chérif et al., 1992). Transcriptomic analyses have revealed that wild-type cucumber contains 406-fold more CsEXO70H4 transcript than the trichome-less tbh mutant (Chen et al., 2014). This suggests that the mechanisms we describe in the Arabidopsis trichome may have more general implications for eurosids.

Materials and Methods

Plant Material and Growth

If not indicated otherwise, plants were grown in standard growth chamber conditions (long day 16 h:8 h, 100 µM photosynthetically active radiation m^{-2} s^{-1}). LT 36W/958 T8 BIOVITALNARVAfluorescent tubes were used. These contain a UV-B peak. All plants were grown in Jiffy soil pellets. The exo70H4-1 mutant was described previously (Kulich et al., 2015), as well as the pmr4-1mutant (Vogel and Somerville, 2000). As a control, a wild-type sibling of the exo70H4-1 mutant was used. As a control for the exo70H4-1 × rdr6-12 double mutant, rdr6-12 (Peragine et al., 2004) was used.

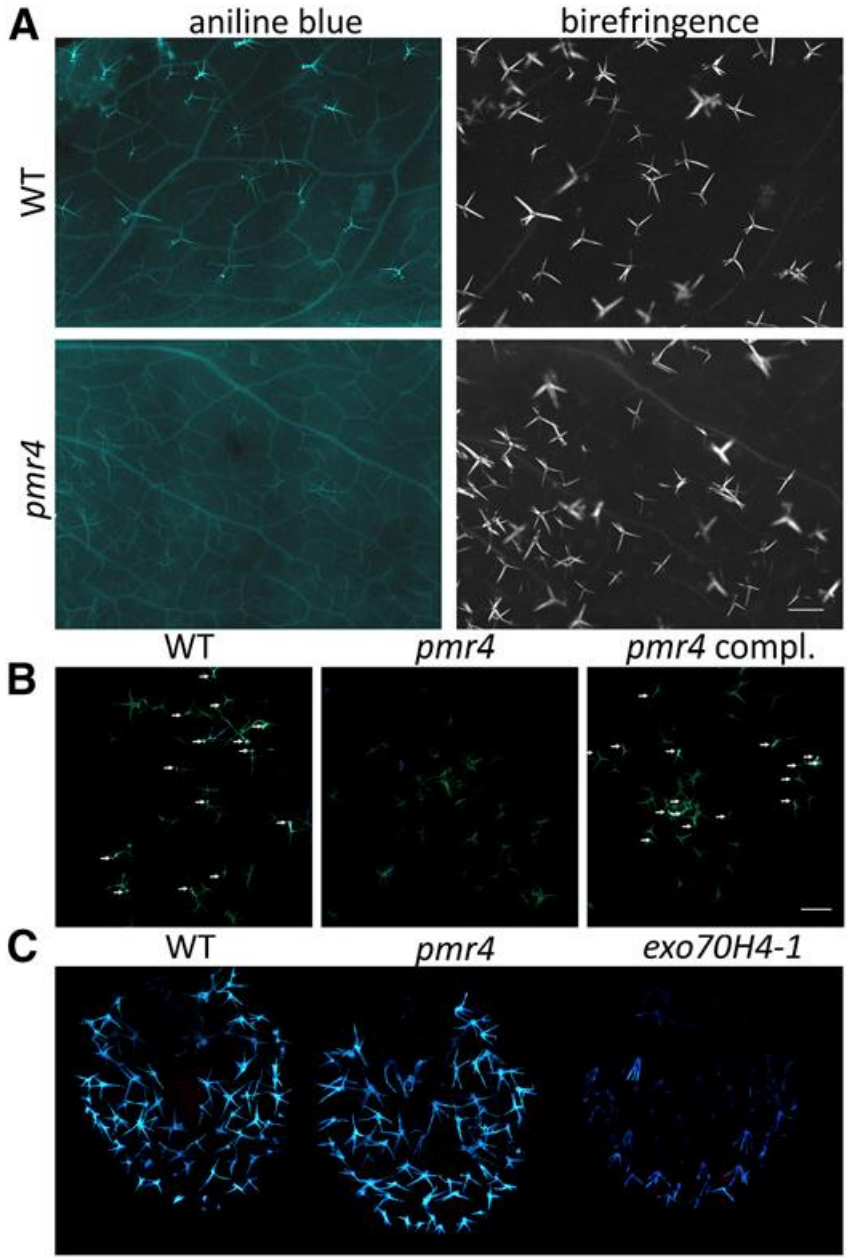

Figure 5. Trichome phenotype of pmr4 mutant. A, Aniline blue staining of callose (left) and cellulose birefringence in polarized light (right) for pmr4 (top) and wild type (WT; bottom) leaves. B, Aniline blue staining of callose on isolated trichomes of wild type, pmr4, and pmr4 mutant complemented with UBQ::GFP:PMR4 construct (pmr4 compl.); arrows point to trichomes with developed callose structures. Scale bar = 500 µm. C, Autofluorescence of phenolic compounds in broken (dead) trichomes of wild type, pmr4, and exo70H4-1, respectively.

Callose Staining and Autofluorescence Visualization

To stain for callose, whole leaves were washed for 3 h in acetic acid:ethanol (1:3) solution,washed three times in deionized water, andincubated overnight in aniline blue solution (150 mM KH_2PO_4 and 0.01% [w/v] aniline blue, pH 9.5). Trichomes were then imaged on leaves or brushed off and imaged.

For autofluorescence development, leaves were placed in between two microscopy slides and dried up overnight. Fifth and sixth leaves of the 24- to 28-d-old rosettes were used for the aniline blue staining and the third youngest visible leaf for autofluorescence observations.

PAMP Treatments

Flg22 (1 μM) or chitosan solution (150 mg/L) with 0.05% Silwet Star wetting agent was sprayed onto the 24-d-old Arabidopsis (Arabidopsis thaliana) rosettes stably transformed with XFP-EXO70H4. Silwet Star (0.05%) was used as a control. Signal was observed 4 to 5 h after the treatment. This experiment was done in triplicate. Spraying was critical factor for the EXO70H4 up-regulation. Protein extract from whole rosettes was used for the western blot analysis, using primary anti-GFP and anti-SEC6 antibodies (Agrisera; AS15 2987 and AS13 2686, respectively).

Construct and Transgenic Line Preparation

For the cloning of all EXO70 paralogs, a multisite gateway approach was used. The EXO70H4 promoter (1 kb upstream) was subcloned into pDONORP4-P1r. GFP in pEN-L1-F-L2 (GFP) was obtained from Karimi et al. (2007). pEN-L1-mCherry-L2 was obtained from Mylle et al. (2013); however, since this construct had a stop codon, we used it as a template to generate a new pDONOR 221-mCherry construct. EXO70 coding sequences were amplified in one or two steps (with att extension primers) and subcloned into the pDONOR P2R-P3 using Gateway BP clonase (Invitrogen). Then, multisite reactions were performed using the EXO70H4 promoter, GFP, EXO70 coding sequence, and destination vector pB7m34GW(BASTA plant selection; Karimi et al., 2007). pDONOR vectors were sequenced using M13 primers. The destination binary constructs were sequenced using M13 primers and two GFP primers (see primer list in Supplemental Table S2). To clone callose synthase PMR4, the genomic fragment was subcloned into pDONOR 221 using Gateway BP clonase and then transferred into the pUBN-GFP vector (Grefen et al., 2010) using Gateway LR clonase. Since the CalS9 genomic fragment is too long to amplify, we isolated the cDNA. This was stitched together from two parts, as none of transcripts had all 42 introns properly spliced. GFP-SEC8 and EXO84b-GFP lines were described previously (Fendrych et al., 2013). All primers in this study are listed in Supplemental Table S2.

All prepared constructs were electroporated into Agrobacterium tumefaciens GV3101 competent cells. The floral dip method (Clough and Bent, 1998) of plant transformation was used, and the transformants were selected on soil by spraying

with BASTA (150 mg/L of glufosinate-NH4). At least five individual transformants were observed in each experiment, and at least two biological replicates were made.

Light Microscopy

Zeiss LSM880 with C-Apochromat 40×/1.2 W Korr FCS M27 objective was used for Figures 1, 4, and 5 [GFP (488): 508–540 nm, chlorophyll (488) 650–721 nm, cell wall autofluorescence (405) 426–502, mCHERRY (561) 597–641]. For Figure 4C and Supplemental Figures S3 and S4, we used Yokogawa CSU-X1 on Nikon Ti-698 E platform, Agilent MLC400 laser box,

and iXON camera (Andor) using filter stringent cubes for GFP and RFP. For Figure 4, A and B, and Supplemental Figure S2, Nikon Eclipse 90i with PlanApo 4×/0.2 objective and Nikon DsFi 2 camera were used. Images were processed using the Fiji platform (Schindelin et al., 2012).

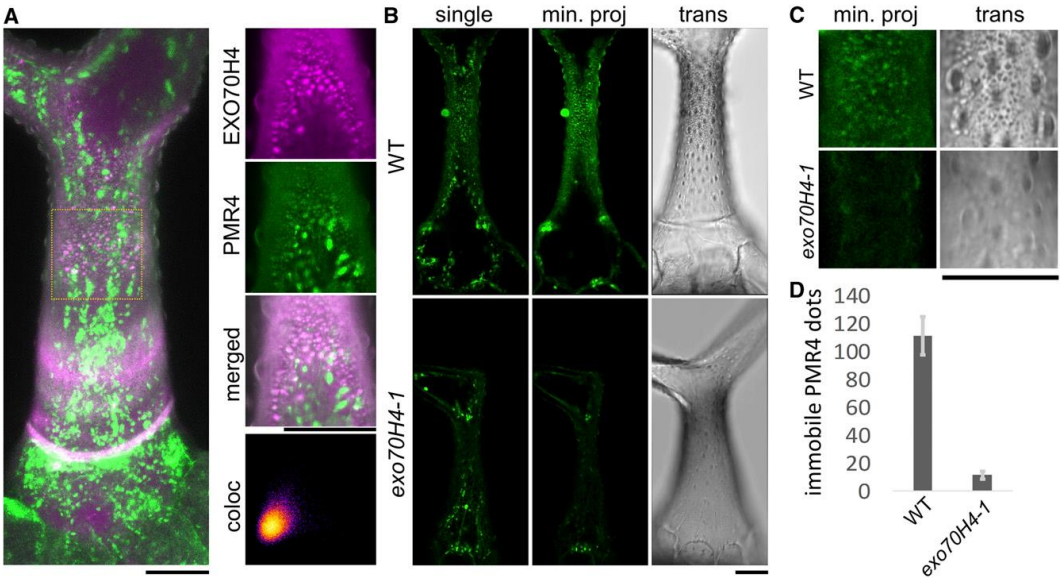

Figure 6. EXO70H4 recruits PMR4 to the ingrowths of the trichome cell wall. A, Left, Overall view of the trichome expressing mCH-EXO70H4 (magenta) and GFP-PMR4 (green). Projection of 14 sections. Yellow dotted square depicts detailed view on the right. Right, Detailed view of a single section with cell wall ingrowths decorated by EXO70H4 and PMR4 with a 2D histogram for the colocalization (Pearson's R value, 0.35; Li's ICQ value, 0,127). B, PMR4-positive cell wall ingrowths are absent in the exo70H4-1 mutant. In the single frame, both the mobile endomembrane fraction and the immobile ingrowths are visible. The mobile fraction is reduced by minimal intensity projection (min. proj.). C, A detail of the ingrowths from B. D, Quantification of the immobile dots in a blind study using the minimal intensity projections. WT, Wild type; bars = 20 µm.

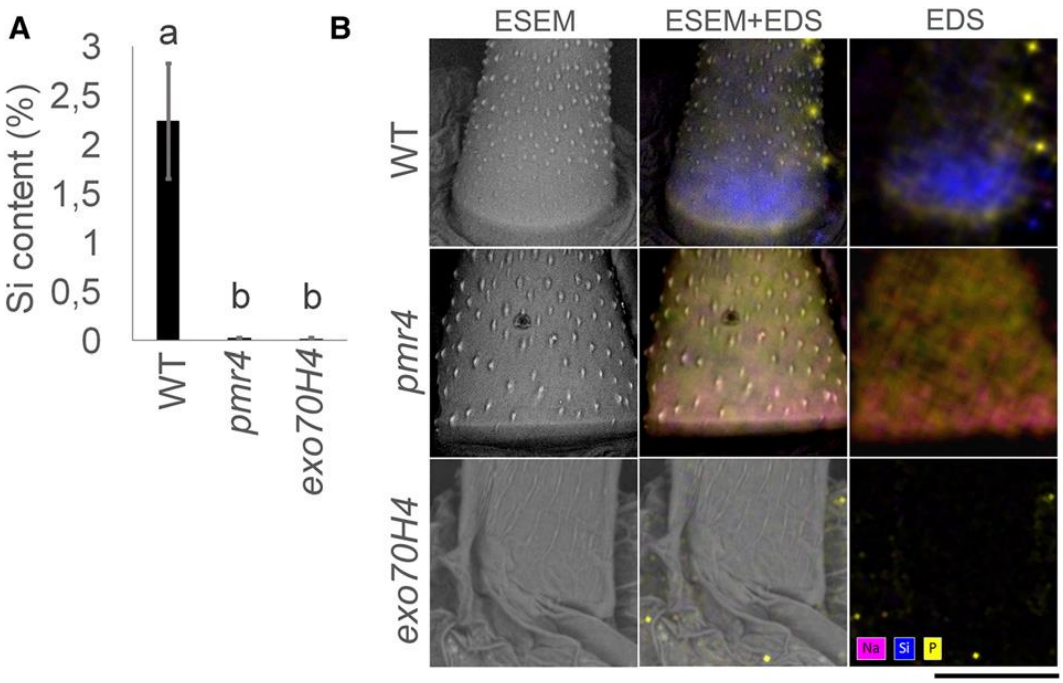

Figure 7. The presence of silica in Arabidopsis trichomes is dependent on callose. A, Quantification of the silica content in multiple genotypes grown on a soil containing 2 mM sodium silicate. Error bars represent SEs. Letters above the bars: mean significant differences (HSD Tukey post hoc test, P , 0.01). B, Examples of trichomes accumulating silicon (blue signal). The accumulation is prominent in the apical domain above the OR. Note that the exo70H4-1 cell wall collapsed due to its mechanical properties. Elements such as sodium (magenta) and phosphate (yellow) also are indicated. Scale bar = 30 mm. WT, Wild type.

ESEM and Energy-Dispersive X-Ray Microanalysis

For a semiquantitative energy-dispersive x-ray microanalysis (EDS), four trichomes from eight leaves were selected for each of the three samples (wild type, pmr4, and exo70H4-1), air dried, and placed on a carbon pad. To maximize detection efficiency and accuracy of the analysis, trichomes were selected according to their shape and shadowing in x-ray maps using a solid-state detector of backscattered electrons and fast EDS mapping. Dried, chemical treatment-free, and conductive coating-free samples were imaged and analysed using ESEM Quanta 650 FEG equipped with EDS silicon drift detector Bruker Quantax 400 XFlash 6/60 under beam energy 10 keV, beam current 100 pA, working distance 10 mm, and water vapor pressure 100 Pa. The ratio of silicon in the sample was calculated as the median values obtained from all trichomes for each sample.

The cell wall of the mature Arabidopsis trichome was in situ opened using two Kleindiek micromanipulators MM3A-EM, thus without any manipulation, cutting, or contamination outside the specimen chamber of ESEM. The inner surface of the trichome (Supplemental Fig. S1) was imaged using gaseous secondary electron

detector under beam energy 10 keV, beam current 50 pA, working distance 11.5 mm, and water vapor pressure 170 Pa.

Acknowledgements

We thank Lukáš Fischer for the motivation to look for the putative EXO70s regulating miRNAs and our technician Marta Čadyová, Patrick Moxon, and Matouš Glanc for a significant improvement of the cloning methods and for constructs provided.

References

Bischoff V, Nita S, Neumetzler L, Schindelasch D, Urbain A, Eshed R,

Persson S, Delmer D, Scheible W-R (2010) TRICHOME BIREFRINGENCE and its homolog AT5G01360 encode plant-specific DUF231 proteins required for cellulose biosynthesis in Arabidopsis. Plant Physiol 153: 590–602

Blümke A, Somerville SC, Voigt CA (2013) Transient expression of the

Arabidopsis thaliana callose synthase PMR4 increases penetration resistance to powdery mildew in barley. Adv Biosci Biotechnol 04: 810–813

Bonke M, Thitamadee S, Mähönen AP, Hauser M-T, Helariutta Y (2003)

APL regulates vascular tissue identity in Arabidopsis. Nature 426: 181– 186

Brennwald P, Rossi G (2007) Spatial regulation of exocytosis and cell polarity:

yeast as a model for animal cells. FEBS Lett 581: 2119–2124

Brugiére T, Exley C (2017) Callose-associated silica deposition in Arabidopsis.

J Trace Elem Med Biol 39: 86–90

Cai G, Faleri C, Del Casino C, Emons AMC, Cresti M (2011) Distribution

of callose synthase, cellulose synthase, and sucrose synthase in tobacco pollen tube is controlled in dissimilar ways by actin filaments and microtubules. Plant Physiol 155: 1169–1190

Chen C, LiuM, Jiang L, Liu X, Zhao J, Yan S, Yang S, Ren H, Liu R, Zhang

X (2014) Transcriptome profiling reveals roles of meristem regulators and polarity genes during fruit trichome development in cucumber (Cucumis sativus L.). J Exp Bot 65: 4943–4958

Chérif M, Menzies JG, Benhamou N, Bélanger RR (1992) Studies of silicon

distribution in wounded and Pythium ultimum infected cucumber plants. Physiol Mol Plant Pathol 41: 371–385

Clough SJ, Bent AF (1998) Floral dip: a simplified method for

Agrobacteriummediated transformation of Arabidopsis thaliana. Plant J 16: 735–743

Cvrčková F, Grunt M, Bezvoda R, Hála M, Kulich I, Rawat A, Zárský V

(2012) Evolution of the land plant exocyst complexes. Front Plant Sci 3: 159

Dong X, Hong Z, Chatterjee J, Kim S, Verma DPS (2008) Expression of

callose synthase genes and its connection with Npr1 signaling pathway during pathogen infection. Planta 229: 87–98

Drakakaki G, van de Ven W, Pan S, Miao Y, Wang J, Keinath NF,

Weatherly B, Jiang L, Schumacher K, Hicks G, et al (2012) Isolation and proteomic analysis of the SYP61 compartment reveal its role in exocytic trafficking in Arabidopsis. Cell Res 22: 413–424

Drdová EJ, Synek L, Pe_cenková T, Hála M, Kulich I, Fowler JE, Murphy

AS, Zárský V (2013) The exocyst complex contributes to PIN auxin efflux carrier recycling and polar auxin transport in Arabidopsis. Plant J 73: 709–719

Elias M, Drdova E, Ziak D, Bavlnka B, Hala M, Cvrckova F, Soukupova

H, Zarsky V (2003) The exocyst complex in plants. Cell Biol Int 27: 199–201

Ellinger D, Glöckner A, Koch J, Naumann M, Stürtz V, Schütt K, Manisseri

C, Somerville SC, Voigt CA (2014) Interaction of the Arabidopsis GTPase RabA4c with its effector PMR4 results in complete penetration resistance to powdery mildew. Plant Cell 26: 3185–3200

Ellinger D, Naumann M, Falter C, Zwikowics C, Jamrow T, Manisseri C,

Somerville SC, Voigt CA (2013) Elevated early callose deposition results in complete penetration resistance to powdery mildew in Arabidopsis. Plant Physiol 161: 1433–1444

Exley C (2015) A possible mechanism of biological silicification in plants.

Front Plant Sci 6: 853

Fauteux F, Chain F, Belzile F, Menzies JG, Bélanger RR (2006) The protective

role of silicon in the Arabidopsis-powdery mildew pathosystem. Proc Natl Acad Sci USA 103: 17554–17559

Fendrych M, Synek L, Pecenková T, Drdová EJ, Sekeres J, de Rycke R,

Nowack MK, Zársky V (2013) Visualization of the exocyst complex dynamics at the plasma membrane of Arabidopsis thaliana. Mol Biol Cell 24: 510–520

Frye CA, Innes RW (1998) An Arabidopsis mutant with enhanced resistance

to powdery mildew. Plant Cell 10: 947–956

Geldner N, Dénervaud-Tendon V, Hyman DL, Mayer U, Stierhof Y-D,

Chory J (2009) Rapid, combinatorial analysis of membrane compartments in intact plants with a multicolor marker set. Plant J 59: 169–178

Ghanmi D, McNally DJ, Benhamou N, Menzies JG, Bélanger RR (2004)

Powdery mildew of Arabidopsis thaliana: a pathosystem for exploring the role of silicon in plant–microbe interactions. Physiol Mol Plant Pathol 64: 189–199

Grefen C, Donald N, Hashimoto K, Kudla J, Schumacher K, Blatt MR

(2010) A ubiquitin-10 promoter-based vector set for fluorescent protein tagging facilitates temporal stability and native protein distribution in transient and stable expression studies. Plant J 64: 355–365

Guerriero G, Hausman J-F, Legay S (2016) Silicon and the plant extracellular

matrix. Front Plant Sci 7: 463

Guseman JM, Lee JS, Bogenschutz NL, Peterson KM, Virata RE, Xie B,

Kanaoka MM, Hong Z, Torii KU (2010) Dysregulation of cell-to-cell connectivity and stomatal patterning by loss-of-function mutation in Arabidopsis chorus (glucan synthase-like 8). Development 137: 1731– 1741

HeiderMR, Gu M, Duffy CM, Mirza AM, Marcotte LL,Walls AC, Farrall

N, Hakhverdyan Z, Field MC, Rout MP, et al (2016) Subunit connectivity, assembly determinants and architecture of the yeast exocyst complex. Nat Struct Mol Biol 23: 59–66

Heider MR, Munson M (2012) Exorcising the exocyst complex. Traffic 13:

898–907

Hodson MJ (2016) The development of phytoliths in plants and its influence

on their chemistry and isotopic composition. Implications for palaeoecology and archaeology. J Archaeol Sci 68: 62–69

Hong D, Jeon BW, Kim SY, Hwang J-U, Lee Y (2016) The ROP2-RIC7

pathway negatively regulates light-induced stomatal opening by inhibiting exocyst subunit Exo70B1 in Arabidopsis. New Phytol 209: 624– 635

Hong Z, Delauney AJ, Verma DP (2001) A cell plate-specific callose synthase

and its interaction with phragmoplastin. Plant Cell 13: 755–768

Huang L, Chen X-Y, Rim Y, Han X, Cho WK, Kim S-W, Kim J-Y (2009)

Arabidopsis glucan synthase-like 10 functions in male gametogenesis. J Plant Physiol 166: 344–352

Hülskamp M, Misŕa S, Jürgens G (1994) Genetic dissection of trichome cell

development in Arabidopsis. Cell 76: 555–566

Iglesias VA, Meins F Jr (2000) Movement of plant viruses is delayed in

a beta-1,3-glucanase-deficient mutant showing a reduced plasmodesmatal size exclusion limit and enhanced callose deposition. Plant J 21: 157–166

Jacobs AK, Lipka V, Burton RA, Panstruga R, Strizhov N, Schulze-Lefert

P, Fincher GB (2003) An Arabidopsis callose synthase, GSL5, is required for wound and papillary callose formation. Plant Cell 15: 2503–2513

Jakoby MJ, Falkenhan D, Mader MT, Brininstool G, Wischnitzki E, Platz

N, Hudson A, Hülskamp M, Larkin J, Schnittger A (2008) Transcriptional profiling of mature Arabidopsis trichomes reveals that NOECK encodes the MIXTA-like transcriptional regulator MYB106. Plant Physiol 148: 1583–1602

Kalmbach L, Hématy K, De Bellis D, Barberon M, Fujita S, Ursache R,

Daraspe J, Geldner N (2017) Transient cell-specific EXO70A1 activity in the CASP domain and Casparian strip localization. Nat Plants 3: 17058

Karimi M, Bleys A, Vanderhaeghen R, Hilson P (2007) Building blocks for

plant gene assembly. Plant Physiol 145: 1183–1191

Kulich I, Pe_cenková T, Sekereš J, Smetana O, Fendrych M, Foissner I,

Höftberger M, Zárský V (2013) Arabidopsis exocyst subcomplex containing subunit EXO70B1 is involved in autophagy-related transport to the vacuole. Traffic 14: 1155–1165

Kulich I, Vojtíková Z, Glanc M, Ortmannová J, Rasmann S, Žárský V

(2015) Cell wall maturation of Arabidopsis trichomes is dependent on exocyst subunit EXO70H4 and involves callose deposition. Plant Physiol 168: 120–131

Law C, Exley C (2011) New insight into silica deposition in horsetail (Equisetum

arvense). BMC Plant Biol 11: 112

Leroux O, Leroux F, Mastroberti AA, Santos-Silva F, Van Loo D,

Bagniewska-Zadworna A, Van Hoorebeke L, Bals S, Popper ZA, de Araujo Mariath JE (2013) Heterogeneity of silica and glycan-epitope distribution in epidermal idioblast cell walls in Adiantum raddianum laminae. Planta 237: 1453–1464

Levy A, Erlanger M, Rosenthal M, Epel BL (2007) A plasmodesmataassociated

b-1,3-glucanase in Arabidopsis. Plant J 49: 669–682

Li S, van Os GMA, Ren S, Yu D, Ketelaar T, Emons AMC, Liu C-M (2010)

Expression and functional analyses of EXO70 genes in Arabidopsis implicate their roles in regulating cell type-specific exocytosis. Plant Physiol 154: 1819–1830

Luo G, Zhang J, Guo W (2014) The role of Sec3p in secretory vesicle targeting

and exocyst complex assembly. Mol Biol Cell 25: 3813–3822

Munson M, Novick P (2006) The exocyst defrocked, a framework of rods

revealed. Nat Struct Mol Biol 13: 577–581

Mylle E, Codreanu M-C, Boruc J, Russinova E (2013) Emission spectra

profiling of fluorescent proteins in living plant cells. Plant Methods 9: 10

Neděla V, Tihlaříková E, Hřib J (2015) The low-temperature method for

study of coniferous tissues in the environmental scanning electron microscope. Microsc Res Tech 78: 13–21

Nielsen ME, Feechan A, Böhlenius H, Ueda T, Thordal-Christensen H

(2012) Arabidopsis ARF-GTP exchange factor, GNOM, mediates transport required for innate immunity and focal accumulation of syntaxin PEN1. Proc Natl Acad Sci USA 109: 11443–11448

Oda Y, Iida Y, Nagashima Y, Sugiyama Y, Fukuda H (2015) Novel coiledcoil

proteins regulate exocyst association with cortical microtubules in xylem cells via the conserved oligomeric golgi-complex 2 protein. Plant Cell Physiol 56: 277–286

Pecenková T, Hála M, Kulich I, Kocourková D, Drdová E, Fendrych M,

Toupalová H, Zársky V (2011) The role for the exocyst complex subunits Exo70B2 and Exo70H1 in the plant-pathogen interaction. J Exp Bot 62: 2107–2116

Peragine A, Yoshikawa M, Wu G, Albrecht HL, Poethig RS (2004) SGS3

and SGS2/SDE1/RDR6 are required for juvenile development and the production of trans-acting siRNAs in Arabidopsis. Genes Dev 18: 2368–2379

Perry CC, Williams RJP, Fry SC (1987) Cell wall biosynthesis during silicification

of grass hairs. J Plant Physiol 126: 437–448

Picco A, Irastorza-Azcarate I, Specht T, Böke D, Pazos I, Rivier-Cordey

A-S, Devos DP, Kaksonen M, Gallego O (2017) The in vivo architecture of the exocyst provides structural basis for exocytosis. Cell 168: 400–412.e18

Robinson NGG, Guo L, Imai J, Toh-E A, Matsui Y, Tamanoi F (1999) Rho3

of Saccharomyces cerevisiae, which regulates the actin cytoskeleton and exocytosis, is a GTPase which interacts with Myo2 and Exo70. Mol Cell Biol 19: 3580–3587

Russo VM, Bushnell WR (1989) Responses of barley cells to puncture by

microneedles and to attempted penetration by Erysiphe graminis f.sp. hordei. Can J Bot 67: 2912–2921

Sabol P, Kulich I, Žárský V (2017) RIN4 recruits the exocyst subunit

EXO70B1 to the plasma membrane. J Exp Bot 68: 3253–3265 Saedler R, Mathur N, Srinivas BP, Kernebeck B, Hülskamp M, Mathur J (2004) Actin control over microtubules suggested by DISTORTED2 encoding the Arabidopsis ARPC2 subunit homolog. Plant Cell Physiol 45: 813–822

Samuel MA, Chong YT, Haasen KE, Aldea-Brydges MG, Stone SL,

Goring DR (2009) Cellular pathways regulating responses to compatible and self-incompatible pollen in Brassica and Arabidopsis stigmas intersect at Exo70A1, a putative component of the exocyst complex. Plant Cell 21: 2655–2671

Samuels A (1993) The effects of silicon supplementation on cucumber fruit:

changes in surface characteristics. Ann Bot 72: 433–440

Samuels AL, Glass ADM, Ehret DL, Menzies JG (1991a) Mobility and

deposition of silicon in cucumber plants. Plant Cell Environ 14: 485–492

Samuels AL, Glass ADM, Ehret DL, Menzies JG (1991b) Distribution of

silicon in cucumber leaves during infection by powdery mildew fungus (Sphaerotheca fuliginea). Can J Bot 69: 140–146

Sangster AG, Hodson MJ (2007) Silica in higher plants. In D Evered,

M O'Connor, eds, Novartis Foundation Symposia: Silicon Biochemistry. John Wiley & Sons, Chichester, UK, pp 90–111

Schindelin J, Arganda-Carreras I, Frise E, Kaynig V, Longair M, Pietzsch

T, Preibisch S, Rueden C, Saalfeld S, Schmid B, et al (2012) Fiji: an open-source platform for biological-image analysis. Nat Methods 9: 676– 682

Sekereš J, Pejchar P, Šantrůček J, Vukašinović N, Žárský V, Potocký M

(2017) Analysis of exocyst subunit EXO70 family reveals distinct membrane polar domains in tobacco pollen tubes. Plant Physiol 173: 1659–1675

Seo DH, Ahn MY, Park KY, Kim EY, Kim WT (2016) The N-terminal UND

motif of the Arabidopsis U-box E3 ligase PUB18 is critical for the negative regulation of ABA-mediated stomatal movement and determines its ubiquitination specificity for exocyst subunit Exo70B1. Plant Cell 28: 2952–2973

Sinlapadech T, Stout J, Ruegger MO, Deak M, Chapple C (2007) The

hyper-fluorescent trichome phenotype of the brt1 mutant of Arabidopsis is the result of a defect in a sinapic acid: UDPG glucosyltransferase. Plant J 49: 655–668

Stegmann M, Anderson RG, Ichimura K, Pecenkova T, Reuter P, _Zársky

V, McDowell JM, Shirasu K, Trujillo M (2012) The ubiquitin ligase PUB22 targets a subunit of the exocyst complex required for PAMPtriggered responses in Arabidopsis. Plant Cell 24: 4703–4716

Stegmann M, Anderson RG, Westphal L, Rosahl S, McDowell JM,

Trujillo M (2013) The exocyst subunit Exo70B1 is involved in the immune response of Arabidopsis thaliana to different pathogens and cell death. Plant Signal Behav 8: e27421

Sunkar R, Zhu J-K (2004) Novel and stress-regulated microRNAs and other

small RNAs from Arabidopsis. Plant Cell 16: 2001–2019

Tian J, Han L, Feng Z, Wang G, Liu W, Ma Y, Yu Y, Kong Z (2015) Orchestration

of microtubules and the actin cytoskeleton in trichome cell shape determination by a plant-unique kinesin. eLife 4: e09351

Tihlaříková E, Neděla V, Shiojiri M (2013) In situ study of live specimens

in an environmental scanning electron microscope. Microsc Microanal 19: 914–918

Töller A, Brownfield L, Neu C, Twell D, Schulze-Lefert P (2008) Dual

function of Arabidopsis glucan synthase-like genes GSL8 and GSL10 in male gametophyte development and plant growth. Plant J 54: 911– 923

Verma DP, Hong Z (2001) Plant callose synthase complexes. Plant Mol Biol

47: 693–701

Vivancos J, Labbé C, Menzies JG, Bélanger RR (2015) Silicon-mediated

resistance of Arabidopsis against powdery mildew involves mechanisms other than the salicylic acid (SA)-dependent defence pathway. Mol Plant Pathol 16: 572–582

Vogel J, Somerville S (2000) Isolation and characterization of powdery

mildew-resistant Arabidopsis mutants. Proc Natl Acad Sci USA 97: 1897–1902

Vukašinović N, Oda Y, Pejchar P, Synek L, Pečenková T, Rawat A,

Sekereš J, Potocký M, _Zárský V (2017) Microtubule-dependent targeting of the exocyst complex is necessary for xylem development in Arabidopsis. New Phytol 213: 1052–1067

Waterkeyn L, Dupont C (1982) L'observation des dépôts pariétaux de silice

au microscope électronique à balayage. Bulletin Societe Royale de Botanique de Belgique 115: 156–160

Webster TR (1992) Developmental problems in Selaginella (Selaginellaceae)

in an evolutionary context. Ann Mo Bot Gard 79: 632–647

Wu H, Turner C, Gardner J, Temple B, Brennwald P (2010) The Exo70

subunit of the exocyst is an effector for both Cdc42 and Rho3 function in polarized exocytosis. Mol Biol Cell 21: 430–442

Yi X, Zhang Z, Ling Y, Xu W, Su Z (2015) PNRD: a plant non-coding RNA

database. Nucleic Acids Res 43: D982–D989

Yue P, Zhang Y, Mei K, Wang S, Lesigang J, Zhu Y, Dong G, Guo W

(2017) Sec3 promotes the initial binary t-SNARE complex assembly and membrane fusion. Nat Commun 8: 14236

Zárský V, Cvrcková F, Potocký M, Hála M (2009) Exocytosis and cell

polarity in plants - exocyst and recycling domains. New Phytol 183: 255–272

Zhang C, Wang L, Zhang W, Zhang F (2013) Do lignification and silicification

of the cell wall precede silicon deposition in the silica cell of the rice (Oryza sativa L.) leaf epidermis? Plant Soil 372: 137–149

Zhao T, Rui L, Li J, NishimuraMT, Vogel JP, Liu N, Liu S, Zhao Y, Dangl

JL, Tang D (2015) A truncated NLR protein, TIR-NBS2, is required for activated defense responses in the exo70B1 mutant. PLoS Genet 11: e1004945

Zhao Y, Liu J, Yang C, Capraro BR, Baumgart T, Bradley RP,

Ramakrishnan N, Xu X, Radhakrishnan R, Svitkina T, Guo W (2013) Exo70 generates membrane curvature for morphogenesis and cell migration. Dev Cell 26: 266–278

21 Simulation-based optimisation of thermodynamic conditions in the ESEM for dynamical *in-situ* study of spherical polyelectrolyte complex particles in their native state

Vilem Neděla[a], Eva Tihlařikova[a], Jiři Maxa[a], Kamila Imrichova[a], Marek Bučko[b], Peter Gemeiner[b]

a *Environmental electron microscopy group, Institute of Scientific Instruments of ASCR, Královopolská 147, 61264 Brno, Czech Republic*

b *Institute of Chemistry, Centre for Glycomics, Slovak Academy of Sciences, Dúbravská cesta 9, 84538 Bratislava, Slovakia*

Keywords

ESEM, Spherical PEC Particles, MC simulations, Thermodynamics, ANSYS, Geant4

Abstract

We present a complex analysis and optimisation of dynamic conditions in the environmental scanning electron microscope (ESEM) to allow *in-situ* observation of extremely delicate wet bio-polymeric spherical particles in their native state. According to the results of gas flow and heat transfer simulations, we were able to develop an improved procedure leading to thermodynamic equilibrium between the sample and chamber environment. To quantify and hence minimise the extent of any sample deformation during specimen chamber pumping, a strength-stress analysis is used. Monte Carlo simulations of beam-gas, -water, and -sample interactions describe beam scattering, absorbed energy, interaction volume and the emission of signal electrons in the ESEM. Finally, we discuss sample damage as a result of drying and the production of beam-induced free radicals. Based on all experimental and simulation results we introduce a Delicate Sample Observation Strategy for the ESEM. We show how this strategy can be applied to the characterization of polyelectrolyte complex spherical particles containing immobilized recombinant cells *E. coli* overexpressing cyclohexanone monooxygenase, used as a model biocatalyst. We present the first native-state electron microscopy images of the viscous core of a halved polyelectrolyte complex capsule containing living cells.

Introduction

The research and development of viable recombinant bacteria with overproduced new enzymes and artificial enzyme cascades is essential for the biocatalytic production of chiral bioactive substances and precursors of potentially new drugs [1]. Considerable efforts have also been devoted to the development of techniques such as immobilization, aimed at enhancing the processing parameters of whole cell biocatalysts, including stability for as many biocatalytic cycles as possible [2]. The immobilization of viable cells renders many advantages including easy separation and reuse of cells, increased stability of cells during repeated biotransformations and storage, increased resistance towards pH changes and reaction temperature as well as the reduction of overall process cost [3]. Moreover, the importance of immobilization has also been demonstrated in other areas such as pancreatic islet cell transplantation [4], bioremediation of polluted environments [5] or controlled drug release [6]. Spherical polyelectrolyte complex (PEC) capsules with a semipermeable membrane and viscous core [7] and spherical PEC beads with a dense polymer network [8] have proven to be well-suited matrices for the enhancement of the biocatalytic efficiency of viable cells via immobilization (see Fig. 1). Preparation and characterization of highly defined PEC capsules for encapsulation of viable recombinant *E. coli* with overproduced Baeyer-Villiger monooxygenases [9] represented the first stage of immobilized biocatalyst development for Baeyer-Villiger biooxidations. Modification of the immobilization protocol led to the preparation of PEC beads [8] as a more economical variant of an immobilized biocatalyst with potentially easier scale-up as compared to PEC capsules. The key step in the preparation of innovative PEC beads was the choice of proper cellulose sulphate, based on the long term experience of the authors [10]. The spherical shape of PEC capsules and beads is invaluable for the investigation of immobilized biocatalyst kinetics including measurements and the determination of apparent and true reaction rates [11]. Sphericity is also a key parameter with a major impact on the mathematical modelling of immobilized biocatalysts for the performance of bioreactors [12].

For the further research and development of these laboratory-produced bio-polymeric spherical microparticles, advanced micro-morphological characterisation is necessary. Shape, size, membrane thickness, permeability and mechanical resistance should be uniform and controlled during and after production [13, 2]. To investigate these parameters correctly, freezing and chemical fixation or any shape distortion must be avoided during observation. Even though a conventional scanning electron microscope (SEM) is very suitable in terms of the large depth of field and high resolution, the need for high vacuum conditions precludes its use [14,15]. Cryo-SEM is also unsuitable since it has been shown to

push the polymer chains apart due to crystal formation in the hydrogel structure and to form an artificial porous structure during rapid freezing and the sublimation of the hydrogel shell [16].

In view of the above, the environmental scanning electron microscope (ESEM) [17,18] seems to be an optimal tool for researching the functional and fully wet/native state of spherical microparticles, although the extremely beam- and environment-sensitive nature of these samples still presents some challenges, as we will show. ESEM allows observation of electrically non-conductive samples in their native and fully wet state in a gaseous (usually water vapour) environment at: pressures ranging from tens to thousands of Pa; reduced sample temperature (commonly down to 2 °C) and a range of relative humidities (RH) [19,20]. Moreover, *in-situ* investigation of these samples at dynamically changing conditions as well as during mechanical [21] and chemical changes allows for complex time lapse studies [22].

In previous studies, several dynamic observations in the ESEM were performed, such as the controlled evaporation of a uranyl brine layer on ice [23] and frost flowers [24]; mechanical tests of carrots [25]; morphological changes of stomatal pores in leaf tissue [26]; volume changes and 3D interpretation of the surface of rice under changing RH [27]. Furthermore, advanced methods for ESEM were introduced, including a method for observation of very susceptible living and surviving biological samples [28] and the Low Temperature Method for ESEM (LTM) [29,30]. The results of LTM were validated by other methods such as cryo-SEM and light microscopy [31]. Using LTM in combination with a new high-efficiency Ionisation Secondary Electron Detector with an electrostatic Separator (ISEDS) for ESEM [32], we recorded the world´s first images of unaffected fresh water rotifers in their native state, and two new species of rotifers were subsequently discovered [33]. An extended version of LTM (ELTM) allows the same sample to be re-used for later analysis in different SEM or ESEM microscopes [34].

Electron-gas interactions in the ESEM result not only in the generation of new signal electrons [35] accelerated and cascade-amplified by the detector's electrostatic/magnetic fields [36] but also in the ionization of gas molecules [37]. Ion bombardment reduces the sample's surface contamination [38] and positive ions help neutralize the negative charge of the sample. This is beneficial for the study of polymer surfaces often contaminated with residual solvents, plasticizers, lowmolecular- weight fractions present in the polymers, or beam-cleaved fragments that are likely to be degassed through the surface. Decontamination processes in the ESEM together with the possibility to observe uncoated electrically non-conductive samples allows the study of specific contrasts that are not seen in conventional

SEM. An example in the case of polymers is given by Gauvin et al. [39]. Moreover, the concentration of positive ions can be controlled when special detectors are used [32,40].

One of the most important challenges when studying soft materials like spherical PEC particles by an electron beam is radiation damage. The electron beam impact on the sample in electron microscopy is quantified by the electron dose (Gy = J kg^{-1}) or dose rate (Gy s^{-1}). A different quantity, which is a measure of the ionizing radiation itself, is called electron flux (D, e^{-} nm^{-2} s^{-1} or C m^{-2}). D is also reported as dose or critical dose [41], however, it does not express the energy that is transferred/absorbed by the sample [42]. D can be represented by the number of electrons reaching a unit surface area of a sample during irradiation, see Eq. (1), and is directly proportional to current density (j, A m^{-2}) and irradiation time ($t$total, s). I0 (A) is the incident current measured by a Faraday cup in vacuum conditions, S (m2) is the total scanned surface area, and ($t$total, s) is the total irradiation time, according to Arnoult et al. [43].

$$D = jt_{total} = \left(\frac{I_0}{S}\right) t_{total} \quad (1)$$

Radiation damage has been shown to reduce with lower beam energy. However, the increase in radiation damage with increasing beam energy appears to be highly non-linear [44]. Ren et al. [45] compared radiation damage of polymer microcapsules with increasing accelerating voltage under dry and wet conditions in the ESEM. Damage is said to occur more quickly for the dry mode; not only because of the irradiation, but also due to the high vacuum in the specimen chamber [45].

The cause of the damage is ionization of the atoms, leading to the formation of molecular radicals and ions, predominantly due to inelastic scattering between incident electrons and the atomic jellium. This causes temporary or permanent chemical and physical changes including the formation of volatile products, mass loss and the formation of unsaturated structures, chain scissions and cross-linking [43]. In the case of polymers, carbon-hydrogen bond cleavage will result in the formation of polymer radicals. The cleavage of carbon-carbon bonds produces small volatile chain fragments, which are readily lost from the sample. Some polymers may lose up to 40% of their volume by these processes [46]. It has been suggested by Egerton et al. [41] and Grubb [47] that damage to a polymer in the form of cross-linking results in the formation of a more radiation-resistant material.

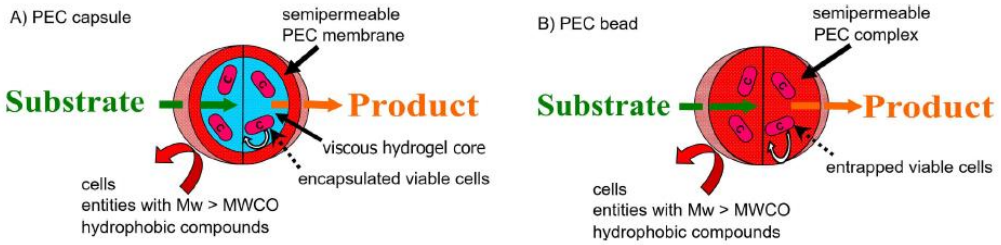

Fig. 1. The structures and function of spherical PEC particles as matrices for the immobilization of viable cells as biocatalysts. A) PEC capsules, B) PEC beads, Mw - molecular weight, MWCO - molecular weight cut-off. Substrates and products of biotransformation freely diffuse through the PEC capsules and beads. Surrounding cells, entities with Mw > MWCO and hydrophobic compounds cannot ingress into capsules and beads.

Another inevitable consequence of electron beam-sample interaction is local heating. The temperature of the sample varies with sample properties (material composition, homogeneity, crystallinity, etc.) and observation conditions in the ESEM (beam current, scan speed, gas type and pressure, working distance, etc.) [29]. It has not yet been possible to measure the actual temperature and gas pressure close to the sample surface (or directly in the beam-scanned area on the sample) in a satisfactory manner in the ESEM [29]. However, there have been some attempts to specify these conditions. One such attempt was the integration of micro sensors for temperature and pressure measurement into the sample holder, described by Leary and Brydson [48].

Another consideration is the flow of gas during pumping. Typically, a controlled sequence of vacuum pumping and water vapour flooding is repeated until most of the dry air is replaced by water vapour [49]. Danilatos et al. [50] introduced modifications to the differentially pumped chamber of the ESEM. They compared two commercial microscopes in terms of pumping efficiency of the pumped volume using a program based on the Direct Simulation Monte Carlo (DSMC) method [51] and the scattering of the primary beam within it [52]. The results of Danilatos' simulations were validated by Maxa et al. [53] using a different counting method and ANSYS software. Furthermore, our group published the results of the simulation of gas flow in a differentially pumped chamber in the environmental SEM AQUASEM II [54] and of a scintillation secondary electron detector for the ESEM [55,56].

In view of the above, although ESEM is a great solution for the study of susceptible wet biological and polymeric samples in their native state, the quality of observation strongly depends on the very precise setting of the working conditions. In practice, real thermodynamic parameters are often significantly different from those required, and their exact value and influence on the sample is not generally known. The most effective way to deal with this problem is a precise description and

determination of conditions in close proximity to the sample, as well as inside the sample, using mathematical and physical simulations, followed by experimental verification. This paper brings together the most comprehensive analysis of these conditions based on simulated results. Thus the aim of this paper is the precise and controlled *in-situ* characterisation of spherical PEC particles, selected as one of the most sensitive and difficult-to-observe samples in our laboratory. This was possible due to simulation-based optimisation of the working conditions, allowing us to work under well-defined and fully controlled environmental conditions in the ESEM. Spherical PEC particles effectively act as a very sensitive sensor allowing visualization of the consequences of thermodynamic changes and beam radiation damage almost in real time in the ESEM. The possibility to obtain detailed information about sensitive samples further pushes the limits of ESEM.

Materials and methods

Preparation of spherical pec particles

As described in a previous study [7], PEC capsules were produced by an air-stripping nozzle with a multiloop reactor via one-step polyelectrolyte complexation of sodium alginate and cellulose sulphate (CS) as polyanions, poly(methylene-co-guanidine) as a polycation, Ca^{2+} as a gelling agent and Na+ as an anti-gelling agent. PEC beads were produced by an air-stripping nozzle without the multiloop reactor via the same reaction of the oppositely charged polymers in a two-step manner [8]. Two sources of CS were used for the preparation of PEC capsules (CS from Across Organics, N.J., USA) and PEC beads (tailor-made CS from Senova, Weimar, Germany).

Cell stocks of recombinant *E. coli* with overexpressed cyclohexanone monooxygenase were kindly donated by Prof. Marko D. Mihovilovic (VUT, Vienna, Austria). The biomass was cultivated and separated from the cultivation medium by centrifugation as reported [8] and used for immobilization in spherical PEC particles (see Fig. 1). Simultaneously, spherical PEC particles without immobilized cells were prepared. Sample stability is very sensitive to storage conditions. Therefore, they were stored in a 50 mM phosphate buffer solution (pH = 7) with ampicillin and 4 g l^{-1} of glucose at 4 °C. They are also sensitive to handling, intensive mixing in solutions with agitators and pressing, and they quickly degrade.

Simplified model of spherical pec particles for simulations

As explained in the section "Preparation of spherical PEC particles" in detail, the capsules and beads are comprised of a 5-component system. These components interact non-covalently, forming a polyelectrolyte complex. After detailed discussion with our co-authors preparing the samples, we agreed on a simplified set of parameters as a model for our simulations, since the parameters of the whole complex are difficult to know. We used the one-monomer-simplified parameters of sodium cellulose sulphate (one monomer formula: $C_6H_9NaO_8S$) (1wt %), sodium alginate ($C_6H_9NaO_7$) (1wt%) [8] and water (98wt%). The density of the simplified material model was calculated to 1010 kg m^{-3}.

Simulations of gas flow, heat transfer and deformations of spherical pec particles in the esem

ANSYS Fluent © software was used for the calculations of temperature changes of the sample and for the calculation of gas flow in the environmental AQUASEM II specimen chamber. The gas flow was calculated by Navier-Stokes equations using the finite volumes method. Because of the compressibility of the gas flow and the assumption of high gradients associated with the supersonic flow in the first pressurelimiting aperture (PLA1, see Fig. 2A, B) a density-based solver was used. Governing equations for additional scalars were solved sequentially using the Implicit Formulation. A calculation schema AUSM (Advection Upstream Splitting Method), which is preferable for supersonic flow solving, was used. For discretization, the second Order and Power Law schemas were used. The boundary conditions were set according to experimental conditions. A water vapour pressure of 684 Pa and temperature of 27 °C was applied in the 3D model of the environmental SEM AQUASEM II specimen chamber. For the heat transfer calculation, ANSYS Fluent uses the following energy Eq. (2):

$$\frac{\partial(\rho E)}{\partial t} + \nabla \cdot [V(\rho E + p)] = \nabla \left[k_{e_{ff}} \nabla T - \sum_j h_j J_j + \tau_{e_{ff}} \cdot V \right] + S_h \qquad (2)$$

where: $\frac{\partial(\rho E)}{\partial t}$ - solves the time dependence of the task, $\nabla \cdot [V(\rho E + p)]$ - solves convection, $k_{e_{ff}} \nabla T$ - solves thermal conduction, $\sum_j h_j J_j$ – solves species diffusion, $\tau_{e_{ff}} \cdot V$ - solves viscous dissipation, S_h - heat sources

Firstly, the natural or mixed convection was calculated and then the proportion between the Grashoff and Reynolds number was used for the calculation. The natural convection buoyancy was calculated using the Rayleigh number. The position of the heating source, simulating the thermal effect of the electron beam in

a voxel, was determined based on the results from MC simulation. The voxel was given a cylindrical shape with dimensions of 1.25×2.0 μm. The calculated heating energy of the electron beam was 2.26×10^{11} W m^{-3} (for conditions 20 keV, 30 pA) and 1.13×10^{12} W m^{-3} (for conditions 20 keV, 150 pA).

The simplified bead model was defined as having a specific heat capacity of 4175 J kg^{-1} K^{-1} and thermal conductivity of 0.637 W m^{-1} K^{-1}, thus the material has similar thermal properties to water [57]. Since we are also interested in the possible benefits of partially surrounding the sample with liquid water before pumpdown, the spherical PEC particle was simulated with two levels of surrounding water (up to 75% and 25% of the height of the particle) with the aim to describe sample conditions after shifting away from thermodynamic equilibrium, when the water level is significantly decreased.

For the first set of simulations, the temperature of the Peltier cooling stage was considered to be equal to the set temperature *T*SET = 2 °C (97% RH at water vapour pressure of 684 Pa). However, the real temperature (*T*REAL) is likely to be different than the set temperature, for reasons that will be discussed later. Therefore, we made a second set of simulations using *T*REAL = 3.5 °C. Figs. 2A-C show the dimensions and 3D model of the simulated volume of the specimen chamber and sample surrounded by liquid water to the level of 75%.

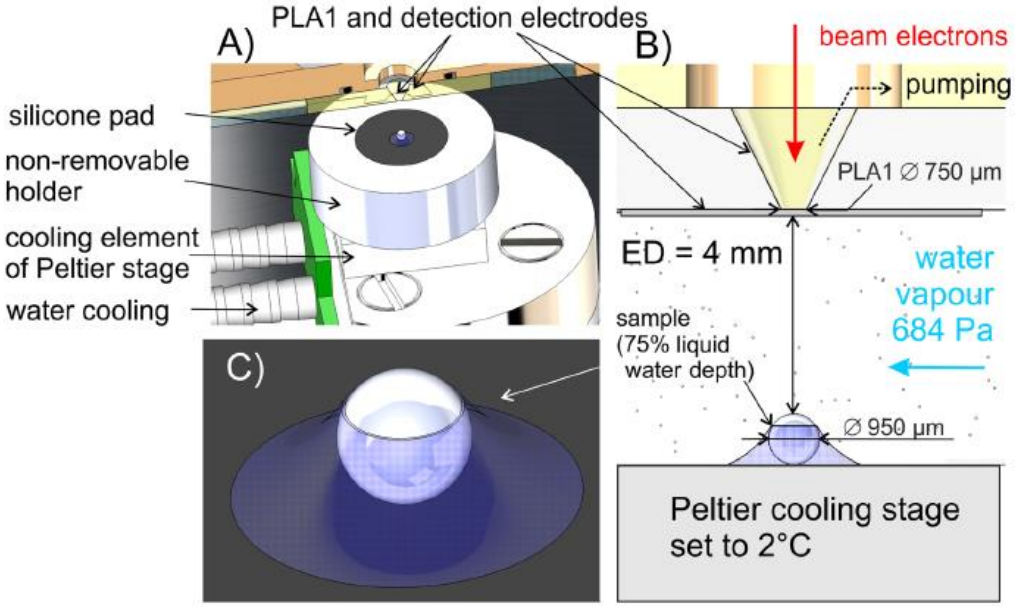

Fig. 2. Visualization of the experimental setup in the ESEM AQUASEM II. A, B) bottom part of the differentially pumped chamber of ESEM with a pressure limiting aperture (PLA1) and self-developed Peltier cooling stage with a silicon pad and sample, C) detail of a spherical PEC particle in the liquid water covering 75% of the sample.

We assume that there is some degree of mechanical stress on the semipermeable membrane of the PEC capsule during the initial chamber pump-down process, and so for simulations of stress and elastic deformation ANSYS Static Structural software was used. It solves the task using the equations of motion. We made a flow analysis through porous medium (representing the semipermeable membrane of the PEC capsule, which is made up of small spherical particles) to deduce the pressure acting on the membrane's walls. The viscous and inertial resistances to flow (*R*v and *R*i) in a porous medium give the total pressure drop through a porous medium and were calculated using the Ergun equation:

$$R_v = \left[\frac{150(1-e)^2}{\varphi^2 D^2 e^3}\right] R_i = \left[\frac{2*1{,}75(1-e)}{\varphi D e^3}\right] \quad (3)$$

where *e* is the porosity of the semipermeable membrane with value of 0,05; φ is the sphericity and *D* is the diameter of the circular area amongst 4 pores with values of 0.7 and 65 nm, respectively. These values were calculated based on the assumption of homogenously distributed pores 50 nm apart. We used radius of 5.4 nm which is the radius of the pores for polysaccharides [9]. The thickness of the membrane was 82.8 μm, as shown later.

According to the given relationships, the *R*v and *R*i values were set for the calculation as 5.2×10^{12} and 5.8×10^{7}, respectively. For the strength calculation, the value of Young's modulus was set to 0.1 MPa [58] and the compressive strength to 0.5 MPa [59].

The conditions for the stress and deformation simulation were set according to the following experimental parameters: beam energy 20 keV, beam current 30 pA, water vapour pressure 684 Pa, a liquid water layer surrounding the particle to 75% of its height, irradiated sample surface actual temperature 3.9 °C and dwell time 235.3 μs.

Monte carlo simulations of electron-gas, -water, -sample interactions

For the simulation of beam electron interactions with the gas environment and signal electron emission from the sample in the ESEM we used the Geant4 platform of CERN [60]. The low energy package was used to extend the range of validity of electromagnetic interactions down to a few eV. For inelastic scattering, we applied the dielectric function theory. The combination of the Mott cross-section with a crosssection based on phonon scattering at low energies was used for the computation of elastic scattering. For validation of the Geant4 module and our simulation setup we executed test simulations consisting of a comparison of total SE and BSE yields and scattering cross-section for a water molecule with

experimental data [61,62]. In order to simulate the impact of primary electron scattering in the ESEM (the so-called "skirt effect") after passing the electron beam through a water vapour environment and a liquid water layer on the sample surface, the electron beam was assumed to be a single spot and 105 electrons were simulated per spot. For the calculation of D_{vacuum} in 1 nm2 of irradiated area per second, Eq. (1) was used (image resolution 768×768 pixels, pixel size 0.53 μm). The resulting values of the electron flux in the conditions of ESEM (D_{ESEM}) equal to D_{vacuum} were multiplied by the coefficient of beam electron loss at a constant gas pressure 684 Pa for specific thicknesses of water layers. The model sample consisted of three levels namely: a water vapour layer (thickness 4 mm, pressure 684 Pa), a liquid water layer (thicknesses 0; 10; 50; 100 and 500 nm) and the spherical PEC particle. Both values of D were calculated for the static position of the electron beam (without scanning) and for a single spot on the sample. Data of the energy loss function needed for the accurate simulation of inelastic scattering events were obtained from experimental measurements [63].

ESEM observation

Samples were stored at 5 °C and were immediately transferred to a silicon pad with T_{SET} 2 °C (see Fig. 2A). The silicon pad, made from a thin wafer, was fixed to the self-developed Peltier cooling stage using thermal paste. Precooled samples were observed in a small droplet of distilled water (approximately 5 μl). Due to the relatively large size of samples (950 μm in diameter) and their beam and environmental sensitivity, we used a combination of our method [28] and self-developed ionization SE detector, integrated into PLA 1 [36]. The opening of the PLA1 was increased to 750 μm in diameter for a larger field of view. We applied a gentle and very slow specimen chamber pumping procedure (speed 203 Pa s^{-1}) under optimised conditions. A faster initial specimen chamber pumping procedure (speed 407 Pa s^{-1}) was used for the observation of spherical PEC particles under conventional conditions and the fastest pumping speed 592 Pa s^{-1} was used for the study of dynamical *in-situ* observation of the cracking of the PEC capsule (discussed later).

All experiments were conducted using environmental SEM AQUASEM II [64] under beam energies of 20 keV and 10 keV and beam currents of 30 pA and 15 pA. Samples were always observed in two steps: 1) control of the level of the covering liquid water layer (dwell time 1.7 μs, image resolution 768×768 pixels) and 2) imaging of the sample surface after the evaporation of the covering water layer (dwell time 235 μs, image resolution 768×768 pixels). The environmental distance (ED) was fixed at 4 mm (see Fig. 2B). Thermodynamic equilibrium adjustments were monitored with Pfeiffer pressure gauges CMR 361–363, and controlled using

a custom-built Peltier cooling stage and custom build hydration system [64]. In the case of all experiments the only gas we used was water vapour.

Results and discussion

Temperature measurement

The real temperature at the surface of the silicon pad was measured *ex-situ* (open specimen chamber) using a FLIR A310 thermal imaging camera (located vertically above the Peltier cooling stage) as well as *insitu* using a GHM 175 thermometer (Greisinger electronics) with a Pt1000 sensor. T_{REAL} was measured to be 3.5 °C for both *ex-situ* as well as *in-situ* measurement. Both temperature measurements were performed while T_{SET} of the Peltier cooling stage was 2 °C. *In-situ* measurement was conducted free of beam irradiation under a water vapour pressure of 684 Pa. The Pt1000 sensor was fixed using thermally nonconductive tape, with a thermally conductive gel on the silicon pad.

Simulations of gas flow and heat transfer in the esem

Knowledge of the values of gas pressure and real temperature alone is not sufficient for observation of susceptible wet samples such as PEC particles in the ESEM. The velocity and direction of the gas flowing closely around the sample's surface should also be considered for selected ED (see Fig. 3A). In the case of our environmental SEM AQUASEM II, with an intentionally increased PLA1 diameter of 750 μm, the velocity of water vapour flow ranges from 9×10^{-4} m s^{-1} for ED=4 mm (sample surface) to 205 m s^{-1} for ED=0 mm (PLA1) (see Fig. 3A). For our simulations, where the model sample was surrounded with liquid water to a depth of 25% and 75%, the velocity of gas flow was very low. In close proximity to the sample, it was approximately constant (from 1.4×10^{-3} m s^{-1} to 9×10^{-4} m s^{-1}) circumferentially from the widest part of the exposed surface to the top of the spherical PEC particle (see Fig. 3A). According to our simulations, a gas pressure inhomogeneity is expected to cause a shift away from thermodynamic equilibrium for ED shorter than 1.3 mm, where gas pressure begins to decrease from 684 Pa for ED = 1.3 mm to 677 Pa for ED = 0.5 mm and 523 Pa for ED = 0 mm (see Fig. 3A). For ED greater than 1.3 mm, the water vapour pressure had a constant value of 684 Pa, corresponding to the value measured with the microscope pressure gauge (Pfeiffer CMR 362). Thus the results of our simulations show that, for the ED used in our experiments (4 mm), gas flow velocity as well as pressure variations are likely to play a negligible role on sample drying. The dependence of RH and sample temperature on ED is shown in Fig. 3B.

Unlike the gas pressure, the actual temperature at the sample surface was significantly different than that expected. The value of the measured real temperature on the silicon pad surface was 3.5 °C rather than the set temperature of 2 °C of the Peltier cooling stage. We estimate that the set and measured values could differ by up to 4 °C when using Peltier cooling stages equipped with replaceable sample holders or when placing the sample on thin cover glass, due to poor thermal contact/conductivity. The influence of these temperature inconsistencies (T_{SET} = 2 °C and T_{REAL}= 3.5 °C) and different levels of water surrounding the sample (25% and 75% depths) on the PEC bead is shown in Fig. 3C.

The simulated temperature of an unirradiated sample with a partially exposed surface was 3.8 °C (liquid water depth 25%) and 3.7 °C (liquid water depth 75%) which was about 1.8 °C and 1.7 °C, respectively, higher than expected. (see black lines in Fig. 3D). The temperature of the irradiated sample additionally increased in the following manner: for a beam current of 30 pA and surrounding water depth 75%, the exposed sample surface temperature increased by 0.2 °C to 3.9 °C. When the surrounding water depth was modelled at 25% of sample height, at the same beam current, the temperature at the sample surface increased again by 0.2 °C, to 4.1 °C. If the sample surface was irradiated with a beam current of 150 pA (a commonly used beam current in the ESEM), its temperature could increase to up to 4.7 °C (water depth 25%) (see blue lines in Fig. 3D).

Fig. 3E provides a two-dimensional interpretation of the temperature distribution of a perpendicularly irradiated surface in the voxel and Fig. 3F shows changes of temperature in the voxel with time. According to the simulations, when irradiation begins, the voxel temperature immediately increases. During the first μs the temperature increases by about 0.15 °C (heating rate 8.6×10^4 °C s^{-1}) for a beam current of 30 pA and about 0.73 °C (heating rate 4.3×10^5 °C s^{-1}) for a beam current of 150 pA. Subsequently, after the first μs, the heating rate changes to 26 °C s^{-1} and 137 °C s^{-1} for 30 pA and 150 pA, respectively, until the whole voxel is irradiated. During the dwell time of 235 μs, the voxel temperature increases by about 0.02 °C (see Fig. 3F). The rate of voxel heating is not dependant on the surrounding water depth. As heat accumulates in the voxel volume, and during slow scan speeds (dwell time 235 μs), the neighbouring voxels are heated as well. Nevertheless, voxel cooling after the end of beam irradiation is very fast with rates approx. 2.5×10^4 °C s^{-1} (30 pA) and 1.3×10^5 °C s^{-1} (150 pA). By the time the beam returns to scan the original pixel (after 139 ms, dwell time 235 μs) or neighbouring pixel (after 181 ms, dwell time 235 μs), the pixel temperatures have returned to their nominal values. Thus, on the timescale of the beam dwell time modelled here, the primary electron beam is not expected to cause significant local heating at the sample surface.

Hence, the most significant factor thus far is the deviation between Peltier set temperature and the actual temperature at the sample surface, leading to calculated RH values of 85% (for surrounding water depth 75% of sample height, 684 Pa, 3.9 °C, 235.3 μs, 20 kV, 30 pA, see Fig. 3F) and 80% (surrounding water depth 75%, 684 Pa, 4.64 °C, 235.3 μs, 150 pA, see Fig. 3F) rather than the expected 97% for the set conditions (684 Pa, 2 °C). Clearly, working at reduced RH will gradually cause the sample surface to dry. For the case of surrounding the sample with a lower level of liquid water, RH will deviate even further.

Simulation of stress and deformation of spherical pec particles in the esem

In our ESEM observations, which we discuss later in this article, we discovered a small elliptical hole (19.7 μm x 16.1 μm) in several PEC capsules from one of the development series. We assume that the hole (see Fig. 4A) was created during production of the spherical particle because its occurrence was always observed in the same place independent of the rotation/position of the capsule during imaging. We did not observe such holes when viewing the capsules with light microcopy (see Fig. 9A), and we assume that placing the capsules in the ESEM resulted in some mechanical forces that allowed the holes to be exposed. Upon electron beam irradiation, we observed that the holes acted as a weak point, causing capsules to collapse. Consequently, the gaseous material of the capsule core escaped (see Fig. 7E,H), followed by the total destruction of the capsule (see Fig. 7F,I).

Based on the above mentioned findings, and given the great importance of the mechanical properties of the spherical PEC particles for their use in practice, we felt it necessary to carry out a detailed strength-stress analysis. To determine the thickness of the semipermeable membrane, the liquid core of a halved PEC capsule was carefully evaporated by shifting away from thermodynamic equilibrium and observed by applying our Delicate Sample Observation Strategy (DSOS) for the ESEM. DSOS is described in detail in the ESEM observations section, later. A membrane thickness of (82.8 ± 2.5) μm was determined from an average of four measurements from the image of the halved PEC capsule (see Fig. 4B). This value is in good agreement with the previously published value of 90 μm (RSD = 5%) measured using optical microscopy [9].

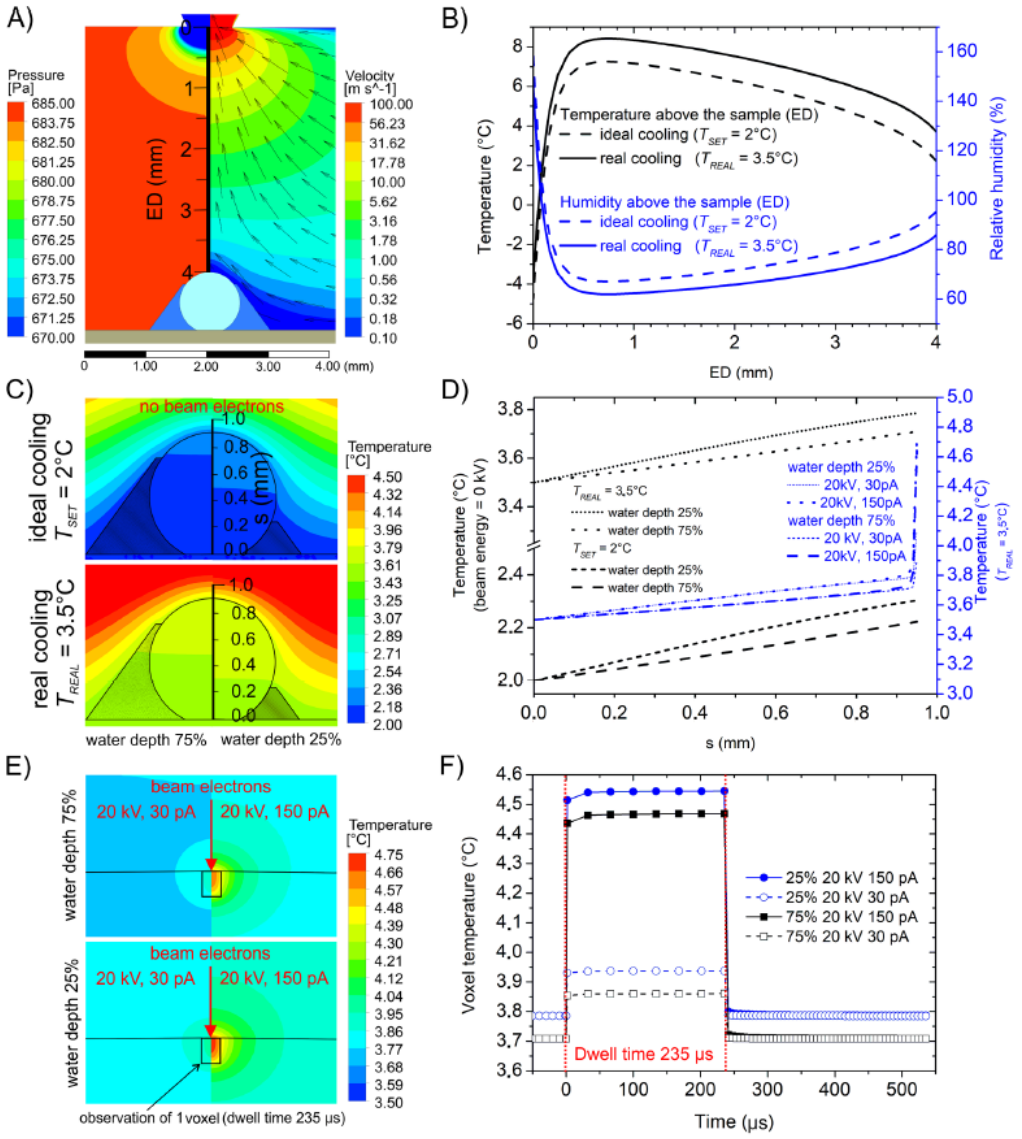

Fig. 3. Simulations of thermodynamic conditions in the vicinity of the sample under experimental conditions in the ESEM AQUASEM II. A, B) the dependence of water vapour pressure, velocity, temperature and relative humidity on the ED; C, D) the temperature gradient inside and closely above the sample under the conditions of ideal and real cooling at 25% and 75% of the surrounding water depth; E) The thermal impact of different beam currents and water depth in the sample's voxel; F) the dependence of voxel temperature on dwell time at various conditions of levels of surrounding water depth and beam current. .

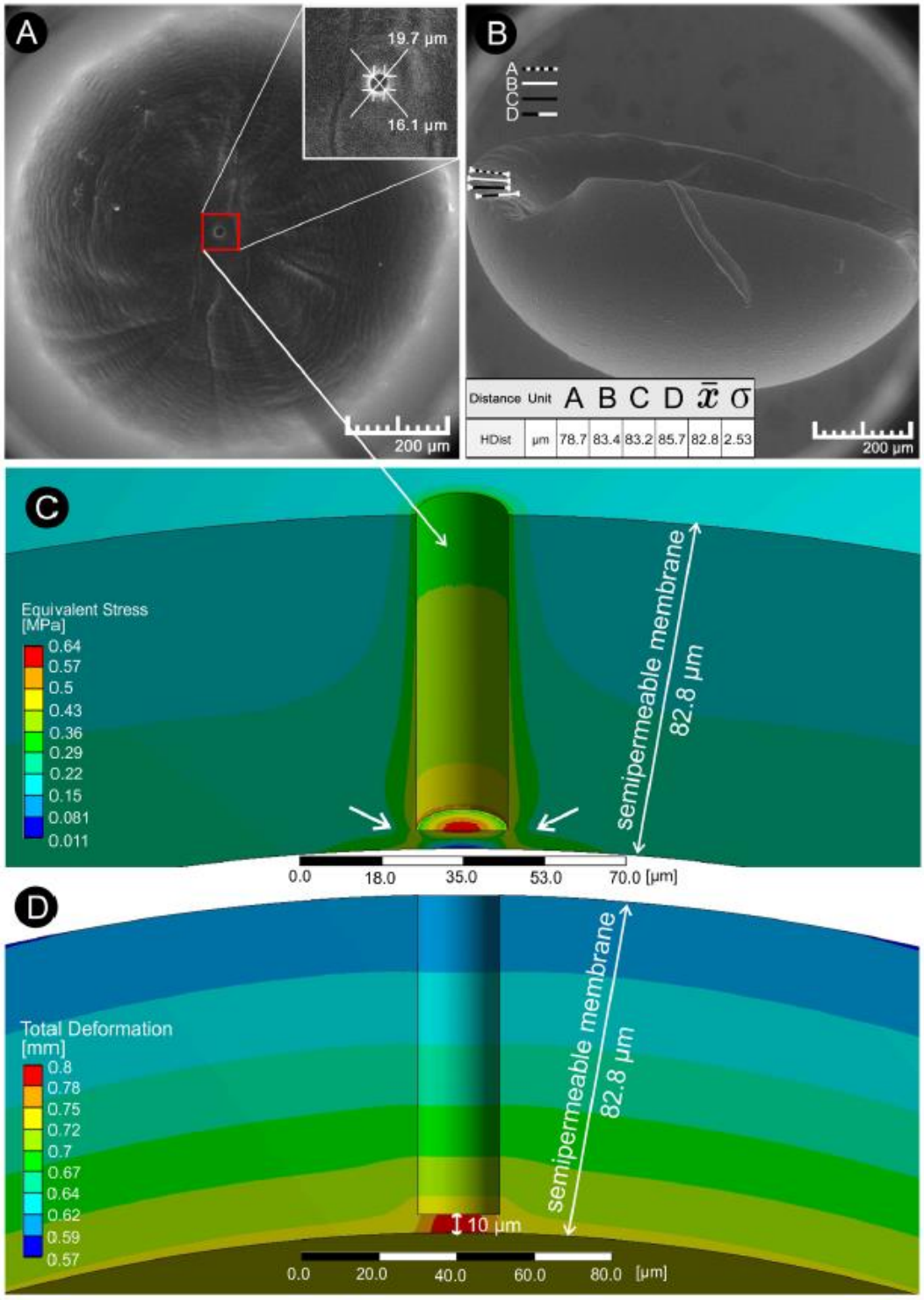

Fig. 4. ESEM image of the partially damaged PEC capsule with a detail of the hole (A) and the halved spherical PEC particle with carefully evaporated liquid core for measurement of semipermeable membrane thickness (B). Results of the strength-stress analysis of the spherical PEC particle (C and D). The cracking of the thinnest part of the membrane is indicated by the highest degree of deformation (D - red region). The crack propagation is indicated by arrows (C – yellow region). The experimental parameters were as follows: water depth of 75%, surface temperature 3.9 °C. The simulation was computed according to the experimental conditions: beam energy 20 keV, beam current 30 time 235.3 µs.

The results of strength-stress analysis of the most susceptible part of the spherical PEC particle surface (middle of the spherical segment) can be seen in Fig. 4C,D. Under thermodynamic conditions corresponding to the experiment (see Fig. 7, 407 Pa s^{-1}) the material of the viscous core in the spherical segment of the PEC capsule is expected to boil. According to the results of our simulations, during conversion from the liquid phase of the core to the gaseous phase, the volume of the sample enlarges. However, the generated vapour leaks out through the pores of the semipermeable membrane. Consequently, a pressure of up to 0.08 MPa is thought to act on the membrane (see Fig. 4C). These results were used for the strength-stress analysis, where the tension was calculated to be up to 0.6 MPa (see Fig. 4C). As soon as the force exceeds the strength limit of the thinnest part of the semipermeable membrane (for our simulation thickness 10 μm, see Fig. 4D), it cracks and excess gas escapes. The cracking of the thinnest part of the membrane is indicated by the highest degree of deformation, see the red region in Fig. 4D. Our simulations also showed that the highest stress intensity in the membrane was at the bottom of the cylindrical hole along its circumference (see in Fig. 4C). In this part it extended diagonally down to the right and left to form a region where the crack in the membrane arose and continued to spread, indicated by arrows in Fig. 4C.

Based on these results, the capsule manufacturing process was improved to avoid the origination of the hole and to optimise its important mechanical properties.

Simulation of primary and signal electron collision in the sample

According to Vezie et al. [65] for the high-resolution study of polymer morphology the yield of secondary electrons (energy around 3 eV) from the sample must be maximized. This occurs when the electron range is approximately twice the secondary electron escape depth (for most polymers the electron range is 400–500 A). The electron ranges in carbon are 460 A and 670 A for beam energies of 0.8 and 1 keV, respectively [66]. Therefore, the optimal beam energy for the study of polymers in SEM is just below 1 keV. The total deposited energy per primary electron decreases with decreasing beam energy, but simultaneously it is confined to a smaller interaction volume, closer to the surface of the sample, leading to an increase in SE yield.

However, the above assumptions require some adaptation for the observation of polymers in ESEM, where beam energy as well as beam current are reduced due to interactions with the imaging gas or in the presence of a liquid layer covering the sample surface. Figs. 5A, B show the impact of the combined environment (constant water vapour layer and increasing thicknesses of liquid water layer) on the irradiation of the sample, for different energies of beam electrons. Results were

obtained using MC simulations without considering any further interactions of the beam with the sample and with the assumption of no charging of the sample surface.

When the value of the water vapour pressure is 684 Pa, in the absence of a liquid water layer, beam electrons with energies below 5 keV are diffused due to collisions with gas molecules. In the case of energy of 1 keV, only 5% of beam electrons are expected to pass through without collision and impact the sample (see Fig. 5A-black curve). Similarly, the energy loss is evident predominantly for electrons with the lowest energies (around 1 keV) where beam electrons reach the sample with approx. 80% of their original energy (20% energy loss, see Fig. 5B-black curve). The beam energy as well as current loss of 5 keV beam electrons starts to be noticeable in the presence of a liquid water layer (see Fig. 5A, B). In the case of 4 mm ED, the effects of water vapour pressure and a liquid water layer may still be appreciable for beam energy of 10 keV, reducing to negligible for energy of 20 keV and higher.

The presence of the water vapour environment and a water layer on the sample surface significantly affects the final beam spot size, the energy of electrons and energy distribution in the spot (Fig. 6A, B). Moreover, it could strongly attenuate the emission of signal electrons from the sample (Fig. 6D).

In a gas pressure environment, the final beam spot size is thus much larger than it is in high vacuum SEM. The water layer on the sample surface additionally prolongs the beam electron path before it reaches the sample surface. In the case of a 500 nm thick water layer, the beam spot size interacting with the PEC surface was almost 5 times bigger than in the absence of a water layer (see Fig. 6B). The water layer also acts as a significant energy absorber, which limits the penetration depth of beam electrons and causes almost a 20% loss of their kinetic energy (see the middle part of Fig. 6A).

The values of electron flux in a vacuum (Dvacuum, e^{-} nm^{-2} s^{-1}) and the dependence of electron flux in ESEM conditions (DESEM, e^{-} nm^{-2} s^{-1}) with increasing thickness of the water layer (up to 500 nm) on the sample surface (at constant pressure of water vapour 684 Pa), for beam currents 30 pA and 150 pA, are shown in Fig. 6C. The value of D increases with increasing value of the beam current and reaches its maximum at vacuum conditions. Moreover, it decreases with the increasing thickness of the water layer on the sample surface proportionally with the amount of electrons absorbed by the environment and deflected outside the area of 1 nm^2. The decrease of D_{ESEM} implies the extent to which the beam spot is scattered (see Fig. 6B). When the beam energy is reduced, the interaction volume becomes smaller. However, as a consequence of beam scattering in the ESEM, the

diameter of the beam spot size increases and the total energy deposition is less localised.

The loss of kinetic energy relates not only to beam electrons passing through the vapour/liquid environment to the sample surface, but also to signal electrons (i.e., secondary and backscattered electrons) emitted from the sample and emitted through the water layer where they can be detected. The permeability of the water layer to signal electrons is limited to about 20 nm, according to Fig. 6D. This figure also shows optimal beam energy for the maximal emission yield of signal electrons in the ESEM. Even though the signal electron yield is said to be maximal for beam energy below 1 keV for polymers in high vacuum SEM, the optimal beam energy in the ESEM appears to be 5–10 keV due to the energy losses in the gaseous environment (ED 4 mm), along with the surface water layer.

Meanwhile, the penetration distance of electrons with initial kinetic energy 50 eV in liquid water reaches a maximum of 2 nm [67]. Therefore, the detection of secondary electrons emitted directly from a wet sample will be strongly attenuated.

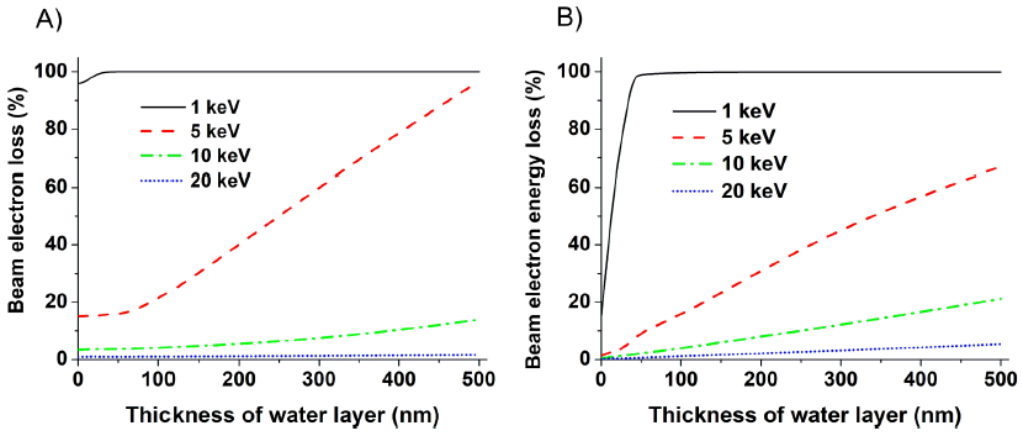

Fig. 5. Dependence of the average amount of beam electron loss A) and beam energy B) for an increasing thickness of water layer for various beam energies after passing through 4 mm water vapour environment with pressure 684 Pa.

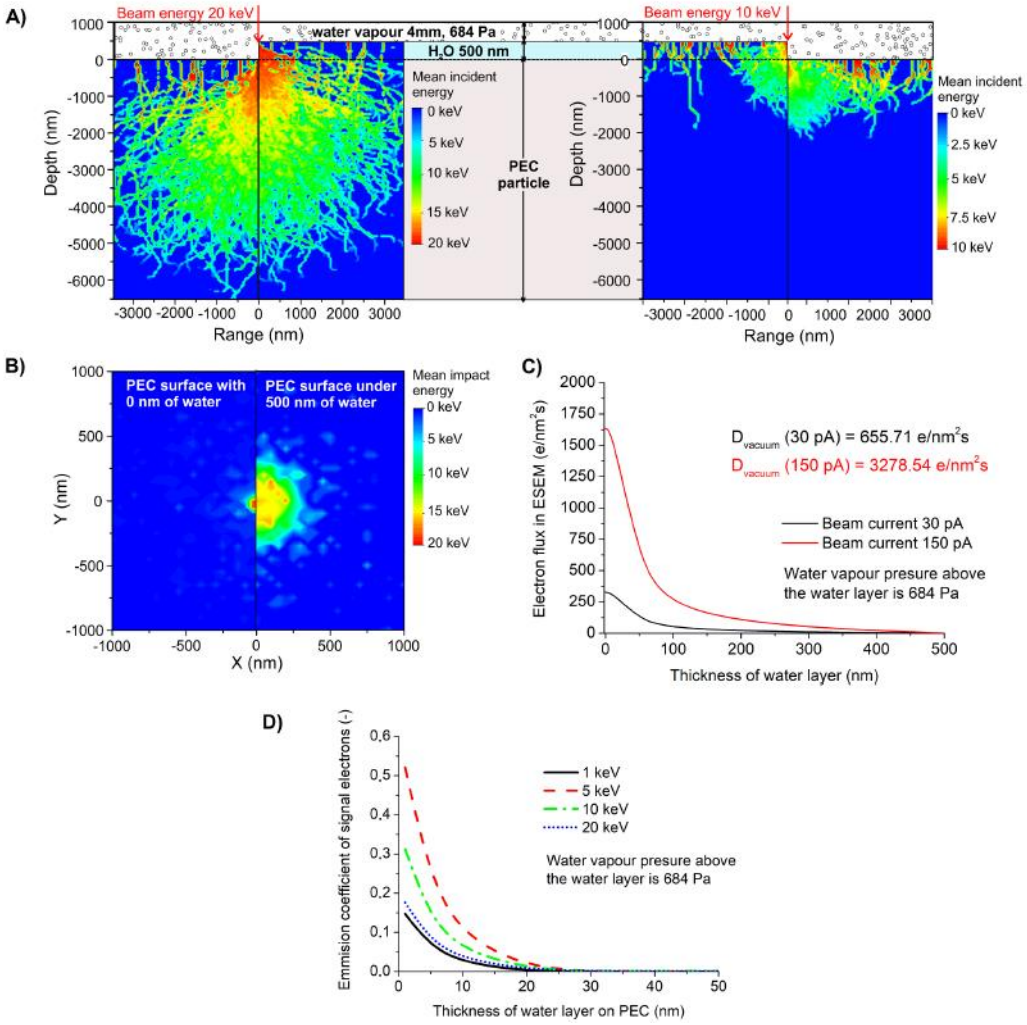

Fig. 6. A) Monte Carlo simulations of the cross-section view of the mean electron energy absorbed in the uncovered sample and sample covered with a 500 nm water layer in the ESEM for beam energies 20 keV (left side) and 10 keV (right side). B) Energy distribution of scattered electron beam on the spherical PEC particle surface in the ESEM for 0 and 500 nm water layer (ED 4 mm, water vapour environment 684 Pa). C) Values of electron flux in a vacuum and the dependence of electron flux on the thickness of the water layer on a spherical PEC particle (curves) at pressure 684 Pa. D) Monte Carlo simulations of signal electrons emission coefficient from the spherical PEC particle covered with increasing thicknesses of the water layer at various beam energies.

ESEM observation

Fig. 7 shows time lapse images of the *in-situ* degradation of spherical PEC particles recorded using a common, but less optimised, observation procedure in the ESEM, for comparison with the optimised procedure outlined later. The observation includes the following steps: a rapid drop of gas pressure (407 Pa s^{-1}) during the initial specimen chamber pumping procedure, followed by several purge-flood cycles, which are applied for the efficient exchange of air to water vapour [49].

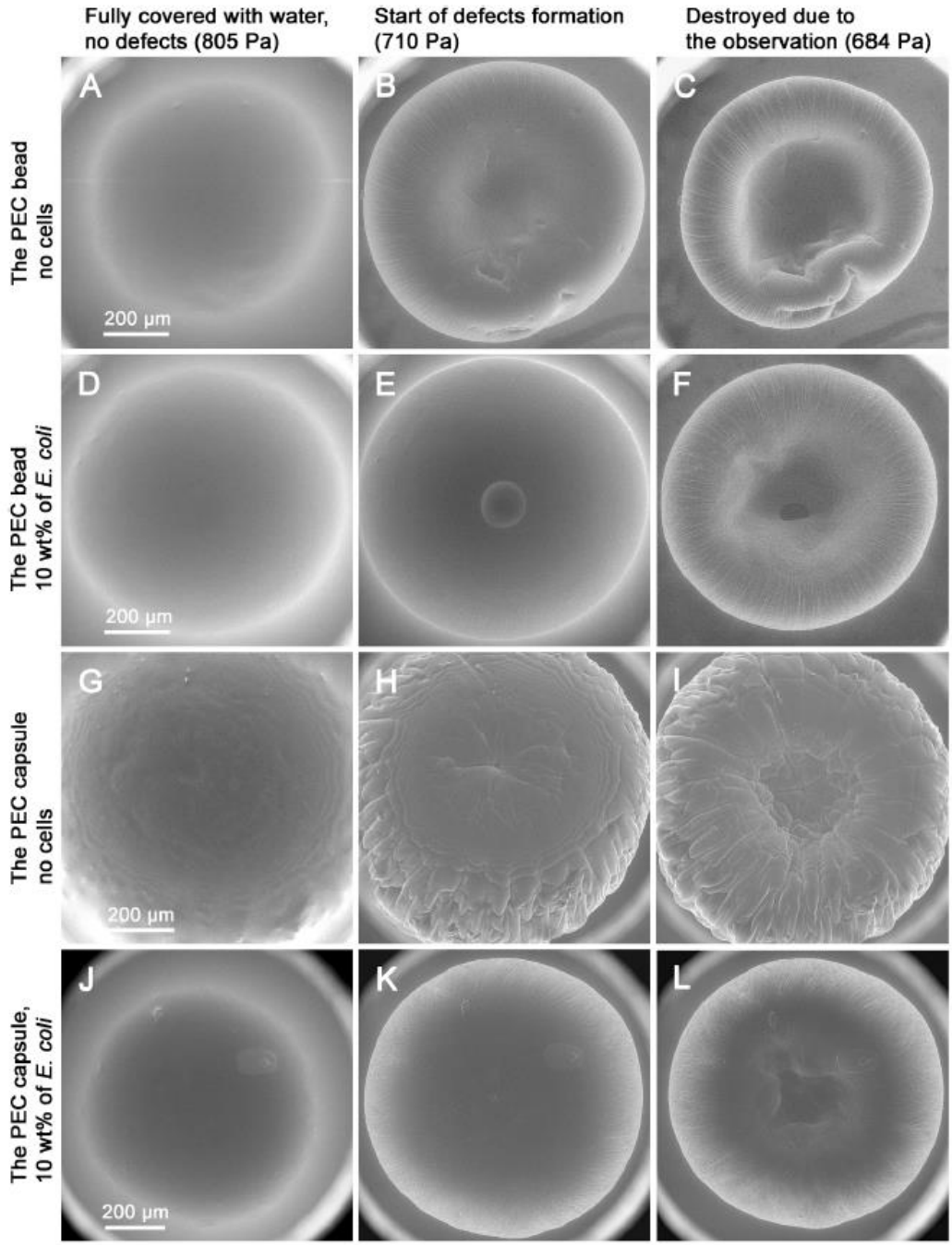

Fig. 7. Common ESEM observation of different spherical PEC particles (A-F PEC capsule; G-L PEC bead). Observation starts in the wet state (the first column). Due to the incorrectly set pressure which does not correspond to the real temperature, the sample is destroyed in a very short time - mostly during two scanned images (dwell time 235 µs), see the second and the third column. Observation conditions: TSET 2.0 °C ≈ TREAL 3.5 °C, 684 Pa, RHREAL 85%, ED 4 mm, beam energy 20 keV, beam current 30 pA.

Consequently, even if there is water around the sample and the sample remains wet all the time, a delicate sample can be damaged due to the rapid changes in gas pressure and temperature around it. Moreover, it is difficult to achieve

thermodynamic equilibrium because the actual sample temperature differs from the set temperature

Images recorded shortly after the initial specimen chamber pumping procedure was completed are shown in Figs. 7A, D, G, J. At this stage, the spherical PEC particles were fully covered with water and free of any destruction, except in Fig. 7G. Despite the fact that all these figures were observed using the same procedure and under RH greater than 100% (corresponding to sample temperatures up to 5 °C at water vapour pressure of 900 Pa), the sample surface in Fig. 7G has dried. This confirmed that the observation of sensitive samples in poorly defined thermodynamic conditions in the ESEM can be very tricky, time consuming and often irreproducible. Images in the middle and right column were recorded at a lower RH, according to the set temperature of 2 °C. Although the real temperature was higher (see the simulation results), the temperature difference was not taken into accout, as is common in typical ESEM observations. Figs. 7B, E, H, K were recorded at the onset of significant deformation of the spherical PEC particles. The images illustrate how quickly ESEM observation can destroy samples. Regardless of whether we observed capsules or beads, the sample damage always began in the middle of the spherical segment, where the sample surface dried first. Here, the sample temperature was the highest and the electron beam irradiation was perpendicular to the sample surface. Due to radiation damage, the polymeric chains have undergone scission, and the mechanical strength of semipermeable membrane was reduced. The forces acting on the outer semipermeable membrane caused the spherical PEC particle to break, the gas escaped and the spherical particle imploded. This process can be seen in Fig. 7E where a small bubble on the sample surface was inflated until it burst and the bead imploded (see Fig. 7F). The totally destroyed spherical particles in the last state of observation can be seen in Figs. 7C,F,I,L. The presence of a semipermeable membrane increased the overall mechanical strength of the capsules, unlike the bead. For this reason, an approximately circular part around the centre of the capsule fell down (see Figs. 7G-L), while the bead's entire upper half broke down (see Figs. 7A-F).

As already indicated, delicate wet samples can also be damaged due to unsuitable parameters of the initial specimen chamber pumping procedure before observation in ESEM. The study of dynamical *in-situ* leakage of the PEC capsule's viscous core and its adhesion to the sample surface is seen in Fig. 8. The leakage was caused due to a very rapid pressure drop during the initial specimen chamber pumping procedure (592 Pa s^{-1}). As shown by the ideal gas law and the results of our further simulations (manuscript in preparation) the most intensive reduction of the temperature occurrs in the first 10 s, when the pumping process starts. During this time, we estimate that the gas temperature drops to −25 °C in the bottom part of the

sample. This could cause sample-freezing onto the silicon pad, during which the volume of the PEC capsule increases as crystals of ice form. Consequently, we postulate that a volume change upon crystallisation caused the observed cracking of the sample. When the pressure approached the target pressure (684 Pa), the sample temperature increased to the value provided by the Peltier cooling stage. Since the semipermeable membrane was frozen, the core was subsequently cooled. Therefore, the core remained in the liquid phase compared to previous experiments. As a result, the viscous core escaped through a crack out (not shown in the images) and covered the surface of the PEC capsule during observation (see Figs. 8A-E). The time-lapse study started as soon as possible, using a slow scanning speed (dwell time 235 μs). While the top part of the capsule was wet, the bottom part was still frozen to the silicon pad (see Fig. 8A). The visible surface of the capsule dried very slowly. Stress in the semipermeable membrane increased and the capsule began to deform (see Fig. 8B). Continuous drying and deformation caused it to break. The semi-liquid inner content (viscous core) became visible on the sample edges and silicon pad (see Fig. 8C, D) until the spherical PEC particle became empty (see Fig. 8E). In the layer covering the rest of the spherical PEC particle, the *E. coli* bacteria, from the inner content, was observed (see Fig. 8F).

According to above presented results, the conventional ESEM observation strategy needs to be optimised for an accurate and gentle study of sensitive samples in their native wet state with minimal damage. A summary of these optimisations is outlined below, in our socalled Delicate Sample Observation Strategy (DSOS).

DSOS should be based on the following steps:

1) Pre-cool samples to minimize large and rapid sample temperature changes in the ESEM

2) Place the pre-cooled sample into a drop of distilled water on the cooling stage

3) Gentle but effective initial pumping process of the ESEM specimen chamber, free of rapid changes in pressure (purge-flood cycles) and temperature

4) A sophisticated cooled sample holder with integrated sample temperature sensor

5) Knowledge of the actual thermodynamic conditions in the vicinity of the sample to minimize sample drying

6) Reduce beam energy, beam current and dwell time as much as possible for

detection of a signal with an acceptable signal-to-noise

7) High efficiency, fast detection systems, which enable working in a wide range of environmental conditions and under conditions mentioned in point 6.

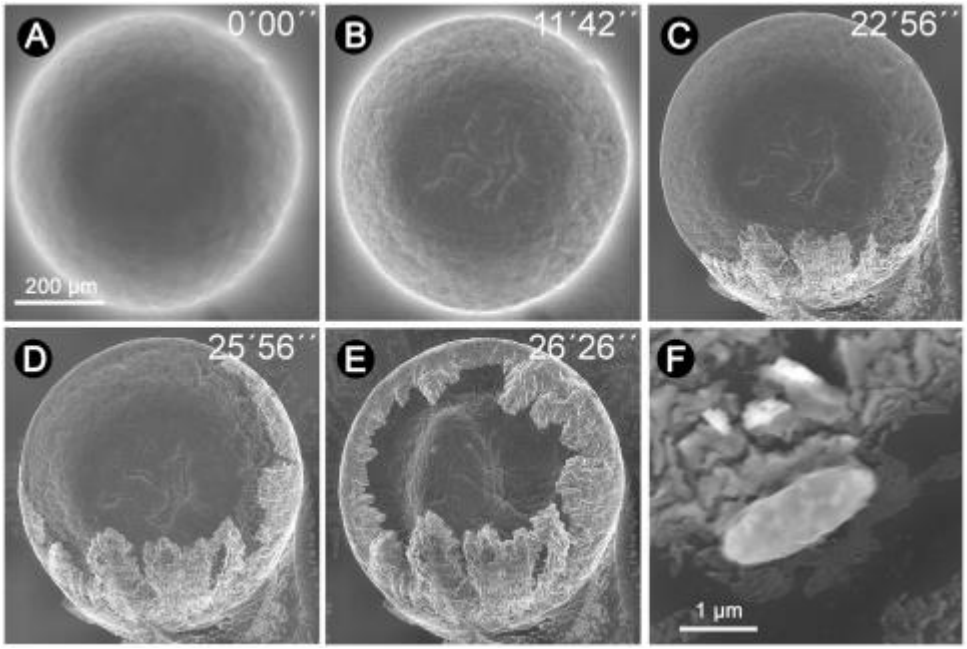

Fig. 8. The PEC capsule containing 10wt% of E. coli. A-E) In-situ deformation of the sample due to leakage of the inner content. C-E) The inner content adhered to the edges of the sample can be seen as a brighter layer. F) The bacteria was found in the adhered layer. Observation conditions: 20 kV, 30 pA, T_{SET} 2.0 °C ≈ T_{REAL} 3.5 °C, 684 Pa, RH_{REAL} 85%, ED 4 mm.

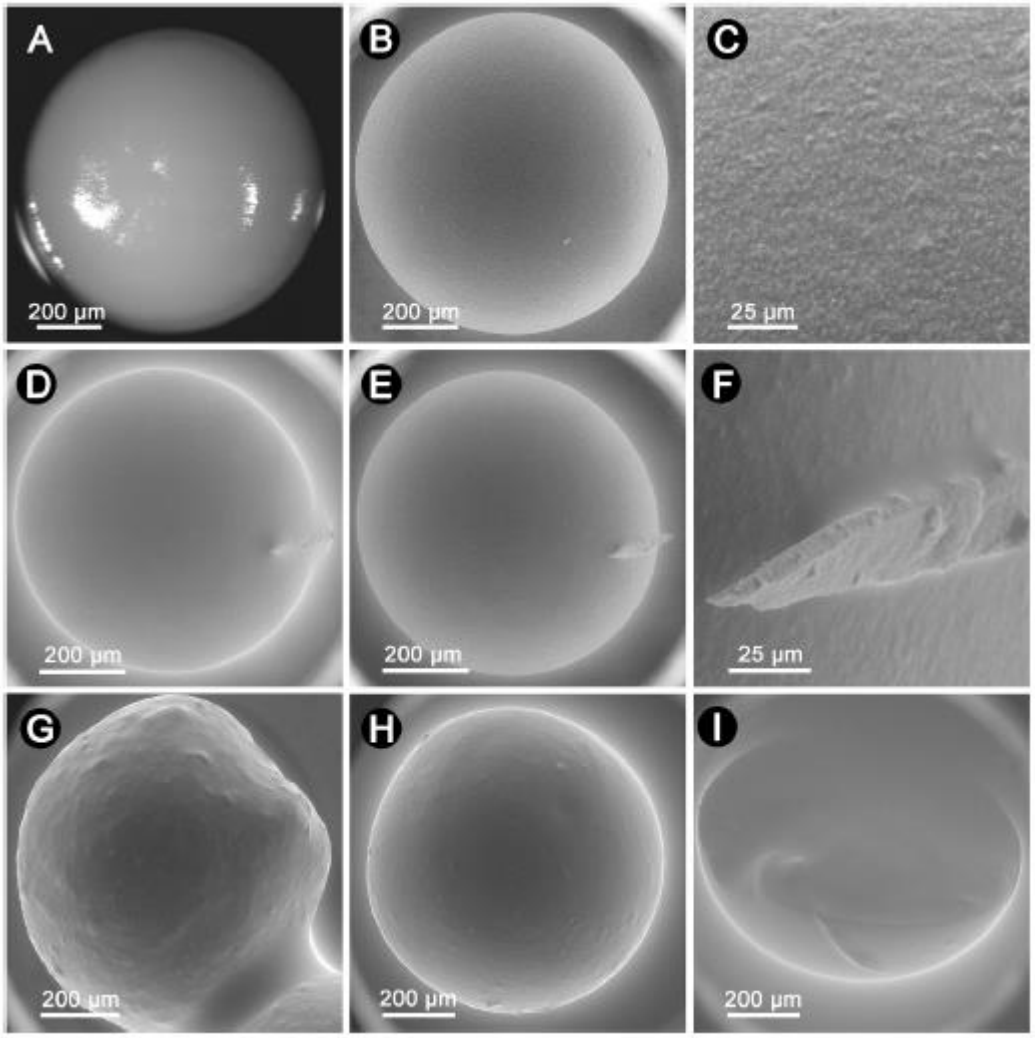

Fig. 9. The PEC capsule containing 10wt% of E. coli. A-E) In-situ deformation of the sample due to leakage of the inner content. C-E) The inner content adhered to the edges of the sample can be seen as a brighter layer. F) The bacteria was found in the adhered layer. Observation conditions: 20 kV, 30 pA, T_{SET} 2.0 °C ≈ T_{REAL} 3.5 °C, 684 Pa, RH_{REAL} 85%, ED 4 mm.

These precautions minimize the electron beam irradiation of the water and sample, thus helping to suppress free radical formation. Moreover, the gentle pumping process ensures more stable thermodynamic conditions in the specimen chamber needed for well controlled revealing of the sample microstructure.

Results obtained after application of DSOS, when very slow initial specimen chamber pumping procedure (speed 203 Pa s^{-1}) and optimised observation conditions were used (beam energy 10 keV, beam current 30 or 15 pA), are shown in Figs. 9B-I. When the thermodynamic conditions in the ESEM are known and fully controlled, the morphological study of very sensitive samples in their native state is possible without damage. The spherical PEC particles show similarity to those observed with a light microscope (Fig. 9A), however, ESEM offers the

potential for studying surface specifics or defects at higher magnification (Fig. 9C). The new strategy brings helpful feedback in defectoscopy and the development of a biotechnological process of spherical PEC particle production (Fig. 9D- H). Figures D-F show the presence of an impurity on the PEC particle. We assume this impurity was incorporated into the semipermeable membrane of the particle during its production process. The detail of the impurity can be seen in Fig. 9F. Surface of the PEC particle with strong corrugation due to cell clustering (Fig. 9G – capsule with 10% of *E. coli* cells) and irregularities of the sphericity of the PEC particles (Fig. 9G, H), which could be caused during the mechanical manipulation of the sample, were also observed.

This new strategy has helped us to further push the limits of ESEM, enabling us to observe an undamaged halved capsule with its intact liquid inner core containing bacteria (see Fig. 9I). We believe that such a result has not previously been achieved in the field of electron microscopy.

Conclusion

In comparison with SEM, ESEM is considered to be less user-friendly and therefore has been less utilized. The sensitivity of delicate samples in their native state to beam radiation and environmental conditions in the ESEM is incomparably higher than the sensitivity of fixed, dried and sputter coated samples in SEM. Therefore, fundamentally different strategies and instrumentation should be used in the ESEM. Our results unveil the high potential of ESEM in the area of dynamical *in-situ* experiments focused on the morphological study of delicate wet samples in their native state without any destruction. We offer the most complex analysis of the majority of physical processes happening before and during sample observation in the ESEM. Based on the analysis, we introduce the Delicate Samples Observation Strategy for ESEM (DSOS) which helps to reveal unique sample information and simplifies the working requirements. Moreover, we can test and calculate mechanical properties of spherical PEC particles (Fig. 4) and characterize their sphericity in the ESEM [8].

According to simulations of gas flow and heat transfer in the ESEM we can conclude that for ED higher than 1.3 mm (or, for a standard PLA 1 with diameter 500 μm, higher than approximately 1 mm) the value of the gas pressure is constant and can be measured by capacitance pressure gauges in the ESEM specimen chamber. For a commonly-used ED higher than 3 mm, we can neglect the influence of the velocity and direction of water vapour flow on the sample. A high thermal power of electron beam (e.g. 20 keV, 150 pA), together with decreasing the amount of water surrounding the sample, act against the realization of thermodynamic

equilibrium. By applying the DSOS, especially by using a beam energy and current down to 10 keV and 30 pA, respectively, the local increase of sample temperature is minimised to only a few tenths of °C. We observed neither an accumulation nor an increase of the sample temperature at commonly-used scanning speeds. Moreover, we can apply the results of our simulations to fully hydrated biological samples, since their specific heat capacity and heat conductivity is similar to the heat capacity and conductivity of spherical PEC particles [68].

Due to the relatively low heat conductivity of polymers, the actual temperature of the area affected by the electron beam is expected to be higher. The local increase in sample temperature can cause irreversible sample dehydration as the delicate thermodynamic equilibrium between gas pressure and sample temperature is shifted to non-equilibrium conditions [64,69]. Moreover, according to Raoult's Law, when the sample in the ESEM contains a liquid phase of water and solutes, conditions for the thermodynamic equilibrium of pure water do not necessarily correspond with the those of the sample [18].

The difference between the T_{SET} and T_{REAL} or actual temperature of the beam irradiated sample surface makes it particularly difficult to achieve thermodynamic equilibrium in the ESEM. When using our selfdeveloped cooling stage, optimised to increase heat transfer, the difference in T_{SET} and T_{REAL} is 1.5 °C. In the case of commonly-used commercial cooling stages, the difference can be significantly higher. Another important issue, which is being neglected in the literature, is the use of a suitable initial specimen chamber pumping procedure. The inappropriately high speed of pumping from atmospheric to working pressure can cause major destruction of delicate samples. This can occur not only as a result of the influence of deformation (see the results of strength-stress analysis) but also due to drying or freezing of the sample in a very short time. During fast pumping of the specimen chamber (592 Pa s^{-1}), we propose that the bottom of the sample is cooled to −25 °C in the first 10 s of the pumping process. Since the sample was likely frozen to the sample holder in our experiments, the PEC capsule broke and the inner viscous core leaked out.

Radiation-induced production of free radicals in water significantly contributes to sample damage. The dissociation energy of the HeO bond in the water molecule is reported to be 499 kJ mol^{-1} at 298 K [70] or 117.59 kcal mol^{-1} [71] which correspond to 5.17 eV and 5.10 eV, respectively. These are the minimal values of the energies needed for dissociation of the HeO bond. Therefore, the interaction of electrons with energy higher than 5.10 eV with water vapour generates additional free radicals which may cause polymer hydrolysis and oxidation on the sample surface [72]. As a result of the interaction of the incident electron with water

molecules in the sample, excitation of orbital electrons in the water molecule arises and it decomposes to few radiolytic species. The radial concentration profile for dominant species (e_{aq}^{-}, H^{*}, $^{*}OH$) produced after an interaction of water with an electron beam of the energy typical for ESEM was published by Royall et al. [44]. They also found that the dominant reactive species is the hydroxyl radical ($^{*}OH$).

By comparing two beam energies, 5 keV and 25 keV, Royall et al. [44] found a drastic increase in the quantities of reactive species for 25 keV. The range of 25 keV primary electrons (PE) spreads reactive species over a wider region and consequently they decay more slowly. We assume that the total number of free radicals increases with increasing energy of primary electrons due to the increased interaction volume in the sample. Simultaneously, with increasing interaction volume, the concentration of free radicals decreases. Since the recombination rate of free radicals is lower at a low concentration, we assume a higher probability of damage to a greater sample volume, as the radicals remain free and diffuse. The scattering of beam electrons in ESEM increases with increasing ED, gas pressure and the thickness of water layer covering the sample. Values D_{vacuum} and D_{ESEM} compare the amount of incident electrons in the original spot size in a vacuum and at a constant value of water vapour pressure in 1 nm^2 per second, at specific beam current and a varying thickness of the water layer for D_{ESEM}. Inelastic interactions of beam electrons with gas molecules and the water layer cause a decrease of electron energy together with an increase in beam scattering and interaction volume. Hence, the energy in the sample is less localised. The SNR in the detected signal is also lower and therefore the resolution in the ESEM decreases.

Based on the above mentioned aspects and our simulations, we assume that free radicals are produced in lower quantities but in a more shallow interaction volume located under the sample surface (see Fig. 6). Application of lower beam energy enhances electron energy loss and beam scattering in the ESEM, hence the final interaction volume in the sample is smaller. Consequently, the amount of free radicals decreases, but their concentration increases, and so the probability of recombination increases. Fig. 9 indicates significantly less damage to the sample when using a lower beam energy. In the case of a 500 nm water layer on the sample, the majority of radicals are produced inside the covering water layer, and can diffuse to the sample surface and cause damage. The decrease of beam energy also causes an increase of the emission coefficient of secondary electrons from the sample; however, in the case of a 500 nm water layer, all of the secondary electrons are absorbed by the layer. The maximal value of the emission coefficient of signal electrons (SE+BSE) was calculated for beam energy 5 keV (see Fig. 6D). The optimal value of beam energy used for research of hydrogels and wet polymers in the ESEM was found to be in the range of 5 to 10 keV.

However, in our dynamical *in-situ* experiment, we observed the evaporation of the covering water layer. This enables the continuous penetration of electrons deeper inside the sample and thus their energy is more localised. Consequently, radiation damage, together with sample drying, results in extensive damage (see Fig. 7). On the other hand, the thinner water layer absorbs a lower amount of signal electrons and in the case of an ultra-thin layer, it is possible for secondary electrons to pass through. This favours better achievable resolution in the ESEM.

We are the first to use electron microscopy to show the native-state thickness of the semipermeable membrane, via our experiments in ESEM. According to the results of our simulations of the size of interaction volume, we can conclude that there is no destruction of the viscous core containing living cells inside the spherical PEC particle, since the thickness of the semipermeable membrane is 82.8 μm. The function/utility of the spherical PEC particle is not influenced at the optimised observation. The biggest challenge was the observation of the halved wet capsule with its undamaged viscous core. DSOS for ESEM, which is based on the results of advanced mathematical-physical simulations, enabled us to be the first-ever to image this liquid viscous core using electron microscopy (see Fig. 9I). For further research, we need to focus on the study and characteristics of the production and diffusion of free radicals in ESEM conditions and on the study of the compensation of radical-sample interaction.

Acknowledgements

The work was supported by the Grant Agency of the Czech Republic [GA 19–03909S] and by the Czech Academy of Sciences [RVO:68081731]. This work was supported by the Slovak Grant Agency for Science VEGA 2/0090/16 and by the Slovak Research and Development Agency under contract no. APVV-15–0227. The authors thank to Tomaš Krajčovič, PhD. (Institute of Chemistry, Slovak Academy of Sciences, Bratislava, Slovakia) for his assistance with the preparation of PEC capsules and beads.

References

[1] M. Bučko, P. Gemeiner, A. Schenkmayerova, T. Krajčovič, F. Rudroff, M.D. Mihovilovič, Baeyer-Villiger oxidations: biotechnological approach, Appl. Microbiol. Biotechnol. 100 (2016) 6585–6599, https://doi.org/10.1007/s00253- 016-7670-x.

[2] M. Polakovič, J. Švitel, M. Bučko, J. Filip, V. Neděla, M.B. Ansorge-Schumacher, P. Gemeiner, Progress in biocatalysis with immobilized viable whole cells: systems development, reaction engineering and applications, Biotechnol. Lett. 39 (2017) 667–683, https://doi.org/10.1007/s10529-017-2300-y.

[3] M. Kadisch, C. Willrodt, M. Hillen, B. Buhler, A. Schmid, Maximizing the stability of metabolic engineering-derived whole-cell biocatalysts, Biotechnol. J. 12 (2017) 1–27, https://doi.org/10.1002/biot.201600170.

[4] M.A. Bochenek, O. Veiseh, A.J. Vegas, J.J. McGarrigle, M. Qi, E. Marchese, M. Omami, J.C. Doloff, J. Mendoza-Elias, M. Nourmohammadzadeh, A. Khan, C.C. Yeh, Y. Xing, D. Isa, S. Ghani, J. Li, C. Landry, A.R. Bader, K. Olejnik, M. Chen, J. Hollister-Lock, Y. Wang, D.L. Greiner, G.C. Weir, B.L. Strand, A.M.A. Rokstad, I. Lacik, R. Langer, D.G. Anderson, J. Oberholzer, Alginate encapsulation as longterm immune protection of allogeneic pancreatic islet cells transplanted into the omental bursa of macaques, Nat. Biomed. Eng. 2 (2018) 810–821, https://doi.org/ 10.1038/s41551-018-0275-1.

[5] A. Partovinia, B. Rasekh, Review of the immobilized microbial cell systems for bioremediation of petroleum hydrocarbons polluted environments, Crit. Rev. Environ. Sci. Technol. 48 (2018) 1–38, https://doi.org/10.1080/10643389.2018. 1439652.

[6] J.S. Patil, M.V. Kamalapur, S.C. Marapur, D.V. Kadam, Ionotropic gelation and polyelectrolyte complexation: the novel techniques to design hydrogel particulate sustained, modulated drug delivery system: a review, Dig. J. Nanomater. Biostructures. 5 (2010) 241–248.

[7] M. Hucik, M. Bučko, P. Gemeiner, V. Štefuca, A. Vikartovska, M.D. Mihovilovič, F. Rudroff, N. Iqbal, D. Chorvat, I. Lacik, Encapsulation of recombinant E. coli expressing cyclopentanone monooxygenase in polyelectrolyte complex capsules for baeyer-villiger biooxidation of 8-oxabicyclo[3.2.1]oct-6-en-3-one, Biotechnol. Lett. 32 (2010) 675–680, https://doi.org/10.1007/s10529-010-0203-2.

[8] T. Krajčovič, M. Bučko, A. Vikartovska, I. Lacik, L. Uhelska, D. Chorvat, V. Neděla, E. Tihlařikova, M. Gericke, T. Heinze, P. Gemeiner, Polyelectrolyte complex beads by novel two-step process for improved performance of viable whole-cell baeyervilliger monoxygenase by

immobilization, Catalysts 7 (2017) 353, https://doi.org/10.3390/catal7110353.

[9] A. Schenkmayerova, M. Bučko, P. Gemeiner, D. Treľova, I. Lacik, D. Chorvat, P. Ačai, M. Polakovič, L. Liptak, M. Rebroš, M. Rosenberg, V. Štefuca, V. Neděla, E. Tihlařikova, Physical and bioengineering properties of polyvinyl alcohol lensshaped particles versus spherical polyelectrolyte complex microcapsules as immobilisation matrices for a whole-cell baeyer–villiger monooxygenase, Appl. Biochem. Biotechnol. 174 (2014) 1834–1849, https://doi.org/10.1007/s12010-014-1174-x.

[10] P. Gemeiner, V. Štefuca, V. Baleš, Biochemical engineering of biocatalysts immobilized on cellulosic materials, Enzyme Microb. Technol. 15 (1993) 551–566, https://doi.org/10.1016/0141-0229(93)90017-V.

[11] V. Štefuca, A. Welwardova, P. Gemeiner, Flow microcalorimeter auto-calibration for the analysis of immobilized enzyme kinetics, Anal. Chim. Acta. 355 (1997) 63–67, https://doi.org/10.1016/S0003-2670(97)81612-1.

[12] V. Štefuca, P. Gemeiner, Investigation of catalytic properties of immobilized enzymes and cells by flow, Microcalorimetry 64 (1999) 69–99, https://doi.org/10.1007/3-540-49811-7_3.

[13] M. Bučko, A. Vikartovska, A. Schenkmayerova, J. Tkač, J. Filip, D. Chorvat, V. Neděla, M.B. Ansorge-Schumacher, P. Gemeiner, Progress in emerging techniques for characterization of immobilized viable whole-cell biocatalysts, Chem. Pap. 71 (2017) 2309–2324, https://doi.org/10.1007/s11696-017-0243-3.

[14] P. Meredith, A.M. Donald, Study of “wet” polymer latex systems in environmental scanning electron microscopy: some imaging considerations, J. Microsc. 181 (1996) 23–35, https://doi.org/10.1046/j.1365-2818.1996.67341.x.

[15] M.J. Garcia-Salinas, A.M. Donald, Use of environmental scanning electron microscopy to image poly(N-isopropylacrylamide) microgel particles, J. Colloid Interface Sci 342 (2009) 629–635, https://doi.org/10.1016/j.jcis.2009.10.064.

[16] L.P.B. Guerzoni, J. Bohl, A. Jans, J.C. Rose, J. Koehler, A.J.C. Kuehne, L. De Laporte, Microfluidic fabrication of polyethylene glycol microgel

capsules with tailored properties for the delivery of biomolecules, Biomater. Sci. 5 (2017) 1549–1557, https://doi.org/10.1039/c7bm00322f.

[17] G.D. Danilatos, Foundations of environmental scanning electron microscopy, Adv. Electron. Electron Phys. 71 (1988) 109–250.

[18] D. Stokes, Principles and practice of variable pressure/environmental scanning electron microscopy (VP-ESEM), John Wiley & Sons, 2008.

[19] G.D. Danilatos, The examination of fresh or living plant material in an environmental scanning electron microscope, J. Microsc. 121 (1981) 235–238, https://doi. org/10.1111/j.1365-2818.1981.tb01218.x.

[20] D.J. Stokes, S.M. Rea, S.M. Best, W. Bonfield, Electron microscopy of mammalian cells in the absence of fixing, freezing, dehydration, or specimen coating, Scanning 25 (2003) 181–184, https://doi.org/10.1002/sca.4950250404.

[21] A.V. Goponenko, B.J. Boyle, K.I. Jahan, M.V. Gerashchenko, D.E. Fomenko, V.N. Gladyshev, Y.A. Dzenis, Use of environmental scanning electron microscopy for in situ observation of interaction of cells with micro- and nanoprobes, Micro Nano Lett 6 (2011) 603, https://doi.org/10.1049/mnl.2011.0166.

[22] C. Appel, C. Bogvad, Heating experiments in the scanning electron microscope, Microsc. Microanal. 17 (2011) 430–431, https://doi.org/10.1017/ S1431927611003023.

[23] J. Krausko, J. Runštuk, V. Neděla, P. Klan, D. Heger, Observation of a brine layer on an ice surface with an environmental scanning electron microscope at higher pressures and temperatures, Langmuir 30 (2014) 5441–5447, https://doi.org/10.1021/la500334e.

[24] X. Yang, V. Neděla, J. Runštuk, G. Ondruškova, J. Krausko, L. Vetrakova, D. Heger, Evaporating brine from frost flowers with electron microscopy and implications for atmospheric chemistry and sea-salt aerosol formation, Atmos. Chem. Phys. 17 (2017) 6291–6303, https://doi.org/10.5194/acp-17-6291-2017.

[25] B.L. Thiel, A.M. Donald, In situ mechanical testing of fully hydrated carrots (daucus carotd) in the environmental sem, Ann. Bot. 82 (1998) 727–733, https://doi.org/ 10.1006/anbo.1998.0732.

[26] J.E. McGregor, A.M. Donald, ESEM imaging of dynamic biological processes: the closure of stomatal pores, J. Microsc. 239 (2009) 135–141, https://doi.org/10.1111/j.1365-2818.2009.03351.x.

[27] X. Tang, M. De Rooij, L. De Jong, Volume change measurements of rice by environmental scanning electron microscopy and stereoscopy, Scanning 29 (2007) 197–205, https://doi.org/10.1002/sca.20064.

[28] E. Tihlařikova, V. Neděla, M. Shiojiri, In situ study of live specimens in an environmental scanning electron microscope, Microsc. Microanal. 19 (2013) 914–918, https://doi.org/10.1017/S1431927613000603.

[29] V. Neděla, E. Tihlařikova, J. Hřib, The low-temperature method for study of coniferous tissues in the environmental scanning electron microscope, Microsc. Res. Tech. 78 (2015) 13–21, https://doi.org/10.1002/jemt.22439.

[30] V. Neděla, J. Hřib, B. Vookova, Imaging of early conifer embryogenic tissues with the environmental scanning electron microscope, Biol. Plant. 56 (2012) 595–598, https://doi.org/10.1007/s10535-012-0062-x.

[31] V. Neděla, J. Hřib, L. Havel, J. Hudec, J. Runštuk, Imaging of norway spruce early somatic embryos with the ESEM, cryo-sem and laser scanning microscope, Micron 84 (2016) 67–71, https://doi.org/10.1016/j.micron.2016.02.011.

[32] V. Neděla, E. Tihlařikova, J. Runštuk, J. Hudec, High-efficiency detector of secondary and backscattered electrons for low-dose imaging in the esem, Ultramicroscopy 184 (2018) 1–11, https://doi.org/10.1016/j.ultramic.2017.08. 003.

[33] E. Michaloudi, S. Papakostas, G. Stamou, V. Neděla, E. Tihlařikova, W. Zhang, S.A.J. Declerck, Reverse taxonomy applied to the brachionus calyciflorus cryptic species complex: morphometric analysis confirms species delimitations revealed by molecular phylogenetic analysis and allows the (re) description of four species, PLoS ONE 13 (2018) 1–25, https://doi.org/10.1371/journal.pone.0203168.

[34] E. Tihlařikova, V. Neděla, B. Đorđević, In-situ preparation of plant samples in esem for energy dispersive x-ray microanalysis and repetitive observation in sem and esem, Sci. Rep. 9 (2019) 2300, https://doi.org/10.1038/s41598-019-38835-w.

[35] A.L. Fletcher, B.L. Thiel, A.M. Donald, Signal components in the environmental scanning electron microscope, J. Microsc. 196 (1999) 26–34, https://doi.org/10.1046/j.1365-2818.1999.00590.x.

[36] V. Neděla, I. Konvalina, B. Lencova, J. Zlamal, Comparison of calculated, simulated and measured signal amplification in a variable pressure sem, Nucl. Instruments Methods Phys. Res. Sect. A Accel. Spectrometers, Detect. Assoc. Equip. 645 (2010), https://doi.org/10.1016/j.nima.2010.12.200.

[37] M. Toth, D.R. Daniels, B.L. Thiel, A.M. Donald, Quantification of electron-ion recombination in an electron-beam-irradiated gas capacitor, j, Phys. D. Appl. Phys. 35 (2002) 1796–1804, https://doi.org/10.1088/0022-3727/35/14/322.

[38] T. Rice, R. Knowles, Ultra high resolution sem on insulators and contaminating samples, Microscopy (2005) 40–42.

[39] R. Gauvin, K. Robertson, J.F. Leberre, J. Finch, B.J. Griffin, Possibility of charge contrast imaging of polymeric materials, Scanning 25 (2003) 240–242.

[40] B.L. Thiel, M. Toth, R.P.M. Schroemges, J.J. Scholtz, G. Van Veen, W.R. Knowles, Two-stage gas amplifier for ultrahigh resolution low vacuum scanning electron microscopy, Rev. Sci. Instrum. 77 (2006), https://doi.org/10.1063/1.2183082.

[41] R.F. Egerton, P. Li, M. Malac, Radiation damage in the tem and sem, Micron 35 (2004) 399–409, https://doi.org/10.1016/j.micron.2004.02.003.

[42] F.M. Ross, Liquid Cell Electron Microscopy, Cambridge University Press, 2016, https://doi.org/10.1017/9781316337455.

[43] C. Arnoult, J. Di Martino, D. Ruch, Prediction and limitation of polymer degradation in environmental sem, Ultramicroscopy 122 (2012) 32–36, https://doi.org/10.1016/j.ultramic.2012.07.027.

[44] C.P. Royall, B.L. Thiel, A.M. Donald, Radiation damage of water in environmental scanning electron microscopy, J. Microsc 204 (2001) 185–195, https://doi.org/10.1046/j.1365-2818.2001.00948.x.

[45] Y.L. Ren, A.M. Donald, Z.B. Zhang, Investigation of radiation damage to microcapsules in environmental sem, Mater. Sci. Technol. 23 (2007) 857–864, https://doi.org/10.1179/174328407x179502.

[46] L.C. Sawyer, D.T. Grubb, Polymer Microscopy, Chapman and Hall, London, 1987.

[47] D.T. Grubb, Radiation damage and electron microscopy of organic polymers, J. Mater. Sci. 9 (1974) 1715–1736, https://doi.org/10.1007/BF00540772.

[48] R. Leary, R. Brydson, Characterisation of esem conditions for specimen hydration control, J. Phys. Conf. Ser. (2010) 241, https://doi.org/10.1088/1742-6596/241/1/012024.

[49] R.E. Cameron, A.M. Donald, Minimizing sample evaporation in the environmental scanning electron microscope, J. Microsc 173 (1994) 227–237, https://doi.org/10.1111/j.1365-2818.1994.tb03445.x.

[50] G.D. Danilatos, Velocity and ejector-jet assisted differential pumping: novel design stages for environmental SEM, Micron 43 (2011) 600–611, https://doi.org/10.1016/j.micron.2011.10.023.

[51] G.A. Bird, Molecular Gas Dynamics and the Direct Simulation of Gas Flows, Clarendon Press, Oxford, 1994, https://doi.org/10.1016/0042-207x(96)80021-2.

[52] G.D. Danilatos, Figure of merit for environmental sem and its implications, J. Microsc 244 (2011) 159–169, https://doi.org/10.1111/j.1365-2818.2011.03521.x.

[53] J. Maxa, M. Bilek, P. Hlavata, P. Vyroubal, K. Lepltova, Comparisons using methods of continuum mechanics and monte carlo at differentially pumped chamber, Adv. Mil. Technol. 11 (2016) 143–150, https://doi.org/10.3849/aimt.01120.

[54] J. Maxa, V. Neděla, The impact of critical flow on the primary electron beam passage through differentially pumped chamber, Adv. Mil. Technol. 6 (2011).

[55] J. Jirak, V. Neděla, P. Černoch, P. Čudek, J. Runštuk, Scintillation se detector for variable pressure scanning electron microscopes, J. Microsc 239 (2010) 233–238, https://doi.org/10.1111/j.1365-2818.2010.03377.x.

[56] J. Maxa, V. Neděla, J. Jirak, P. Vyroubal, K. Hladka, Analysis of gas flow in a secondary electron scintillation detector for esem with a new system of pressure limiting apertures, Adv. Mil. Technol. 7 (2012).

[57] A.T. Akinshilo, J.O. Olofinkua, O. Olaye, Flow and heat transfer analysis of the sodium alginate conveying copper nanoparticles between two parallel plates, Shahid Chamran Univ. Ahvaz. 3 (2017) 258–266, https://doi.org/10.22055/JACM. 2017.21514.1105.

[58] G. Kaklamani, D. Cheneler, L.M. Grover, M.J. Adams, J. Bowen, Mechanical properties of alginate hydrogels manufactured using external gelation, j, Mech. Behav. Biomed. Mater. 36 (2014) 135–142, https://doi.org/10.1016/j.jmbbm.2014.04.013.

[59] U. Oyeagu, C. Nwuche, C. Ogbonna, J. Ogbonna, Addition of fillers to sodium alginate solution improves stability and immobilization capacity of the resulting calcium alginate beads, Iran. J. Biotechnol. 16 (2018) 67–73, https://doi.org/10.21859/ijb.1824.

[60] S. Agostinelli, GEANT4 collaboration - A simulation toolkit, nucl. instrum, Methods Phys. Res., Sect. A. 506 (2003) 250.

[61] D.C. Joy, A database on electron-solid interactions, Scanning 17 (1995) 270–275, https://doi.org/10.1002/sca.4950170501.

[62] G.D. Danilatos, Electron scattering cross-section measurements in esem, Micron 45 (2012) 1–16, https://doi.org/10.1016/j.micron.2012.10.002.

[63] P. De Vera, I. Abril, R. Garcia-Molina, Inelastic scattering of electron and light ion beams in organic polymers, J. Appl. Phys. 109 (2011), https://doi.org/10.1063/1. 3581120.

[64] V. Neděla, Controlled dehydration of a biological sample using an alternative form of environmental sem, J. Microsc. 237 (2010) 7–11, https://doi.org/10.1111/j. 1365-2818.2009.03216.x.

[65] D.L. Vezie, E.L. Thomas, W.W. Adams, Low-voltage, high-resolution scanning electron microscopy: a new characterization technique for polymer morphology, Polymer (Guildf) 36 (1995) 1761–1779, https://doi.org/10.1016/0032-3861(95)90923-P.

[66] S. Okayama, K. Kanaya, Penetration and energy-loss theory of electrons in solid targets, j, Phys. D. Appl. Phys. 5 (1972) 43–51, https://doi.org/10.1088/0022-3727/5/1/308.

[67] K. Wiklund, J.M. Fernndez-Varea, B.K. Lind, A monte carlo program for the analysis of low-energy electron tracks in liquid water, Phys. Med. Biol. 56 (2011) 1985–2003, https://doi.org/10.1088/0031-9155/56/7/005.

[68] L. Li, M. Liang, B. Yu, S. Yang, Analysis of thermal conductivity in living biological tissue with vascular network and convection, Int. J. Therm. Sci. 86 (2014) 219–226, https://doi.org/10.1016/j.ijthermalsci.2014.07.006.

[69] D. Stokes, Investigating biological ultrastructure using environmental scanning electron microscopy (ESEM), Sci. Technol. Educ. Microsc. an Overv. Investig. 2 (2006) 564–570 https://www.researchgate.net/profile/Debbie_Stokes/publication/240635965_Investigating_Biological_Ultrastructure_using_Environmental_Scanning_Electron_Microscopy_(ESEM)/links/0c96052fa214c8fd5f000000.pdf.

[70] V.I. Vedeneyev, L.V. Gurvich, V.N. Kondratyev, V.A. Medvedev, Y.L. Frankevich, Bond Energies, Ionization Potentials and Electron Affinities, St. Martin's Press, New York, 1962.

[71] B. Ruscic, A.F. Wagner, L.B. Harding, R.L. Asher, D. Feller, D.A. Dixon, K.A. Peterson, Y. Song, X. Qian, C.Y. Ng, J. Liu, W. Chen, D.W. Schwenke, On the enthalpy of formation of hydroxyl radical and gas-phase bond dissociation energies of water and hydroxyl, J. Phys. Chem. A. 106 (2002) 2727–2747, https://doi.org/10.1021/jp013909s.

[72] S. Kitching, A.M. Donald, Beam damage of polypropylene in the environmental scanning electron microscope: an ftir study, J. Microsc 190 (1998) 357–365, https://doi.org/10.1046/j.1365-2818.1998.00346.x.

22 Physical and Bioengineering Properties of Polyvinyl Alcohol Lens-Shaped Particles Versus Spherical Polyelectrolyte Complex Microcapsules as Immobilisation Matrices for a Whole-Cell Baeyer–Villiger Monooxygenase

Andrea Schenkmayerová & Marek Bučko & Peter Gemeiner & Dušana Treľová & Igor Lacík & Dušan Chorvát Jr. & Pavel Ačai & Milan Polakovič & Lukáš Lipták & Martin Rebroš & Michal Rosenberg & Vladimír Štefuca & Vilém Neděla & Eva Tihlaříková

Keywords

Polyelectrolyte complex microcapsules, LentiKats®, Confocal laser scanning microscopy, Inverse size exclusion chromatography, Environmental scanning electron microscopy, Baeyer–Villiger biooxidation

Abstract

Direct comparison of key physical and chemical-engineering properties of two representative matrices for multipurpose immobilisations was performed for the first time. Polyvinyl alcohol lens-shaped particles LentiKats® and polyelectrolyte complex microcapsules were characterised by advanced techniques with respect to the size distribution of the particles, their inner morphology as revealed by fluorescent probe staining, mechanical resistance, size-exclusion properties, determination of effective diffusion coefficient and environmental scanning electron microscope imaging. While spherical polyelectrolyte complex microcapsules composed of a rigid semipermeable membrane and a liquid core are almost uniform in shape and size (diameter of 0.82 mm; RSD=5.6 %), lens-shaped LentiKats® are characterised by wider size distribution (diameter of 3.65 mm; RSD=10.3 % and height of 0.341 mm; RSD=32.3 %) and showed the same porous structure throughout their whole volume at the mesoscopic (micrometre) level. Despite differences in their inner structure and surface properties, the pore diameter of~2.75 nm for regular polyelectrolyte complex microcapsules and~1.89 nm for LentiKats® were similar. These results were used for mathematical modelling, which provided the estimates of the effective diffusion coefficient of sucrose. This value was $1.67\times10^{-10}m^2\ s^{-1}$ for polyelectrolyte complex microcapsules and $0.36\times10^{-10}m^2\ s^{-1}$ for LentiKats®. Recombinant cells Escherichia coli-overexpressing enzyme cyclopentanone monooxygenase were immobilised in polyelectrolyte complex microcapsules and LentiKats® for comparison of their

operational stability using model Baeyer–Villiger oxidation of (±)-cis-bicyclo [3.2.0] hept-2-en-6-one to regioisomeric lactones as important chiral synthons for potential pharmaceuticals. Both immobilisation matrices rendered high operational stability for whole-cell biocatalyst with no reduction in the biooxidation rate over 18 repeated reaction cycles.

Introduction

The research and development of immobilised biosystems has accelerated since the early 1980s mainly due to remarkable improvements in the techniques used to produce beads with entrapped biomaterials. Highly productive devices have enabled the preparation of beads with a controlled, narrow distribution of size and shape from a laboratory scale to an industrial scale [1]. Water-soluble polysaccharides were the most frequently used materials for entrapment due to the simple and nontoxic formation of hydrogel beads by ionotropic gelation using divalent cations such as Ca^{2+} [2]. However, the development of thermoreversible gelification of polyvinylalcohol (PVA) in the form of lens-shaped particles, known as LentiKats® [3] allowed many applications due to the higher catalytic efficiency, mechanical stability, as well as the lower mass transfer resistance and cost of these particles with entrapped cells or enzymes [4, 5]. Moreover, the permeability of conventionally prepared PVA particles can be modified to entrap specific enzymes within the matrix (www.genialab.com).

Despite the advantages of the latter, PVA particles have been characterised only with respect to their geometry and partially to their mechanical properties (www.genialab.com); a more detailed physical–chemical characterisation is needed. Additionally, techniques involving immobilisation into capsules with semipermeable membranes have been developed in parallel with the above-mentioned entrapment techniques. The dramatic improvement of the encapsulation protocol has been achieved via the development of a multiloop reactor for a continuous encapsulation procedure based on the polyelectrolyte complexation of sodium alginate and cellulose sulphate as polyanions, poly(methylene-co-guanidine) as a polycation, $CaCl_2$ as a gelling agent and NaCl as an antigelling agent [6, 7]. The reactor [8] enabled the laboratory production of uniform polyelectrolyte complex (PEC) microcapsules with a controlled shape and size, as well as a controlled membrane thickness, permeability and mechanical resistance [9]. The characterisation and control of the newer PEC microcapsule properties, including the inner structure and surface properties [10], was inevitable to determine the proper function and predictability of PEC microcapsule behaviour in important applications such as the immunoisolation of Langerhans islets for the treatment of

diabetes [11] and the stabilisation and reuse of enzymes and bacterial cells as biocatalysts [12–14].

Based on the above-mentioned characteristics, gel entrapment and encapsulation may be considered as representative for the immobilisation of whole cells. The biotechnological applications of gel entrapment and encapsulation are well documented [1]. Interestingly, however, the characterisation of immobilisation techniques, including PEC microcapsules and PVA particles, has been performed mainly via a trial-and-error approach, and a systematic comparison based on the physical–chemical parameters of the immobilisates prepared by these techniques is still lacking. This evolution in research is supported by the observation that the comparison of immobilisation devices, which enabled the development of entrapment techniques more than 20 years ago, occurred much later [15]. This delay is also true for the techniques and parameters recommended for the characterisation of capsules and beads applied in biotechnology and medicine, published in 2009 [16]. Additionally, despite the wide range of applications of immobilisation techniques developed in the 1980s, additional fundamental research into the behaviour of immobilised microbes was introduced relatively recently [17].

Recently, significant improvements have been achieved with the encapsulation of recombinant Escherichia coli cells overproducing enzymes from the group of Baeyer–Villiger monooxygenases (BVMOs) within PEC microcapsules, including increased cell storage stability [18], increased operational stability [14] and preserved cell viability [19]. The present increased interest in research on BVMOs may provide fundamental insights into the molecular mechanisms of catalysis mediated by BVMOs [20] and by the successful construction of novel amperometric biosensors to monitor the Baeyer–Villiger (BV) biooxidation [21]. BVMOs are also attractive for industrial applications as they catalyse the enantioselective BV biooxidation of cyclic ketones to corresponding lactones as chiral precursors of natural and bioactive compounds [22–24]. Therefore, BVMOs are undoubtedly suitable for immobilisation in industrially relevant LentiKats® PVA gel particles [25], and the industrial-scale production of these particles has already been applied in several processes (www.lentikats.eu).

Themain objective of this study is, in conjunction with our previous results [1, 25], to compare and characterise LentiKats® PVAparticles and PECmicrocapsules for immobilisation of the same biocatalytic system. Recombinant E. coli-overproducing cyclopentanone monooxygenase (CPMO) was used as a model biocatalyst for entrapment in LentiKats® and encapsulation into PEC microcapsules. The enantioselective BV biooxidation of (±)-cis-bicyclo[3.2.0] hept-2-en-6- one to the corresponding lactones (1R, 5S)-3-oxabicyclo [3.3.0] oct-

6-en-2-one and (1S, 5R)-3- oxabicyclo [3.3.0] oct-6-en-2-one [25] was chosen as a model biotransformation. The size distribution analysis of LentiKats® and PEC microcapsules, visualisation of their inner structure, determination of their mechanical stability and molecular weight cut-off, mathematical modelling of mass transfer, and determination of the diffusion coefficients were performed. Complementary morphological characterisation of LentiKats® and PEC microcapsule surfaces was performed by environmental scanning electron microscope (ESEM). The operational stability of cells immobilised in LentiKats® and PEC microcapsules was also investigated.

Material and Methods

Material

High-viscosity, high-mannuronic- acid sodium alginate from ISP Alginates (Girvan, UK) and cellulose sulphate sodium salt from Acros Organics (New Jersey, USA) were used in the PEC microcapsule preparation. The poly (methylene-co-guanidine hydrochloride) from Scientific Polymer Products Inc. (Ontario, USA), supplied as a 35 % (w/v) aqueous solution, was lyophilised prior to use. LentiKats® were prepared at a large scale by LentiKats (Stráž pod Ralskem, Czech Republic). (±)-Cis-bicyclo [3.2.0] hept-2-en-6-one was from Fluka (Sigma Aldrich), (1R, 5S)-3-oxabicyclo [3.3.0] oct-6-en-2-one from Fluka and (1S, 5R)-3-oxabicyclo [3.3.0] oct-6-en-2-one from Aldrich. The LBamp agar medium consisted of (grams per liter): agar 15, peptone 10, yeast extract 5, NaCl 10 and ampicillin 0.2. The LBamp medium for cell growth consisted of (grams per liter): peptone 10, yeast extract 5, NaCl 10 and ampicillin 0.2. The TB_{amp} medium consisted of (grams per liter): tryptone 12, yeast extract 24, glycerol 5, $K_2HPO_4.3H_2O$ 16.4, KH_2PO_4 2.3 and ampicillin 0.2.

Cultivation of Cells

Glycerol stocks of recombinant E. coli BL21(DE3) with pET22b+overexpressing cyclopentanone monooxygenase (EC 1.14.13.16) from Comamonas sp. NCIMB 9872 were stored at −80 °C. The cells were streaked on an LBamp agar Petri dish and grown overnight at 37 °C.

Propagation of Cells for Encapsulation

A single colony from the Petri dish was inoculated into 10 mL liquid LB_{amp} medium and cultivated for 12 h at 37 °C on a rotary shaker at 200 rpm. The inoculum was pipetted into TB_{amp} media (1 % [v/v]) and grown at 37 °C and 200 rpm until reaching an OD_{620} of 0.6. Induction was performed by the addition of isopropyl β-

D-1-thiogalactopyranoside (IPTG) to a final concentration of 0.25 mM for 2 h at 30 °C and 180 rpm. The centrifuged biomass was suspended in polyanion solution (2 % [w/v] of dry cell weight) and used for encapsulation.

Propagation of Cells for Immobilisation in LentiKats®

E. coli was cultivated as described previously [25]. After 20 h of cultivation, IPTG (0.25 mM) was used for enzyme induction. Then, 950 mL of biomass (0.99 g of dry cell weight) was harvested (2,750 g, 4 °C, 30 min), resuspended in 6 mL of distilled water and the centrifuged cells were used for entrapment. To obtain a high concentration of cells within the immobilisates, three successive 12-h cultivations of LentiKats® were performed in LB_{amp} media at 37 °C and 200 rpm. During the fourth batch, the induction by the addition of IPTG to a final concentration of 0.25 mM and incubation for 2 h at 30 °C and 180 rpm were performed.

Immobilisation Procedures

Encapsulation

PEC microcapsules were created as described in previous work with1-min polycomplexation [12]. PEC microcapsules without cells were used for the physical characterisation. PEC microcapsules containing cells were prepared with 2 % (w/v) dry cell weight suspended in the polyanion solution.

Laboratory LentiKats® Preparation

PVA particles containing cells were prepared using the LentiKat Printer® (www.lentikats.eu). Four grams of polyvinyl alcohol and 2.4 g of polyethylene glycol were melted in distilled water (27.6 mL) and cooled to 40 °C, and the concentrated biomass (6 mL) was added. Particles were dried in an airflow cabinet and re-swelled in the stabilising solution (0.1 M Na_2SO_4). Five grams of particles were propagated in 25 mL of LB medium (100 mL Erlenmeyer flask, 37 °C, 200 rpm, ampicillin 50 mg L^{-1}) for three repeated batches (max. 12 h each). After 2 h of cultivation of the fourth repeated batch, IPTG (0.25 mM) was used for enzyme induction (30 °C, 180 rpm, 2 h).

Large-Scale LentiKats® Preparation

PVA particles without immobilised biomass were prepared at a large scale by LentiKats (Czech Republic) (www.lentikats.eu).

Determination of Particle Size Distribution

Measurements of the PEC microcapsule diameter and membrane thickness were performed with a LM6-3 optical microscope (Kvant, Slovakia) [12]. LentiKats® diameter was measured with a STM 723 stereomicroscope (Kvant, Slovakia) supplied with an Olympus C-4000 ZOOM digital camera (Tokyo, Japan) connected to a PC operating with Impor 5.0 Professional Image Analysis software (Kvant, Bratislava, Slovakia) and Cam2Com Version 2.0.0.22 software. The average diameter and standard deviation were obtained by the analysis of 50 randomly selected particles.

Microscopic Investigation of the Inner Structure

LentiKats® and PEC microcapsules were stained for at least 24 h using the fluorescent dye trisodium 8-hydroxypyrene-1.3.6-trisulfonate (pyranine) (Invitrogen Molecular Probes, 0.1 mM). Pyranine was recommended through personal communication with Dr. R. Stloukal from LentiKats, Czech Republic [26]. The samples were incubated in a 10^{-1} mM solution of pyranine for at least 24 h, removed and washed in a 0.9 % NaCl solution. For imaging in transmission and fluorescence contrast modes, a confocal laser scanning head (LSM 510 META NLO) coupled to the Axiovert 200 M inverted microscope stand (both Zeiss, Germany) was used. Zeiss PlanNeofluar ×2.5/0.075 and PlanApochromat ×10/0.45 lenses were used to visualise whole PEC microcapsules and LentiKats®, and Zeiss PlanApochromat ×20/0.75 and a C-Apochromat ×40/1.2 W water immersion objective were used to visualise the details of their inner structure. Pyranine fluorescence was excited by a 488-nm line from an argon ion laser, and transmission was imaged simultaneously using the same laser. For fluorescence detection, the 488-nm dichroic filter and a BP 500–550-nm band-pass emission filter were used.

Owing to the necessity of advanced surface characterisation of samples with higher resolution and large depth of field, both types of matrices were investigated using non-commercial experimental ESEM AQUASEM II developed by the group of Environmental Electron Microscopy (ISI ASCR in Brno, Czech Republic) in cooperation with Tescan Company. In view of the fact that matrices are very sensitive to electron beam, they must be observed in fully wet and native state. Due to the relatively big size of samples, a combination of two newly published methods [27, 28] and special improvement of detector were used. The gentle and slow sample chamber pumping procedure, an ionisation detector of secondary electrons [29] (beam current up to 40 pA) enhanced for larger field of view (850 μm) and our observation protocol for reduced sample temperatures (1 °C and 750 Pa of water vapours for PEC; −20 °C and 540 Pa of air for LentiKats®) were combined. Samples were incubated in 0.9 % NaCl solution for a time of transport, removed

and observed in small droplet (approximately 10 ml) of distilled water. Both types of matrices were observed at beam accelerating voltage 20 kV and a sample to second pressure limiting aperture distance 4 mm. For thermodynamic equilibrium adjustment control, Pfeiffer pressure gauges CMR 261 and CMR 263, a custom build Peltier stage and a hydration system were used.

Mechanical Strength Measurement

The mechanical properties of the LentiKats® and PEC microcapsules were determined in compression mode using the Texture Analyser TA-XT2i (Stable Micro Systems, Godalming, UK) equipped with a mobile probe and Texture Expert Exceed 2.64 software. Compression measurements were conducted for up to 95 % of LentiKats® and PEC microcapsule deformation at a compression speed of 0.5 mm s^{-1} on 50 LentiKats® and 50 PEC microcapsules per batch. The compression data were also used for the determination of the LentiKats® height from the first non-zero value of recorded force. The results are represented by the bursting force for the PEC microcapsules and the force required to deform LentiKats® by 70 % of their height.

Inverse Size Exclusion Chromatography (iSEC)

The molecular weight cut-off (MWCO) determination of LentiKats® and PEC microcapsules was performed using inverse size exclusion chromatography (iSEC). Briefly, 10 mL of a packed volume of either analysed LentiKats® or PEC microcapsules was placed on a glass Omnifit chromatographic column of 10×150 mm (Omnifit, Cambridge, UK). Pullulan/dextran standards (Polymer Laboratories, American Polymer Standard Corp. and Polysciences) and protein standards (HMW kit from Sigma Aldrich, LMW kit from GE Healthcare) were injected into the column at a concentration of 3 mg mL^{-1} for the polysaccharide standards and a few milligrams per milliliter for the protein standards, following the recommendation from the producers, via the 100 μL loop injector using 50 mM phosphate buffer (pH~7) as the mobile phase applied at a 0.2 mL min^{-1} flow rate. The elution volume for each standard was determined as the volume at which 50 % of the standard was eluted. This quantity was used to determine the chromatographic partition coefficients providing the MWCO of column packing in the form of the molecular weight and viscosity radius R_η as described elsewhere [30, 31]. The Waters SEC setup was equipped with a Waters 2410 refractive index detector. WinGPC 7.2 software (Polymer Standard Service, Mainz, Germany) was used for data acquisition and evaluation.

Mathematical Modelling of the Mass Transfer Governing iSEC

The mathematical modelling of the iSEC results for sucrose was based on the linear driving force chromatography model [32]. This model assumes that, for a linear adsorption isotherm, a chromatographic peak broadening caused by the effects of axial dispersion, liquid-film and particle mass transfer can be represented by a single model parameter, the apparent diffusion coefficient D_{La}:

$$\varepsilon \frac{\partial c_s}{\partial t} + (1-\varepsilon) K_{SEC} \frac{\partial c_s}{\partial t} = -u\varepsilon \frac{\partial C_5}{\partial z} + \varepsilon D_{La} \frac{\partial^2 c_s}{\partial z^2} \quad (1)$$

$$t = 0 \quad 0 \le z \le L \quad c_S = 0 \quad (2)$$

$$t > o \quad z = 0 \quad u(C_s - C_{s0}) = D_{La} \frac{\partial c_s}{\partial z} \quad (3)$$

$$z = L \quad \frac{\partial c_s}{\partial z} = 0 \quad (4)$$

where ε is the bed void fraction, cs is the solute (sucrose) concentration in the mobile phase, t is time, K_{SEC} is the sucrose partition coefficient determined by iSEC, z is the axial coordinate, $u = \frac{4V}{\pi d^2 \varepsilon}$ is the mobile phase interstitial velocity, V ̇= 0:2 mL min^{-1} is the volume flow rate, and d=10 mm is the column diameter. The Van Deemter theory permits the exact quantification of the axial dispersion and mass transfer contributions to the total dispersion effect through the height equivalent to a theoretical plate HETP (see Supplementary data) [33]. The commercial process engineering software Athena Visual Workbench (Stewart & Associates Engineering Software, Madison, WI; www.athenavisual.com) was used for the modelling [34].

Investigation of Baeyer–Villiger Biooxidation

A total of 0.5 g of wet cell weight (0.1 g dry mass) or 5 g of immobilisates containing cells was added to 25 mL of biotransformation medium (50 mM phosphate buffer and 4 g L^{-1} glucose, pH 7). Biooxidation was initialised by the addition of the substrate (±)-cis-bicyclo[3.2.0] hept- 2-en-6-one (1:2, v/v in ethanol) to 0.5 g L−1 at 175 rpm and 25 °C. After the conversion reached 100 %, the centrifuged cells and immobilisates were washed with phosphate buffer and stored in the refrigerator (4 °C) overnight in biotransformation medium. One biotransformation was performed each day. The withdrawn samples were analysed via gas chromatography.

Cell Viability Measurement

Cell viability measurements were described elsewhere [19].

Gas Chromatography

The concentrations of substrates and products during bioconversion with PEC microcapsules and free cells were measured by Trace GC Ultra and ITQ 900 MS from Thermo Scientific using an Rt®-2330NB column (105 m, 0.32 mm ID, 0.10 μm df), Restek. Prior to analysis, samples of medium from the biotransformation were extracted with dichloromethane (1:1, v/v) containing 0.5 mg mL^{-1} methyl benzoate as an internal standard. As the carrier gas, helium was used at flow of 1 mL min^{-1}. The injector operated at 200 °C in splitless mode with a split flow of 50 mL min^{-1}. The column temperature program was set as follows—isotherm at 80 °C for 10 min, subsequent heating to 200 °C at a rate of 5 °C min^{-1} and isotherm at 200 °C for 20 min. The MS transfer line temperature was 200 °C. The bioconversion with LentiKats® was analysed via GC as reported previously [25].

Results and Discussion

Particle Size Distribution

Particle size distribution is a parameter that determines immobilisate uniformity and the reproducibility of the preparation. Additionally, the size of the immobilisate is one of essential parameters influencing its mass transfer properties. Finding a compromise between the sizes of the immobilised cell particles so they are large enough to be easily filtered from the reaction media but still small enough to preserve suitable diffusion properties is important. Images of PEC microcapsules and LentiKats® from microscopes are shown in the supplement [Fig. S1]. The measured diameter of the spherical PEC microcapsule d_{PEC}=0.82 mm (RSD=5.6 %) is smaller than that of the LentiKats® circular base d_{LK}=3.65 mm (RSD=10.3 %). LentiKats® are lens-shaped, and their height is 0.341 mm (RSD=32.3 %) (texture analyser result). Based on Fig. 1, the PEC microcapsules are more uniform in diameter, and also, their circular shape is more regular than LentiKats® (see Fig. 2c) which have a broader diameter distribution. PEC microcapsules are more uniform in diameter than LentiKats®, which have a broader diameter distribution. This difference might be due to the different preparation techniques. PEC microcapsules were prepared via a laboratory encapsulation device that allows the reproducible formation of uniform microcapsules, whereas the process of large-scale production of LentiKats® is not able to provide sufficiently uniform particles.

Inner Structure

PEC microcapsules consist of a polymeric membrane (0.09 mm, RSD=5.0 %) that is strongly stained with pyranine and a liquid core-free from a fluorescent signal (Fig. 1). The highest fluorescence intensity is localised in the outer part of the PEC microcapsule membrane (approx. 0.04 mm). Because pyranine is anionic, we assume a residual positive charge in this area, which is in accordance with previously reported data [10]. Well visible surface microstructure of the PEC microcapsule was characterised also using a specially designed ionisation detector for ESEM capable to record low-energy secondary electrons, typically emitted from ones to tens of nanometres thick surface layer. Figure 1c shows relatively smooth and clean surface of the PEC microcapsule with very good plasticity and with very low amount of defects, visible as small outgrowth on the surface. PEC microcapsule surface waviness was induced as a consequence of the small controlled decrease of the relative humidity in the sample vicinity, highlighted by white arrow in Fig. 1c. The right part region below the top of the sphere is fully hydrated and relatively smooth. On the contrary, natural surface roughness of the PEC microcapsule is expectable and resulted from the process of sample formation (see Fig. 1c, structure insight white square).

Interestingly, the structure of the LentiKats® surface membrane (Fig. 2a) is optically unresolvable (most likely due to very small pores). The interior of LentiKats® featured a sponge-like structure with pores at the micrometre scale (Fig. 2b, detail on Fig. S2). Those pores most likely serve as a space for colony-forming microorganisms under growing conditions [26]. Interestingly, these sponge-like pores were practically inaccessible to polyethylene glycol (PEG) solutes greater than 8,000 Da as confirmed by batch sorption experiments (data not shown) using PEGs of molar mass between 300 and 12,000 Da, indicating that they are not open toward the surrounding environment. This finding corresponds to the results obtained by iSEC introduced below. The above-mentioned findings were independently proven also by direct observation of LentiKats® surface using the ESEM. In view of the previous results, the thin nano-layer closing the pores was mechanically violated, and pores were studied using the ESEM. Figure 3a shows upper and lower parts of surface of two LentiKats® suitably situated and observed in the mutually closed position. The lower LentiKats® shows complicated surface with many small pores approximately 4 μm in diameter. The surface of the upper LentiKats® is smooth and free of micrometric pores with typical uneven edge. Figure 3b shows the lower part of surface free of mechanical stress documenting closed pores corresponding with results of fluorescence microscopy and iSEC.

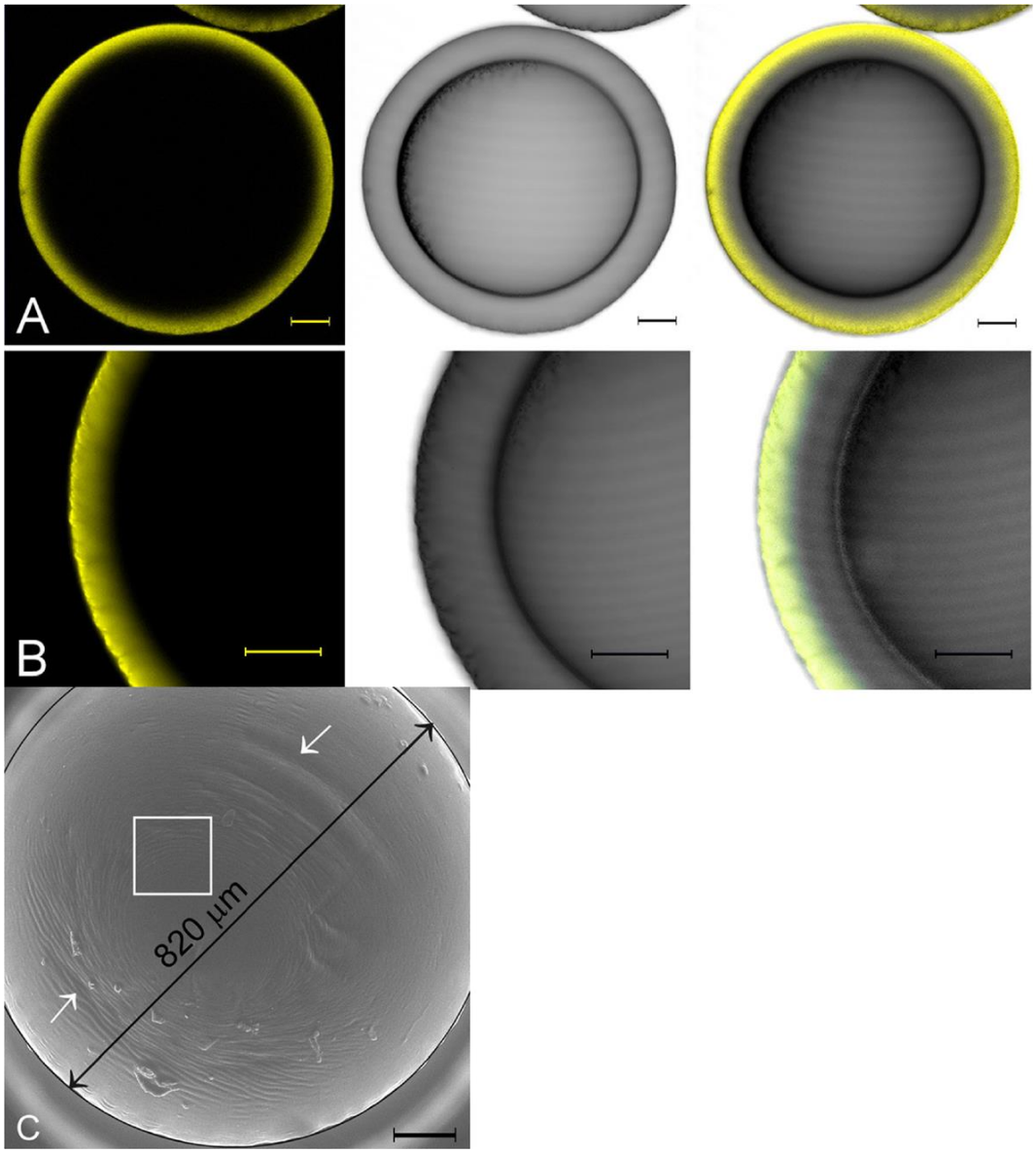

Fig. 1 a Whole PEC microcapsule structure visualised with pyranine via confocal laser scanning microscopy fluorescence in the transmission and combined modes, respectively. b Membrane detail. c The PEC microscapsule imaged by ESEM with highlighted circularity and diameter measurement (black line), surface waviness due to sample dehydration (white arrow) and natural surface roughness (white square). The scale bar indicates 100 µm

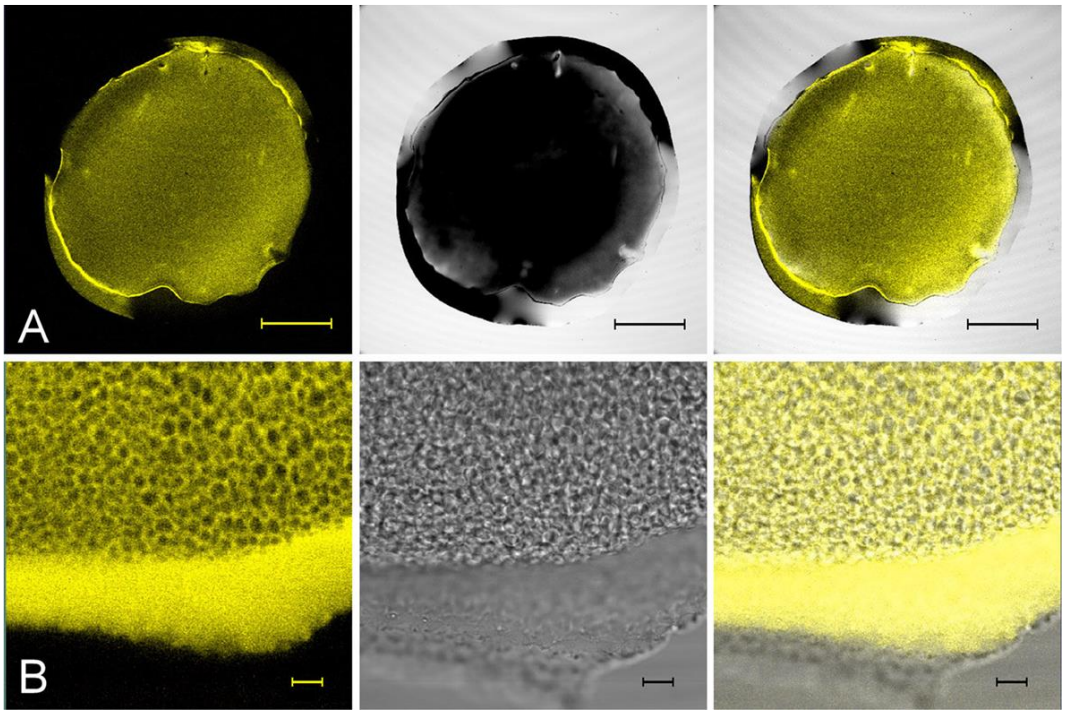

Fig. 2 a Whole LentiKats® structure visualised with pyranine via confocal laser scanning microscopy in the combined fluorescence and transmission mode. The scale bar indicates 1 mm. b LentiKats® detail. The scale bar indicates 10 μm

Mechanical Strength

The average force needed to deform LentiKats® by 70 % was 217.1 g/LentiKats® (RSD= 39 %) and to burst PEC microcapsules, 3.2 g/microcapsule (RSD=19 %). Because of their mechanical robustness, LentiKats® are designed to be used in stirred bioreactors in batch [35] or continuous mode [4]. For the large-scale use of PEC microcapsules, the bioreactor has to be capable of mixing with low shear stress, since microcapsules are fragile when intensive mixing is applied. In our previous papers, PEC microcapsules were successfully used in a small calorimetric packed-bed reactor [14] and in a reactor mildly agitated by air using a ceramic air stone as a bubble sparger [13].

Pore Size Distribution

For the determination of the diffusion and permeability properties of hydrogels, two factors are of main interest: the solute diffusion rate and the particle size exclusion properties [16].

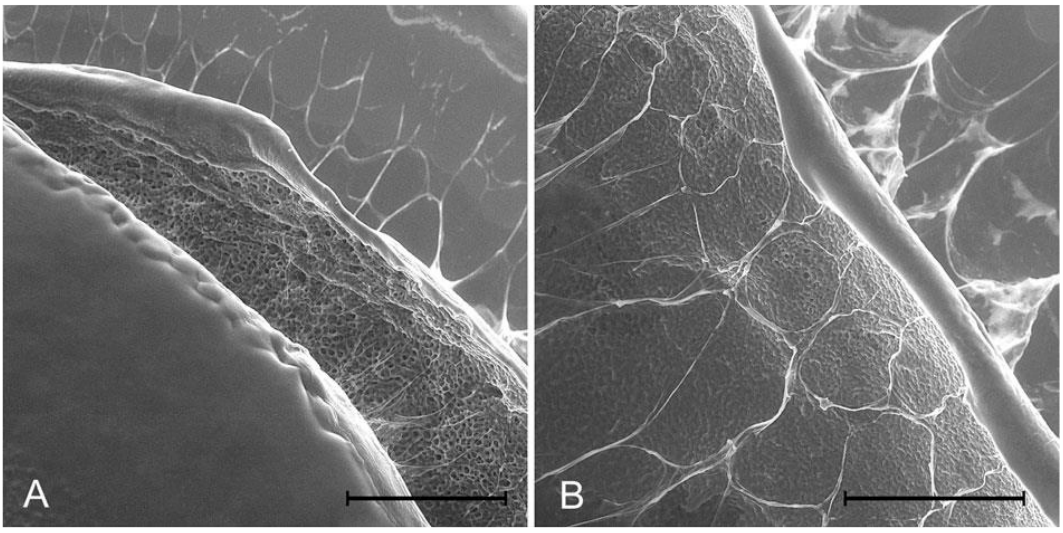

Fig. 3 a ESEM image of two LentiKats® surfaces, pores are open after the mechanical stress. b The nonaffected sponge-like structure with closed pores. The scale bar indicates 200 μm

Polysaccharide elution chromatograms (Fig. S3 supplement) are broad, which is in agreement with previously reported results [30]. This observation is likely connected to the large sizes of the solute molecule (e.g., slower movement of large molecules in stagnant liquid phase) and is partly caused by the polydispersity of dextran and pullulan standards. However, elution chromatograms are also broad for monodisperse protein standards, which indicates that the peak broadening may be likewise caused by low column efficiency resulting from axial and radial dispersion effects. The protein and polysaccharide calibrations of the column packed with PEC microcapsules or LentiKats® are shown in the form of $(1-K_{SEC})=f(M)$ in Fig. 4. The differential distributions, obtained as the first derivative of the calibration curve providing the information on the pore size distributions [9] are depicted as insets in Fig. 4. The data show that the protein differential distributions are narrower than the polysaccharide differential distributions. Furthermore, the differential distributions obtained for the PEC microcapsules are narrower than those of LentiKats®. This observation indicates that the PEC microcapsule membrane pores are more uniform in size. Table 1 contains the evaluated MWCO values from the iSEC analysis (Fig. 4) using either polysaccharide or protein standards and the evaluated values of the viscosity radii. In the case of LentiKats®, the MWCO for the protein standards is approximately twofold higher than for the polysaccharide standards. Considering that the polyvinyl alcohol matrix of LentiKats® has a non-ionic characteristic without strong interactions with either of the used standards, this result is understandable and reflects the globular conformation of the proteins and the statistical coil conformation of the pullulans. Hence, the MWCO based on proteins and polysaccharides equal to 14,200 Da and 7,600 Da, respectively, provides the same value for the viscosity radius of ~2.0 nm, which characterises

the exclusion limit of this material. In contrast, the MWCO value for PEC microcapsules determined by both types of standards is approximately the same and equals∼40,000 Da. The different viscosity radii of polysaccharides (5.4 nm) and proteins (2.8 nm) may be assumed to be caused by electrostatic interactions between proteins and the residual charge of the PEC microcapsule membrane. Therefore, in the case of PEC microcapsules, the data obtained via non-interacting polysaccharide standards are considered representative for the adequate characterisation of pore size for this type of material. In summary, PEC microcapsules are more permeable than the batch of LentiKats® tested in this experiment. Taking into account the objective of a whole-cell Baeyer–Villiger monooxygenase immobilisation, both matrices are suitable. In case of the need of enzyme immobilisation, there is a possibility to modify both matrices, so the pores are small enough to not permit the leakage of the enzyme (www.genialab.com) [13]. Subsequently, the permeability as well as pore diameter would be decreased.

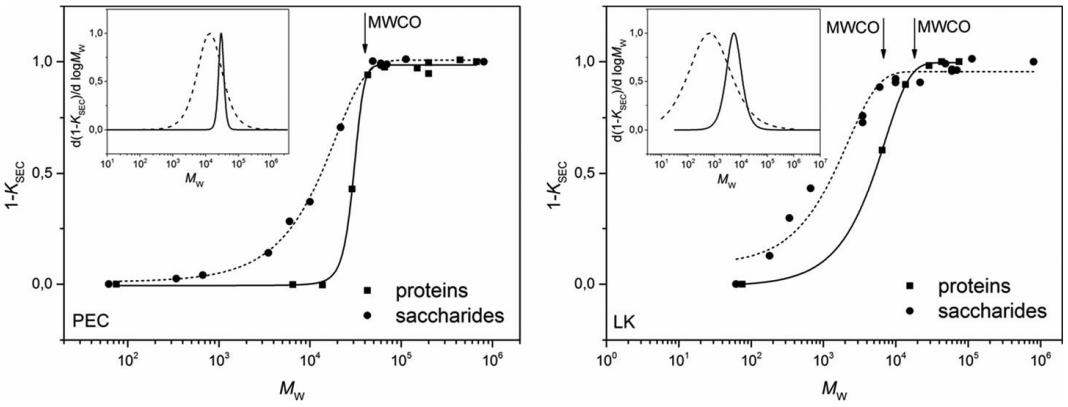

Fig. 4 PEC microcapsules and LentiKats® iSEC experimental results are scattered as closed square for protein and closed circle for saccharide calibration. The data are fitted with the Boltzmann function, with its first derivative providing the pore size distribution [9] determined with black line protein and broken line polysaccharide calibration (data in the inset graph)

Table 1 Experimentally determined MWCO and Rη values of PEC microcapsules and LentiKats® based on iSEC data

	Calibration standards	MWCO [Da]	R_η [nm]
PEC microcapsules	Polysaccharides	44,700	5.42
	Proteins	38,000	2.75
LentiKats®	Polysaccharides	7,600	2.04
	Proteins	14,200	1.89

Particle Mass Transfer Characteristics

The experimental and model iSEC elution chromatograms of sucrose are in good agreement [supplementary data Fig. S4]. The HETP values obtained by the modelling were 0.76 cm for the PEC microcapsules and 3.13 cm for the LentiKats® (Table 2). Table 2 also presents the transport parameters, D_L and k_L, calculated from the correlation equations specified in the supplementary data [36, 37]. Using these three parameters and the van Deemter [33] and Glueckauf [38] equations, the effective diffusion coefficient De of sucrose was evaluated. Table 2 also compares the De values with the diffusion coefficient of sucrose in water, $D=4.6\times 10^{-10}$ m^2 s^{-1} [39]. The De for the PEC microcapsules was 36 % of D, whereas that for LentiKats® was only 8 % of D (Table 2).

These experimentally determined values of the D_e/D ratio were compared with the values obtained from a predictive equation (Eq. 9 in Supplementary Data) that requires knowledge of the particle porosity, tortuosity and pore hindrance factor. The particle porosity was approximated by the sucrose K_{SEC} values 0.975 for the PEC microcapsules and 0.703 for LentiKats® (iSEC results). The particle tortuosity, 1.01 for the PEC microcapsules and 1.17 for LentiKats®, was calculated from the corresponding porosity using an equation proposed by Barrande et al. [40], which was verified for a number of gel materials. Finally, the pore hindrance factor was obtained from the Renkin equation [41]. This equation has a single parameter that is the ratio of the solute hydrodynamic radius and pore radius. The latter radius was represented by the viscosity radius of polysaccharides from Table 1.

Table 2 presents the predicted values of the D_e/D ratio, which were 0.65 for the PEC microcapsules and 0.20 for LentiKats®. The predicted values were approximately twice as high as the experimental values of this ratio. Nonetheless, the experimental and predicted values confirmed a relatively low effective diffusivity of sucrose for both gel-type materials. These observations are, however, consistent with the heterogeneous nature of the structure of both materials described

above. The overall mass transfer rate can be expected to be controlled by the dense shell layer in the case of the PEC microcapsules and by the intrinsic polymer network of LentiKats®. The porosity of these substructures is lower than the mean particle porosity estimated from the distribution coefficient, which includes the contribution of the dilute core of PEC microcapsules or micrometre-scale pores of LentiKats®. This finding also implies that the true tortuosity values for these substructures could be higher than the calculated ones for the entire particle. Both these effects indicate that the predicted D_e/D values should be lower than those given in Table 2.

Another source of the uncertainty of the predictive equation is the assumption of the pore cylindrical shape in the Renkin equation. With respect to the experimental D_e values, the main uncertainties represent the use of the half height of lens-shaped particles as their single characteristic dimension, especially for the estimation of DL, and the accuracy of the D_L and k_L predictions for the relatively small column used in the iSEC experiments. Despite these issues, the experimental D_e values represent a good basis for the assessment of the effect of mass transfer on the overall rate of biotransformation processes.

Biocatalytic Properties of Immobilised Cells

The comparison of the two immobilisation methods was focused not only on the physical parameters but also on the biocatalytic efficiency. The model of BV biotransformation using E. coli-overexpressing CPMO was chosen. In Fig. 5, the conversion of CBCH in the second hour for each of 18 cycles is shown for free cells, PEC microcapsules and LentiKats®. During the first 8 days, the reaction performed by the free cells was slower. We believe the reason for this slowness involves oxygen transport. As removing samples also involves the removal of cells, the reaction was started in a 250-mL flask with 70 mL of biotransformation media, whereas the PEC microcapsules and LentiKats® were placed in 100-mL flasks with 25 mL of biotransformation media. Each new cycle with free cells was initiated by reducing the media volume by the volume of the removed samples. These changes could increase the oxygen transfer rate and increase the reaction rate. In the 18^{th} cycle, the free cells were suspended in 25 mL of media in a 100-mL flask to ensure that the concentration of cells and all the conditions were the same as those for the PEC microcapsules and LentiKats®. The progress of the reaction under these conditions was the same for all three systems tested. The reaction was complete in 2 h. Confocal laser scanning microscopy viability measurements of the cells showed that the viability of free cells was 98 % after 18 cycles and that the viability of cells encapsulated in PEC was 95 %. The viability of cells entrapped in LentiKats® was not tested because a sufficient number of cells could not be washed

out of the intact LentiKats® matrix and melting the PVA would cause cell death. However, the high viability of free and encapsulated cells suggests that more than 18 cycles could be performed.

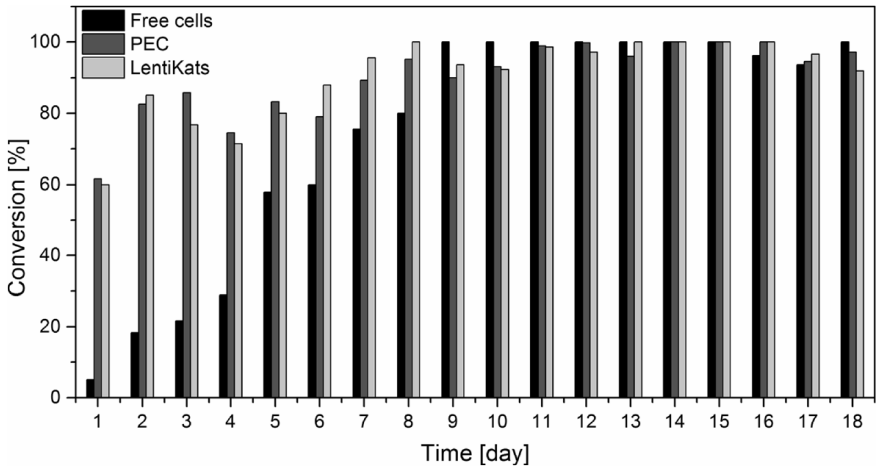

Fig. 5 Evolution of substrate CBCH (0.5 g L−1) conversion during 18 repeated biooxidations performed with 0.5 g of free cells (20 % dry cell weight), 5 g of PEC microcapsules and 5 g of LentiKats® at 25 °C and 175 rpm. The conversion during the second hour of the reaction is compared

Conclusion

In this paper, we report the characterisation and comparison of two methods of immobilisation: entrapment into polyvinyl alcohol lens-shaped LentiKats® and encapsulation in polyelectrolyte complex microcapsules composed of sodium alginate, cellulose sulphate and poly(methylene-co-guanidine). Both types of immobilisation matrices were fluorescently stained with pyranine. Confocal laser scanning microscopy revealed that the polyelectrolyte complex microcapsule membrane has a residual positive charge in the outer layer. Thus, polysaccharide standards are more representative in the inverse size exclusion measurements of the pore size distribution than proteins evincing electrostatic interactions. The advanced morphological characterisation of LentiKats® by ESEM prove the inner sponge-like structure with micrometre dimensions serving as spaces for cell propagation under growth conditions. Testing the mechanical strength with the texture analyser device encourages the use of robust LentiKats® in stirred bioreactors, and the more fragile polyelectrolyte complex microcapsules should be protected from shear stress. Measuring the particle size distribution using microscopy methods and the pore size distribution using inverse size exclusion chromatography provided the values needed to model the effective diffusion coefficient of sucrose for the polyelectrolyte complex microcapsules and LentiKats®. The experimental and predicted values were compared, and a relatively low effective diffusivity for both matrices was confirmed. However, each

system has its good and bad points; both immobilisation matrices proved to be suitable for the selected bioengineering model. Enclosed recombinant E. coli - overexpressing cyclopentanone monooxygenase underwent 18 successive Baeyer– Villiger biotransformations without a loss of efficiency. We believe that this article represents a step forward to address the missing features in the physical and biocatalytic characterisation of polyelectrolyte complex microcapsules and LentiKats®. At this stage of the research, it is clear that highly defined polyelectrolyte complex microcapsules are suitable as standard for laboratory investigation of encapsulated biocatalysts with the challenging tasks of production upscale and cost reduction. On the other hand, LentiKats® is undoubtedly an appropriate matrix for applications of immobilised biocatalysts including whole-cell Baeyer– Villiger monooxygenases for production of valuable chiral synthons.

Acknowledgements

This work was supported by the Slovak Grant Agency for Science VEGA 1/0229/12, by the Slovak Research and Development Agency under contract No. APVV-0302-10 and No. APVV-0486-10 as well as Grant Agency of the Czech Republic GA14-22777S. We thank Prof. Marko D. Mihovilovic (VUT, Vienna, Austria) for providing the expression strain E. coli-overexpressing CPMO and Dr. Radek Stloukal from LentiKats (Czech Republic) for personal communication.

References

1. Bučko, M., Mislovičová, D., Nahálka, J., Vikartovská, A., Šefčovičová, J., Katrlík, J., Tkáč, J.,Gemeiner, P., Lacík, I., Štefuca, V., Polakovič, M., Rosenberg, M., Rebroš, M., Šmogrovičová, D., & Švitel, J. (2012). Chemical Papers, 66, 983–998. doi:10.2478/s11696-012-0226-3.

2. Gerbsch, N., & Buchholz, R. (1995). FEMS Microbiology Reviews, 16, 259–269. doi:10.1111/j.1574-6976. 1995.tb00173.x.

3. Jekel, M., Buhr, A., Willke, T., & Vorlop, K. D. (1998). Chemical Engineering & Technology, 21, 275–278.

4. Rebroš, M., Rosenberg, M., Grosová, Z., Krištofíková, L., Paluch, M., & Sipöcz, M. (2009). Applied Biochemistry and Biotechnology, 158, 561–70.

5. Trögl, J., Krhůtková, O., Pilařová, V., Dáňová, P., Holíček, R., Kohlová, M., Hejda, S., Smrčka, J., Boušková, A., & Křiklavová, L. (2012). International Journal of Environmental Science and Technology, 9, 425–432. doi:10.1007/s13762-012-0048-4.

6. Lacík, I., Briššová, M., Anilkumar, A. V., Powers, A. C., & Wang, T. G. (1998). Journal of Biomedical Materials Research, 39, 52–60. doi:10.1002/(SICI)1097-4636(199801)39:1<52::AID-JBM7>3.0.CO;2-H.

7. Lacík, I. (2006). Australian Journal of Chemistry, 59, 508–524. doi:10.1071/CH06197.

8. Anilkumar, A. V., Lacík, I., & Wang, T. G. (2001). Biotechnology and Bioengineering, 75, 581–589. doi:10. 1002/bit.10077.

9. Briššová, M., Lacík, I., Powers, A. C., Anilkumar, A. V., & Wang, T. J. (1998). Biomedical Materials Research, 39, 61–70. doi:10.1002/(SICI)1097-4636(199801)39:1<61::AID-JBM8>3.0.CO;2-G.

10. Podskočová, J., Chorvát, D., Kolláriková, G., & Lacík, I. (2005). Laser Physics, 15, 545–551.

11. Rokstad, A.M.A., Lacík, I., de Vos, P. and Strand, B.L. (2014) Adv. Drug Del. Rev. 67-68, 111-130. doi:10.1016/j.addr.2013.07.010.

12. Bučko, M., Vikartovská, A., Lacík, I., Kolláriková, G., Gemeiner, P., Pätoprstý, V., & Brygin, M. (2005). Enzyme and Microbial Technology, 36, 118–126. doi:10.1016/j.enzmictec.2004.07.006.

13. Vikartovská, A., Bučko, M., Mislovičová, D., Pätoprstý, V., Lacík, I., & Gemeiner, P. (2007). Enzyme and Microbial Technology, 41, 748–755. doi:10.1016/j.enzmictec.2007.06.010.

14. Bučko, M., Schenkmayerová, A., Gemeiner, P., Vikartovská, A., Mihovilovič, M. D., & Lacík, I. (2011). Enzyme and Microbial Technology, 49, 284–288. doi:10.1016/j.enzmictec.2011.05.013.

15. Prüsse, U., Bilancetti, L., Bučko, M., Bugarski, B., Bukowski, J., Gemeiner, P., Lewińska, D., Manojlovic, V.,Massart, B., Nastruzzi, C., Nedovic, V., Poncelet, D., Siebenhaar, S., Tobler, L., Tosi, A., Vikartovská, A., & Vorlop, K. D. (2008). Chemical Papers, 62, 364–374. doi:10.2478/s11696-008-0035-x.

16. de Vos, P., Bučko, M., Gemeiner, P., Navrátil,M., Svitel, J., Faas,M., Strand, B. L., Skjak-Braek, G.,Morch, Y. A., Vikartovská, A., Lacík, I., Kolláriková, G., Orive, G., Poncelet, D., Pedraz, J. L., & Ansorge-Schumacher, M. B. (2009). Biomaterials, 30, 2559–2570. doi:10.1016/j.biomaterials.2009.01.014.

17. Junter, G. A., & Jouenne, T. (2004). Biotechnology Advances, 22, 633–658. doi:10.1016/j.biotechadv.2004.06.003.

18. Hucík, M., Bučko, M., Gemeiner, P., Stefuca, V., Vikartovská, A.,Mihovilovic,M. D., Rudroff, F., Iqbal, N., Chorvát, D., Jr., & Lacík, I. (2010). Biotechnology Letters, 32, 675–80. doi:10.1007/s10529-010-0203-2.

19. Schenkmayerová, A., Bučko, M., Gemeiner, P., Chorvát, D., Jr., & Lacík, I. (2012). Biotechnology Letters, 34, 309–14. doi:10.1007/s10529-011-0765-7.

20. Bosserman, M. A., Downey, T., Noinaj, N., Buchanan, S. K., & Rohr, J. (2013). ACS Chemical Biology, 8, 2466–2477. doi:10.1021/cb400399b.

21. Schenkmayerová, A., Bučko, M., Gemeiner, P., & Katrlík, J. (2013). Biosensors & Bioelectronics, 50, 235–238. doi:10.1016/j.bios.2013.06.061.

22. de Gonzalo, G., Mihovilovic, M. D., & Fraaije, M. W. (2010). ChemBioChem, 11, 2208–2231. doi:10.1002/cbic.201000395.

23. Leisch, H., Morley, K., & Lau, C. K. (2011). Chemical Reviews, 111, 4165–4222. doi:10.1021/cr1003437.

24. Balke, K., Kadow, M., Mallin, H., Saß, S., & Bornscheuer, U. T. (2012). Organic & Biomolecular Chemistry, 10, 6249–6265. doi:10.1039/C2OB25704A.

25. Rebroš, M., Lipták, L., Rosenberg, M., Bučko, M., & Gemeiner, P. (2014). Letters in Applied Microbiology, 58, 556–563. doi:10.1111/lam.12227.

26. R. Stloukal, Lentikats Czech Republic, personal communication, 2013.

27. Neděla, V., Hřib, J., & Vooková, B. (2012). Biological Plantarum, 56, 595–598. doi:10.1007/s10535-012-0062-x.

28. Tihlaříková, E., Neděla, V., & Shiojiri, M. (2013). Microscopy and Microanalysis, 19, 914–918. doi:10.1017/S1431927613000603.

29. Neděla, V., Konvalina, I., Lencová, B., & Zlámal, J. (2011). Nuclear Instrumentation and Methodology, A 645, 79–83. doi:10.1016/j.nima.2010.12.200.

30. Briššová,M., Petro,M., Lacík, I., Powers, A. C., &Wang, T. (1996). Analytical Biochemistry, 242, 104–111. doi:10.1006/abio.1996.0435.

31. Hoesli, C. A., Kiang, R. L., Mocinecova, D., Speck, M., Moskova, D. J., Donald-Hague, C., Lacík, I., Kieffer, T. J., & Piret, J. M. (2012). Journal of Biomedical Materials Research Part B: Applied Biomaterials, 100, 1017–1028. doi:10.1002/jbm.b.32667.

32. Guiochon, G., Fellinger, A., Shirazi, D. G., & Katti, A. M. (2006). Fundamentals of Preparative and Nonlinear Chromatography (2nd ed.). Amsterdam: Academic.

33. Van Deemter, J. J., & Zuiderweg, F. J. (1956). Chemical Engineering Science, 5, 271–289. doi:10.1016/0009-2509(96)81813-6.

34. Stewart, W. E., Caracotsios, M., & Sørensen, J. P. (1992). AIChEJ, 38, 641–650. doi:10.1002/aic.690380502.

35. Grosová, Z., Rosenberg, M., Gdovin, M., Sláviková, L., & Rebroš, M. (2009). Food Chemistry, 116, 96– 100. doi:10.1016/j.foodchem.2009.02.011.

36. Chung, S. F., &Wen, C. Y. (1968). AIChEJ, 14, 857–866. doi:10.1002/aic.690140608.

37. Wilson, E. J., & Geankoplis, C. J. (1966). Indian Engineering of Chemical Fundamentals, 5, 9–14. doi:10.1021/i160017a002.

38. Glueckauf, E., & Coates, J. I. (1947). Journal of Chemical Society, 1315-1321. doi:10.1039/JR9470001315

39. Dojčanský, J., & Longauer, J. (2000) in Chemical engineering II (in Slovak: Chemické inžinierstvo II), Malé Centrum, Bratislava.

40. Barrande, M., Bouchet, R., & Denoyel, R. (2007). Analytical Chemistry, 79, 9115–9121. doi:10.1021/ ac071377r.

41. Renkin, E. M. (1954). Journal of General Physiology, 38, 225–243.

23 Polyelectrolyte Complex Beads by Novel Two-Step Process for Improved Performance of Viable Whole-Cell Baeyer-Villiger Monoxygenase by Immobilization

Tomáš Krajčovič [1], Marek Bučko [1], Alica Vikartovská [1], Igor Lacík [2], Lucia Uhelská [2], Dušan Chorvát [3], Vilém Neděla [4], Eva Tihlaříková [4], Martin Gericke [5], Thomas Heinze [5] and Peter Gemeiner [1]

1 *Department of Glycobiotechnology, Institute of Chemistry, Slovak Academy of Sciences, Dúbravská cesta 9, SK-845 38 Bratislava, Slovakia;*
2 *Polymer Institute, Slovak Academy of Sciences, Dúbravská cesta 9, SK-845 41 Bratislava, Slovakia;*
3 *Department of Biophotonics, International Laser Centre, Ilkovičova 3, SK-841 04 Bratislava, Slovakia;*
4 *Department of Electron Microscopy, Institute of Scientific Instruments of the ASCR v.v.i., Královopolská 147, CZ-612 64 Brno, Czech Republic;*
5 *Institute of Organic Chemistry and Macromolecular Chemistry, Centre of Excellence for Polysaccharide Research, Friedrich Schiller University of Jena, Humboldtstrasse 10, D-07743 Jena, Germany;*

Keywords

polyelectrolyte complex beads; environmental scanning electron microscopy; confocal laser scanning microscopy; Baeyer-Villiger biooxidation; cyclohexanone monoxygenase; immobilization; viable whole-cell biocatalyst

Abstract

A novel immobilization matrix for the entrapment of viable whole-cell Baeyer–Villiger monooxygenase was developed. Viable recombinant *Escherichia coli* cells overexpressing cyclohexanone monooxygenase were entrapped in polyelectrolyte complex beads prepared by a two-step reaction of oppositely-charged polymers including highly defined cellulose sulphate. Immobilized cells exhibited higher operational stability than free cells during 10 repeated cycles of Baeyer–Villiger biooxidations of rac-bicyclo[3.2.0]hept-2-en-6-one to the corresponding lactones (1*R*,5*S*)-3-oxabicyclo-[3.3.0]oct-6-en-3-one and (1*S*,5*R*)-2-oxabicyclo-[3.3.0]oct-6-en-3-one. The morphology of polyelectrolyte complex beads was characterised by environmental scanning electron microscopy; the spatial distribution of polymers in the beads and cell viability were examined using confocal laser scanning microscopy, and the texture was characterised by the mechanical resistance measurements.

Introduction

The immobilization of viable whole-cell biocatalysts has long been considered an important method for ensuring their recyclability and stabilisation for the development of the industrial production of chemical specialities and chiral drug precursors [1]. In particular, the combination of viable recombinant cells with overproduced enzymes and their immobilization facilitates recyclability and renders possible a continuous bioreactor arrangement with high application potential [2].

One of the validated techniques for immobilizing viable recombinant cells is their encapsulation in polyelectrolyte complex (PEC) capsules, which afforded promising results in the previous development of encapsulated viable whole-cell biocatalysts [3–5]. PEC capsules have been produced by a single-step polyelectrolyte complexation of oppositely-charged polyanion (PA) aqueous solutions consisting of cellulose sulphate (CS), high-viscosity sodium alginate and living bacterial cells with a polycation solution of poly(methylene-co-guanidine) (PMCG), CaCl2 as gelling and NaCl as antigelling agents [6]. PA microdrops have been air-stripped by a coaxial nozzle into a polycation solution flowing in a multiloop chemical reactor for the preparation of spherical and monodispersed PEC capsules [7]. This encapsulation protocol preserved the high viability of the encapsulated recombinant *Escherichia coli* (*E. coli*) cells with overproduced ezymes from the group of Baeyer– Villiger monooxygenases (BVMOs) as well as their long-term storage and operational stability [4,8–10].

The development of encapsulation techniques, including the PEC capsules, has progressed towards a precise and targeted characterisation of the morphology, physicochemical properties of capsules, biocompatibility and their changes over time, using the latest techniques [11,12] for applications in biotechnology and medicine. Additionally, there is also an increased effort to optimise immobilization by predicting and modelling the bioengineering parameters of potential industrial processes [13]. On the other hand, current practice in industrial applications of immobilized biocatalysts [14] does not entail the consistent characterisation of the immobilization procedure and influence over the geometry, size, stability of composition, mechanical and diffusion properties of immobilized cell particles. This could lead to an incomplete knowledge of the immobilization parameters and methods for their control as well as the unsubstantiated exclusion of promising immobilization techniques for industrial use. The current development and production of tailormade CS is crucial for further research into innovative and improved PEC capsules [15]. Parameters such as the origin of cellulose, molecular weight (MW), viscosity and degree of substitution (DS) of the CS significantly

influence the successful formation of PEC capsules. Hence, the selection of commercial, tailor-made CS by the process described in [15], which, to the best of our knowledge, alone meets the latter scientific requirements, is essential for the encapsulation of cells. Although the production of PEC capsules with semipermeable membranes has been useful for the development of viable whole-cell biocatalysts under laboratory conditions, it entails a relatively complex encapsulation procedure and considerable consumption of PMCG and washing solutions using a continuous, one-step protocol. In addition, for more robust uses, PEC capsules with immobilized whole-cell biocatalysts have proved to be fragile during intensive mixing [10], and it was necessary to use fluidised-bed bioreactors [5] or mini packed-bed reactors with a low flow-rate [9]. Hence, it is desirable to develop protocols for the preparation of PEC beads with enhanced mechanical properties, with a lower consumption of PMCG and washing solutions, and with a simpler cation immobilization procedure.

The present work sought to develop PEC beads with entrapped viable cells complexed in the whole volume of the beads. Another aim was the use of imaging techniques to characterise the morphology of PEC beads and cells in the native state, the spatial distribution of the polymer within PEC beads and the mechanical resistance of the PEC beads. Viable recombinant *E. coli* (*Escherichia coli*) cells overproducing cyklohexanone monooxygenase (CHMO) from the group of BVMOs were used as a model biocatalyst in this study. Currently, there is increased interest in research into novel enzymes and the industrial applications of BVMOs, as they catalyse the enantioselective BV biooxidation of a wide range of cyclic ketones to the corresponding lactones as chiral precursors of natural and bioactive compounds as well as potential drugs [16–19]. The study also sought to determine the operational stability of PEC beads with immobilized recombinant *E. coli* cells with CHMO during repeated Baeyer–Villiger (BV) biooxidations as well as the influence of repeated biotransformations on the viability of cells.

Results and Discussion

Production of PEC Bads with Immobilized E. coli Containing CHMOProduction of PEC Bads with Immobilized E. coli Containing CHMO

The development of PEC beads was performed following a modified protocol originally developed for the one-step encapsulation of viable *E. coli* cells with overproduced BVMO in PEC capsules [4,9]. In the present work, PEC beads were prepared by a two-step procedure. This included the gelation of PA microdrops with cells in a solution of CaCl2 in the first step followed by polyelectrolyte complexation with PMCG in the second step, and finally washing in a physiological saline solution. This immobilization protocol resulted in less stringent and simpler

conditions including higher utility and approximately a 2-fold decrease in the consumption of expensive PMCG and washing solutions for the preparation of immobilized viable *E. coli* with CHMO as compared with the PEC capsules previously used [9]. Use of the two-step procedure for the preparation of PEC beads led to an approximately one-third cost reduction as compared with the previous production of PEC capsules. Irrespective of this, a narrow size distribution of PEC beads of 0.64 ± 0.03 mm (Figure 1), high cell viability as well as higher operational stability of immobilized cells than in free cells was achieved, as detailed subsequently.

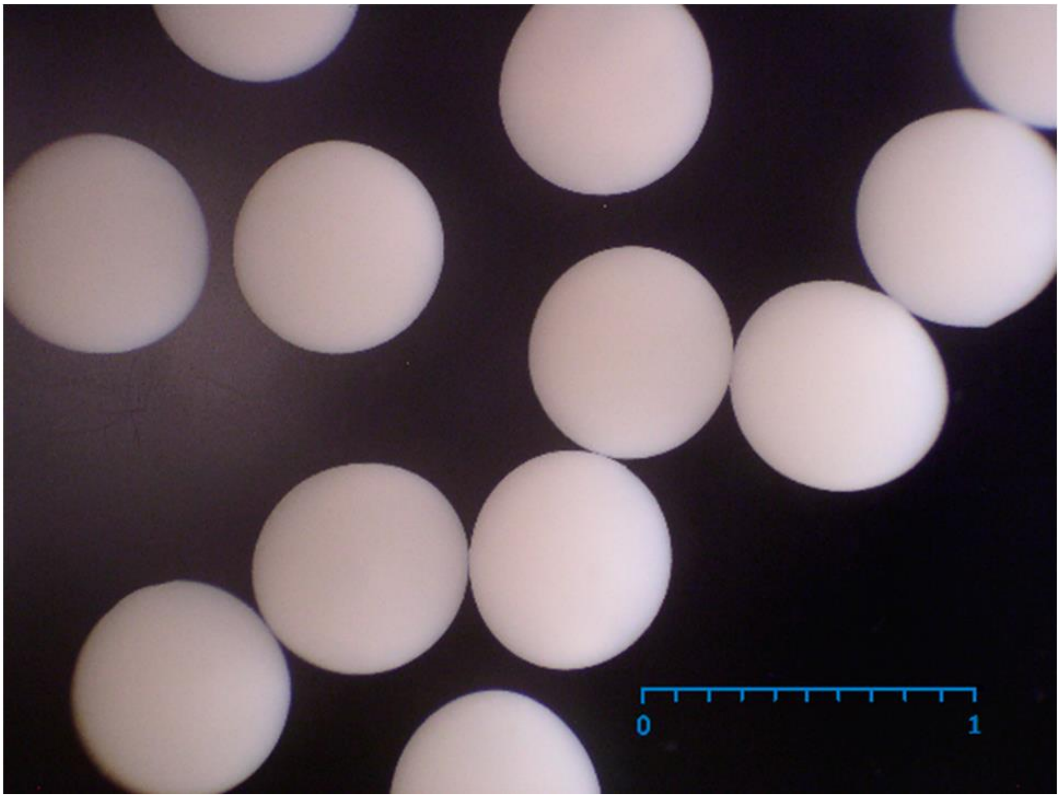

Figure 1. Photomicrography of uniform polyelectrolyte complex (PEC) beads with entrapped recombinant E. coli (Escherichia coli) cells with overexpressed cyklohexanone monooxygenase (CHMO). The immobilization yield was 100%. The scale bar is 1 mm.

Suitability of Cellulose Sulphate

The selection of suitable CS as the polyanion component is the key to polyelectrolyte complexation with the PMCG polycation, which is crucial for the integrity, mechanical and chemical resistance and biocompatibility of PEC beads. CS with a DS of 1.45 and a molecular weight of 400,000 g/mol–500,000 g/mol was used for the preparation of the PEC beads using a two-stage procedure including gelation and complexation steps. The substitution did not apparently depolymerise the cellulose, because the DS of 1.45 was in good agreement with the increase in

MW of the starting cellulose (254,700 g/mol). The crystallinity index of the bleached kraft pulp (BKP) CrI of 50 ± 3%, determined by the method developed by [20] showed a relatively high proportion of the amorphous phase distorted by the supra-molecular structure of the starting cellulose. If a similar crystallinity is exhibited by the spruce sulphite pulp (SSP) used in this work, a relatively high proportion of the amorphous phase should afford a more homogeneous distribution of substitution in the overmolecular cellulose structure. The amorphous phase also affords the availability of the polycations (PMCG) forming the PEC complex as well as better permeability of substrates and products for a biocatalytic reaction in that part of PEC beads in which the CS is incorporated.

Repeated Biotransformations Using Immobilized Cells

Stabilisation of the high enzyme activity of cells to achieve the maximum substrate conversion in repeated biotransformation cycles is one of the most important parameters in respect of the profitability of immobilized whole-cell biocatalysts [1]. At the same time, when using live cells, the need to maintain the highest degree of cell viability is also important. Over the course of 10 repeated BV biooxidations of bicyclo[3.2.0]hept-2-ene-6-one to regioisomeric lactones (1*R*,5*S*)-3-oxabicyclo-[3.3.0]oct-6-en-3-one and (1*S*,5*R*)-2-oxabicyclo-[3.3.0]oct-6-en-3-one, a high and stable conversion rate was observed using *E. coli* cells with CHMO immobilized in PEC beads (Figure 2). For up to 8 cycles, conversion rates of 100–93 ± 4% were achieved. After the 9th and 10th cycles, decreases to 85 ± 6% and 65 ± 5%, respectively were observed. In contrast with these findings, unprotected free cells exhibited a distinct decrease of 85 ± 6% in substrate conversion of the BV biooxidation in the 4th cycle, which showed a steady decline to 48 ± 6% in the 10th cycle. Cell stabilization within mild and physiological microenvironment of the PEC beads may contribute to higher stability of immobilized cells and delayed their deactivation compared to free cells (Figure 2).

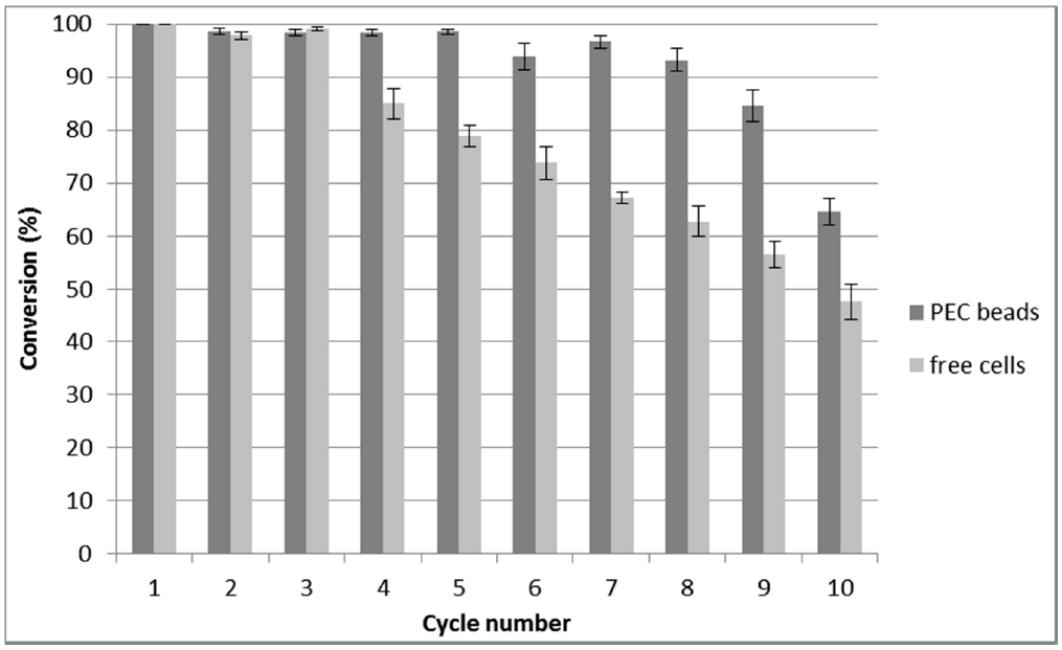

Figure 2. Conversion of bicyclic substrate to enantiomerically pure lactones using free and PEC immobilized E. coli cells containing CHMO enzyme catalysing Baeyer–Villger BV biooxidation. The graph shows the conversion rate in reaction time of 120 min. PEC: polyelectrolyte complex; BV: Baeyer–Villiger.

Morphology of PEC Beads

To investigate the morphology of the PEC beads, the confocal laser scanning microscopy arrangement described in the previous section was used (Figure 3). The beads contained Rhodamine 123 and Eosin Y as fluorescent tracer dyes of a concentration of 10−6 mol/L and were incubated for 15−30 min. These two non-covalently bound fluorescent tracer dyes were employed to monitor the distribution of the residual opposite charge within the PEC microcapsule [21]. Anionic Eosin Y (Figure 3A) was predominantly localised in the outer region of the PEC bead, and its concentration dropped sharply towards the bead interior. On the other hand, cationic Rhodamine 123 (Figure 3B) was observed in the entire volume of the PEC bead, with a higher intensity at the outer region and a lower intensity in the centre. Unlike in the previous study on polyelectrolyte capsules [21], no specific layers or internal structures were observed in the present study. It is worth noting that the spatial distribution of the fluorescence reflects the concentration of the dye molecules, corresponding to the residual free-charged groups of the matrix, rather than the spatial distribution of polymer components in the bead.

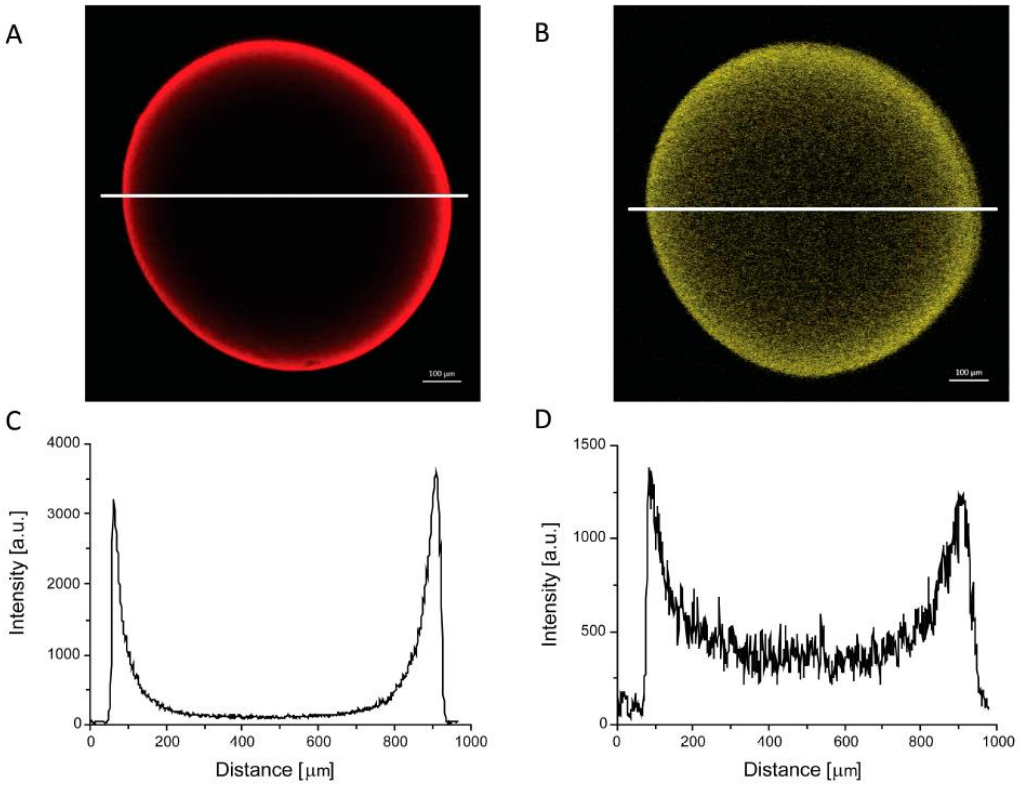

Figure 3. Image of PEC beads obtained by confocal laser scanning microscopy. Visualisation of the spatial distribution of fluorescence of Eosin Y (A) and Rhodamine 123 (B); Profiles of fluorescence intensity distribution, estimated along the white line for the respective tracer dye (C,D).

Cell Viability

Cell viability prior to and after biotransformation was measured by the intake of PI by the necrotic cells [8]. The viability of immobilized cells of *E. coli* with CHMO under different conditions and after 10 repeated biotransformation cycles (Figure 4) was evaluated. The viability in all cases remained within an 85−95% range.

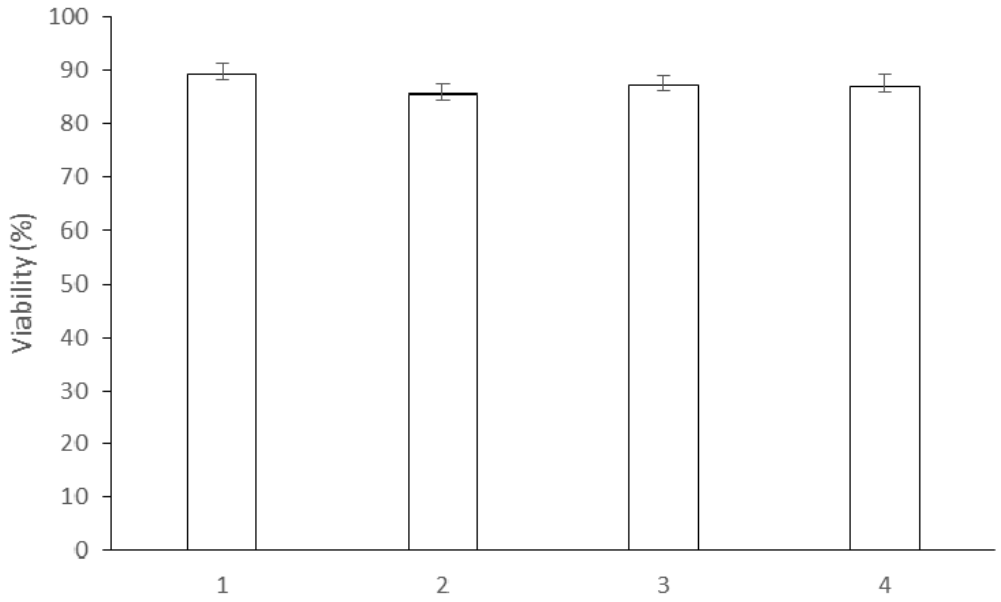

Figure 4. Viability of recombinant E. coli cells with CHMO in different preparations. 1: PEC beads after 10 biotransformation cycles; 2: PEC beads prior to biotransformations; 3: free cells after 10 biotransformation cycles; 4: free cells prior to biotransformations.

The high viability of cells immobilized in PEC beads was identical with that of free cells prior to biotransformations. This demonstrates the excellent biocompatibility of the novel PEC beads and their ability to preserve the physiological microenvironment for immobilized cells. At the same time, the nontoxicity of the PEC complex with CS in capsules [22] was also confirmed in the PEC beads developed in the present work. In addition, the high cell viability which did not vary after 10 biotransformation cycles demonstrates the preservation of the physiological conditions for immobilized cells during biotransformations.

Environmental Scanning Electron Microscopy (ESEM)

The PEC beads with and without *E. coli* cells showed a very regular spherical shape with a relatively smooth surface free from cracks and corrugations that was maintained after repeated biotransformations (Figure 5A–C). *E. coli* cells in their native state covered with a very thin liquid layer of a solution are shown in Figure 5D. The PEC bead microstructure was significantly improved compared with the microstructure described in a previous study, where the roughness of the PEC capsule surface with *Gluconobacter oxydans* cells was higher [5]. A slight wrinkling of the PEC bead surface without cells is commonly formed during polyelectrolyte complexation (highlighted by white dashed arrows in Figure 5A). In all cases, good roundness and bead regularity as well as low size distribution were demonstrated using ESEM. A slightly blurred image of *E. coli* cells partially covered by a small layer of the solution exhibited the unique possibility to depict

fully wet cells in their native state using the ESEM AQUASEM II (Figure 5D) equipped with custom-built detectors of signal electrons with a very high detection efficiency [23]. A lower quality of this image was caused by the unprocessed state of these live cells, depicted without the use of any preparation technique such as chemical fixation, drying or metal coating [24] as well as their imaging under a very low beam current and a relatively high pressure of water vapour in the specimen chamber of the ESEM.

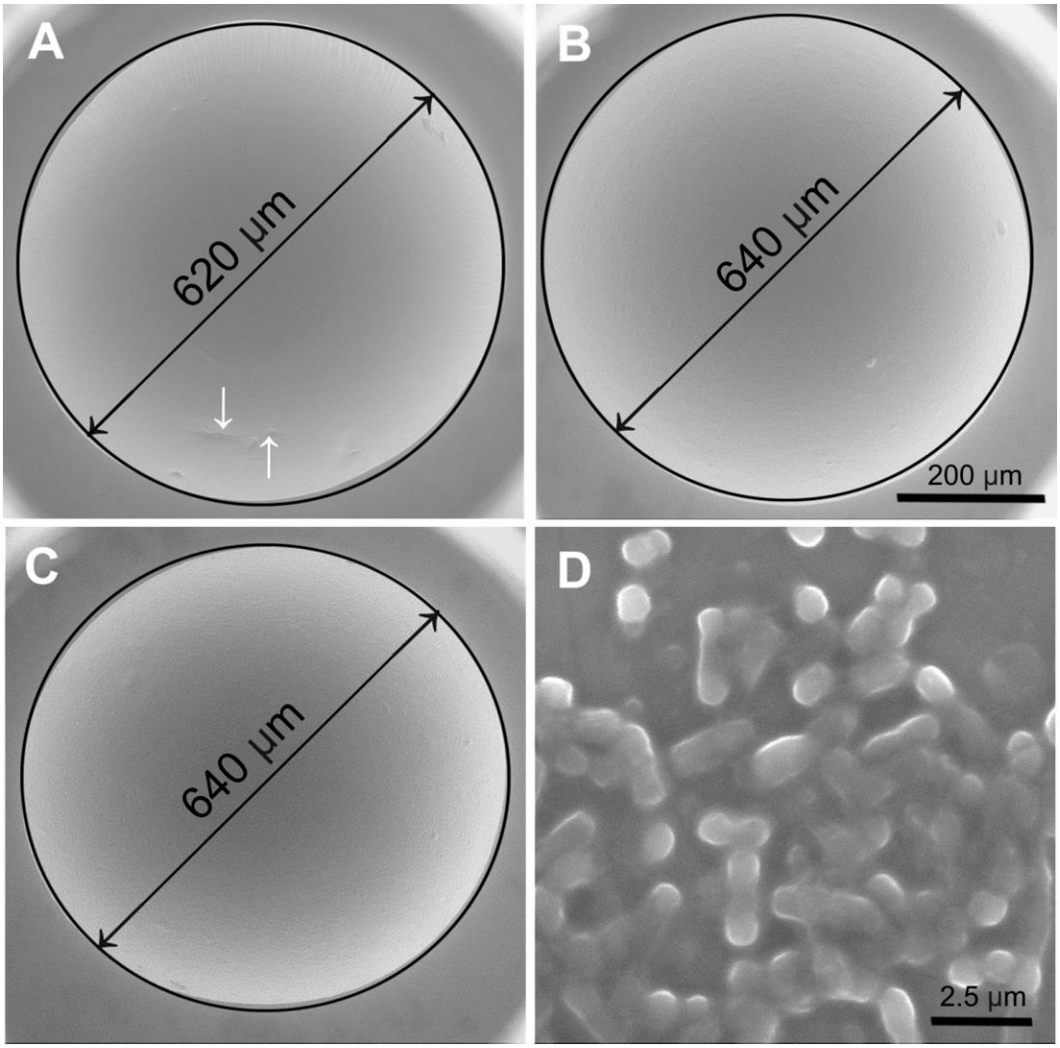

Figure 5. Microstructure of PEC bead surface free from cells (A), PEC bead with 10% (w/v) of wet E. coli cells prior to biotransformations (B), PEC bead with 10% (w/v) of wet E. coli cells after 10 biotransformation cycles (C), free live E. coli cells (D) in aqueous solution of phosphate buffer recorded by environmental scanning electron microscopy (ESEM) AQUASEM II with highlighted circularity and diameter measurement (black lines). The surface corrugation is due to cells clustering (A, white dashed arrow). The scale bar indicates 200 µm in (A–C) and 2.5 µm in (D).

Mechanical Resistance

Figure 6 depicts a typical course of the force during measurement of the mechanical resistance of PEC beads. The point marked by the arrow represents the bursting force required for mechanical disruption of the PEC bead. The average bursting force of PEC beads with entrapped cells prior to biotransformations was 0.95 ± 0.04 g/bead, which was close to the average bursting force of 1.16 ± 0.26 g/bead obtained for PEC beads after 10 biotransformation cycles. Practically the same mean values of bursting force prior to and after biotransformations showed that the mechanical strength of the PEC complex in the beads was not influenced either by mechanical forces induced by mixing or the sequestering agents such as phosphate buffer present in the reaction media.

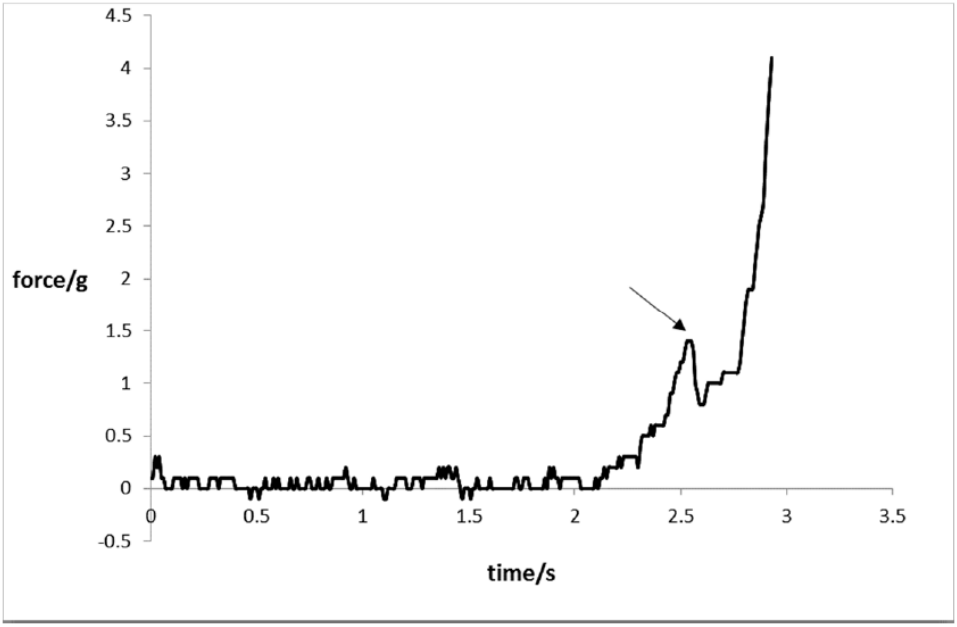

Figure 6. Time evolution of compression force applied onto a single PEC bead with immobilized cells after the 10th biotransformation cycle, measured during mechanical resistance test. The arrow indicates the moment of bead disruption.

It is also important to note that the PEC complex found throughout the volume of PEC beads provides additional mechanical resistance to the cells compared with the previously reported PEC capsule which contains the PEC membrane and the liquid core [25]. This can be seen in the course of the compression force where, after the disruption of a PEC bead at the point indicated by the arrow, a small decrease in the force occurred, followed by an increase in the bead resistance. On the other hand, the bursting of the PEC capsule observed previously [25] was followed by a sharp drop in force caused by the immediate and irreversible PEC capsule collapse.

Materials and Methods

Characterisation Polymers

High-viscosity, high-mannuronic acid sodium alginate from ISP Alginate (Girvan, UK) with the following chemical composition (determined by 1H NMR) was employed: fraction of alginate consisting of guluronic acid FG = 0.41, fraction of alginate consisting of mannuronic acid F_M = 0.59; fractions of alginate consisting of dimers and trimers of gluronic acid (G) and mannuronic acid (M): F_{GG} = 0.21, F_{GM} = F_{MG} = 0.20, F_{MM} = 0.39; F_{GGM} = F_{MGG} = 0.03, F_{MGM} = 0.18, F_{GGG} = 0.18, NG>1 = 8. PMCG from Scientific Polymer Products Inc. (Ontario, NY, USA), supplied as a 35% (*w/v*) aqueous solution, was lyophilised prior to use. The fluorescent tracer dyes Rhodamine 123 and Eosin Y were obtained from Acros Organics (Geel, Belgium). Water-soluble CS with the required DS, dynamic viscosity and MW was provided by Senova Biotechnologieunternehmen (Weimar, Germany). The derivative was prepared in accordance with the literature by the homogeneous conversion of spruce sulphite pulp (MW_{Cuen} 254, 700 g/mol from Borregaard ChemCell, Sarpsborg, Norway) with SO3-pyridine complex in the ionic liquid 1-butyl-3-methylimidazolium chloride (BMIMCl) with *N*,*N*-dimethylformamide as a dipolar aprotic co-solvent in order to improve the miscibility of the reaction mixture [15]. The final product had a DS of 1.45 and a dynamic viscosity of 15.6 mPa·s in 0.9% NaCl aqueous solution. The viscosity average molecular weight of around 500,000–600,000 g/mol corresponds to the weight average molecular weight of CS in the range from 310,000 to 460,000 g/mol determined by size exclusion chromatography [15]. These values were similar to those of the starting cellulose of 254,700 g/mol [15]. Sharp peaks characteristic of CS originating from sulphate groups were observed at 1256 cm^{-1} (δ SO_2) and 805 cm^{-1} (δ SO).

A Flash 2000 CHNS/O Analyser (Thermo Fisher Scientific, Waltham, MA, USA) was used for elemental analyses. The DS was calculated from the elemental composition as described in the literature [15]. Size exclusion chromatography (SEC) of CS was performed on a JASCO system (PU- 980 isocratic pump, RI-930 refractive index detector, Suprema guard column and columns (100 Å, 1000 Å, 3000 Å, in series) with 1 M Na2HPO4 (pH = 9, 200 mg/L NaN3) as eluent (flow-rate: 1 mL/min, sample, concentration: 0.5 mg/mL). A viscometer (Brookfield Programmable DV-II+ Instrument, Middleboro, MA, USA) equipped with Thermostat Julabo F12 (Seelbach, Germany) was employed to determine the dynamic viscosity of CS solutions in an 0.9% NaCl aqueous solution. The viscosity average molecular weight of CS was determined from the intrinsic viscosity in 0.5 M NaCl at 25 °C (Mark Houwink parameters: α = 0.94, K = $6.37 \cdot 10^{-6}$ mL/g) in accordance with the literature [26]. Fourier-transform infra red (FTIR) spectra were measured using a Nicolet 6700 spectrometer (Thermo Fisher Scientific, Waltham,

MA, USA) equipped with DTGS detector and Omnic 8.0 software (Thermo Fisher Scientific, Waltham, MA, USA). The spectra were collected in the range from 4000 cm^{-1} to 400 cm^{-1} at a resolution of 4 cm^{-1}; the number of scans was 128. Diamond Smart Orbit ATR accessory was applied to solid-state measurements.

Cultivation of Cells

Cell stocks of *E. coli* overexpressing CHMO (EC1.14.13.22) from *Acinetobacter calcoaceticus* NCIMB 9871 were stored at −80 °C. The recombinant *E. coli* strain was kindly donated by Prof. Marko D. Mihovilovič (TU Vienna, Austria). Cells, streaked at LB_{amp} agar Petri dish containing 10 g/L of peptone, 5 g/L of yeasts extract, 10 g/L of NaCl, 15 g/L of agar and 0.2 g/L of ampiciline, were cultivated in an incubator at 37 °C to afford colonies of approximately 1 mm size. A single colony from LB_{amp} agar was inoculated to a 10 mL of LB_{amp} medium in an Erlenmayer flask and allowed to grow at 37 °C in an orbital shaker at 150 rpm for 12 h. 1% of the inoculum (*v/v*) was pipetted into a TB_{amp} medium and cultivated at 37 °C in an orbital shaker at 150 rpm for 12 h. The addition of isopropyl β-D-1-thiogalactopyranoside (IPTG) to the final concentration of 0.25 mM to the medium, during shaking at 25 °C in an orbital shaker at 200 rpm for 2 h, induced the synthesis of CHMO enzyme. The biomass was separated from the medium by centrifugation at 15 °C and 4000× *g* for 15 min and used for biotransformation experiments and immobilization.

Preparation of Polyelectrolyte Complex Beads

A suspension of cells was prepared in a solution of 1.8% (*w/v*) of PA consisting of 0.9% (*w/v*) of sodium alginate and 0.9% of CS in 0.9% (*w/v*) NaCl at pH = 7 to the final concentration of 10% of wet cells. The PA solution with the cells was added dropwise into a stirred gelation solution of 1.0% (*w/v*) of CaCl2 using a custom-made coaxial air-stripping extrusion device. The time of gelation was 10 min and the collection time was 1 min. Subsequently, the prepared beads were separated from the gelation medium and transferred into a stirred solution containing 1.8% (*w/v*) of PMCG and 0.9% (*w/v*) of NaCl at pH = 7 for 10 min in order to undergo polyelectrolyte complexation. The polyelectrolyte complex beads were washed with 0.9% (*w/v*) of NaCl and used in biotransformation.

Repeated Biotransformations

PEC beads with immobilized cells (10% *w/w*) and free *E. coli* cells were transferred into a reaction medium containing 50 mM phosphate buffer (pH = 7), 0.2 g/L of ampiciline and 4 g/L of glucose. Model Baeyer–Villiger biooxidation resulting in the production of lactone regioisomers (1*S*,5*R*)-2- oxabicyclo[3.3.0]oct-6-en-3-one

and (1*R*,5*S*)-3-oxabicyclo-[3.3.0]-oct-6-en-2-one [27] was initiated by the addition of substrate rac-bicyclo[3.2.0]hept-2-en-6-one in ethanol (volume ratio 1:9) to the reaction medium to a final concentration of 0.5 g/L. The reaction conditions were 25 °C and 150 rpm in an orbital shaker. Substrate and produced lactones in samples were extracted in dichlormethane with methyl benzoate as internal standard (0.5 mg/mL) and analysed using gas chromatography as reported previously [9]. After each biotransformation, the PEC beads containing cells, and the free cells, were separated from the reaction medium by filtration (encapsulated cells) or centrifugation (free cells), washed with a substrate-free medium and subjected to another biotransformation cycle.

Confocal Laser Scanning Microscopy

The internal structure of the PEC beads was characterised using confocal laser scanning microscopy (CLSM). Images of the PEC beads were recorded simultaneously in transmission, reflection and fluorescence modes using a laser scanning microscope head LSM 510 META on Axiovert 200M stand (both from Carl Zeiss, Jena, Germany). A Zeiss PlanApochromat 10x/0.45 lens was used to visualise the whole beads. Laser lines of 488 nm for Rhodamine 123 and 543 nm for Eosin Y were used for excitation. Two channels with band-pass filter 500–550 nm for detection of the reflected light and a long-pass filter LP 560 nm were used for fluorescence.

Cell Viability

The CLSM confocal laser scanning microscopy system described for the investigation of the PEC bead structure was also used for cell viability imaging. Cells necrosis was detected using fluorescence of propidium iodide by LSM 510 META NLO microscope (Carl Zeiss, Jena, Germany) equipped with the C-Apochromat 40xW/corr water immersion objective. Viability of the encapsulated cells was determined after mild disruption of the beads in a test tube. The mixture was carefully stirred so as to ensure that the remains of beads did not affect the measurement. The cells were incubated for 10 min with 1 μM of propidium iodide (PI). Fluorescence was initiated by the 543 nm line of HeNe laser and an LP 560 nm long-pass emission filter was used for PI fluorescence detection. The cell viability was evaluated as a ratio of the number of the surviving bacterial cells to the total number of bacterial cells. The number of viable bacterial cells was calculated as the difference between the total number of bacterial cells and the number of necrotic cells identified by propidium iodide fluorescence. The total number of cells was counted from the respective transmission image in accordance with the literature [8].

Environmental Scanning Electron Microscopy

Due to the very high sensitivity of PEC beads to electron beam irradiation resulting in radiation damage and a high risk of surface dehydration, images of the beads were recorded under conditions of carefully controlled and very slowly reduced relative humidity (from 100% to 90%) in a specimen chamber of the ESEM AQUASEM II developed by the group of Environmental Electron Microscopy (ISI ASCR in Brno, Czech Republic) in cooperation with TESCAN (Brno, Czech Republic). A sophisticated hydration system with heated needle valve (35 °C) was used as an additional water supply in the microscope. PEC beads and *E. coli* cells were observed in a small droplet of aqueous solution of 50 mM phosphate buffer (pH = 7), ampicillin 0.2 g/L and glucose 4 g/L, at a reduced beam accelerating voltage of 10 kV and very low beam current of 30 pA. A specially modified ionisation detector of secondary electrons [28] affording a low beam current observation with a large field of view (up to 850 μm) was used.

Mechanical Strength

The mechanical properties of the PEC beads were determined in compression mode using a Texture Analyser TA-XT2i (Stable Micro Systems, Godalming, UK) equipped with a mobile probe and Texture Expert Exceed 2.64 software (Stable Micro Systems, Godalming, UK). Compression measurements were conducted at a compression speed of 0.5 mm/s to the point at which 95% of 50 PEC beads per batch were deformed. The bursting force is the result of this compression test.

Conclusions

This work focused on the development of an immobilization procedure providing PEC beads for the entrapment of viable recombinant *E. coli* cells with overexpressed cyclohexanone monooxygenase. Uniform and stable PEC beads were successfully produced by a two-step procedure including ionotropic gelation and polyelectrolyte complexation. The PEC beads were prepared under less stringent conditions with a lower consumption of polycation and washing solutions than for the PEC capsules previously used. These characteristics are highly advantageous for a potential production scale-up of Baeyer–Villiger biooxidations using entrapped viable cells. Accordingly, it was important that the performance of cells entrapped in PEC beads for a model Baeyer–Villiger biooxidation, expressed as their operational stability, was enhanced over that of free cells. The PEC beads preserved high cell viability and enabled faster and more precise handling with cells during repeated Baeyer–Villiger biooxidations. Further studies using environmental scanning electron microscopy confirmed the stability of the dimensions and the sphericity of the PEC beads. In addition, both the surface

morphology and the mechanical resistance of the PEC beads remained unchanged prior to and after biotransformations.

Acknowledgements

This work was supported by the Slovak Grant Agency for Science VEGA 2/0090/16 and by the Slovak Research and Development Agency under contracts no. APVV-15-0227 and APVV-14-0858. This publication is the result of the project implementation: Applied research in the field of industrial biocatalysis, ITMS code: 26240220079 supported by the Research & Development Operational Programme funded by the ERDF. The authors are indebted to P. Laudeley (Institute of Organic Chemistry and Macromolecular Chemistry, Friedrich Schiller University of Jena) for her assistance with the synthesis of tailored CS.

References

1. Kadisch, M.; Willrodt, C.; Hillen, M.; Bühler, B.; Schmid, A. Maximizing the stability of metabolic engineering-derived whole-cell biocatalysts. *Biotechnol. J.* **2017**, *12*, doi:10.1002/biot.201600170.

2. Wachtmeister, J.; Rother, D. Recent advances in whole cell biocatalysis techniques bridging from investigative to industrial scale. *Curr. Opin. Biotechnol.* **2016**, *42*, 169–177, doi:10.1016/j.copbio.2016.05.005.

3. Bučko, M.; Vikartovská, A.; Lacík, I.; Kolláriková, G.; Gemeiner, P.; Pätoprstý, V.; Brygin, M. Immobilization of a whole-cell epoxide-hydrolyzing biocatalyst in sodium alginate-cellulose sulfate-poly(methylene-coguanidine) capsules using a controlled encapsulation process. *Enzyme Microb. Technol.* **2005**, *36*, 118–126, doi:10.1016/j.enzmictec.2004.07.006.

4. Hucík, M.; Bučko, M.; Gemeiner, P.; Štefuca, V.; Vikartovská, A.; Mihovilovic, M.D.; Rudroff, F.; Iqbal, N.; Chorvát, D., Jr.; Lacík, I. Encapsulation of recombinant *E. coli* expressing cyclopentanone monooxygenase in polyelectrolyte complex capsules for Baeyer-Villiger biooxidation of 8-oxabicyclo[3.2.1]oct-6-en-3-one. *Biotechnol. Lett.* **2010**, *32*, 675–680, doi:10.1007/s10529-010-0203-2.

5. Bertóková, A.; Vikartovská, A.; Bučko, M.; Gemeiner, P.; Tkáč, J.; Chorvát, D.; Štefuca, V.; Neděla, V. Biooxidation of 2-phenylethanol to phenylacetic acid by whole-cell *Gluconobacter oxydans* biocatalyst immobilized in

polyelectrolyte complex capsules. *Biocatal. Biotransform*. **2015**, *33*, 111–120, doi:10.3109/10242422.2015.1053470.

6. Lacík, I.; Briššová, M.; Anilkumar, A.V.; Powers, A.C.; Wang, T. New capsule with tailored properties for the encapsulation of living cells. *J. Biomed. Mater. Res.* **1998**, *39*, 52–60, doi:10.1002/(SICI)1097-4636(199801)39:1<52::AID-JBM7>3.0.CO;2-H.

7. Anilkumar, A.V.; Lacik, I.; Wang, T.G. A novel reactor for making uniform capsules. *Biotechnol. Bioeng.* **2001**, *75*, 581–589, doi:10.1002/bit.10077.

8. Schenkmayerová, A.; Bučko, M.; Gemeiner, P.; Chorvát, D., Jr.; Lacík, I. Viability of free and encapsulated *Escherichia coli* overexpressing cyclopentanone monooxygenase monitored during model Baeyer–Villiger biooxidation by confocal laser scanning microscopy. *Biotechnol. Lett.* **2012**, *34*, 309–314, doi:10.1007/s10529- 011-0765-7.

9. Bučko, M.; Schenkmayerová, A.; Gemeiner, P.; Vikartovská, A.; Mihovilovič, M.D.; Lacík, I. Continuous testing system for Baeyer-Villiger biooxidation using recombinant *Escherichia coli* expressing cyclohexanone monooxygenase encapsulated in polyelectrolyte complex capsules. *Enzyme Microb. Technol.* **2011**, *49*, 284–288, doi:10.1016/j.enzmictec.2011.05.013.

10. Schenkmayerová, A.; Bučko, M.; Gemeiner, P.; Treľová, D.; Lacík. I.; Chorvát, D., Jr.; Ačai, P.; Polakovič, M.; Lipták, L.; Rebroš, M.; et al. Physical and bioengineering properties of polyvinyl alcohol lens-shaped particles versus spherical polyelectrolyte complex microcapsules as immobilization matrices for a whole-cell Baeyer- Villiger monooxygenase. *Appl. Biochem. Biotechnol.* **2014**, *174*, 1834–1849, doi:10.1007/s12010-014-1174-x.

11. De Vos, P.; Bučko, M.; Gemeiner, P.; Navrátil, M.; Švitel, J.; Faas, M.; Strand, B.L.; Skjak-Braek, G.; Morch, Y.A.; Vikartovská, A.; et al. Multiscale requirements for bioencapsulation in medicine and biotechnology. *Biomaterials* **2009**, *30*, 2559–2570, doi:10.1016/j.biomaterials.2009.01.014.

12. Rokstad, A.M.A.; Lacík, I.; de Vos, P.; Strand, B.L. Advances in biocompatibility and physico-chemical characterization of micorspheres for cell encapsulation. *Adv. Drug Deliv. Rev.* **2014**, *67–68*, 111–130, doi:10.1016/j.addr.2013.07.010.

13. Polakovič, M.; Švitel, J.; Bučko, M.; Filip, J.; Neděla, V.; Ansorge-Schumacher, M.B.; Gemeiner, P. Progress in biocatalysis with immobilized viable whole cells: Systems development, reaction engineering and applications. *Biotechnol. Lett.* **2017**, *39*, 667–683, doi:10.1007/s10529-017-2300-y.

14. Liese, A.; Seelbach, K.; Buchholz, A.; Haberland, J. Processes. In *Industrial Biotransformations*, 2nd ed.; Liese, A., Seelbach, K., Wandrey, C., Eds.; Wiley-VCH Verlag GmbH&Co.: Weinheim, Germany, 2006; pp. 147–513, ISBN 3-527-31001-0.

15. Gericke, M.; Liebert, T.; Heinze, T. Interaction of ionic liquids with polysaccharides, 8–synthesis of cellulose sulfates suitable for polyelectrolyte complex formation. *Macromol. Biosci.* **2009**, *9*, 343–353, doi:10.1002/mabi.200800329.

16. Bučko, M.; Gemeiner, P.; Schenkmayerová, A.; Krajčovič, T.; Rudroff, F.; Mihovilovič, M.D. Baeyer-Villiger oxidations: Biotechnological approach. *Appl. Microbiol. Biotechnol.* **2016**, *100*, 6585–6599, doi:10.1007/s00253-016-7670-x.

17. Leisch, H.; Morley, K.; Lau, C.K. Baeyer-Villiger Monooxygenases: More Than Just Green Chemistry. *Chem. Rev.* **2011**, *111*, 4165–4222, doi:10.1021/cr1003437.

18. Balke, K.; Kadow, M.; Mallin, H.; Saß, S.; Bornscheuer, U.T. Discovery, application and protein engineering of Baeyer–Villiger monooxygenases for organic synthesis. *Org. Biomol. Chem.* **2012**, *10*, 6249–6265, doi:10.1039/C2OB25704A.

19. Rudroff, F.; Fink, M.J.; Pydi, R.; Bornscheuer, U.T.; Mihovilovic, M.D. First chemo-enzymatic synthesis of the (*R*)-Taniguchi lactone and substrate profiles of CAMO and OTEMO, two new Baeyer-Villiger monooxygenases. *Monatsh. Chem.* **2017**, *148*, 157–165, doi:10.1007/s00706-016-1873-9.

20. Ju, X.; Bowden, M.; Brown, E.E.; Zhang, X. An improved X-ray diffraction method for cellulose crystallinity measurement. *Carbohyd. Polym*. **2015**, *123*, 476–481, doi:10.1016/j.carbpol.2014.12.071.

21. Podskočová, J.; Chorvát, D., Jr.; Kolláriková, G.; Lacík, I. Characterization of polyelectrolyte microcapsules by confocal laser scanning microscopy and atomic force microscopy. *Laser Phys.* **2005**, *15*, 545–551.

22. Zhang, L.Y.; Yao, S.J.; Guan, Y.X. Effects of poly(methylene-co-guanidine) in microbial growth in an alginate/cellulose sulphate-CaCl2/poly(methylene-co-guanidine) capsule system. *Process Biochem.* **2005**, *40*, 189–193, doi:10.1016/j.procbio.2003.12.003.

23. Neděla, V.; Tihlaříková, E.; Runštuk, J.; Hudec, J. High-efficiency detector of secondary and backscattered electrons for low-dose imaging in the ESEM. *Ultramicroscopy* **2018**, *184*, 1–11, doi:10.1016/j.ultramic.2017.08.003.

24. Tihlaříková, E.; Neděla, V.; Shiojiri, M. In Situ study of live specimens in an environmental scanning electron microscope. *Microsc. Microanal.* **2013**, *19*, 914–918, doi:10.1017/S1431927613000603.

25. Bučko, M.; Vikartovská, A.; Gemeiner, P.; Lacík, I.; Kolláriková, G.; Marison, I.W. *Nocardia tartaricans* cells immobilized in sodium alginate-cellulose sulfate-poly(methylene-co-guanidine) capsules: Mechanical resistance and operational stability. *J. Chem. Technol. Biotechnol.* **2006**, *81*, 500–504, doi:10.1002/jctb.1466.

26. Kishino, K.; Kawai, T.; Nose, M.; Saitoh, M.; Kamide, K. Dilute Solution Properties of sodium cellulose disulphate. *Eur. Polym. J.* **1981**, *17*, 623–630, doi:10.1016/0014-3057(81)90101-4.

27. Mihovilovic, M.D.; Rudroff, F.; Grötzl, B.; Kapitan, P.; Snajdrova, R.; Rydz, J.; Mach, R. Family clustering of Baeyer–Villiger monooxygenases based on protein sequence and stereopreference. *Angew. Chem. Int. Ed.* **2005**, *44*, 3609–3613, doi:10.1002/anie.200462964.

28. Neděla, V.; Konvalina, I.; Lencová, B.; Zlámal, J. Comparison of calculated, simulated and measured signal amplification in a variable pressure SEM. *Nucl. Instrum. Meth. A* **2011**, *645*, 79–83, doi:10.1016/j.nima.2010.12.200.

24 Fractal characteristics of pore structure of compacted bentonite studied by ESEM and MIP methods

Haiquan Sun[1], David Mašín1, Jan Najser[1], Vilém Neděla[2], Eva Navrátilová[2]

1 Faculty of Science, Charles University, Albertov 6, 128 43 Prague, Czech Republic
2 Institute of Scientific Instruments, The Czech Academy of Sciences, Královopolská 147, 612 64 Brno, Czech Republic

Keywords

Bentonite, ESEM, Fractal dimension, Microstructure, MIP, Suction

Abstract

In this paper, we aim to clarify microstructure of bentonite from Cerny vrch deposit in the Czech Republic. We adopt results of ESEM and MIP experiments performed at various suctions along wetting and drying paths on bentonite samples compacted from powder to two different initial dry densities. The data were used for quantification of fractal dimension characteristics of pores of different sizes. Two different methods of calculating fractal dimension were used for MIP data, and one method was used for evaluation of ESEM images. Fractal dimensions obtained from MIP data, combined with the measured pore size density functions, allowed us to identify two different pore families: micropores and macropores. Macropores can be further subdivided into fine macropores and coarse macropores based on fractal analysis. The pore systems were further distinguished by different responses to suction changes and to compaction effort. In general, we observed slight increase in fractal dimension with increasing suction and with increasing dry density.

Introduction

Over the past few decades, bentonite has been an extensively studied material, thanks to its application as a buffer material in the planned repositories of spent nuclear fuel. It is now well accepted that bentonite structure is composed of different pore families. Typically, two predominant pore sizes are identified: macropores, formed between silt-sized aggregates of clay particles, and micropores, which represent the pore system within these aggregates. This distinction has been a basis for development of models describing mechanical and coupled hydro-mechanical behaviour of these materials [1, 10, 16, 28, 36, 37, 47].

Although the simple distinction of two pore systems is efficient for model formulation, various recent studies indicate that the pore structure of bentonite and

its evolution during wetting and drying cycles is actually more complex. Wang et al. [54] identified four major pore sizes in MX80 bentonite. Similarly, four pore sizes were suggested by Přikryl and Weishauptová [41] for bentonite from Czech deposit. Lloret and Villar [32] observed emergence of a new mode in pore size density function during wetting, located between two pore size peaks of ascompacted material. This is consistent with observation by Manca et al. [34], who identified that bi-modal pore size distribution curve of bentonite transforms to mono-modal after saturation. Similarly, conclusions reached other researchers at different soil types [5, 38, 46]. In the cited studies, it was observed that mono-modal distribution transforms back to bi-modal in subsequent drying. However, Seiphoori et al. [49] and Burton et al. [3] observed that the double porosity structure did not recover when drying after wetting. Romero et al. [46] assumed two pore families in compacted Boom clay, but elaborated more on selection of delimiting pore size between micropores and macropores. Detailed review of the microstructure of compacted unsaturated clays has been presented by Romero and Simms [45].

In this work, we studied microstructure of Czech bentonite from Cerny vrch deposit, denoted as B75. This bentonite has been used as a buffer material in Mock-Up- Josef model of nuclear waste repository [50]. Microstructure determines pore shape, pore specific surface and pore size distribution. These properties are related to the cation exchange capacity, permeability and sorption capacity, which are important properties considered in the design of high-level nuclear waste repositories. Most of the bentonite microstructure evaluation is based on quantification of global quantities (like micro- and macrovoid ratio), or on visual evaluations of ESEM images and pore size distributions measured by MIP method. In this work, we aim for a more quantitative evaluation using a fractal theory. It gives us better insight into the pore structure, and it also allows us to better identify different pore families based on their sizes, which is a supporting argument for microstructurally based bentonite material models.

The fractal theory was first introduced by Mandelbrot [35]. The Euclidian or topological dimension is an integer; one represents line, two represents surface, and three represents volume. However, the fractal dimension is a real number, for a line its value varies between 1 and 2, and for surface varies between 2 and 3. The fractal dimension can be used to analyse the pore systems of porous medium based on self-similarity of pore geometry. Fractal dimension has been proven to be an efficient tool to describe and study the pore irregularity and surface roughness of different porous materials, such as the heterogeneities of pore spaces in sedimentary rocks [13, 31, 56], the fractal characteristic of micropores on the fracture surface of sandstone [18, 23, 52], the fractal description of particle fragmentation related to fracture energy [58] and shear strength [59] and the methane and gas adsorption of

coals [15, 30, 33]. The fractal dimension of clay related to its structure has also been studied by many researchers [4, 12, 20, 44, 45, 53].

Various techniques have been applied to analyse the pore structure of compacted bentonite. One of the methods is based on the digital image analysis using scanning electron microscopy (SEM) [26, 29, 30, 44, 55], environmental scanning electron microscopy (ESEM) [11, 29, 45] or transmission electron microscopy (TEM) [42] microphotographs. The other common methods include evaluation of mercury intrusion porosimetry test (MIP) [9] and the nitrogen gas adsorption–desorption tests [57, 60, 61]. Among all the methods, SEM, ESEM and MIP are most frequently used to investigate the pore structures of compacted bentonite [29, 39, 40]. Because bentonite is a clay sensitive to water, the pore structure would change with changing water content. The advantage of ESEM to SEM is that in ESEM the relative humidity can be controlled observing the fabric change with time or relative humidity, while with SEM we can only observe dry samples. The image analysis can only show two-dimensional pictures and local information, which does not represent complete 3D structure of the pores.

In this paper, we adopted results of ESEM and MIP methods to study bentonite microstructure using fractal theory. The ESEM method was selected as a representative photography method, giving detailed insight into the pore shape and structure, but providing only 2D images. MIP method was selected to supplement ESEM method, as it provides 3D information on pore sizes, which is, however, expressed in terms of cumulative volumes only, without information on pore shapes. Experiments on samples with different initial dry densities under different relative humidity conditions reported by Sun et al. [51] were adopted to evaluate the fractal characteristics.

Materials

The commercial compacted Czech bentonite B75 was used in this study. The montmorillonite content was around 60%, and initial water content about 10%. The chemical composition of bentonite B75 is shown in Table 1, and the cation exchange capacity is shown in Table 2.

The bentonite powder was used to prepare the compacted samples. This powder was uniaxially compacted in the laboratory mould to reach the desired initial dry densities of 1.27 g/cm^3 and 1.90 g/cm^3. The initial water content of the powder was around 10%. The height of the sample was 10 mm and the diameter was 50 mm. The manufactured bentonite was cut into small pieces. Tests on two groups of samples were evaluated in this paper. Samples from the first group were dried in the oven for more than 48 h with temperature of 105 °C. Subsequently, the dried

samples were put in the desiccator with suction control by different vapour pressure. Samples from the second group were initially compacted, directly dried by two different methods (freeze-drying and oven-drying) and adopted in ESEM measurements. All the evaluations were done on samples from the first group, except of evaluations from the ‘‘The effect of oven-drying and freeze-drying on fractal dimension using ESEM images’’ section.

Table 1 Chemical composition of bentonite B75 [19]

Component	Weight (%)
SiO_2	51.91
Al_2O_3	15.52
Fe_2O_3	8.89
TiO_2	2.28
CaO	4.6
MgO	2.22
Na_2O	1.21
K_2O	1.27
P_2O_5	0.4
MnO	0.11
FeO	2.95
SO_3	0.09
$CaCO_3$	11.71
CO_2	5.15
Lost-drying	10.65

Table 2 Cation exchange capacity of bentonite B75

Cation	mmol/100 g
Ca^{2+}	47.27
Na^{+}	15.39
K^{+}	2.01
Mg^{2+}	15.80
H^{+}	< 0.5

Each desiccator was in equilibrium with different chemical saturated salt solution corresponding to different relative humidity. In this paper, suctions of 286.7 MPa,

38 MPa and 3.29 MPa were imposed on the compacted bentonite for wetting path. After equilibration, the samples for MIP tests were freeze-dried before the measurement. The detailed information and procedures were described in [51].

Methods

Environmental scanning electron microscopy

The environmental scanning electron microscopy (ESEM) tests have been performed using Quanta 650 FEG scanning electron microscope at the Institute of Scientific Instruments of the Czech Academy of Sciences, Brno. Samples of compacted bentonite were equilibrated at suction of 286.7 MPa before their placement into ESEM cell. The samples were placed in a special conical holder and cooled by a Peltier stage. This holder allows minimising sample shift in conditions of very high relative humidity as well as better cooling which is necessary for sample stabilisation and repeatability of observation. Conditions of observation were kept constant throughout the experiment. The samples of the bentonites were observed in water vapour environment under increasing and then decreasing relative humidity (wetting and drying). The water vapour pressure of 93 Pa (relative humidity of 10%) was determined as optimal initial state for the experiment. Then, the vapour pressure was gradually increased up to 850 Pa (relative humidity 97%). After the maximum value of the relative humidity was reached, the relative humidity was gradually decreased again down to 10%. The microphotographs were taken at each stage. The time interval between vapour pressure changes was 15 min. Similar interval was used by other researchers [29, 39].

Mercury intrusion porosimetry tests

Mercury intrusion porosimetry (MIP) is based on the capillary law governing non-wetting liquid (with contact angle bigger than 90°) penetration into small pores. The pore entrance diameter (D) can be calculated from the intrusion pressure, p, the surface tension of mercury, σ_{Hg}, the contact angle between the mercury and soil surface, $\theta_{n\omega}$, and the equivalent entrance diameter, D,$D = -\left(4\sigma_{Hg}\, cos\, \theta_{nw}\right) / P$. In this study, the θ_{nw} = 130° and σ_{Hg} = 0.484 N/m at 25 °C were considered in pore diameter calculation.

The tests were performed at the Department of Inorganic Technology at the University of Chemistry and Technology Prague (Apparatus AutoPore IV, Micromeritics). All the samples for this measurement were freeze-dried. The apparatus has two pressure regimes: one is the low one from 0.01 to 0.2 MPa which can measure the pore radius between 100 and 3 μm, and the other is the high regime from 0.2 to 400 MPa which corresponds to the pore radius between 3 μm to 1.5 nm.

It is noted that the MIP method cannot detect nanopores below approximately 3 nm, and these results were thus not adopted in the evaluation.

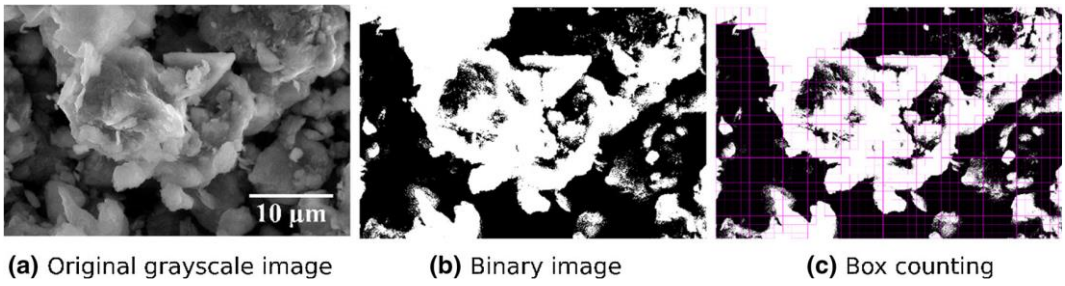

Fig. 1 Examples of ESEM microphotographs of compacted bentonite used for box counting fractal dimension methods, the original greyscale image (a), binary image (b), box counting (c)

Fractal dimension calculation theory

Fractal dimension calculated from ESEM images

For fractal dimension analysis, the original greyscale microphotographs taken from ESEM apparatus must be transformed into binary images. The binary image contains only two colours, black and white. Typically, the black colour represents pores and the white colour represents the solid skeleton. The greyscale threshold value was used to separate the solid and pore. An appropriate global threshold value was chosen to apply to all microphotographs.

There are many methods to calculate fractal dimension from microphotographs taken from ESEM tests, such as box counting method [30], probability statistic method [14] or Fourier method [48]. The box counting method, which has been widely used in rocks and soils [30] characterising the pore distribution and fractal dimension, was chosen to determine the fractal dimension of compacted bentonite. The procedures of calculating fractal dimension are shown in Fig. 1 including the original greyscale ESEM photograph (Fig. 1a), the binary image after applied threshold value (Fig. 1b) and the binary image used in box counting to measure the fractal dimension (Fig. 1c). The size of the box was denoted as e. The number of boxes which cover solid surface was then marked as N(ε). This procedure was repeated with different box sizes with corresponding covering counts N obtained, so the box counting fractal dimension D_b could be calculated with Eq. (1) [17, 30]:

$$D_b = -\lim_{e \to 0} \frac{ln(N(\varepsilon))}{ln(\varepsilon)} \quad (1)$$

The fractal dimension is equal to the slope of natural logarithms N(ε) versus ε.

In this paper, the free software ImageJ [43] and associated open-source plug-ins [22] were used to process the microphotographs and to analyse the results.

Fractal dimension calculated from MIP data

The results of MIP were often used for the analysis of pore structure of materials like coal, clay and so on. For calculation of the pore surface fractal dimension D_s, Eq. (2) based on Menger fractal dimension model has usually been used by other researchers [21, 27, 44, 45], which is related to derivative of the cumulative intrusion volume as a function of intrusion pressure:

$$log\left[\left(dV_p \,/\, dv_{max}\right) / \, d_p\right] \alpha (D_s - 4)\, log\, p \qquad (2)$$

where p is the intrusion pressure (MPa), V_p is the cumulative volume intruded for a given pressure p, V_{max} is the total volume intruded for the maximum intrusion pressure and D_s is the surface fractal dimension. The interval zones of self-similarity and the different types of pore structure can be obtained from the linear sections of $log\left[\left(dV_p \,/\, dv_{max}\right) / \, d_p\right]$ versus *log p*, the slope of which yields the values of fractal dimension.

Fractal dimension calculated from MIP data

The results of MIP were often used for the analysis of pore structure of materials like coal, clay and so on. For calculation of the pore surface fractal dimension D_s, Eq. (2) based on Menger fractal dimension model has usually been used by other researchers [21, 27, 44, 45], which is related to derivative of the cumulative intrusion volume as a function of intrusion pressure:

$$log\left[\left(dV_p \,/\, dv_{max}\right) / \, d_p\right] \alpha (D_s - 4)\, log\, p \qquad (2)$$

where p is the intrusion pressure (MPa), V_p is the cumulative volume intruded for a given pressure p, V_{max} is the total volume intruded for the maximum intrusion pressure and D_s is the surface fractal dimension. The interval zones of self-similarity and the different types of pore structure can be obtained from the linear sections of $log\left[\left(dV_p \,/\, dv_{max}\right) / \, d_p\right]$ versus *log p*, the slope of which yields the values of fractal dimension.

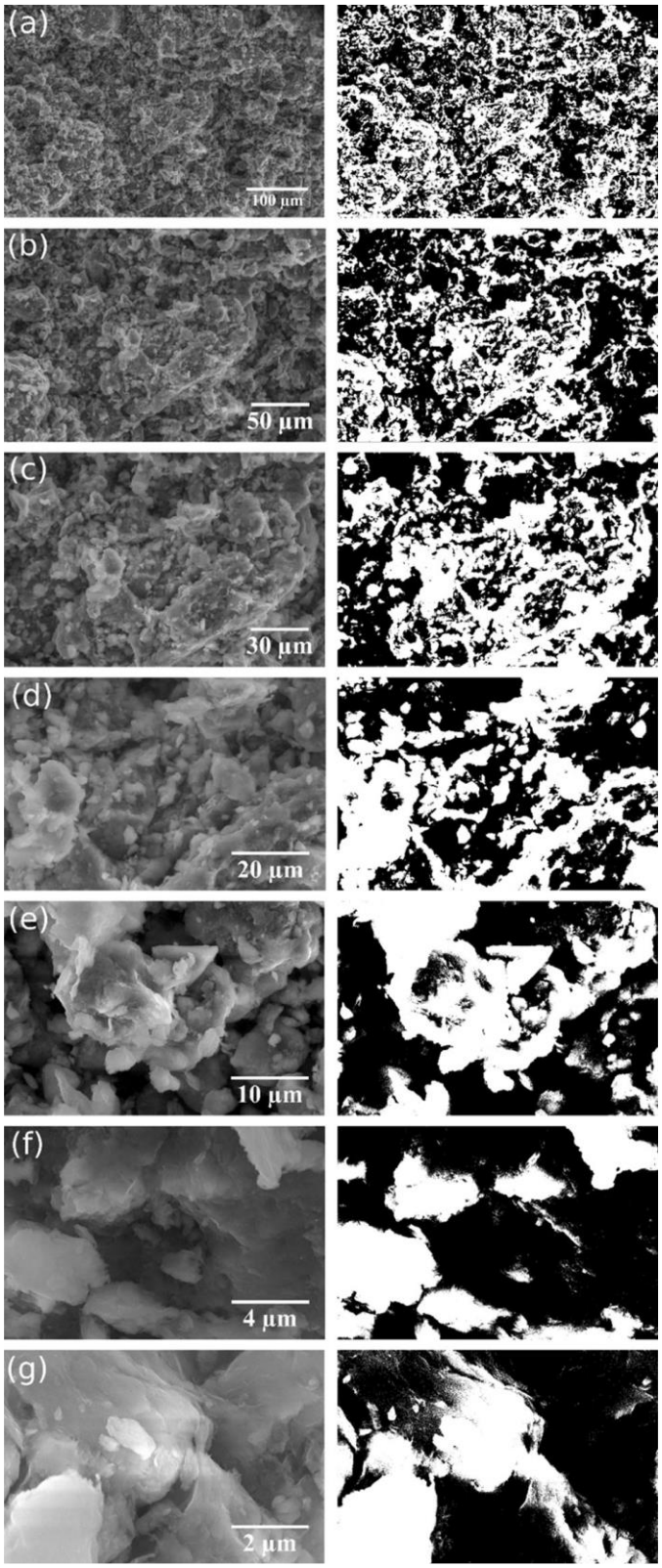

Fig. 2 ESEM observation of freeze-dried compacted bentonite (ρd = 1.27 g/cm^3) under different magnifications: a ×800, b ×1500, c ×2500, d 95000, e ×10,000, f ×25,000, g ×50,000. Left: original greyscale images; right: binary images

Fractal dimension calculated from MIP data

The results of MIP were often used for the analysis of pore structure of materials like coal, clay and so on. For calculation of the pore surface fractal dimension D_s, Eq. (2) based on Menger fractal dimension model has usually been used by other researchers [21, 27, 44, 45], which is related to derivative of the cumulative intrusion volume as a function of intrusion pressure:

$$log\left[\left(dV_p \,/\, dv_{max}\right) / \, d_p\right] \alpha (D_s - 4)\, log\, p \tag{2}$$

where p is the intrusion pressure (MPa), V_p is the cumulative volume intruded for a given pressure p, V_{max} is the total volume intruded for the maximum intrusion pressure and D_s is the surface fractal dimension. The interval zones of self-similarity and the different types of pore structure can be obtained from the linear sections of $log\left[\left(dV_p \,/\, dv_{max}\right) / \, d_p\right]$ versus $log\ p$, the slope of which yields the values of fractal dimension.

Another method is based on thermal dynamic relation of porous medium in the process of mercury intrusion porosimetry [62]. It is considering the equilibrium of surface energy increased by mercury intrusion and work done by surroundings, which is used to calculate the fractal dimension (denoted as D_z) using the following equations:

$$ln(W_n) = ln(Q_n) + C \tag{3}$$

$$\text{Let} \qquad Q_n = r_n^{2-D_z} V_n^{D_z/3} \tag{4}$$

$$W_n = \sum_{i=1}^{n} \overline{p_i} \Delta V \tag{5}$$

Substituting Eqs. (4) and (5) into Eq. (3) leads to:

$$(n(W_n) r_n^2) = D_z\, ln\left(V_n^{\frac{1}{3}} \,/\, r_n\right) + C' \tag{6}$$

where i means the ith intrusion step, n means the total intrusion number, $\overline{p_i}$ is the average intrusion pressure for ith intrusion, $\overline{p_i}\Delta V$ is the increased intrusion volume for ith intrusion, r is the pore radius, C and C′ are constants, D_z is the fractal dimension calculated from thermal dynamic relations, W_n is the accumulated surface energy and Q_n is a function of pore radius and pore volume. Both the methods [Eqs. (2) and (6)] were used for calculation of fractal dimension in this paper.

Results and discussion

Observation scale effects on fractal dimension using ESEM images

Figure 2 shows the ESEM microphotographs of compacted bentonite with initial dry density of 1.27 g/cm^3 under different magnifications. The pore size was measured by ImageJ software. Obviously, with magnification increase, the pore size decreases. The range of pore diameters roughly corresponding to each magnification is shown in Table 3. It is obvious from images that the compacted bentonite has multiple pore systems. The clay matrix looks homogeneous under low magnification in Fig. 2a, but with increasing magnification, details of structure of the aggregates become clear. Two pore families were visually identified by Sun et al. [51]: macropores and micropores (see Fig. 3). In this work, we investigate the data by evaluating the surface fractal dimension.

Table 3 Typical pore diameter under different magnifications

Magnification	800	1500	2500	5000	10,000	25,000	50,000
Pore diameter (μm)	10–25	6–10	4–8	2–4	1.5–3	0.5–1	0.02–0.1

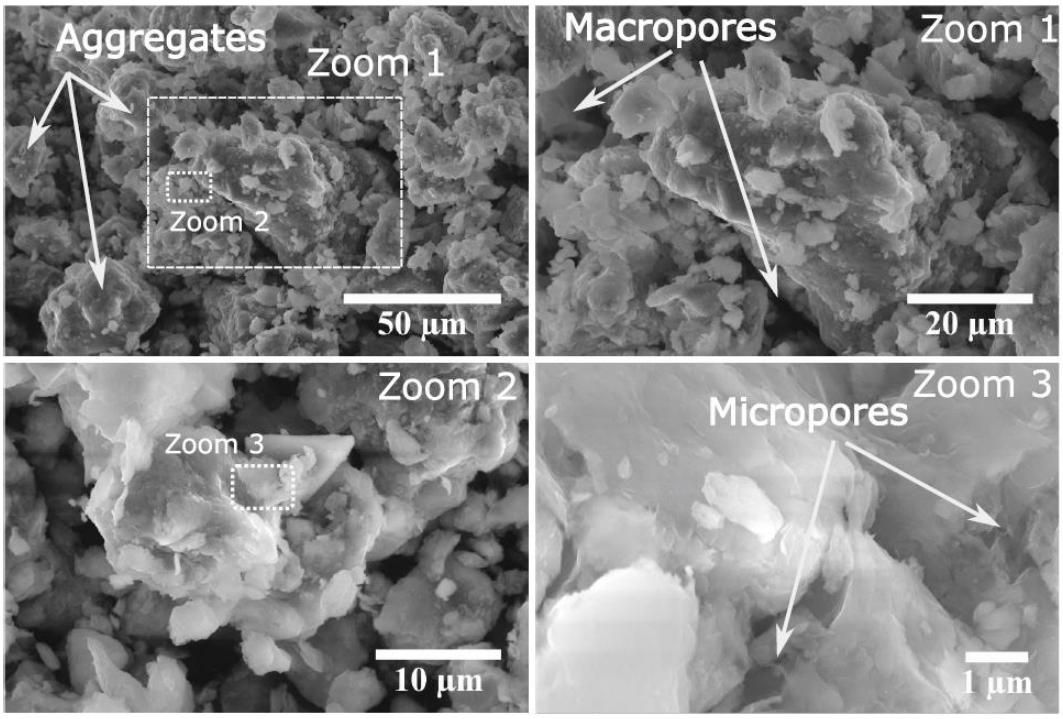

Fig. 3 ESEM micrographs of compacted bentonite with a dry density of 1.27 g/cm^3 with pore families of macropores and micropores [51]

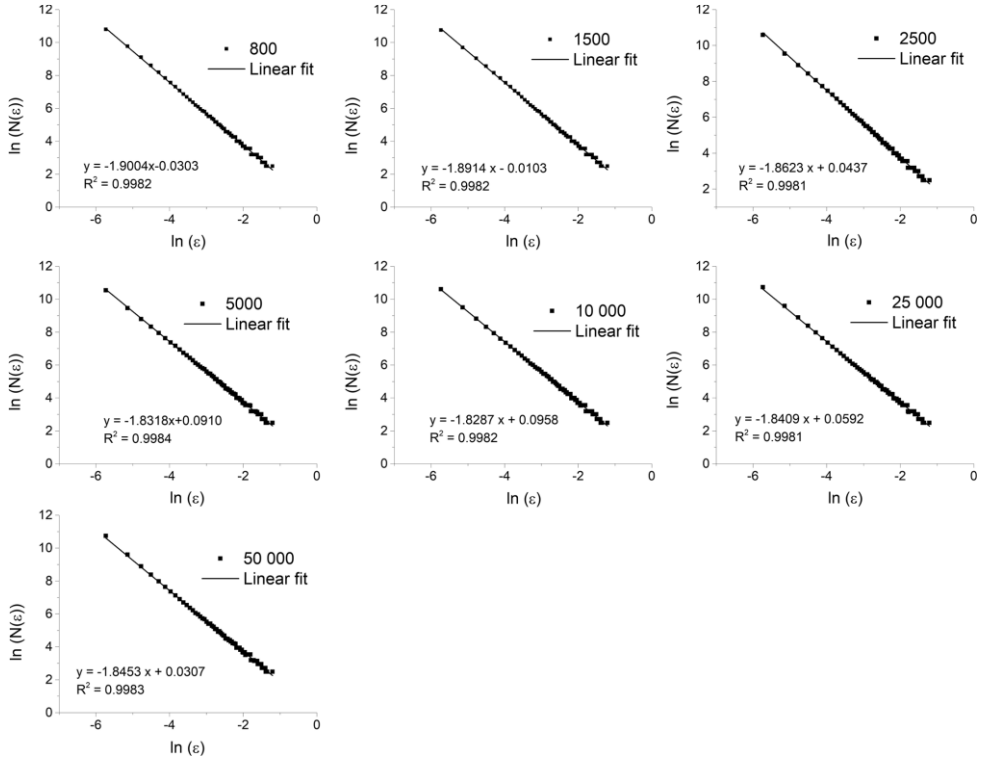

Fig. 4 Surface fractal dimension (Db) of dry density of 1.27 g/cm3 with different magnifications from ESEM microphotographs

Although the microphotographs are in two dimensions, they still represent surface roughness under different magnifications. The surface fractal dimension (Db) was used to analyse the roughness of the clay surface. Because of the 2D images, the surface fractal dimension will be between 1 and 2. The box counting method mentioned above and demonstrated in Fig. 1 was used. Figures 4 and 5 show the results of box counting methods for dry density of 1.27 g/cm^3 and 1.9 g/cm^3 separately. The linear equation with the real box counting data has a high correlation coefficient of more than 0.997 for all the cases, which indicates that the pore structures of compacted bentonite have high fractal characteristics. The relation between fractal dimension and magnification for low and high dry density samples is shown in Fig. 6. The results show a decrease in Db with increasing magnification, which is followed by an increase at high magnifications. (The increase is, however, indicated by few data points only.) Db has a linear relationship with logarithm of magnification for both dry densities until the threshold value at magnification of 10,000 for lower dry density and 25,000 for higher dry density samples. The same linear trend was observed for soils by Dathe et al. [6] and for rocks by Liu et al. [31]. At low magnification, the microphotographs contain more aggregates than those at high magnification, which makes the surface more irregular.

Finally, we also evaluated possible effect of porosity on fractal dimension (Fig. 7). This figure shows that fractal dimension does not correlate significantly with the porosity.

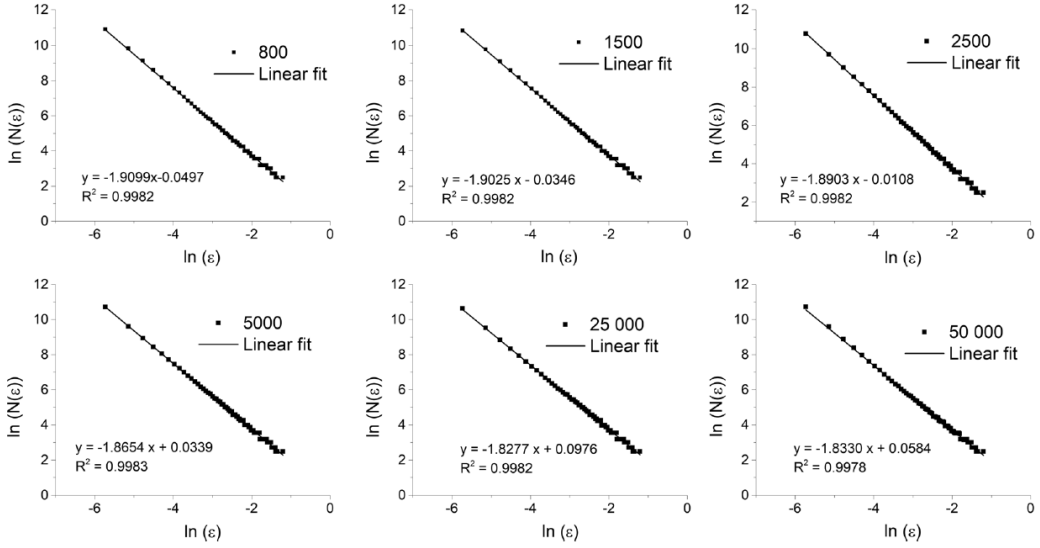

Fig. 5 Surface fractal dimension (Db) of dry density of 1.90 g/cm3 with different magnifications from ESEM microphotographs

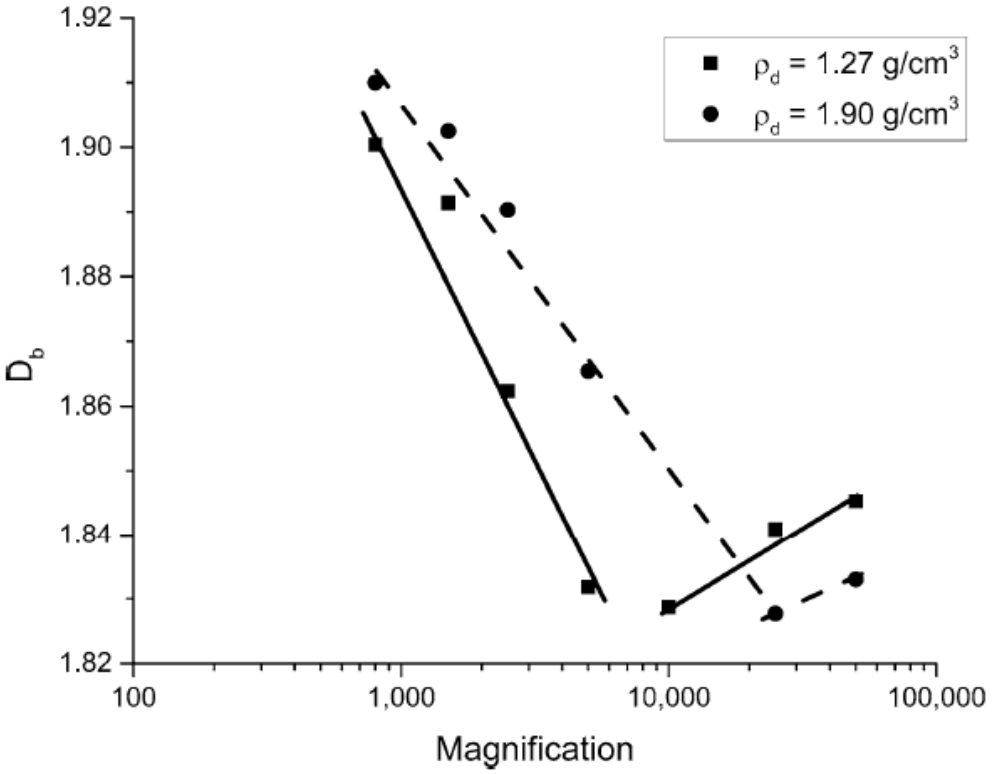

Fig. 6 Surface fractal dimension (Db) versus magnification, low dry density of 1.27 g/cm^3 (a) and high dry density of 1.9 g/cm^3 (b)

The effect of oven-drying and freeze-drying on fractal dimension using ESEM images

It is generally accepted that different drying techniques have different influence on the microstructure of compacted clays. Delage and Lefebvre [8] summarised the

water volume and total mercury intrusion volume of Champlain clay, which verified that freeze-drying can preserve its original microstructure. The oven-drying produces large shrinkage, especially for high water content samples. Keiser et al. [24] studied influence of three different drying techniques (drying in ambient air, oven-drying and freeze-drying) on the grain size of clay. The results showed that soil with high clay content (>39%) was sensitive to drying techniques.

Figure 8 shows microphotographs of the freeze-dried and oven-dried samples for medium dry density of 1.6 g/ cm^3 compacted bentonite at various magnifications. The initial water content was around 10%, and the samples were identical before drying. The details of freeze-drying and oven-drying methods were described in [51].

In order to investigate the drying method, influence of the microstructure of compacted bentonite on surface fractal dimension (Db) was calculated on freeze-dried and oven-dried samples. Three initial dry densities of 1.27 g/ cm^3, 1.6 g/cm^3 and 1.9 g/cm^3 with initial water content of 10% were studied. Surface fractal dimension (Db) versus magnification for the two drying methods is shown in Fig. 9a, b and c for low, medium and high dry density samples, respectively. The fractal dimension decreased with increasing magnification regardless of the drying method. The fractal dimension was almost the same at low magnification, while the difference is increasing with magnification increase. The fractal dimension calculated from oven-dried samples shows a higher value at higher magnification for medium and high dry density samples, while little effect is observed on low dry density samples. Recall that the higher the fractal dimension, the rougher the surface is. The fractal dimension reflects that oven-drying may change the original structure which makes the clay surface more irregular with higher pore surface fractal dimension.

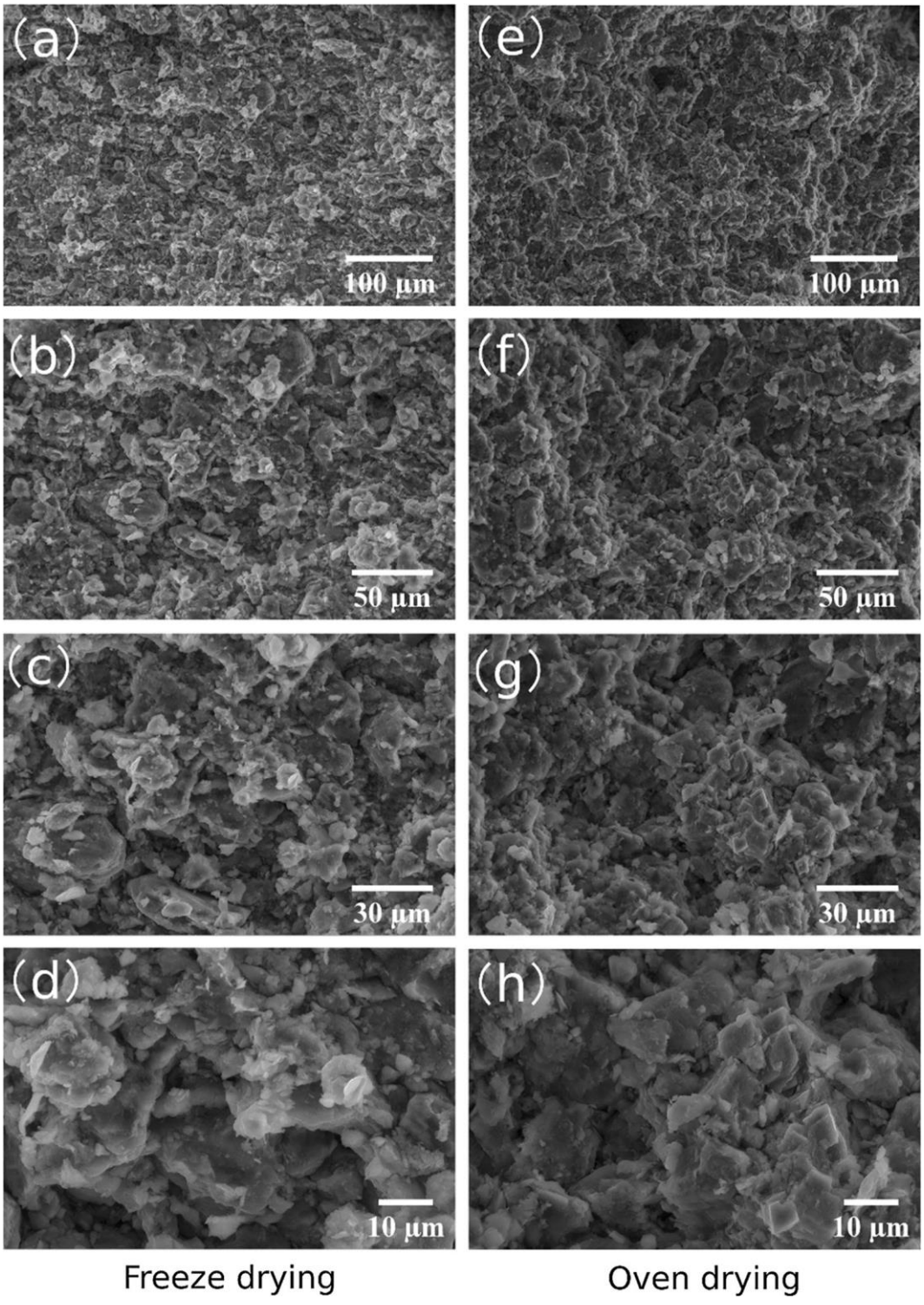

Fig. 8 Dry density of 1.60 g/cm^3 bentonite dried by freeze-drying (left) and oven-drying (right) with magnification of ×800 (a, e), ×1500 (b, f), ×2500 (c, g) and ×5000 (d, h)

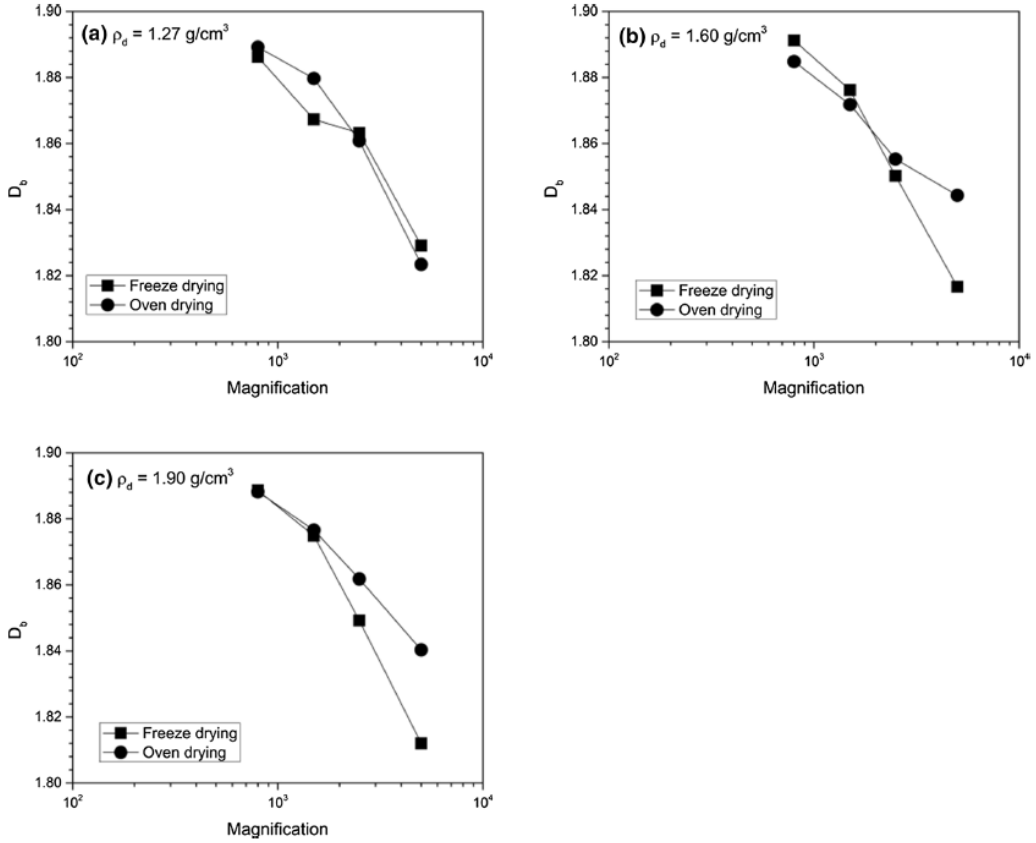

Fig. 9 Surface fractal dimension (D_b) of freeze-dried and oven-dried samples along with magnification for both dry densities

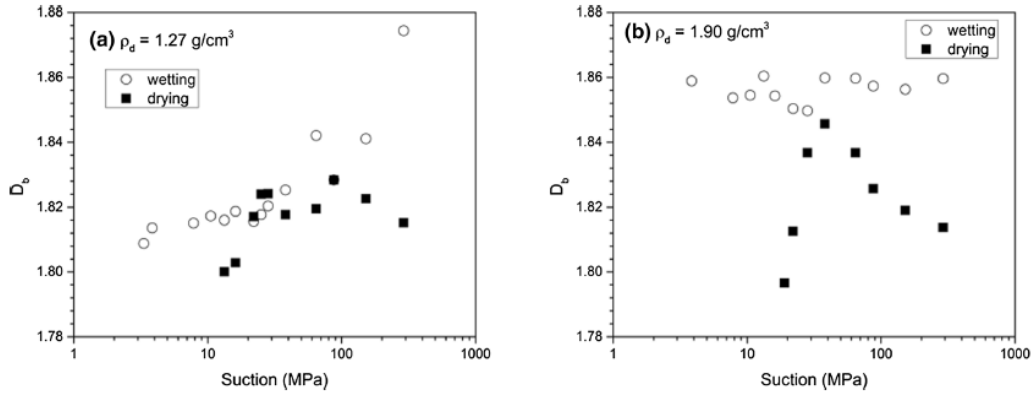

Fig. 10 Surface fractal dimension (D_b) versus suction with drying and wetting cycles, low dry density of 1.27 g/cm^3 (a) and high dry density of 1.90 g/cm^3 (b)

Table 4 Initial porosity measured by MIP test

	286.7 (%)	38 (%)	3.24 (%)
1.27	42.99	46.07	51.59
1.90	13.75	17.70	23.90

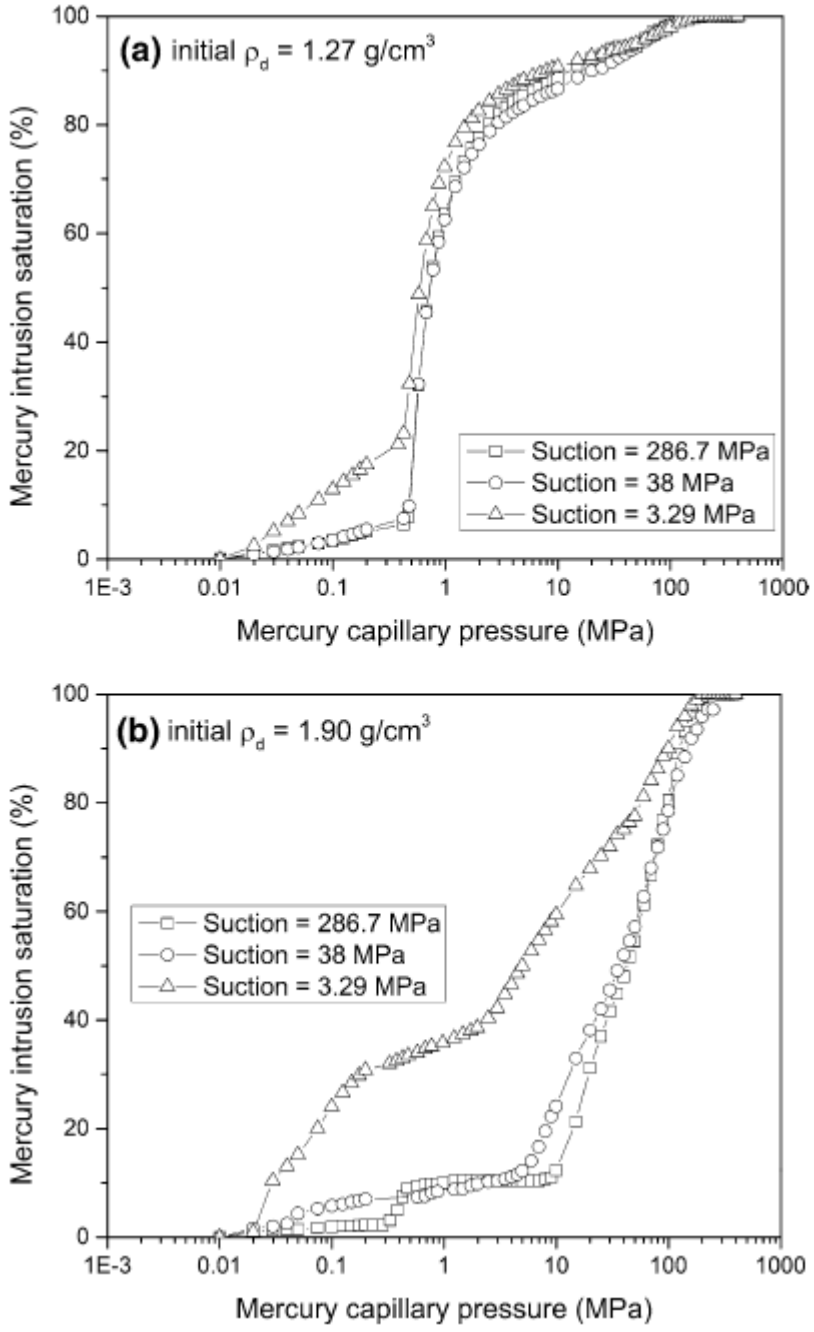

Fig. 11 Mercury intrusion saturation versus mercury capillary pressure

The effect of wetting and drying cycles on fractal dimension using ESEM images

In general, the water content influences the behaviour of compacted bentonite. The volume of soil increases when water is adsorbed, and consequently, the microstructure is affected. The clay surface was observed in different stages under various relative humidities. The compacted ovendried bentonite was first equilibrated at suction of 286.7 MPa; then, it was placed into ESEM cell and it was controlled by wetting path (relative humility 10% to 97%) and subsequently by drying path. (Relative humidity was decreased back to 10%.)

The bentonite samples compacted to dry density of 1.27 g/cm^3 and 1.9 g/cm^3 were used for ESEM observation. Twenty-four microphotographs were taken for each dry density for both wetting and drying paths. The suction can be calculated from relative humidity using Eq. (7):

$$S_t = (RT\rho_w / \omega)\, ln(1 / RH) \qquad (7)$$

where S_t is the total suction (kPa); R is the molar gas constant, which is equal to 8.314462 J/(mol K); T is the absolute temperature (K); ρ_w is the density of water; ω is the molecular mass of water vapour, which is equal to 18.016 g/mol; RH is the relative humidity of the system which is defined as the ratio of partial pressure of vapour over saturation vapour pressure.

Considering the sharp increase in swelling volume of bentonite aggregates under high relative humidity conditions [51], the magnification of 2500 was chosen for observation. It is detailed enough when compared with lower magnifications, and still the aggregates can be tracked along all relative humidities. Fractal dimension was evaluated from each microphotograph with magnification of 2500. The surface fractal dimension (D_b) versus suction is shown in Fig. 10 for dry densities of 1.27 g/cm^3 and 1.9 g/cm^3. It can be seen that for low dry density samples the fractal dimension decreased with wetting. Fractal dimension increased with drying up to suction of approximately 20 MPa, and then it decreased again for suction above 100 MPa. For high dry density samples, fractal dimension is independent of suction for wetting, while sharp increase followed by a slight decrease in D_b can be seen during drying. Similar phenomenon was observed by Beddoe and Lang [2] for cement paste and [25] for unsaturated soils.

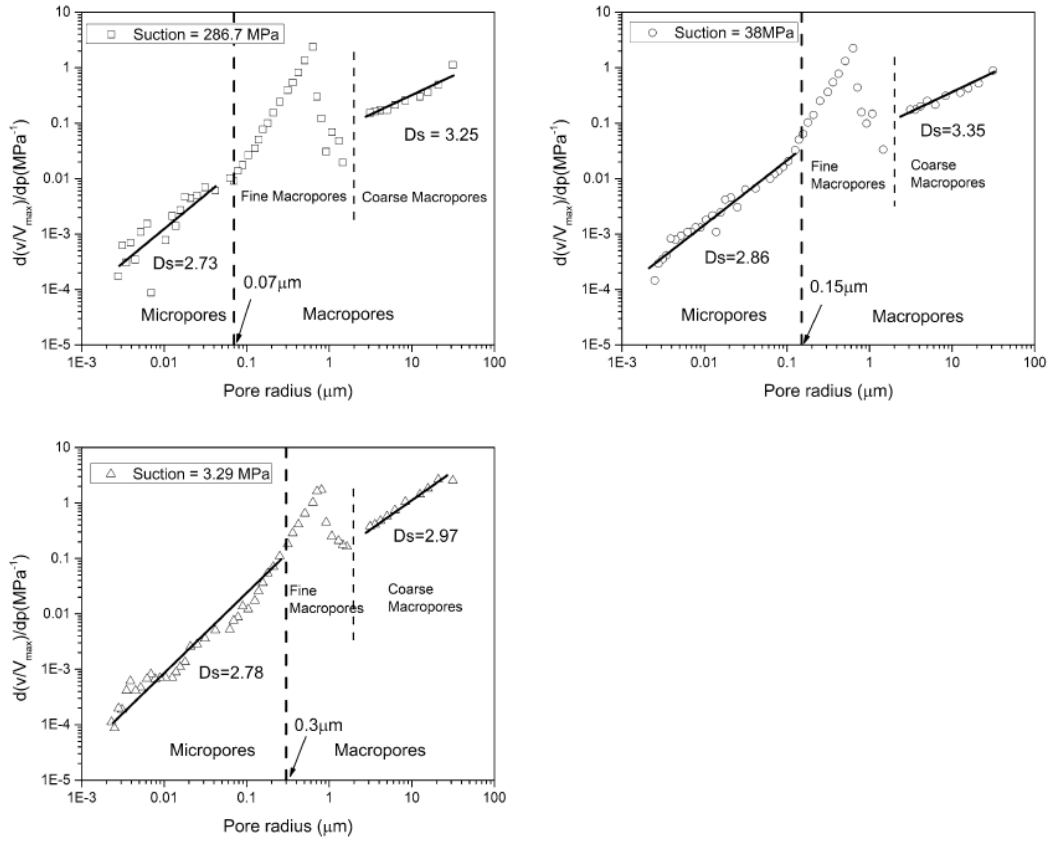

Fig. 12 Fractal dimension Ds versus applied pressure for dry density of 1.27 g/cm^3 under a suction = 286.7 MPa, b suction = 38 MPa, c suction = 3.29 MPa

Suctions effects on fractal dimension in MIP measurements

Pore surface fractal dimension Ds from MIP

The porosity measured by mercury intrusion porosimetry is shown in Table 4. It decreases with increasing dry density and suction. Figure 11 shows the original data of mercury capillary pressure versus mercury intrusion saturation degrees. The mercury intrusion saturation degree is equal to the intruded mercury volume divided by the total intruded mercury volume.

Figures 12 and 13 show the pore surface fractal dimension D_s versus pore radius from MIP data for low and high dry density samples, respectively. The fractal dimension was calculated from Eq. (2). An attempt was made to identify the interval zones of self-similarity and the different types of pore structures from the linear sections shown in Figs. 12 and 13. There, the values of D_s can be calculated from the curve slope. Figures 12 and 13 show the surface fractal dimension of dry density samples of 1.27 g/cm^3 and 1.90 g/cm^3 under three suctions. According to [7], a surface fractal dimension, D_s, which is equal to 2 representing a fissure-like porosity, while D_s is equal to 3 representing a more space-filling volumetric pore

structure. This concept was used in boom clay by Romero and Simms [45] and Romero [44] and in unsaturated soils by Farulla and Jommi [12].

In order to describe different pore size domains based on pore geometry, data for both dry densities and all suctions were plotted in one graph (Fig. 14a). Both micropores and macropores can be clearly identified based on the fractal analysis. Inside the family of macropores, fine macropores and coarse macropores can be distinguished (indicated by dashed lines in Figs. 12 and 14). Micropores are represented by parallel regression lines of all samples demonstrating similar values of surface fractal dimension D_s. It shows that this domain representing the pores inside the aggregates is compaction-insensitive. However, close to the micro–macro boundary, D_s of high density samples is influenced by applied suction (Fig. 15). The size of the micropores domain is therefore not uniquely defined and depends on the value of suction. These results confirm quantitatively the qualitative evaluation presented by Sun et al. [51].

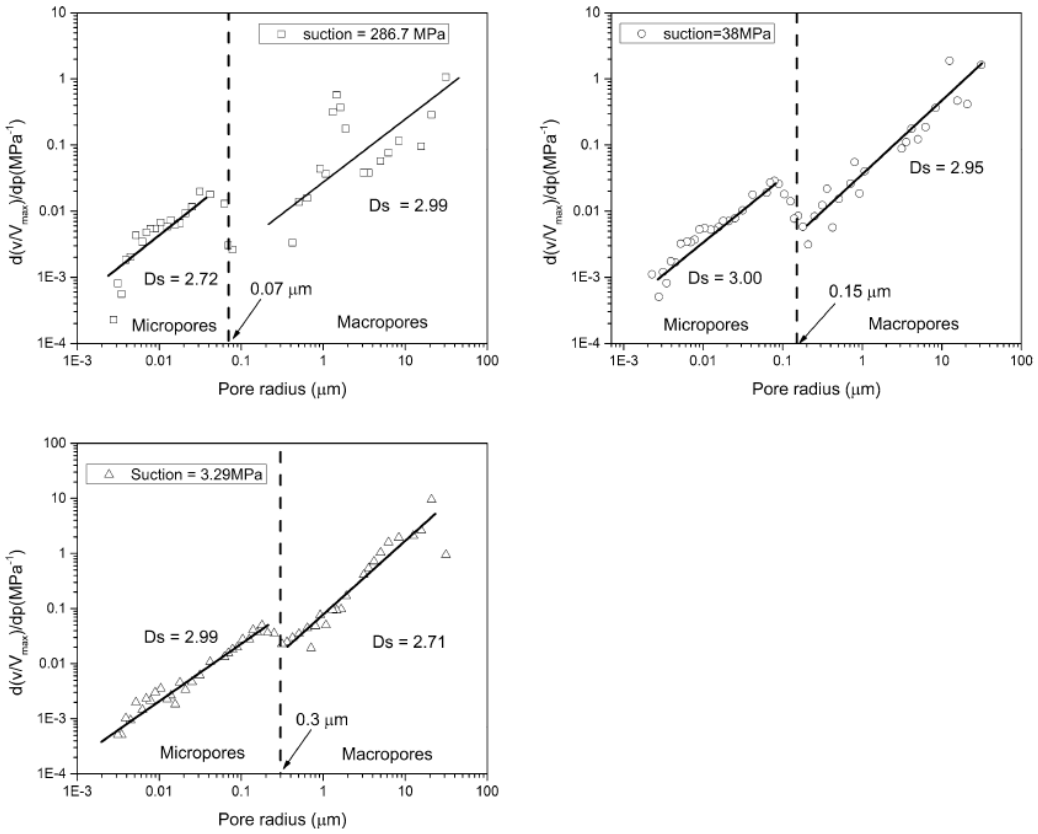

Fig. 13 Fractal dimension Ds versus applied pressure for dry density of 1.90 g/cm^3 under a suction = 286.7 MPa, b suction = 38 MPa, c suction = 3.29 MPa

The actual value of surface fractal dimension for both pore families is shown in Fig. 16. As is also clear from Fig. 14, the pores exhibit approximately similar value of

Ds. The Ds of macropores is slightly higher in the case of low dry density samples, whereas for high dry density, the values are similar. When the trend of Ds values is compared with the fractal dimension Db calculated from box counting method (Fig. 6), the Db decreased with magnification and then a little increased. (This increase can, however, be caused by small number of pores present in the evaluated images at high magnifications.) This trend is supported by Ds values, which are higher for bigger pore radius and lower for smaller pore radius. The micropores exhibit similar Ds values in the range 2.72–3.0 (Table 5, Fig. 16). It suggests similar shape of the pores, which can be described as a space-filling volumetric structure [45]. The fractal dimension of macropores in low dry density samples at high suction exceeds the value of 3. This can be caused by more complex shape of these pores, which can be also combined with microcracks. Similar values were observed by Romero and Simms [45].

Thermal fractal dimension from MIP [Eq. (6)]

Figures 17 and 18 show the pore surface fractal dimension D_z calculated from Eq. (6). The D_z is constant in all pressure ranges compared with the fractal dimension D_s.

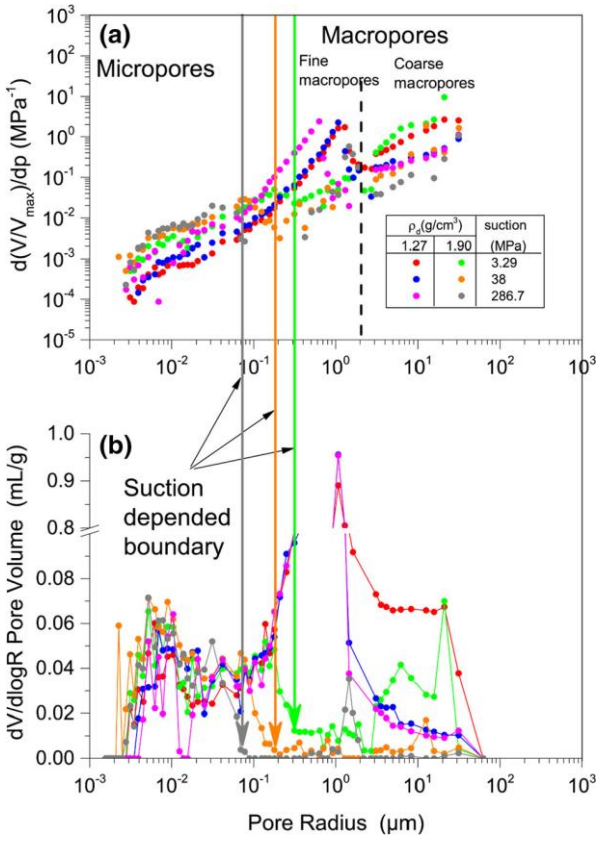

Fig. 14 Fractal dimension (a) and pore size distribution (b) with pore radius under each suction level for both dry densities

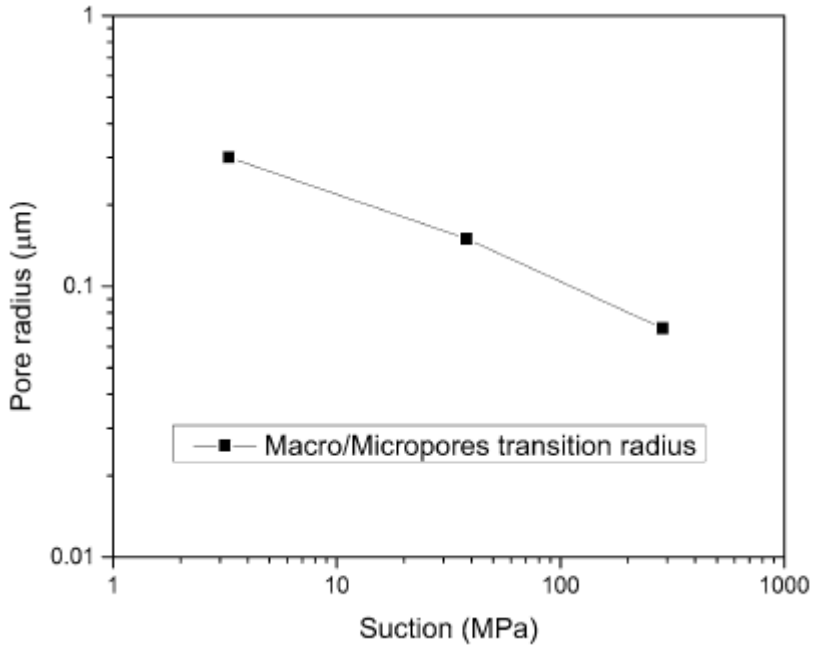

Fig. 15 Transition pore radius changing with suction for high dry density

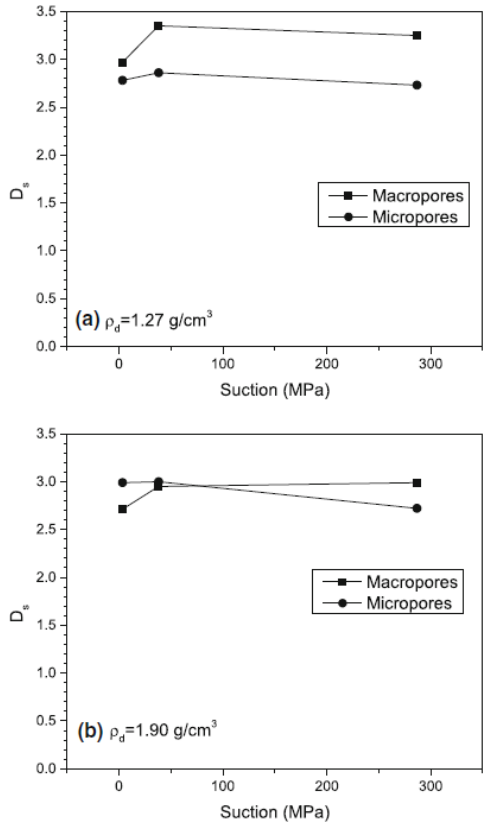

Fig. 16 Fractal dimension versus suction for various pore systems: a dry density of 1.27 g/cm^3 and b dry density of 1.9 g/cm^3

Table 5 Fractal dimension Ds with pore systems for both dry densities

Suction/MPa	1.27 g/cm^3		1.90 g/cm^3	
	Macropores	Micropores	Macropores	Micropores
286.7	3.25	2.73	2.99	2.72
38	3.35	2.86	2.95	3.00
3.29	2.97	2.78	2.71	2.99

The correlation coefficient of fitting curves of these MIP data is greater than 0.98, which indicates a good linear relationship. The fractal dimension D_z of low and high dry density samples under each suction level is shown in Fig. 19. It can be seen that, as a general trend, fractal dimension slightly increased with the suction increase. This observation is consistent with pore surface fractal dimension (D_b) evaluated using ESEM images in wetting tests, but no clear comparison is possible with D_b evaluated using drying tests and with D_s variation with suction. High dry density samples have higher fractal dimension than low dry density samples.

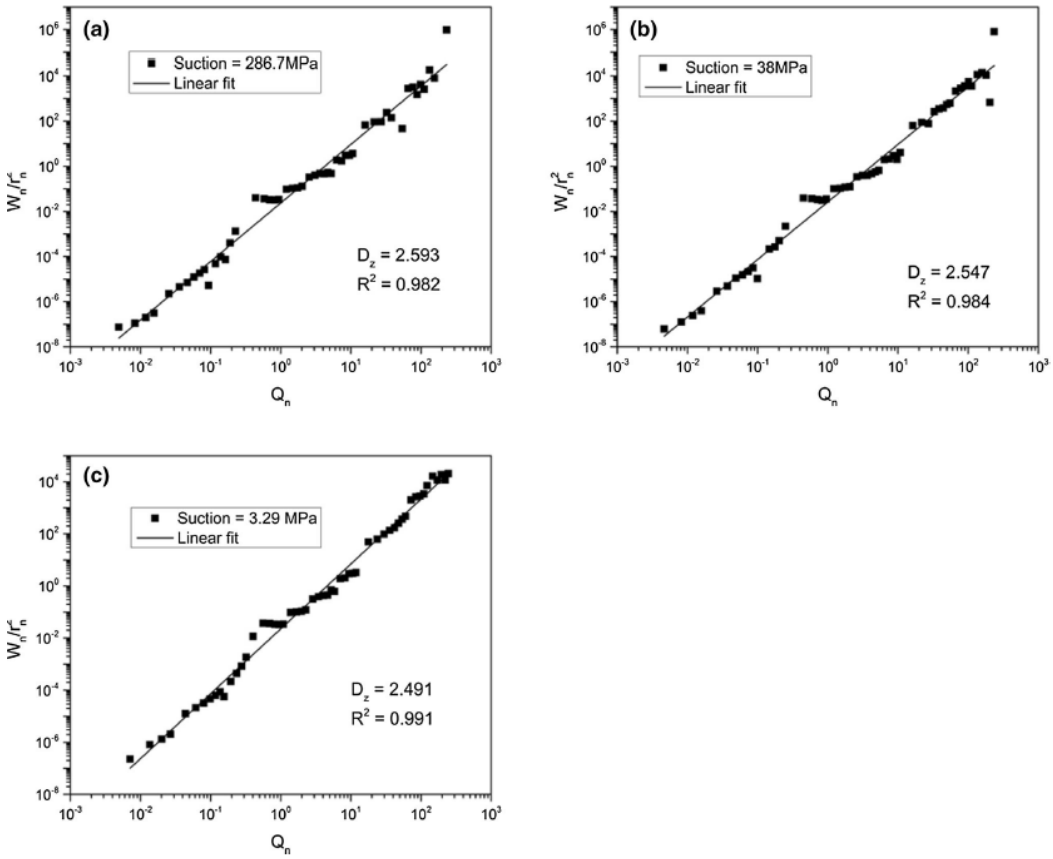

Fig. 17 Fractal dimension D_z of low dry density of 1.27 g/cm^3 under a suction = 286.7 MPa, b suction = 38 MPa, c suction = 3.29 MPa

Discussion on the differences between results obtained using ESEM and MIP methods

The MIP method is characterising indirectly the features of the solid–pore interfaces. The MIP provides a limited information, however, as it describes the surface/volume accessible by mercury only. The fractal dimension calculation is based on ideal fractal structure of Menger Sponge, which may vary with the scale D_s. The thermal fractal dimension (D_z) calculated from MIP is based on the thermal dynamic relation of porous medium in the process of mercury intrusion, which makes the fractal dimension constant through all the pressure range. Contrary, the fractal dimension calculated from ESEM uses images which cover most macropores (2500X), but the smallest and largest pores cannot be quantified using this magnification, it only represents 2D sections through the samples, and evaluation of pore boundaries is subject to uncertainties. The fractal dimensions obtained from both results thus cannot be compared directly; however, both give an insight into the pore structure characteristics quantifiable by these methods.

Conclusions

The fractal dimension of compacted bentonite using samples of different dry densities was studied by ESEM and MIP tests at different suctions. The influence of pore size, wetting and drying cycles, suction and compaction energy on fractal dimension were discussed and analysed. The different approaches based on box counting method (D_b), Menger fractal dimension model (D_s) and thermal dynamic relation (D_z) were applied. The following conclusions can be made:

1. The fractal analysis using box counting method on ESEM images proved high fractal characteristics of bentonite pore system. The fractal dimension decreases with increasing magnification due to more smooth and regular structures observed under high magnifications. However, the fractal dimension increases again when approaching extremely high magnifications. The effect of freeze-drying and oven-drying was investigated, showing higher fractal dimension of oven-dried samples. This indicates certain change in the pore structure of the samples exposed to oven-drying.

2. Two pore size domains were defined based on the fractal analysis of MIP data, namely micropores and macropores. The macropores can be subdivided into fine macropores and coarse macropores. The zones influenced by suction and different compaction energy were identified. An estimation of pore geometry of different size domains can be made based on the value of fractal dimension D_s. Pore size domains determined from fractal analysis correlate with size domains obtained by visual evaluation of MIP

distribution curves. The fractal analysis of MIP data thus proved to be a useful tool, which complements the information obtained from MIP distribution curves.

3. Comparison of the different methods of fractal analysis is problematic, due to different nature of methods used in evaluation. We can, however, conclude that often fractal dimension decreases slightly with decreasing suction (D_b evaluated using wetting tests, D_s on low dry density samples and D_z for both dry densities).

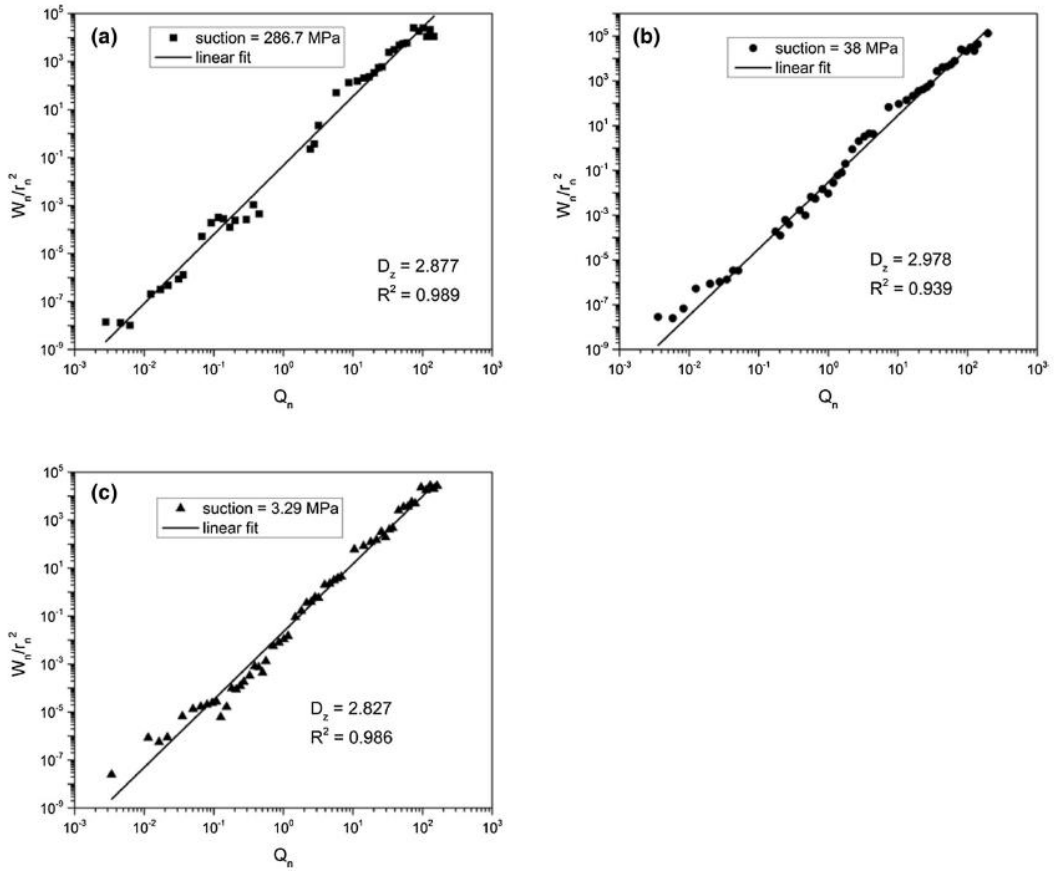

Fig. 18 Fractal dimension Dz of low dry density of 1.90 g/cm3 under a suction = 286.7 MPa, b suction = 38 MPa, c suction = 3.29 MPa

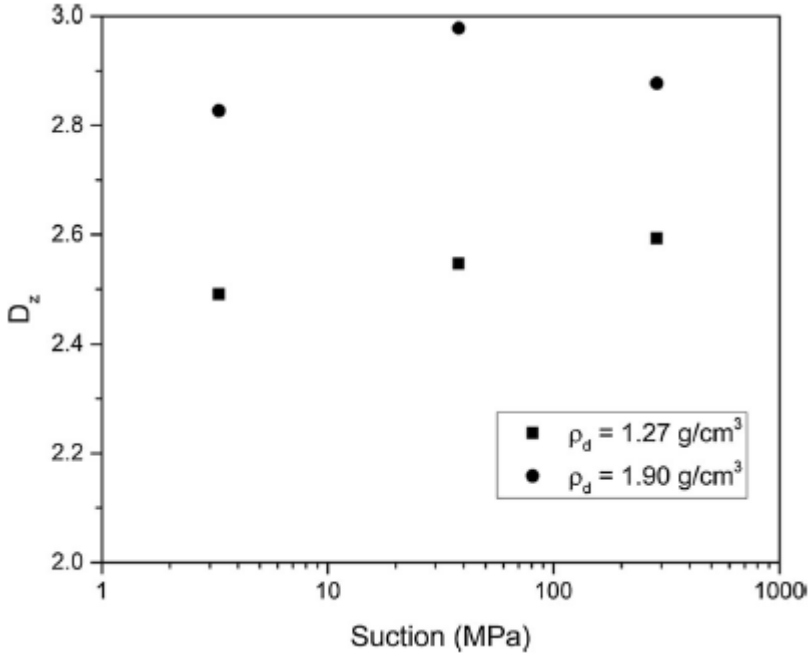

Fig. 19 Fractal dimension D_z versus suction for both dry densities

Acknowledgements

This project receives funding from the Euratom Research and Training Programme 2014–2018 under grant agreement No. 745942. The first author acknowledges support by the grants Nos. 846216 and 1476119 of the Charles University Grant Agency. Institutional support by Center for Geosphere Dynamics (UNCE/SCI/006) is greatly appreciated.

References

1. Alonso E, Vaunat J, Gens A (1999) Modelling the mechanical behaviour of expansive clays. Eng Geol 54:173–183

2. Beddoe RE, Lang K (1994) Effect of moisture on fractal dimension and specific surface of hardened cement paste by small-angle X-ray scattering. Cem Concr Res 24(4):605–612

3. Burton GJ, Pineda JA, Sheng D, Airey D (2015) Microstructural changes of an undisturbed, reconstituted and compacted high plasticity clay subjected to wetting and drying. Eng Geol 193:363–373

4. Cui ZD, Zhao LZ, Yuan L (2016) Microstructures of consolidated Kaolin clay at different depths in centrifuge model tests. Carbonates Evaporites 31(1):47–60

5. Cuisinier O, Laloui L (2004) Fabric evolution during hydromechanical loading of a compacted silt. Can Geotech J 28:483–499

6. Dathe A, Eins S, Niemeyer J, Gerold G (2001) The surface fractal dimension of the soil–pore interface as measured by image analysis. Geoderma 103(1–2):203–229

7. De Las Cuevas C (1997) Pore structure characterization in rock salt. Eng Geol 47(1–2):17–30

8. Delage P, Lefebvre G (1984) Study of the structure of a sensitive Champlain clay and of its evolution during consolidation. Can Geotech J 21(1):21–35

9. Delage P, Audiguier M, Cui YJ, Howat MD (1996) Microstructure of a compacted silt. Can Geotech J 33:150–158

10. Della VG, Jommi C, Romero E (2013) A fully coupled elastic– plastic hydromechanical model for compacted soils accounting for clay activity. Int J Numer Anal Methods Geomech 37(5):503–535

11. Deng H, Hu X, Li HA, Luo B, Wang W (2016) Improved porestructure characterization in shale formations with FESEM technique. J Nat Gas Sci Eng 35:309–319

12. Farulla CA, Jommi C (2005) Suction controlled wetting–drying cycles on a compacted scaly clay. In: Proceedings of international conference on problematic soils, vol 25, p 27

13. Flavio SA, Stefan L, Gregor PE (1998) Quantitative characterization of carbonate pore systems by digital image analysis. AAPG Bull 82(10):1815–1836

14. Florindo JB, Bruno OM (2014) Fractal descriptors based on the probability dimension: a texture analysis and classification approach. Pattern Recogn Lett 42:107–114

15. Friesen WI, Mikula RJ (1987) Fractal dimensions of coal particles. J Colloid Interface Sci 120(1):263–271

16. Gens A, Alonso EE (1992) A framework for the behaviour of unsaturated expansive clays. Can Geotech J 29(6):1013–1032

17. Grau J, Méndez V, Tarquis AM, Diaz MC, Saa A (2006) Comparison of gliding box and box-counting methods in soil image analysis. Geoderma 134(3–4):349–359

18. Hansen JP, Skjeltorp AT (1988) Fractal pore space and rock permeability implications. Phys Rev B 38(4):2635

19. Hausmannova L, Vasicek R (2014) Measuring hydraulic conductivity and swelling pressure under high hydraulic gradients. Geol Soc Lond Spec Publ 400:293–301 (SP400-36)

20. Hyslip JP, Vallejo LE (1997) Fractal analysis of the roughness and size distribution of granular materials. Eng Geol 48(3–4):231–244

21. Jommi C, Sciotti A (2003) A study of the microstructure to assess the reliability of laboratory compacted soils as reference material for earth constructions. In: Proceedings of the 2nd international conference on structural and construction engineering, vol 3, pp 2409–2415. Balkema

22. Karperien A (2013) FracLac for ImageJ. Charles Sturt University, Dubbo

23. Katz A, Thompson AH (1985) Fractal sandstone pores: implications for conductivity and pore formation. Phys Rev Lett 54(12):1325

24. Keiser L, Soreghan GS, Joo YJ (2014) Effects of drying techniques on grain-size analyses of fine-grained sediment. J Sediment Res 84(10):893–896

25. Khoshghalb A, Pasha AY, Khalili N (2015) A fractal model for volume change dependency of the water retention curve. Géotechnique 65(2):141–146

26. Komine H, Ogata N (1999) Experimental study on swelling characteristics of sand-bentonite mixture for nuclear waste disposal. Soils Found 39(2):83–97

27. Korvin G (1992) Fractal models in the earth sciences. Elsevier Science Limited, Amsterdam

28. Li J, Yin ZY, Cui Y, Hicher PY (2017) Work input analysis for soils with double porosity and application to the hydromechanical modeling of unsaturated expansive clays. Can Geotech J 54(2):173–187

29. Lin B, Cerato AB (2014) Applications of SEM and ESEM in microstructural investigation of shale-weathered expansive soils along swelling-shrinkage cycles. Eng Geol 177:66–74

30. Liu X, Nie B (2016) Fractal characteristics of coal samples utilizing image analysis and gas adsorption. Fuel 182:314–322

31. Liu K, Ostadhassan M, Zhou J, Gentzis T, Rezaee R (2017) Nanoscale pore structure characterization of the Bakken shale in the USA. Fuel 209:567–578

32. Lloret A, Villar MV (2007) Advances on the knowledge of the thermo-hydro-mechanical behaviour of heavily compacted ‘‘FEBEX’’ bentonite. Phys Chem Earth 32:701–715

33. Mahamud M, López O ´ , Pis JJ, Pajares JA (2003) Textural characterization of coals using fractal analysis. Fuel Process Technol 81(2):127–142

34. Manca D, Ferrari A, Laloui L (2016) Fabric evolution and the related swelling behaviour of a sand/bentonite mixture upon hydro-chemo-mechanical loadings. Géotechnique 66(1):41–57

35. Mandelbrot BB (1977) Fractals: form, chance and dimension. Freeman, San Francisco

36. Mašín D (2013) Double structure hydromechanical coupling formalism and a model for unsaturated expansive clays. Eng Geol 165:73–88

37. Mašín D (2017) Coupled thermohydromechanical double-structure model for expansive soils. ASCE J Eng Mech 143(9):04017067

38. Monroy R, Zdravkovic L, Ridley A (2010) Evolution of microstructure in compacted London Clay during wetting and loading. Géotechnique 60(2):105–119

39. Montes-H G (2005) Swelling–shrinkage measurements of bentonite using coupled environmental scanning electron microscopy and digital image analysis. J Colloid Interface Sci 284(1):271–277

40. Niu WJ, Ye WM, Song X (2019) Unsaturated permeability of Gaomiaozi bentonite under partially free-swelling conditions. Acta Geotech. https://doi.org/10.1007/s11440-019-00788-9 (inprint)

41. Přikryl R, Weishauptová Z (2010) Hierarchical porosity of bentonite-based buffer and its modification due to increased temperature and hydration. Appl Clay Sci 47(1–2):163–170

42. Pyun SI, Rhee CK (2004) An investigation of fractal characteristics of mesoporous carbon electrodes with various pore structures. Electrochim Acta 49(24):4171–4180

43. Rasband WS (2016) ImageJ. U. S. National Institutes of Health, Bethesda, Maryland, USA. https://imagej.nih.gov/ij/

44. Romero MEE (1999) Characterisation and thermo-hydro-mechanical behaviour of unsaturated Boom clay: an experimental study. Universitat Politécnica de Catalunya, Barcelona

45. Romero E, Simms PH (2008) Microstructure investigation in unsaturated soils: a review with special attention to contribution of mercury intrusion porosimetry and environmental scanning electron microscopy. Geotech Geol Eng 26:705–727

46. Romero E, Della VG, Jommi C (2011) An insight into the water retention properties of compacted clayey soils. Ge´otechnique 61(4):313

47. Sánchez M, Gens A, Villar MV, Olivella S (2016) Fully coupled thermo-hydro-mechanical double-porosity formulation for unsaturated soils. Int J Geomech 16(6):D4016015

48. Schepers HE, Van Beek JH, Bassingthwaighte JB (1992) Four methods to estimate the fractal dimension from self-affine signals (medical application). IEEE Eng Med Biol Mag 11(2):57–64

49. Seiphoori A, Ferrari A, Laloui L (2014) Water retention behaviour and microstructural evolution of MX-80 bentonite during wetting and drying cycles. Géotechnique 64(9):721–734

50. Stastka J, Smutek J (2015) Experimental works with bentonite pellets at the CEG. In: LUCOEX conference and workshop—fullscale demonstration tests in technology development of repositories for disposal of radioactive waste, Oskarshamn, Sweden, pp 179–184

51. Sun H, Mašín D, Najser J, Neděla V, Navrátilová E (2019) Bentonite microstructure and saturation evolution in wetting– drying cycles evaluated using ESEM, MIP and WRC measurements. Géotechnique 69(8):713–726

52. Turcotte DL (2002) Fractals in petrology. Lithos 65(3–4):261–271

53. Vallejo LE (1996) Fractal analysis of the fabric changes in a consolidating clay. Eng Geol 43(4):281–290

54. Wang Q, Cui YJ, Tang AM, Li XL, Ye WM (2014) Time- and density-dependent microstructure features of compacted bentonite. Soils Found 54(4):657–666

55. Watt GR, Griffin BJ, Kinny PD (2000) Charge contrast imaging of geological materials in the environmental scanning electron microscope. Am Miner 85(11–12):1784–1794

56. Wong PZ, Howard J (1986) Surface roughening and the fractal nature of rocks. Phys Rev Lett 57:637–642

57. Xiang G, Xu Y, Xie S, Fang Y (2017) A simple method for testing the fractal dimension of compacted bentonite immersed in salt solution. Surf Rev Lett 24(03):1750040

58. Xu Y (2018) The fractal evolution of particle fragmentation under different fracture energy. Powder Technol 323:337–345

59. Xu Y (2018) Shear strength of granular materials based on fractal fragmentation of particles. Powder Technol 333:1–8

60. Xu Y (2018) Fractal model for the correlation relating total suction to water content of bentonites. Fractals 26(03):1850028

61. Yang F, Ning Z, Liu H (2014) Fractal characteristics of shales from a shale gas reservoir in the Sichuan Basin, China. Fuel 115:378–384

62. Zhang B, Li S (1995) Determination of the surface fractal dimension for porous media by mercury porosimetry. Ind Eng Chem Res 34(4):1383–1386

25 Effect of the preparation of lime putties on their properties

Eva Navrátilová1, Eva Tihlaříková1, Vilém Neděla1, Pavla Rovnaníková2 & Jaroslav Pavlík3

1 *The Czech Academy of Science, Institute of Scientific Instruments, Brno, 612 64, Czech Republic.*
2 *Institute of Chemistry, Faculty of Civil Engineering, Brno University of Technology, Brno, 602 00, Czech Republic.*
3 *Lhoist, Lime kiln Čertovy schody a.s., Tmaň, 267 21, Czech Republic.*

Abstract

In the study of lime as the basic component of historical mortars and plasters, four lime putties prepared from various kinds of lime of various granulometry and by various ways of preparation were evaluated. The rheological properties and micro-morphologic changes, growing of calcite crystals, and rate of carbonation were monitored. The lime putty prepared from lump lime achieves the best rheological properties, yield stress 214.7 Pa and plastic viscosity 2.6 Pa·s. The suitability of this lime putty was checked by testing the development of calcium hydroxide and calcite crystals using scanning electron microscopy and environmental scanning electron microscopy. The disordered crystals of calcium hydroxide exhibit better carbonation resulting in the large crystals of calcite; therefore, the mortar prepared from the lump lime has the highest flexural strength and compressive strength 0.8/2.5 MPa, its carbonation is the fastest and exhibits the longest durability. Also, thanks to the micro-morphological characterization of samples in their native state by means of environmental scanning electron microscopy, the new way of lime putty preparation by mixing was proven. The preparation consists in the mechanical crash of the lime particles immediately after hydration. This enables the properties of putty prepared from lump lime to be nearly reached.

Introduction

In the past lime putty was traditional material with a wide application in construction. It used to be prepared from lump lime and it featured good workability, plasticity and durability. The traditional preparation of lime putty was replaced by modern chemical-technological processes. Lime putty is essential for the restoration of historic plaster, wall painting, sgraffito etc[1]. Lime putty is obtained by the hydration of calcined limestone in an excess of water according to the following equation:

$$CaO + H_2O \rightarrow Ca(OH)_2 + 65\ kJ.\ mol^{-1} \quad (1)$$

It is a strongly exothermic reaction which leads to the enlargement of volume. The ratio of change in the particles' volume of CaO to $Ca(OH)_2$ is 16.9/33.2. Lime putty is an aqueous suspension of calcium hydroxide particles. A small proportion of calcium carbonate can be present due to incomplete calcination of limestone or reaction with carbon dioxide. The process of hydration of CaO is dependent upon the reactivity of quicklime, which is influenced by the temperature of calcination of CaCO3. CaO is released from limestone and the pore structure of grains is generated during calcination. The physical properties of quicklime, such as porosity, density, grain size and hydration rate, are dependent on the temperature of calcination. Furthermore, the process of CaO hydration is dependent on the distribution of particle size, the quantity and quality of the added water, the temperature of the water, the presence of impurities in the quicklime, and the presence of ions in the mixing water[2,3]. The specific surface area is the most reliable parameter which can be used to evaluate the reactivity of quicklime. The higher specific surface area of quicklime is the reason for its higher reactivity[4–7]. The burning of CaO leads to changes in the microstructure and these differences in the microstructure of CaO crystals burnt at different temperatures result in different hydration activity of CaO[8]. The hydration process of quicklime is also affected by the particle size of CaO. The finer particles are more sintered and thus they cause a low reactivity of quicklime. The coarser particles will contain some amount of unburned $CaCO_3$, which is an inert material in quicklime[4,9]. Various methods and the temperature of hydration of CaO lead to obtaining lime putty with a different morphology, size, and size distribution of calcium hydroxide crystals. The calcium hydroxide crystals with a size of approximately 100 –110 nm originate during the hydration in the excess of water and at a lower temperature[5]. Calcium hydroxide hydrated in the excess of water exhibits crystals which have clearly visible edges. Calcium hydroxide hydrated in a smaller amount of water is without the sharp edges of crystal and tends to form agglomerates[10].

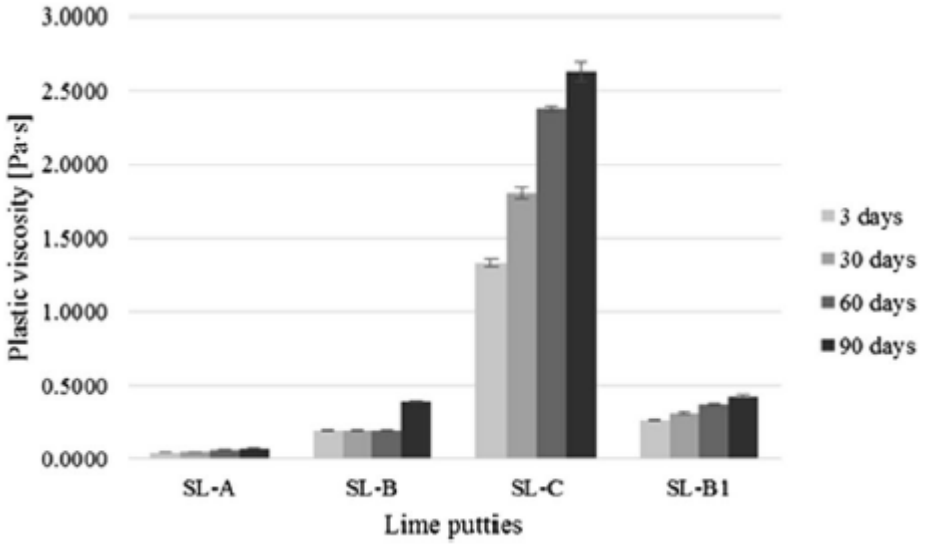

Figure 1. Average values of plastic viscosity of lime putties at different ages.

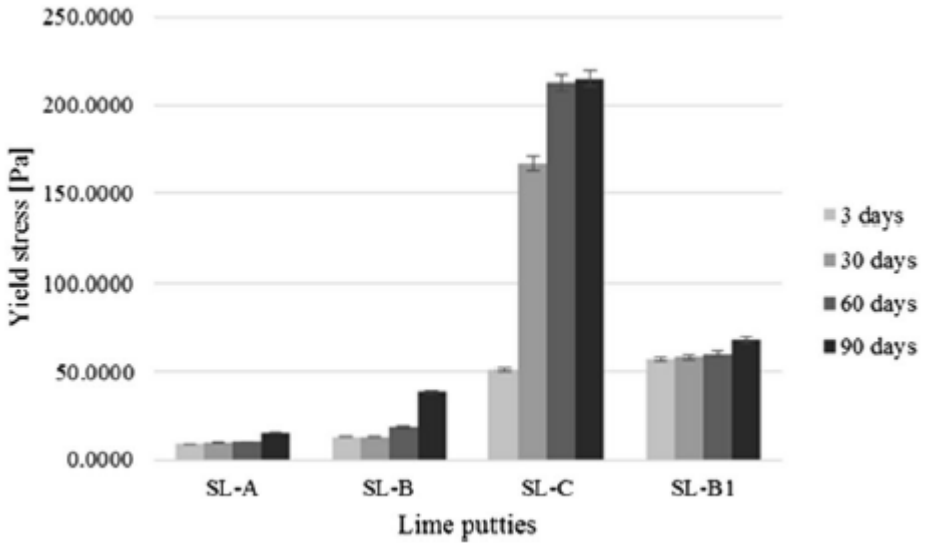

Figure 2. Average values of yield stress of lime putties at different ages.

The long-term maturing of lime putty in an excess of water has a beneficial effect on its quality. Such stored lime putty has better plasticity, workability, and it retains sufficient water to prepare plaster of a high durability[11–13]. The microstructure of calcium hydroxide is changed during the maturing of lime putty[14,15] and the $Ca(OH)_2$ crystals diminish. The $Ca(OH)_2$ crystals with a size of between 37–50 nm occur in freshly hydrated lime - the crystals have a size of 34 nm at the age of two months and 28 nm at the age of 14 months. The specific surface area of the calcium hydroxide increases with this reduction in the size of the calcium hydroxide crystals[11,14–16]. Furthermore, the calcium hydroxide crystals change their form from large prismatic crystals to submicrometre plate crystals and secondary nucleation

of nanometre plate crystals[11,15,17]. The change in the original prismatic crystals into smaller submicrometre plate crystals with a higher specific surface area leads to an increased adsorption of water and thereby increases plasticity and workability[10,11,15,17]. Atzeni *et al.*[16] examined the effect of the maturation of lime putty on its viscosity. They prepared three lime putties with different times of maturation. Observation of the lime putties by TEM revealed that the calcium hydroxide crystals reduce in size over time. The oldest lime putty showed the greatest shear resistance and it was even more viscous than the three-month-old lime putty as well as the non-matured lime putty. The non-matured lime putty contains the agglomerates of calcium hydroxide and these agglomerates are covered by a thin film of water, which acts as a lubricant, and so this lime putty is extremely fluid. The prolonged ageing of lime putty leads to a higher viscosity, which is caused by the change in its microstructure and the specific surface area of calcium hydroxide during the ageing process. Analogous to the investigation of lime, Paiva *et al.*[18] prepared lime mortars with a different maturation period. The mortars matured for seven days were more viscous in their fresh state, showed higher strengths at the age of 90 days, and exhibited a lower capillary absorption coefficient than the mortars without maturation. Margalha *et al.*[19] found that slaked lump lime provides a binder with a higher proportion of active lime than powdered lime. The mortars prepared from the micronized lime show a higher porosity with larger pores, leading to a reduction in their mechanical strengths. The mortars prepared from lump lime exhibit higher strengths, but they require over-ageing treatment because of their shrinking.

Results

Rheology of the lime putties

The results of the measurement of the plastic viscosity and the yield stress of lime putties SL-A, SL-B, SL-C, and SL-B1 during their maturation at the age of 3, 30, 60, and 90 days are shown in Figs 1 and 2. The graphs show an increase in the plastic viscosity and the yield stress of the lime putties with a prolonged period of maturation. The increase in the values of the plastic viscosity and the yield stress in lime putties SL-A, SL-B, and SL-B1 is not so apparent at the ages of 3, 30, and 60 days compared to lime putty SL-C. The values of the plastic viscosity and the yield stress of lime putty SL-B increase significantly at the age of 90 days. The increase in the values of the plastic viscosity and the yield stress is slow at the age of 90 days for lime putties SL-A and SL-B1. The highest plastic viscosity and yield stress were found in the sample from lump lime C. Lime putty SL-A, prepared from lime containing grains under 90 μm, showed the lowest plastic viscosity and yield stress. Lime putty SL-B, prepared from lime containing grains under 200 μm, reached only

slightly higher values of plastic viscosity and yield stress than lime putty SL-A. However, the differences in the values of yield stress and plastic viscosity were greater at the age of 90 days for lime putties SL-A and SL-B. The disruption of the particles by mixing affected the plastic viscosity and yield stress of lime putty SL-B1, which reached higher values of plastic viscosity and yield stress than lime putty SL-B, which was not exposed to mixing after hydration, and the grains of the lime are not in any way disrupted. The results of the rheological measurements are consistent with previously published results[16,18,19].

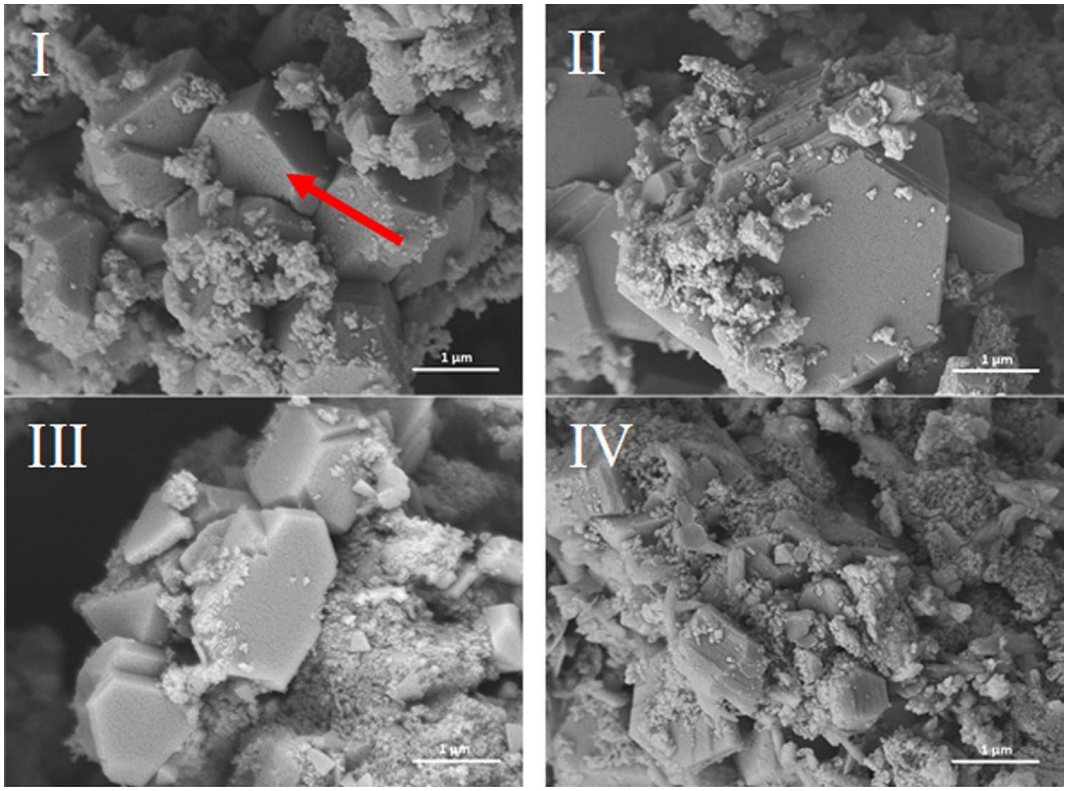

Figure 3. Lime putty SL-A at the age of 3 days (I), 30 days (II), 60 days (III) and 90 days (IV).

Image of the microstructure of the lime putties

Figures 3–6 illustrate the microstructure of lime putties SL-A, SL-B, SL-C, and SL-B1 during their maturation at the age of 3, 30, 60, and 90 days. Figures 3I and 4I show the prismatic hexagonal crystals of calcium hydroxide created in samples SL-A and SL-B. Lime putties SL-C and SL-B1 do not contain the significant crystals of calcium hydroxide which are present in samples SL-A and SL-B. The crystals in these cases are coated with a layer of hydrogel ($Ca(OH)_2$.aq), which is already discernible after three days of hydration (maturation) Figs 5I and 6I. During the maturation of all the lime putty samples, the regular hexagonal crystals of calcium hydroxide are transformed into smaller irregular crystals which are coated with a layer of hydrogel. The gradual transformation of the calcium hydroxide crystals is

well evident in Figs 3II– IV, 4II–IV, 5II–IV, and 6II–IV. The transformation of the calcium hydroxide crystals and hydrogel formation of lime putties SL-A and SL-B is slower than in the samples SL-C and SL-B1. The micrographs in Figs 5III and 6III show the calcium hydroxide crystals coated with a layer of hydrogel which originates faster and more intensively in samples SL-C and SL-B1. Conversely, the micrographs in Figs 3III and 4III present the microstructure of lime putties SL-A and SL-B with clearly visible crystals of calcium hydroxide. The layer of hydrogel increases during the maturation of lime putties. The amount of hydrogel is greatest at the age of 90 days in sample SL-C and in sample SL-B1 Figs 5IV and 6IV. The formation of hydrogel on the surface of the crystals of calcium hydroxide proceeds best in sample SL-C, which was prepared from lump lime where the regular hexagonal crystals of calcium hydroxide were not fully developed. The process of particle disruption immediately after hydration enables the acceleration of the process of hydrogel formation on the surface of the crystals of calcium hydroxide, and, moreover, the process of transformation of the regular crystals of calcium hydroxide to the smaller irregular ones is faster. The microstructure images of lime putties confirm the results provided by the performed rheological measurements.

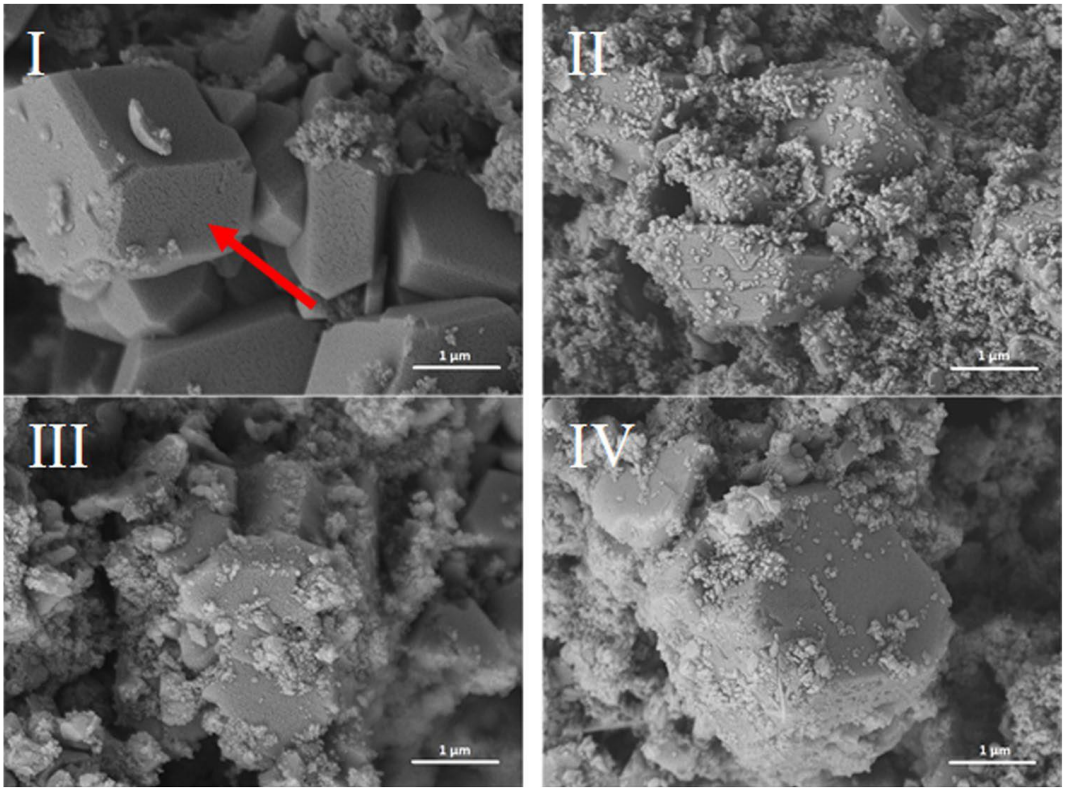

Figure 4. Lime putty SL-B at the age of 3 days (I), 30 days (II), 60 days (III) and 90 days (IV).

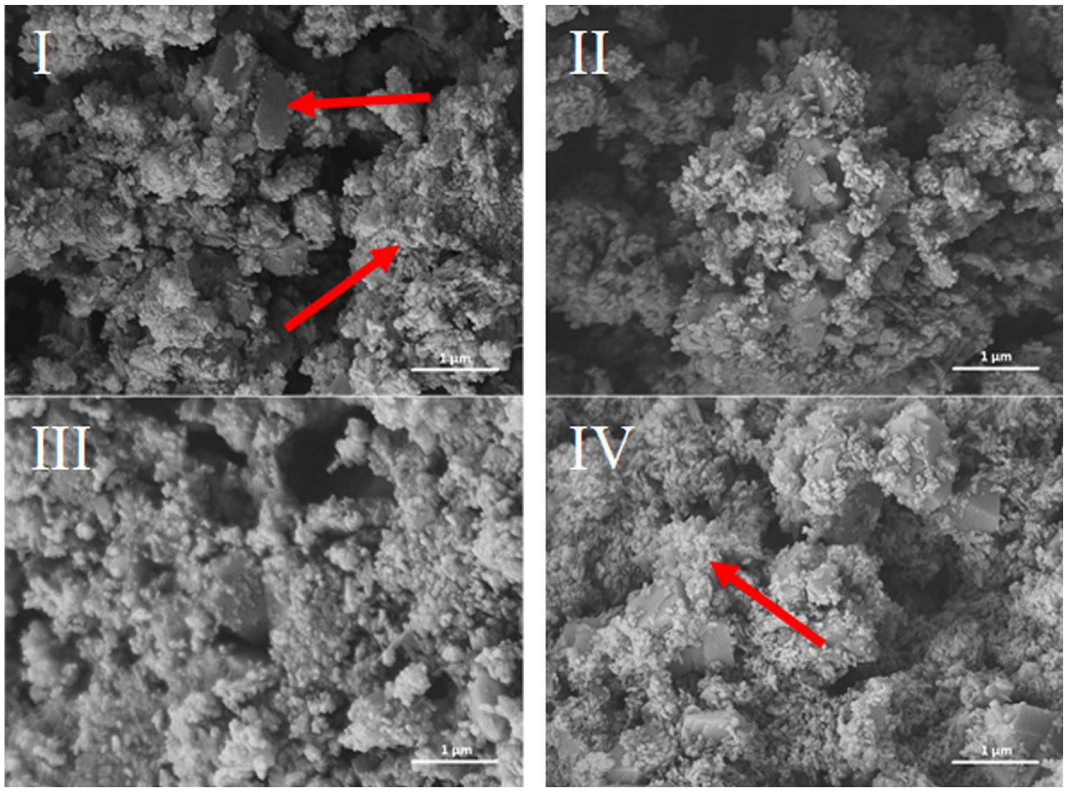

Figure 5. Lime putty SL-C at the age of 3 days (I), 30 days (II), 60 days (III) and 90 days (IV).

The HR-ESEM images of lime putty SL-A without preparation of the sample and sputtering at the age of 3 and 30 days are shown in Fig. 7. Owing to the sophisticated and, in this work, experimentally proven method for the preparation of samples for HR-SEM, the images from the HR ESEM provide very similar information: significant hexagonal crystals of calcium hydroxide see Fig. 7I. The regular hexagonal crystals of calcium hydroxide are gradually transformed into smaller irregular crystals coated with a layer of hydrogel during the maturation of lime putty Fig. 7II. The HR-ESEM is a preferable method for observing micro-morphological changes during the maturation of lime putties because it is not necessary to use complicated sample preparation methods. Incorrectly sputter coated samples can lead to the formation of artefacts which can distort the micro-morphological interpretation. The HR-SEM is a suitable method for the evaluation of morphological changes during the maturation of lime putties; however, this method places heightened demands on the sample preparation, and, therefore, it can introduce inaccuracies into the characterization of the microstructure. The HR-ESEM is a more accurate, faster, and easier method for the evaluation of the morphology lime putties, as the samples are not treated at all before their observation[20,21]. Thus, there are no artefacts distorting the microstructural interpretation.

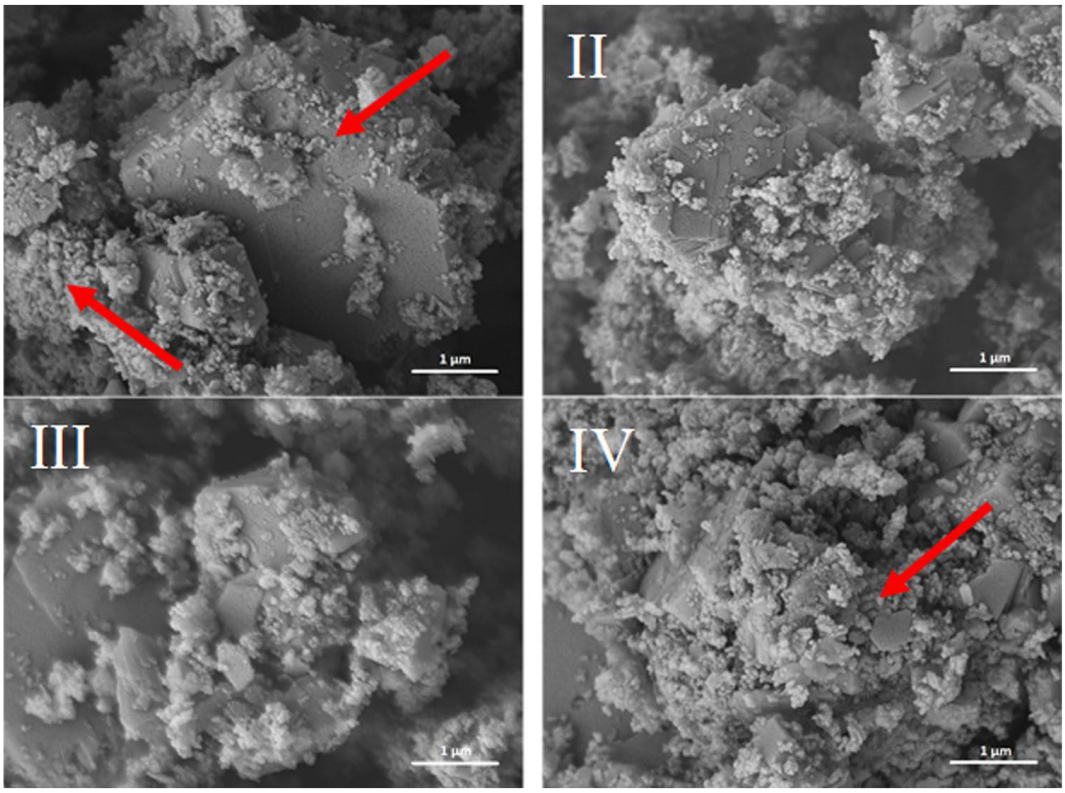

Figure 6. Lime putty SL-B1 at the age of 3 days (I), 30 days (II), 60 days (III) and 90 days (IV).

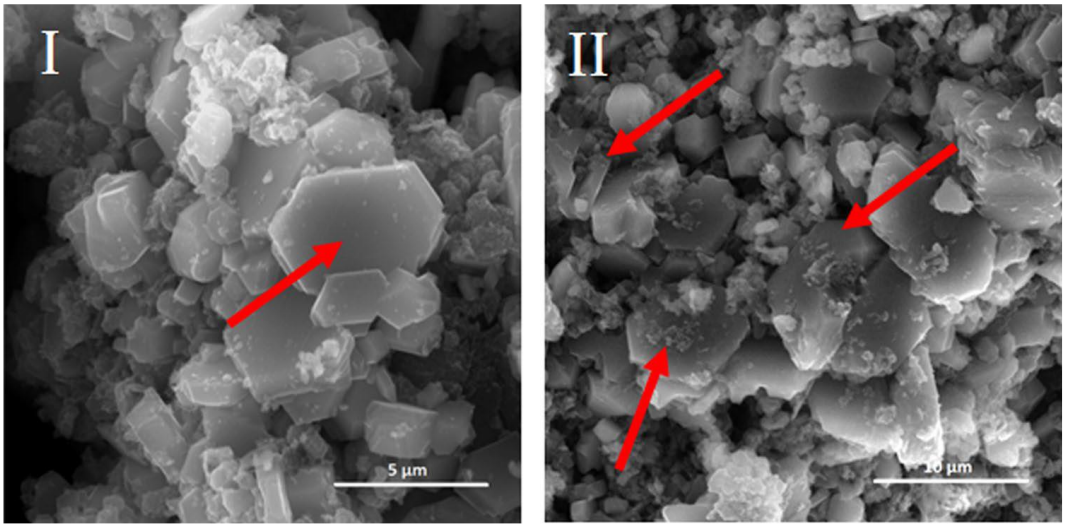

Figure 7. The lime putty SL-A at the age of 3 days (I) and 30 days (II).

The same specific differences in the sample morphology may also be caused due to the samples drying and coating of a metal layer for SEM observation. Conversely, observation in ESEM does not require the above processes and the samples are observed naturally wet and without any modifications. The surface morphology of the crystals observed using the ESEM are somewhat smooth and free of sharp edges and micro-cracks see Fig. 7I and II vs. Fig. 3I and II.

Microstructure of carbonated lime putties

Figure 8 shows the development of calcite crystals in carbonated lime putties C-SL-A, C-SL-B, C-SL-C, and C-CL-B1 after 14 days of storage in a box with a high concentration (20%) of CO_2 and humidity (70%). The length of the side of the calcite crystals was measured. The regular crystals which grew separately were selected for measurement. The images in Fig. 8 and Table 1 show the different development of calcite crystals in the carbonated lime putties. The size of calcite crystals is affected by the preparation method of the lime putties and the granulometry of lime. The smallest calcite crystals were developed in lime putty C-SL-A, which was prepared from lime with a grain size of under 90 μm Fig. 8I; whereas the larger crystals originated in lime putty C-SL-B Fig. 8II. The largest calcite crystals were found in lime putty C-SL-C Fig. 8III. The method of preparation, i. e. the mixing of lime putty SL-B1, affected the size of the calcite crystals C-SL-B1 Fig. 8IV. The mixing process leads on to the easier dissolution of the grains of quicklime, subsequently to the formation of larger crystals of calcium hydroxide.

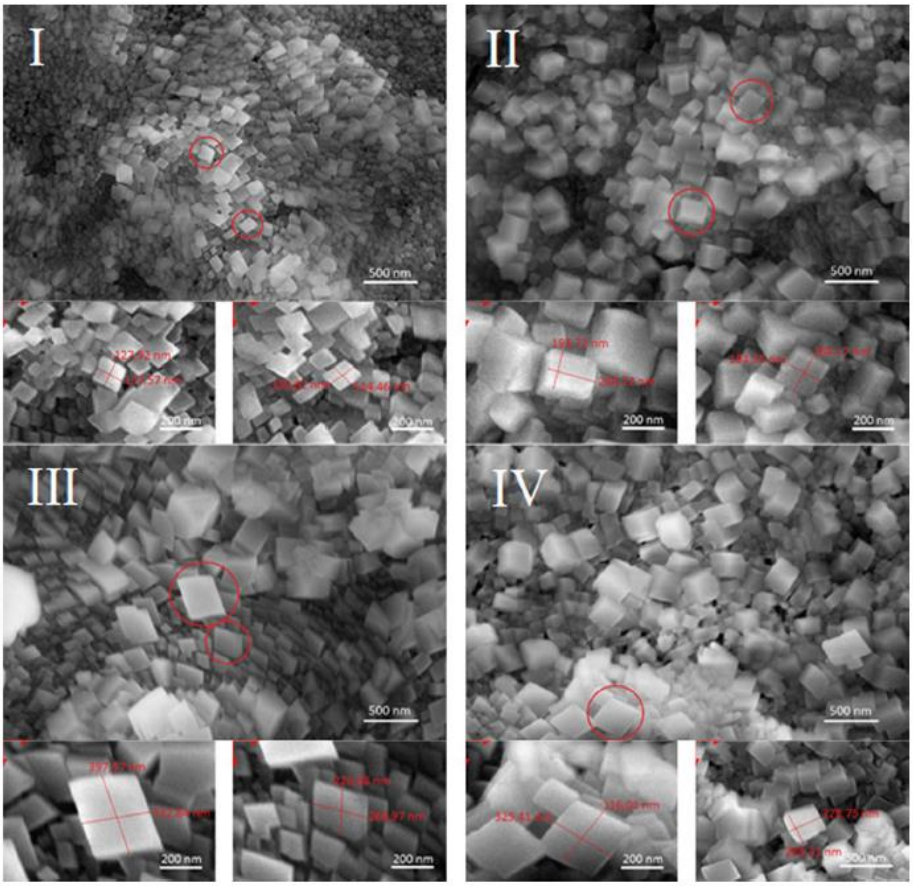

Figure 8. Microstructure of carbonated lime putties C-SL-A (I), C-SL-B (II), C-SL-C (III) and C-SL-B1 (IV).

Table 1. Average side length of the calcite crystals. The repeatability limit was calculated for each value

	C-SL-A	C-SL-B	C-SL-C	C-SL-B1
Average side length of calcite crystals side [nm]	128.84 ± 10.77	236.00 ± 13.18	309.67 ± 14.96	244.06 ± 14.18

Differential thermal analysis of the carbonated lime putties

The results of differential thermal analysis of carbonated lime putties C-SL-A, C-SL-B, C-SL-C, and C-CL-B1 after 14 days of storage in a CO_2 environment are demonstrated in Fig. 9. The curves TG and DTG show that the carbonation process for the individual lime putties is different. The carbonation of lime putty samples C-SL-A and C-SL-B proceeded similarly. The smaller grains in lime A lead to a lower content of calcium hydroxide and a higher content of calcium carbonate (25.2% $Ca(OH)_2$ and 65.7% $CaCO_3$) compared to lime B (20.0% $Ca(OH)_2$ and 68.7% $CaCO_3$). Sample C-SL-C, prepared from lump lime, carbonates very quickly (2.8% $Ca(OH)_2$ and 85.8% $CaCO_3$). Sample C-SL-B1 contained less calcium hydroxide and, actually, more calcium carbonate (8.9% $Ca(OH)_2$ and 80.0% $CaCO_3$) than lime putty C-SL-B due to the process of activation.

Strengths of lime mortars

The effect of lime putty preparation on the carbonation process was also assessed by determining the strengths of lime mortars. The results of the tensile and compressive strengths measurements of lime mortars M-A, M-B, M-C, and M-B1 at the age of 28 days are illustrated in Table 2. The strengths of the lime mortars vary depending on the granulometry of the original quicklime from which the lime putties and the mortars were prepared. Mortar M-B, prepared from lime putty SL-B, reached higher strengths than mortar M-A, which was prepared from lime putty SL-A. Mortar M-C, which was prepared from the putty made from lump lime, reached the highest strengths.

The effect of the method of preparation of lime putty is also noticeable because mortar M-B1 achieved higher strengths than mortar M-B. Both of these lime mortars were prepared from lime with the same granulometry, but lime putty SL-B1 was mixed, unlike lime putty SL-B.

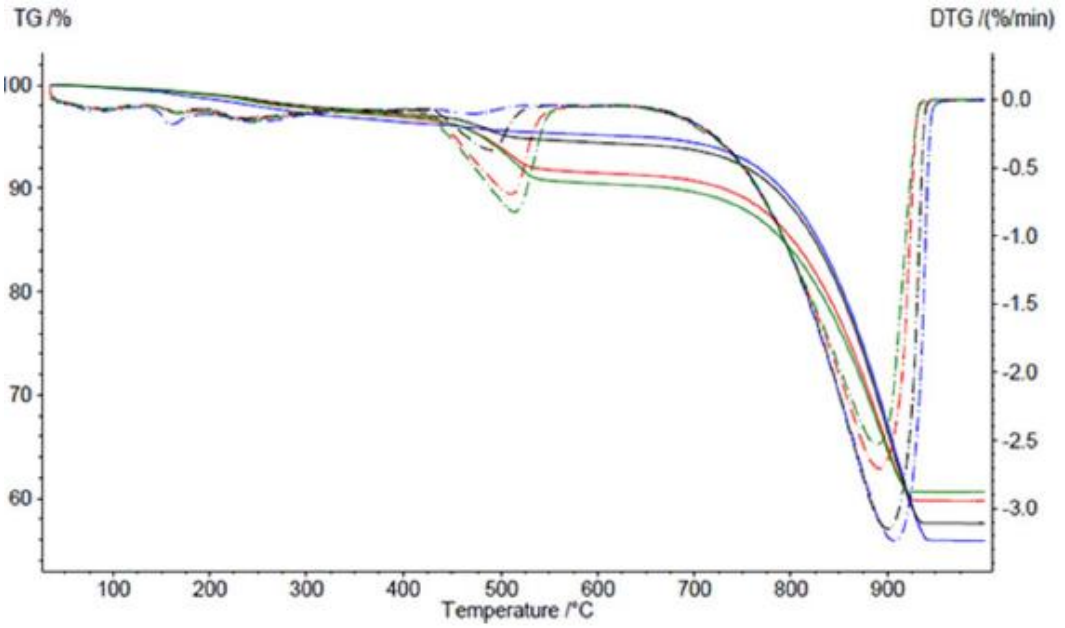

Figure 9. Differential thermal analysis of the carbonated lime putties C-SL-A, C-SL-B, C-SL-C and C-SL-B1, red curve – C-SL-A, green curve – C-SL-B, blue curve – C-SL-C, black curve – C-SL-B1.

Table 2. Average strengths of lime mortars M-A, M-B, M-C and M-B1 at 28 days. The repeatability limit was calculated for each value.

	MA	MB	MC	MB1
Flexural strength [MPa]	0.5 ± 0.01	0.6 ± 0.02	0.8 ± 0.02	0.7 ± 0.03
Compressive strength [MPa]	1.3 ± 0.06	1.5 ± 0.05	2.5 ± 0.08	1.8 ± 0.05

Discussion

The aim of the article was to analyse the development of the lime putties in the dependence on time by means of selected methods giving accurate results. The found results exactly characterize the lime putties' properties and correspond with the results published by other authors. The authors of the article consider a high potential in the micro-morphological characterization of the lime putties in their native state, so without any sample treatment with minimum occurrence of artefacts, by means of ESEM. The article presents an evaluation of the results obtained by means of classic SEM and ESEM for the objective arbitration.

Four lime putties prepared in different ways from quicklimes with varying granulometry were analysed in the dependence on the maturation time. During the maturation of lime putties, the regular hexagonal crystals of calcium hydroxide are transformed into smaller irregular crystals which are coated with a layer of

hydrogel. The rheological properties are dependent on the amount of hydrogel produced during the ageing of lime putties.

- The use of lump lime or mixing a suspension of lime for the preparation of lime putty leads to the formation of incompletely regular calcium hydroxide crystals and a high amount of hydrogel formation. It results in a faster formation of calcium carbonate, the growth of larger calcite crystals, and higher strengths of lime mortars.
- The values of plastic viscosity and yield stress increase with the increasing period of maturation. The use of aged limes leads to obtaining an intermediate product of higher quality for the preparation of lime mortars.
- The process of particle disruption during the mixing of lime putty helps accelerate the hydrogel formation as well as increasing plastic viscosity and yield stress.
- The use of lump lime or the mechanical disruption of lime particles is the most suitable for the properties of lime putty and, consequently, for the preparation of lime mortars.
- Matured lime putties prepared from lump lime and by mixing lime putty are the most suitable for the preparation of mortar.

The most important contribution of the article in the field of conservation and restoration of historical mortars consists in the new way of lime putties preparation by means of mechanical crush of the lime particles. Mortars produced from such prepared lime putty achieved similar properties as mortars made from the matured lime putty prepared from lump lime. An advantage of the new way of lime putty preparation is the use of commonly available powder lime without the necessity of using more difficult to obtain lump lime. The presented results exhibited that mortars with higher strengths can be prepared from common powder lime. These mortars will be more durable with a higher resistance to environmental influences and contaminated atmosphere.

Table 3. Grain content of lime A and B.

Lime	<0.063 [µm]	0.063–0.090 [µm]	0.090–0.200 [µm]	>200 [µm]
A	15.18	14.04	3.41	2.77
B	14.14	9.85	4.62	2.86

Methods

Limes

Lime A with a grain size of under 90 μm, lime B with a grain size of under 200 μm, and lump lime with a grain size from 10 mm to 63 mm (Lime kiln, Čertovy schody a.s., Tmaň) were used to prepare the lime putties. Lime A and lime B are mixtures of lime burned partially (70%) in the co-current regenerative furnace at 1000 °C and in the countercurrent shaft furnace (30%) at 1300 °C. Lime C is a mixture of lime burned in the co-current regenerative furnace at 1100 °C (50%) and in the countercurrent shaft furnace at 1300 °C (50%). The content of total CaO/active CaO in lime A was 96.05/93.74, in lime B 94.08/88.34, and in lime C 95.87/92.33. The reactivity of lime expressed as the time taken to reach a temperature of 60 °C, according to EN 459-2, was 2.3 min for lime A, 2.6 min for lime B, and 3.5 min for lime C.

The granulometry of lime A and lime B is shown in Table 3. Lime A contains more fine particles under 0.063 μm and no particles above 200 μm. Lime B contains less fine particles under 0.063 μm and exhibits a higher content of particles below 200 μm and above 200 μm.

Preparation of the lime putties and the lime mortars

Lime putties SL-A, SL-B, and SL-C were prepared by mixing 200 g of lime and 640 ml of deionized water. Lime putty SL-B1 was prepared by mixing 200 g of lime and 640 ml of deionized water and this lime putty was mixed (25,000 rev/min) for 5 minutes after its hydration. The fresh lime putties were immediately stored in plastic bottles and they were supplemented with water to avoid reaction with CO_2 and air drying. The samples were then kept in closed bottles at a temperature of 20 ± 1 °C. Samples SL-A, SL-B, SL-C, and SL-B1 were stored in a box with 70% humidity and a 20% concentration of CO_2 for 14 days for accelerated carbonation. Lime mortars M-A, M-B, M-C, and M-B1 were prepared from the lime putties and sand with a ratio of 1:3. The lime mortars were placed in moulds with dimensions of 40 × 40 × 160 mm. Specimens were stored under laboratory conditions at a temperature of 20 ± 1 °C and a relative humidity of 50 ± 5% after their removal from the moulds.

Rheology

The rheological properties of lime putties SL-A, SL-B, SL-C, and SL-B1after 3, 30, 60, and 90 days' maturation were monitored by a Discovery Hybrid Rheometer HR-1 (parallel plate diameter of 25 mm with roughened surface). The rheological

properties of the lime putties were determined from the curves of flow with the increasing and decreasing shear rate in the range from 0 sec−1 to 200 sec−1 over 2 minutes. The values of yield stress and plastic viscosity were determined according to the Bingham model,

$$\tau = \tau_0 + \mu\dot{\gamma} \quad (2)$$

where τ [Pa] is the shear stress, τ_0 is the yield stress, μ [Pa·s] is the plastic viscosity, and $\dot{\gamma}$ [s^{-1}] is the shear strain rate[22]. Temperature of the measurement apparatus and the laboratory were kept constant at 20 (±0.5) °C.

Observation in SEM and ESEM

Lime putty samples SL-A, SL-B, SL-C, and SL-B1 were observed in the high resolution scanning electron microscope (HR-SEM) JSM6700F JEOL (with a beam energy of 5 keV, a working distance of 8 mm, and an Everhart-Thornley detector) after 3, 30, 60, and 90 days. The samples of the lime putties were prepared for observation in the SEM in the following manner: the samples were rinsed with 10 ml of acetone to remove water and 10 ml of diethyl ether for drying. Next, the samples were dried in a nitrogen atmosphere in order to eliminate the influence of CO_2, and the samples were sputtered.

The sample of lime putty SL-A was observed in the environmental scanning electron microscope (ESEM) AQUASEM II (with a beam energy of 20 keV, a water vapour pressure of 800 Pa, and an ionization detector) after 3 and 30 days. The sample was studied directly without sputtering.

The different development of the calcite crystals in carbonated lime putties C-SL-A, C-SL-B, C-SL-C a C-SLB1 was monitored with the high resolution environmental scanning electron microscope (HR-ESEM) QUANTA 650 FEG (with a beam energy of 10 keV, water vapour pressure of 200 Pa, and a GSED detector). The samples were studied directly without sputtering. The length of the side of the calcite crystals was measured using the Scandium software.

Differential thermal analysis

The differential thermal analysis of carbonated lime putties C-SL-A, C-SL-B, C-SL-C, and C-SL-B1 was performed using the thermal analyser NETSCH STA 2500 after 14 days of being stored in a box with 70% humidity and a 20% concentration of CO_2. The used instrument exhibits accuracy with an error ±10%. The measurement was carried out under a nitrogen atmosphere.

Strengths

The flexural strength and compressive strength of lime mortars M-A, M-B, M-C, and M-B1 were determined at 28 days according to EN 1015-11.

All presented data was calculated as average value from the repeated five measurements and standard deviation and repeatability limit (probability level 95%) were calculated.

Acknowledgements

This paper has been worked out under the project No. L100651601, the Ministry of Education, Youth and Sports of the Czech Republic (project LO1212), the research infrastructure was funded by the Ministry of Education, Youth and Sports of the Czech Republic and the European Commission (project CZ.1.05/2.1.00/01.0017). This paper also supported by the project No. LO1408 "AdMaS UP - Advanced Materials, Structures and Technologies", supported by Ministry of Education, Youth and Sports under the "National Sustainability Programme I".

References

1. Kotík, P. *et al*. Lime, first ed., Society of Technology of Architectural Heritage, Prague, 2001 (76 pages), ISBN 80-902668-8-6 (In Czech).

2. Kemperl, J. & Maček, J. Precipitation of calcium carbonate from hydrated lime of variable reactivity, granulation and optical properties. *J. Miner. Process.* **93**, 84–88 (2009).

3. Commandré, J. M., Salvador, S. & Nzihou, A. Reactivity of laboratory and industrial limes. *Chem. Eng. Res. Design.* **85**, 473–480 (2007).

4. Chiaia, B., Fantilli, A. P. & Ventura, G. A chemo-mechanical model of lime hydration in concrete structures. *Constr. Build. Mater.* **29**, 308–315 (2012).

5. Potgieter, H. J., Potgieter, S. S., Moja, S. J. & Maluba-bafubiandi, A. An empirical study of factors influencing lime slaking. Part I: production and storage conditions. *Miner. Eng.* **15**, 201–203 (2002).

6. Shi, H., Zhao, Y. & Li, W. Effects of temperature on the hydration characteristic of free lime. *Cem. Concr. Res.* **32**, 789–793 (2002).

7. Giles, D. E., Ritchie, I. M. & Xu, B. A. The kinetics of dissolution of slaked lime. *Hydrometallurgy* **32**, 119–128 (1993).

8. Whittington, B. I. The chemistry of CaO and Ca(OH)2 relating to the Bayer process. *Hydrometallurgy* **43**, 13–35 (1996).

9. Moropoulou, A., Bakolas, A. & Aggelakopoulou, E. The effects of limestone characteristics and calcination temperature to the reactivity of the quicklime. *Cem. Concr. Res.* **31**, 633–639 (2001).

10. Rosell, J. R., Haurie, L., Navarro, A. & Cantalapiedra, I. R. Influence of the traditional slaking process on the lime putty characteristics. *Constr. Build. Mater.* **55**, 423–430 (2014).

11. Rodrigues-Navarro, C., Hansen, E. & Ginell, W. S. Calcium hydroxide crystal evolution upon aging of lime putty. *J. Am. Ceram. Soc.* **81**, 3032–3034 (1998).

12. Cardoso, F. A., Fernandes, H. C., Pileggi, R. F., Cincotto, M. A. & John, V. M. Carbide lime and industrial hydrated lime characterization. *Powder Technol.* **195**, 143–149 (2009).

13. Cizer, Ő., Van Balen, K., Elsen, J. & Van Gemert, D. Real-time investigation of reaction rate and mineral phase modifications of lime carbonation. *Constr. Build. Mater.* **35**, 741–751 (2012).

14. Romagnoli, M., Gualtieri, M. L., Hanuskova, M., Rattazzi, A. & Polodoro, C. Effect of drying method on the specific surface area of hydrated lime: A statistical approach. *Powder Technol.* **246**, 504–5010 (2013).

15. Mascolo, G., Mascolo, M. C., Vitale, A. & Marino, O. Microstructure evolution of lime putty upon aging. *J. Cryst. Growth* **312**, 2363–2368 (2010).

16. Atzeni, C., Farci, A., Floris, D. & Meloni, P. Effect of aging on rheological properties of lime putty. *J. Am. Ceram. Soc.* **87**, 1746–1766 (2004).

17. Ruiz-Agudo, E. & Rodriguez-Navarro, C. Microstructure and Rheology of Lime Putty. *Langmuir* **26**, 3868–3877 (2010).

18. Paiva, H., Velosa, A., Veiga, R. & Ferreira, V. M. Effect of maturation time on the fresh and hardened properties of an air lime mortar. *Cem. Concr. Res.* **40**, 447–451 (2010).

19. Margalha, G., Veiga, R. & de Brito, J. Traditional methods of mortar preparation: The hot lime mix method. *Cem. Concr. Compos.* **33**, 469–804 (2011).

20. Neděla, V., Tihlaříková, E. & Hřib, J. The low-temperature method for study of coniferous tissues in the environmental scanning electron microscope. *Microscope Res. Tech.* **78**, 13–21 (2015).

21. Schenkmayerová, A. *et al*. Physical and bioengineering properties of polyvinyl alcohol lens-shaped particles versus spherical polyelectrolyte complex microcapsules as immobilisation matrices for a whole-cell baeyer–villiger monooxygenase. *Appl. Biochem. Biotechnol.* **174**, 1834–1849 (2014).

22. Medina, C., Banfill, P. F. G., Sánchez de Rojas, M. I. & Frías, M. Rheological and calorimetric behaviour of cements blended with containing ceramic sanitary ware and construction/demolition waste. *Constr. Build. Mater.* **40**, 822–831 (2013).

26 Observation of a Brine Layer on an Ice Surface with an Environmental Scanning Electron Microscope at Higher Pressures and Temperatures

Ján Krausko[1,2], Jiří Runštuk[3], Vilém Neděla[3], Petr Klán[1,2], and Dominik Heger[1,2]

1 *Department of Chemistry, Faculty of Science, Masaryk University, Kamenice 5, 62500 Brno, Czech Republic*
2 *RECETOX, Faculty of Science, Masaryk University, Kamenice 5, 62500 Brno, Czech Republic*
3 *Institute of Scientific Instruments of the ASCR, v.v.i., Královopolská 147, 61264 Brno, Czech Republic*

Abstract

Observation of a uranyl-salt brine layer on an ice surface using backscattered electron detection and ice surface morphology using secondary-electron detection under equilibrium conditions was facilitated using an environmental scanning electron microscope (ESEM) at temperatures above 250 K and pressures of hundreds of Pa. The micrographs of a brine layer over ice grains prepared by either slow or shock freezing provided a complementary picture of the contaminated ice grain boundaries. Fluorescence spectroscopy of the uranyl ions in the brine layer confirmed that the species exists predominately in the solvated state under experimental conditions of ESEM.

Introduction

Natural ice and snow accumulate and concentrate significant amounts of impurities that can be stored or chemically transformed, and eventually released to the environment.[1–4] The impurities are rejected from the freezing solution to the ice grain boundaries, free ice surfaces, or liquid/brine inclusions.[1] Information about compartmentation and phase speciation of chemical impurities in ice is thus essential for the assessment of their fate. The location of impurities and their interactions with the water molecules of ice, still not sufficiently clarified, must be studied at lower temperatures because thawing erases the information. Various techniques such as absorption,[5–7] fluorescence,[8] or X-ray photoelectron[9] spectroscopies have been utilized on solid ice samples. Microscopy is one of the few direct methods for observing ice impurities and evaluating their location and compartmentation.[10–12]

Low-temperature scanning electron microscopy (LTSEM)[13] has already been used for the observation of natural[14–16] and laboratory-generated ice surfaces, grain

boundaries,[17] vitrified sulfuric acid,[18] as well as solid impurities at the grain boundaries or dust particles/coagulated solutes[14] on the grain surfaces, for example.[19,20] LTSEM requires low pressure in the specimen chamber (usually below 10^{-4} Pa) which causes potentially undesirable ice sublimation, called (thermal) etching, revealing impurities that would otherwise remain buried under the ice surface. When the impurities keep their location while the surrounding ice sublimes, a 3D morphology of the ice boundaries is revealed. Various shapes of coagulated impurities, such as grain boundary filaments formed from triple junction tubes (also called veins),[19] thin ridges,[14] cobweb-like structures,[21] nodules, sheets, as well as stems and leaves,[20] have been observed. A site-specific energy-dispersive spectrometer for X-ray microanalysis built into the LTSEM,[21] and a confocal optical microscopy coupled with Raman spectroscopy, [12] were used to determine unambiguously that the observed features are concentrated impurities excluded from the solutions.

The environmental scanning electron microscope (ESEM) has been constructed for observation of various wet nonconductive samples at high pressures.[22] Maintaining a water vapor pressure on the order of 10^3 Pa or more obviates the need for conductive surface coating, and allows the sample to be preserved essentially in its natural form.[23] As a result, the sample surface structure is highly hydrated, thus the technique is suitable for the investigation of dynamic processes, such as sample solidification or dissolution. Only a few studies have examined noncontaminated ice at high pressures using the ESEM.[24] Leu and co-workers examined ice particle sizes in thin ice films;[25,26] Zimmermann and co-workers observed ice nucleation on various solid supports, such as silver iodide, kaolinite, or montmorillonite;[27] and Varanasi and co-workers observed frost formation on hydrophobic surfaces coated, for example, with a thin layer of (tridecafluoro-1,1,2,2-tetrahydrooctyl)trichlorosilane at 260 K.[28] Neshyba and coworkers showed well-resolved surfaces of hexagonal ice crystals possessing strands which are characteristic for growing and ablating facets.[29] Pedersen and co-workers observed ice crystals growing into contact.[30] In most of the previous studies of ice, SEM has been used at pressures below 0.1 Pa and temperatures below 180 K.

In this work, we used a customized ESEM[31] to study uranyl ion-containing brine layers on the ice surfaces at environmentally relevant temperatures (above 250 K) and pressures (below 700 Pa). A uranyl salt indicator was used to obtain high contrast ESEM images in electron backscattering mode to resolve small-scale features, such as grain boundaries filled with brine, and at the same time to get information about uranyl ion chemical speciation in the frozen solution using fluorescence spectroscopy.[32]

Experimental section

Uranyl nitrate hexahydrate (Lachema, p. a.) and perchloric acid (70%, redistilled; Aldrich) were used. Crystalline uranyl perchlorate was prepared from solid uranyl nitrate through repeated cycles of dissolution and evaporation of perchloric acid (70%).[33] Ultrapure water for semiconductor purposes with a resistance of 18 MΩ cm^{-1} was used in all experiments. Uranyl nitrate hexahydrate was dissolved in a stock solution of perchloric acid (pH = 1.0) prior to the experiments. Uranyl ion concentration was 1.01×10^{-2} mol dm^{-3}. The fluorescence emission spectra were obtained on an Aminco-Bowman AB2 spectrofluorimeter or an Edinburgh Instruments (FLSP 980) spectrofluorimeter in 10 mm fluorescence cuvettes (293 K) or 10 mm glass test tubes at 270 or 254.7 K; the excitation wavelength was 414 nm. The fluorescence excitation and emission spectra were corrected by using a reference detector for the intensity of the excitation source and a correction file, respectively, and the spectra were normalized. The lifetimes are given in the format: mean ± standard deviation of the mean with the number of measurements (n) enclosed in parentheses.

ESEM Description

An environmental scanning electron

microscope (ESEM) AQUASEM II was used for imaging of the ice samples. It allows observation of nonconductive, wet, or liquid samples at a specimen chamber pressure below 2000 Pa. This apparatus was built at the Institute of Scientific Instruments, Academy of Sciences of the Czech Republic and has been previously described.[23,34,35] The microscope is equipped with a directly heated tungsten hairpin cathode, a YAG:Ce^{3+} (trivalent cerium doped yttrium−aluminum garnet) detection system for backscattered electrons. A unique ionization detector for secondary electrons uses a thin biased indium tin oxide detection electrode sputtered on a signal electron face surface of the scintillation single crystal YAG:Ce^{3+}, and a newly patented[36] ionization secondary electron detector with an electrostatic separator. For observation of wet samples and implementation of dynamic in situ experiments, the microscope was equipped with three capacity gauges (Pfeiffer CMR 262) used for the exact measurement of gas pressures, including water vapor, and a custom-made Peltier stage for sample cooling to −30 °C. Water vapors are efficiently supplied via a hydration system equipped with temperature and vapor flow controllers. A micrometric valve provided a precise and reproducible flow control of water vapor. The system was equipped with a special heating system for temperature stabilization and fine control of the water vapor flow. Heating of the ∼0.2 L water tank and a micrometric valve also prevented possible water

condensation caused by polytropic expansion of water vapor in the valve. The temperature of the water vapor in the water tank was measured by a precise temperature sensor, heat-shielded from the water tank wall, and controlled by a proportional-integral-derivative (PID) controller with an accuracy of 0.1 °C. The whole system was additionally insulated against thermal affection from ambient and suppression heat loss. The strength of this microscope lies in its ability to evacuate the specimen chamber very slowly, as well as the ability to reach high humidity conditions in the sample vicinity without purge-flood cycles. The ability to control temperature in the vicinity of the sample allowed us to study ice under precisely controlled conditions.

ESEM Sample Preparation

Aqueous (aq) samples were frozen under atmospheric pressure on a 0.375 mm thick silicon pad of 8 mm diameter that was cooled by a Peltier block. The initial pad temperature was above −1 °C. The droplet exposed to freezing was about 3 mm in diameter. The solidification was seeded by snowflakes formed from air humidity at the opening of the bottle which was cooled by liquid nitrogen using a dissecting needle. Water vapor was allowed to condense on the ice sample to compensate for evaporation or sublimation losses. When the ice was prepared by cooling without seeding, it grew suddenly from the undercooled solution at temperatures around −7 °C.

Ice sphere (artificial snow) samples were prepared by spraying very fine droplets of a liquid into a vessel containing liquid nitrogen using a Teflon nebulizer (airbrush). The ice spheres were moved directly from the liquid nitrogen onto the precooled silicon pad (T = 255 K), which was immediately inserted into the sample chamber that was pumped to reach the working pressure.

ESEM Operation

ESEM examination of the ice samples was performed at temperatures from 273 to 255 K in a mixed water vapor/ air atmosphere at the pressures of 450−700 Pa, at which the partial pressure of water vapor was in the range of 200−300 Pa. The partial pressures of air and water vapor were adjusted separately before the experiment was carried out. A micrometric valve in the hydration system was opened, and the pressure of the water vapor was measured and adjusted. The partial pressure of the water vapor was measured similarly.

Results and Discussion

We utilized a customized ESEM[31] at temperatures above 250 K and pressures below 700 Pa in order to study the brine-layer covered ice surfaces. Under these conditions, the phenomena of etching and subsequent stripping of impurities are largely suppressed. Figure 1 shows the comparison of the experimental conditions used in this research (in black) to those employed by others (in gray). The solid curve indicates equilibrium between the ice and water-vapor phases. Pressures between 400 and 700 Pa, ~50% water-vapor saturation and temperatures above 250 K were utilized in our experiments. Under such conditions, the dynamic equilibrium between vaporization and water vapor condensation was maintained, thus changes in the structure of the frozen samples were largely suppressed.

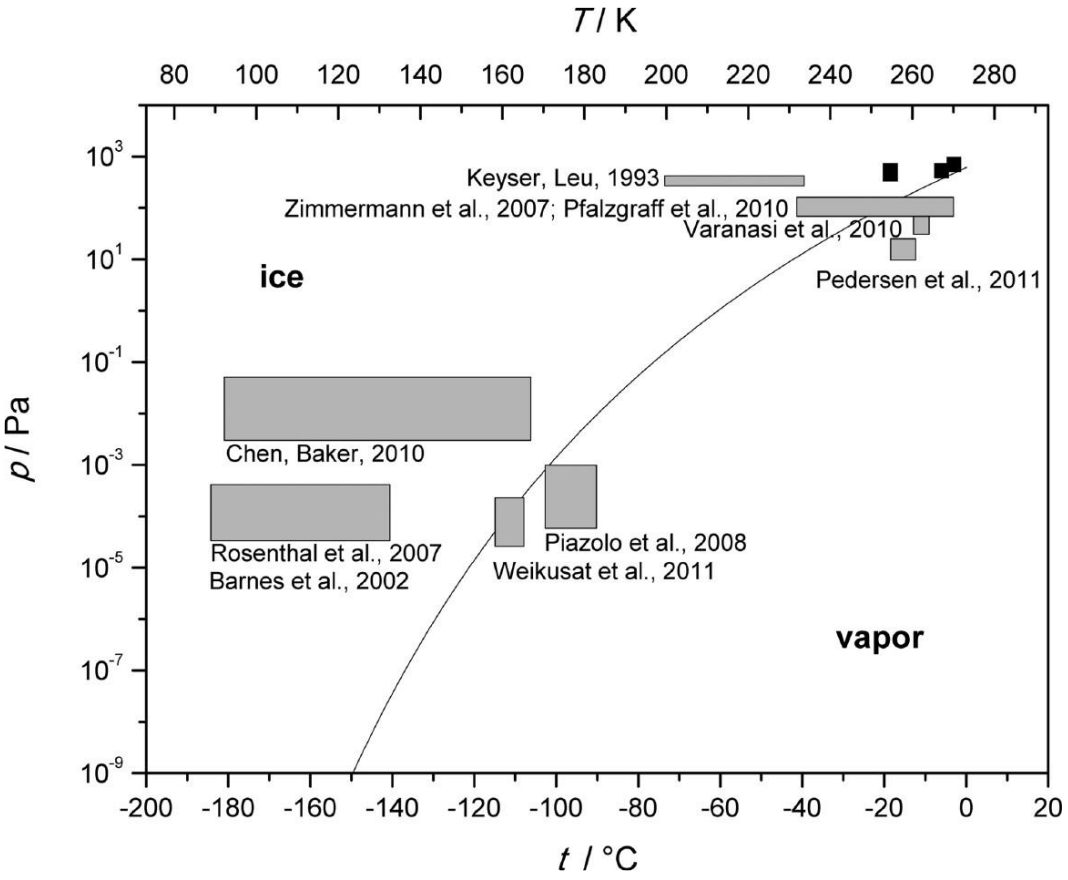

Figure 1. Phase equilibrium between ice and water vapor,[37] and ESEM working ranges used by us (in black) and others (in gray).[14,17,21,25,27−30,38−40]

Figure 2a shows an ESEM image of an ice sample prepared by freezing of pure water under atmospheric pressure inside the specimen chamber. A water droplet of about 3 mm diameter was placed on a precooled silicon pad (272 K) and seeded by a small submillimeter ice crystal. After solidification, the sample was cooled to 270 K, and the pressure was reduced to 695 Pa. Different shapes and sizes of the ice grains (30−200 μm) can be distinguished. Due to the detection of secondary electrons (SE), which is sensitive mostly to surface topography, the ice grain

boundaries are visible as black lines with a bright halo. This is caused by enhanced emission of secondary electrons from the sample edges, known as the "edge effect".[41] This typically appears in sample images observed by secondary electron detectors situated in the specimen chamber of electron microscopes.[41] At this temperature, the ice crystals are covered by a disordered interface (also called quasi liquid layer),[42] which is, however, too thin to be detected by this technique.[43]

Uranyl nitrate solutions (0.01 M) acidified by perchloric acid to pH = 1 were used in all our experiments because hydrolysis of the uranyl ion is suppressed, and only a single species (a hydrated uranyl ion) is present under these conditions.[33,44] Freezing a 0.01 M solution of uranyl salt produced an ice of similar morphology (Figure 2b) to that of pure (noncontaminated) ice (Figure 2a). The experimental temperature of 267 K was well above the eutectic temperature of the uranyl nitrate hexahydrate−water system (T_{eu} = 253.1 K)[45] as well as of the perchloric acid−water system (T_{eu} = 213 K);[46] therefore, the uranyl ion must have been dissolved in the brine (liquid) layer. We do not expect any substantial uranyl ion incorporation into the ice lattice because of its size.[47] Since the amount of backscattered electrons (BSE) is related to the atomic number of the elements present, the $_{92}$U-rich regions appeared brighter, whereas the regions consisting of water molecules remained dark. This color pattern also agrees with what was previously observed for vitrified impurities on the ice surface.48 The difference between pure ice and a frozen uranyl salt solution is largely manifested in the channels and pools of concentrated uranyl ion solutions (bright) along with the individual ice grains (black). The channels containing the uranyl ion enclose whole grains. Such a complete wetting of grain boundaries is expected on the ice surface when three phases-solid, liquid, and vapor-are in equilibrium.[18] Pools are usually largest at the meeting points of three crystals, although some may also be present on the surface.[49] The uranyl ion-containing liquid layer is expected to be considerably more concentrated (by several orders of magnitude) than the parent solution due to the freezing concentration effect.[5] This system is most probably in a thermodynamic equilibrium because the freezing process was slow. The orientations of the ice grains[50] could support an argument for what we are actually seeing on the micrographs: that the dark parts are crystals, and the light ribbons are grain boundaries. Unfortunately, our microscopic setup could not be used for polarization measurements at these temperatures. Instead, thawing the uranyl-contaminated ice samples at elevated temperatures (Supporting Information, SI, Movies S1 and S2) helped us to understand the observed features. These movies, made of a series of images of the same location, observed by both the SE and BSE detectors, demonstrate grain boundary metamorphism and the gradual flooding and expansion of the uranyl-containing layer over the ice surface. It is apparent that the crystal shape changed

considerably during the measurement, and that the thawing started from the edge of the crystals.

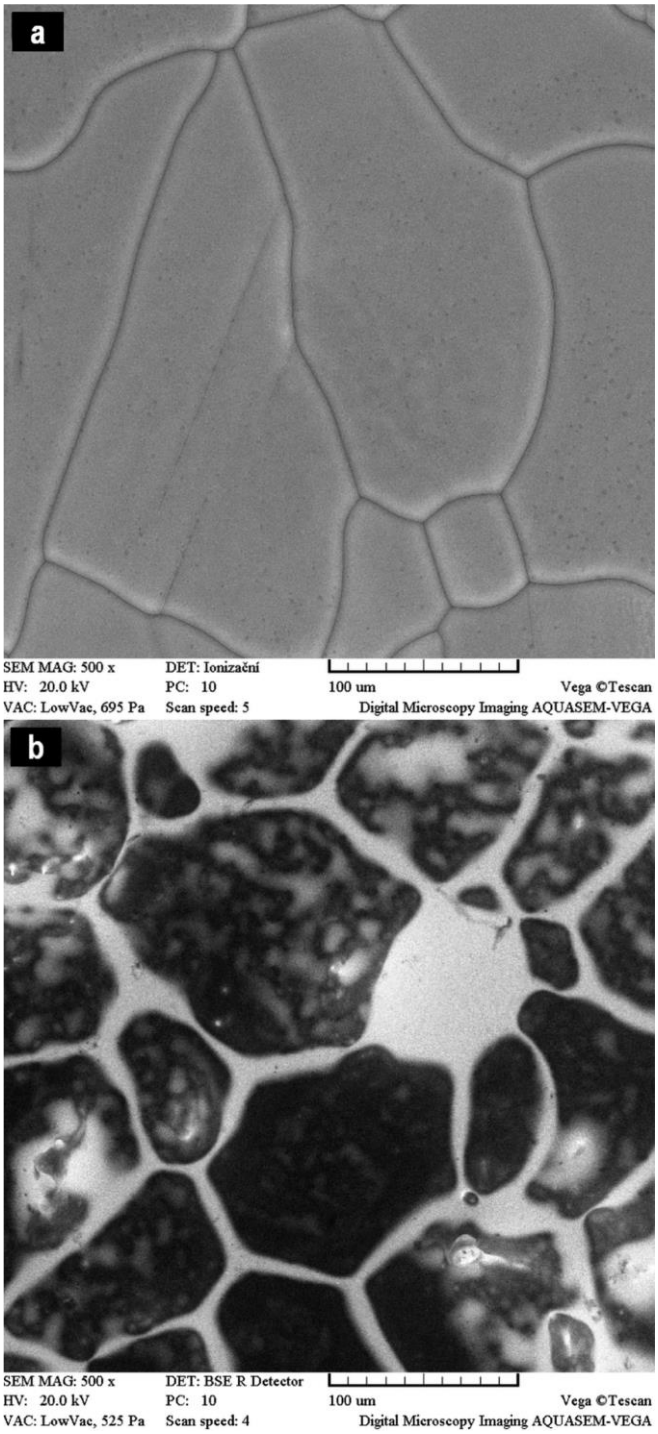

Figure 2. An ESEM image of ice prepared by freezing a droplet inside the specimen chamber: (a) frozen pure water; SE detector mode; 270 K, 695 Pa; (b) a frozen uranyl salt solution; c = 10^{-2} M; BSE detector mode; 267 K, 525 Pa.

Alternatively, ice spheres and contaminated ice spheres were produced by spraying (nebulization) pure water (Figure 3) or a 0.01 M uranyl salt aq solution (Figures 4 and 5) into liquid nitrogen, and then warming to 255 K inside a microscope chamber. The ice spheres thus prepared have already been found to have a relatively large specific surface area,[8] and can be used as a proxy for natural snow.[51,52] These round-shaped spheres were of 20−200 μm diameter, some of them connected by necks to form chains.

Clearly, the ice spheres prepared from uranyl aq solutions (Figures 4 and 5) possessed a much rougher surface compared to those of pure ice (Figure 3). The ice surface morphology (bulges) was clearly captured by a detector of secondary electrons (Figure 4), whereas a high uranyl salt concentration localized at the grain boundaries was revealed by the BSE detector (Figure 5). Close inspection of this image reveals grain boundaries on the surface of ice spheres as white curves. The ice spheres were evidently composed of multiple ice grains or crystals of 5−50 μm in size, and the ice grains were completely wetted by concentrated brine. The brighter spots on the surface of ice spheres in Figure 5 probably correspond to bulges that may also contain uranyl ions.

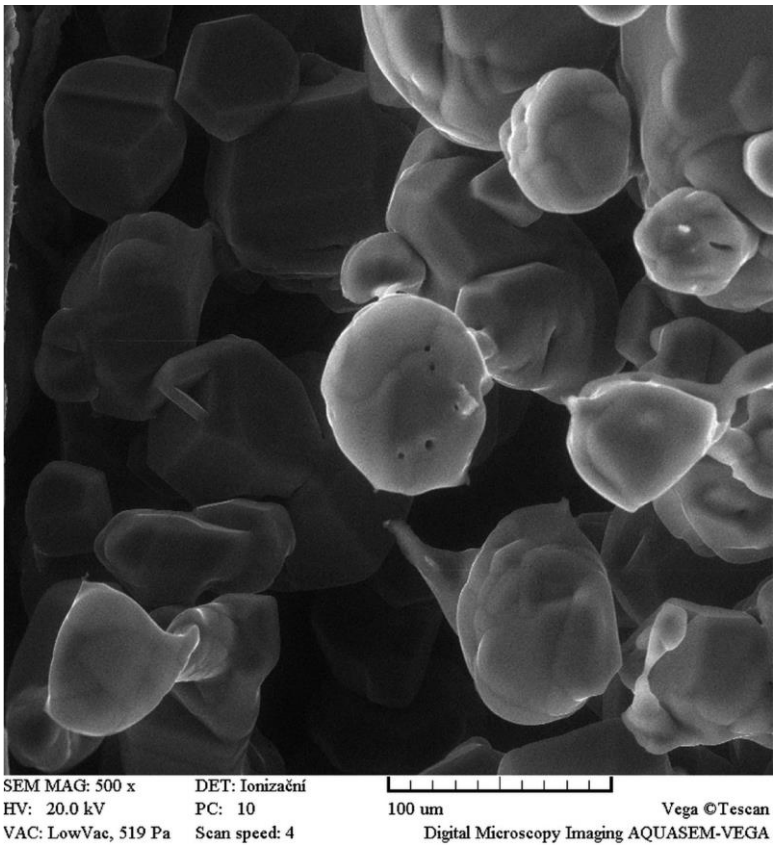

Figure 3. ESEM images of ice spheres prepared by spraying fine droplets of pure water into liquid nitrogen; SE detector mode; 255 K; and 519 Pa.

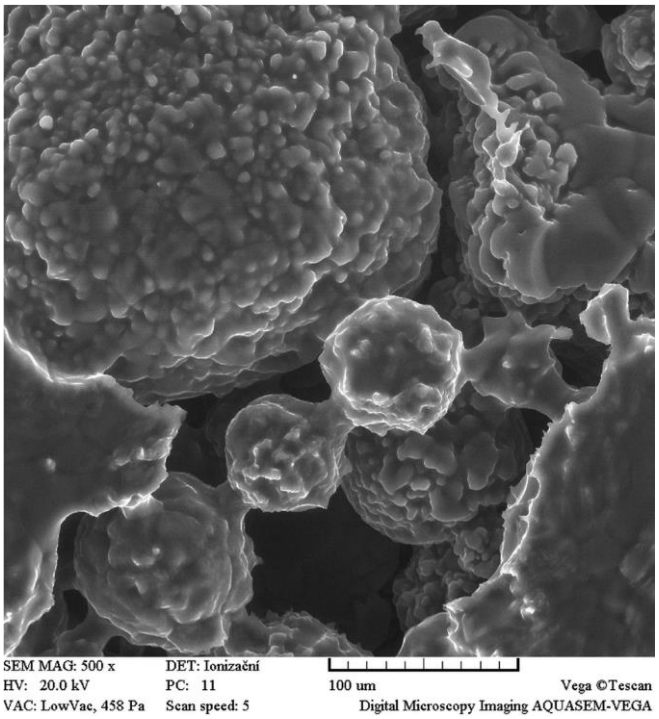

Figure 4. ESEM images of ice spheres prepared from a 0.01 M uranyl salt solution by spraying fine droplets into liquid nitrogen; SE detector mode, 255 K, 458 Pa. Figures 4 and 5 show identical sample positions.

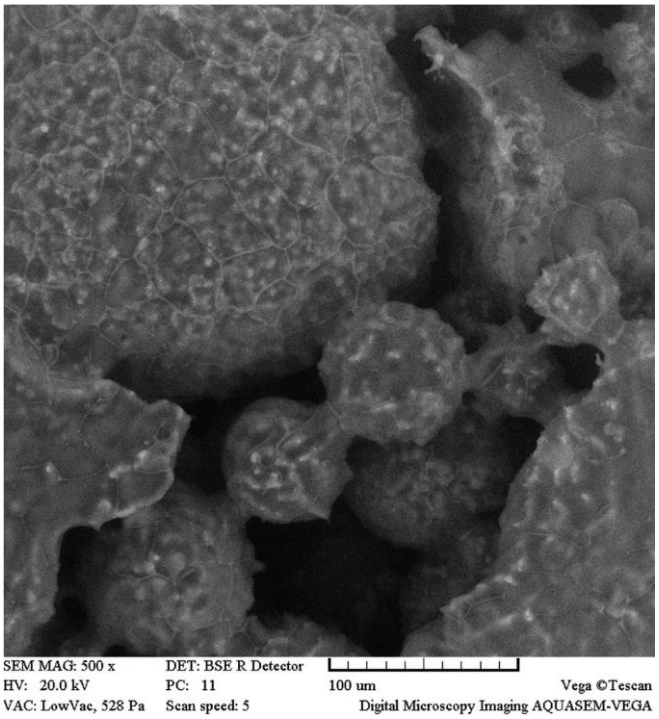

Figure 5. ESEM images of ice spheres prepared from a 0.01 M uranyl salt solution by spraying fine droplets into liquid nitrogen; BSE detector mode, 255 K, 528 Pa; Figures 4 and 5 show identical sample

positions.

In order to get information about the phase speciation of the uranyl ion and its microenvironment in the ice samples, the corresponding frozen aq solutions were subjected to luminescence analysis. The luminescence lifetime of crystalline uranyl nitrate is known to depend considerably on its degree of hydration (for example, dihydrate: τ = 499 μs; trihydrate: τ = 838 μs; hexahydrate τ = 699 μs).[32,33] In our work, the luminescence lifetime of uranyl perchlorate crystals was found to be 283 ± 10 μs (SI Figure S1). In addition, the dependence of the uranyl ion luminescence lifetime on the perchloric acid concentration has been observed to be nearly linear (SI Figure S2) at ClO4 − concentrations between 0.3 and 10 M (0.1 M aq $HClO_4$: τ = 2 μs; 11 M aq $HClO_4$: τ = 65 μs).[53]

We used this linear regression equation to estimate the perchloric acid concentration in the brine. The monoexponential lifetime of uranyl salt aq solutions frozen at 267 K was (12.3 ± 0.3) μs (n = 5) (SI Table S1). Such slow freezing apparently caused rejection of the solute solution into the veins and onto the surface of a polycrystalline ice matrix, along with a substantial increase in the local concentration of perchloric acid.[7,54,55] On the basis of the reported linear dependence of the uranyl ions' luminescence lifetime on perchloric acid concentration,[53] we estimate that the final perchlorate concentration was 1.5 M (see Scheme 1). This resulting concentration also agrees with the equilibrium concentration at 267 K and atmospheric pressure within the experimental range of accuracy.[45] However, this estimation does not take into account effects of temperature, or effects caused by an increase in the uranyl ions concentration during freezing.

The ice spheres prepared by spraying a uranyl salt solution (c = 0.01 M) into liquid nitrogen provided three major luminescence lifetimes (0.59 ± 0.09) μs (n = 4), (3.03 ± 0.06) μs (n = 4) and (291 ± 6) μs (n = 4) at 255 K (SI Table S1). The shock freezing thus probably created a rather heterogeneous speciation of uranyl ions. The major contribution (∼80%; $\tau \approx 3$ μs) to the emission intensity corresponds to the uranyl ion at a slightly elevated perchlorate acid concentration (0.5 M) compared to that of the initial solution ($\tau \approx 2$ μs). The second contribution (∼15%, $\tau \approx 0.5$ μs) comes when the microenvironment does not contain perchlorate ions. Only a small luminescence fraction (∼5%, $\tau \approx 290$ μs) can be assigned to uranyl perchlorate crystals (see Scheme 1).

Our ESEM and fluorescence analyses thus provided unequivocal evidence that freezing the uranyl salt aq solutions causes rejection of a solute to the ice grain boundaries to form a more concentrated brine layer at temperatures above the eutectic temperature, regardless of the rate and method of freezing (at 270 or 77 K). However, uranyl ion speciation was largely dependent on experimental conditions.

A gradual, slow freezing of the sample created a homogeneous and prominent increase of the perchloric acid concentration in the brine and its expulsion to the space between the ice grains. Since the system is most probably in thermodynamic equilibrium, the uranyl ion concentration corresponds to that estimated from the phase diagram.

Scheme 1. Microenvironmental Speciation upon Slow (267 K) and Fast (77 K) Freezing of a Uranyl Perchlorate Solution [a]

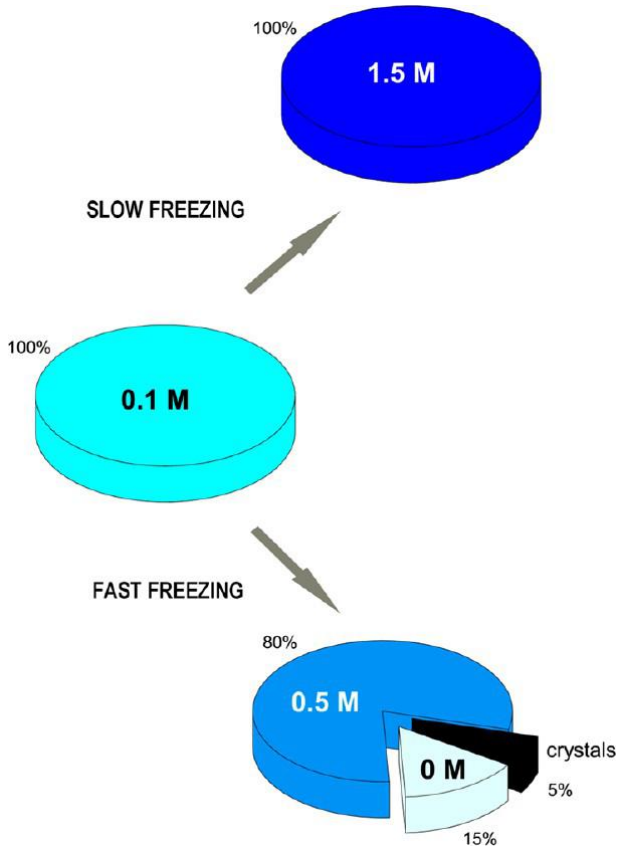

[a] Estimates of the molar concentrations of perchloric acid in the brine layer and their relative abundances in the isolated compartments are given. For detailed information, see SI Table S1.

In contrast, shock freezing by spraying an aq solution into liquid nitrogen and luminescence analysis performed at elevated temperatures provided evidence of a heterogeneous distribution and speciation of the uranyl salt dissolved in the brine. Under such conditions, the frozen system cannot reach equilibrium, and small ice grains with a larger specific surface are formed resulting in a lower brine concentration compared to that obtained by slow freezing at 270 K. In addition, shock freezing caused nonhomogenous distribution of the uranyl ion, such that the uranyl ion regions free of the perchlorate ions, as well as the regions where uranyl perchlorate concentrations exceeded the concentration limits (the uranyl crystals were formed), are apparent from the fluorescence lifetimes. This observation is

analogous to our previous observations using methylene blue as a concentration effect indicator,[5] and can evidently be anticipated for many other contaminants,[9,56] including those of environmental relevance.[57] Many chemical compounds are expected to form a brine layer on the ice surfaces.1 The specific behavior of individual chemical contaminants in freezing ice stems from various equilibrium thermodynamic concentrations and interfacial energies, characterized by dihedral solid−liquid angles at the grain boundaries on the microscopic scale.[18,48]

In this pilot project, a rather large concentration (10 mM) of uranyl salt was used for detailed observation of the brine on the ice surface. Such a value is at least 3 orders of magnitude larger than that of the highest natural occurrence.[58] Nevertheless, when the system is in a thermodynamic equilibrium the local concentration of the brine, defined by the phase diagram, is not dependent on the initial solution concentration.

Conclusions

It was demonstrated that the ESEM method allows for the observation of ice and its liquid uranyl salt inclusions at elevated temperatures and pressures that had not been accessible before. Furthermore, our combined ESEM and luminescence experimental data provided evidence of uranyl phase speciation, compartmentation, and microenvironmental properties. ESEM of ice samples could be applied in many relevant scientific fields, such as environmental and material sciences or cryobiology.[59,60]

Acknowledgements

The project was supported by the Grant Agency of the Czech Republic (P503/10/0947, P.K.; GA14-22777S, V.N., and by the Czech Ministry of Education (LO1214). Jakob Wirz and Todd Hammond are acknowledged for fruitful discussions.

References

1 Bartels-Rausch, T.; Jacobi, H. W.; Kahan, T. F.; Thomas, J. L.; Thomson, E. S.; Abbatt, J. P. D.; Ammann, M.; Blackford, J. R.; Bluhm, H.; Boxe, C.; Domine, F.; Frey, M. M.; Gladich, I.; Guzmán, M. I.; Heger, D.; Huthwelker, T.; Klán, P.; Kuhs, W. F.; Kuo, M. H.; Maus, S.; Moussa, S. G.; McNeill, V. F.; Newberg, J. T.; Pettersson, J. B. C.; Roeselová, M.; Sodeau, J. R. A review of air−ice chemical and physical interactions (AICI): liquids, quasi-liquids, and solids in snow. Atmos. Chem. Phys. 2014, 14, 1587−1633.

2 Klan, P.; Holoubek, I. Ice (Photo)chemistry. Ice as a Medium for Long-Term (Photo)chemical Transformations-Environmental Implications. Chemosphere 2002, 46, 1201−1210.

3 Domine, F.; Bock, J.; Voisin, D.; Donaldson, D. J. Can We Model Snow Photochemistry? Problems with the Current Approaches. J. Phys. Chem. A 2013, 117, 4733−4749.

4 O'Concubhair, R.; Sodeau, J. R. The Effect of Freezing on Reactions with Environmental Impact. Acc. Chem. Res. 2013, 46, 2716−2724.

5 Heger, D.; Jirkovsky, J.; Klan, P. Aggregation of Methylene Blue in Frozen Aqueous Solutions Studied by Absorption Spectroscopy. J. Phys. Chem. A 2005, 109, 6702−6709.

6 Heger, D.; Klan, P. Interactions of Organic Molecules at Grain Boundaries in Ice: A Solvatochromic Analysis. J. Photochem. Photobiol., A 2007, 187, 275−284.

7 Heger, D.; Klanova, J.; Klan, P. Enhanced Protonation of Cresol Red in Acidic Aqueous Solutions Caused by Freezing. J. Chem. Phys. B 2006, 110, 1277−1287.

8 Heger, D.; Nachtigallova, D.; Surman, F.; Krausko, J.; Magyarova, B.; Brumovsky, M.; Rubes, M.; Gladich, I.; Klan, P. Self-Organization of 1-Methylnaphthalene on the Surface of Artificial Snow Grains: A Combined Experimental-Computational Approach. J. Phys. Chem. A 2011, 115, 11412−11422.

9 Krepelova, A.; Huthwelker, T.; Bluhm, H.; Ammann, M. Surface Chemical Properties of Eutectic and Frozen NaCl Solutions Probed by XPS and NEXAFS. ChemPhysChem 2010, 11, 3859−3866.

10 Mulvaney, R.; Wolff, E. W.; Oates, K. Sulfuric-Acid at Grain- Boundaries in Antarctic Ice. Nature 1988, 331, 247−249.

11 Cheng, J.; Soetjipto, C.; Hoffmann, M. R.; Colussi, A. J. Confocal Fluorescence Microscopy of the Morphology and Composition of Interstitial Fluids in Freezing Electrolyte Solutions. J. Phys. Chem. Lett. 2010, 1, 374−378.

12 Baker, I.; Iliescu, D.; Obbard, R.; Chang, H.; Bostick, B.; Daghlian, C. P., Microstructural characterization of ice cores. In Annals of Glaciology, Vol 42, 2005, Dowdeswell, J.; Willis, I. C., Eds. 2005; Vol. 42, pp 441−444.

13 Blackford, J. R. Sintering and Microstructure of Ice: A Review. J. Phys. D Appl. Phys. 2007, 40, R355−R385.

14 Barnes, P. R. F.; Wolff, E. W.; Mallard, D. C.; Mader, H. M. SEM Studies of the Morphology and Chemistry of Polar Ice. Microsc. Res. Techniq. 2003, 62, 62−69.

15 Domine, F.; Lauzier, T.; Cabanes, A.; Legagneux, L.; Kuhs, W. F.; Techmer, K.; Heinrichs, T. Snow metamorphism as revealed by scanning electron microscopy. Microsc. Res. Techniq. 2003, 62, 33−48.

16 Spaulding, N. E.; Meese, D. A.; Baker, I. Advanced microstructural characterization of four East Antarctic firn/ice cores. J. Glaciol. 2011, 57, 796−810.

17 Barnes, P. R. F.; Mulvaney, R.; Wolff, E. W.; Robinson, K. A Technique for the Examination of Polar Ice Using the Scanning Electron Microscope. J. Microsc.-Oxford 2002, 205, 118−124.

18 McCarthy, C.; Blackford, J. R.; Jeffree, C. E. Low-Temperature- SEM Study of Dihedral Angles in the Ice-I/Sulfuric Acid Partially Molten System. J. Microsc. 2013, 249, 150−157.

19 Cullen, D.; Baker, I. Observation of Impurities in Ice. Microsc. Res. Techniq. 2001, 55, 198−207.

20 Cullen, D.; Baker, I. Observation of Sulfate Crystallites in Vostok Accretion Ice. Mater. Charact. 2002, 48, 263−269.

21 Rosenthal, W.; Saleta, J.; Dozier, J. Scanning Electron Microscopy of Impurity Structures in Snow. Cold. Reg. Sci. Technol. 2007, 47, 80−89.

22 Danilatos, G. D. Foundations of Environmental Scanning Electron Microscopy. Adv. Electron. El. Phys. 1988, 71, 109−250.

23 Nedela, V.; Hrib, J.; Vookova, B. Imaging of Early Conifer Embryogenic Tissues with the Environmental Scanning Electron Microscope. Biol. Plantarum 2012, 56, 595−598.

24 Waller, D.; Stokes, D. J.; Donald, A. M. Improvements to a Cryosystem to Observe Ice Nucleating in a Variable Pressure Scanning Electron Microscope. Rev. Sci. Instrum. 2008, 79.

25 Keyser, L. F.; Leu, M. T. Morphology of Nictric-acid and Water Ice Films. Microsc. Res. Techniq. 1993, 25, 434−438.

26 Leu, M.-T.; Keyser, L. F. Vapor-deposited Water and Nitric Acid Ices: Physical and Chemical Properties. Int. Rev. Phys. Chem. 2009, 28, 53−109.

27 Zimmermann, F.; Ebert, M.; Worringen, A.; Schutz, L.; Weinbruch, S. Environmental Scanning Electron Microscopy (ESEM) as a New Technique to Determine the Ice Nucleation Capability of Individual Atmospheric Aerosol Particles. Atmos. Environ. 2007, 41, 8219−8227.

28 Varanasi, K. K.; Deng, T.; Smith, J. D.; Hsu, M.; Bhate, N. Frost Formation and Ice Adhesion on Superhydrophobic Surfaces. Appl. Phys. Lett. 2010, 97.

29 Pfalzgraff, W. C.; Hulscher, R. M.; Neshyba, S. P. Scanning Electron Microscopy and Molecular Dynamics of Surfaces of Growing and Ablating Hexagonal Ice Crystals. Atmos. Chem. Phys. 2010, 10, 2927−2935.

30 Pedersen, C.; Mihranyan, A.; Stromme, M. Surface Transition on Ice Induced by the Formation of a Grain Boundary. PLoS One 2011, 6.

31 Tihlarikova, E.; Nedela, V.; Shiojiri, M. In Situ Study of Live Specimens in an Environmental Scanning Electron Microscope. Microsc. Microanal. 2013, 19, 914−918.

32 Leung, A. F.; Hayashibara, L.; Spadaro, J. Fluorescence Properties of Uranyl Nitrates. J. Phys. Chem. Solids 1999, 60, 299−304.

33 Lubal, P.; Havel, J. Spectrophotometric and Potentiometric Study of Uranyl Hydrolysis in Perchlorate Medium. Is Derivative Spectrophotometry Suitable for Search of the Chemical Model? Chem. Pap. 1997, 51, 213−220.

34 Nedela, V. Methods for Additive Hydration Allowing Observation of Fully Hydrated State of Wet Samples in Environmental SEM. Microsc. Res. Techniq. 2007, 70, 95−100.

35 Nedela, V. Controlled Dehydration of a Biological Sample Using an Alternative form of Environmental SEM. J. Microsc.-Oxford 2010, 237, 7−11.

36 Nedela, V.; Jirak, J. Ionisation Detector for Environmental Scanning Electron Microscope. Eur. Pat. 2010, EP 2 195 822 B1.

37 Murphy, D. M.; Koop, T. Review of the Vapour Pressures of Ice and Supercooled Water for Atmospheric Applications. Q. J. R. Meteor. Soc. 2005, 131, 1539−1565.

38 Chen, S.; Baker, I. Observations of the Morphology and Sublimation-induced Changes in Uncoated Snow Using Scanning Electron Microscopy. Hydrol. Process. 2010, 24, 2041−2044.

39 Piazolo, S.; Montagnat, M.; Blackford, J. R. Sub-structure Characterization of Experimentally and Naturally Deformed Ice Using Cryo-EBSD. J. Microsc. 2008, 230, 509−519.

40 Weikusat, I.; De Winter, D. A. M.; Pennock, G. M.; Hayles, M.; Schneijdenberg, C.; Drury, M. R. Cryogenic EBSD on Ice: Preserving a Stable Surface in a Low Pressure SEM. J. Microsc. 2010, 242, 295− 310.

41 Cizmar, P.; Vladar, A. E.; Ming, B.; Postek, M. T. Simulated SEM Images for Resolution Measurement. Scanning 2008, 30, 381− 391.

42 Li, Y.; Somorjai, G. A. Surface Premelting of Ice. J. Phys. Chem. C 2007, 111, 9631−9637.

43 Sazaki, G.; Asakawa, H.; Nagashima, K.; Nakatsubo, S.; Furukawa, Y. How do Quasi-Liquid Layers Emerge from Ice Crystal Surfaces? Cryst. Growth Des. 2013, 13, 1761−1766.

44 Meinrath, G. Aquatic Chemistry of Uranium. Freiberg On-line Geosci. 1998, 1, 1−100.

45 Cohen-Adad, R.; Lorimer, J. W.; Phillips, S. L.; Salomon, M. A Consistent Approach to Tabulation of Evaluated Solubility Data - Application to the Binary Systems RbCl−H2O and UO2(NO3)2−H2O. J. Chem. Inf. Comp. Sci. 1995, 35, 675−696.

46 Kirgintsev, A. N.; Trushnikova, L. N.; Lavent'eva, V. G. Solubility of Inorganic Substances in Water, Handbook; Khimiya: Leningrad, Otd., 1972; p 245.

47 Dent, A. J.; Ramsay, J. D. F.; Swanton, S. W. An EXAFS study of uranyl ion in solution and sorbed onto silica and montmorillonite clay colloids. J. Colloid Interface Sci. 1992, 150, 45−60.

48 Blackford, J. R.; Jeffree, C. E.; Noake, D. F. J.; Marmo, B. A. Microstructural evolution in sintered ice particles containing NaCl observed by low-temperature scanning electron microscope. Proc. Inst. Mech. Eng. L−J. Mater.-Des. Appl. 2007, 221, 151−156.

49 Rempel, A. W.; Waddington, E. D.; Wettlaufer, J. S.; Worster, M. G. Possible Displacement of the Climate Signal in Ancient Ice by Premelting and Anomalous Diffusion. Nature 2001, 411, 568−571.

50 Iliescu, D.; Baker, I.; Chang, H. Determining the orientations of ice crystals using electron backscatter patterns. Microsc. Res. Techniq. 2004, 63, 183−187.

51 Kurkova, R.; Ray, D.; Nachtigallova, D.; Klan, P. Chemistry of Small Organic Molecules on Snow Grains: The Applicability of Artificial Snow for Environmental Studies. Environ. Sci. Technol. 2011, 45, 3430−3436.

52 Ray, D.; Kurkova, R.; Hovorkova, I.; Klan, P. Determination of the Specific Surface Area of Snow Using Ozonation of 1,1- Diphenylethylene. Environ. Sci. Technol. 2011, 45, 10061−10067.

53 Bouby, M.; Billard, I.; Bonnenfant, A.; Klein, G. Are the Changes in the Lifetime of the Excited Uranyl Ion of Chemical or Physical Nature? Chem. Phys. 1999, 240, 353−370.

54 Takenaka, N.; Tanaka, M.; Okitsu, K.; Bandow, H. Rise in the pH of an unfrozen solution in ice due to the presence of NaCl and promotion of decomposition of gallic acids owing to a change in the pH. J. Phys. Chem. A 2006, 110, 10628−10632.

55 Robinson, C.; Boxe, C. S.; Guzman, M. I.; Colussi, A. J.; Hoffmann, M. R. Acidity of frozen electrolyte solutions. J. Chem. Phys. B 2006, 110, 7613−7616.

56 Cho, H.; Shepson, P. B.; Barrie, L. A.; Cowin, J. P.; Zaveri, R. NMR investigation of the quasi-brine layer in ice/brine mixtures. J. Chem. Phys. B 2002, 106, 11226−11232.

57 Sander, R.; Bottenheim, J. A compilation of tropospheric measurements of gas-phase and aerosol chemistry in polar regions. Earth Syst. Sci. Data 2012, 4, 215−282.

58 Tokunaga, T. K.; Kim, Y.; Wan, J. M.; Yang, L. Aqueous Uranium(VI) Concentrations Controlled by Calcium Uranyl Vanadate Precipitates. Environ. Sci. Technol. 2012, 46, 7471−7477.

59 Kirsebom, H.; Mattiasson, B. Cryostructuration as a Tool for Preparing Highly Porous Polymer Materials. Polym. Chem. 2011, 2, 1059−1062.

60 Kirk, S.; Skepper, J.; Donald, A. M. Application of Environmental Scanning Electron Microscopy to Determine Biological Surface Structure. J. Microsc.-Oxford 2009, 233, 205−224.

27 Evaporating brine from frost flowers with electron microscopy and implications for atmospheric chemistry and sea-salt aerosol formation

Xin Yang[1], Vilém Neděla[2], Jiří Runštuk[2], Gabriela Ondrušková[3,4], Ján Krausko[3,4], Ľubica Vetráková[3,4], and Dominik Heger[3,4]

1 British Antarctic Survey, Natural Environment Research Council, Cambridge, UK
2 Environmental Electron Microscopy Group, Institute of Scientific Instruments of the CAS, Brno, Czech Republic
3 Department of Chemistry, Faculty of Science, Masaryk University, Kamenice 5/A8, 625 00 Brno, Czech Republic
4 Research Centre for Toxic Compounds in the Environment (RECETOX), Masaryk University, Kamenice 5/A29, 625 00 Brno, Czech Republic

Abstract.

An environmental scanning electron microscope (ESEM) was used for the first time to obtain well-resolved images, in both temporal and spatial dimensions, of lab-prepared frost flowers (FFs) under evaporation within the chamber temperature range from-5 to-18 °C and pressures above 500 Pa. Our scanning shows temperature-dependent NaCl speciation: the brine covering the ice was observed at all conditions, whereas the NaCl crystals were formed at temperatures below -10 °C as the brine oversaturation was achieved. Finger-like ice structures covered by the brine, with a diameter of several micrometres and length of tens to 100 μm, are exposed to the ambient air. The brine-covered fingers are highly flexible and cohesive. The exposure of the liquid brine on the micrometric fingers indicates a significant increase in the brine surface area compared to that of the flat ice surface at high temperatures; the NaCl crystals formed can become sites of heterogeneous reactivity at lower temperatures. There is no evidence that, without external forces, salty FFs could automatically fall apart to create a number of sub-particles at the scale of micrometres as the exposed brine fingers seem cohesive and hard to break in the middle. The fingers tend to combine together to form large spheres and then join back to the mother body, eventually forming a large chunk of salt after complete dehydration. The present microscopic observation rationalizes several previously unexplained observations, namely, that FFs are not a direct source of sea-salt aerosols and that saline ice crystals under evaporation could accelerate the heterogeneous reactions of bromine liberation.

Introduction

Ice and snow constitute an important reaction medium on Earth and are known to accumulate and concentrate significant amounts of impurities that are stored, transformed, and eventually released. The knowledge of the exact location and speciation of these chemical impurities in ice and snow under various environmental conditions is crucial for assessing their reactivity (McNeill et al., 2012; Bartels-Rausch et al., 2014; Gudipati et al., 2015) and further fate.

The ions originating from sea salt (including, for example, Na^+, Cl^-, and Br^-/ have been widely observed in polar regions in media such as aerosols, snow packs, and ice cores (DeAngelis et al., 1997; Rankin and Wolff, 2003; Fischer et al., 2007; Legrand et al., 2016). The sea salts trapped in snow packs form a large chemical reservoir and therefore embody a significant part of chemical reactions in the polar boundary layer (Abbatt et al., 2012). Conversely, inactive ions such as Na^+ recorded in ice cores could serve as a palaeoclimate proxy for the past climate (Rankin and Wolff, 2003; Abram et al., 2013). Although the sea spray and bubble bursting in the open ocean surface dominate sea-salt aerosol (SSA) production on most of Earth, the winter SSA peaks observed at most near-coastal sites in polar regions (Wagenbach et al., 1998; Rankin et al., 2004) are clearly out of phase with the distance to the open water. Several lines of evidence suggest that winter sea salt cannot derive only from the long-range transport of the aerosol produced over the open ocean. The winter maximum observed seems inconsistent with the fact that the nearest open water is hundreds of kilometres further away in the given season because of extended sea ice. In ice cores, significantly higher concentrations of salts are found in glacial periods, when sea ice was even more widespread and furthermore when relevant models do not suggest any greater transport (Mahowald et al., 2006). The most direct evidence of the salt that should originate from zones covered with sea ice arises from the composition of sea-salt aerosol and ice cores. Frequent episodes when the sulfate / sodium [SO_4^{2-} / Na^+] ratio is below that of seawater, despite the addition of the non-sea-salt sulfate resulting from the oxidation of dimethlysulfide, are observed (Wagenbach et al., 1998). This is believed to occur due to the effect of mirabilite ($Na_2SO_4.10H_2O$) precipitating from the brine when the temperature drops below -6.4 °C (Wagenbach et al., 1998; Jourdain et al., 2008 ; Butler et al., 2016b; Marion et al., 1999), a segregation inapplicable to sea spray particles.

The sea ice microstructure is permeated by brine channels and pockets that contain concentrated seawater-derived brine. Cooling sea ice results in further formation of pure ice within these pockets as thermal equilibrium is attained, resulting in a smaller volume of increasingly concentrated residual brine (Light et al., 2003;

Butler et al., 2016b). A fraction of such concentrated brine will be expelled upwards to form a thin layer of brine on the sea ice surface, where frost flower (FFs) can grow under a certain weather condition. The formation of mirabilite results in removing the major portion of the dissolved SO_4^{2-} from the brine, with less effect on the Na^+ due to its large abundance compared to the sulfate (e.g. Butler et al., 2016b). The SSA produced from these residual brines consequently displays a depleted [SO_4^{2-} / Na^+] ratio. However, for sea spray particles, the Na2SO4 will not be fractionated in the atmosphere or the following deposition, even when these particles are exposed to sub-zero temperatures: the precipitated mirabilite remains within the body of the aerosol and has no effective pathway to escape.

FFs are commonly observed on fresh sea ice and preferentially grow on small-scale roughness nodules sticking above the surface or out of the brine, which is typically colder by 5 °C compared to bulk ice (Domine, 2005; Galley et al., 2015); at these conditions, the supersaturation of water vapour is frequently achieved (Style and Worster, 2009). Frost flowers often consist of feather-like dendritic ice crystal structures, and their surface can be covered by concentrated brine (Perovich and Richter-Menge, 1994; Barber et al., 2014; Galley et al., 2015). A detailed chemical composition analysis was performed, finding, inter alia, that FFs can reach the salinity of the concentrated brine of 120 practical salinity units (Douglas et al., 2012), which is in the effective range of the mirabilite precipitation (Butler et al., 2016b). FFs have the specific surface area of 185 (+80–50) $cm^2\ g^{-1}$, measured by methane adsorption; such a specific surface area is about 5 times lower than that of freshly fallen snow. The surface area of FFs is estimated to be $1.4 m^2$ per m^2 of ice surface (Domine, 2005). The fragile structure plus extremely high brine salinity (Rankin, 2002) make FFs the likely cause of chemical reactions (e.g. heterogenous, photochemical, and redox; Perovich and Richter-Menge, 1994; Kaleschke et al., 2004; Simpson et al., 2007) and source for SSA (Wagenbach et al., 1998; Wolff et al., 2003). However, recent studies propose that FFs are not as important as assumed previously (Obbard et al., 2009; Roscoe et al., 2011; Abbatt et al., 2012). In particular, a recent wind tunnel experiment indicated that FFs are not a direct source of SSA (Roscoe et al., 2011). Apart from saline FFs, the snow lying on sea ice can be contaminated by seawater (or saline) through various pathways (Domine et al., 2004). These contaminated salty snows have been hypothesized to act as an efficient source of SSA (via blowing snow) and bromine (Yang et al., 2008; Legrand et al., 2016; Zhao et al., 2016; Levine et al., 2014). The relative importance of these two sea-ice-sourced SSA to the polar winter sea-salt budget is still under debate (e.g. Huang and Jaeglé, 2017; Xu et al., 2016; Rhodes et al., 2017). In any case (FFs or salty snow), the formation of SSA from salty ice particles requires its size to be reduced via the loss of water through either the evaporation or the

sublimation processes, depending on the temperature. Until now, there was no detailed image at the microphysical scale to indicate what happens to saline ice under evaporation or sublimation. Moreover, current atmospheric chemical models consider the solutes' impurities on ice to be present in a diluted liquid solution on the ice surface (Domine et al., 2013). Such a model is generally unsatisfactory in describing the real situation, and thus more realistic parameters for modelling are needed. Some of us previously showed that the concentration increase of nonpolar (Heger et al., 2011; Kania et al., 2014; Krausko et al., 2015a, b) and polar compounds (Heger et al., 2005, 2006; Heger and Klan, 2007; Krausková et al., 2016) can even lead to their crystallization under certain conditions.

In this study, we grew FFs in a laboratory and inspected them using an environmental scanning electron microscope (ESEM) to obtain some information about the state of impurities in/on the ice. The preparation of the FF samples to mimic the FFs naturally produced on sea ice is detailed in Sect. 2 together with the related information on the ESEM. The scanning results are presented in Sect. 3, the atmospheric implications are discussed in Sect. 4, and the conclusions are available in Sect. 5.

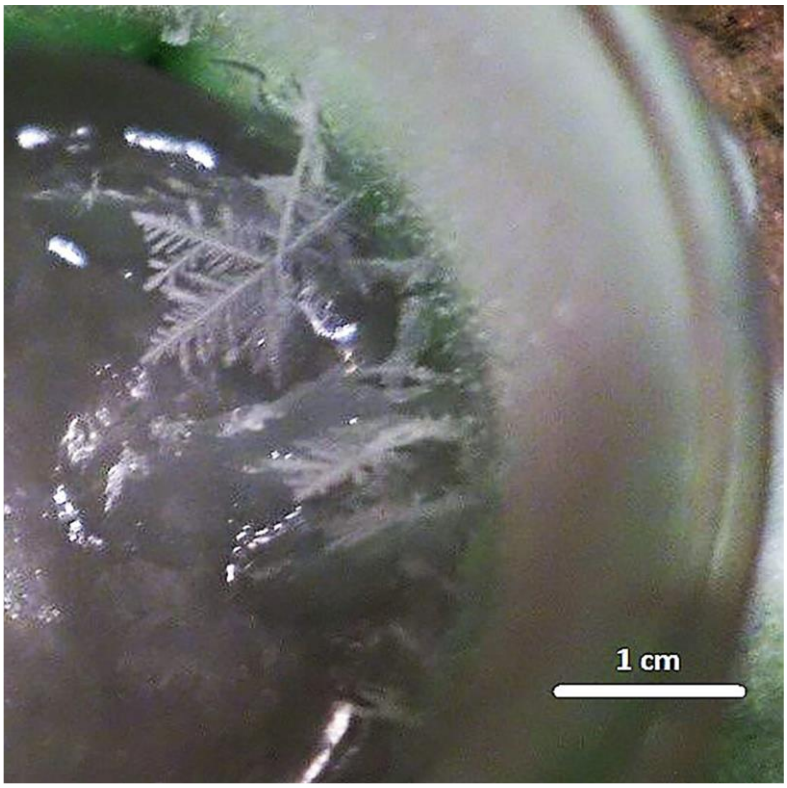

Figure 1. A frost flower (FF) grown in a polystyrene-isolated beaker in a walk-in cold room, at the temperature of -30 °C. Both pure water FFs and saline FFs were prepared for further microscopic scanning (see the text for details).

Methods

Growth of the frost flowers and preparation of the samples

The FFs were prepared in a custom-built 2m×2m walk-in cold chamber. Inspired by the natural condition at which FFs grow (Style and Worster, 2009) and exploiting previous methods of preparation (Roscoe et al., 2011), we cooled the walk-in cold chamber down to -30 °C and inserted vessels containing pure water or an aqueous solution of NaCl (3.5% w/w, similar to that of seawater) at 20 °C. The vessels were isolated with styrofoam to minimize the contact cooling of the solution by the floor of the walk-in chamber and to promote cooling by the air. We typically observed the following course of events: first, hoarfrost appeared on the sides of the beaker; then, an ice crust formed on the water level; subsequently, dendrite-shaped icy features (considered to be FFs) grew gradually, as shown in Fig. 1. After the ice reached a certain thickness, the FFs stopped growing and were collected into a pre-cooled vial to be stored at the temperature of liquid nitrogen. Care was taken to collect only the FFs from the ice surface, avoiding the hoarfrost condensed on the walls of the beaker. The FFs were fragile and fragmented during the manipulation. The FFs grown on the surface of pure water were powdery; however, those grown from the brine were sticky, and therefore two spatulas were needed to place them into the vials. We attempted to follow growth conditions similar to the natural ones; our sampling method guarantees that the features were grown on the ice surface, and thus the examined samples are believed to be very similar to natural FFs.

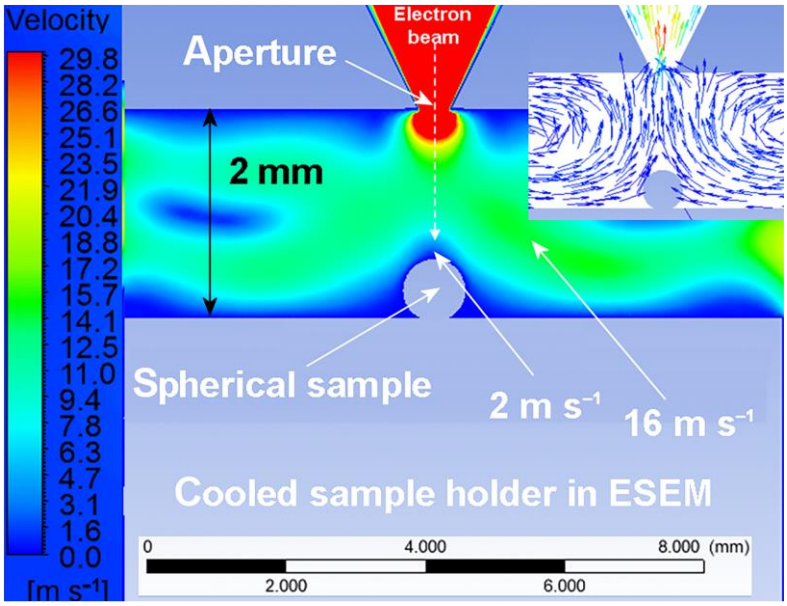

Figure 2. The ANSYS Inc. fluent-based simulation of the water vapour velocity distribution and the direction of the vapour flow in the vicinity of the sample surface in the specimen chamber of the applied ESEM AQUASEM II.

Environmental scanning electron microscope

The ESEM (AQUASEM II) is unique in the observation of nonconductive, wet, or liquid samples, with the specimen chamber pressure as high as 2000 Pa and temperatures ranging from 0 to -30 °C (Tihlarikova et al., 2013). The indicated temperature is measured on the sample holder. The temperature of the ice surface is estimated to differ by no more than 2 °C from that of the holder on which the temperature is measured. This estimate is based on the observation of the ice surface melting. The major source of the heat is the energy from the electrons used for scanning.

The conditions inside the chamber allow for the observation of ice samples in conditions similar to those under which ice and snow occur naturally. No conductive coating of the sample is needed, because the positive ions resulting from the electron–gas ionization in high-gas-pressure conditions of the ESEM discharge the accumulated charge. The strength of this apparatus lies in the delicate control of the dynamic conditions in the specimen chamber via an originally designed hydration system enhanced with temperature and vapour flow control and an advanced cooling system integrated in the sample holder. The specimen chamber can be evacuated very slowly, with the possibility of reaching high humidity conditions in the sample vicinity without purge– flood cycles (Nedˇela et al., 2015). The water vapour temperature is estimated to be around 10 °C. Care was taken to direct the steam away from the sample to prevent any heat-up. The regulation of the temperature in the vicinity of the sample allows us to study ice in precisely controlled conditions (Krausko et al., 2014). The temperature, pressure, and relative humidity in the chamber of the ESEM can be set close to the frost point to cause ice sublimation or gradual growth. The ESEM is equipped with a tungsten hairpin cathode as a source of electrons and also with two custom-built detectors (Neděla et al., 2011): an ionization detector for secondary electrons (surface sensitive to provide information about the morphology of the ice surface) and a highly material sensitive detector of backscattered electrons. A comparison of these two modes on identical samples yields complementary information on the morphology of the ice surface and ice grain boundaries contaminated by impurities.

As shown in Fig. 2, water vapour flows around the sample and through the detector's aperture during the scanning of the sample. The flow speed varies from $2ms^{-1}$ on the sample surface to $16ms^{-1}$ at the distance of 0.7mm above the sample surface (simulated for the experimental pressure of 300 Pa in the specimen chamber of the ESEM AQUASEM II and for the spherical shape of the sample). The flow is influenced by the shape of the sample, pumping speed, and ESEM aperture

diameter. The flow speed was simulated as described previously (Maxa, 2011, 2016).

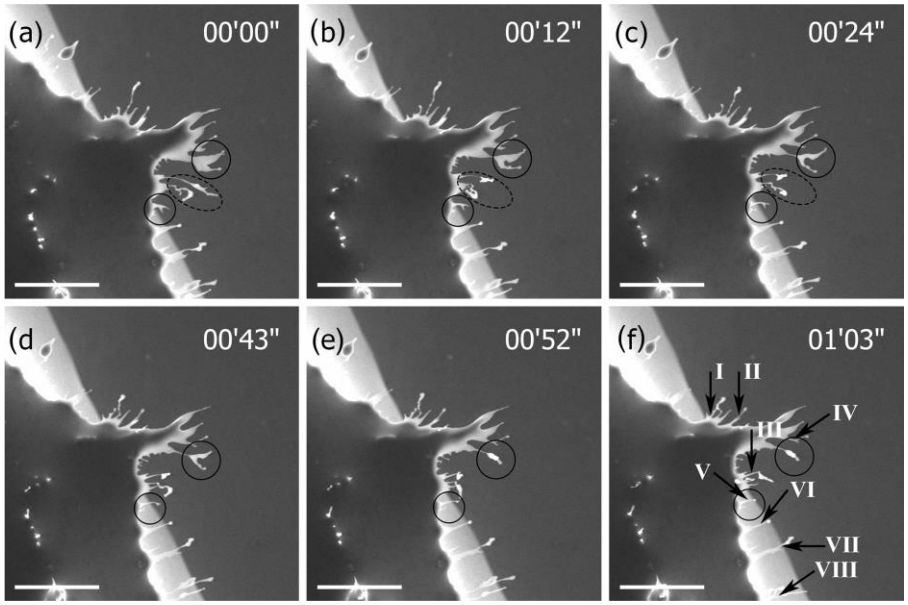

Figure 3. The dynamical in situ images of the formation of brine fingers during slow evaporation of water from the frost flower. The individual fingers bending and flapping around are highlighted in circles. The width of the seven indicated necks in Fig. 3f is measured as d_I =(2.23±0.43) μm, mean ±standard error of the mean. Imaged with the applied ESEM AQUASEM II; beam energy at 20 keV, ionization detector, water vapour pressure of 348 Pa, sample holder temperature of -5.2 °C, and sample-to-aperture distance of 2 mm. Scale bar: 100 μm. A video of this case is attached (S1).

Results and discussions

FFs at a high temperature: brine fingers formation

The FFs were scanned at the chamber temperature of -5.2 °C. Figure 3 shows many spikes sticking out from the main ice body; here, these will be referred to as fingers. The smooth texture is indicative of surfaces covered with a layer of a solution in contrast to the dry ice crystal surface observed at temperatures below -30 °C and pressures below 50 Pa (McCarthy et al., 2007; Blackford, 2007; Pfalzgraff et al., 2010; Bartels-Rausch et al., 2014). The image differs from that of a water drop also in the irregular and non-spherical features. Thus, we are of the opinion that the exposed fingerlike spikes consist of ice covered with brine. More arguments to support this interpretation will be proposed in the following parts of the text. The brine is expected to become more concentrated as a result of the loss of water during progressive evaporation. The exposed thin fingers can be as much as 100 μm long, still remaining quite cohesive and hard to break. In Fig. 3f, we estimate the thickness of the fingers' necks at their most narrow points to be d =(2.23±0.43) μm; the given values are mean ±standard error of the mean. In some cases, a rounded sphere appeared on the top of a finger during evaporation, as encircled in Fig. 3. At temperatures exceeding ~ -10 °C, which is well above the eutectic point temperature

($T_{Eutectic}$ D=21.21 °C; Brady, 2009), the concentrated brine was always observed as liquid, and no NaCl crystals were perceived. The viscosity of the concentrated brine at the 20 °C is not even 2 times higher than that of pure water (Weast et al., 1987). Although we did not find any reference to the values of the brine viscosity at sub-zero temperatures, the viscosity of seawater at zero temperature is only slightly higher than that of pure water (1.3 times; Sharqawy et al., 2010), and the viscosity of supercooled water at -17 °C is only 3.8 times larger compared to that at 20 °C (Dehaoui et al., 2015). Therefore, we do not assume that the viscosity of the brine will increase significantly enough to be the only explanation for the formation of the fingers. The fingers were observed to easily bend and flap following the airflow in the chamber (Fig. 3, oval, and Supplement S1). When these fingers are close enough to one another, they may tangle together to join into a larger one.

The relative humidity in our experiments was set to be slightly below the frost point, and therefore slow loss of the water from the sample could be observed. Thus, the micrographs obtained already at the beginning of the observations are not fully undisturbed; we assume that the water evaporates faster from the brine of a lower concentration compared to the more concentrated one (in accordance with Raoult's law). The vapour pressures above the water, ice, and saturated brine (8.3% w=w) at -5 °C are 422, 402, and 403 Pa, respectively. These values were calculated from the applied equations for the vapour pressure above the water and ice as adopted from Buck (1981); for the brine, the relevant formulae are proposed within the article by Perovich and Richter- Menge (1994):

$$e_w = [1.0007 + 3.46 \times 10^{-6} p] \times [6.1121 \times e^{\frac{(17.966 \times t)}{(247.15 + t)}}]$$

$$e_i = [1.0003 + 4.18 \times 10^{-6} p] \times [6.1115 \times e^{\frac{(22.452 \times t)}{(272.55 + t)}}]$$

$$e_b = e_\omega (1 - 0.000537 \times S_b)$$

where e_w is the saturation vapour pressure above the water, e_i is the saturation vapour pressure above the ice, e_b is the saturation vapour pressure above the brine, p is the atmospheric pressure in millibars, S_b is the brine salinity in parts of mass per thousand, and t is the temperature in °C. In an additional experiment with pure water FFs (not shown here), we found out that they sublimate markedly faster than brine-covered FFs.

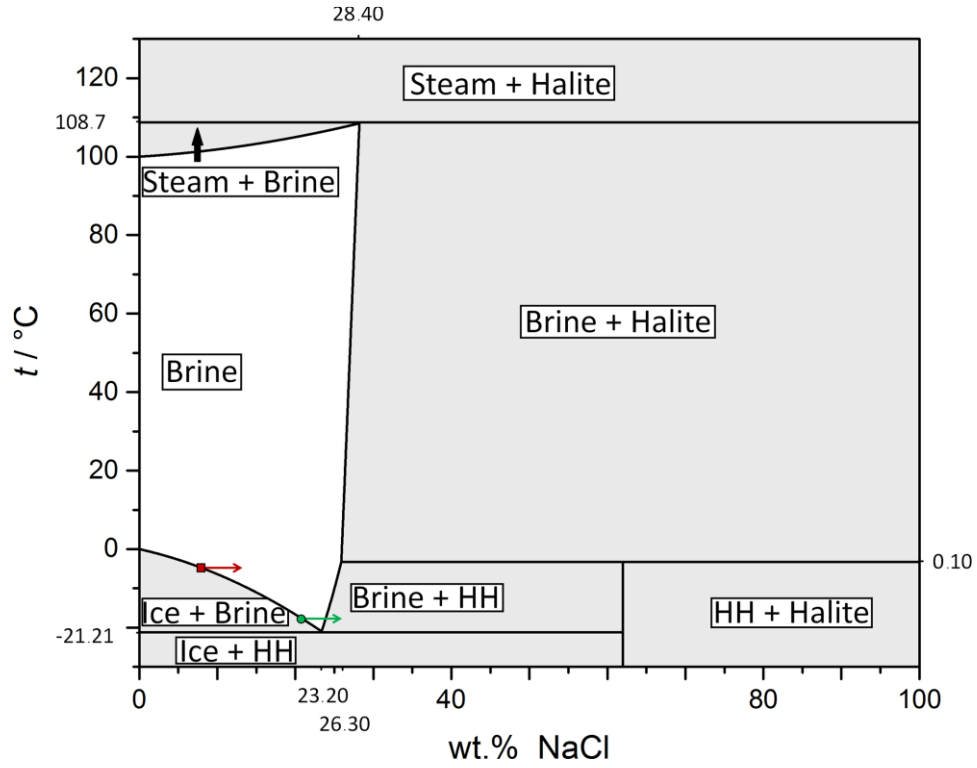

Figure 4. The phase diagram for a water–NaCl system. Indicated (red and green arrows) are our experimental conditions at about -5 and -17 °C. HH stands for hydrohalite ($NaCl.2H_2O$). Based on equations from Brady (2009).

At the temperature of -5.2 °C and concentration of NaCl lower than 8.3% (w=w), the phase diagram (Fig. 4) indicates the presence of a liquid solution of NaCl and ice. Therefore, if the equilibrium conditions are established, there will be ice and ca. 8.3%NaCl solution covering its surface. As the water is gradually evaporated from the brine, the ice must melt to maintain the equilibrium concentration. This process is represented with the red arrow in the phase diagram of Fig. 4. This rationalizes well our observations: the evaporation of the water from the brine on the fingers causes its concentration to increase above the equilibrium concentration; therefore, the water must be supplied from the ice body towards the brine fingers to dilute the brine. This process results in gradual melting of the ice body until all the ice is melted.

An examination of the sequences of the micrographs suggests that the evaporation proceeds faster from the main ice body than from the fingers. This can be seen in the video of Supplement S1 as the fingers exhibit a relatively stable shape even if the main ice body gradually abates. Thus, the concentration of the brine in the surface layer of the fingers is deemed to be higher than that on the main body. We can speculate that the higher concentration of NaCl on the fingers is a result of previous water vapour evaporation from the brine on the fingers. Possibly, the most concentrated solution is found on the tips of the fingers, where small spheres are

sometimes formed. The increased local concentration of salt would effectively lower the water vapour evaporation and hence reduce further melting of the ice forming the fingers' interior, thus not allowing its breakaway from the main body. For example, if the NaCl saturation concentration of 25%(w=w) is reached at -5 °C, the water partial pressure drops to 365 Pa from the 403 Pa at the brine equilibrium concentration (8.3 %).

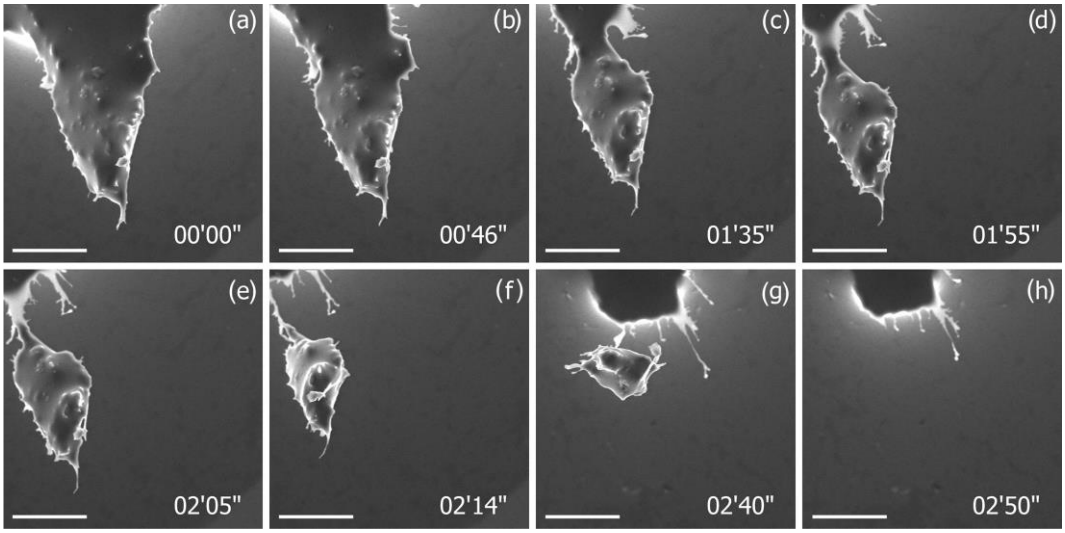

Figure 5. The dynamical in situ micrographs of a large (~100 μm) brine-covered piece of ice formation and breakaway during slow evaporation of water from the frost flower. Imaged with the ESEM AQUASEM II; beam energy at 20 keV, ionization detector, water vapour pressure of 348 Pa, sample holder temperature of -5.2 °C, and sample-to-aperture distance of 2 mm. Scale bars: 100 μm. A video of this case is attached (Supplement S2).

A particular consequence of a higher rate of water evaporation from the side wall of a finger and the main ice body compared to the fingertip is the formation and propagation of gulfs. This is well exemplified in Fig. 5, where the process resulted in the breakaway of large pieces of ice (> 100 μm) from the mother body. First, a very deep gulf was formed which later separated the two pieces by a very thin neck, eventually leading to the breaking off of the two parts (Supplement S2). This case indicates that the evaporation or sublimation process indeed could cause a large ice particle to fall aside, but this phenomenon is not common, as we noticed it only once in all our observations (20 experiments). Moreover, there is no evidence that the brine fingers can fall apart to form a number of micrometre-sized particles.

The understanding of the structure of FFs is still far from complete. The 3-D X-ray micro computer tomography experiments suggest that salt impurities are present mostly on the ice surface (Hutterli et al., 2008). Such a finding is consistent with our observation and can be well understood, taking into account the genesis of FFs, where the brine wicks on the already formed ice to develop a highly saline surface skim (Domine, 2005). In contrast, the dynamics of freezing forces the solutes to

segregate and form the veins of freeze-concentrated solutions engulfed by the ice (Blackford, 2007; Cheng et al., 2010; McCarthy et al., 2013; Bogdan et al., 2014; Krausko et al., 2014). The solutes in the freeze-concentrated solution, here probably in the surface layer only, experience not only an increased concentration (Heger et al., 2005; Kania et al., 2014; Krausko et al., 2015a) but also a changed pH (Heger et al., 2006; Krausková et al., 2016; Papadimitriou et al., 2016; Rérolle et al., 2016) and polarity (Heger and Klan, 2007). Recently, it was noticed that, for a frozen solution, the surface brine layer is interconnected with the interior veins system (Walker et al., 2013).

Overall, ice covered with brine seems to offer the most reasonable explanation for the objects denoted as fingers, aptly characterizing all our observations and also corresponding to the previous studies (Domine, 2005; Cheng et al., 2010). The observed generation of fingers can be the energetically most feasible path to deal with a large amount of concentrated brine being relatively quickly formed on an ice body, whose volume gradually decreases. Further water evaporation would concentrate the brine, eventually forming NaCl crystals. The final product of the evaporation is shown in Fig. S3. Typically, a sample was dried within 30 min in the microscopic chamber (depending on the exact experimental condition), the relative humidity embodying the most important factor (Neděla et al., 2015).

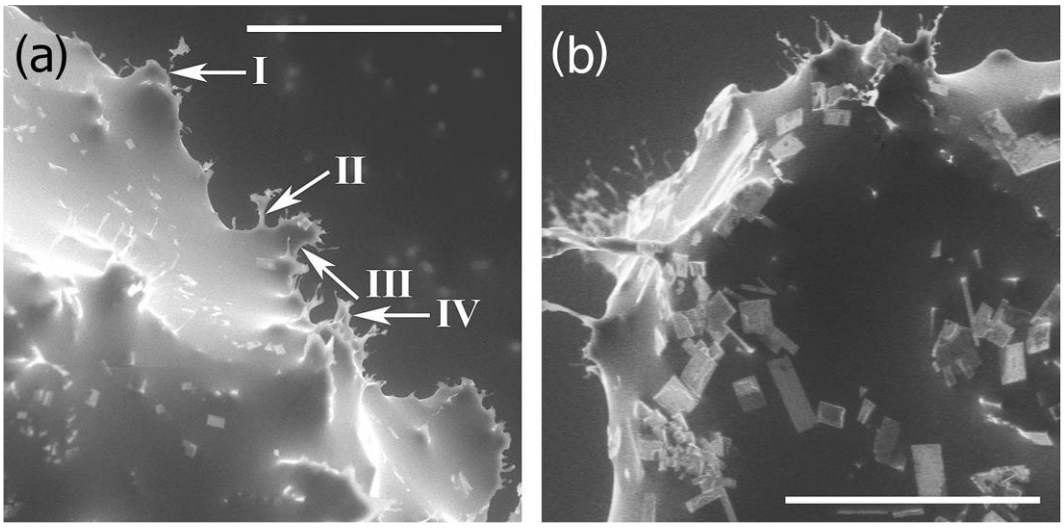

Figure 6. (a, b) The frost flower micrograph detailing the surface scattered by the NaCl crystals and the finger structures. Compared to the situation at a higher temperature (Figs. 3 and 4), the brine fingers looked stiffer, appeared more rarely, and the angle at the base was larger. The widths of the four indicated necks measured are d_I D0.87, d_{II} D3.78, d_{III} D26.30, and d_{VI} D13.60 μm. Scale bars: 200 μm. Figure 6b shows that the salt crystals can be found also on the protruding fingers. Microscopic conditions: ESEM AQUASEM II, ionization detector, air pressure of 520 Pa, sample holder temperature of -17.0 °C, and sample-to-aperture distance of 2 mm.

FFs at a low temperature: NaCl crystal formation

The evaporation of FFs at the temperature of -17 °C was also scanned, as shown in Figs. 6–9. Additionally to the liquid brine observed at -5 °C, we saw a large number of salt crystals widely spread on not only the ice surface layer but also the surfaces of the fingers (Fig. 6b). Apparently, as we observed the salt crystals, brine, and ice together at these conditions, the sample cannot be in the thermodynamic equilibrium (Fig. 4).

The fingers at -17 °C were less numerous and more robust compared to those observed at higher temperatures, with their necks typically reaching tens of micrometres or more (Fig. 6). The flexibility of the fingers is demonstrated in Figs. 7 and S4 by the observation of thin neck tethering and eventual pulling back a large piece of ice to the main ice body. Together with our additional scanning performed at the temperatures of -10 and -12 °C (not shown), we witnessed that chamber temperatures progressively decreasing below -10°C effectively increase the formation of crystals and reduce the number of fingers, indicating that the brine microphysical feature under sublimation or the evaporation process is temperature sensitive. Figure 8 clearly shows that salt crystals are widely formed on the surface brine layer during water evaporation from the FFs, eventually growing into a large cluster of crystals covering most of the surface. The dynamics of the process is shown by successive images joined into the video in S5. The size of the crystals varies from a few micrometres at an early stage to more than one hundred micrometres at a later stage. It is also possible to discern that salt crystals freely move on the brine surface, occasionally sinking below the surface. This can provide some indication of the thickness of the brine on the ice surface. It should be noted that, at the temperature of -17 °C, air with the relative humidity of ca. 20% was always used instead of the pure water vapour applied at -5 °C, thus setting slightly evaporative conditions in the microscopic chamber.

We suppose that the sample heated up from the liquid nitrogen temperature to -17 °C would allow the brine layer to approach the thermodynamic equilibrium concentration of 20% (w=w). Referring to the mirabilite, fast dissolution of hydrohalite crystals is expected upon warming (Butler and Kennedy, 2015; Butler et al., 2016b); therefore, the observations are dependent on the temperature and pressure in the microscope's chamber and not on the thermal history of the sample. Further water evaporation can easily cause the oversaturation of the brine solution to a concentration exceeding 24%(w=w) and thus result in the consequent formation of salt crystals. Presumably, this occurs in our microscopic chamber at the above-indicated observation temperatures. We can exclude the assumption that the formed crystals are made of water ice as they grow (in size and number) during the

evaporation process. The saturation can be reached via increasing the brine concentration by only 3 %, which can easily happen. This process is represented by the green arrow in the phase diagram of Fig. 4. The formation of salt crystals, besides ice melting, is apparently the second mechanism of reducing the brine concentration. Which mechanism prevails then depends on the subtle balance of the apour pressure and temperature in the microscopic chamber. Under thermodynamic equilibrium conditions, the crystallization would effectively reduce the salt concentration of the brine to the quasi-equilibrium state of ca. 24 %, and a further decrease would occur by the ice melting to 20 %, which still seems to play an important role even at this temperature. For the above considerations, we deliberately separated the three-phase system to two systems in two phases, ice with brine and brine with NaCl crystals, to estimate the equilibrium conditions. The NaCl crystallization heat is slightly exothermic (-3.9 kJ mol^{-1}; Sanahuja and Cesari, 1984), and therefore the crystallization process also supplies some heat for further water evaporation.

We should admit that we do not have any reliable method to decide what kinds of salt crystals are formed in our observations, namely, whether they are anhydrous NaCl (halite) or dihydrate $NaCl.2H_2O$ (hydrohalite). However, the prevailing morphological shapes lead us to prefer the presence of NaCl. The binary phase diagram for water–NaCl (Fig. 4) suggests the stability region of NaCl at temperatures higher than 0.11 °C; below this temperature, only $NaCl.2H_2O$ is stable. Halite crystallizes in the cubic crystal structure, whereas hydrohalite does so in the monoclinic one. The hydrohalite crystals rapidly recrystallize to anhydrous halite and brine at temperatures of > 0.11 °C; the reverse recrystallization of halite to hydrohalite is slow even in contact with a saturated sodium chloride solution (Bode et al., 2015).

In aerosol simulating chambers under the conditions of preferential homogenous nucleation, the formed crystal structures do not correspond to those of the phase diagram. Halite crystals were observed at the temperature where the bulk phase diagram predicts the formation of hydrohalite. Only below a certain temperature (varying in two independent experiments: -38.2 °C; Wagner et al., 2012 and -21.2 °C; Wise et al., 2012), the efflorescence of hydrohalite crystals resulted from homogeneous crystallization at a specified relative humidity. In contrast, heterogeneous nucleation on available surfaces, such as ice surface, resulted in the growth of thermodynamically stable hydrohalite. Hydrohalite was found to crystallize from an oversaturated aqueous solution (brine) below the temperature of -0.1 °C (Light et al., 2009, 2003).

According to the bulk state diagram for the sodium chloride–water system, the formation of $NaCl.2H_2O$ should occur at both sub-zero temperatures and concentrations not exceeding 61.9 %. Even though we cannot estimate the oversaturation in the brine surface layer, we do not suppose that the water sublimation from the brine is rapid enough to increase the concentration above 61 %; respecting this argument, $NaCl.2H_2O$ hydrohalite crystals should be formed. Conversely, the shape of the most (but not all) of the salt crystals is close to rectangular, and therefore the cubic structure of halite can be inferred. The variety of NaCl crystal morphologies is presented in Fig. 9. It can be argued that, similarly to the non-thermodynamic homogeneous crystallization in aerosol chambers, halite preferentially crystallizes also in the conditions of our observation, for reasons we are currently unable to explain.

It is interesting to note that an anomalous increase of the water heat capacity with decreasing temperature is reduced and even eliminated with the increasing concentration of the NaCl in the solution. The isobaric heat capacity c_p of 23% brine at -17.2 °C equals ca. 3.3 kJ $°C^{-1}kg^{-1}$ (Archer and Carter, 2000), which is substantially less compared to the c_p of water at the same temperature (4.3 kJ $°C^{-1}$ kg^{-1}/. Conversely, the c_p of ice (1.98 kJ $°C^{-1}$ kg^{-1} at -17.2 °C) is still much lower than that of water or brine (Haida et al., 1974). Therefore, at thermal gradients, ice will change its temperature faster than the liquid parts of the system.

Atmospheric implications

Although our laboratory-prepared FFs can be regarded as one particular example of the natural FF, we cannot determine how representative this example is, especially as the FF's interior structure has not been detailed yet. However, we can consider our observations a good model for the general case of sea ice, with the limitation to the ice–NaCl system. It should be stressed that NaC and Cl^- comprise 85.7% of the total salt in seawater by mass (Millero et al., 2008). The remaining 14.3% of solutes may play an important role in the geochemistry of FFs and thus may be important for certain considerations. In particular, the precipitated ikaite and mirabilite from seawater, at -2 and -6.4 °C, respectively, may possibly act as nucleation centres for NaCl (Butler et al., 2016a). Obviously, the omission of other salts in this study is a limitation to representing real FFs. We should also stress that our observations were performed at the chamber pressure of p = ~ 600 Pa, which is substantially lower compared to low atmospheric conditions; therefore, direct implications for the natural FF should be made with care and questioned in further work. Nevertheless, our observations reveal some possibly relevant facts, and these are outlined below.

In atmospheric chemistry

Exposing a progressively concentrated brine to the ambient air, following the evaporation of water, may have a significant atmospheric implication, especially in atmospheric chemistry. Depending on the original position of the brine, namely, if it was located on the ice surface or buried in-between the ice crystals in the vein channels and pockets, the evaporation of the surrounding ice may increase the brine surface area by several times or even more than an order of magnitude. This could potentially accelerate the heterogeneous reactions; one particularly important reaction is bromide liberation, $HOBr(g)+Br^- \rightarrow Br_2(g)$, which is believed to be the direct source of bromine from the saline particles in polar regions (Fan and Jacob, 1992).

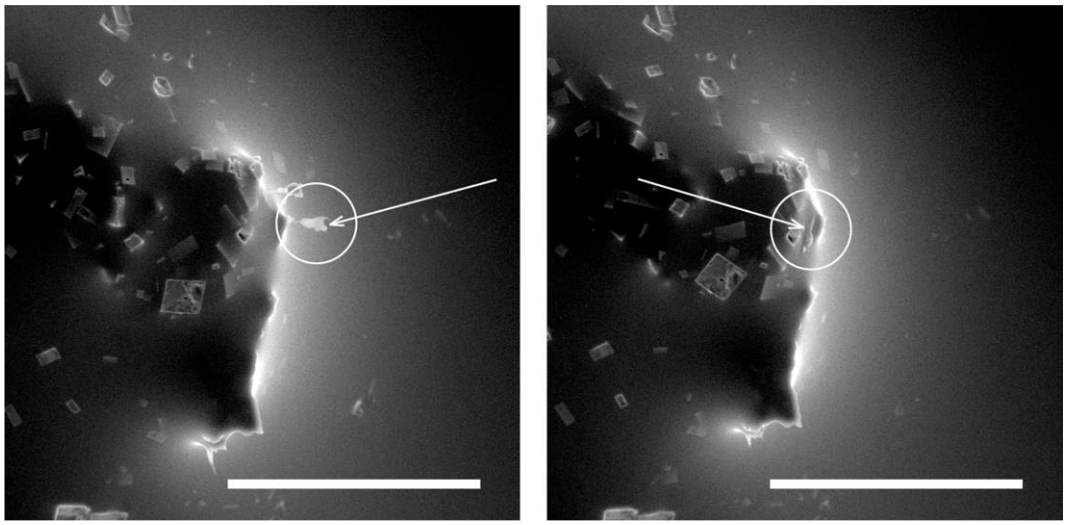

Figure 7. The frost flower micrograph showing a finger combining back to its mother body (circled). Conditions: ESEM AQUASEM II, ionization detector, air pressure of 520 Pa, sample holder temperature of -17.0 °C, and sample-to-aperture distance of 2 mm. The second image was recorded 10 s after the first one. Scale bars: 200 μm. A video visualizing the dynamics during evaporation is attached (S4).

As reflected in the images taken, the exposed brine fingers may tangle together and combine with the mother body to form a large chunk of salt in the end (Fig. S3). Therefore, the increase in the surface area of the brine due to the exposure of the brine fingers to the ambient air could only be efficient during the evaporating period as aged FFs may exhibit a reduced area due to the formation of a precipitate. Thus, the acceleration of heterogeneous chemistry due to the evaporation process likely applies to fresh FFs and salty snows but not aged ones.

Compared to the crystals lying on the sea ice surface, those aloft snow particles may be more prone to losing their water (Mann et al., 2000). Therefore, salty blowing snow particles lofted from the surface may suffer from rapid loss of water and

enhanced bromide liberation, as reflected in recent measurements (Jacobi et al., 2012; Lieb-Lappen and Obbard, 2015). Note that the effects of air ventilation in snow packs on snow chemistry, via the abovementioned sublimation process, remain unknown to date and thus deserve further in situ measurement.

Even though atmospheric conditions on Earth do not often allow for the formation of hydrohalite from bulk brine or in aerosols (Koop et al., 2000; Cziczo and Abbatt, 2000; Wagner and Mohler, 2013), we demonstrate that the local concentration on ice covered with brine exposed to desiccation by wind ventilation can easily meet these conditions. In the real world, an extremely dry conditions is not common in most sea-ice-covered zones; however, the wind ventilation effect could also cause ice water loss even under a high-relative-humidity condition (Thorpe and Mason, 1966). The ventilation effect is efficient and could dominate the water loss in the chamber even when the relative humidity is close to 100 %. Under the Earth's atmospheric conditions, it could be possible that the ventilation effect is strong enough to trigger NaCl crystal formation. However, anhydrous crystals are not easily prevented from deliquescing; most likely, these crystals will be soon diluted to form brine again. From the general point of view, the impact of the temperature and ventilation effects on saline brine microphysical features, as observed in this study, is interesting and may have significant implications for atmospheric chemistry and climate, for example, with respect to ice nucleation (Wagner and Mohler, 2013).

The sea-salt aerosol produced from saline particles could effectively form a large reservoir of various chemical compounds. Moreover, these aloft SSA could easily become chemically active once they are airborne; they can get acidified quickly by absorbing naturally generated or anthropogenic sulfate or nitrate gases, which is a key step for bromide liberation from saline particles (Abbatt et al., 2012). The models integrating these airborne SSA as a source of bromine can aptly capture the observed bromine explosion and ozone depletion events often occurring in polar spring time (Yang et al., 2010; Legrand et al., 2016; Zhao et al., 2016; Theys et al., 2011).

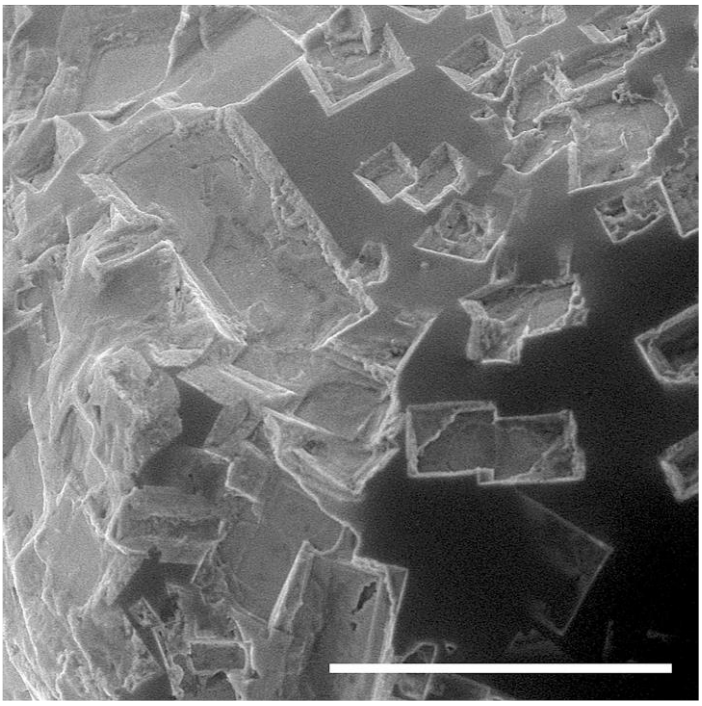

Figure 8. The NaCl crystals are clearly seen on the top of the surface brine layer of the frost flower. During the gradual process of evaporation, the individual ice crystals were moving on the brine surface at first, eventually growing into a large cluster of crystals. Conditions: ESEM AQUASEM II, ionization detector, air pressure of 510 Pa, sample holder temperature of -15.0 °C, and sample-toaperture distance of 2 mm. Scale bars: 200 μm. A video visualizing the formation of these crystals is attached (S5).

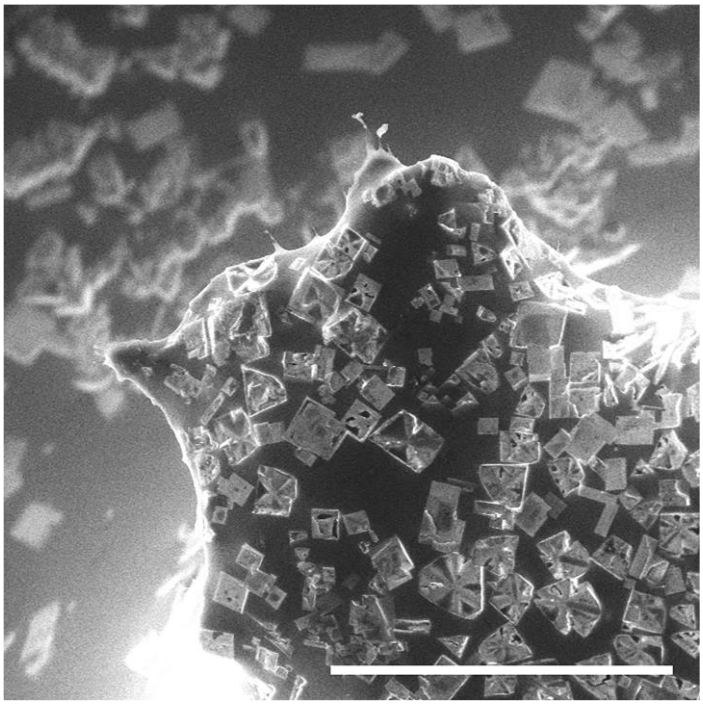

Figure 9. The NaCl crystal morphologies formed on the frost flower. Conditions: ESEM AQUASEM II, ionization detector, air pressure of 520 Pa, sample holder temperature of -15.0 °C, and sample-to-aperture distance of 2 mm. Scale bar: 200 μm.

In sea-salt aerosol formation

It seems that, without external forces such as collisions or wind cropping, evaporation itself will not automatically cause particle splitting to form sub-particles. The sticky brine fingers tend to combine back to the mother body (as shown in Fig. 7) rather than to fly away to form sub-particles. The leftover of FFs' evaporation is normally a large chunk of salt, as shown in Fig. S3. Thus, the present study supplies a clear microphysical picture in the explanation of why FFs could not be a direct source of SSAs, which is in accordance with the observation by Roscoe et al. (2011) that no SSAs were detected at wind tunnel speeds up to 12 ms^{-1}. Blowing snow on sea ice, as hypothesized by Yang et al. (2008), can produce SSA through a sublimation process. Recent modelling studies have shown that this process could reproduce well the polar winter SSA peaks in most polar sites (Levine et al., 2014; Huang and Jaeglé, 2017; Rhodes et al., 2017). As indicated in the present study, FFs are ruled out as a direct source of SSA, thus making blown salty snow particles more likely to be an efficient SSA source, as suggested previously.

Regarding less-salty snow particles, it is not clear whether the sublimation process will cause splitting. There is always a potential for large snow particles, e.g. ones with the size of hundreds of micrometres, to split during the evaporation process, especially when the surface brine skim is discontinuous. However, for much smaller particles (tens of micrometres or less), the splitting is less likely compared to the larger ones. Although the results of this study indicate that the ratio (of the number of SSAs formed from one snow particle) could be close to 1, the dependences of the ratio on the particle initial size and salt content are not known. In the original formula for the parameterization of SSA production from blown snow (Yang et al., 2008), the ratio is assumed to be a unit; however, a large ratio of 5 was applied in a recent model integration (Huang and Jaeglé, 2017).

Conclusions

An ESEM was used, for the first time, to obtain a detailed microphysical picture of evaporating frost flowers prepared from NaCl solution. The thorough scanning, in both temporal and spatial dimensions reveals a secret world of FFs in their evaporation period.

The evaporation of water from the brine causes ice melting underneath as it supplies the melting water to dilute the locally increased salt concentration. This process results in the formation of naked fingers standing out of the main body of the FFs. These fingers covered with the concentrated brine supply an enhanced surface area where (heterogeneous) reactions, exemplified by bromide release, could be

boosted. Whether this microphysical picture, taken for saline FFs in this study, applies also to less-saline snowpacks on sea ice and to blown salty snow particles, requires further investigation.

The exposed brine fingers are rather sticky and flexible at a higher temperature (e.g. -5 °C); they, however, become stiff with the temperature dropping due to a lower amount of liquid in the brine. A multitude of micrometric NaCl crystals were observed in the brine layer at temperatures below -10 °C, indicating that the brine's microphysical feature is temperature sensitive, thus changing the physical and optical properties of the FFs. As a newly discovered aspect, the presence of NaCl crystals should be considered with respect to possible atmospheric heterogeneous reactivity and the distribution of ions in bulk ice.

It is very likely that, without external forces, the evaporation process itself will not automatically cause a saline crystal to fall apart to produce aerosol size particles. The sticky brine fingers tend to tangle each other and eventually unite with the main body instead of forming multi-sub-particles, indicating that FFs are not a direct source of SSA, which is consistent with previous suggestions (Roscoe et al., 2011). This technique allows us to observe liquid NaCl brine on the ice surface and the process of its evaporation.

Acknowledgements

This work was supported by the BAS Collaboration Fund, UK, and Czech Science Foundation (GA14-22777S, GA15-12386S); the affiliated RECETOX research infrastructure is funded by projects of the Czech Ministry of Education (LO1214, LM2011028). Xin Yang gratefully acknowledge financial support from NERC/UK through project BLOWSEA (NE/J023051/1).

References

Abbatt, J. P. D., Thomas, J. L., Abrahamsson, K., Boxe, C., Granfors, A., Jones, A. E., King, M. D., Saiz-Lopez, A., Shepson, P. B., Sodeau, J., Toohey, D. W., Toubin, C., von Glasow, R., Wren, S. N., and Yang, X.: Halogen activation via interactions with environmental ice and snow in the polar lower troposphere and other regions, Atmos. Chem. Phys., 12, 6237–6271, doi:10.5194/acp-12-6237-2012, 2012.

Abram, N. J., Wolff, E. W., and Curran, M. A. J.: A review of sea ice proxy information from polar ice cores, Quaternary Sci. Rev., 79, 168–183, doi:10.1016/j.quascirev.2013.01.011, 2013.

Archer, D. G., and Carter, R. W.: Thermodynamic Properties of the NaCl C H2O System. 4. Heat Capacities of H2O and NaCl(aq) in Cold-Stable and Supercooled States, J. Phys. Chem. B, 104, 8563–8584, doi:10.1021/jp0003914, 2000.

Barber, D. G., Ehn, J. K., Pucko, M., Rysgaard, S., Deming, J. W., Bowman, J. S., Papakyriakou, T., Galley, R. J., and Sogaard, D. H.: Frost flowers on young Arctic sea ice: The climatic, chemical, and microbial significance of an emerging ice type, J. Geophys. Res.-Atmos., 119, 11593–11612, doi:10.1002/2014jd021736, 2014.

Bartels-Rausch, T., Jacobi, H.-W., Kahan, T. F., Thomas, J. L., Thomson, E. S., Abbatt, J. P. D., Ammann, M., Blackford, J. R., Bluhm, H., Boxe, C., Domine, F., Frey, M. M., Gladich, I., Guzmán, M. I., Heger, D., Huthwelker, Th., Klán, P., Kuhs, W. F., Kuo, M. H., Maus, S., Moussa, S. G., McNeill, V. F., Newberg, J. T., Pettersson, J. B. C., Roeselová, M., and Sodeau, J. R.: A review of air–ice chemical and physical interactions (AICI): liquids, quasi-liquids, and solids in snow, Atmos. Chem. Phys., 14, 1587–1633, doi:10.5194/acp-14-1587-2014, 2014.

Blackford, J. R.: Sintering and microstructure of ice: a review, J. Phys. D Appl. Phys., 40, R355–R385, doi:10.1088/0022- 3727/40/21/r02, 2007.

Bode, A. A. C., Pulles, P. G. M., Lutz, M., Poulisse, W. J. M., Jiang, S., Meijer, J. A. M., van Enckevort, W. J. P., and Vlieg, E.: Sodium Chloride Dihydrate Crystals: Morphology, Nucleation, Growth, and Inhibition, Cryst. Growth Des., 15, 3166–3174, doi:10.1021/acs.cgd.5b00061, 2015.

Bogdan, A., Molina, M. J., Tenhu, H., Bertel, E., Bogdan, N., and Loerting, T.: Visualization of Freezing Process in situ upon Cooling and Warming of Aqueous Solutions, Scientific Reports, 4, 7414, doi:10.1038/srep07414, 2014.

Brady, J. B.: Magma in a Beaker: Analog Experiments with Water and Various Salts or Sugar for Teaching Igneous Petrology, Canadian Mineralogist, 47, 457–471, doi:10.3749/canmin.47.2.457, 2009.

Buck, A. L.: New Equations for Computing Vapor-Pressure and Enhancement Factor, J. Appl. Meteorol., 20, 1527–1532, doi:10.1175/1520-0450(1981)020<1527:nefcvp>2.0.co;2, 1981.

Butler, B. M. and Kennedy, H.: An investigation of mineral dynamics in frozen seawater brines by direct measurement with synchrotron X-ray powder diffraction, J. Geophys. Res.-Oceans, 120, 5686–5697, doi:10.1002/2015jc011032, 2015.

Butler, B. M., Papadimitriou, S., and Kennedy, H.: The effect of mirabilite precipitation on the absolute and practical salinities of sea ice brines, Mar. Chem., 184, 21–31, doi:10.1016/j.marchem.2016.06.003, 2016a.

Butler, B. M., Papadimitriou, S., Santoro, A., and Kennedy, H.: Mirabilite solubility in equilibrium sea ice brines, Geochim. Cosmochim. Ac., 182, 40–54, doi:10.1016/j.gca.2016.03.008, 2016b.

Cheng, J., Soetjipto, C., Hoffmann, M. R., and Colussi, A. J.: Confocal Fluorescence Microscopy of the Morphology and Composition of Interstitial Fluids in Freezing Electrolyte Solutions, J. Phys. Chem. Lett., 1, 374–378, doi:10.1021/jz9000888, 2010.

Cziczo, D. J. and Abbatt, J. P. D.: Infrared observations of the response of NaCl, MgCl2, NH4HSO4, and NH4NO3 aerosols to changes in relative humidity from 298 to 238 K, J. Phys. Chem. A, 104, 2038–2047, doi:10.1021/jp9931408, 2000.

DeAngelis, M., Steffensen, J. P., Legrand, M., Clausen, H., and Hammer, C.: Primary aerosol (sea salt and soil dust) deposited in Greenland ice during the last climatic cycle: Comparison with east Antarctic records, J. Geophys. Res.-Oceans, 102, 26681– 26698, doi:10.1029/97jc01298, 1997.

Dehaoui, A., Issenmann, B., and Caupin, F.: Viscosity of deeply supercooled water and its coupling to molecular diffusion, P. Natl. Acad. Sci. USA, 112, 12020–12025, doi:10.1073/pnas.1508996112, 2015.

Domine, F.: Specific surface area, density and microstructure of frost flowers, Geophys. Res. Lett., 32, L13502, doi:10.1029/2005gl023245, 2005.

Domine, F., Sparapani, R., Ianniello, A., and Beine, H. J.: The origin of sea salt in snow on Arctic sea ice and in coastal regions, Atmos. Chem. Phys., 4, 2259–2271, doi:10.5194/acp-4-2259-2004, 2004.

Domine, F., Bock, J., Voisin, D., and Donaldson, D. J.: Can We Model Snow Photochemistry? Problems with the Current Approaches, J. Phys. Chem. A, 117, 4733–4749, doi:10.1021/jp3123314, 2013.

Douglas, T. A., Domine, F., Barret, M., Anastasio, C., Beine, H. J., Bottenheim, J., Grannas, A., Houdier, S., Netcheva, S., Rowland, G., Staebler, R., and Steffen, A.: Frost flowers growing in the Arctic ocean-atmosphere–sea ice–snow interface: 1. Chemical composition, J. Geophys. Res., 117, D00R09, doi:10.1029/2011jd016460, 2012.

Fan, S. M. and Jacob, D. J.: Surface Ozone Depletion in Arctic Spring Sustained by Bromine Reactions on Aerosols, Nature, 359, 522–524, doi:10.1038/359522a0, 1992.

Fischer, H., Siggaard-Andersen, M. L., Ruth, U., Rothlisberger, R., and Wolff, E.: Glacial/interglacial changes in mineral dust and sea-salt records in polar ice cores: Sources, transport, and depo-sition, Rev. Geophys., 45, Rg1002, doi:10.1029/2005rg000192, 2007.

Galley, R. J., Else, B. G. T., Geilfus, N.-X., Hare, A. A., Babb, D., Papakyriakou, T., Barber, D. G., and Rysgaard, S.: Micrometeorological and Thermal Control of Frost Flower Growth and Decay on Young Sea Ice, Arctic, 68, 79–92, doi:10.14430/arctic4457, 2015.

Gudipati, M. S., Abou Mrad, N., Blum, J., Charnley, S. B., Chiavassa, T., Cordiner, M. A., Mousis, O., Danger, G., Duvernay, F., Gundlach, B., Hartogh, P., Marboeuf, U., Simonia, I., Simonia, T., Theulé, P., and Yang, R.: Laboratory Studies Towards Understanding Comets, Space Sci. Rev., 197, 101–150, doi:10.1007/s11214-015-0192-5, 2015.

Haida, O., Matsuo, T., Suga, H., and Seki, S.: Calorimetric Study of Glassy State 10. Enthalpy Relaxation at Glass-Transition Temperature of Hexagonal ice, J. Chem. Thermodyn., 6, 815–825, doi:10.1016/0021-9614(74)90227-4, 1974.

Heger, D. and Klan, P.: Interactions of organic molecules at grain boundaries in ice: A solvatochromic analysis, J. Photochem. Photobiol. A-Chem., 187, 275–284, doi:10.1016/j.jphotochem.2006.10.012, 2007.

Heger, D., Jirkovsky, J., and Klan, P.: Aggregation of methylene blue in frozen aqueous solutions studied by absorption spectroscopy, J. Phys. Chem. A, 109, 6702–6709, doi:10.1021/jp050439j, 2005.

Heger, D., Klanova, J., and Klan, P.: Enhanced protonation of cresol red in acidic aqueous solutions caused by freezing, J. Phys. Chem. B, 110, 1277–1287, doi:10.1021/jp0553683, 2006.

Heger, D., Nachtigallova, D., Surman, F., Krausko, J., Magyarova, B., Brumovsky, M., Rubes, M., Gladich, I., and Klan, P.: Self-Organization of 1-Methylnaphthalene on the Surface of Artificial Snow Grains: A Combined Experimental-Computational Approach, J. Phys. Chem. A, 115, 11412–11422, doi:10.1021/jp205627a, 2011.

Huang, J. and Jaeglé, L.: Wintertime enhancements of sea salt aerosol in polar regions consistent with a sea ice source from blowing snow, Atmos. Chem. Phys., 17, 3699–3712, doi:10.5194/acp-17-3699-2017, 2017.

Hutterli, M. A., Huthwelker, T., Miedaner, M. M., Enzmann, F., Ammann, M., Schneebeli, M., Maus, S., Stampanoni, M., Jones, A. E., and Wolff, E.: A 3D X-ray micro computer tomography perspective of sea ice, frost flowers and snow as sources of reactive halogens, European Geophysical Union Spring Meeting, Vienna, 13–18 April, 2008.

Jacobi, H. W., Voisin, D., Jaffrezo, J. L., Cozic, J., and Douglas, T. A.: Chemical composition of the snowpack during the OASIS spring campaign 2009 at Barrow, Alaska, J. Geophys. Res.- Atmos., 117, D00r13, doi:10.1029/2011jd016654, 2012.

Jourdain, B., Preunkert, S., Cerri, O., Castebrunet, H., Udisti, R., and Legrand, M.: Year-round record of size-segregated aerosol composition in central Antarctica (Concordia station): Implications for the degree of fractionation of sea-salt particles, J. Geophys. Res.-Atmos., 113, D14308, doi:10.1029/2007jd009584, 2008.

Kaleschke, L., Richter, A., Burrows, J., Afe, O., Heygster, G., Notholt, J., Rankin, A. M., Roscoe, H. K., Hollwedel, J.,Wagner, T., and Jacobi, H. W.: Frost flowers on sea ice as a source of sea salt and their influence on tropospheric halogen chemistry, Geophys. Res. Lett., 31, L16114, doi:10.1029/2004gl020655, 2004.

Kania, R., Malongwe, J. K. E., Nachtigallová, D., Krausko, J., Gladich, I., Roeselová, M., Heger, D., and Klán, P.: Spectroscopic Properties of Benzene at the Air–Ice Interface: A Combined Experimental–Computational Approach, J. Phys. Chem. A, 118, 7535–7547, doi:10.1021/jp501094n, 2014.

Koop, T., Kapilashrami, A., Molina, L. T., and Molina, M. J.: Phase transitions of sea-salt/water mixtures at low temperatures: Implications for ozone chemistry in the polar marine boundary layer, J. Geophys. Res.-Atmos., 105, 26393–26402, 2000.

Krausko, J., Runštuk, J., Neděla, V., Klán, P., and Heger, D.: Observation of a Brine Layer on an Ice Surface with an Environmental Scanning Electron Microscope at Higher Pressures and Temperatures, Langmuir, 30, 5441–5447, doi:10.1021/la500334e, 2014.

Krausko, J., Malongwe, J. K. E., Bičanová, G., Klán, P., Nachtigallová, D., and Heger, D.: Spectroscopic Properties of Naphthalene on the Surface of Ice Grains

Revisited: A Combined Experimental–Computational Approach, J. Phys. Chem. A, 119, 8565–8578, doi:10.1021/acs.jpca.5b00941, 2015a.

Krausko, J., Ondrušková, G., and Heger, D.: Comment on "Photolysis of Polycyclic Aromatic Hydrocarbons on Water and Ice Surfaces" and on "Nonchromophoric Organic Matter Suppresses Polycyclic Aromatic Hydrocarbon Photolysis in Ice and at Ice Surfaces", J. Phys. Chem. A, 119, 10761–10763, doi:10.1021/acs.jpca.5b08276, 2015b.

Krausková, L, Procházková, J., Klašková, M., Filipová, L., Chaloupková, R., Malý, S., Damborský, J., and Heger, D.: Suppression of protein inactivation during freezing by minimizing pH changes using ionic cryoprotectants, Int. J. Pharm., 509, 41– 49, doi:10.1016/j.ijpharm.2016.05.031, 2016.

Legrand, M., Yang, X., Preunkert, S., and Theys, N.: Year-round records of sea salt, gaseous, and particulate inorganic bromine in the atmospheric boundary layer at coastal (Dumont d'Urville) and central (Concordia) East Antarctic sites, J. Geophys. Res.- Atmos., 121, 997–1023, doi:10.1002/2015jd024066, 2016.

Levine, J. G., Yang, X., Jones, A. E., and Wolff, E. W.: Sea salt as an ice core proxy for past sea ice extent: A processbased model study, J. Geophys. Res.-Atmos., 119, 5737–5756, doi:10.1002/2013jd020925, 2014.

Lieb-Lappen, R. M. and Obbard, R. W.: The role of blowing snow in the activation of bromine over first-year Antarctic sea ice, Atmos. Chem. Phys., 15, 7537–7545, doi:10.5194/acp-15-7537- 2015, 2015.

Light, B., Maykut, G. A., and Grenfell, T. C.: Effects of temperature on the microstructure of first-year Arctic sea ice, J. Geophys. Res.: Oceans, 108, 33–1, doi:10.1029/2001jc000887, 2003.

Light, B., Brandt, R. E., and Warren, S. G.: Hydrohalite in cold sea ice: Laboratory observations of single crystals, surface accumulations, and migration rates under a temperature gradient, with application to "Snowball Earth", J. Geophys. Res., 114, C07018, doi:10.1029/2008jc005211, 2009.

Mahowald, N. M., Lamarque, J. F., Tie, X. X., and Wolff, E.: Seasalt aerosol response to climate change: Last Glacial Maximum, preindustrial, and doubled carbon dioxide climates, J. Geophys. Res.-Atmos., 111, D05303, doi:10.1029/2005jd006459, 2006.

Mann, G. W., Anderson, P. S., and Mobbs, S. D.: Profile measurements of blowing snow at Halley, Antarctica, J. Geophys. Res.- Atmos., 105, 24491–24508, doi:10.1029/2000jd900247, 2000.

Marion, G. M., Farren, R. E., and Komrowski, A. J.: Alternative pathways for seawater freezing, Cold Reg. Sci. Technol., 29, 259–266, doi:10.1016/s0165-232x(99)00033-6, 1999.

Maxa, J.: Comparisons Using Methods of Continuum Mechanics and Monte Carlo at Differentially Pumped Chamber, Advances in Military Technology, 11, 143–150, doi:10.3849/aimt.01120, 2016.

Maxa, J. and Neděla, V: Impact of the Critical Flow on Conditions of the Primary Electron Beam Passage Through the Differentially Pumped Chamber, Publishing Group of University of Defence, 6, 39–46, 2011.

McCarthy, C., Cooper, R. F., Kirby, S. H., Rieck, K. D., and Stern, L. A.: Solidification and microstructures of binary ice- I/hydrate eutectic aggregates, American Mineralogist, 92, 1550– 1560, doi:10.2138/am.2007.2435, 2007.

McCarthy, C., Blackford, J. R., and Jeffree, C. E.: Lowtemperature- SEM study of dihedral angles in the ice-I/sulfuric acid partially molten system, J. Microscopy, 249, 150–157, doi:10.1111/jmi.12003, 2013.

McNeill, V. F., Grannas, A. M., Abbatt, J. P. D., Ammann, M., Ariya, P., Bartels-Rausch, T., Domine, F., Donaldson, D. J., Guzman, M. I., Heger, D., Kahan, T. F., Klán, P., Masclin, S., Toubin, C., and Voisin, D.: Organics in environmental ices: sources, chemistry, and impacts, Atmos. Chem. Phys., 12, 9653–9678, doi:10.5194/acp-12-9653-2012, 2012.

Millero, F. J., Feistel, R., Wright, D. G., and McDougall, T. J.: The composition of Standard Seawater and the definition of the Reference-Composition Salinity Scale, Deep-Sea Res. Pt. I, 55, 50-72, doi:10.1016/j.dsr.2007.10.001, 2008.

Neděla, V., Konvalina, I., Lencova, B., and Zlámal, J.: Comparison of calculated, simulated and measured signal amplification in a variable pressure SEM, Nuclear Instruments & Methods in Physics Research Section a-Accelerators Spectrometers Detectors and Associated Equipment, 645, 79–83, doi:10.1016/j.nima.2010.12.200, 2011.

Neděla, V., Tihlaříková, E., and Hřib, J.: The low-temperature method for study of coniferous tissues in the environmental scanning electron microscope, Microscopy Research and Technique, 78, 13–21, doi:10.1002/jemt.22439, 2015.

Obbard, R. W., Roscoe, H. K., Wolff, E. W., and Atkinson, H. M.: Frost flower surface area and chemistry as a function of salinity and temperature, J. Geophys. Res., 114, D20305, doi:10.1029/2009jd012481, 2009.

Papadimitriou, S., Loucaides, S., Rérolle, V., Achterberg, E. P., Dickson, A. G., Mowlem, M., and Kennedy, H.: The measurement of pH in saline and hypersaline media at sub-zero temperatures: Characterization of Tris buffers, Mar. Chem., 184, 11–20, doi:10.1016/j.marchem.2016.06.002, 2016.

Perovich, D. K. and Richter-Menge, J. A.: Surface characteristics of lead ice, J. Geophys. Res., 99, 16341, doi:10.1029/94jc01194, 1994.

Pfalzgraff, W. C., Hulscher, R. M., and Neshyba, S. P.: Scanning electron microscopy and molecular dynamics of surfaces of growing and ablating hexagonal ice crystals, Atmos. Chem. Phys., 10, 2927–2935, doi:10.5194/acp-10-2927-2010, 2010.

Rankin, A. M.: Frost flowers: Implications for tropospheric chemistry and ice core interpretation, J. Geophys. Res., 107, 4, doi:10.1029/2002jd002492, 2002.

Rankin, A. M. and Wolff, E. W.: A year-long record of sizesegregated aerosol composition at Halley, Antarctica, J. Geophys. Res.-Atmos., 108, 4775, doi:10.1029/2003jd003993, 2003.

Rankin, A. M., Wolff, E. W., and Mulvaney, R.: A reinterpretation of sea-salt records in Greenland and Antarctic ice cores?, in: Annals of Glaciology, edited by: Jacka, J., Annals of Glaciology- Series, Int Glaciological Soc, Cambridge, 39, 276–282, 2004.

Rérolle, V., Ruiz-Pino, D., Rafizadeh, M., Loucaides, S., Papadimitriou, S., Mowlem, M., and Chen, J.: Measuring pH in the Arctic Ocean: Colorimetric method or SeaFET?, Methods in Oceanography, 17, 32–49, doi:10.1016/j.mio.2016.05.006, 2016.

Rhodes, R. H., Yang, X., Wolff, E. W., McConnell, J. R., and Frey, M. M.: Sea ice as a source of sea salt aerosol to Greenland ice cores: a model-based study, Atmos. Chem. Phys. Discuss., doi:10.5194/acp-2017-100, in review, 2017.

Roscoe, H. K., Brooks, B., Jackson, A. V., Smith, M. H., Walker, S. J., Obbard, R. W., and Wolff, E. W.: Frost flowers in the laboratory: Growth, characteristics, aerosol, and the underlying sea ice, J. Geophys. Res., 116, D12301, doi:10.1029/2010jd015144, 2011.

Sanahuja, A. and Cesari, E.: Enthalpy of Solution of KCl and NaCl in Water at 298.15 K, J. Chem. Thermodyn., 16, 1195–1202, doi:10.1016/0021-9614(84)90192-7, 1984.

Sharqawy, M. H., Lienhard, J. H., and Zubair, S. M.: Thermophysical properties of seawater: a review of existing correlations and data, Desalination and Water Treatment, 16, 354–380, doi:10.5004/dwt.2010.1079, 2010.

Simpson, W. R., von Glasow, R., Riedel, K., Anderson, P., Ariya, P., Bottenheim, J., Burrows, J., Carpenter, L. J., Frieß, U., Goodsite, M. E., Heard, D., Hutterli, M., Jacobi, H.-W., Kaleschke, L., Neff, B., Plane, J., Platt, U., Richter, A., Roscoe, H., Sander, R., Shepson, P., Sodeau, J., Steffen, A., Wagner, T., and Wolff, E.: Halogens and their role in polar boundary-layer ozone depletion, Atmos. Chem. Phys., 7, 4375–4418, doi:10.5194/acp-7- 4375-2007, 2007.

Style, R. W. and Worster, M. G.: Frost flower formation on sea ice and lake ice, Geophys. Res. Lett., 36, L11501, doi:10.1029/2009gl037304, 2009.

Theys, N., Van Roozendael, M., Hendrick, F., Yang, X., De Smedt, I., Richter, A., Begoin, M., Errera, Q., Johnston, P. V., Kreher, K., and De Mazière, M.: Global observations of tropospheric BrO columns using GOME-2 satellite data, Atmos. Chem. Phys., 11, 1791–1811, 10.5194/acp-11-1791-2011, 2011.

Thorpe, A. D. and Mason, B. J.: The evaporation of ice spheres and ice crystals, Br. J. Appl. Phys., 17, 541–548, doi:10.1088/0508- 3443/17/4/316, 1966.

Tihlarikova, E., Nedela, V., and Shiojiri, M.: In Situ Study of Live Specimens in an Environmental Scanning Electron Microscope, Microsc. Microanal., 19, 914–918, doi:10.1017/s1431927613000603, 2013.

Wagenbach, D., Ducroz, F., Mulvaney, R., Keck, L., Minikin, A., Legrand, M., Hall, J. S., and Wolff, E. W.: Sea-salt aerosol in coastal Antarctic regions, J. Geophys. Res.-Atmos., 103, 10961– 10974, doi:10.1029/97jd01804, 1998.

Wagner, R. and Mohler, O.: Heterogeneous ice nucleation ability of crystalline sodium chloride dihydrate particles, J. Geophys. Res.-Atmos., 118, 4610–4622, doi:10.1002/jgrd.50325, 2013.

Wagner, R., Möhler, O., and Schnaiter, M.: Infrared Optical Constants of Crystalline Sodium Chloride Dihydrate: Application To Study the Crystallization of Aqueous Sodium Chloride Solution Droplets at Low Temperatures, J. Phys. Chem. A, 116, 8557– 8571, doi:10.1021/jp306240s, 2012.

Walker, R. L., Searles, K., Willard, J. A., and Michelsen, R. R. H.: Total reflection infrared spectroscopy of water-ice and frozen aqueous NaCl solutions, J. Chem. Phys., 139, 244703, doi:10.1063/1.4841835, 2013.

Weast, R. C., Astle, M. J., and Beyer, W. H.: CRC handbook of chemistry and physics : a ready-reference book of chemical and physical data, CRC Press, Boca Raton, 1987.

Wise, M. E., Baustian, K. J., Koop, T., Freedman, M. A., Jensen, E. J., and Tolbert, M. A.: Depositional ice nucleation onto crystalline hydrated NaCl particles: a new mechanism for ice formation in the troposphere, Atmos. Chem. Phys., 12, 1121–1134, doi:10.5194/acp-12-1121-2012, 2012.

Wolff, E. W., Rankin, A. M., and Rothlisberger, R.: An ice core indicator of Antarctic sea ice production?, Geophys. Res. Lett., 30, 2158, doi:10.1029/2003gl018454, 2003.

Xu, L., Russell, L. M., and Burrows, S. M.: Potential sea salt aerosol sources from frost flowers in the pan-Arctic region, J. Geophys. Res.-Atmos., 121, 10840–10856, doi:10.1002/2015jd024713, 2016.

Yang, X., Pyle, J. A., and Cox, R. A.: Sea salt aerosol production and bromine release: Role of snow on sea ice, Geophys. Res. Lett., 35, L16815, doi:10.1029/2008gl034536, 2008.

Yang, X., Pyle, J. A., Cox, R. A., Theys, N., and Van Roozendael, M.: Snow-sourced bromine and its implications for polar tropospheric ozone, Atmos. Chem. Phys., 10, 7763–7773, doi:10.5194/acp-10-7763-2010, 2010.

Zhao, X., Strong, K., Adams, C., Schofield, R., Yang, X., Richter, A., Friess, U., Blechschmidt, A. M., and Koo, J. H.: A case study of a transported bromine explosion event in the Canadian high arctic, J. Geophys. Res.-Atmos., 121, 457–477, doi:10.1002/2015jd023711, 2016.

28 The morphology of ice and liquid brine in an environmental scanning electron microscope: a study of the freezing methods

Ľubica Vetráková[1], Vilém Neděla[1], Jiří Runštuk[1], and Dominik Heger[2]

1 *Environmental Electron Microscopy Group, Institute of Scientific Instruments of the Czech Academy of Sciences, Brno, Czech Republic*

2 *Department of Chemistry, Faculty of Science, Masaryk University, Brno, Czech Republic*

Abstract.

The microstructure of polycrystalline ice with a threading solution of brine controls its numerous characteristics, including the ice mechanical properties, ice–atmosphere interactions, sea ice albedo, and (photo)chemical behavior in and on the ice. Ice samples were previously prepared in laboratories in order to study various facets of ice–impurity interactions and (photo)reactions to model natural ice–impurity behavior. We examine the impact of the freezing conditions and solute (CsCl used as a proxy for naturally occurring salts) concentrations on the microscopic structure of ice samples via an environmental scanning electron microscope. The method allows us to observe the ice surfaces in detail, namely, the free ice, brine puddles, brine-containing grain boundary grooves, individual ice crystals, and imprints left by entrapped air bubbles at temperatures higher than -25 °C. The amount of brine on the external surface is found proportional to the solute concentration and is strongly dependent on the sample preparation method. Time-lapse images in the condition of slight sublimation reveal subsurface association of air bubbles with brine. With rising temperatures (up to -14 °C), the brine surface coverage increases to remain enhanced during the subsequent cooling and until the final crystallization below the eutectic temperature. The ice recrystallization dynamics identify the role of surface spikes in retarding the ice boundaries' propagation (Zener pinning). The findings thus quantify the amounts of brine exposed to incoming radiation, available for the gas exchange, and influencing other mechanical and optical properties of ice. The results have straightforward and indirect implications for artificially prepared and naturally occurring salty ice, respectively.

Introduction

Ice and snow are important reaction media in which chemical compounds (impurities) can be accumulated, transformed, and released back to other

compartments in the environment (Bartels-Rausch et al., 2014). The location and time evolution of impurities within a frozen sample are crucial in multiple respects: they determine the mechanical and optical properties of the material and thus must be considered in relation to snowpack stability, avalanches, sea ice mechanics, and climate change research (Blackford et al., 2007; Hobbs, 2010; Dash et al., 2006; Wåhlin et al., 2014). The location of impurities most probably influences the compounds' reactivity because their availability to incoming light radiation and/or gaseous reactants substantially differs depending on whether the impurities are located on the ice surface or buried in the frozen bulk (Hullar and Anastasio, 2016; Bartels-Rausch et al., 2014). However, the information combining the reactivity of compounds with their locations is essentially missing. Excepting low concentrations of HF, NH_4^+ , HCl, HNO_3, and formaldehyde (Perrier et al., 2002; Thibert and Domine, 1998, 1997), impurities are usually not incorporated into the ice lattice (Krausková et al., 2016; Hobbs, 2010; Wilson and Haymet, 2008). As ice is highly intolerant to impurities, these are segregated to an unfrozen freeze-concentrated solution (FCS) during the growth of ice crystals. The FCS can be located in the lamellae and veins between the ice crystals, (micro)pockets within the ice structure, or puddles and grain boundary grooves on the ice surface. When the mixture is cooled below the eutectic temperature (T_{eu}), the FCS may crystallize or vitrify (Salnikova et al., 2015; Bogdan et al., 2014; Imrichova et al., 2019).

To determine the actual positions of chemical compounds in ice samples, various microscopic techniques are used, including optical (Bogdan et al., 2014; Bogdan and Molina, 2017), fluorescence (Cheng et al., 2010; Roessl et al., 2015), electron (Blackford et al., 2007; Chen and Baker, 2010; Rosenthal et al., 2007; Barnes et al., 2002), and confocal Raman (Dong et al., 2009) microscopies. While optical microscopy can be applied at environmentally relevant temperatures and pressures, very low pressure conditions (10^{-4} to 10-2 Pa) are needed in the specimen chamber of a conventional scanning electron microscope (SEM). At such low pressures, ice sublimes very rapidly due to its high vapor pressure (Blackford, 2007); for that reason, ice samples are observable only at very low temperatures (below -120 °C) in a SEM (Blackford et al., 2007). These conditions are far from naturally relevant ones. Conversely, however, electron microscopy resolves fine structures 2 orders of magnitude smaller compared to those examined with optical microscopy, and its depth of field is much larger. Moreover, the ice surface appears opaque in a SEM, and its surface topography is thus defined significantly better than possible via optical microscopy (Blackford, 2007). In order for electron microscopy to be usable at higher pressures, the environmental scanning electron microscope (ESEM) was designed (Danilatos, 1993). An ESEM can operate at specimen chamber pressures of up to thousands of pascals, and such capability allows frozen samples to be

inspected at higher temperatures, even up to the samples' melting point. To prevent ice sublimation, water vapor can be purged into the specimen chamber; thus, the imaging is performed under closer-to natural conditions. Further, ionization of the gas in the specimen chamber of the ESEM prevents the sample from being charged, rendering the technique very convenient for imaging electrically nonconductive samples without the need of conductive coating. ESEMs are therefore becoming increasingly popular within research into pure ice (Nair et al., 2018; Magee et al., 2014; Chen et al., 2017) and ice–impurity interactions under static and dynamically changing conditions (Krausko et al., 2014; Yang et al., 2017). While electron microscopy visualizes the sample surface in detail, microcomputed tomography has been recently applied to investigate solute locations in the frozen bulk (Hullar and Anastasio, 2016). Using this technique, the authors were able to visualize the locations of solutes (CsCl or rose bengal), gas, and ice in 3-D.

Salt solutions are abundant in the natural environment; seawater alone represents 96.5% of water on the Earth (Gleick, 1993). In wintertime, sea ice covers an area of up to 7% of the Earth's surface and, as such, embodies one of the largest biomes (Thomas, 2017). Salts and ice also coexist in sea aerosols (Knipping et al., 2000; Zobrist et al., 2008), in coastal regions (on frost flowers; Douglas et al., 2012), and in ice cores (Ohno et al., 2006, 2005; Vega et al., 2018).

Well-conceived laboratory investigation of the ice– impurity interaction has the potential to simplify complex natural systems. Laboratory-based studies of the (photo)chemical reactions of frozen aqueous solutions have improved the understanding of the (photo)chemistry occurring in cold environments (Bartels-Rausch et al., 2014; Klanova et al., 2003). However, the dissonance between results from individual laboratories as regards the photodegradation rates (Kahan et al., 2010; Ram and Anastasio, 2009) points to the fact that there still remain key factors influencing the reactivity in a frozen solution that were not comprehended previously.

The impurities' locations were most often deduced from the sample preparation methods; for example, freezing an aqueous solution involved the precondition of placing the impurities inside the ice matrix. Subsequent breaking of the ice into small pieces was proposed to bring the impurities to the ice surface (Kahan et al., 2010); this assumption was recently questioned (Hullar et al., 2018). Other studies suggested that freezing an aqueous solution places the impurities prevalently inside the ice interior, whereas deposition of the organics from the vapor phase accommodates them on the ice surface (Ondrušková et al., 2018; Vetráková et al., 2017; Krausko et al., 2015a, b; Kania et al., 2014; Heger et al., 2011; Hullar et al., 2018; Bartels-Rausch et al., 2013). Conversely, nebulizing the solution into liquid

nitrogen was assumed to produce ice spheres with the organic impurities on their surfaces (Kurkova et al., 2011).

To establish a direct proof of salt location in frozen samples, we herein applied various methods to freeze caesium chloride (CsCl) solutions.We had intended to determine how the ice impurities' location and surface availability are affected by the freezing technique, temperature, and salt concentrations. The ESEM technology was utilized for the visualization due to its ability to represent the samples' surface topography together with the impurities' locations. CsCl was chosen as the model salt, being similar to NaCl and providing very good microscopic contrast; thus, the presence of brine on the surface of the frozen samples can be clearly monitored, with indirect implications towards the location of sea water brine on sea ice.

Methods

The microscopic images were recorded using an AQUASEM II, a Tescan VEGA SEM modified at the Institute of Scientific Instruments of the Czech Academy of Sciences (Tihlarikova et al., 2013; Nedela, 2007). This ESEM is capable of imaging wet, electrically nonconducting samples at chamber pressures as high as 2000 Pa and temperatures down to -27 °C. The advantages of the AQUASEM II in the imaging of frozen samples has been described previously (Krausko et al., 2014; Yang et al., 2017).

Preparation of the samples

CsCl solutions with the concentrations of 0.005, 0.05, and 0.5M were prepared by dissolving an appropriate amount of CsCl in Milli-Q H_2O. The molar concentrations correspond to molalities of 0.005, 0.050, and 0.512 mol kg^{-1}, respectively, using the solution densities at 20 °C published by Reiser et al. (2014); the positions of these concentrations can be realized on the phase diagram for the CsCl–water (Fig. 1) (Gao et al., 2017). The concentrations are proxies for natural salt occurrence in coastal snow (5 mM) (Beine et al., 2012; Douglas et al., 2012), up to the concentration in sea water (0.5 M) (Massom et al., 2001; Thomas, 2017). Prior to the measurement, the solutions had been filtered through a 0.45 μm filter to exclude impurities that might interfere with the microscopic observations. The solutions were frozen at atmospheric pressure via four distinct methods:

I. Spontaneous freezing of a droplet without seeding. A droplet was put onto the silicon sample holder (cooling stage) of the ESEM at room temperature (about 23 °C). The temperature of the cooling stage, controlled by a Peltier cooler, was lowered gradually (the cooling rate corresponded to approximately 0.5 °C s^{-1}) until the sample

froze spontaneously, with the estimated freezing rate being (154±13) mm s^{-1}. The nucleation temperature ranged from -16 to -18 °C in the replicate experiments. After becoming frozen, the sample was cooled down to the initial observation temperature of -22 to -25 °C.

II. Freezing of a droplet with seeding. A droplet was placed onto the cooling stage of the ESEM and its temperature was set to -2 °C; then, after thermal equilibration, several small ice crystals were added to the edge of the sample to initiate the nucleation process. The estimated freezing rate reached about 0.2mm s^{-1}. Subsequently, the temperature of the cooling stage was lowered down to the initial observation value.

III. Spraying into a vessel containing liquid nitrogen (LN). Small ice spheres (similar to artificial snow) were formed and then transferred onto the microscope cooling stage precooled to -25 °C.

IV. Fragmentation of an LN-frozen sample. The applied CsCl solution enclosed in a hard gelatine capsule (diameter of 8mm, approx. height of 25 mm, and sample level was at ~ 10 mm) was immersed in LN. After freezing, the sample was fragmentized with a scalpel; thus, irregularly shaped pieces were formed, and the former interior of the sample was revealed. The fragments from the interior of the sample were transferred onto the ESEM cooling stage precooled to -25 °C.

In methods I and II, the freezing rates were estimated by observing the process of freezing the 0.05M CsCl solution with a high-speed camcorder (Phantom V611, Vision Research, Inc., 3000 fps) and via analyzing the movement of the freezing interface. As regards method I, the interface was nicely visible, and the calculated freezing rates were very reproducible; method II, however, exhibited a very poorly visible interface, allowing only rough estimation of the freezing rate.

During the open-chamber freezing process, a thin layer of ice from the deposited moisture was formed on the surfaces of the frozen samples in all of the preparation methods. This layer protected the samples from sublimating while the specimen chamber was being pumped down. The layer exhibited a structure very different from that of the frozen samples (Fig. S18 in the Supplement); thus, the desublimated ice was always readily distinguishable from the original ice sample. The sublimation of the deposited layer was monitored at the start of the ESEM imaging; as soon as the layer had sublimated, the imaged surface of the frozen sample was affected by the sublimation process to only a very small extent. We can infer this fact because we had also followed further sublimation of the ice samples, as will be reported in the near future. By further extension, the effect of ice sublimation could be more pronounced in temperature cycling and ice dynamics experiments.

Table 1. The major parameters of the freezing methods I–IV.

	The temperature of the cooling medium*	Sample size	Observed part
I	−16 °C	$d \approx 4$ mm	surface
II	−2 °C	$h \approx 1$ mm	
III	−196 °C	$d \approx 100$–300 µm	
IV		$d = 8$ mm $h \approx 10$ mm	interior

* The temperature of the cooling medium just before the nucleation started.

Imaging in the ESEM

The electron beam energy of 20 keV and a YAG:Ce^{3+} scintillation backscattered electron (BSE) detector, sensitive to the region encompassing the top 1500 nm, were employed for the imaging. In a number of instances, the samples were represented with an ionization detector of secondary electrons, recording mainly signals from the thin subsurface layer (up to 5 nm); the device enabled us to obtain information about the topology of the surface (Neděla et al., 2015). In all of the measurements, a low beam current (40 pA) and a short dwell time (14 µs) were employed to minimize radiation damage to the frozen samples. During the experiments, we maintained the nitrogen gas partial pressure of 500 Pa inside the specimen chamber. Besides the nitrogen gas, water vapor was also purged into the chamber; the relative humidity was kept slightly below the sublimation curve values to prevent moisture condensation on the ice surface. Somewhat slow ice sublimation was observed, as conditions exactly matching the sublimation curve are difficult to establish inside the specimen chamber of the ESEM. For a fresh sample, the initial temperature of the cooling stage was usually set to -25 °C (occasionally being -22 or -23:5 °C). Then, the temperature was gradually changed, and its impact on the brine abundance on the surface of the sample was monitored.

The indicated temperatures relate to the Peltier cooler placed inside the cooling stage. However, the temperature of the sample differs from that of the Peltier cooler; we detected differences of up to 2 °C between the data provided by the sensor of the cooler and the temperature of the sample measured with both a sensor frozen inside the ice and a thermal camera (Flir A310) in atmospheric conditions. The temperature settled significantly more slowly in the sample than in the cooling stage: we observed a lag of about 3 min for when the value of -18 °C was reached. Additionally, heating the sample surface with an electron beam (also considering the relatively warm gas purged through the specimen chamber) and the subsequent

cooling due to the ice sublimation and/or water evaporation from the brine might affect the surface temperature during the imaging. The images were typically recorded with the magnification of 500 (image resolution of ~ 0:5 μm), although a resolution up to 10 times higher is feasible.

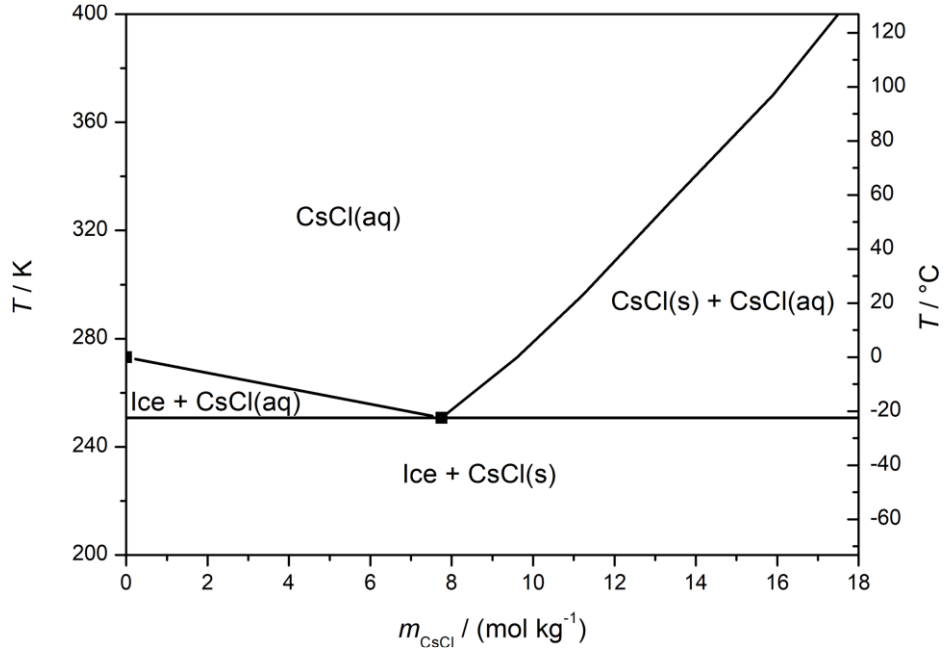

Figure 1. The CsCl–water phase diagram; adopted from Gao et al. (2017).

Estimating the brine surface coverage

We used a BSE detector that has high sensitivity to atoms with large atomic numbers; thus, in the gray scale ESEM images, the sample surface covered with the CsCl is white, whereas the gray areas represent the ice. To estimate the extent of the sample surface covered with the brine, Mountains® software (Digital Surf) was applied. This software facilitates selecting pixels with brightness above the chosen threshold; the pixels are then highlighted. By overlaying the highlighted mask and the white areas in the original image, the best-fitting threshold is chosen to represent the brine and to exclude the ice (Fig. S1).

A constant threshold could not be employed for all of the images due to the fact that, during the actual image acquisition, the parameters of the detector (and thus the brightness and contrast of the image) were often changed based on the intensity of the detected signal to avoid underexposure or overexposure. If the signal is locally too intensive (e.g., there are spots with a large amount of the brine), the detector sensitivity must be reduced during the image acquisition to prevent oversaturation; thus, spots with a low amount of the brine might not be visible in the image, and the surface coverage could become underestimated. Conversely,

with the CsCl signal too low, the brightness of the brine might be comparable to that of the surface irregularities (as the detector is also sensitive to the morphology of the sample, albeit to a limited extent only), leading to them being misinterpreted as small brine-containing spots. Such a situation would then cause overestimated brine surface coverage. The estimated coverage can therefore be directly compared exclusively in samples with similar amounts of the salt (similar concentrations), where the detector response differences are negligible. The uncertainty of the manual threshold selection procedure is indirectly deducible from the variance of the surface coverage in the sequence of the images recorded at the same temperature soon after one another; the relevant value was in units of percentage.

Results and discussion

Representative examples of the surfaces of the non-seeded samples, seeded samples, and ice spheres of three CsCl concentrations (0.5, 0.05, and 0.005 M) are displayed in Fig. 2. These images were recorded at the very beginning of the microscopic observations, and their surfaces are thus very little affected by the sublimation and specific conditions inside the specimen chamber of the ESEM (e.g., low pressure and possible interactions with the electron beam); we therefore assume that the observed features had resulted from the various freezing conditions. When BSEs are detected, merely the material contrast is revealed in most cases. The white areas in the images represent the CsCl-containing brine or CsCl crystals, while the dark or gray regions indicate the ice. Certain limited topographical information is also obtained; it is visualized via various shades of gray. We measured > 50 samples and analyzed the acquired micrographs. From these, we then evaluated the impact of the freezing method and the salt concentration on the appearance of the surfaces of the frozen samples, location of the brine, and sizes of the ice crystals and grain boundary grooves.

Appearance of the surface of the frozen samples

Non-seeded samples (Fig. 2, left column)

The brine was located mainly at the grain boundary grooves. For the CsCl concentration of 0.005 M, the grooves were very visible; no brine puddles were located on the sample surface. As the concentration was increased to 0.05 M, the grain boundary grooves became thicker and small brine puddles appeared on the surface. The surfaces of the samples (0.005 and 0.05 M) were not smooth, with visible small humps. The surface of the most concentrated sample (0.5 M) was already almost completely covered with a brine layer at the beginning of the observations; during the procedure, the surface became completely brine-flooded due to the slow, gradual ice sublimation. Thus, the ice grains and grain boundary grooves could not be sufficiently recognized in this case.

Seeded samples (Fig. 2, middle column)

The amount of CsCl at the grain boundaries was apparently much smaller compared to that in the non-seeded samples: the grain boundaries were barely visible in the microscopic images of the 0.005 and 0.05M seeded samples, and the surface of the 0.5M seeded sample was not brine-flooded. However, brine puddles were abundant on the surfaces of the seeded samples. The surfaces were not smooth, with numerous humps formed (vide infra).

Ice spheres (Fig. 2, right column)

Spraying the solution into the LN led to the formation of ice spheres, with typical diameters ranging between 100 and 300 μm. Their prevalently regular and spherical shapes indicate that the droplets froze during levitation above the LN surface due to the inverse Leidenfrost effect: if they had frozen inside the LN volume, the shapes would have been pear-like (Adda-Bedia et al., 2016). The surfaces of the spheres were smooth, lacking visible humps and almost without brine puddles. For the concentration of 0.005 M, the grain boundaries were nearly invisible, exhibiting very little brine on the sphere surfaces. As regards the CsCl concentrations of 0.05 and 0.5 M, the brine was freeze-concentrated in the grain boundary grooves and at joints between neighboring spheres.

Sizes of the ice crystals

The average sizes of the ice crystals on the surfaces of the frozen samples depended on both the freezing method and the solution concentration (Table 2). The largest ice crystals were detected in the seeded droplet (the average sizes of 105, 91, and 48 μm for 0.005, 0.05, and 0.5M CsCl, respectively). These crystals exhibited oblong shapes, and therefore their longer and shorter dimensions were evaluated separately; the average dimensions determined are listed in Table 2. As the larger crystals often exceeded the field of view of the ESEM (Fig. S2, distance F), the calculated sizes are biased towards lower values; thus, the average sizes should be somewhat larger. The smallest ice crystals were formed in the supercooled non-seeded droplet; the average size equaled 44, 33, and 26 μm for 0.005, 0.05, and 0.5MCsCl, respectively. Medium ice crystals (average size of 50, 55, and 39 μm for 0.005, 0.05, and 0.5MCsCl, respectively) were observed on the surfaces of the ice spheres.

In our experiments, the freezing of the seeded samples promoted the slowest freezing rates, as the ice crystals developed from a solution with a low degree of supercooling (the temperature of the droplet was -2 °C) and the progress of the crystallization front proved to be about 0.2mm s^{-1}. This freezing technique produced

the largest ice crystals. The freezing rates for the non-seeded samples (150 mm s^{-1}) and ice spheres were much higher compared to those in the previous case, and thus substantially smaller ice crystals had been produced. The ice crystals in the non-seeded samples and in the ice spheres were about half the size of those in the seeded samples.

Our examination of the large crystals at low supercooling is parallel to the findings by Macklin and Ryan, who investigated large crystal discs at low supercooling of pure water (Macklin and Ryan, 1966). The patterns in our micrographs show sizable disc-like crystals formed at low supercooling (Fig. 2b), whereas 16 °C supercooling (Fig. 2a) delivers numerous small crystals. The fact that faster freezing rates promote a high number of small ice crystals and slower ones form a few large ice crystals is well recognized and efficiently utilized by productive freezing and lyophilization techniques (Kasper and Friess, 2011; Jameel, 2010; Cao et al., 2003).

As mentioned above, the ice crystal size difference between the samples frozen under high and low supercooling was expected. However, we were rather surprised that the ice crystals in the non-seeded supercooled droplet appeared smaller than those in the ice spheres prepared by spraying a solution into the LN. Although LN boils at the very low temperature of -196 °C, its ability to quickly cool the sample down is reduced due to the inverse Leidenfrost effect (Adda- Bedia et al., 2016). An alternative reason for comparatively large ice crystals forming during the nebulization of a solution into LN may consist of a different freezing mechanism: at freezing rates from 210 to 2×10^{-6} mm s^{-1}, morphological instability of the ice surface is predicted, whereas outside this range linear progression of the ice front is expected (Wettlaufer, 1992; Maus, 2019). The prediction was made for a 3.5% solution of NaCl and varied in other compositions. The linear relationship between the freezing rate and the dimension of the formed lamellae holds only with temperatures of morphologically unstable growth; thus, if a high freezing rate induces linear growth of ice in ice spheres' preparation, the resulting ice crystal sizes cannot be used for comparison with the slower methods.

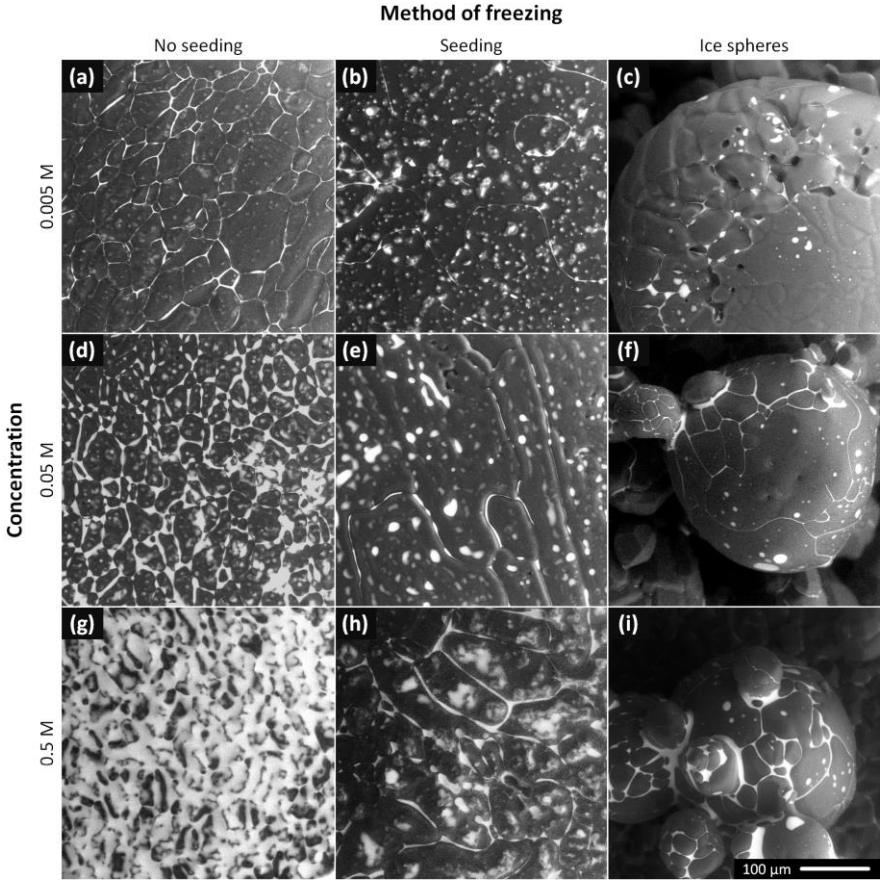

Figure 2. The ESEM images of the frozen samples prepared from the 0.005, 0.05, and 0.5MCsCl solutions via spontaneous freezing of a supercooled (non-seeded) droplet (a, d, g), freezing a droplet seeded with ice crystals (b, e, h), and spraying the solution into LN (c, f, i). The images were acquired at the very beginning of the observations, at the following temperatures: -22°C (f, h, i), -23:5 °C (a–c), and -25 °C (d, e, g). The gray areas represent the ice, and the white regions denote the CsCl brine. Images of two additional samples for each freezing method and concentration are provided in Figs. S7–S15.

Table 2. The average diameters (and their standard errors of the mean) of the ice crystals on the surface of the frozen samples prepared from the 0.005, 0.05, and 0.5MCsCl solutions via the three freezing methods. The ice crystals in the seeded samples had oblong shapes; therefore, the average sizes of the longer and shorter sides of the crystals were evaluated separately. The number of crystals used for the analysis is presented in Table S1.

Concentration	Average diameters of the ice crystals (μm)				
	Non-seeded	Seeded droplets			Ice
		overall	longer	shorter	
0.005	44 ± 3	105 ± 11	135 ± 19	75 ± 8	50 ± 7
0.05	33 ± 2	91 ± 19	125 ± 25	53 ± 8	55 ± 2
0.5	26 ± 2	48 ± 4	65 ± 6	31 ± 2	39 ± 4

Another aspect affecting the crystal sizes consists of the concentration of the solutes. Generally, the ice crystals were smaller when the solute concentration had increased. The observation is in accordance with the conclusion proposed by multiple natural ice core studies, namely, that high-impurity ice exhibits, as a rule, smaller grains than low-impurity ice at the same depth (Eichler et al., 2017). The explanation of this phenomenon may relate to the solution viscosity bewater molecules to the crystal surface, and an increase in

the viscosity hinders the crystal growth (Braslavsky, 2015). The CsCl solution viscosity increases at concentration values higher than approximately 2 mol kg^{-1} (Goldsack and Franchetto, 1977; Nakai et al., 1995). The concentration in the veins of the freezing CsCl solution is expected to be within such a range, as the eutectic composition corresponds to about 7.7 mol kg^{-1} (Gao et al., 2017). A further factor influencing the ice crystal sizes possibly relates to a decreased heat capacity of the solution due to the presence of a solute (Bonner and Cerutti, 1976; Gao et al., 2017); thus, the solution may be cooled more effectively and the ice may propagate at a quicker pace, leading to smaller ice crystals. Changes in the above-described aspects could also cause altered microscopic convection patterns within the sample being frozen; these were previously shown to play a major role in the freezing of macroscopic quantities of sea water (Wettlaufer et al., 1997).

Brine on the surface of the frozen samples

Effects of the salt concentration

Typically, the brine on the surface of the frozen samples increased in amount with rising concentration of the salt. Such behavior is not surprising, as the maximum concentration of a salt in the brine and the proportion of the brine to the ice at each temperature are given by the liquidus curve in the phase diagram; the amount of the liquid brine increases with the salt concentration and temperature.

The grain boundary grooves became substantially thicker when the concentration had increased. The average widths of the brine-filled grain boundary grooves related to the concentration are given in Table 3. The measurements are displayed in S17. The average groove widths for the 0.005M samples might be overestimated, as many grooves were so thin that they were almost invisible or their widths approached the image resolution (approx. 0.5 μm). The grain boundary grooves could not be determined for the non-seeded sample with the CsCl concentration of 0.5 M, as the ice crystals were barely visible below the brine layer; the layer covered nearly the whole surface of the sample.

Impact of the freezing method on the surface coverage

The brine surface coverage in relation to the freezing method was estimated for the frozen 0.05M solutions. While the brine covered (18:2_4:0)% and (9:0±2:8)% of the surface in the non-seeded and the seeded samples, respectively, it occupied only (4:1±1:5)% in the ice spheres (Table S3). These estimates are based on the detected relative brine surface coverage in five independent samples for each freezing method. However, the estimated surface coverage might be strongly dependent on the intensity of the detected signal, as discussed in the Methods section. Regrettably, neither the thickness of the brine layer nor the absolute amount of the salt on the surface can be directly evaluated using the ESEM; we can nevertheless estimate the relative amount of the salt on the surface of the sample, presuming that the thickness of the surface brine is similar to channels' width. Therefore, we estimated the relative amount of the salt on the surface of the frozen samples prepared from 0.05MCsCl via the freezing methods I–III, exploiting the assumption that the thickness of the surface layer equals 1.5 μm. As a result, the relative amounts of the salt on the surface were 9 %, 4.5 %, and 26% for the non-seeded droplets, seeded droplets, and ice spheres, respectively. The calculations are provided in the Supplement.

The location of the CsCl brine within the sample and the related surface coverage were presumably dependent on the freezing rate and its directionality. In the globally supercooled non-seeded sample (cooled from the bottom), we suppose the crystallization was directed from the bottom upwards, as shown previously by Suzuki et al. (2007) for a supercooled water droplet on a silicon surface; thus, the salt was prevalently expelled from the bulk to the surface of the sample as the abrupt crystallization proceeded. Conversely, the seeded sample probably started to crystallize from the surface, close to the edge of the sample as the first place in touch with the seeding crystals. Even though small vertical temperature gradients were to be expected through the solution, we considered crystallization from the surface more likely, in accordance with a related study that suggested that

crystallization on the surface was 1×10^{10} more probable than the corresponding process in the bulk (Shaw et al., 2005). Because the given freezing method promoted slower freezing rates, we speculate that most of the salt was expelled from the growing ice towards the bottom of the frozen sample. Thus, only a small portion of the salt could be seen on the surface. The lowest brine surface coverage was detected in the ice spheres created by the freezing of micrometric droplets from the surface inwards; however, due to the large specific surfaces of the ice spheres, the estimated relative amount of the salt on the surface was the highest among the techniques discussed. Nevertheless, a large portion of CsCl solution was expelled by the growing ice from the surface of the sphere towards the center, and the CsCl brine inclusions were trapped below the surface. Other arguments supporting this assumption are presented in the chapter discussing the interior of the frozen samples.

Effects of the temperature

As regards the seeded droplet of the 0.005MCsCl solution, the brine surface coverage was studied as a function of temperature (Figs. 3 and 4, Movie S1). The temperature of the sample reacts relatively slowly when the cooling stage temperature has been changed; therefore, the surface coverage variations are continuous, not stepwise. For this sample, about 20% of the surface was covered with the CsCl brine, initially at -23:4 °C. Note that such surface coverage is, unexpectedly, larger than that found on average even in the more concentrated seeded sample (c= 0.05 M) within the previous section. The explanation may lie in the stochastic behavior of the freezing process; however, we identify the most important factor in the difference of the instrumental settings, which, for reasons already outlined above, does not allow quantitative comparison of the micrographs. The brine was located mainly on the ice surface humps (Fig. 3); apparently, these had functioned as points around which the brine gathered and crystallized. To a major extent, the humps seem to be artifacts of the low-pressure conditions in the microscope, as will be discussed in the following section.

When the temperature was gradually increased, the area of the brine-covered surface grew larger (Fig. 4). Such behaviour was expected, as the liquid fraction in the partially frozen sample increases with the temperature in the region between the T_{eu} and the melting point. At the highest temperature examined, -12 °C, about 80% of the surface was covered with the brine. Subsequently, the temperature was abruptly lowered from -12 to -23:3 °C, and the brine surface coverage fraction decreased from about 80% to approximately 40 %. According to the CsCl–water phase diagram (Fig. 1), the equilibrium concentration of the CsCl brine equals 7.7 mol kg^{-1} at -23 °C and 3.9 mol kg^{-1} at -12 °C (Gao et al., 2017), meaning that if a

constant amount of the CsCl salt on the surface is assumed, the brine volume on the frozen surface should approximately double after the temperature had increased from -23 to -12 °C. Even though it is not possible to evaluate the volume from the microscopic images, we documented well that the brine surface coverage had risen by factor of 4 during the warming, becoming much larger than the increase implied by the phase diagram. Presumably, the brine volume can be inferred indirectly from the surface coverage if spreading of the brine on the ice surface is governed mainly by the surface tension. We interpret the change in the brine volume as the central cause of the observed surface coverage variations, and we also suppose that the observed 4-fold rise in the coverage indicates an even larger volume alteration because the brine thickness will increase too. The strong relationship between the brine volume and surface coverage is indirectly demonstrated in Fig. 4; the coverage follows the same trend as the relative amount of brine in the frozen sample (w_{brine}) calculated from the phase diagram using the following formula:

$$w_{brine} = \frac{m_{aq}}{m_{fr} - m_{aq}}$$

where m_{aq} is the molality of the aqueous solution of salt (that can be approximated by the concentration of the salt in case of low concentrations) and m_{fr} is the molality of the brine in the frozen sample (it is dependent on temperature and can be inferred from the liquidus curve of the phase diagram). Thus, we are of the opinion that the change of the brine volume is the main cause of the surface coverage variation.

Table 3. The average widths of the CsCl brine-filled grain boundary grooves for the frozen samples prepared from the 0.005, 0.05, and 0.5MCsCl solutions via the three freezing methods. The uncertainties represent the pooled standard deviations. The numbers of independent samples used for the calculation are listed in Table S2. The average width of the grain boundary grooves for the 0.5M non-seeded sample was not determined because the brine layer covered almost the whole surface of this sample. ND stands for not determined.

Concentration	Average widths of the grain boundary grooves (μm)		
	Non-seeded samples	Seeded samples	Ice spheres
0.005	1.3 ± 0.5	1.1 ± 0.3	1.2 ± 0.3
0.05	2.1 ± 0.9	1.1 ± 0.3	1.9 ± 0.5
0.5	ND	5.7 ± 2.0	3.3 ± 1.1

During the cooling phase, the decrease in the brine volume (and correspondingly also the surface coverage) by half was expectable, considering the phase diagram; however, the surface coverage by the end of the experiment was significantly larger compared to the initial stage, despite the essentially equal temperatures (-23.4 vs. -23.3 °C). Moreover, the temperature decrease down to -27 °C at the end of the

experiment led to a surface coverage of about 30 %, which, despite the temperature being 3.6 °C lower, exceeded the amount of coverage found at the initial stage by 10 %.

The results of this temperature cycling experiment indicate that, as the ice from the surface was required to melt during the heating in order to double the volume of the brine, a formerly inaccessible portion of the brine (restrained due to being trapped in the ice interior) surfaced. This increased the amount of the CsCl salt on the surface, and the brine volume rose dramatically above the expectations stemming from the phase diagram. The subsequent cooling of the sample lowered the volume by half, as expected, indicating that the overall amount of the CsCl salt on the surface had not changed at the cooling stage. This observation implies that the temperature cycling may result in enhanced accumulation of the brine on the frozen surface during the heating phase.

In the experiment, the CsCl started to crystallize from the brine at -27 °C only after a time delay (Fig. 3i). The salt crystallization front propagated along the brine-filled grain boundaries and puddles (Figs. 3, S3, Movie S1). The salt crystals exhibited fine dendritic structures and remained at the humps for a longer period. The brine left on the surface produced voids in the ice bulk; similarly, vertical, gravity driven brine drainage is known to cause sea ice density to decrease (Timco and Frederking, 1996). We are currently investigating the details of salt crystallization and ice sublimation in salt-containing samples under various conditions.

In other experiments, the cooling stage temperature of -25 °C was sufficient for the brine to crystallize after a prolonged period. The hitherto published T_{eu} values of the CsCl-H_2O mixture range from -24:83 to -22.3 °C (Cohen-Adad, 1991; Dubois et al., 1993; Fujiwara and Nishimoto, 1998; Monnin and Dubois, 1999; Chen et al., 2005; Gao et al., 2017). The thermal camera measurements in atmospheric conditions (without the reduced pressure environment of the ESEM sample chamber) showed that the sample was about 2 °C warmer than indicated by the sensor of the Peltier cooler. Further warming of the sample during the ESEM experiments was to be expected, especially due to the effects of the electron beam and the relatively warm gas purged through the specimen chamber; conversely, the surface cooling embodied an expectable process too, considering the ice sublimation and water evaporation from the brine. These factors could contribute to the salt crystallization on the sample surface, even when the temperature of the stage does not change; still, the overall temperature difference between the surface of the frozen samples and the cooler will likely not exceed 2 °C.

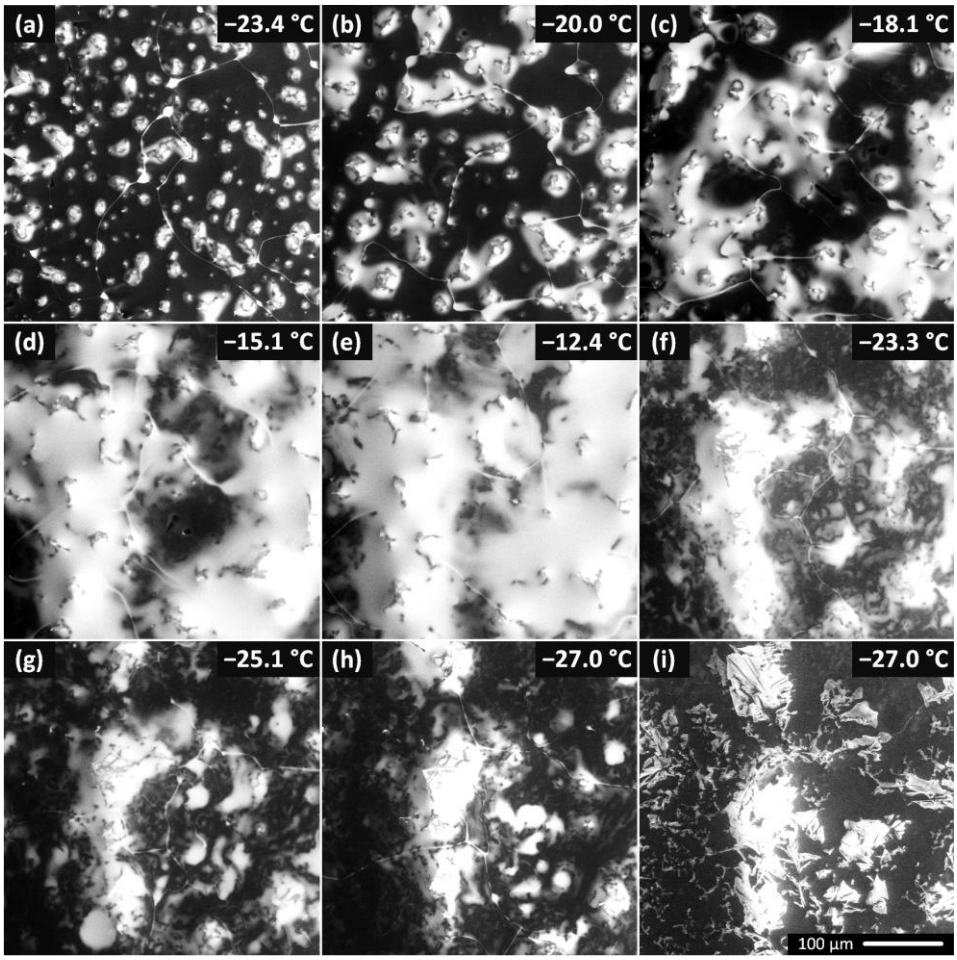

Figure 3. The brine surface coverage as a function of temperature for the seeded 0.005M sample. The temperature was first increased stepwise from -23.4 to -12.4 °C and then decreased to -27 °C. The corresponding numerical values of the brine surface coverage are given in Fig. 4. A movie from this experiment is included in the Supplement (Movie S1). Panels (h) and (i) display the salt crystals forming from the brine. The crystals formed along the grain boundaries and on the humps where the brine had accumulated previously. The crystallization started a minute after the cooling stage temperature had been set to -27 °C. The air pressure in the microscope chamber was 500 Pa during the sequence. The scale in panel (i) is valid for all the images.

The observed ice surface coverage changes have consequences for the interaction with radiation under natural conditions: the higher the brine volume on the ice surface, the more absorbing the surface compared to the condition of dry ice surface, which is highly scattering (Light et al., 2009, 2003). Thus, the temperature increase with the subsequent spread of the brine on the surface may lead to the surface darkening, resulting in higher solar radiation absorption and further increase in the temperature. Conversely, the brine crystallizing on the ice surface would result in larger reflection of the radiation, as the crystals would scatter the light substantially more effectively compared to the liquid brine (Carns et al., 2016; Light et al., 2016). These effects, together with the number and sizes of inclusions, ice grains, and location and characteristics of the absorbing particles, influence the overall absorption properties of icy bodies (Warren, 2019).

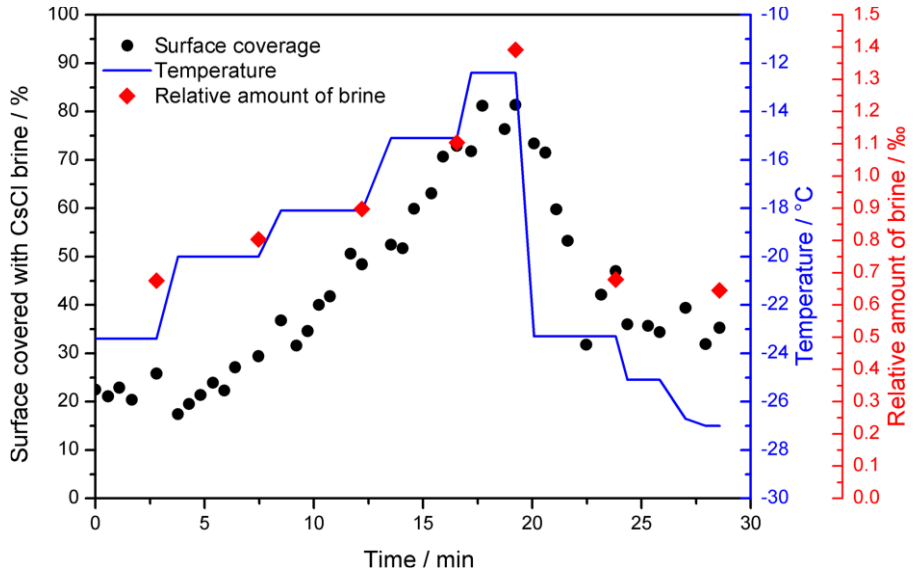

Figure 4. The relative brine surface coverage in the frozen seeded droplet (c(CsCl)=0.005 M) at varying temperatures. The representative images used for the calculation are displayed in Fig. 3. The temperature of the cooling stage during the measurement is indicated with the blue pattern. The red diamonds denote the relative amount of brine in the frozen sample, based on the phase diagram (Fig. 1); temperatures 2 °C higher than those of the cooling stage were used for the calculation to better represent the sample temperature.

Formation of the humps

The surface humps were observed in the numerous non seeded and seeded samples, often in co-location with the brine puddles. The time-lapse images revealed the humps forming at places where the puddles had been located previously (Fig. 5). The humps usually exhibited broader bases and thin tips; the brine was located mainly at the bases, not on the tips (Figs. S4, S5). As the sublimation continued, the tips became even thinner. In some cases, the thin tip separated from the body of a hump and fell off (Fig. S4). From these observations we infer that the humps are predominantly formed during microscopic examinations due to ice sublimating from the frozen samples; we do not expect the humps to originally have been present on the surface of the samples. The formation of the humps appears to be facilitated by the brine puddles on the ice surface: when the surface is covered with the brine, the sublimation from the given spot is retarded and a hump is formed. Such formation might be an artefact caused by experimentation in a low-pressure environment. Previously, similar observations had been explained in terms of charged peaks formed by etching in the SEM (Barnes et al., 2002).

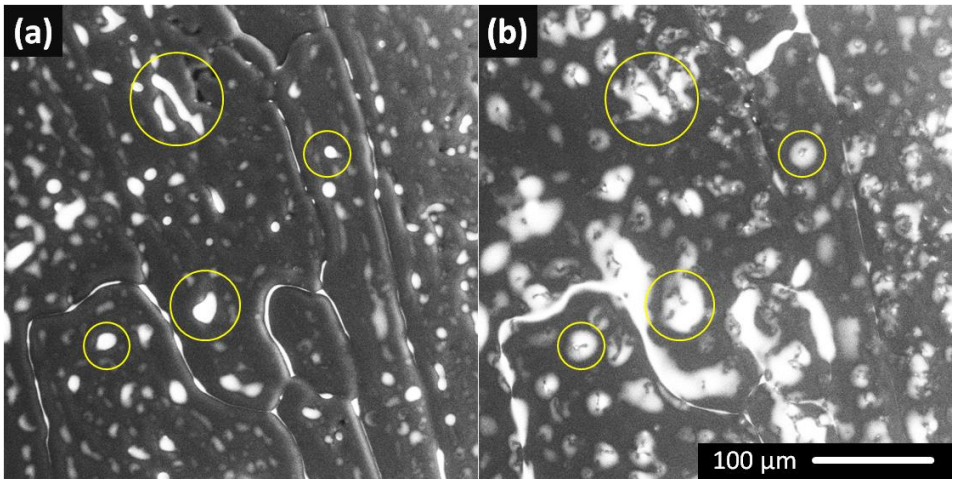

Figure 5. The ESEM images of the seeded sample prepared from the 0.05M CsCl solution at the very beginning of the observation (a) and after 90 s (b). The images were recorded at the temperature of -25 °C. As conditions below the sublimation curve had been set inside the specimen chamber, sublimation of the top layer of the ice was presumed during the time interval between two images. It is clearly visible that the humps formed at spots previously covered with the brine; four examples of such spots are encircled.

Dynamics of the ice surface

The dynamics of the frozen samples' surfaces could be observed even at -23 °C. The CsCl brine-filled grain boundaries were not static: their positions changed swiftly over time. Interestingly, the positions of the humps on the ice surface did not change accordingly. A representative example is shown in Fig. 6 and Movie S1. The surface of the seeded droplet from the 0.005 M CsCl solution was observed at -23.4 °C. As is demonstrated by the yellow arrow, whose position remains constant in all the panels in Fig. 6, the indicated hump was originally encircled by brine-filled channels (Fig. 6a). We suppose the channels denote the ice grain boundary positions. As time progressed, the grain boundary on the right-hand side performed an apparent gradual movement through the hump, while the hump did not change. The brine channel moved from the spot marked with the arrow tip to that marked with the red dot in Fig. 6d (distance 31 µm, time 1 min and 40 s), thus advancing by approximately 19 µm min^{-1}. It was also observed that the humps had caused the directional propagation of the ice boundaries to decelerate; several such examples are presented in Movie S1. A larger brine volume surfaced at the triple junctions of the ice grains. The dynamics of the process, together with the sampling being relatively slow compared to the ice boundary movement, lend the brine reservoirs the appearance of propagating comet-like objects; this effect is demonstrated via the related encircled points in Movie S1. These brine pools occasionally appear at

the locations of caverns formed by bubbles, thus delineating the grain boundary, which would otherwise be difficult to observe.

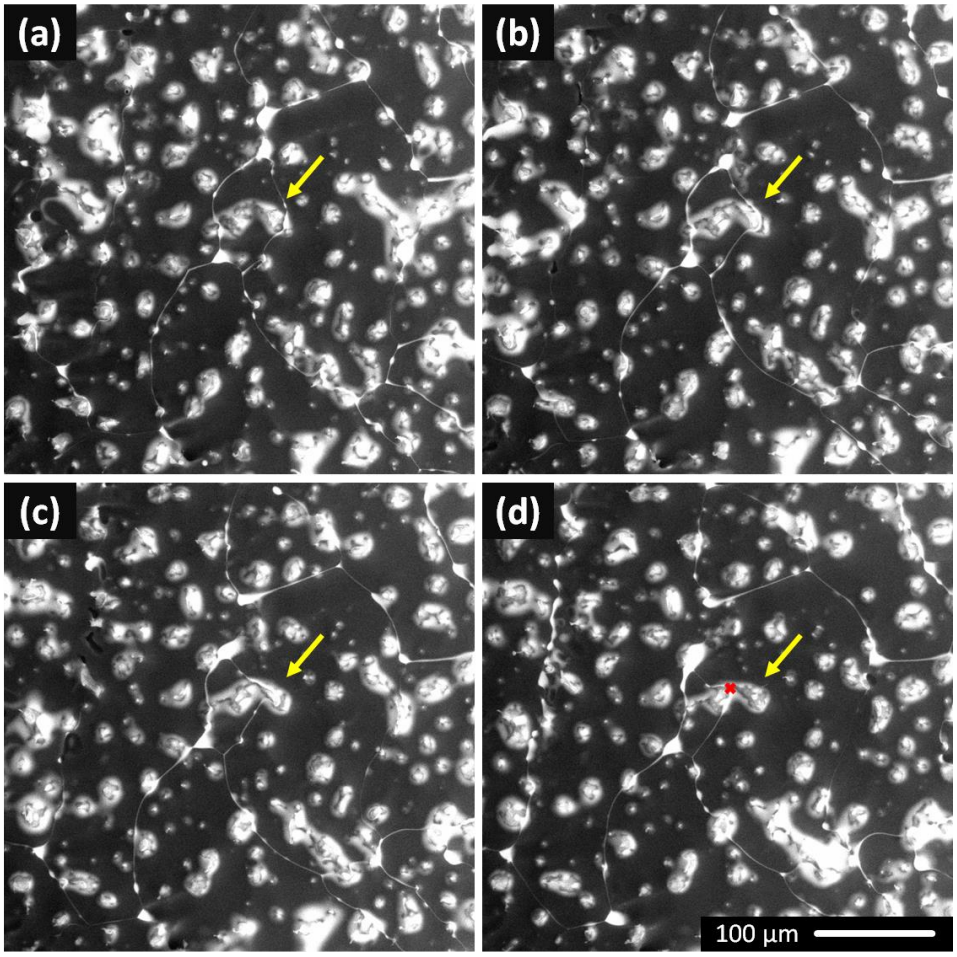

Figure 6. The ice surface dynamics observed at -23.4 °C and 500 Pa. The brine-filled grain boundaries (white channels) shifted their positions over time, while the positions of the humps did not change. An example is indicated by the yellow arrow pointing to a CsCl-filled channel moving through a hump. The arrow indicates the initial position of the brine channel in all of the figures. The sample was prepared from the 0.005 M CsCl solution by freezing a droplet seeded with ice at -2 °C. The distance between the brine channel (red point) and the arrow tip (where the movement started) is 31 µm; the channel moved by ~19 µm min^{-1}. The time interval between the images is approximately 30 s. The scale in (d) is valid for all of the images.

The fact that ice is a very dynamic medium that allows for reconstitution at subzero temperatures was previously evidenced using, for example, time-lapse X-ray tomography; up to 60% of the total ice mass recrystallized during 12 h at -15 °C (Pinzer and Schneebeli, 2009; Hullar and Anastasio, 2016). Our research team is not the first one to have observed the disjointed behavior of the ice surface in relation to the underlying ice crystals; fresh ice growing in steps of 100– 4000 nm to traverse the ice grains regardless of the boundaries was already noticed for planar ice growth (Ketcham and Hobbs, 1968). Moreover, the observed mutual interactions between the surface humps and the ice grain boundaries, causing

temporal retardation of the boundaries and partial draft of the hump (in the direction of the boundary motion) can be classified as Zener slow-mode pinning (Eichler et al., 2017). New ice grain formation (probably ascribable to the grain-boundary bulges mechanism) and the subsequent ice crystal growth are visualized in Fig. 7 (Steinbach et al., 2017). In this context, however, another explanation is also acceptable, as discussed below.

The actual reason why the brine channels were dynamic while the humps remained static is not entirely clear to us. The causes of the recrystallization process are nevertheless appropriately summarized by Steinbach; the relevant factors include the thermal gradients and strains in the samples (Steinbach et al., 2017). Two possibilities are considered in this respect.

Firstly, the movement of the brine channels could be induced by a temperature gradient across the surface of the frozen ice. The sample was prepared from a hemispherical droplet by cooling from the bottom. Thus, the height was not constant across the sample and would be the most prominent in the center, allowing the temperature gradient to rise across the surface. A thermal camera was used to estimate the temperature gradients throughout the sample during cooling outside the ESEM chamber; it was not experimentally feasible to insert the camera into the chamber. As the temperature of the sample dropped from 0 to -18 °C, the temperature at the center of the surface was approximately 2.7 °C higher than at the periphery. This difference had presumably been caused by the greater thickness of the sample at the central section. However, after the sample was cooled down and its temperature became approximately constant (which typically took about 3 min), the gradient was reduced, albeit in an opposite manner: the center was about 0.2–0.3 °C colder than the periphery, producing a small temperature gradient throughout the sample even after the cooling. Regrettably, as the experiment was not conducted in the ESEM chamber, the effects of the gas flow on the one hand and sublimation on the other are not included. Under a temperature gradient, the solute would exhibit higher concentration at the colder end of the brine inclusion and lower concentration at the warmer end, resulting in migration of the brine inclusions toward the warmer region of the ice (Light et al., 2009). The behavior observed in the present study indicates that the water molecules at the brine-filled grain boundaries are redistributed much faster than those on the ice surface. The dissolved salt may diffuse through the veins to increase the salt concentration on one side and decrease it on the other. Where the concentration increases, the ice grain boundaries will melt and where it decreases the ice will grow to maintain equilibrium conditions.

The sample presented in Fig. 6 was sufficiently cooled down, as enough time had elapsed since the last temperature adjustment; therefore, we assume there might be a temperature gradient of only several tenths of a degree Celsius across the sample.

A second hypothesis to explain the apparent movement of the brine channels focuses on the ice sublimation from the sample surface. The brine channels were not necessarily perpendicular to the surface; the angle between the surface and the channels might have been low, and therefore the sublimation of a thin layer of ice from the surface could theoretically result in apparent movement of the brine channels while the appearance of the humps would not change markedly. Similar reasoning had been employed for the sublimation of ice crystals that are not perpendicularly oriented to explain the observed excessive width of the ice grain grooves (Cullen and Baker, 2001). The sublimation rate largely depends on both the amount of water vapor purged into the chamber and the temperature. We do not know the complete time required for our samples to sublimate because the process was not aimed at in our experiments; contrariwise, we intended to prevent sublimation of the samples. We usually imaged the samples for about 30 min, and they never sublimated during this period. The sample height at the start of the imaging corresponded to approximately 1mm (based on the working distance of the ESEM). The upper limit of the (vertical) sublimation rate can thus be calculated if full sublimation of the sample is assumed to materialize within 30 min; the (vertical) sublimation rate would then be 33 μm min^{-1}. The brine channel (Fig. 6) moved by ~ 19 μm min^{-1}. If the apparent movement of the brine channel is caused solely by the sublimation, the angle between the channel and the horizontal line will be 60°.

We are, however, uncertain if the reason for these unusual dynamics of the frozen surface consists of one of the previously described conditions, both of them, or a completely different process.

Interior of the frozen samples

Sublimation

The subsurface structure of the samples was revealed after partial sublimation of the ice from the surface made from the 0.005MCsCl solution (Fig. 8). Subsurface hollows were observed in all types of samples, namely, the non-seeded and seeded ones as well as the ice spheres. The numbers and sizes of the hollows nevertheless differed: the hollows in the nonseeded samples were small (units of micrometers) but numerous, those in the seeded samples were scarce, and those in the LN-prepared ice spheres were numerous, with the size varying from units to 100 μm. The formation of these hollows is presumably associated with air bubbles trapped below the ice surface. For all the freezing methods, opening the hollows by further sublimation often revealed them to be partially filled with the brine (Fig. 8); the co-

location of the brine with gases suggests that the brine in the veins is airsaturated. The presence of gases in the brine had been shown previously to ease the ice recrystallization and boundary migration (Harrison, 1965). Recently, brine inclusions trapped below the ice surface co-located with air bubbles were found (Hullar and Anastasio, 2016). The co-location of the brine and the bubbles was most pronounced for the ice spheres, formed by freezing microdroplets of the solution with LN at temperatures close to -196 °C. The ice spheres were most likely frozen from the surface inwards; therefore, the entrapment of the brine and air inside the structure was anticipated, as was also observed in fractured samples in a similar manner (McCarthy et al., 2013). Conversely, the seeding method allows slow ice crystallization, leading to major expulsion of the air either out of the solution or downward, towards the bottom; we are nevertheless unsure of the details of such scenarios.

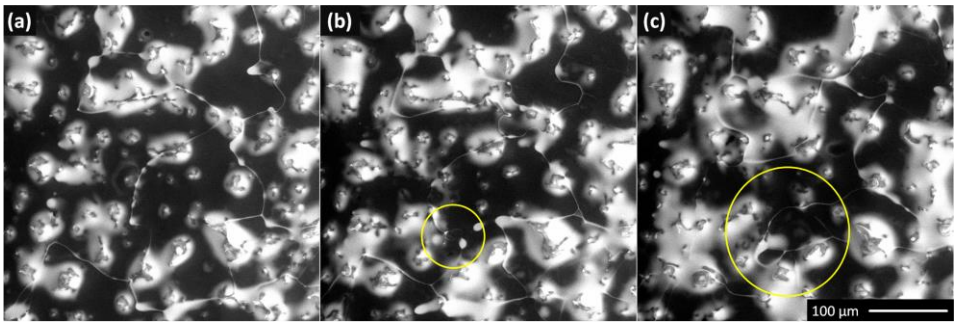

Figure 7. The ice surface dynamics observed at -23.4 °C and 500 Pa. Newly formed ice grains are encircled.

Our recent study of the ice spheres prepared from NaCl solution revealed that, besides the eutectic crystallization, part of the solution vitrified under the conditions of fast cooling (Imrichova et al., 2019). The differential scanning calorimetry indicated the melting of the glass at -91 °C upon progressive heating, further allowing cold crystallization of NaCl and water at -76 °C. As the ice spheres are inspected at a much higher temperature in the present study, we expect the salt to be crystalline or dissolved in liquid brine during the observations.

Fragmentation

An additional technique to observe the interior of a frozen sample consisted of fragmenting the LN-frozen macroscopic ice samples and inspecting the pieces originated from the given interior in the ESEM. Representative images of the fragments are displayed in Fig. 9; it is clearly visible that the ice and the brine are arranged in parallel lamellae in the original interior of the fragmentized sample. The brine lamellae appear as lines on the micrograms. These lamellae were approximately equidistant within one facet of the fragment; however, when various

facets are compared within one sample, the distances between the lamellae might differ significantly. The closer brine lamellae spacing for the lower-right facet in Fig. 9b was approximately 10 μm; the wide-spaced zrrangement (at 40 μm) is displayed on the upper-left facet. The lamellae were long and narrow. The parallel structure of the lamellae was sparsely interrupted by the bridge connecting two adjacent brine layers across the ice plate; several examples of these are encircled in Fig. 9a. Only a few bridges were typically recognized on the individual facets. We cannot determine if these features were present in the samples naturally or only through sample fragmentation (Maeda et al., 2003).

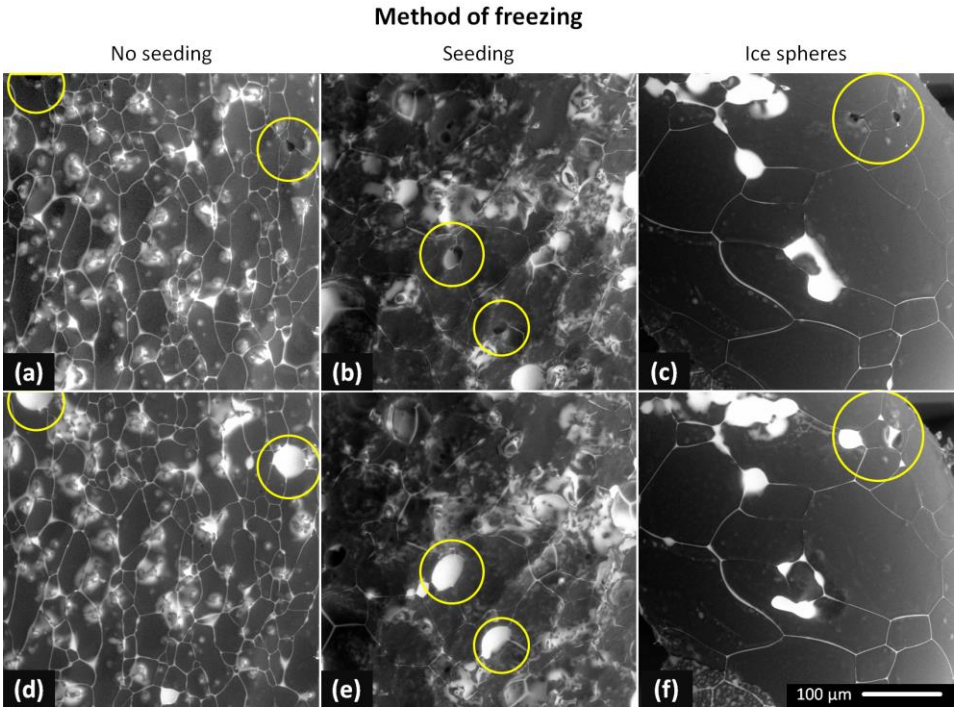

Figure 8. The ESEM images of the partially sublimated frozen samples prepared from the 0.005MCsCl solution: the non-seeded droplet (a and d, -25 °C); the seeded droplet (b and e, -25 °C); and the ice sphere (c and f, -23 °C). The hollows in the internal structure were revealed after the initial sublimation of the ice from the surface (a, b, and c). Further sublimation showed the hollows filled with the brine (d, e, and f); the time interval between the upper and the lower images was about 1 min. The gray areas represent the ice, while the white regions indicate the CsCl brine.

The structures observed in the interior of the LN-frozen samples resembled the lamellar eutectic structure of alloys (Losert et al., 1998; Yan et al., 2017) or the pattern often recognized when sea ice is formed (Anderson and Weeks, 1958; Petrenko and Whitworth, 1999;Weeks, 2010; Thomas, 2017; Nagashima and Furukawa, 1997; Shokr and Sinha, 2015). This pattern is generated due to the constitutional supercooling of the liquid ahead of the freezing interface. It has long been known that the fastest freezing produces dendritic structures, whereas gradual slow freezing is characterized by cellular and planar structures, respectively (Rohatgi and Adams, 1967; Trivedi and Kurz, 1994). The linear solidification

region is also reached upon very fast freezing (Wettlaufer, 1992). As a matter of fact, the microscopic structure of ice and brine is a complicated function of the thermal gradient and rate of freezing (Losert et al., 1998; Yan et al., 2017; Maus, 2007). The spacing of the parallel lamellae of pure ice separated by brine layers, created in a direction perpendicular to that of freezing, is characteristic of particular freezing rates and salt identities and concentrations. In terms of freezing salt solutions (NaCl, KCl and LiCl), the spacing between the perpendicular lamellae was experimentally found to be proportional to the inverse square root of the freezing rate (Rohatgi and Adams, 1967). The same paper reported that the maximum freezing rate, as well as its average, was inversely proportional to the square of the distance from the chill. At the same time, an increase in the solute concentration is responsible for the larger spacing between the lamellae. It is therefore conceivable that the uneven spacing observed in Fig. 9b is due to unequal temperatures and/or concentrations in the growth of the individual ice facets. Another contributing factor could be the altered relative angle of the facets towards the detector, which would result in biased observed spacing. Using the theoretically predicted instability for the 0.035% NaCl solution, (Wettlaufer, 1992) we can conclude, for the observed 10 μm spacing, that the freezing rate can range from 0.1 to 10^{-5} mm s^{-1}. Thus, the freezing of the 16 °C supercooled sample can proceed 1000 times (or more) faster than that of the LN-immersed capsules.

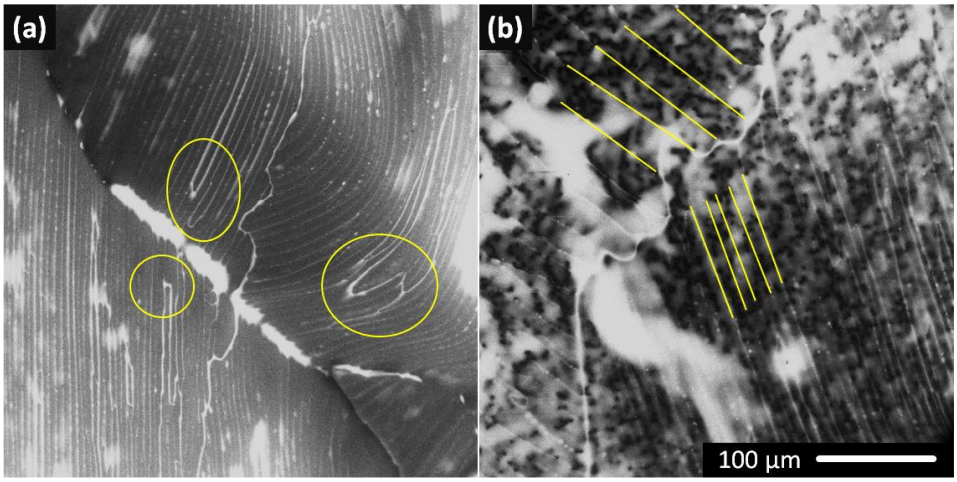

Figure 9. The interior of the fragmentized LN-frozen sample of 0.05M CsCl imaged with the ESEM at -25 °C. The gray areas represent the ice, and the white regions indicate the CsCl brine. The brine was arranged in densely spaced parallel lamellae. Bridging of the ice was rare within a facet; examples of the effect are highlighted in (a). The brine lamellae were equidistantly spaced within a facet. However, the distances between the lamellae might differ significantly among the facets (b). Images of two additional samples for this freezing method are provided in Fig. S16.

It is interesting to note that lamellar brine arrangement was not observed in any other sample, namely, neither on the surface of the LN-frozen macroscopic sample (Fig. S6) nor on or below the surface of the ice spheres (Figs. 2 and 8, righthand

columns). Instead, structures resembling a cellular arrangement rather than a lamellar interface are formed in the small samples (Weeks, 2010; Losert et al., 1998). We can only speculate if the absence of lamellar growth in the micrometric ice spheres is due to the higher freezing rate or the exposure to a lower temperature gradient compared to the macroscopic sample with a diameter of 8mm immersed in LN. Two significantly different ice sample structures were observed, even though LN was used as the coolant in both cases. A recent study of the inverse Leidenfrost effect of levitating drops on the surface of LN revealed a strong dependence of the freezing time on the size of the droplet (Adda- Bedia et al., 2016); therefore, the size and surface properties of micrometric ice spheres in contrast to those of gelatine capsules can be among important contributing factors as regards the described difference.

Relevance to previous observations

The ESEM observation presented herein employed a proprietarily developed detection system allowing the use of very low currents (40 pA) and short dwell times (14 μs) to minimize the samples' degradation during the imaging (Nedela et al., 2018). The electric field was not found to influence the ice growth (Rohatgi et al., 1974). There was a subtle magnetic field present in our microscopic chamber. Thus, our observations differed from the natural conditions mostly due to the low pressure of 500 Pa inside the chamber.

In the experiments, CsCl was used as the solute thanks to its high contrast between the caesium atom and the oxygen and hydrogen of ice when BSEs are detected. It served as the model compound for monovalent chlorides, abundantly present in the environment. CsCl solutions exhibit properties relatively similar to those of NaCl; in particular, the eutectic temperatures important for this study are very close to each other (T_{eu} (CsCl)=-23 °C, T° (NaCl)=-21.21 °C) (Brady, 2009). The tested concentrations ranged over 2 orders of magnitude. The values within 500–50mM define the concentration of NaCl in seawater, and therefore they are also descriptive of fresh sea ice in the given context (Massom et al., 2001; Thomas, 2017). NaCl concentrations reaching up to 160mM were detected immediately next to a highway treated against road icing; 50mM of a salt solution can thus be considered a concentration potentially found farther from roads or in their close vicinity when the salt was already partly flushed away (Notz and Worster, 2009; Labadia and Buttle, 1996). The values discovered in surface snows in Arctic coastal regions or on the surface of frost flowers span between 10–100mM but may also be as low as 5mM (Beine et al., 2012; Douglas et al., 2012; Maus, 2019). A similar concentration was used in the report on solute locations in ice by Hullar and Anastasio (2016).

The principal finding presented within our study is embodied in the very strong sensitivity of the ice-brine morphology and brine distribution to the freezing method (Figs. 2, 3, 9). Even for identical solution concentrations, the method and direction of freezing strongly modify the appearance of the ice surface morphology. In all of the experiments, we observed a clear difference between the interconnected system of the brine in the grain boundary grooves and the predominantly separated brine puddles. At the lowest salt concentrations, free ice surfaces dominated. As the concentration rose, the grain boundary grooves broadened, and both the amount and the size of the brine puddles increased; however, some parts of the surface would remain bare even at the highest concentrations. Partial surface wetting had been invoked previously (Domine et al., 2013).

The directionality of freezing influences to a large extent the amount of brine exposed on the surface. Freezing from the outside inwards segregates the brine inside the ice matrix, whereas the same process starting from the bottom expels the brine to the ice surface. The directionality of freezing was previously shown to play a key role in determining the final distribution of impurities at the macroscopic scale for the formation of ice on seawater (Wettlaufer et al., 1997). With the samples cooled from the top by air at -20 °C, it was observed that the salt is retained in the mushy layer of ice until it reaches a critical height. After this stage, plumes (capsules) of a saturated salt solution (having a higher density and low temperature) migrate downwards, leaving space for a less concentrated solution and thus faster growth of the ice. Such a procedure then reduces the sea ice density (Timco and Frederking, 1996). Our freezing methods differ from that related to natural sea water in the rates and directionality. By extension, we would like to imply that the role of material convection in relation to the drop size should be considered for the modeling of the freezing process.

The distinct ice grain sizes and textures shown for the various freezing methods (Figs. 2, 8, 9, and Table 2) indicate possible differences in the mechanical, thermal, and optical properties of the ice, influencing, for example, the samples' permeability for percolating solutions or their optical properties. Related changes could affect numerous properties of ice, having geological consequences, such as the impact on sea ice desalination and melting; further, the variations might influence also the energy balance of ice and aerosols and rates of the (photo)chemical reaction (Thomas, 2017). In our experiments, the samples were invariably placed on the silicon pad in the microscope. This procedure renders the observation different from that of natural sea ice, where the brine from the ice may leak into the seawater (Notz and Worster, 2009). Nevertheless, our observations can be considered a good model for salty ice on solid ground.

The distinct ice grain sizes and textures shown for the various freezing methods (Figs. 2, 8, 9, and Table 2) indicate possible differences in the mechanical, thermal, and optical properties of the ice, influencing, for example, the samples' permeability for percolating solutions or their optical properties. Related changes could affect numerous properties of ice, having geological consequences, such as the impact on sea ice desalination and melting; further, the variations might influence also the energy balance of ice and aerosols and rates of the (photo)chemical reaction (Thomas, 2017). In our experiments, the samples were invariably placed on the silicon pad in the microscope. This procedure renders the observation different from that of natural sea ice, where the brine from the ice may leak into the seawater (Notz and Worster, 2009). Nevertheless, our observations can be considered a good model for salty ice on solid ground.

The ice sublimation effects displayed in Fig. 8 suggest the character of the behavior of salty ice samples exposed to dry winds in the nature, namely, samples in which gradual brine accumulation is expected.

Connection to previous microscopic observations

In previous studies of frozen aqueous solutions, two regions were described: one of the uncontaminated, pure ice matrix, and the other with impurities concentrated in liquid-like compartments above their eutectic temperatures (Krausko et al., 2014; Thomas, 2017; Lake and Lewis, 1970; Rohatgi and Adams, 1967). The impurities' inclusion was observed via several microscopic methods for both laboratory-prepared samples and natural ice and snow. However, the imaging methods reaching -20 °C or more did not have a resolution large enough to visualize the impurities in the grain boundary grooves and were blind to the ice topography. For this reason, the impurities in the grain boundary grooves of polycrystalline ice were then observed in high vacuum via the use of a low temperature (< -80 °C) SEM (Barnes et al., 2003; Cullen and Baker, 2001; Blackford et al., 2007; Rosenthal et al., 2007). Our technique facilitates the observation of all the aspects: the liquid brine puddles, brine in the grain boundary grooves, and, to some extent, ice topology. The aim in this context is to summarize the previous observations, with a focus on the dimensions of the observed impurities' elements; first, attention is paid to the veins of subtle impurities and grain boundary grooves and, second, the larger puddles are discussed.

Observing the grain boundary grooves and veins

Typically, in the procedures adopted to observe the impurities, the ice samples were repeatedly exposed to "etching", e.g., ice sublimation at a higher temperature (-20°C) (Rosenthal et al., 2007; Cullen and Baker, 2001). The analysis allowed

examination of pure ice crystals surrounded by veins containing the impurities. Using the energy dispersive X-ray technique, the veins were found to contain elements (e.g., Cl, S, Na, Mg) corresponding to the common minerals (NaCl, sulfates) for natural glacier samples (Cullen and Baker, 2001). At certain instances, the grain boundary impurities would coagulate to form filaments that can eventually peel off the ice due to differing thermal expansion coefficients. The diameters of the filaments varied between 0.2 and 2.5 μm, and the dimension of the nodes (the meeting points of four grains) was approximately 5 μm (Blackford et al., 2007; Rosenthal et al., 2007). However, the diameter of the groove formed by the sample sublimation at 253K for 8 weeks reached as high as 250 μm. The apparent size of the sublimation groove can be biased by the fact that the ice crystals do not need to be oriented perpendicularly to the plane of observation. The observation most relevant to the ice spheres presented herein is that of the NaCl solution (0.043 M) nebulized into LN and observed at -120 °C (Blackford et al., 2007). The newly prepared ice spheres exhibited sub-micrometer fine filaments of salt on the surface, whereas sintering at -25 °C allowed separated patches (up to 100 μm in diameter) and filaments threading the ice crystals due to metamorphism (Blackford, 2007; Domine et al., 2013). Further sublimation of the ice striped the filaments and showed that they form 3-D interconnected structures, also indicating that each filament has a star-like geometry, which is appropriately explained via considering the surface energies of the ice and the brine.

All the dimensions of the veins observed previously correspond very well to those of the grain boundary grooves reported in the present paper (Table 3). The grain boundary grooves are formed at positions where two neighboring ice grains meet on the ice surface; thus, they thread each individual ice grain. Apparently, the amount of the brine on the ice surface was not sufficient to fill the groove around all the ice grains due to low brine concentration and/or the freezing method concentrating the brine towards the interior of the ice matrix (Fig. 2c, e, f). Even for the most concentrated samples, the grain boundary grooves were found to range below 6 μm on average. The ice grain boundary grooves were predicted to increase their width with rising temperature and upon aging; (Nye, 1991) for example, under certain conditions, the values of 0.3 and 0.7mm are assumed after 10 and 100 d, respectively, at 0 °C.

Observation of the brine puddles

The advantage of optical microscopic methods and X-ray tomography consists of the possibility of working at atmospheric pressure and an arbitrary temperature; the central drawback of these approaches rests in the compromised spatial resolution (Blackford, 2007). Importantly, optical microscopy maintains the transparency of

ice to visible light, causing the image to include the subsurface information (Eichler et al., 2017); this aspect can be considered a benefit or a drawback, depending on the situation. Thus, the applied method relied on imaging the larger brine patches, but the brine in the subtle ice boundary grooves could not be represented.

The fluorescence microscopy technique exploiting a pH indicator showed a major difference between frozen water and a 0.1mMsolution of NaCl at -7 °C (Cheng et al., 2010): the former left pools of the solution around the ice crystals (approx. 12 μm wide), whereas the latter was specific in that the solute was mostly rejected towards the edge of the microscopic field of view, leaving only a few thin brine channels in the bulk of the ice. Another study based on fluorescence microscopy was intended to assess the amount of aggregation of bovine serum albumin labeled by a fluorescence probe (Roessl et al., 2015). Fast freezing rates produced more puddles of proteins, while slow ones led to fewer larger patches (millimeter sized), with the protein contained in a more concentrated solution. Such results agree with those assessing the extent of aggregation via the spectroscopy of methylene blue (Heger et al., 2005). The patches containing various salts were shown, via X-ray fluorescence imaging, to increase their surface concentrations with decreasing temperatures (Tokumasu et al., 2016). In the referenced study by Tokumasu et al. (2016) the patches were determined to be about 30 μm wide at temperatures from -5 to -15 °C. The optical microscopy and Raman spectroscopy of ice core samples detected microscopic impurities assigned to salt crystals and dust scattered through the ice matrix (Eichler et al., 2017). Eichler et al.'s report did not find any signal for liquid inclusions in the form of pools or veins around the ice grains at -15 °C. The resolution of the microscopy corresponded to 3 μm pixel^{-1}, a value higher than the dimension

of most of the grain boundary grooves measured in our experiments. Therefore, it appears probable that the method did not facilitate discerning the ice grain boundaries (Eichler et al., 2017). Recently, the Raman microscopy of ice revealed the dependence of the brine puddles' width on the temperature; the width increased from 10 μm at -20 °C to 20 μm at -10 °C for 0.6M NaCl solutions (Malley et al., 2018). Interior images of laboratory-frozen CsCl aqueous solutions (1 mM) were acquired with X-ray microtomography (Hullar and Anastasio, 2016). Slow freezing in a refrigerator led to the formation of large pools of impurities (tens to hundreds of micrometers), whereas dumping the sample into liquid nitrogen produced small segregations, namely, ones sized below the voxel size of 16 μm. The impurities were often associated with the air bubbles. The ice grain boundaries were not visualized as their dimensions were below the resolution of the applied method. Quantification of the overall amount of the CsCl present in the samples revealed that a substantial part of the CsCl was not detected in the analysis; thus, it must have

been present in the sub-detection compartments in the bulk of the ice matrix. Based on the current study, we suggest that the amount of missing brine can be located in the veins. A similar conclusion was drawn in one of the first attempts to quantify the amount of air in ice, with the success not exceeding 50 %–66 %: there remained 33 %–50% of air deemed to form bubbles too small to be discernible with the magnification of 160 times (Carte, 1961).

The present study suggests that the remaining solute is likely to be found in not only the puddles of the highly concentrated solution but also the veins or grain boundary grooves threading the crystals. The problem of the varying behavior of the surface brine puddles as opposed to the brine in the ice grain grooves should be examined in more detail. The difference in the dynamics of these two environments (Fig. 6) suggests the possibility of physically and/or chemically distinct behaviors; however, comprehensive research in the given respect is yet to be conducted.

Relevance to impurity locations anticipated in previous laboratory experiments

The observed strong dependence of the ice microstructure on the freezing method suggests that inferring the locations of impurities exclusively from the way the sample was prepared is not straightforward; subtle details, such as the particular sample geometry and material properties of its cover, may play a significant role. Although we found satisfactory reproducibility of the freezing methods, variability was noticed within our research and other investigations in cases when the freezing rates had not been precisely controlled (Malley et al., 2018). Certain variance of values should always be supposed, even when the cooling protocol is kept unaltered as the freezing remains stochastic (Vetráková et al., 2017; Krausková et al., 2016; Heger et al., 2006; Heger and Klan, 2007). Importantly, a generalizable conclusion can be drawn from our current observations: for instances where the freezing occurs from the surface inwards, the impurities are to be expected inside the ice matrix, whereas when the process starts from the cooled pad, brine expulsion to the ice surface is likely to materialize. This justified and expectable result should be applied to review the experiments in which the impurities' locations were inferred merely based on the freezing procedure.

Thus, we can also assume, exploiting current and previous observations (Krausko et al., 2014; Blackford et al., 2007), that the impurities will be contained primarily inside ice spheres prepared by solution nebulization into LN. Experimental procedures essentially identical to our method for the preparation of the spheres were described by Kurkova et al. (2011); however, these authors proposed that the impurities prevail on the outer surfaces of the ice spheres in the ice–air interface. The difference between the present study and the approach adopted by Kurkova et

al. (2011) lies in that salt solutions are used in our case, whereas Kurkova et al. (2011) applied dilute organic compound solutions (with $CuCl_2$ in some instances). We acknowledge that utilizing inorganic salts as a proxy for organic compounds is only partly descriptive, but we assume that the compounds, inorganic or organic, experience similar positions. It is interesting to notice that ice spheres prepared from a solution of 1,1-diphenylethylene allowed complete conversion when exposed to ozone at 188K but did not facilitate the same conversion at 268K (Ray et al., 2013); the lower temperatures possibly enabled the ozone to enter the inside of the ice spheres, this being an ability restricted by higher temperatures. All our numerous attempts to visualize low concentrations of organic compounds ended unsuccessfully, as we had not observed significant differences from frozen pure water (data not shown).

In the present paper, we propose evidence for structural differences between the surface (Figs. 2–7) and the interior of the investigated ice samples (Fig. 9). In the ice broken via mechanical impact, we cannot bring any evidence for the supposed cleavage “along defected sites such as veins and pockets” (Kahan et al., 2010). From Fig. 9 we can infer that the sample disintegrated perpendicularly to the lamellae. Certainly, after cutting the ice, some amount of impurities will surface; however, our current observations indicate that most of the compounds still remain inside the ice interior. No flowing out of the brine was observed at -25 °C, even though the sample had slowly sublimated. Therefore, it seems unlikely that by crushing the original ice cubes the organic impurities from the interior of the ice matrix could ascend to the ice–air interface in an appreciable quantity, as was suggested by Kahan et al. (2010); such a process would probably not occur unless the sample were exposed to increased temperatures for a prolonged time or strong sublimation. Structurally, it can be proposed that even though the impurities frozen out of the solution may slightly rearrange after the ice was crushed, they will not be present in the quasi-liquid layer but in the grooves around the ice crystals. In our opinion, the faster disappearance in the experiments by Kahan et al. (2010) of the anthracene fluorescence signal in crushed ice as compared to ice cubes might be explained instead by specific optical properties of crushed ice (McFall and Anastasio, 2016).

Conclusions

We documented high sensitivity of the brine-ice topology towards freezing procedures. The experimental setup of our ESEM allowed us to image the brine puddles together with ice grain grooves and free ice surfaces for a wide range of CsCl concentrations and various freezing methods previously applied in the laboratory examination of ice. The ice grain sizes and the brine surface coverage

were found to be determined by not only the initial solution concentration but, crucially, also by the freezing method and the thermal history of the sample. The freezing method also influenced the sizes and distribution of the air bubbles, which tend to collocate with the brine. Therefore, the thermodynamic state of the sample (the temperature and impurities' concentrations) is not the sole factor for determining the shape of the frozen water: The freezing rate and directionality play a critical role in the brine distribution and will thus influence the transport properties within sea ice, including the thermal conductivity and permeability. The presented micrographs clarified the possible porosity and pore microstructure of salty ice. Strong hysteresis, resulting in the brine accumulating on the ice surface, was found during the warming–cooling cycle. The rheology of ice is strongly related to the freezing rates; in our experiments, these were directly measured or inferred from the spacing of the lamellae in the ice samples' interior, with the latter of these approaches being applied in cases of morphological instability. The interior of the in-capsule, LN-frozen ice samples exhibited regularly spaced layers of ice and brine and did not reconstruct during the observation. Besides the static snapshots, we were able to document the ice sublimation and recrystallization dynamics. During the latter, the surface humps retarded the ice grain boundary migration. The recognition of the impurities' locations within frozen samples should help to reinterpret previous assumptions and to rationalize the observed behavior for laboratory experiments, all with the goal of describing the complex interactions in natural ice. The obtained knowledge can also serve as an input for physical and chemical models.

Acknowledgements

The research was supported by Czech Science Foundation (19-08239S). We thank Jiří Hudec for helping us with the thermal camera measurements and Vojtěch Svak for providing his know-how as regards the high-speed camera operation. We also thank the reviewers for constructive suggestions that improved the quality of the paper.

References

Adda-Bedia, M., Kumar, S., Lechenault, F., Moulinet, S., Schillaci, M., and Vella, D.: Inverse Leidenfrost Effect: Levitating Drops on Liquid Nitrogen, Langmuir, 32, 4179–4188, https://doi.org/10.1021/acs.langmuir.6b00574, 2016.

Anderson, D. L. and Weeks, W. F.: A theoretical analysis of seaice strength, Eos, Trans. Am. Geophys. Union, 39, 632–640, https://doi.org/10.1029/TR039i004p00632, 1958.

Barnes, P. R. F., Mulvaney, R., Wolff, E. W., and Robinson, K.: A technique for the examination of polar ice using the scanning electron microscope, J. Micros.-Oxford, 205, 118–124, https://doi.org/10.1046/j.0022-2720.2001.00981.x, 2002.

Barnes, P. R. F., Wolff, E. W., Mallard, D. C., and Mader, H. M.: SEM studies of the morphology and chemistry of polar ice, Micros. Res. Tech., 62, 62–69, https://doi.org/10.1002/jemt.10385, 2003.

Bartels-Rausch, T., Wren, S. N., Schreiber, S., Riche, F., Schneebeli, M., and Ammann, M.: Diffusion of volatile organics through porous snow: impact of surface adsorption and grain boundaries, Atmos. Chem. Phys., 13, 6727–6739, https://doi.org/10.5194/acp-13-6727-2013, 2013.

Bartels-Rausch, T., Jacobi, H.-W., Kahan, T. F., Thomas, J. L., Thomson, E. S., Abbatt, J. P. D., Ammann, M., Blackford, J. R., Bluhm, H., Boxe, C., Domine, F., Frey, M. M., Gladich, I., Guzmán, M. I., Heger, D., Huthwelker, Th., Klán, P., Kuhs,W. F., Kuo, M. H., Maus, S., Moussa, S. G., McNeill, V. F., Newberg, J. T., Pettersson, J. B. C., Roeselová, M., and Sodeau, J. R.: A review of air-ice chemical and physical interactions (AICI): liquids, quasi-liquids, and solids in snow, Atmos. Chem. Phys., 14, 1587–1633, https://doi.org/10.5194/acp-14-1587-2014, 2014.

Beine, H., Anastasio, C., Domine, F., Douglas, T., Barret, M., France, J., King, M., Hall, S., and Ullmann, K.: Soluble chromophores in marine snow, seawater, sea ice and frost flowers near Barrow, Alaska, J. Geophys. Res., 117, D00R15, https://doi.org/10.1029/2011jd016650, 2012.

Blackford, J. R.: Sintering and microstructure of ice: a review, J. Phys. D Appl. Phys., 40, R355–R385, https://doi.org/10.1088/0022-3727/40/21/r02, 2007.

Blackford, J. R., Jeffree, C. E., Noake, D. F. J., and Marmo, B. A.: Microstructural evolution in sintered ice particles containing NaCl observed by low-temperature scanning electron microscope, P. Inst. Mechan. Eng. Part L, 221, 151–156, https://doi.org/10.1243/14644207jmda134, 2007.

Bogdan, A. and Molina, M. J.: Physical Chemistry of the Freezing Process of Atmospheric Aqueous Drops, The J. Phys. Chem. A, 121, 3109–3116, https://doi.org/10.1021/acs.jpca.7b02571, 2017.

Bogdan, A., Molina, M. J., Tenhu, H., Bertel, E., Bogdan, N., and Loerting, T.: Visualization of Freezing Process in situ upon Cooling and Warming of Aqueous Solutions, Sci. Rep., 4, 7414, https://doi.org/10.1038/srep07414, 2014.

Bonner, O. D. and Cerutti, P. J.: The partial molar heat capacities of some solutes in water and deuterium oxide, The J. Chem. Thermodynam., 8, 105–112, https://doi.org/10.1016/0021- 9614(76)90082-3, 1976.

Brady, J. B.: MAGMA IN A BEAKER: ANALOG EXPERIMENTS WITH WATER AND VARIOUS SALTS OR SUGAR FOR TEACHING IGNEOUS PETROLOGY, Can. Mineral., 47, 457–471, https://doi.org/10.3749/canmin.47.2.457, 2009.

Braslavsky, I.: 15. Control of ice formation in biological samples, Cryobiology, 71, 168, https://doi.org/10.1016/j.cryobiol.2015.05.021, 2015.

Cao, E., Chen, Y., Cui, Z., and Foster, P. R.: Effect of freezing and thawing rates on denaturation of proteins in aqueous solutions, Biotechnol. Bioeng., 82, 684–690, https://doi.org/10.1002/bit.10612, 2003.

Carns, R. C., Light, B., and Warren, S. G.: The spectral albedo of sea ice and salt crusts on the tropical ocean of Snowball Earth: II. Optical modeling, J. Geophys. Res.-Oceans, 121, 5217–5230, https://doi.org/10.1002/2016jc011804, 2016.

Carte, A. E.: Air Bubbles in Ice, P. Phys. Soc. London, 77, 757–768, https://doi.org/10.1088/0370-1328/77/3/327, 1961.

Chen, N. J., Morikawa, J., Kishi, A., and Hashimoto, T.: Thermal diffusivity of eutectic of alkali chloride and ice in the freezing– thawing process by temperature wave analysis, Thermochim. Acta, 429, 73–79, https://doi.org/10.1016/j.tca.2004.11.010, 2005.

Chen, S. and Baker, I.: Observations of the morphology and sublimation-induced changes in uncoated snow using scanning electron microscopy, Hydrol. Process., 24, 2041–2044, https://doi.org/10.1002/hyp.7689, 2010.

Chen, X., Shu, J., and Chen, Q.: Abnormal gas-liquid-solid phase transition behaviour of water observed with in situ environmental SEM, Sci. Rep., 7, 46680, https://doi.org/10.1038/srep46680, 2017.

Cheng, J., Soetjipto, C., Hoffmann, M. R., and Colussi, A. J.: Confocal Fluorescence Microscopy of the Morphology and Composition of Interstitial Fluids in Freezing Electrolyte Solutions, J. Phys. Chem. Lett., 1, 374–378, https://doi.org/10.1021/jz9000888, 2010.

Cohen-Adad, R.: Caesium Chloride, in: Alkali Metal and Ammonium Chlorides in Water and Heavy Water (Binary Systems), Pergamon, Amsterdam, 375–412, 1991.

Cullen, D. and Baker, I.: Observation of impurities in ice, Micros. Res. Tech., 55, 198–207, https://doi.org/10.1002/jemt.10000, 2001.

Danilatos, G. D.: Introduction to the ESEM Instrument, Micros. Res. Tech., 25, 354–361, https://doi.org/10.1002/jemt.1070250503, 1993.

Dash, J. G., Rempel, A. W., and Wettlaufer, J. S.: The physics of premelted ice and its geophysical consequences, Rev. Modern Phys., 78, 695–741, https://doi.org/10.1103/RevModPhys.78.695, 2006.

Domine, F., Bock, J., Voisin, D., and Donaldson, D. J.: Can We Model Snow Photochemistry? Problems with the Current Approaches, J. Phys. Chem. A, 117, 4733–4749, https://doi.org/10.1021/jp3123314, 2013.

Dong, J. P., Hubel, A., Bischof, J. C., and Aksan, A.: Freezing- Induced Phase Separation and Spatial Microheterogeneity in Protein Solutions, J. Phys. Chem. B, 113, 10081–10087, https://doi.org/10.1021/jp809710d, 2009.

Douglas, T. A., Domine, F., Barret, M., Anastasio, C., Beine, H. J., Bottenheim, J., Grannas, A., Houdier, S., Netcheva, S., Rowland, G., Staebler, R., and Steffen, A.: Frost flowers growing in the Arctic ocean-atmosphere–sea ice–snow interface: 1. Chemical composition, J. Geophys. Res., 117, D00R09, https://doi.org/10.1029/2011jd016460, 2012.

Dubois, M., Royer, J. J., Weisbrod, A., and Shtuka, A.: Recostruction of Low-temperature Binary Phase Diagrams Using a Constrained Least Squares Method – Application to the H2O CsCl System, Eur. J. Mineral., 5, 1145–1152, 1993.

Eichler, J., Kleitz, I., Bayer-Giraldi, M., Jansen, D., Kipfstuhl, S., Shigeyama,W.,Weikusat, C., andWeikusat, I.: Location and distribution of micro-inclusions in the EDML and NEEM ice cores using optical microscopy and in situ Raman spectroscopy, The Cryosphere, 11, 1075–1090, https://doi.org/10.5194/tc-11-1075- 2017, 2017.

Fujiwara, S. and Nishimoto, Y.: Nonbiological Complete Differentiation of the Enantiomeric Isomers of Amino Acids and Sugars by the Complexes of Gases with the Eutectic Compounds of Alkali Chlorides and Water, Anal. Sci., 14, 507–514, https://doi.org/10.2116/analsci.14.507, 1998.

Gao, D., Li, D., and Li, W.: Solubility of RbCl and CsCl in pure water at subzero temperatures, heat capacity of RbCl(aq) and CsCl(aq) at T = 298.15 K, and thermodynamic modeling of RbClCH2O and CsCl + H_2O systems, The J. Chem. Thermodynam., 104, 201–211, https://doi.org/10.1016/j.jct.2016.09.031, 2017.

Gleick, P. H.: Water in Crisis. A Guide to the World's Fresh Water Resources, Oxford University Press, 1993. Goldsack, D. E. and Franchetto, R.: Viscosity of Concentrated Electrolyte Solutions. 1. Concentration Dependence at Fixed Temperature, Can. J. Chem.-Rev. Can. Chim., 55, 1062–1072, https://doi.org/10.1139/v77-148, 1977.

Harrison, J. D.: Measurement of Brine Droplet Migration in Ice, J. Appl. Phys., 36, 3811–3815, https://doi.org/10.1063/1.1713953, 1965.

Heger, D. and Klan, P.: Interactions of organic molecules at grain boundaries in ice: A solvatochromic analysis, J. Photochem. Photobiol. A-Chem., 187, 275–284, https://doi.org/10.1016/j.jphotochem.2006.10.012, 2007.

Heger, D., Jirkovsky, J., and Klan, P.: Aggregation of methylene blue in frozen aqueous solutions studied by absorption spectroscopy, J. Phys. Chem. A, 109, 6702–6709, https://doi.org/10.1021/jp050439j, 2005.

Heger, D., Klanova, J., and Klan, P.: Enhanced protonation of cresol red in acidic aqueous solutions caused by freezing, J. Phys. Chem. B, 110, 1277–1287, https://doi.org/10.1021/jp0553683, 2006.

Heger, D., Nachtigallova, D., Surman, F., Krausko, J., Magyarova, B., Brumovsky, M., Rubes, M., Gladich, I., and Klan, P.: Self-Organization of 1-Methylnaphthalene on the Surface of Artificial Snow Grains: A Combined Experimental-Computational Approach, J. Phys. Chem. A, 115, 11412–11422, https://doi.org/10.1021/jp205627a, 2011.

Hobbs, P. V.: Ice Physics, OUP Oxford, ISBN 9780199587711, 2010.

Hullar, T. and Anastasio, C.: Direct visualization of solute locations in laboratory ice samples, The Cryosphere, 10, 2057–2068, https://doi.org/10.5194/tc-10-2057-2016, 2016

Hullar, T., Magadia, D., and Anastasio, C.: Photodegradation Rate Constants for Anthracene and Pyrene Are Similar in/on Ice and in Aqueous Solution, Environ. Sci. Technol., 52, 12225–12234, https://doi.org/10.1021/acs.est.8b02350, 2018.

Imrichova, K., Vesely, L., Gasser, T. M., Loerting, T., Nedela, V., and Heger, D.: Vitrification and increase of basicity in between ice Ih crystals in rapidly frozen dilute NaCl aqueous solutions, J. Chem. Phys., 151, 014503, https://doi.org/10.1063/1.5100852, 2019.

Jameel, F.: Formulation and process development strategies for manufacturing biopharmaceuticals, edited by: Hershenson, S., John Wiley & Sons, 2010.

Kahan, T. F., Zhao, R., Jumaa, K. B., and Donaldson, D. J.: Anthracene Photolysis in Aqueous Solution and Ice: Photon Flux Dependence and Comparison of Kinetics in Bulk Ice and at the Air-Ice Interface, Environ. Sci. Technol., 44, 1302–1306, https://doi.org/10.1021/es9031612, 2010.

Kania, R., Malongwe, J. K. E., Nachtigallová, D., Krausko, J., Gladich, I., Roeselová, M., Heger, D., and Klán, P.: Spectroscopic Properties of Benzene at the Air–Ice Interface: A Combined Experimental–Computational Approach, The J. Phys. Chem. A, 118, 7535–7547, https://doi.org/10.1021/jp501094n, 2014.

Kasper, J. C. and Friess, W.: The freezing step in lyophilization: Physico-chemical fundamentals, freezing methods and consequences on process performance and quality attributes of biopharmaceuticals, Eur. J. Pharma. Biopharma., 78, 248–263, https://doi.org/10.1016/j.ejpb.2011.03.010, 2011.

Ketcham, W. M. and Hobbs, P. V.: Step Growth on Ice During Freezing of Pure Water, Philos. Magazine, 18, 659–661, https://doi.org/10.1080/14786436808227468, 1968.

Klanova, J., Klan, P., Heger, D., and Holoubek, I.: Comparison of the effects of UV, H2O2=UV and gamma- irradiation processes on frozen and liquid water solutions of monochlorophenols, Photochem. Photobiol. Sci., 2, 1023–1031, https://doi.org/10.1039/b303483f, 2003.

Knipping, E. M., Lakin, M. J., Foster, K. L., Jungwirth, P., Tobias, D. J., Gerber, R. B., Dabdub, D., and Finlayson-Pitts, B. J.: Experiments and Simulations of Ion-Enhanced Interfacial Chemistry on Aqueous NaCl Aerosols, Science, 288, 301–306, https://doi.org/10.1126/science.288.5464.301, 2000.

Krausko, J., Runštuk, J., Neděla, V., Klán, P., and Heger, D.: Observation of a Brine Layer on an Ice Surface with an Environmental Scanning Electron Microscope at Higher Pressures and Temperatures, Langmuir, 30, 5441–5447, https://doi.org/10.1021/la500334e, 2014.

Krausko, J., Malongwe, J. K. E., Bièanová, G., Klán, P., Nachtigallová, D., and Heger, D.: Spectroscopic Properties of Naphthalene on the Surface of Ice Grains Revisited: A Combined Experimental–Computational Approach, The J. Phys. Chem. A, 119, 8565–8578, https://doi.org/10.1021/acs.jpca.5b00941, 2015a.

Krausko, J., Ondrušková, G., and Heger, D.: Comment on “Photolysis of Polycyclic Aromatic Hydrocarbons on Water and Ice Surfaces” and on “Nonchromophoric Organic Matter Suppresses Polycyclic Aromatic Hydrocarbon Photolysis in Ice and at Ice Surfaces”, The J. Phys. Chem. A, 119, 10761–10763, https://doi.org/10.1021/acs.jpca.5b08276, 2015b.

Krausková, L’., Procházková, J., Klašková, M., Filipová, L., Chaloupková, R., Malý, S., Damborský, J., and Heger, D.: Suppression of protein inactivation during freezing by minimizing pH changes using ionic cryoprotectants, Int. J. Pharma., 509, 41– 49, https://doi.org/10.1016/j.ijpharm.2016.05.031, 2016.

Kurkova, R., Ray, D., Nachtigallova, D., and Klan, P.: Chemistry of Small Organic Molecules on Snow Grains: The Applicability of Artificial Snow for Environmental Studies, Environ. Sci. Technol., 45, 3430–3436, https://doi.org/10.1021/es104095g, 2011.

Labadia, C. F. and Buttle, J. M.: Road salt accumulation in highway snow banks and transport through the unsaturated zone of the Oak Ridges Moraine, southern Ontario, Hydrol. Process., 10, 1575–1589, https://doi.org/10.1002/(sici)1099-1085(199612)10:12<1575::aid-hyp502>3.0.co;2-1, 1996.

Lake, R. A. and Lewis, E. L.: Salt rejection by sea ice during growth, J. Geophys. Res., 75, 583–597, https://doi.org/10.1029/JC075i003p00583, 1970.

Light, B., Maykut, G. A., and Grenfell, T. C.: Effects of temperature on the microstructure of first-year Arctic sea ice, J. Geophys. Res.-Oceans, 108, 33/31–33/16, https://doi.org/10.1029/2001jc000887, 2003.

Light, B., Brandt, R. E., and Warren, S. G.: Hydrohalite in cold sea ice: Laboratory observations of single crystals, surface accumulations, and migration rates under a temperature gradient, with application to “Snowball Earth”, J. Geophys. Res., 114, C07018, https://doi.org/10.1029/2008jc005211, 2009.

Light, B., Carns, R. C., and Warren, S. G.: The spectral albedo of sea ice and salt crusts on the tropical ocean of Snowball Earth: 1. Laboratory measurements, J. Geophys. Res.-Oceans, 121, 4966– 4979, https://doi.org/10.1002/2016jc011803, 2016.

Losert, W., Shi, B. Q., and Cummins, H. Z.: Evolution of dendritic patterns during alloy solidification: Onset of the initial-instability, P. Natl. Acad. Sci. USA, 95, 431–438, https://doi.org/10.1073/pnas.95.2.431, 1998.

Macklin,W. C. and Ryan, B. F.: Habits of Ice Grown in Supercooled Water and Aqueous Solutions, Philos. Magazine, 14, 847–860, https://doi.org/10.1080/14786436608211977, 1966.

Maeda, N., Israelachvili, J. N., and Kohonen, M. M.: Evaporation and instabilities of microscopic capillary bridges, P. Natl. Acad. Sci. USA, 100, 803–808, https://doi.org/10.1073/pnas.0234283100, 2003.

Magee, N. B., Miller, A., Amaral, M., and Cumiskey, A.: Mesoscopic surface roughness of ice crystals pervasive across a wide range of ice crystal conditions, Atmos. Chem. Phys., 14, 12357– 12371, https://doi.org/10.5194/acp-14-12357-2014, 2014.

Malley, P. P. A., Chakraborty, S., and Kahan, T. F.: Physical Characterization of Frozen Saltwater Solutions Using Raman Microscopy, ACS Earth Space Chem., 2, 702–710, https://doi.org/10.1021/acsearthspacechem.8b00045, 2018.

Massom, R. A., Eicken, H., Hass, C., Jeffries, M. O., Drinkwater, M. R., Sturm, M., Worby, A. P., Wu, X., Lytle, V. I., Ushio, S., Morris, K., Reid, P. A., Warren, S. G., and Allison, I.: Snow on Antarctic sea ice, Rev. Geophys., 39, 413–445, https://doi.org/10.1029/2000rg000085, 2001.

Maus, S.: Prediction of the cellular microstructure of sea ice by morphological stability theory, Physics and Chemistry of Ice, edited by: Kuhs, W. F., 371–382 pp., 2007.

Maus, S.: Interactive comment on The Cryosphere Discuss., The Cryosphere Discuss., https://doi.org/10.5194/tc-2019-13, 2019.

McCarthy, C., Blackford, J. R., and Jeffree, C. E.: Lowtemperature- SEM study of dihedral angles in the ice-I/sulfuric acid partially molten system, J. Micros., 249, 150–157, https://doi.org/10.1111/jmi.12003, 2013.

McFall, A. S. and Anastasio, C.: Photon flux dependence on solute environment in water ices, Environ. Chem., 13, 682, https://doi.org/10.1071/en15199, 2016.

Monnin, C. and Dubois, M.: Thermodynamics of the CsCl-H2O system at low temperatures, Eur. J. Mineral., 11, 477–482, 1999.

Nagashima, K. and Furukawa, Y.: Solute Distribution in front of an Ice/Water Interface during Directional Growth of Ice Crystals and Its Relationship to Interfacial Patterns, The J. Phys. Chem. B, 101, 6174–6176, https://doi.org/10.1021/jp963172k, 1997.

Nair, M., Husmann, A., Cameron, R. E., and Best, S. M.: In situ ESEM imaging of the vapor-pressure-dependent sublimationinduced morphology of ice, Phys. Rev. Materials, 2, 040401(R), https://doi.org/10.1103/PhysRevMaterials.2.040401, 2018.

Nakai, T., Sawamura, S., and Taniguchi, Y.: Effect of pressure on the viscosity of aqueous cesium-chloride solution at 25 _C, J. Molec. Liqu., 65–6, 365–368, https://doi.org/10.1016/0167- 7322(95)00832-4, 1995.

Nedela, V.: Methods for additive hydration allowing observation of fully hydrated state of wet samples in environmental SEM, Micros. Res. Tech., 70, 95–100, https://doi.org/10.1002/jemt.20390, 2007.

Nedela, V., Tihlarikova, E., Runstuk, J., and Hudec, J.: Highefficiency detector of secondary and backscattered electrons for low-dose imaging in the ESEM, Ultramicroscopy, 184, 1–11, https://doi.org/10.1016/j.ultramic.2017.08.003, 2018.

Neděla, V., Konvalina, I., Oral, M., and Hudec, J.: The Simulation of Energy Distribution of Electrons Detected by Segmental Ionization Detector in High Pressure Conditions of ESEM, Micros. Microanal., 21, 264–269, https://doi.org/10.1017/S1431927615013483, 2015.

Notz, D. and Worster, M. G.: Desalination processes of sea ice revisited, J. Geophys. Res., 114, C05006, https://doi.org/10.1029/2008jc004885, 2009.

Nye, J. F.: The rotting of temperate ice, J. Cryst. Growth, 113, 465– 476, https://doi.org/10.1016/0022-0248(91)90081-F, 1991.

Ohno, H., Igarashi, M., and Hondoh, T.: Salt inclusions in polar ice core: Location and chemical form of watersoluble impurities, Earth Planet. Sci. Lett., 232, 171–178, https://doi.org/10.1016/j.epsl.2005.01.001, 2005.

Ohno, H., Igarashi, M., and Hondoh, T.: Characteristics of salt inclusions in polar ice from Dome Fuji, East Antarctica, Geophys. Res. Lett., 33, L08501, https://doi.org/10.1029/2006gl025774, 2006.

Ondrušková, G., Krausko, J., Stern, J. N., Hauptmann, A., Loerting, T., and Heger, D.: Distinct Speciation of Naphthalene Vapor Deposited on Ice Surfaces at 253 or 77 K: Formation of Submicrometer-Sized Crystals or an Amorphous Layer, The J. Phys. Chem. C, 122, 11945–11953, https://doi.org/10.1021/acs.jpcc.8b03972, 2018.

Perrier, S., Houdier, S., Domine, F., Cabanes, A., Legagneux, L., Sumner, A. L., and Shepson, P. B.: Formaldehyde in Arctic snow. Incorporation into ice particles and evolution in the snowpack, Atmos. Environ., 36, 2695–2705, 2002.

Petrenko, V. F. and Whitworth, R. W.: Physics of ice, Oxford University Press, Oxford, 1999. Pinzer, B. R. and Schneebeli, M.: Snow metamorphism under alternating temperature gradients: Morphology and recrystallization in surface snow, Geophys. Res. Lett., 36, L23503, https://doi.org/10.1029/2009gl039618, 2009.

Ram, K. and Anastasio, C.: Photochemistry of phenanthrene, pyrene, and fluoranthene in ice and snow, Atmos. Environ., 43, 2252–2259, https://doi.org/10.1016/j.atmosenv.2009.01.044, 2009.

Ray, D., Malongwe, J. K. E., and Klán, P.: Rate Acceleration of the Heterogeneous Reaction of Ozone with a Model Alkene at the Air–Ice Interface at Low Temperatures, Environ. Sci. Technol., 47, 6773–6780, https://doi.org/10.1021/es304812t, 2013.

Reiser, S., Horsch, M., and Hasse, H.: Temperature Dependence of the Density of Aqueous Alkali Halide Salt Solutions by Experiment and Molecular Simulation, J. Chem. Eng. Data, 59, 3434– 3448, https://doi.org/10.1021/je500420g, 2014.

Roessl, U., Leitgeb, S., and Nidetzky, B.: Protein freeze concentration and micro-segregation analysed in a temperaturecontrolled freeze container, Biotechnol. Rep., 6, 108–111, https://doi.org/10.1016/j.btre.2015.03.004, 2015.

Rohatgi, P. K. and Adams, C. M.: Ice–Brine Dendritic Aggregate formed on Freezing of Aqueous Solutions, J. Glaciol., 6, 663– 679, https://doi.org/10.1017/s0022143000019936, 1967.

Rohatgi, P. K., Jain, S. M., and Adams, C. M.: Effect of Magnetic and Electrical Fields on Dendritic Freezing of Aqeous Sulutions of Sodium Chloride Materials, Sci. Eng., 15, 283–290, https://doi.org/10.1016/0025-5416(74)90062-7, 1974.

Rosenthal, W., Saleta, J., and Dozier, J.: Scanning electron microscopy of impurity structures in snow, Cold Reg. Sci. Technol., 47, 80–89, https://doi.org/10.1016/j.coldregions.2006.08.006, 2007.

Salnikova, M., Varshney, D., and Shalaev, E.: Heterogeneity of Protein Environments in Frozen Solutions and in the Dried State, in: Lyophilized Biologics and Vaccines, edited by: Varshney, D. and Singh, M., Springer, New York, NY, 2015.

Shaw, R. A., Durant, A. J., and Mi, Y.: Heterogeneous Surface Crystallization Observed in Undercooled Water, The J. Phys. Chem. B, 109, 9865–9868, https://doi.org/10.1021/jp0506336, 2005.

Shokr, M. and Sinha, N.: Sea Ice: Physics and Remote Sensing, edited by: Mongraph, G., John Wiley and Sons, 600 pp., 2015.

Steinbach, F., Kuiper, E.-J. N., Eichler, J., Bons, P. D., Drury, M. R., Griera, A., Pennock, G. M., and Weikusat, I.: The Relevance of Grain Dissection for Grain Size Reduction in Polar Ice: Insights from Numerical Models and Ice Core Microstructure Analysis, Front. Earth Sci., 5, 66, https://doi.org/10.3389/feart.2017.00066, 2017.

Suzuki, S., Nakajima, A., Yoshida, N., Sakai, M., Hashimoto, A., Kameshima, Y., and Okada, K.: Freezing of water droplets on silicon surfaces coated with various silanes, Chem. Phys. Lett., 445, 37–41, https://doi.org/10.1016/j.cplett.2007.07.066, 2007.

Thibert, E. and Domine, F.: Thermodynamics and kinetics of the solid solution of HCl in ice, J. Phys. Chem. B, 101, 3554–3565, 1997.

Thibert, E. and Domine, F.: Thermodynamics and kinetics of the solid solution of HNO3 in ice, J. Phys. Chem. B, 102, 4432– 4439, 1998.

Thomas, D. N.: Sea Ice, Wiley-Blackwell, Chichester, UK, 2017.

Tihlarikova, E., Nedela, V., and Shiojiri, M.: In situ study of live specimens in an environmental scanning electron microscope, Micros. Microanal., 19, 914–918, https://doi.org/10.1017/S1431927613000603, 2013.

Timco, G.W. and Frederking, R. M.W.: A review of sea ice density, Cold Reg. Sci. Technol., 24, 1–6, https://doi.org/10.1016/0165- 232X(95)00007-X, 1996.

Tokumasu, K., Harada, M., and Okada, T.: X-ray Fluorescence Imaging of Frozen Aqueous NaCl Solutions, Langmuir, 32, 527– 533, https://doi.org/10.1021/acs.langmuir.5b04411, 2016.

Trivedi, R. and Kurz, W.: Solidification microstructures: A conceptual approach, Acta Metallur. Material., 42, 15–23, https://doi.org/10.1016/0956-7151(94)90044-2, 1994.

Vega, C. P., Isaksson, E., Schlosser, E., Divine, D., Martma, T., Mulvaney, R., Eichler, A., and Schwikowski-Gigar, M.: Variability of sea salts in ice and firn cores

from Fimbul Ice Shelf, Dronning Maud Land, Antarctica, The Cryosphere, 12, 1681–1697, https://doi.org/10.5194/tc-12-1681-2018, 2018.

Vetráková, L'., Vykoukal, V., and Heger, D.: Comparing the acidities of aqueous, frozen, and freeze-dried phosphate buffers: Is there a "pH memory" effect?, Int. J. Pharmaceut., 530, 316–325, https://doi.org/10.1016/j.ijpharm.2017.08.005, 2017.

Wåhlin, J., Leisinger, S., and Klein-Paste, A.: The effect of sodium chloride solution on the hardness of compacted snow, Cold Reg. Sci. Technol., 102, 1–7, https://doi.org/10.1016/j.coldregions.2014.02.002, 2014.

Warren, S. G.: Optical properties of ice and snow, Philos. Trans. A Math. Phys. Eng. Sci., 377, 20180161, https://doi.org/10.1098/rsta.2018.0161, 2019.

Weeks, W. F.: On Sea Ice, On Sea Ice, 1–665 pp., 2010.

Wettlaufer, J. S.: Directional solidification of salt water: deep and shallow cells, Europhys. Lett., 19, 337–342, https://doi.org/10.1209/0295-5075/19/4/015, 1992.

Wettlaufer, J. S., Worster, M. G., and Huppert, H. E.: Natural convection during solidification of an alloy from above with application to the evolution of sea ice, J. Fluid Mechan., 344, 291–316, https://doi.org/10.1017/s0022112097006022, 1997.

Wilson, P. W. and Haymet, A. D. J.: Workman-Reynolds freezing potential measurements between ice and dilute salt solutions for single ice crystal faces, J. Phys. Chem. B, 112, 11750–11755, 2008.

Yan, F., Xiong,W., and Faierson, E.: Grain Structure Control of Additively Manufactured Metallic Materials, Materials, 10, 1260, https://doi.org/10.3390/ma10111260, 2017.

Yang, X., Neděla, V., Runštuk, J., Ondrušková, G., Krausko, J., Vetráková, L'., and Heger, D.: Evaporating brine from frost flowers with electron microscopy and implications for atmospheric chemistry and sea-salt aerosol formation, Atmos. Chem. Phys., 17, 6291–6303, https://doi.org/10.5194/acp-17- 6291-2017, 2017.

Zobrist, B., Marcolli, C., Pedernera, D. A., and Koop, T.: Do atmospheric aerosols form glasses?, Atmospheric Chemistry and Physics, 8, 5221–5244, https://doi.org/10.5194/acp-8-5221- 2008, 2008.

29 Conclusion

The first part of the habilitation thesis contains an introduction to the issue of environmental scanning electron microscopy and a description of its current state in the world, including a commented set of citations of author's articles defining his contribution to the field. In the next part of the thesis, a set of twenty-five most important author's articles published in impacted scientific journals is systematically arranged. These articles document the gradual development of his scientific work starting with redesigning and rebuilding of the SEM VEGA from Tescan company leading to the creation of the ESEM AQUASEM II prototype followed by the first results of biological samples research. Subsequently, next articles deals with gas flow simulations to optimize the design of a differentially pumped chamber of ESEM AQUASEM II and the development of the Scintillation SE detector for variable pressure SEM. Articles dealing with the Monte Carlo simulations of the signal electron-gas and electron-sample interactions to understand and optimize the operation of an ionization detector for ESEM are presented as well. The article High-efficiency detector of secondary and backscattered electrons for low-dose imaging in the ESEM, published in the prestigious scientific journal Ultramicroscopy, brings significant results that push the boundaries of ESEM's possibilities in the field of signal electron detection. This paper presents for the first time a highly sensitive backscattered electron scintillation detector for ESEM and especially a combined secondary electron detector containing the new ISEDS, which is currently one of the most sensitive detectors for ESEM in the world. The ISEDS is also the first in the world to enable energy filtration of detected electrons in ESEM. The following series of articles contains unique results of in-situ study of biological samples in dynamically changing conditions of the ESEM specimen chamber. From the point of view of interdisciplinary research in the field of plant biology, the articles presenting the new Low-Temperature method for ESEM and its extended version Extended-Temperature method in the article In-situ preparation of plant samples in ESEM for energy dispersive x-ray microanalysis and repetitive observation in SEM and ESEM are crucial. The above mentioned methods, in combination with ISEDS, enabled for the first time in the world to display highly sensitive rotifers in their native state in ESEM and thus contributed to the discovery of new species of these aquatic organisms. A series of articles focused on the development of a method for imaging highly sensitive PEC capsules and beads culminated in the article named Simulation-based optimization of thermodynamic conditions in the ESEM for a dynamic in-situ study of spherical polyelectrolyte complex particles in their native state, published in the journal Ultramicroscopy. This article pushes the boundaries of ESEM's current possibilities with its breakthrough results in the field of studying

samples of biopolymers and hydrogels. Further articles present the results of dynamic in-situ experiments focused on changes and behaviour of bentonite as a suitable material for use in nuclear waste repositories. The habilitation thesis ends with several articles with a high impact factor in the field of physical and environmental chemistry. The articles deal with the research of morphological changes of ice containing salt impurities in dynamically changing conditions of the ESEM specimen chamber, e.g. during melting, sublimation and temperature cycling. The published results make it possible to understand and explain the important processes associated with the formation of sea ice, its importance as a reaction medium and the release of salts back into the atmosphere in the form of aerosols and reactive halogens depleting the ozone layer.

The habilitation thesis summarizes author's results from many years of research and development of unique methods and instrumentation in the field of environmental scanning electron microscopy. These results broaden the boundaries of possibilities and applicability of ESEM for interdisciplinary and internationally excellent research. The author focused on several areas: 1) development and implementation of prototypes of unique ultrasensitive detectors of signal electrons which, unlike commercially available detectors, are able to image sensitive samples under low energy and very low current of electron beam, hence with minimal radiation damage; 2) development of own Monte Carlo simulation programs to understand the physical processes accompanying signal generation and its amplification in gas for image formation in ESEM, which is crucial for the optimization of the efficiency of our detectors; 3) thermodynamics simulations for accurate setting of optimal conditions (values of gas pressure, temperature and relative humidity) in the proximity to the observed sample to prevent its drying, or for the implementation of advanced in-situ studies of samples in dynamically changing conditions in the ESEM specimen chamber; 4) advanced and dynamical in-situ experiments in defined environmental conditions, which are beyond the capabilities of commercially available electron microscopes. Thanks to the achieved results, new methods, unique instrumentation and advanced modifications of electron microscopes, significant progress has been made not only in environmental scanning electron microscopy, research of wet susceptible biological and polymer samples, but also in many other disciplines.